Thèse n° 9513

Welded moment connections with highly dissipative panel zones for enhanced seismic performance of steel moment frames

Présentée le 29 avril 2022

Faculté de l'environnement naturel, architectural et construit
Laboratoire des structures métalliques résilientes
Programme doctoral en génie civil et environnement

pour l'obtention du grade de Docteur ès Sciences

par

Andronikos SKIADOPOULOS

Acceptée sur proposition du jury

Prof. K. Beyer, présidente du jury
Prof. D. Lignos, directeur de thèse
Prof. M. Engelhardt, rapporteur
Prof. J. Hajjar, rapporteur
Prof. B. Stojadinovic, rapporteur

École
polytechnique
fédérale
de Lausanne

2022

Acknowledgments

This PhD Thesis would not have been possible without the assistance and honest support of many people. As an expression of my deep appreciation and sincere gratitude, this section is dedicated to them.

First and foremost, I would like to sincerely thank my PhD Thesis supervisor, Professor Dimitrios Lignos. Thank you for giving me the opportunity to pursuit my PhD with you. Under your continuously insigful and highly demanding supervision as well as your extensive work quality, I was able to grow as a scientist and as a professional. Thank you for being supportive and attentive at all times. Most importantly, thank you for entrusting me before, during and after my doctoral studies, with the countless hours and effort spent on discussing research matters and for advancing me. Working under your guidance was a pleasure and a true honor.

I am also very greatful to the jury members of this doctoral thesis, Prof. K. Beyer (EPFL), Prof. B. Stojadinovic (ETH-Zürich), Prof. M. Engelhardt (UT Austin) and Prof. J. Hajjar (Northeastern University) for their valuable comments and insightful discussion.

Special credits should be also given to all those who passionately contributed to the experimental program of this doctoral thesis. I would like to thank EPFL and Nippon Steel Corporation (NSC) for financially supporting my research. I sincerely thank M. Arita-san from NSC for his professionalism, the thorough quality of work and insightful discussions. I would also like to thank the rest of the NSC team, including S. Hiroshima-san and the laboratory technicians of the Hasaki Research and Development Center for their hard and top-quality work. I also thank Dr. Y. Suzuki for his contribution to the initial development of this project and for his invaluable comments. Many thanks are also given to the test specimen fabricator company Techno Steel Daishin, the test specimen welder Mr. Kenta Yoshiba and Mr. Shun Ri who conducted the ultrasonic testing. Finally, thanks are given to the technicians of GIS at EPFL and my colleague Selimcan Ozden for contributing in material testing.

I sincerely thank the RESSLab family for making my life more enjoyable in and out of campus and for the countless discussions and assistance in research matters. I thank Prof. Ahmed Elkady (University of Southampton) for his invaluable feedback and (fantastic) support during my first research steps; highly appreciated. I also thank Prof. Alain Nussbaumer and Dr. Albano de Castro e Sousa for their support and very insightful comments on this doctoral thesis. I should express my honest gratitude and admiration to Dr. Hiroyuki Inamasu for all the memorable experiences we share and his invaluable support and contribution on me and my thesis. I sincerely thank Dr. Hammad El-Jisr for all the moments of laugh we share and the countless discussions and help on research issues, as well as Dr. Nenad Bijelic for his motivational and always warm and helpful spirit. I thank Dr. Alexander Hartloper, Dr. Konstantinos Bakalis, Martina Paronesso, Diego Heredia, Selimcan Ozden, Mohamed Abouelkair, Prof. Asai Tatsauya (Nagoya University), Dr. Gabriele Granello, Athina Spinasa, Nitesh Karmacharya, Bikram Oli, Kusum Shrestha, Lucas Mathevet, Colin Vaccari and Dr. Matthew Sjaarda for all the enjoyable moments we share. I thank the RESSLab super-secretary Karin Pasche and ex-secretary Luisa Proietti for always dealing successfully with multidimentional topics and for contributing to a lively work environment. Finally, I would like to thank EPFL Professor Emeritus John Botsis and Dr. Georgios Pappas from ETH-Zürich for their invaluable insights and contribution on fracture-related topics.

My appreciation and gratitude go to the Professors of National Technical University of Athens (NTUA) that supported my pursuit of doctoral studies (Prof. Ch. Gantes, Prof. D. Vamvatsikos, Prof. N. Lagaros). Especially, I thank Prof. Ch. Gantes for initially inspirating me and afterwards supporting and motivating me towards the research direction I followed.

During my PhD studies, I had the pleasure of making some amazing friends with whom I spent unforgettable and relaxing moments. Dr. Pepe Tsili, Fani Stampo, Alex, Bill, Foivo, Angelika, Aspa, Kathrin, Dimitri, thank you all for making my life more pleasant and fulfilling.

Hoping that the reader still follows the acknoledgments section, I would like to express my deepest love for my friends and family. I thank Solon, the mechanical engineering expert. I specially thank Kostis, my NTUA-mate for all the stimulating discussions and great memories, as well as Christos. I would like to express my admiration and gratitude to Serafino, Athi and Athinagoras for their unconditional support and for always inspirating me. I wholeheartedly thank my uncle Kostas Skiadopoulos for being the reason why I followed and embraced the beauty of Civil Engineering and for supporting me throughout the years. I would like to express my greatfulness and unconditional love to Kiriaki for tolerating, encouraging and supporting me (especially during the last couple of months) and for always sharing enjoyable and pleasant memories. Finally, this doctoral thesis is dedicated to my always inspiring and admirable brother George, as well as my father Aris and my mother Maria for their unconditional love and support in all my pursuits and endeavors.

Andronikos Skiadopoulos

Lausanne, April 15, 2022

Abstract

Research conducted after the 1994 Northridge earthquake in the U.S. and the 1995 Kobe earthquake in Japan led to the development of today's pre-qualified beam-to-column connections for capacity-designed steel moment resisting frames (MRFs). Welded moment connections feature weld backing bars that should be removed after the execution of complete joint penetration groove welds at the bottom beam flange-to-column flange joint. On the other hand, advancements in steel and weld materials, as well as fabrication techniques, allow for the exploitation of simplified weld details at this location. In welded moment connections for seismic applications, the participation of the beam-to-column web panel zones in the energy dissipation is generally limited during an earthquake event. In such a design context, beam local buckling is likely even at modest lateral drift demands, thereby engendering structural repair costs in the aftermath of earthquakes. The primary reasons for such a seismic design practice are twofold. The first one relates to known limitations of panel zone design models that compromise our ability to effectively balance the seismic design of fully restrained beam-to-column connections. The second one relates to the panel zone kinking that could increase the fracture potential of beam-to-column connections. However, recent experiments in the literature provide controversial results regarding the same matter.

This doctoral thesis aims at advancing the state-of-knowledge regarding the seismic design and behavior of steel MRFs with highly dissipative panel zones. A new panel zone design model was first developed. This model addresses the limitations of all available panel zone models in the literature. The model was validated thoroughly with about 100 available experiments that encompass a broad range of geometric parameters. The panel zone model can effectively enable a balanced seismic design of welded moment connections with inelastic panel zones. One step further, this thesis revisited the current detailing of welded connections. Simplifications in their fabrication process were proposed by intentionally keeping a customized beveled backing bar in place, without impairing the connection's ductility under cyclic loading. The proposed connection weld detail is substantiated by continuum finite element analyses and full-scale experiments on welded moment connections with highly dissipative panel zones. It is demonstrated that, contrary to the current design paradigm, a stable hysteretic response is achieved up until lateral drift demands of at least 7% rad, thereby diminishing the cyclic deterioration in story shear resistance. As such, the seismic stability of steel MRFs is only governed by global P-Delta effects. Quantitative seismic response characteristics of steel MRFs with highly dissipative panel zones through large-scale systel-level parametric studies were also provided. It is shown that steel MRFs with highly inelastic panel zones, have up to two times lower mean annual frequency of collapse than corresponding results with steel MRFs designed with the current status quo. It is also demonstrated that steel MRFs with inelastic panel zones, enjoy up to 50% reduction in residual story drift ratios at a design-basis earthquake; their beam-to-column connections do not experience fractures due to panel zone kinking; and local buckling in steel beams is very limited even at low probability of occurrence seismic events.

Keywords

Steel moment resisting frames, Panel zones, Panel zone models, Full-scale experiments, Welded beam-to-column connections, Beveled weld backing bars, Seismic stability, Structural repairs, Collapse risk.

Résumé

Les différents études menées après les séismes de Northridge aux Etats-Unis en 1994 et de Kobe au Japon en 1995 ont conduit au développement des liaisons poutre-poteau actuellement utilisées lors du dimensionnement en capacité des cadres métalliques (MRF). Les connections rigides soudés, qui constituent l'objectif principal de cette thèse de doctorat, comportent des plaques d'appuis de soudure qui doivent être retirées après la réalisation d'une soudure à pénétration complète à la jonction entre l'aile inférieure de la poutre et celle de la colonne. D'autre part, les progrès réalisés dans le domaine de l'acier, des matériaux de soudure et des techniques de fabrication permettent aujourd'hui d'exploiter des détails de soudure simplifiés. Lors d'un événement sismique, la quantité d'énergie dissipée par les angles de cadre rigides est généralement limitée. Avec une telle conception, le voilement des poutres est probable même à des déplacements inter-étages modestes, ce qui engendre des coûts de réparation structurelles post-sismique. Deux sont les raisons principales qui justifient une telle pratique en conception parasismique. La première est liée aux limites présentés par les modèles utilisés pour dimensionner les angles de cadre rigides, ce qui nous obligent de les dimensionner élastiquement. La deuxième concerne la grande ampleur des déformations au cisaillement que les angle de cadre peut subir pendant un séisme, ce qui peut causer une augmentation du potentiel de fracture des assemblages poutre-poteau. Cependant, des études conduits récemment fournissent des résultats controversés sur ce même sujet.

Cette thèse de doctorat vise à faire progresser l'état des connaissances concernant la conception et le comportement sismique des MRF en acier avec des angles de cadres à haute énergie de dissipation. Un nouveau modèle de dimensionnement des angles de cadre a d'abord été développé. Ce modèle aborde les limites des modèles d'angles de cadre disponibles dans la littérature. Le modèle a été validé de manière approfondie en utilisant environ 100 tests expérimentaux qui englobent un large éventail de paramètres géométriques. Le modèle d'angle de cadre proposé permet de dimensionner les connexions rigides soudées poutre-poteau en considérant un angle de cadre inélastique. De plus, cette thèse a aussi revisité les détails actuels des assemblages soudés. Des simplifications liés à leur fabrication ont été proposées en gardant intentionnellement en place une plaque d'appui biseautée personnalisée, sans altérer la ductilité de la connexion sous chargement cyclique. Le détail de soudure proposé est étayé par des analyses aux éléments finis et des essais à grande échelle sur des connexions poutre-poteau rigides soudées avec des angles de cadres à haute énergie de dissipation. Il est démontré que, contrairement à la conception actuelle, une réponse hystérétique stable est obtenue jusqu'à des déplacement inter-étage d'au moins 7 % rad, diminuant ainsi la détérioration cyclique de la résistance au cisaillement de l'étage. Ainsi, la stabilité sismique des MRF en acier n'est gouvernée que par les effets P-Delta globaux. Grâce à des études paramétriques, la thèse de doctorat a également fourni des caractéristiques quantitatives de la réponse sismique des MRF en acier avec des angles de cadre à haute énergie de dissipation. Il est démontré que les MRF en acier composé d’angles de cadres à haute énergie de dissipation ont une fréquence annuelle moyenne d'effondrement jusqu'à deux fois inférieure par rapport aux résultats obtenu avec des MRF en acier conçus selon les approches courantes. Il est également démontré que les MRF en acier avec des angles de cadre inélastiques bénéficient d'une réduction allant jusqu'à 50 % des déplacements inter-étage relatifs résiduels lors d'un tremblement de terre de référence ; leurs assemblages poutre-poteau ne subissent pas de fractures dues à de grandes déformations de cisaillement des angles de cadre ; et le voilement des poutres en acier est très limité même à des événements sismiques à faible probabilité d'occurrence.

Mots-clés

Cadre rigide en acier, Angle de cadre, Modèle d’angle de cadre, Essais à grande échelle, Connexions soudées poutre-poteau, Plaque d’appuis de soudure, Stabilité sous charge sismique, Réparations structurelles, Probabilité d'effondrement.

Contents

Acknowledgments .... **v**
Abstract .... **vii**
Keywords .... **viii**
Résumé .... **ix**
Mots-clés .... **x**
List of Figures .... **xv**
List of Tables .... **xxiii**
Chapter 1 Introduction **25**
1.1 Research background 25
1.2 Problem statement and research objectives 31
1.3 Thesis outline 32
Chapter 2 Development of inelastic panel zone database **35**
2.1 Introduction 36
2.2 Assembled database description 38
2.2.1 Beam/column material and geometric characteristics 41
2.2.2 Panel zone material and geometric characteristics 43
2.2.3 Digitized data 44
2.2.4 Decomposed deformation quantities 45
2.2.5 Predicted panel zone resistance and demand 46
2.2.6 Measured panel zone model quantities 48
2.3 Maximum attained lateral drift demands prior to connection fracture 49
2.4 Assessment of commonly used panel zone design models 50
2.5 Balanced design aspects 52
2.6 High-fidelity continuum finite-element model validations 54
2.7 Summary and conclusions 56
Chapter 3 Proposed panel zone model for seismic design of steel moment-resisting frames **59**
3.1 Introduction 60
3.2 Mechanics of panel zone behavior through CFE analysis 65
3.2.1 Description and validation of CFE modeling approach 65
3.2.2 Deduced panel zone performance parameters 67

3.3 Discussion 68

3.4 Proposed panel zone model 69

3.4.1 Panel zone elastic stiffness 69

3.4.2 Panel zone shear strength 71

3.4.3 Proposed panel zone model validation 75

3.5 Effect of doubler plates 76

3.6 Effect of axial load 79

3.6.1 Interior columns 80

3.6.2 End columns 81

3.7 Limitations of the present study 82

3.8 Summary and conclusions 82

3.9 Dedication 83

Chapter 4 Proposed backing bar detail in welded beam-to-column connections for seismic applications 85

4.1 Introduction 86

4.2 Methodology 89

4.3 Employed fracture mechanics methods, primary assumptions and sensitivity analyses 90

4.4 Continuum finite element modeling for informing fracture mechanics methods 92

4.5 Overview and scope of fracture analysis 95

4.6 Assessment of pre-Northridge WUF-B connections 96

4.6.1 Effect of fillet weld reinforcement on J-integral demand 99

4.6.2 Effect of axial load on J-integral demand 100

4.7 Assessment of post-Northridge WUF-W connections 101

4.7.1 Effect of panel zone design distortions 103

4.7.2 Beam depth effect 104

4.7.3 Beam flange thickness effect 105

4.7.4 Column flange thickness effect 106

4.7.5 Weld toe size effect 106

4.8 Limitations 106

4.9 Summary and conclusions 107

Chapter 5 Full-scale experiments of cyclically loaded welded moment connections with highly dissipative panel zones and simplified weld details 109

5.1 Introduction 109

5.2 Test objectives and anticipated seismic performance 112

5.3 Overview of the test program 113

5.3.1 Test specimens 113

5.3.2 Specimen fabrication 115

5.3.3 Test apparatus 117

5.3.4 Instrumentation plan and deduced measurements 119

5.3.5 Ancillary tests 121

5.3.6 Applied loading protocols 123

5.4 Experimental results and discussion 124

5.4.1 Qualitative summary of experimental behavior 124

5.4.1.1 Performance of beveled backing bars 133

5.4.1.2 Ultimate failure modes 134

5.4.2 Quantitative assessment of test results 137

5.4.2.1 Prequalification limits 137

5.4.2.2 Decomposition of inelastic deformations and assessment of balanced design 138

5.4.2.3 Twist demands in the column 140

5.4.2.4 Column flange local deformations 141

5.4.2.5 Strain demands at critical locations 143

5.4.3 Effect of loading history and implications on structural collapse and predictive modeling. 144

5.5 Predictive models and implications on collapse safety 145

5.6 Limitations of the present study 147

5.7 Summary and conclusions 148

Chapter 6 Seismic demands of steel moment resisting frames with inelastic beam-to-column web panel zones 151

6.1 Introduction 152

6.2 Proposed modeling approach for beam-to-column connections with inelastic panel zones 154

6.2.1 Behavioral insights 154

6.2.2 Shell element modeling approach 154

6.2.3 Macro-model approach 155

6.2.4 Validation and comparison with system level behavior 156

6.2.5 Modeling of beam flange fracture 157

6.3 Archetype steel buildings 158

6.4 Nonlinear building models 160

6.5 Nonlinear static analysis 161

6.6 Nonlinear response history analysis 163

6.6.1 Collapse risk evaluation 163

6.6.2 Seismic demands at discrete seismic intensities of interest 166

6.6.3 Engineering demand parameter hazard curves 168

6.7 Summary and conclusions 172

Chapter 7 Conclusions and future work 175

7.1 Summary 175

7.2 Conclusions 176

7.2.1 Proposed panel zone model for the seismic design of fully restrained beam-to-column connections ... 176

7.2.2 Hysteretic behavior of welded connections with highly dissipative panel zones and simplified weld details ... 177

7.2.3 Seismic demands of steel moment resisting frames with inelastic beam-to-column web panel zones ... 179

7.3 Recommendations for future research ... 180

Appendix A. Design drawings of test specimens ... 181

Appendix B. Design drawings of the test specimen lateral support system ... 191

Appendix C. Detailed instrumentation plan ... 203

Appendix D. Welding procedure specifications and ultrasonic test results ... 215

D.1 Weld electrode mill certificates ... 216

D.2 Welding procedure specifications ... 218

D.3 Ultrasonic test results ... 239

Appendix E. Material test results ... 243

E.1 Monotonic material test results ... 244

E.2 Cyclic material test results ... 245

E.3 Material test results from measured experimental strain histories ... 250

Appendix F. Detailing requirements and design procedure of the proposed welded connections and summary of experimental results of test specimens ... 253

F.1 Detailing requirements and design procedure of the proposed welded connections ... 254

F.2 Summary of experimental results of Specimen 1 ... 257

F.3 Summary of experimental results of Specimen 2 ... 261

Appendix G. Design summaries of steel moment resisting frames with elastic and dissipative panel zones ... 265

References ... 281

Curriculum Vitae ... 295

List of Figures

Figure 1.1 Typical pre-Northridge fully restrained welded unreinforced flange-bolted web (WUF-B) beam-to-column connection detailing. 25

Figure 1.2 Characteristic beam-to-column connection fractures in Northridge 1994 earthquake [original image courtesy: Prof. M. D. Engelhardt]. 26

Figure 1.3 Schematic illustration of the beam-to-column connection fractures in Northridge 1994 earthquake [image adapted from Krawinkler et al. (1971); Tremblay et al. (1995)]. 26

Figure 1.4 Typical post-Northridge fully restrained welded unreinforced flange-welded web (WUF-W) beam-to-column connection detailing. 27

Figure 1.5 Welded unreinforced flange-welded web beam-to-column connection test results........ 28

Figure 1.6 Beam-to-column connection test results with inelastic panel zone (Krawinkler 1978)........ 29

Figure 1.7 Reduction of area in the through-thickness direction versus sulfur content for conventional and high performance steel (data from nipponsteel.com). 31

Figure 2.1 Comparison of panel zone and subassembly responses. 36

Figure 2.2 Typical cruciform subassembly test configurations. 38

Figure 2.3 Representative beam-to-column connection typologies included in the assembled inelastic panel zone database. 39

Figure 2.4 Typical access hole geometries. 39

Figure 2.5 Histograms depicting geometric and material properties of the assembled inelastic panel zone experimental data. 42

Figure 2.6 Measured R_y boxplots for the beam and column steel materials. 43

Figure 2.7 Panel zone: (a) model (Krawinkler 1978); (b) cross-sectional characteristic dimension; (c) connection characteristic dimensions; and (d) action forces. 44

Figure 2.8 Typical digitized local and global responses along with representative histograms of panel zone and subassembly response parameters. 45

Figure 2.9 Column-loaded interior subassembly decomposition of deformations. 46

Figure 2.10 Representative example of data extraction. 48

Figure 2.11 Maximum story drift ratio versus beam span-to-depth ratio of the collected data........ 49

Figure 2.12 Probability of connection failure given SDR and γ for different beam-to-column connection types. 51

Figure 2.13 Comparison of theoretical and measured panel zone elastic stiffness, K_e. 51

Figure 2.14 Comparison of theoretical and measured panel zone strength at $4\gamma_y$ versus t_{cf}. 52

Figure 2.15 Plastic rotation contribution of beam and panel zone versus the $R_u/R_{n,pl}$ ratio. 53

Figure 2.16 (a) Normalized maximum attained beam end moment versus $R_u/R_{n,pl}$; and (b) $R_u/R_{n,pl}$ versus normalised maximum attained panel zone shear distortion. 54

Figure 2.17 Continuum finite element model schematics. 55

Figure 2.18 Comparison between CFE Model 1 and 2 prediction and test data of SPEC-6, Ricles et al. (2004). 55

Figure 3.1 Panel zone kinematics and mathematical model assumptions. 61

Figure 3.2 Comparison of analytically derived, K_e, and measured, $K_{e,m}$, panel zone elastic stiffness...... 63

Figure 3.3 Comparison of inelastic panel zone test data without doubler plate: (a) $K_p/K_{p,m}$ versus t_{cf}; (b) $V_p/V_{p,m}$ versus t_{cf}; and (c) first cycle envelopes for panel zone measured shear stiffness and strength deduction (data extracted from Kim et al. (2015), specimen 3). 64

Figure 3.4 Detailed and reduced-order continuum finite element models. 66

Figure 3.5 Comparison between CFE model prediction and test data: (a)-(b) data reproduced from FEMA (1997); (c)-(d) data reproduced from Ricles et al. (2004b). 67

Figure 3.6 Deduced panel zone performance parameters... 68

Figure 3.7 Representative continuum finite element analysis results with varying web panel zone aspect ratio and column flange thickness. 69

Figure 3.8 Shear stress distributions at γ_y, $4\gamma_y$ and $6\gamma_y$: (a) slender; and (b) stocky and shallow panel zones. 70

Figure 3.9 (a) Deviation of predicted K_e from measured one, $K_{e,m}$, with respect to K_f/K_e; and (b) normalized panel zone stiffness at representative shear distortion levels with respect to K_f/K_e. 72

Figure 3.10 Normalized average shear stress at γ_y, $4\gamma_y$ and $6\gamma_y$ for the: (a) web; and (b) flange. 74

Figure 3.11 Comparison of measured and predicted panel zone hysteretic responses. 75

Figure 3.12 Comparison of the proposed panel zone stiffness and shear strength at $4\gamma_y$ and $6\gamma_y$ versus the measured ones from inelastic panel zone test data without doubler plates. 76

Figure 3.13 Continuum finite element model CJP and fillet weld details. 78

Figure 3.14 Relative difference in the average shear stresses between the doubler plate and the column web versus accumulated panel zone shear distortion. 78

Figure 3.15 Comparison of measured and predicted response of panel zones with fillet- and CJP-welded doubler plates. 79

Figure 3.16 Panel zone relative difference between the panel zone shear strength with/without applied axial load versus accumulated panel zone shear distortion for interior columns. 81

Figure 3.17 Panel zone relative reduction due to axial force versus accumulated panel zone shear distortion for both interior and exterior columns (8-story steel MRF). 81

Figure 4.1 Welded unreinforced flange-bolted web (WUF-B) pre-Northridge connection: (a) typical configuration; (b) potential locations for crack initiation; and (c) typical bottom beam flange-to-column flange connection detail [adopted from Paret (2000), credit: Prof. J. Fisher] and schematic of additional flaw profile along the beam flange width. 86

Figure 4.2 Fracture pattern observed during the 1994 Northridge earthquake in a welded unreinforced flange, bolted-web connection (photo courtesy: Professor Michael Engelhardt). 87

Figure 4.3 Typical welded unreinforced flange-welded web (WUF-W) pre-qualified connection detailing. 88

Figure 4.4 J-integral computation specifics for a typical beam flange-to-column flange connection........ 91

Figure 4.5 Continuum finite element model of a beam-to-column connection; global model and submodel variants. 93

Figure 4.6 Continuum finite element sensitivity analyses results. 94

Figure 4.7 Backing bar geometry: (a) conventional detail; and (b) beveled detail. 95

Figure 4.8 Bottom beam flange-to-column flange weld detail along with their respective continuum finite element submodels. 97

Figure 4.9 J-integral comparisons for a typical pre-Northridge WUF-B connection and its model variants: (a) J-integral versus story drift ratio; and (b) effect of bevel angle, θ_b, on J-integral. 98

Figure 4.10 Effect of fillet weld reinforcement on J-integral for pre-Northridge WUF-B connection detailing depending on the assumed continuum finite element submodel. 99

Figure 4.11 Effect of column tensile axial force on J-integral for pre-Northridge WUF-B connections. 101

Figure 4.12 Pre-qualified WUF-W connection: (a) applied force versus story drift ratio; and (b) normalized panel zone shear distortion versus story drift ratio. 102

Figure 4.13 Pre-qualified WUF-W connections with weak and strong panel zones. 103

Figure 4.14 Fracture assessment of pre-qualified WUF-W connections with a beveled backing bar...... 105

Figure 5.1 Illustration of typical welded unreinforced flange-welded web connection detailing. 110

Figure 5.2 (a) Hysteretic responses of welded unreinforced flange-welded web beam-to-column connections with variable design panel zone distortions, γ_d; deformed shapes for the (b) $2\gamma_y$ (at 3% rad lateral drift demand); and the (c) $22\gamma_y$ (at 6% rad lateral drift demand) cases [source: Shin (2017)]. 111

Figure 5.3 Overview of the beam-to-column connection (unit: millimeters)... 114

Figure 5.4 Fabrication of test specimen – welding preparation in the upright position. 115

Figure 5.5 Fabrication of the beam-to-column connection – beveled backing bar details. 116

Figure 5.6 Fabrication of the beam-to-column connection – completion of CJP welding details. 116

Figure 5.7 Fabrication of the beam-to-column connection – removal of weld runoff tabs. 117

Figure 5.8 Identified locations of weld discontinuities after ultrasoning testing for Specimen 2 (unit: millimeters). 117

Figure 5.9 Overview of the test setup (unit: millimeters).. 118

Figure 5.10 Instrumentation plan at the panel zone and the load application locations (unit: millimeters). 119

Figure 5.11 Illustration of the rigid body motion rotation... 120

Figure 5.12 Cyclic true stress-strain behavior of representative uniaxial loading protocols in the column web. 122

Figure 5.13 Loading protocols for the beam-to-column connection test specimens. 124

Figure 5.14 Story shear resistance versus story drift ratio. 126

Figure 5.15 Panel zone shear force versus normalized panel zone shear distortion............................... 127

Figure 5.16 Specimen 1 bottom beam flanges at characteristic loading excursions. 128

Figure 5.17 Specimen 2 bottom beam flanges at characteristic loading excursions. 129

Figure 5.18 Panel zone deformation at characteristic loading excursions.. 130

Figure 5.19 Yield pattern around the beveled backing bar of the bottom flange of the steel beam (Specimen 1)... 130

Figure 5.20 Specimen 1 crack patterns at characteristic lateral drift demands of: (a) +6% rad; (b) -7% rad; (c) +7% rad; and (d) -8% rad.. 131

Figure 5.21 Specimen 2 crack patterns at characteristic loading excursions: (a-b) 39th (-10.0% rad); (c) 48th (+10.0% rad); and (d) 50th (-10% rad).. 133

Figure 5.22 Backing bar deformations (Specimen 2, at a 10% rad lateral drift demand). 134

Figure 5.23 Ultimate failure modes of Specimen 1 after the test completion. 135

Figure 5.24 Ultimate failure modes of Specimen 2 after the test completion. 136

Figure 5.25 Deformation pattern of the test specimens after the completion of the test program. 137

Figure 5.26 Beam moment at the column face versus story drift ratio. 138

Figure 5.27 Moments at the beam ends at the column face location versus beam chord rotations and moments at the column at the panel zone top horizontal edge location versus column chord rotations. . 139

Figure 5.28 Contributions of the panel zone, the beams and the column to the story drift ratio at characteristic lateral loading excursions. 140

Figure 5.29 Column twist demands at characteristic lateral loading excursions. 141

Figure 5.30 Column flange local deformations at characteristic lateral loading excursions. 142

Figure 5.31 Yield pattern at the panel zone kinking locations due to column flange local deformations at characteristic lateral drift demands of Specimen 2. 142

Figure 5.32 Stress and strain demands 50 mm away from the bottom panel zone kinking location for Specimens 1 and 2. 144

Figure 5.33 Comparisons of simulated versus experimental results. 146

Figure 5.34 Response comparisons of welded connections with elastic and highly dissipative panel zones. 147

Figure 6.1 Hysteretic response of subassemblies with variable panel zone inelastic shear distortions. .. 153

Figure 6.2 Schematic representation of panel zone modeling approaches. 155

Figure 6.3 Panel zone shell element model versus macro-model for the DBE-scaled FEMA P695 far-field ground motion set: (a) peak story drift ratio distributions; and (b) peak γ/γ_y distributions. 157

Figure 6.4 Schematic illustration of workflow for modeling of beam flange fracture during nonlinear response history analysis. 158

Figure 6.5 Three- and five-bay, four-story steel buildings. 159

Figure 6.6 Pushover analysis results for the four-story, three-bay MRF 162

Figure 6.7 Seismic hazard curves for the three-bay moment resisting frames. 163

Figure 6.8 IDA curves for the three-bay, four-story steel MRF with $\gamma_d = 10\gamma_y$. 164

Figure 6.9 Collapse fragility curves for the four-story steel MRFs: (a) three-bay steel MRFs; and (b) five-bay steel MRFs. Probabilities of collapse in 50 years and mean annual frequency of collapse for the four-story steel MRFs: (c) three-bay steel MRFs; and (d) five-bay steel MRFs. 165

Figure 6.10 Peak story drift ratio distributions near collapse for the three-bay MRFs. 166

Figure 6.11 Effect of targeted panel zone distortion on engineering demand parameters of interest for the four-story, three-bay MRF. 167

Figure 6.12 Exceedance functions for the number of beam end fractures per MRF at MCE. 168

Figure 6.13 (a) Peak γ/γ_y for the most critical panel zone along the building height for the four-story, 3-bay, MRF with $\gamma_d = 10\gamma_y$; and (b) distribution of peak γ/γ_y for selected seismic intensities. 169

Figure 6.14 Hazard curves for engineering demand parameters of interest for the four-story, three-bay MRFs. 170

Figure 6.15 Expected global and local engineering demand parameters at DBE for the three-bay MRFs. 171

Figure 6.16 Expected number of beam end fractures per MRF at MCE: (a) three-bay; and (b) five-bay.171

Figure A.1 Test specimen general plan drawings. 182

Figure A.2 Test specimen detailed drawings. 183

Figure A.3 Beam-to-column connection drawings.. 184

Figure A.4 Test specimen west beam drawings. 185
Figure A.5 Test specimen east beam drawings. 186
Figure A.6 Test specimen column drawings. 187
Figure A.7 Test specimen column weld drawings. 188
Figure A.8 Test specimen actuator adapter plate drawings. 189
Figure A.9 Test specimen list of bolts and rods. 190
Figure B.1 Lateral support system general plan drawings. 192
Figure B.2 Lateral support system overview drawings. 193
Figure B.3 Lateral support system piece location drawings. 194
Figure B.4 Lateral support system angle overview drawings. 195
Figure B.5 Lateral support system angle P1 drawings. 196
Figure B.6 Lateral support system angle P2 drawings. 197
Figure B.7 Lateral support system angle P3 drawings. 198
Figure B.8 Lateral support system beam P4 drawings. 199
Figure B.9 Lateral support system beam P5 drawings. 200
Figure B.10 Lateral support system list of bolts and rods. 201
Figure C.1 Instrumentation plan – top side general plan drawings. 204
Figure C.2 Instrumentation plan – bottom side general plan drawings. 205
Figure C.3 Instrumentation plan – column strain gauge drawings. 206
Figure C.4 Instrumentation plan – west beam strain gauge drawings. 207
Figure C.5 Instrumentation plan – east beam strain gauge drawings. 208
Figure C.6 Instrumentation plan – LVDT (Part A) drawings. 209
Figure C.7 Instrumentation plan – LVDT (Part B) drawings. 210
Figure C.8 Instrumentation plan – LVDT (Part C) drawings. 211
Figure C.9 Instrumentation plan – Rosette and potentiometer drawings. 212
Figure C.10 Instrumentation plan – beam end string pot drawings. 213
Figure D.1 Mill certificate of the T49J0T1-1CA-UH5 weld electrode. 216
Figure D.2 Mill certificate of the YGW-18 weld electrode. 217
Figure D.3 Shear tab-to-column face welding procedure specification of Specimen 1 east beam. 219
Figure D.4 Top beam flange-to-column face welding procedure specification of Specimen 1 east beam. 220
Figure D.5 Bottom right beam flange-to-column face welding procedure specification of Specimen 1 east beam. 221
Figure D.6 Bottom left beam flange-to-column face welding procedure specification of Specimen 1 east beam. 222
Figure D.7 Beam web-to-column face welding procedure specification of Specimen 1 east beam. 223
Figure D.8 Shear tab-to-column face welding procedure specification of Specimen 1 west beam. 224

Figure D.9 Top beam flange-to-column face welding procedure specification of Specimen 1 west beam. 225

Figure D.10 Bottom right beam flange-to-column face welding procedure specification of Specimen 1 west beam. 226

Figure D.11 Bottom left beam flange-to-column face welding procedure specification of Specimen 1 west beam. 227

Figure D.12 Beam web-to-column face welding procedure specification of Specimen 1 west beam. 228

Figure D.13 Shear tab-to-column face welding procedure specification of Specimen 2 east beam. 229

Figure D.14 Top beam flange-to-column face welding procedure specification of Specimen 2 east beam. 230

Figure D.15 Bottom right beam flange-to-column face welding procedure specification of Specimen 2 east beam. 231

Figure D.16 Bottom left beam flange-to-column face welding procedure specification of Specimen 2 east beam. 232

Figure D.17 Beam web-to-column face welding procedure specification of Specimen 2 east beam. 233

Figure D.18 Shear tab-to-column face welding procedure specification of Specimen 2 west beam. 234

Figure D.19 Top beam flange-to-column face welding procedure specification of Specimen 2 west beam. 235

Figure D.20 Bottom right beam flange-to-column face welding procedure specification of Specimen 2 west beam. 236

Figure D.21 Bottom left beam flange-to-column face welding procedure specification of Specimen 2 west beam. 237

Figure D.22 Beam web-to-column face welding procedure specification of Specimen 2 west beam. 238

Figure D.23 Locations of welds subjected to ultrasonic test. 239

Figure D.24 Ultrasonic test results. 241

Figure E.1 Representative monotonic coupon test before and after test (Column flange, 2nd test). 244

Figure E.2 Monotonic coupon test results: (a) beam web; (b) beam flange; (c) column web; and (d) column flange. 244

Figure E.3 Representative cyclic coupon test before and after test (Column flange, loading protocol 3). 245

Figure E.4 Beam web coupon test and simulation results. 246

Figure E.5 Beam flange coupon test and simulation results. 247

Figure E.6 Column web coupon test and simulation results. 248

Figure E.7 Column flange coupon test and simulation results. 249

Figure E.8 Experimental strain histories: Specimen 1. 250

Figure E.9 Experimental strain histories: Specimen 2. 250

Figure E.10 Beam web coupon test and simulation results based on experimental strain histories: (a) Specimen 1; and (b) Specimen 2. 251

Figure E.11 Beam flange coupon test and simulation results based on experimental strain histories: (a) Specimen 1; and (b) Specimen 2. 251

Figure E.12 Column web coupon test and simulation results based on experimental strain histories: (a) Specimen 1; and (b) Specimen 2. 251

Figure E.13 Column flange coupon test and simulation results based on experimental strain histories: (a) Specimen 1; and (b) Specimen 2. 252

Figure F.1 Proposed welded unreinforced moment connection detailing. 254

Figure F.2 Beam-to-column connection detailing of Specimen 1. 257

Figure F.3 Schematic of the test setup of Specimen 1 258

Figure F.4 Specimen 1 hysteretic responses of: (a) subassembly; (b) panel zone; (c) west beam; and (d) east beam. 259

Figure F.5 Characteristic views of Specimen 1 during the experiment. 260

Figure F.6 Beam-to-column connection detailing of Specimen 2. 261

Figure F.7 Schematic of the test setup of Specimen 2 262

Figure F.8 Specimen 2 hysteretic responses of: (a) subassembly; (b) panel zone; (c) west beam; and (d) east beam. 263

Figure F.9 Characteristic views of Specimen 2 during the experiment. 264

Figure G.1 Design spectrum and archetype MRF periods. 266

Figure G.2 Plan view of the three- and five-bar steel MRFs. 267

Figure G.3 Elevation view of the four-story steel MRFs: (a) three-bay; and (b) five-bay. 267

Figure G.4 Elevation view of the eight-story steel MRFs: (a) three-bay; and (b) five-bay 268

Figure G.5 Elevation view of the twelve-story steel MRFs: (a) three-bay; and (b) five-bay. 268

Figure G.6 Elevation view of the twenty-story steel MRFs: (a) three-bay; and (b) five-bay 269

Figure G.7 Drift and stability coefficient checks for the four-, eight-, twelve- and twenty-story, three-bay MRFs. 275

Figure G.8 Drift and stability coefficient checks for the four-, eight-, twelve- and twenty-story, five-bay MRFs. 276

List of Tables

Table 2.1 Summary of pre-Northridge beam-to-column connection detailing testing programs in the assembled database (in alphabetical order). 40

Table 2.2 Summary of post-Northridge beam-to-column connection detailing testing programs in the assembled database (in alphabetical order). 41

Table 2.3 Lognormal distribution parameters and correlation coefficients for γ/γ_y and SDR. 50

Table 3.1 Statistical parameters for the linear regression curves of the $a_{eff} - K_f/K_e$ relationships. 74

Table 3.2 Normalized average shear stress values and expressions in the web and the flanges, based on the proposed model. 75

Table 3.3 Virtual test matrix for the examination of doubler plate effectiveness. 77

Table 3.4 Virtual test matrix for the examination of the axial load effect. 80

Table 4.1 CFE analyses beveled backing bar geometry characteristics. 95

Table 4.2 Post-Northridge subassembly CFE analysis matrix. 102

Table 5.1 Measured dimensions of the test specimens. 114

Table 5.2 Measured and nominal material properties of the test specimens. 121

Table 5.3 Calibrated parameters of multiaxial constitutive law for the steel material of columns and beams. 123

Table 5.4 Chemical composition of steel materials. 123

Table 6.1 Archetype steel MRF first mode periods and global performance factors. 160

Table D.1 Overview of the weld procedure specifications of both test specimens. 218

Table D.2 Overview of the ultrasonic test results of both test specimens. 240

Table E.1 Calibrated parameters of multiaxial constitutive law for the steel material of columns and beams. 245

Table F.1 Testing program information of Specimen 1. 257

Table F.2 Material properties and test specimen details of Specimen 1. 258

Table F.3 Key experimental observations of Specimen 1. 260

Table F.4 Summary of Specimen 1 experimental results. 260

Table F.5 Testing program information of Specimen 2. 261

Table F.6 Material properties and test specimen details of Specimen 2. 262

Table F.7 Key experimental observations of Specimen 2. 264

Table F.8 Summary of Specimen 2 experimental results. 264

Table G.1 Archetype steel MRF panel zone shear resistance over panel zone shear demand values and first mode periods. 270

Table G.2 Four-story, three-bay steel MRF design. 271

Table G.3 Four-story, five-bay steel MRF design. 271

Table G.4 Eight-story, three-bay MRF design. 271

Table G.5 Eight-story, five-bay MRF design. 271

Table G.6 Twelve-story, three-bay MRF design. 272

Table G.7 Twelve-story, five-bay MRF design.. 272
Table G.8 Twenty-story, three-bay MRF design.. 273
Table G.9 Twenty-story, five-bay MRF design. 274
Table G.10 SCWB ratio for the four-story, three-bay MRF 277
Table G.11 SCWB ratio for the four-story, five-bay MRF 277
Table G.12 SCWB ratio for the eight-story, three-bay MRF 277
Table G.13 SCWB ratio for the eight-story, five-bay MRF... 277
Table G.14 SCWB ratio for the twelve-story, three-bay MRF 278
Table G.15 SCWB ratio for the twelve-story, five-bay MRF 278
Table G.16 SCWB ratio for the twenty-story, three-bay MRF 279
Table G.17 SCWB ratio for the twenty-story, five-bay MRF 279

Chapter 1 Introduction

1.1 Research background

Steel moment-resisting frames (MRFs) are commonly used as lateral load-resisting systems in seismic regions. Steel MRFs can sustain high ductility demands if proper structural detailing is employed along with principles of capacity design (Fardis 2018; Uang and Bruneau 2018). In capacity-designed steel MRFs, inelastic deformations are mostly concentrated near the steel beam ends and the first story column fixed ends (AISC 2016a; BCJ 2016; CEN 2004a; CSA 2019). Design rules applied to steel MRF beam-to-column connections after the 1994 Northridge earthquake in California and the 1995 Kobe earthquake in Japan, limited the participation of the beam-to-column panel zones in the energy dissipation of beam-to-column connections. In this context, cyclic deterioration in flexural strength of steel beams due to local buckling is anticipated even at modest lateral drift demands (Lignos and Krawinkler 2013). This is a challenging issue from a repairability standpoint.

Surveys in steel MRF buildings after the 1994 Northridge earthquake highlighted that pre-Northridge fully restrained welded unreinforced flange-bolted web (WUF-B) beam-to-column connections (see Fig. 1.1) with highly inelastic panel zones and deep beams (i.e., beam depths of more than 500mm) experienced premature fractures (FEMA 2000a; Youssef et al. 1995).

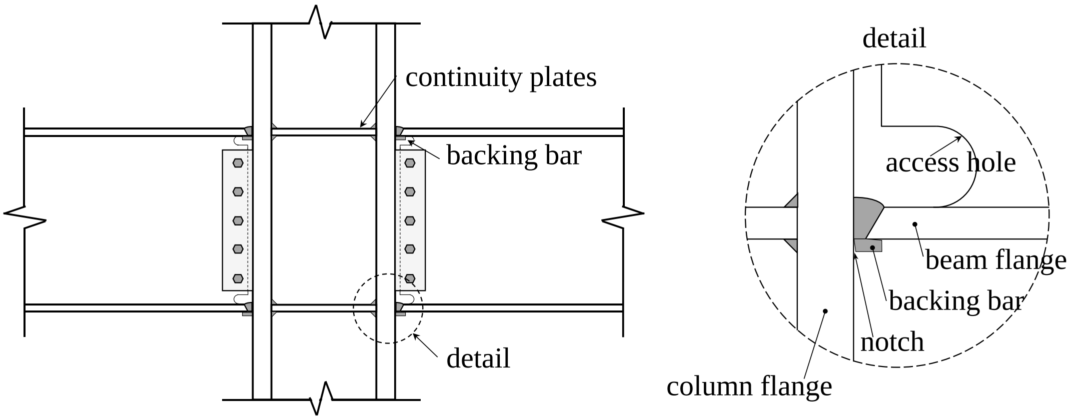

Figure 1.1 Typical pre-Northridge fully restrained welded unreinforced flange-bolted web (WUF-B) beam-to-column connection detailing.

Commonly observed fracture types for the same connections are shown in Figs. 1.2 and 1.3. Referring to Fig. 1.1, the presence of the weld backing bar was creating a geometric notch in the bottom beam flange, leading to high strain demands nearby that region. This notch, in combination with the inelastic panel zone kinking (see Fig. 1.3), necessitated high toughness requirements in the column and weld materials (Whittaker et al. 1998), particularly for connection designs that featured deep beams (Chi et al. 1997). The fracture toughness of the weld material, which comprised semi-automatic, self-shielded, flux-cored arc welding process (FCAW-SS) was found to be fairly poor (Chi et al. 2000; FEMA 2000a), thereby leading to fractures in the weld material and the heat affected zone (see Fig. 1.2a and Fig. 1.3, Types 1 and 2). Moreover, the inferior fracture toughness through the column thickness direction was found to be inadequate compared to the fracture toughness requirements in this location (Krawinkler 1995). This often lead to divot fracture (see Fig. 1.2b and Fig. 1.3, Types 4, 8) and fracture through the column flange and web material (Miller 1998) as shown in Fig. 1.3 (i.e., Types 3, and 5-6).

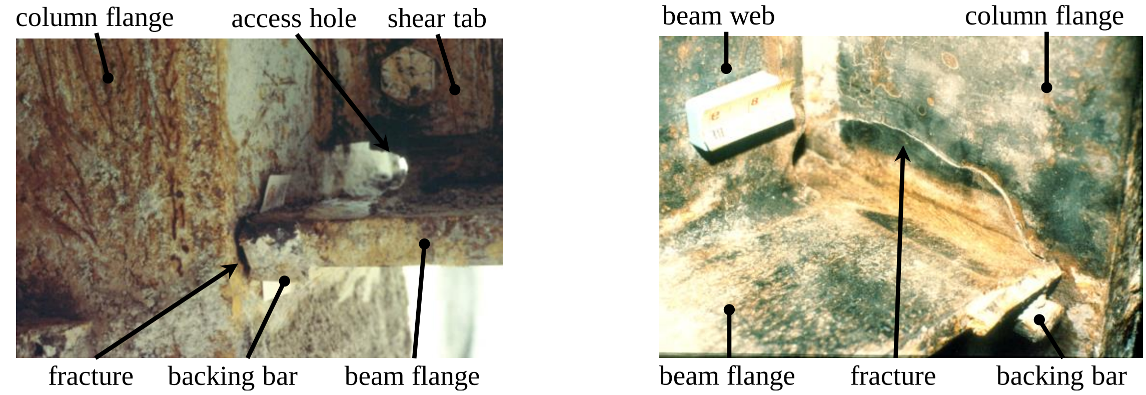

(a) fracture in the beam flange to column flange heat affected zone

(b) divot fracture

Figure 1.2 Characteristic beam-to-column connection fractures in Northridge 1994 earthquake [original image courtesy: Prof. M. D. Engelhardt].

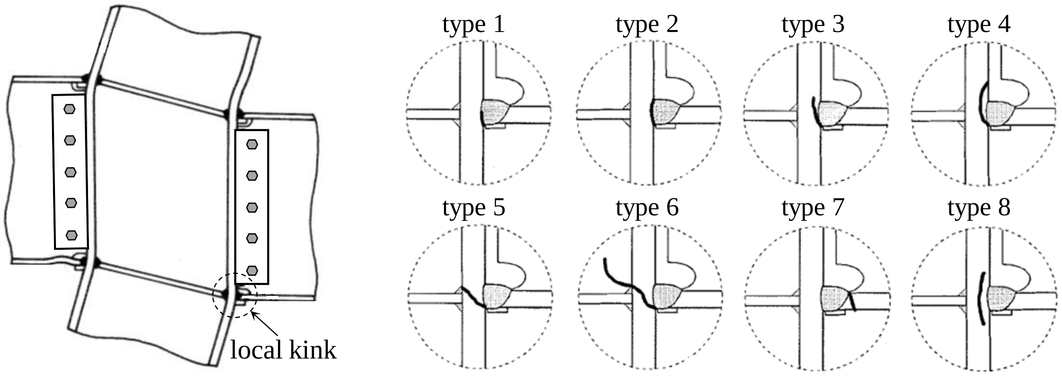

Figure 1.3 Schematic illustration of the beam-to-column connection fractures in Northridge 1994 earthquake [image adapted from Krawinkler et al. (1971); Tremblay et al. (1995)].

The non-optimized weld access hole geometry often caused high stress concentration near the beam flanges, thereby resulting in tearing nearby this location (Ricles et al. 2000) as shown in Fig. 1.3 (see Type 7). Finally, the tendency towards scrap-based steel production and inferior quality control resulted in uncertainty in the upper bound yield stress of the respective steel beams (FEMA 2000a; Tremblay et al. 1995). As a result, the yield stress of the weld metal was often under-matched with respect to the base metal's yield stress. As a consequence, this often leads to brittle fracture at the beam flange-to-column flange weld material.

The above findings constitute a great contribution for the further development of today's prequalified beam-to-column connections. Experimental studies on WUF-B connections with improved welding procedures, weld and base metal materials as well as an optimal access hole geometry (Han et al. 2007; Stojadinović et al. 2000) showed that this configuration was still inadequate to meet the established seismic performance requirements. As such, a tendency towards welded unreinforced flange-welded web (WUF-W) connections was established, based on experimental work (Lee et al. 2002, 2005c; b; Ricles et al. 2000, 2002a; b) and corroborating finite element studies (Chi et al. 1997; El-Tawil et al. 1998; Lu et al. 2000; Mao et al. 2001). A typical post-Northridge WUF-W connection, which is shown in Fig. 1.4, leverages a weld metal with improved fracture toughness requirements for the execution of the complete joint penetration (CJP) weld between the beam flange-to-column flange connection. An optimized access hole geometry is also employed with rigorous specifications in the bottom beam flange weld backing bar. Moreover, an essentially elastic panel zone design is preferred in order to minimize strain localization due to kinking at the beam flange-to-the column face interface.

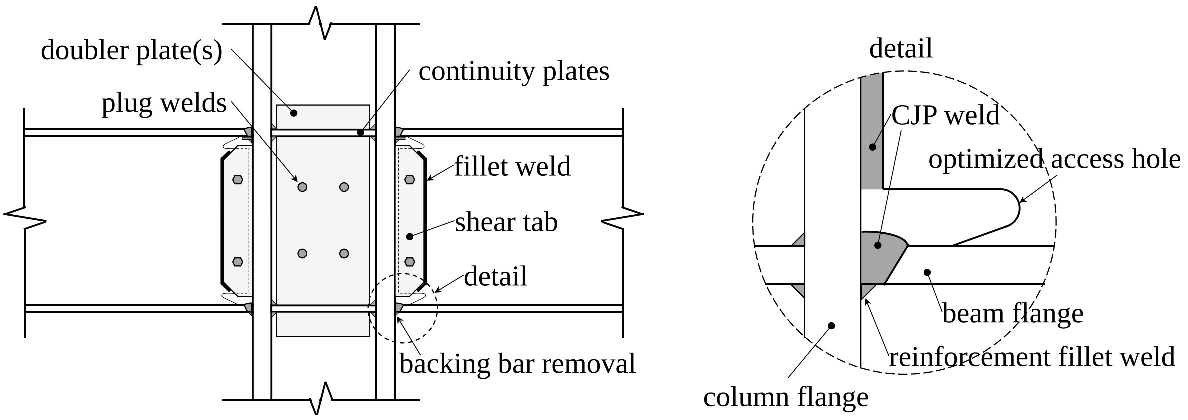

Figure 1.4 Typical post-Northridge fully restrained welded unreinforced flange-welded web (WUF-W) beam-to-column connection detailing.

Figure 1.5a illustrates test results of a WUF-W beam-to-column connection designed as per AISC (2016a; b; c) with elastic panel zones (Shin 2017). At a lateral drift demand of 3% rad, local buckling initiates within the dissipative zone of the steel beam(s), while at 4% rad, there is prominent story shear resistance degradation. Cyclic deterioration of flexural strength increases the earthquake-induced collapse risk of steel MRFs (Lignos and Krawinkler 2011). Moreover, at modest lateral drift demands, the need of structural repairs at the steel MRF beam ends may be imperative (see Fig. 1.5a).

Research (Chi and Uang 2002; Ricles et al. 2004b) suggests that once local geometric instabilities occur in the beam ends, the adjacent column is subjected to increased twisting demands, thereby compromising its lateral load resistance (Elkady and Lignos 2018a; Ozkula et al. 2017). To limit the deformations within the beam-to-column panel zone, thick doubler plates may be imperative [e.g., Ricles et al. (2000); Sato et al. (2007); Shin (2017)]. Oftentimes, this involves welding near the k-area of steel columns and could potentially cause fabrication problems (Barsom and Pellegrino 2000; Nikolaidou et al. 2013).

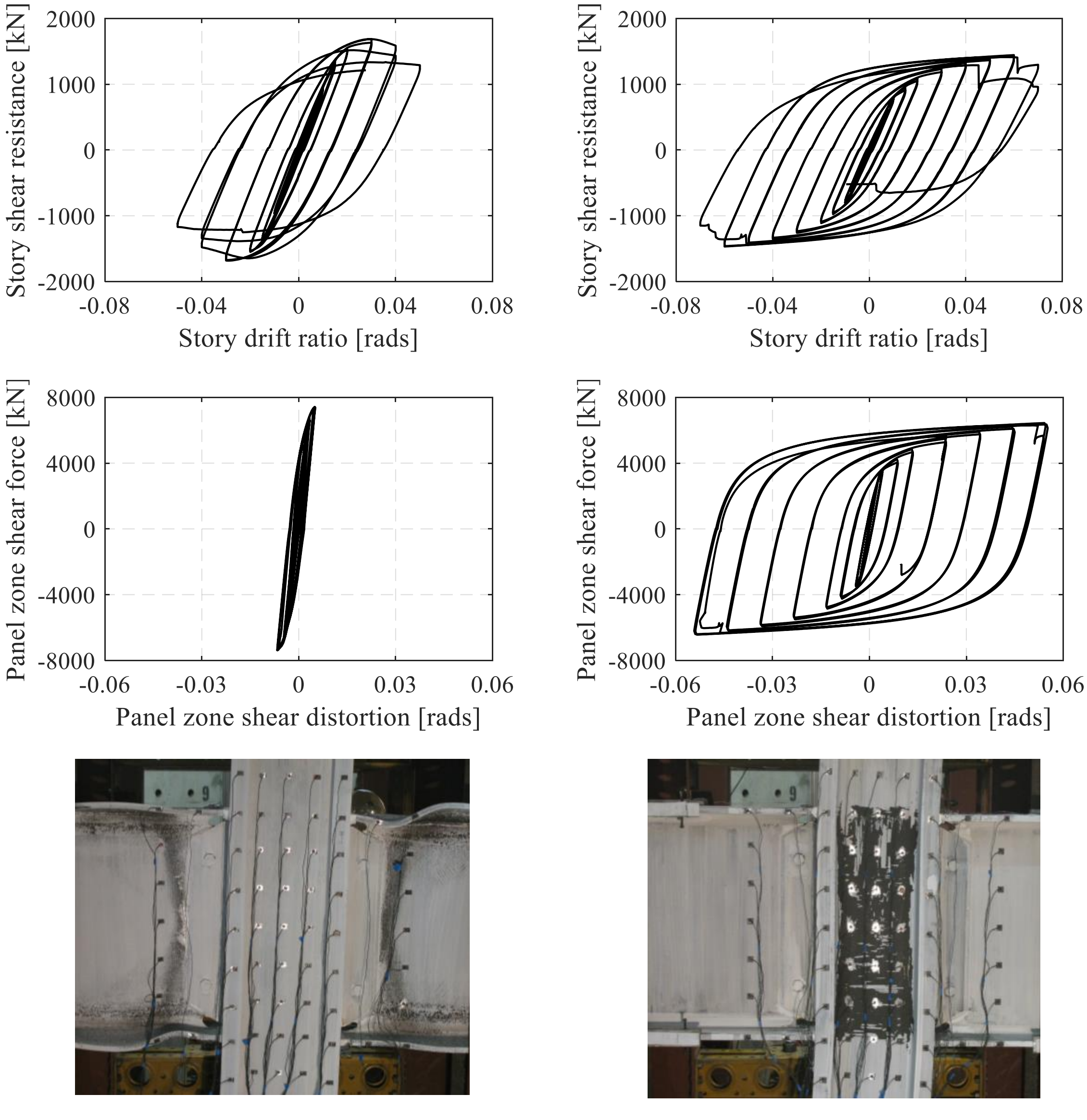

(a) elastic panel zone design

(b) highly inelastic panel zone design

Figure 1.5 Welded unreinforced flange-welded web beam-to-column connection test results - First row: global response; Second row: panel zone response; Third row: connection caption at lateral drift demand of 4% rad [images adopted from Shin (2017)].

From a life-safety standpoint, beam-to-column connections designed according to AISC 358-16 (AISC 2016c) meet the prequalification criteria. While ensuring the life-safety is the utmost objective of current building seismic provisions, the impact of seismic events on direct and indirect financial losses has gained attention over the past decade (Aslani and Miranda 2005; Bonowitz 2009; Comerio 2006; FEMA 2012; Porter 2021; Ramirez and Miranda 2012). Along these lines, methodologies to quantify the time to recovery by means of structural and nonstructural element repairs and downtime have evolved (FEMA 2012, 2018; Furley et al. 2021; Terzic et al. 2021). Hwang and Lignos (2017) used the loss estimation methodology by Ramirez and Miranda (2012) and found that in low- to mid-rise steel MRFs designed in high seismicity zones, structural repairs due to beam-to-column connection damage attributable to local buckling in the steel beam ends is on the order of 20% of the total replacement cost of a steel frame building during a design-basis earthquake (i.e., 10% probability of occurrence over a 50 year service life) without considering downtime. In this regard, prior research has focused on limiting damage on structural building components to minimize functional recovery (Molina Hutt et al. 2021).

Minimizing structural damage in buildings reduces the financial losses in the advent of mainshock-aftershock seismic excitations (Song et al. 2014). Moreover, from a collapse safety standpoint, mobilizing a non-degrading component hysteretic response such as that in Fig. 1.5b decreases the collapse risk in the mainshock-aftershock earthquake sequences (Li et al. 2014; Shokrabadi et al. 2018). Within such a context, existing concepts for steel MRF beam-to-column connection seismic designs should be revisited, so as to minimize structural repairs and downtime in the aftermath of earthquakes.

Back in the early 1970s, experimental studies on inelastic panel zone beam-to-column connections demonstrated the beneficial aspects of panel zone shear yielding (Fielding and Huang 1971; Krawinkler et al. 1971; Krawinkler and Popov 1982; Popov et al. 1985). Figure 1.6a depicts a characteristic example of the stable panel zone hysteretic response. In this test, the beam-to-column connection reached 6% rad lateral drift demands (see Fig. 1.6b) without major damage in the steel beams of the beam-to-column connection. On the other hand, the results should be carefully interpreted due to scale effects that did impact the overall beam-to-column connection performance in steel MRF buildings during the 1994 Northridge earthquake (Mahin 1998; Malley 1998).

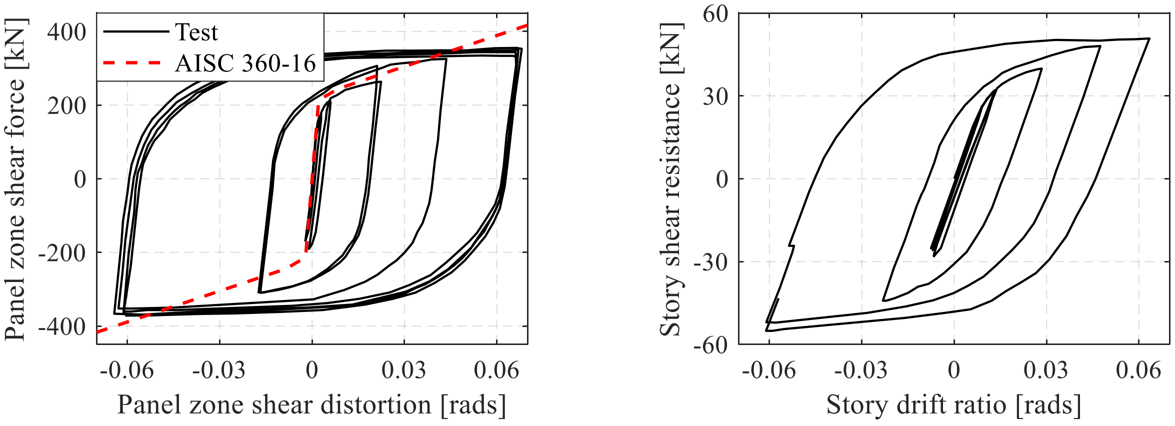

(a) panel zone response

(b) global response

Figure 1.6 Beam-to-column connection test results with inelastic panel zone (Krawinkler 1978).

More recent studies on WUF-W beam-to-column connection tests (Kim and Lee 2017; Lee et al. 2005b; Lin et al. 2000; Rahiminia and Namba 2013; Shin 2017) with highly inelastic panel zones (i.e., shear distortions higher than $10\gamma_y$, where γ_y is the panel zone distortion at yield) demonstrated a satisfactory connection performance without significant strength and stiffness deterioration at 6% rad lateral drift demands. Figure 1.5b depicts a stable hysteretic response up to 6% rad lateral drift demands of one of those connections, which can be directly contrasted with the current design paradigm (see Fig. 1.5a). Referring to Fig. 1.5b, the ultimate failure mode involved beam flange fracture in the CJP weld. The story shear resistance in this beam-to-column connection without doubler plates is marginally smaller compared to the nominally identical beam-to-column connection with doubler plates highlighted in Fig. 1.5a. In the former, the beam participation to the lateral drift demands is nearly three times less than that of the latter. As such, the associated twist demands in the adjoining column were greatly reduced in this case.

Despite the promising performance of beam-to-column connections with inelastic panel zones (i.e., distortions higher than $1-4\gamma_y$), balancing their shear resistance relative to the shear demand of the adjoining steel beams relies on the availability of reliable panel zone strength models for design. Available panel zone stiffness and strength models (Kim et al. 2015; Kim and Engelhardt 2002; Krawinkler 1978; Lee et al. 2005c) in the literature exhibit a number of limitations. This is particularly evident in cases where column cross sections feature thick flanges (thickness higher than 50mm) as suggested in the literature (Brandonisio et al. 2012; El-Tawil et al. 1999; Kim and Engelhardt 2002; Krawinkler 1978; Lee et al. 2005c; Qi et al. 2020; Soliman et al. 2018). Indicatively, a comparison between the predicted (AISC 2016b) and measured panel zone behavior is shown in Fig. 1.6a for available experimental data. Another reason why beam-to-column connection designs that promote panel zone yielding are not favoured is an existing perception that allowing for panel zone shear yielding in steel MRF beam-to-column connections, a soft story collapse mechanism may be triggered (Castro et al. 2005; Tsai and Popov 1990).

Regardless of the advancement in the performance of current fully restrained prequalified welded unreinforced flange beam-to-column connections, their fabrication is time consuming due to the rigorous specifications in the beam flange to column face welding (FEMA 2000a; Miller 2017; Popov et al. 1998). The specifications include removal of the bottom beam flange backing bar, weld root back gouging, ultrasonic testing to inspect potential deficiencies and fillet weld reinforcement of the outer bottom beam flange fiber to column face connection. On the other hand, quality control and fabrication technique improvements lead to simplifications in other structural details such as column splices (Shaw et al. 2015; Stillmaker et al. 2016), and continuity and doubler plate detailing in fully restrained beam-to-column connections (Reynolds and Uang 2022).

Steel making practices, to date, offer high performance steel materials (Kanno 2016) with improved mechanical properties depending on the application. For instance, for structural details that utilize plates with thicknesses higher than 38mm, lamellar tearing may occur due to the high strains imposed in the through-thickness plate direction (i.e., Z-direction) during the cooling process of the welding procedure (AISC 2016a). In this case, steel-making practices offer increased through-thickness properties by limiting the sulfur content, which is one of the main causes of anisotropy in steels. By limiting sulfur, the brittleness reduces and the weldability is improved. Figure 1.7 indicates that high performance steel ensures increased reduction in area property (ASTM 2018a) by controlling the sulfur content. High performance steel with improved through-thickness direction properties does not only eliminate the steel anisotropy, but also increases the fracture toughness in all directions (Barsom and Korvink 1998; Malley and Frank 2000; Miki et al. 2002). In Europe, it is suggested that Z35 quality class be met according to CEN (2004b) for connections subjected to high though-thickness strains. Within this context, divot fracture (see Fig. 1.2b) that could potentially be an issue in post-Northridge WUF-W connections (Lin et al. 2000) may be alleviated.

The general consensus from the above findings is that today's fabrication and material advancements could be further exploited for the seismic design of fully restrained welded beam-to-column connections that promote panel zone shear yielding. Structural detailing simplifications at the beam flange to column face connections may also be possible.

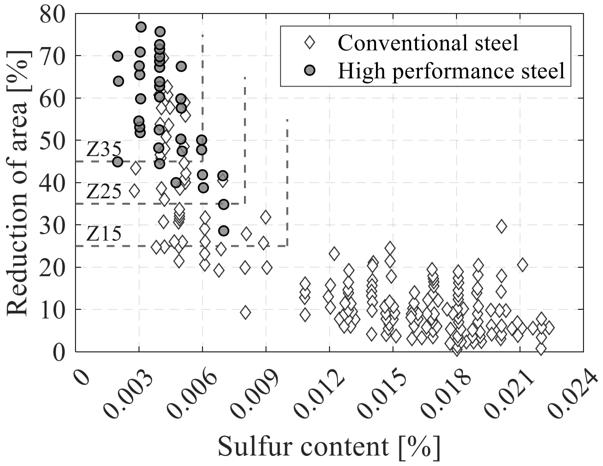

Figure 1.7 Reduction of area in the through-thickness direction versus sulfur content for conventional and high performance steel (data from nipponsteel.com).

1.2 Problem statement and research objectives

The previous section suggests that the current status quo in prequalified WUF-W beam-to-column connections may necessitate structural repairs in the aftermath of earthquakes. Depending on the building occupancy, downtime may be appreciable. Moreover, the beam end local instabilities lead to increased twist demands in steel MRF columns, thereby compromising their lateral load-carrying capacity. To ensure limited inelastic deformations within the beam-to-column panel zone, thick doubler plates may be imperative. On the other hand, by engineering the beam-to-column connections so as to balance the energy dissipation between the panel zone and the steel beams, a stable beam-to-column hysteretic response can be achieved for seismic intensities with a low probability of occurrence. At the same instance, the column twist demands and the welding complexity in the doubler plates can be tolerated. Motivated by the above, this thesis aims at advancing the state-of-the-art in fully restrained WUF-W beam-to-column connections in modern steel MRFs designed in seismic regions. The main research objectives of this doctoral thesis are summarized as follows,

- Develop a reliable model for the seismic design of steel MRF panel zones for balancing the overall seismic performance of beam-to-column connections under cyclic loading.
- Develop simplified structural detailing rules for fully restrained WUF-W beam-to-column connections by waiving some of the current weld specifications at the beam flange-to-column flange location.
- Conduct full-scale beam-to-column connection experiments to validate the proposed concepts and to characterize the ultimate failure modes of the proposed connections at large lateral drift demands associated with structural collapse.
- Conduct system-level studies of steel MRF buildings that utilize variable targeted panel zone inelastic deformations to benchmark their seismic collapse risk and their expected repairability requirements within the framework of performance-based earthquake engineering.

1.3 Thesis outline

This doctoral thesis comprises seven chapters, including the introduction and the conclusions. Four of them are part of peer-reviewed journal articles; two of them are already published and two are under review. One more article is planned to be submitted as a peer-reviewed journal paper. For the chapters that are reproduced from journal articles, detailed information is provided at the beginning of each chapter regarding the list of authors, their contribution and the full bibliographic information of the published article. A set of appendices complements the experimental program described in Chapter 5 and the system-level study described in Chapter 6.

Chapter 2 summarizes the state-of-the-art in experimental research of fully restrained beam-to-column connections. The collected test data emphasize on beam-to-column connections that feature inelastic panel zones. A comprehensive database is assembled for this purpose and is made publicly available, together with fully digitized panel zone and subassembly global hysteretic responses. The gathered dataset aids the beam-to-column connection performance assessment and the evaluation of available panel zone models, some of which are currently used in the seismic design of steel MRFs. The assembled database constitutes a valuable source for validation of multi-fidelity finite element models. This chapter is reproduced from the peer-reviewed journal article by Skiadopoulos and Lignos (2021).

Chapter 3 proposes a mechanics-based panel zone model for the seismic design of steel unreinforced beam-to-column connections. The model is informed by continuum finite element analyses for a broad range of panel zone geometries. Comparisons with pertinent experimental data presented in Chapter 2 suggest that the developed panel zone model provides a remarkable accuracy in predicting the panel zone stiffness and strength, while it tackles limitations of all available panel zone models in the literature. The effect of the column axial load and the utilization of doubler plates on the panel zone response are interrogated. This chapter is reproduced from the journal article by Skiadopoulos et al. (2021).

Chapter 4 revisits the current detailing of welded unreinforced flange-welded web beam-to-column connections as part of steel MRFs. The rigorous and resource-consuming bottom beam flange backing bar treatment necessitates its removal, weld root back gouging, thorough crack inspection and fillet reinforcement. Given the improved quality control as well as the weld and base metal specifications and practice to date, simplifications in the fabrication process are proposed by a beveled backing bar configuration. An optimized beveled unreinforced backing bar configuration is developed that minimizes the fracture potential at the beam flange to column face connection detail. This chapter is reproduced from the accepted peer-reviewed manuscript by Skiadopoulos and Lignos (2022a).

Chapter 5 presents the experimental results of fully restrained WUF-W beam-to-connection full scale subassemblies. Their beam-to-column web panel zones, which were designed with the proposed model from Chapter 3, achieve highly inelastic panel zone shear distortions. Moreover, the beam flange to column face weld detailing is based on the recommendations that were developed as part of Chapter 4. Two loading protocols are employed in the testing program; the reversed cyclic symmetric loading protocol (AISC 2016a), and the SAC near-fault loading protocol, followed by a collapse-consistent lateral loading history. The results suggest that WUF-W beam-to-column connections with the proposed structural detailing achieve superior lateral drift demands (above 7% rads) without practically experiencing nonlinear geometric instabilities. While the weld backing bars were kept in place after the completion of demand-critical groove welds in the beam flange-column flange, these did not experience fractures.

Chapter 6 proposes a modeling approach to explicitly simulate the hysteretic response of panel zones in steel MRFs. The fracture potential in inelastic beam-to-column connections is considered based on numerical model updating. The adopted modeling approach, which is thoroughly validated with available experimental data, is incorporated into system-level nonlinear simulations in order to quantify the seismic demands of prototype steel MRFs with variable panel zone targeted inelastic distortions. The steel MRFs range from 4 to 20 stories. The seismic collapse risk of the examined steel MRFs is first quantified and compared with that of steel MRF designs that follow the current design paradigm. Hazard curves for local and global engineering demand parameters are developed in the context of performance-based earthquake engineering. These tools are employed to examine the effect of the panel zone inelasticity on the seismic stability and the expected level of structural repairs at pertinent seismic intensities of interest to the engineering profession. This chapter is reproduced from the accepted peer-reviewed manuscript by Skiadopoulos and Lignos (2022b).

Chapter 7 summarizes the primary conclusions of this study. Limitations as well as suggestions for future work are discussed.

A series of appendices supplement the experimental data described in Chapter 5 and the system-level study described in Chapter 6. These appendices include the drawings of the experimental setup, the lateral support system and the instrumentation plan described in Chapter 5. The ultrasonic test certificates together with the welding procedure specification and pertinent information regarding the material properties of the weld and base metal are also summarized in the appendices. Finally, a brief design summary of the steel MRF designs presented in Chapter 6 is also provided.

Chapter 2 Development of inelastic panel zone database

Bibliographic details

This chapter presents the post-print version of the article with the following full bibliographic details:

Skiadopoulos, A., and Lignos, D. G. (2021). “Development of inelastic panel zone database.” *Journal of Structural Engineering*, American Society of Civil Engineers, 147(4), 04721001.

DOI: https://doi.org/10.1061/(ASCE)ST.1943-541X.0002957.

Author’s contribution

Concerning the material presented in this chapter, Andronikos Skiadopoulos developed the methodology, assembled the inelastic panel zone database, analyzed the data, created the figures, wrote the manuscript draft and revised the manuscript. The co-author contributed in developing the methodology presented in this chapter, supervising the work conducted by Andronikos Skiadopoulos, funding acquisition, and reviewing and editing the original and final manuscript drafts.

2.1 Introduction

Modern capacity-designed steel moment resisting frames (MRFs) in seismic regions comprise beam-to-column connections that usually experience limited inelastic behavior in their panel zone web joint during an earthquake. Related experimental studies (Kim and Lee 2017; Lee et al. 2005a, 2002; Lin et al. 2000; Rahiminia and Namba 2013; Shin and Engelhardt 2013a; Tsai and Chen 2000) that examined the behavior of beam-to-column connections designed with either weak panel zones or with a more balanced design approach, suggest that a properly detailed beam-to-column joint may reach up to high lateral drift demands (e.g., 6%), without experiencing much strength and stiffness deterioration as shown in Fig. 2.1a. This agrees with early seminal work on the topic (Fielding and Huang 1971; Ghobarah et al. 1992; Krawinkler et al. 1971; Popov et al. 1985; Popov and Pinkney 1969; Slutter 1981; Tsai and Popov 1988). On the other hand, premature fracture due to excessive panel zone kinking should be prevented at modest lateral drift demands (Chi et al. 1997; El-Tawil et al. 1999; Lu et al. 2000; Mao et al. 2001; Ricles et al. 2004b). This may be achieved by properly balancing the panel zone shear strength with respect to the shear demand coming from the intersecting beam(s) and column.

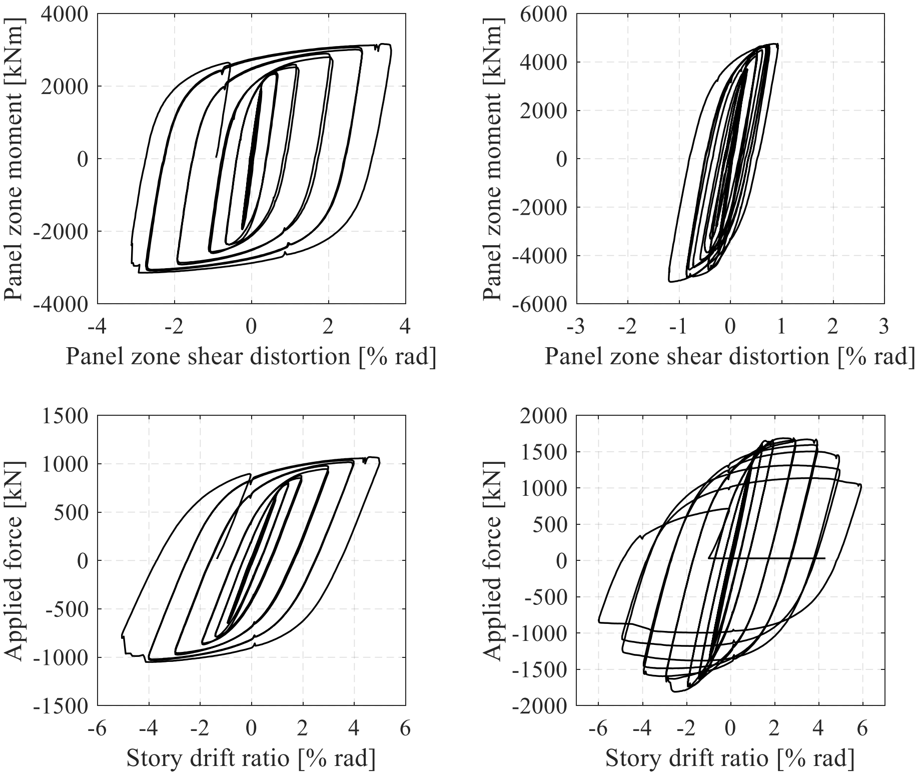

(a) weak panel zone design (b) strong panel zone design

Figure 2.1 Comparison of panel zone and subassembly responses: (a) weak [test data digitized from SPEC-6, Ricles et al. (2004b)]; and (b) strong [test data digitized from SPEC-3, Ricles et al. (2004b)] panel zone design.

The state-of-the-art in panel zone strength modeling (Kim and Engelhardt 2002; Krawinkler 1978; Lee et al. 2005c; Lin et al. 2000), which is adopted in current seismic provisions worldwide (AISC 2016b; CEN 2005) may lead to an appreciable panel zone shear strength overestimation (Brandonisio et al. 2012; El-Tawil et al. 1999; Jin and El-Tawil 2005; Kim and Engelhardt 2002; Krawinkler 1978; Lee et al. 2005c; Qi et al. 2018; Soliman et al. 2018). In lieu of the absence of a robust panel zone strength model, the current design paradigm (AISC 2016b; CEN 2005) tends to concentrate the inelastic deformations in steel or composite steel beams by means of flexural yielding followed by inelastic local buckling, which may be challenging to repair in the aftermath of earthquakes depending on the level of strength and stiffness deterioration as shown in Fig. 2.1b. From a collapse risk standpoint, this may be an important consideration in mainshock-aftershock series.

In the above discussion, the role of the slab is essential. Particularly, the composite action increases the strain demand on the bottom flange of a beam, thereby increasing the fracture potential at the same location (Hajjar et al. 1998; Kim and Lee 2017; Leon et al. 1998). This effect is more apparent in shallow composite steel beams due to the neutral axis shifting towards the upper beam flange (Jones et al. 2002). On the other hand, the panel zone demand decreases while the beam’s effective depth increases due to the presence of the slab (Elkady and Lignos 2014; Kim and Engelhardt 2002).

Following the 1994 Northridge and the 1995 Kobe earthquakes, generous resources were allocated with emphasis on experimental earthquake engineering to comprehend the above challenges in beam-to-column connections by means of full-scale physical testing (Malley 1998; NSF 2004). In line with the cyclic inelastic behavior of panel zone joints in steel MRFs, over 100 experiments have been conducted since the early 1970. The general consensus is that most of the aforementioned data are getting lost over time. They are largely available only in technical reports (often only in hard copies); hence, they cannot be efficiently reused by the research and practice communities. Such dataset constitutes a valuable resource to comprehend the behavior of beam-to-column connections featuring inelastic panel zones by means of simulation-based engineering science and to potentially lead to new paradigms in beam-to-column seismic connection design.

To address the knowledge gap, this chapter describes a compiled inelastic experimental panel zone database, including the methodology undertaken to digitize and systematically document the available experimental data. The assembled database of physical experiments, including the digitized force-story drift ratio and deduced panel zone shear force-inelastic shear distortion relations, along with pertinent material and geometric properties are publicly available through the Zenodo data storage repository (doi: http://www.doi.org/10.5281/zenodo.3689756, Skiadopoulos and Lignos 2020). A comprehensive synthesis of the database is also presented herein, including a number of limitations of available panel zone strength models used in seismic design of modern steel MRFs. A number of recommendations for continuum finite element (CFE) modeling of beam-to-column connections with inelastic panel zones is provided through comprehensive model validation examples. The CFE models are also made publicly available.

2.2 Assembled database description

The collected database comprises 100 tests of steel beam-to-column connection subassemblies, which were mostly subjected to symmetric cyclic loading histories. The test data is gathered from 24 experimental programs on both pre- and post-Northridge connection typologies. While hollow structural sections are not uncommon in columns, the focus herein is on beam-to-column connections comprising wide-flange cross sections. Referring to Fig. 2.2, the test configurations involved exterior and interior beam-to-column connections that were either loaded from the beam(s) (see Figs. 2.2a and 2.2c) or the column (see Figs. 2.2b and 2.2d). The connection types are depicted in Fig. 2.3. These mainly comprise:

- Welded unreinforced flange-welded web connection (WUF-W) (Fig. 2.3a).
- Reduced beam section connection (RBS) (Fig. 2.3b).
- Welded unreinforced flange-bolted web connection (WUF-B) (Fig. 2.3c).
- Bolted flange plate connection (BFP) (Fig. 2.3d).
- Welded flange plate connection (WFP) (Fig. 2.3e).
- Kaiser bolted bracket connection (KBB) (Fig. 2.3f).
- Bolted unstiffened and stiffened extended end-plate connection (BEEP) (Fig. 2.3g).
- Welded unreinforced flange-welded web composite steel beam connection with or without RBS (Fig. 2.3h).

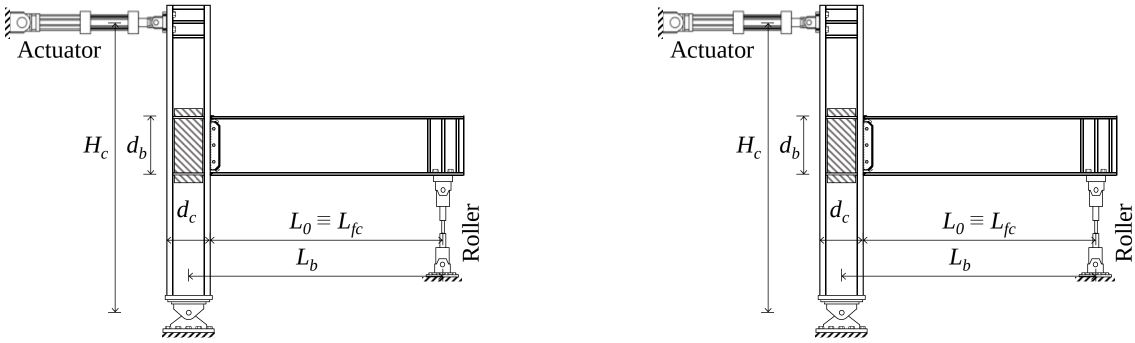
Actuator
H_c
d_b
d_c
$L_0 \equiv L_{fc}$
L_b
Roller
Actuator
H_c
d_b
d_c
$L_0 \equiv L_{fc}$
L_b
Roller

(a) exterior, loaded from beam (b) exterior, loaded from column

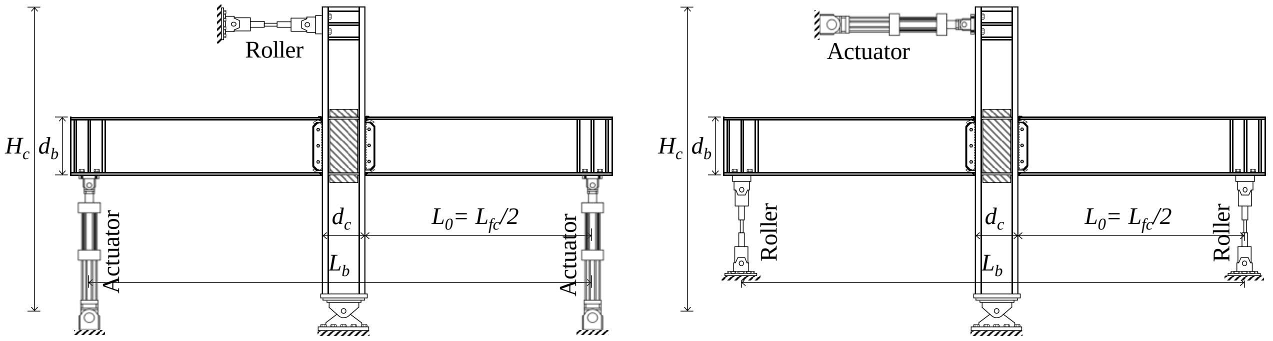
Roller
H_c
d_b
Actuator
d_c
$L_0= L_{fc}/2$
L_b
Actuator
Actuator
H_c
d_b
Roller
d_c
$L_0= L_{fc}/2$
L_b
Roller

(c) interior, loaded from beams (d) interior, loaded from column

Figure 2.2 Typical cruciform subassembly test configurations.

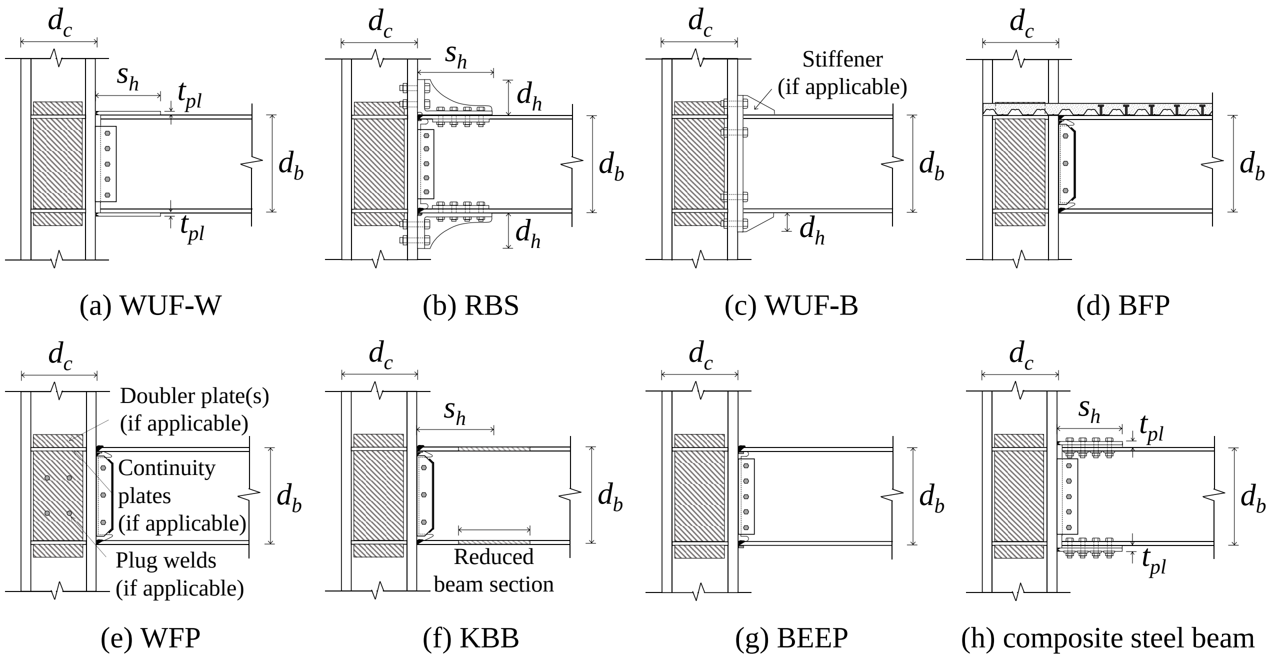
d_c
s_h
t_{pl}
d_b
d_h
Stiffener
(if applicable)
(a) WUF-W
(b) RBS
(c) WUF-B
(d) BFP
Doubler plate(s)
(if applicable)
Continuity
plates
(if applicable)
Plug welds
(if applicable)
Reduced
beam section
(e) WFP
(f) KBB
(g) BEEP
(h) composite steel beam

Figure 2.3 Representative beam-to-column connection typologies included in the assembled inelastic panel zone database.

The assembled dataset includes 23 exterior (Figs. 2.2a and 2.2b) and 16 interior (Figs. 2.2c and 2.2d) pre-Northridge connections with bare steel beams (FEMA 1997; Fielding and Huang 1971; Ghobarah et al. 1992; Kim et al. 2015; Kim and Lee 2017; Krawinkler et al. 1971; Popov et al. 1985; Slutter 1981). These mainly involved self-shielded flux-cored arc (FCAW-SS) complete joint penetration (CJP) welds in the beam flange-to-column face connections. These welds featured a E70T-4 weld electrode. The backing bars at both beam flanges were left in place after welding. In these tests, the access hole geometry of Fig. 2.4a was adopted. Two experimental programs (Kim and Lee 2017; Uang et al. 2000) employed retrofitted pre-Northridge connection configurations with a composite slab in place. A summary of the gathered data is shown in Table 2.1 including basic material and geometric characteristics of the respective test specimens (i.e., connection type, presence of slab, presence of reduced beam section, beam depth, d_b, panel zone aspect ratio, d_b/d_c and column steel grade).

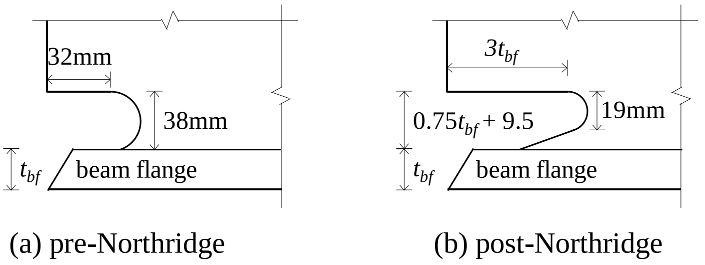
32mm
38mm
t_{bf}
beam flange
(a) pre-Northridge
$3t_{bf}$
$0.75t_{bf}$+ 9.5
19mm
(b) post-Northridge

Figure 2.4 Typical access hole geometries.

Table 2.1 Summary of pre-Northridge beam-to-column connection detailing testing programs in the assembled database (in alphabetical order).

Reference	Connection type	Slab	RBS	d_b (mm)	d_b/d_c	Column steel grade
FEMA (1997)	WUF-B	-	-	754-912	2.0-2.2	A572 Gr. 50
Fielding and Huang (1971)	WUF-W	-	-	629	1.6	A36
Ghobarah et al. (1992)	BEEP	-	-	358/406	1.0-1.3	not reported
Kim et al. (2015)	KBB	-	-	912	2.3	A572 Gr. 50
Kim and Lee (2017)	Retrofit	Yes	-	500	1.3	SM490
Krawinkler et al. (1971)	WUF-B	-	-	254/348	1.3-1.5	A36
Popov et al. (1985)	WUF-B	-	-	457-476	0.9-1.0	A572 Gr. 50
Slutter (1981)	WUF-B	-	-	602	1.7	A36
Uang et al. (2000)	Retrofit	Yes	-	912	1.9	A36

Similarly, 47 post-Northridge connection tests with bare steel beams are included in the assembled database (Chi and Uang 2002; Ciutina and Dubina 2008; Engelhardt et al. 2000; Kosarieh and Danesh 2016; Lee et al. 2005a, 2002; Rahiminia and Namba 2013; Ricles et al. 2000, 2004b; Sato et al. 2007; Schneider and Teeraparbwong 2000; Shin 2017; Stojadinović et al. 2000; Tsai and Chen 2000). Nine subassemblies with steel beams composite with a reinforced concrete slab (Engelhardt et al. 2000; Ricles et al. 2004b) were also collected. One test involved a composite steel beam as part of a sub-system with two wide-flange steel columns (Del Caprio et al. 2014, 2016).

Thirty-two (32) of the collected specimens include doubler plates to control the anticipated inelastic panel zone web shear distortion. Post-Northridge connection doubler plates, which were mainly fabricated from A572 Gr. 50 steel (nominal yield stress, f_y = 345MPa), were mostly attached to the respective column web with CJP welds of either E70T-1 or E71T-8 weld electrode. Horizontal doubler plate and plug welds (see Fig. 2.3a) were employed, when necessary, according to AWS (2016).

The distinction between pre- and post-Northridge beam-to-column connections is associated with the connection detailing and welding specifications. These mainly include:

- Removal of the bottom backing bar and fillet weld reinforcement of the beam flange-to-column face CJP root weld in the latter connection typology.
- Rigorous specification and practice for welding in the latter connection typology in accordance with AWS (AWS 2016; Barsom et al. 2000; Johnson 1997; Miller 2017). Beam flange-to-column face welds are deemed demand critical. From the approved processes for such welds, typically FCAW-SS is utilized and from the permitted weld electrodes, E70T-6 and E70TG-K2.
- Improved access hole geometry for minimizing stress concentrations according to Ricles et al. (2002a) subsequent to the SAC studies (Ricles et al. 2000). This is shown in Fig. 2.4b.
- While the WUF-B connection was the common practice prior to Northridge 1994 earthquake, this is not anymore the case for intermediate and special MRFs according to AISC (2016c).

The assembled dataset of post-Northridge beam-to-column connections, together with pertinent geometric and material characteristics, are summarized in Table 2.2.

Table 2.2 Summary of post-Northridge beam-to-column connection detailing testing programs in the assembled database (in alphabetical order).

Reference	Connection type	Slab	RBS	d_b (mm)	d_b/d_c	Column steel grade
Chi and Uang (2002)	WUF-B	-	Yes	912	1.3	A992 Gr. 50
Ciutina and Dubina (2008)	WUF-W	-	-	360	1.2	S235
Del Caprio et al. (2014)	WUF-W	Yes	Yes	353	1.1	A572 Gr. 50
Engelhardt et al. (2000)	WUF-W/ WUF-B	Yes	Yes	912	2.0-2.1	A572 Gr. 50
Kosarieh and Danesh (2016)	WFP	-	-	400	1.1	S235
Lee et al. (2002)	WUF-W	-	-	617	1.5-1.6	A992 Gr. 50
Lee et al. (2005a)	WUF-W	-	Yes	600/700	1.5-1.6	SM490
Rahiminia and Namba (2013)	WUF-W	-	-	400	1.3	SM490A
Ricles et al. (2000)	WUF-W	-	-	912	2.0-2.1	A572 Gr. 50
Ricles et al. (2004b)	WUF-W	Yes	Yes	757/912	1.1-1.3	A572 Gr. 50
Sato et al. (2007)	BFP	-	-	757/780	1.9	A992 Gr. 50
Schneider and Teeraparbwong (2000)	BFP	-	-	602/754	1.6-1.9	A572 Gr. 50
Shin (2017)	WUF-W/BFP	-	-	599-912	0.9-2.0	A992 Gr. 50
Stojadinović et al. (2000)	WUF-B	-	-	754	2.0	A572 Gr. 50
Tsai and Chen (2000)	WUF-W	-	Yes	600	2.0	A572 Gr. 50

2.2.1 Beam/column material and geometric characteristics

Figure 2.5 shows histograms depicting important material and geometric parameters of the assembled inelastic panel zone database. While most of the pre-Northridge tests employed WUF-B connections, the post-Northridge connections mainly employed WUF-W (with/without RBS) and BFP/WFP connections (see Fig. 2.5a). Referring to Fig. 2.5b, the gathered beam-to-column connections feature beam-to-column depth aspect ratios, d_b/d_c, ranging from 0.9 to 2.3. The columns employ both stocky and deep cross sections with flange thicknesses, t_{cf}, ranging from 10 to 80mm as shown in Fig. 2.5c. The variation of the above parameters is of particular interest for the assessment of existing panel zone strength models as well as the development of new ones. From Fig. 2.5d, the beam depths, d_b, range from 250 to 900 mm and the respective shear span-to-beam depth ratios, L_o/d_b (L_o: beam shear span from column face to beam inflection point, as per Fig. 2.2) range from about 2.5 to 8 (see Fig. 2.5e). Since d_b and L_o/d_b affect the fracture potential of beam-to-column connections (El-Tawil et al. 1999; FEMA 2000a), the variation of these parameters aids the beam-to-column connection performance assessment discussed hereinafter. Referring to Fig. 2.5f, while the significant majority of pre-Northridge connections are comprised of A36 (nominal yield stress, f_y = 250MPa) steel beams, the ones in post-Northridge connections employ A572 or A992 Gr 50 steel (f_y = 345MPa) or equivalent. The collection process includes the measured geometric and material properties of the respective steel beams and columns, when available.

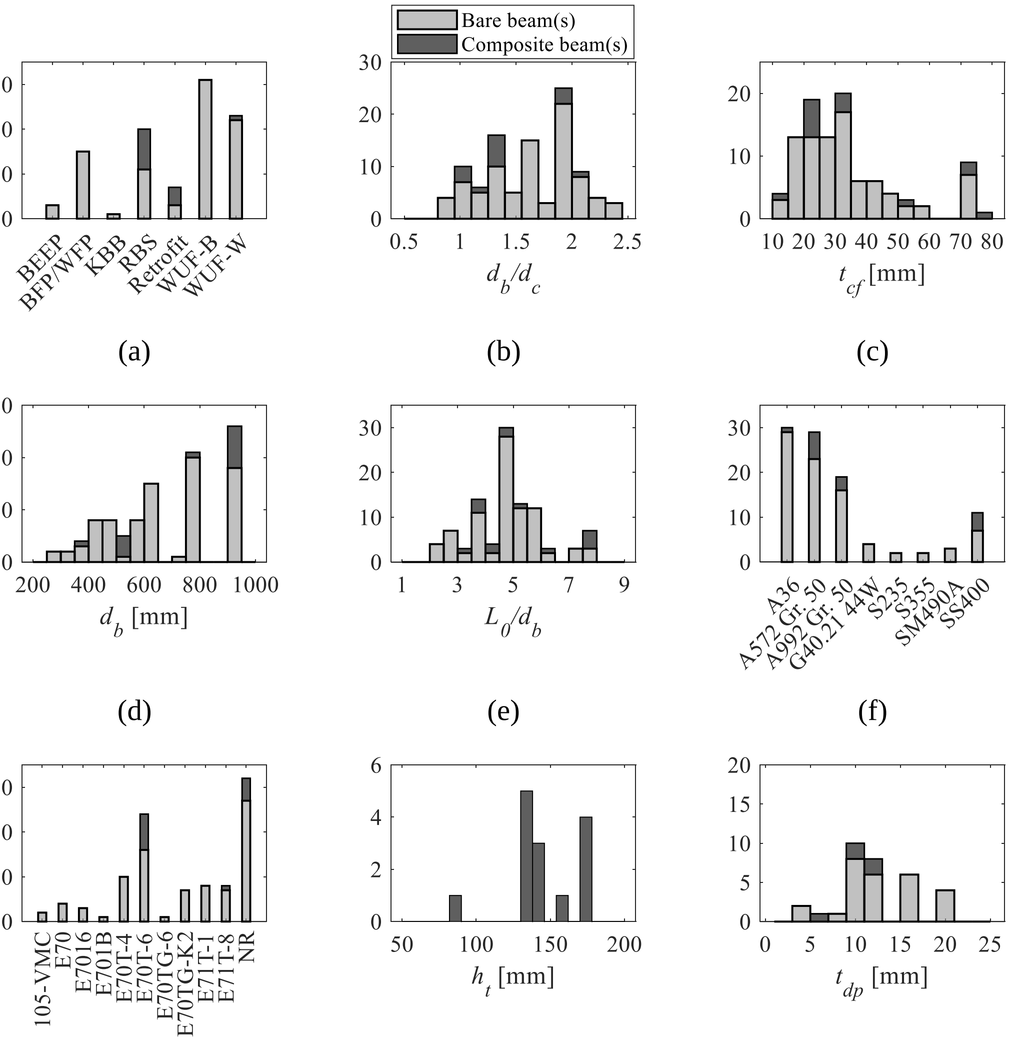

(a) (b) (c)

(d) (e) (f)

(g) (h) (i)

Figure 2.5 Histograms depicting geometric and material properties of the assembled inelastic panel zone experimental data.

Since the beam-to-column connection cyclic performance is highly dependent on the construction detailing, such as the presence of the weld backing bar, the weld electrode and the access hole geometry (FEMA 2000a), this information is also reported in the assembled database. Referring to Fig. 2.5g, the variation of beam-to-column face weld electrodes (mainly E70T-4, E70T-6, E71T-1 and E71T-8) is significant. Finally, nearly 60 specimens (mainly in post-Northridge connections) have the bottom beam flange backing bar removed, according to AWS (2016).

With regard to the composite action, the slab and deck geometry, the concrete and reinforcement material properties as well as the shear stud geometric and material properties are systematically collected. The above parameters are useful to infer the degree of composite action and, thus, the composite steel beam plastic flexural resistance according to current design standards (AIJ 2007, 2010; AISC 2016c; a; CEN 2004c; a). Referring to Fig. 2.5h, the total slab depth, h_t, of the collected dataset varies from 80 to 180mm. Nine tests have a deck rib oriented in parallel to the beam, while in the rest, the deck rib is oriented perpendicular to the steel beam. Finally, the measured cylinder concrete compressive strength varies from 21 to 47 MPa. In most of the collected tests, the 28 days compressive strength was reported by the experimentalists. The degree of composite action as per AISC (2016a; b), ranges from 7-49% . Finally, from the collected tests, 25 employ one doubler plate, while seven employ two. The doubler plate thickness, t_{dp}, ranges from 4-20mm as shown in Fig. 2.5i.

Figure 2.6 shows the measured R_y (i.e., ratio of the measured yield stress to specified minimum yield stress) boxplots for all the beams and column materials. The central line represents the median, while the bottom and top box edges the 25th and 75th percentiles of the collected sample. Extreme values (i.e., '-' symbol) and outliers (i.e., '+' symbol) are also depicted in the boxplots. According to the US practice, the recommended R_y value (i.e., R_y = 1.1) for A572 and A992 Gr 50 steels is consistent with the collected data, whereas for A36 steel, the proposed value of 1.5 according to AISC (2016a) seems to be well above those obtained from the data (i.e., 1.25). The same applies for European steel (i.e., for S235), where a value of R_y = 1.4 is recommended (Braconi et al. 2013). However, in this case the number of material data was only limited to six.

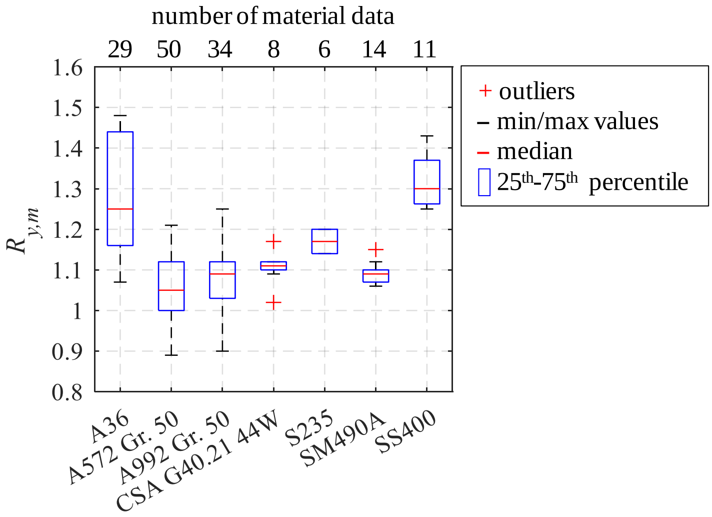

Figure 2.6 Measured R_y boxplots for the beam and column steel materials.

2.2.2 Panel zone material and geometric characteristics

To quantify the panel zone shear resistance, based on available panel zone models (see Fig. 2.7a), its material and geometric characteristics are identified. Thus, the beam and column cross-sectional (see Fig. 2.7b) and material properties (as described in the previous section) along with the doubler and continuity plate geometric (see Fig. 2.7c) and material properties are systematically documented in the database.

If doubler plates are present, their number, n_{dp}, their thickness, t_{dp}, their measured yield stress, f_{ydp}, and the distance between the plug welds (if applicable) (see Fig. 2.7c) are archived in the database. The continuity plate thickness, t_{cp}, and the depth, d_{cp}, (see Fig. 2.7c) are also documented. The material properties of these plates are not collected because they were not available, in most of the respective experimental reports.

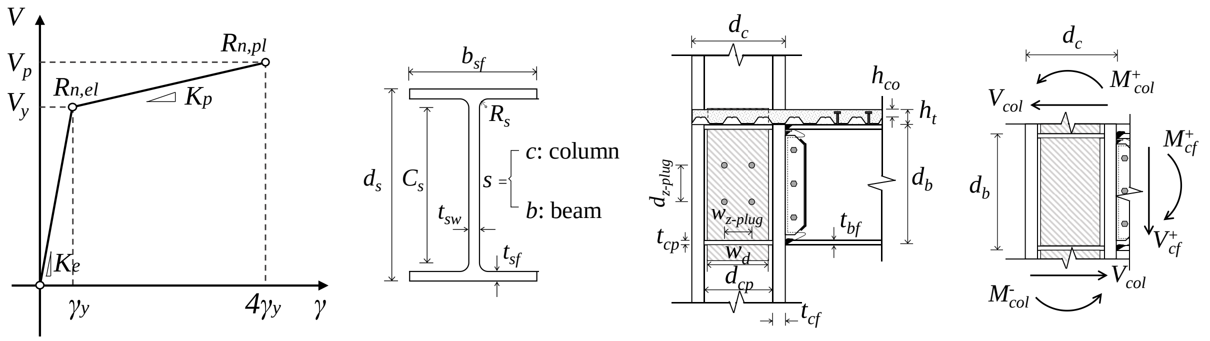

(a) Krawinkler model (b) cross section (c) connection geometry (d) action forces

Figure 2.7 Panel zone: (a) model (Krawinkler 1978); (b) cross-sectional characteristic dimension; (c) connection characteristic dimensions; and (d) action forces.

In WUF-W and WUF-B connections, it is assumed that their effective depth equals $d_{eff} = d_b - t_{cf}$. In KBB connections, d_{eff} is defined from the centroidal distance between the bolt groups of the two brackets (AISC 2016c), meaning $d_{eff} = d_b + d_h$ (see Fig. 2.3f). In BEEP connections, studies have shown that rib stiffeners increase the lever arm, thus decreasing the demand in the panel zone (D'Aniello et al. 2017). However, the collected connections (Ghobarah et al. 1992) are all unstiffened. We assume that $d_{eff} = d_b - t_{bf}$ holds true in this case. For bare beam interior subassemblies, the beam effective depth is the same for the two column faces (i.e., $d^+_{eff} = d^-_{eff}$). For composite steel beams under sagging, the effective depth is assumed to be, $d^+_{eff} = d_b + h_t - h_{co}/2 - t_{bf}/2$ (see Fig. 2.7c) in a similar manner with El Jisr et al. (2019) because the force acting at the top flange is shifted due to the presence of the slab (Elkady and Lignos 2014; Kim and Engelhardt 2002). While Castro et al. (2005) provides a more thorough consideration of the composite effect on the panel zone demand, herein the authors chose to interpret the composite beam subassembly data based on the above effective depth assumption to retain simplicity in the computations.

2.2.3 Digitized data

The panel zone and subassembly global hysteretic diagrams are fully digitized. In particular, the panel zone shear force, V_{pz}, versus shear distortion, γ, and the applied force, F, versus story drift ratio (SDR) relationships are deduced. The digitization process was conducted with a software called Digitizer (Lignos and Krawinkler 2012). During this process, nearly 20 digitized data per loading interval are identified. In regions where the Bauschinger effect is evident on the deduced hysteretic diagram, the digitized data density is increased. This leads to a sufficient accuracy for assessing the panel zone inelastic behavior. Representative digitization examples are shown in Figs. 2.8a and 2.8b for the panel zone and the global subassembly responses, respectively.

The maximum attained panel zone shear distortion, γ_{max}, and peak story drift ratio, SDR_{max}, of each connection prior to failure is automatically extracted. Hereinafter, failure is defined based on a 20% loss of the connection's flexural capacity. This may be due to fracture or beam/column local and/or member nonlinear geometric instabilities.

We consider the maximum positive and negative cyclic interval values as shown in Figs. 2.8a and 2.8b, to identify γ_{max} and SDR_{max}, respectively. The histograms of γ_{max} (normalized by γ_y, which is the panel zone yield shear distortion angle) and SDR_{max} are depicted in Figs. 2.8c and 2.8d. From these figures, a large portion of the deduced γ_{max} and SDR_{max} range between 4-12γ_y and 5-6%, respectively. It is noteworthy that a considerable number of beam-to-column panel zone webs reached a shear distortion of more than 12γ_y.

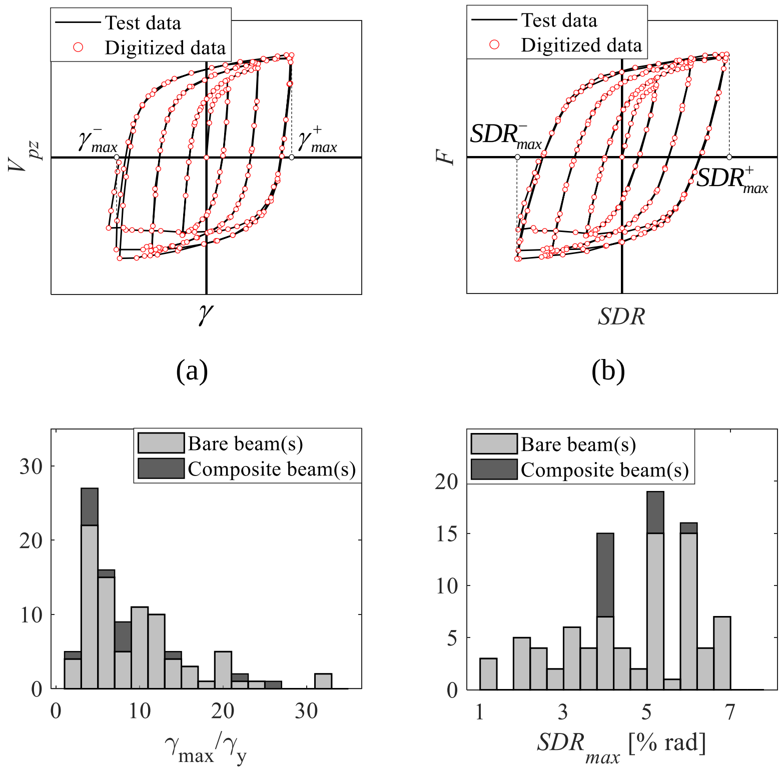

(a) (b)

(c) (d)

Figure 2.8 Typical digitized local and global responses along with representative histograms of panel zone and subassembly response parameters.

2.2.4 Decomposed deformation quantities

The deduced $V_{pz} - \gamma$ relation is provided in the database as a characteristic of the digitized panel zone hysteretic diagrams. If the available panel zone data was not in this form, force equilibrium and geometric compatibility principles were applied to deduce V_{pz} and γ. Figure 2.9 shows a typical column-loaded interior subassembly decomposition of deformations for the panel zone, the beams and the column. Based on Fig.

2.9a, the panel zone contribution to SDR, θ_{pz}, is related to γ by Eq. (2.1). Additionally, the chord rotation of the beam, θ_b', and the column, θ_c', are related to their contribution to SDR by Eqs. (2.2) and (2.3), respectively (see Figs. 2.9b and 2.9c). If the global response and the chord rotations of the beam(s) and the column are the only available information, then γ is calculated by combining Eqs. (2.1), (2.2) and (2.3), given that $SDR = \theta_{pz} + \theta_b + \theta_c$.

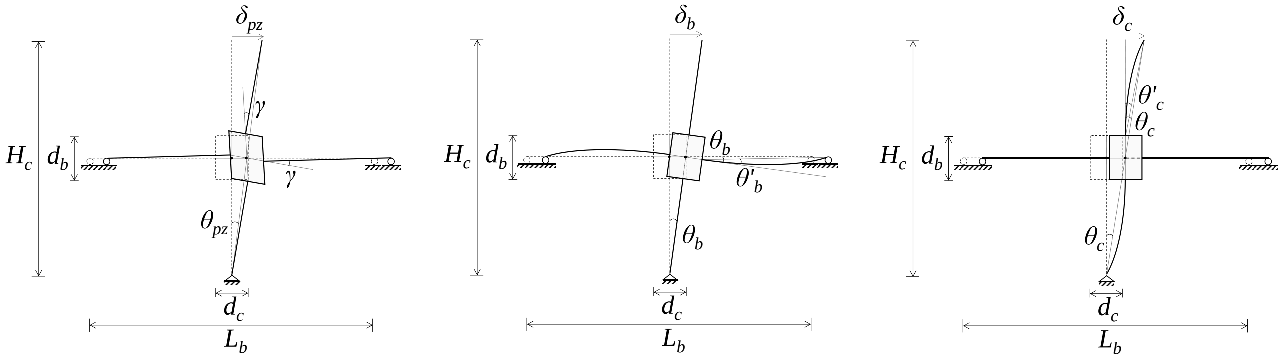

(a) panel zone (b) beam (c) column

Figure 2.9 Column-loaded interior subassembly decomposition of deformations.

$$\theta_{pz} = \gamma\left(1 - \frac{d_c}{L_b} - \frac{d_b}{H_c}\right) \tag{2.1}$$

$$\theta_b = \theta_b' \cdot \frac{L_b - d_c}{L_b} \tag{2.2}$$

$$\theta_c = \theta_c' \cdot \frac{H_c - d_b}{H_c} \tag{2.3}$$

2.2.5 Predicted panel zone resistance and demand

The AISC (2016b) panel zone model, which is a refined version of the one proposed by Krawinkler (1978), is expressed in Eqs. (2.4) and (2.5) for elastic and inelastic panel zone design, respectively (see Fig. 2.7a). In these equations, the nomenclature is in accordance with Figs. 2.7b and 2.7c. In Europe, CEN (2005) considers the contribution of the column web in a similar manner with $R_{n,el}$. If continuity plates are present, Eq. (2.6) is employed to account for the plastic flexural resistance of the column flanges in the kinking locations. Modifications of the Krawinkler (1978) model, which were found in the literature (Kim and Engelhardt 2002; Lee et al. 2005c; Lin et al. 2000), are also included in the database.

$$R_{n,el} = 0.6 \cdot f_y \cdot d_c \cdot t_w \tag{2.4}$$

$$R_{n,pl} = 0.6 \cdot f_y \cdot d_c \cdot t_w \cdot \left(1 + \frac{3 \cdot b_{cf} \cdot t_{cf}^2}{d_b \cdot d_c \cdot t_w}\right) \tag{2.5}$$

$$V_{wp,Rd} = \frac{0.9 f_y A_v}{\sqrt{3}} + \frac{4 M_{pl,fc,Rd}}{d_b - t_{bf}} \tag{2.6}$$

$$\frac{4M_{pl,fc,Rd}}{d_b - t_{bf}} \leq \frac{2M_{pl,fc,Rd} + 2M_{pl,st,Rd}}{d_b - t_{bf}}$$

Where, A_v is the effective shear area of the column; $M_{pl,fc,Rd}$ is the design plastic moment resistance of a column flange in the panel zone kinking locations; and $M_{pl,st,Rd}$ is the design plastic moment resistance of a continuity plate. When doubler plates are utilized, according to AISC (2016b), the effective panel zone thickness for the shear strength computation in Eqs. (2.4) and (2.5) should be replaced by $t_w = t_{cw} + n_{dp} \cdot t_{dp}$. On the other hand, only one doubler plate is accounted for as per CEN (2005) [see clause 6.2.6.1(6)], even in cases where two are present.

According to today's practice, the panel zone shear demand, R_u [see Eq. (2.7)] should be less or equal to either $R_{n,el}$, or, $R_{n,pl}$. Herein, we compute the panel zone shear demand based on force equilibrium (see Fig. 2.7d), by assuming that the probable moment, $M_{b,pr}$, is attained at the anticipated beam plastic hinge locations according to Eq. (2.8):

$$\begin{gathered}\text{Interior joints: } R_u = V_{bf}^{+} + V_{bf}^{-} - V_{col} = \frac{M_{cf}^{+}}{d_{eff}^{+}} + \frac{M_{cf}^{-}}{d_{eff}^{-}} - V_{col} \\ \text{Exterior joints: } R_u = V_{bf}^{+} - V_{col} = \frac{M_{cf}^{+}}{d_{eff}^{+}} - V_{col}\end{gathered} \tag{2.7}$$

$$\begin{gathered}M_{b,pr} = C_{pr} \cdot R_y \cdot f_{yb} \cdot Z_{eb} \\ C_{pr} = \frac{f_{yb} + f_{ub}}{2f_{yb}} \leq 1.2 \\ \text{For WUF-W connections, } C_{pr} = 1.4\end{gathered} \tag{2.8}$$

where, Z_{eb} is the effective plastic modulus of the beam within the assumed plastic hinge location; f_{yb} is the specified minimum yield stress of the beam; f_{ub} is the specified minimum tensile stress of the beam.

For RBS connections, $M_{b,pr}$ is calculated at the centre of the RBS (i.e., M_{RBS}) and is transferred to the column face, according to Eq. (2.9). The same holds true for BFP, WFP and KBB connections, whose plastic hinge is shifted by s_h from the column face (see Figs. 2.3d, 2.3e and 2.3f):

$$M_{cf} = M_{RBS} + V_{RBS} \cdot s_h \tag{2.9}$$

where, V_{RBS} is the shear force at the centre of the RBS.

In the above computations, when the measured material properties are employed, $R_y \cdot f_{yb}$ is replaced by f_{ybm}, which represents the measured yield stress of the beam web or flange. For the panel zone demand computation, an effective yield stress weighted based on the beam web and flanges area is accounted (i.e., f_{yb-avg}). For the panel zone shear strength computation, the measured column web yield stress, f_{ycw}, is considered for the web contribution, while that of the column flange, f_{ycf}, for the flange contribution. When doubler plate(s) are present, their yield stress, f_{ydp}, is accounted for their contribution in the panel zone shear strength. Same assumptions hold true for composite steel beam-to-column connections.

The V_{col} computation [see Eq. (2.7)] is based on a force equilibrium of the statically determinate interior or exterior subassembly systems of Fig. 2.2. Regardless of the loading application [load applied on beam(s) or column], the R_u prediction equation does not change. However, this differs for interior and exterior subassemblies due to the different number of beams employed (i.e., two versus one, respectively), as shown in Eq. (2.10).

$$R_u = \frac{aM_{cf}}{d_{eff}} \cdot \left(\frac{1 - \frac{ad_c}{2L_b} - \frac{d_b}{H_c}}{1 - \frac{ad_c}{2L_b}} \right) \tag{2.10}$$

where $a = 1$ for exterior joints and $a = 2$ for interior joints

2.2.6 Measured panel zone model quantities

The digitized first cycle envelope shown in Fig. 2.10a is utilized to deduce the measured panel zone response parameters of interest and to compare with available panel zone model predictions. The measured parameter deduction is achieved through a MATLAB code (doi: http://www.doi.org/10.5281/zenodo.3689756, Skiadopoulos and Lignos 2020). This script automates the panel zone parameter extraction process.

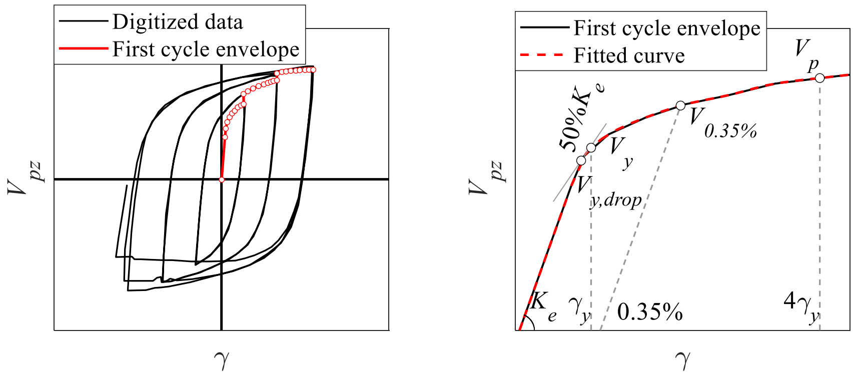

(a) first cycle envelope (b) panel zone deduced quantities

Figure 2.10 Representative example of data extraction.

The deduced parameters of interest are shown in Fig. 2.10b. They comprise: (a) the elastic panel zone stiffness, K_e, which is identified based on the the first few digitized data points. If the data resolution is not sufficient, then K_e is extracted from the first unloading excursion; (b) the yield shear strength, V_y, at a shear distortion angle γ_y, according to Krawinkler (1978); (c) the yield shear strength, $V_{y,drop}$, corresponding to a 50% drop in K_e; and (d) the panel zone shear strength, $V_{0.35\%}$, corresponding to the 0.35% inelastic shear distortion offset, according to the Japanese provisions (AIJ 2012). Moreover, the post-yield panel zone shear strength, V_p, at $4\gamma_y$ is reported.

2.3 Maximum attained lateral drift demands prior to connection fracture

According to AISC (2016a), prequalified connections, shall not exhibit more than 20% loss of their nominal flexural resistance at a targeted SDR = 4%. Figure 2.11 shows the SDR_{max} versus L_0/d_b for the collected pre- and post-Northridge connections. It is observed that more than half of the pre-Northridge connections do not comply with the above prequalification criteria. This is attributed to well-known issues related to the material, geometry and connection construction practices as discussed in FEMA (2000a). In Figure 2.11, pre-Northridge tests (Fielding and Huang 1971; Ghobarah et al. 1992; Krawinkler et al. 1971; Slutter 1981) that achieved the AISC's 4% drift target were comprised of shallow cross sections. Test specimens featuring deep cross sections (Engelhardt and Husain 1993; FEMA 1997) are representative of those that failed in the 1994 Northridge earthquake and are among the ones with high fracture potential as shown in Fig. 2.11.

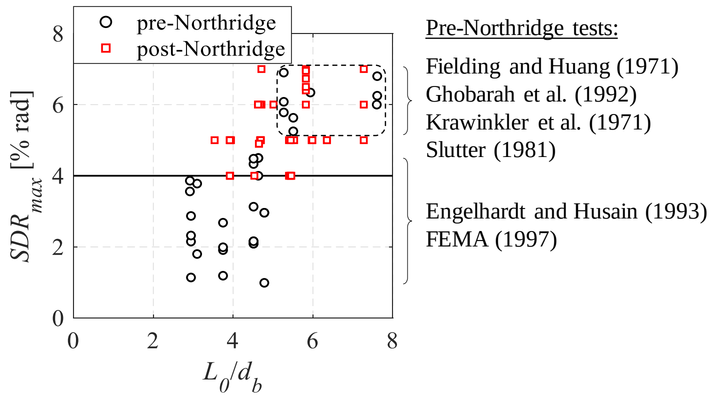

Pre-Northridge tests:

Fielding and Huang (1971)
Ghobarah et al. (1992)
Krawinkler et al. (1971)
Slutter (1981)

Engelhardt and Husain (1993)
FEMA (1997)

Figure 2.11 Maximum story drift ratio versus beam span-to-depth ratio of the collected data.

A series of experimental (Lee et al. 2005b; Ricles et al. 2000, 2002a) and finite element studies (Chi et al. 1997; El-Tawil et al. 1999; Lu et al. 2000; Mao et al. 2001) proposed modifications in the respective beam-to-column connection typologies, leading to a substantial connection performance improvement. The test data are also superimposed in Fig. 2.11. While these data points satisfy the AISC (2016a) prequalification criteria, there is no consensus with regard to the level of acceptable panel zone inelastic shear distortions. To provide insight regarding this matter, the probability of connection failure given SDR and γ is quantified. A joint (bivariate) lognormal cumulative distribution is assumed. The null hypothesis of the predictor variables following lognormal distribution was accepted with a 5% significance level according to the Kolmogorov-Smirnov (Kolmogorov 1933; Smirnov 1939) and Shapiro-Wilk (Shapiro and Wilk 1965) [or Shapiro-Francia (Shapiro and Francia 1972) for leptokurtic samples with kurtosis > 3] goodness-of-fit tests. The correlation coefficient, ρ, of the predictor variables is shown in Table 2.3. It is observed that ρ is diverging from zero (i.e., higher than 0.2) for all connection types, rendering the predictor variables dependent. That being said, the probability density function (i.e., PDF) of the bivariate lognormal distribution accounts for this collinearity.

Table 2.3 Lognormal distribution parameters and correlation coefficients for γ/γ_y and SDR.

Connection type	pre-Northridge		post-Northridge		BFP/WFP		Composite steel beam(s)	
Variable (X)	γ/γ_y	SDR	γ/γ_y	SDR	γ/γ_y	SDR	γ/γ_y	SDR
Mean (μ_X)	5.9	2.7	7.6	4.9	8.6	6.0	7.3	4.4
St. deviation (σ_X)	2.0	1.6	1.8	1.2	1.9	1.1	2.0	1.2
Correlation coeff. (ρ)	0.77		0.23		0.36		0.19	

Figure 2.12 illustrates the corresponding joint cumulative distribution functions per connection type. The probability of failure in pre-Northridge connections (see Fig. 2.12a) is qualitatively much higher than that of post-Northridge connections (see Fig. 2.12b), regardless of the attained SDR and γ. Interestingly, reinforced beam-to-column connections (i.e., BFP and WFP) (see Fig. 2.12c) enjoy a decreased probability of failure compared to the typical unreinforced post-Northridge connection (i.e., WUF-W) regardless of the respective inelastic panel zone shear distortion. Referring to Fig. 2.12d, composite steel beams are likely to experience a larger probability of failure at a given SDR compared to their bare beam counterparts. To "digest" the deduced results at $4\gamma_y$, which is considered a possible panel zone inelastic shear distortion target in balanced design of beam-to-column connections, and at SDR = 4%, pre-Northridge connections have at least 30% probability of failure whereas post-Northridge connections do not exhibit more than a 2% chance. At $6\gamma_y$, the respective probabilities of failure become at least 50% and 5% respectively. Noteworthy is the performance of reinforced connections that can easily attain $10\gamma_y$ at SDR = 4% without experiencing any loss of strength due to premature fracture and/or beam local buckling. This agrees with prior work (El Jisr et al. 2019).

2.4 Assessment of commonly used panel zone design models

The assembled database may be utilized for the assessment of available panel zone models; hence, their applicability range may be identified along with potential limitations to be addressed in future research. Figure 2.13 shows a comparison of the analytical panel zone elastic shear stiffness, K_e, which is predicted by a number of available models, and the deduced one from the assembled data, $K_{e,m}$. From this figure, the AISC (2016b); CEN (2005) and Kim and Engelhardt (2002) models consistently overestimate K_e by nearly 30%. When the panel zone geometry comprises two doubler plates, CEN (2005) only accounts for one [see clause 6.2.6.1(6)]. The CEN (2005) and the AISC (2016b) models attain a comparable accuracy only when both doubler plates are considered in the panel zone shear strength computations. Referring to Fig. 2.13, the Lin et al. (2000) model provides reasonable panel zone elastic stiffness predictions. This model considers the bending deformation mode within the panel zone in an empirical fashion. Same observations hold true for the collected composite steel beams.

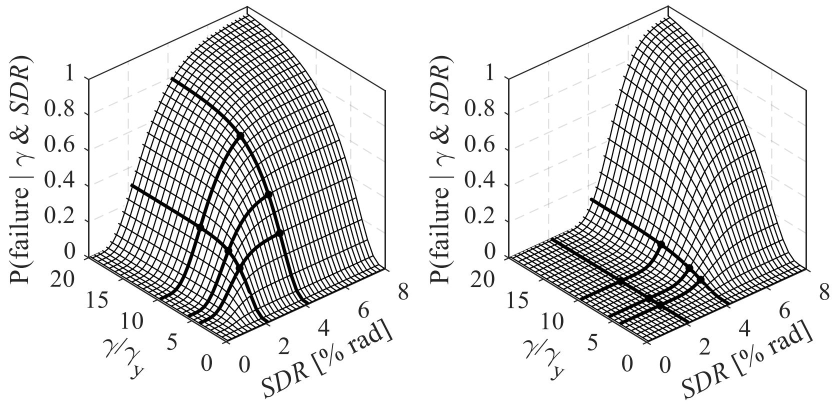

(a) pre-Northridge (b) post-Northridge

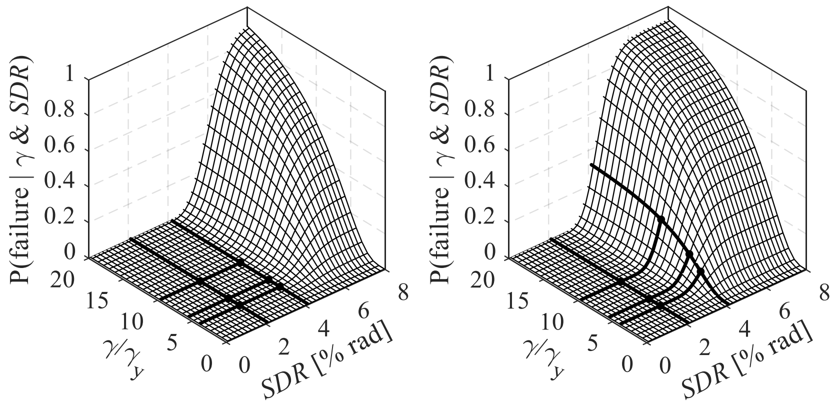

(c) BFP/WFP (d) composite steel beam(s)

Figure 2.12 Probability of connection failure given SDR and γ for different beam-to-column connection types.

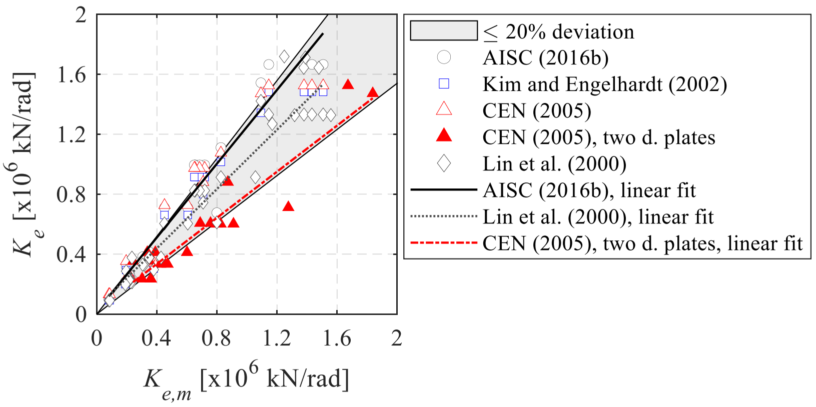

Figure 2.13 Comparison of theoretical and measured panel zone elastic stiffness, K_e.

Figure 2.14 shows the prediction of V_p according to all the available panel zone models with respect to t_{cf}. In this figure, the straight lines indicate the respective trends. The predicted V_p values are normalized with respect to the measured values $V_{p,m}$. It is observed that the AISC (2016b) model overestimates V_p by 20% to 40% for thick column flanges (t_{cf} > 50mm) regardless of the presence of the composite slab. This is a well-known issue, which has been reported in a number of studies (Brandonisio et al. 2012; El-Tawil et al. 1999; Jin and El-Tawil 2005; Kim and Engelhardt 2002; Krawinkler 1978; Lee et al. 2005c; Qi et al. 2018; Soliman et al. 2018). In Fig. 2.14, the models by Lee et al. (2005c) and Lin et al. (2000) deviate from the measured values. Noteworthy is the opposite trend of the CEN (2005) model [i.e., Eq. (2.6)] to that of the AISC (2016b) model [i.e., Eq. (2.5)]. Indeed, in the absence of continuity plates, CEN (2005) disregards the panel zone post-yield shear strength. As such, in shallow columns comprising stocky cross sections (i.e., W14x398) that, typically, do not necessitate continuity plates, the panel zone “ultimate” strength equals V_y. This generally underestimates by more than 20% the panel zone shear strength. Finally, in specimens utilizing two doubler plates, accounting only for one leads to a shear strength underestimation by 20%.

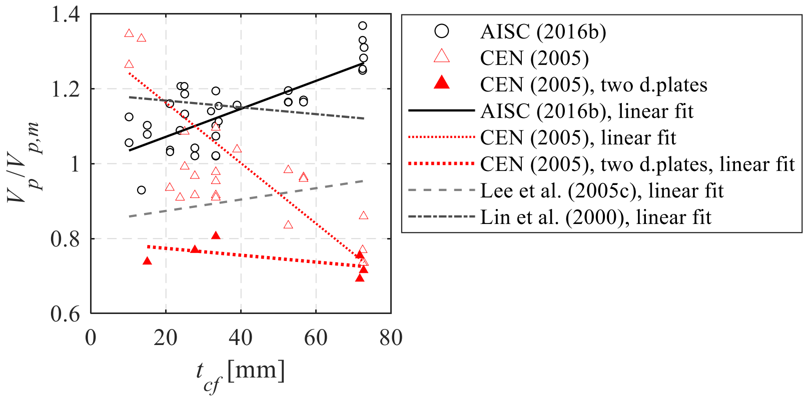

Figure 2.14 Comparison of theoretical and measured panel zone strength at $4\gamma_y$ versus t_{cf}.

2.5 Balanced design aspects

Panel zone yielding delays the inelastic deformation concentration in steel beams (Lee et al. 2005a; Ricles et al. 2004b). Figure 2.15 shows the beam and panel zone plastic rotation contribution to the total one versus the strength ratio, $R_u/R_{n,pl}$, for all the available tests. In this figure, the plastic rotation contribution is normalized with respect to the total connection plastic rotation. The efficiency of the $R_u/R_{n,pl}$ ratio to describe the panel zone weakness relies on the accuracy of $R_{n,pl}$ and R_u. The former is based on a well-established panel zone model (Krawinkler 1978) in the literature as per AISC (2016b). The latter assumes hardening in the beam flexural resistance calculation as per C_{pr}, regardless of the panel zone weakness. When the panel zone is weak (i.e., $R_u/R_{n,pl}$>1), the beam inelastic demand is expected to be lower than that in their strong panel zone counterparts. As such, C_{pr} in weak panel zones is expected to be lower than that in the strong ones. However, this differentiation is not made herein due to lack of pertinent research. Regardless of this limitation, the $R_u/R_{n,pl}$ ratio is rational for the panel zone weakness categorization (El Jisr et al. 2019; Lee et al. 2005a). The results suggest that for $R_u/R_{n,pl}$ > 1.5, the beam’s contribution to the total plastic deformation of the subassembly is fairly limited. When $R_u/R_{n,pl}$ ranges from about 1.1 to 1.4, a balanced design of the respective beam-to-column connection may be possible.

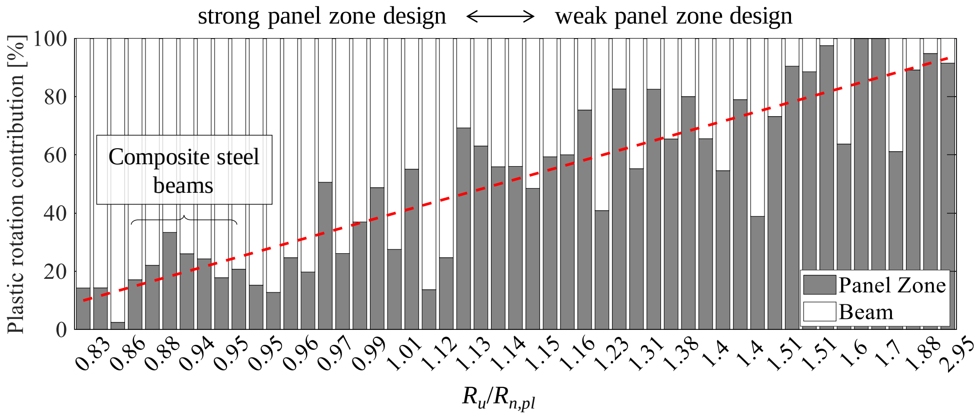

Figure 2.15 Plastic rotation contribution of beam and panel zone versus the $R_u/R_{n,pl}$ ratio.

For $R_u/R_{n,pl}$ < 0.95, the inelastic behavior is mostly concentrated in the steel beams. The panel zone participation in this case varies depending on the presence of the slab (see Fig. 2.15) as well as the respective material variability of the steel beams and columns. Generally, the panel zone contribution to the overall plastic rotation of a beam-to-column connection increases when the slab is present due to the higher probable flexural demand that a panel zone joint experiences (Elkady and Lignos 2014).

Figure 2.16a shows how the ratio of the deduced maximum moment at the column face, $M_{cf,m,max}$ to the probable moment, M_{pr}, varies with respect to the $R_u/R_{n,pl}$ ratio. The results suggest that when $R_u/R_{n,pl}$ > 1.2, the beam does not reach M_{pr}. In this figure, the collected WUF-W bare post-Northridge connections have been highlighted. The probable moment has been estimated with a peak connection strength factor C_{pr} = 1.4 according to AISC (2016c). Although inconclusive, because of the limited number of tests, the above value seems to be unrealistically high. Moreover, the AISC (2016a) provisions do not specify whether the bare or the composite steel beam flexural plastic resistance should be used in the M_{pr} computation. Herein, it is found that $M_{pr,composite}$ is a more realistic representation of the expected maximum beam moment. Although in deep beams (i.e., d_b > 700mm) this observation is not critical, in shallow beams (i.e., d_b < 500mm), which are highlighted in Fig. 2.16a, the estimated composite flexural resistance may be underestimated by nearly 50% due to the neutral axis shifting from the presence of the concrete slab.

Figure 2.16b shows the relation between $R_u/R_{n,pl}$ and γ_{max}/γ_y ratios for all the assembled data. It is observed that for a targeted $R_u/R_{n,pl}$ = 1.2, post-Northridge connections can withstand shear distortions up to about $10\gamma_y$ without experiencing premature fracture. Moreover, in composite steel beam subassemblies, the attained panel zone shear distortions may increase by nearly 30% compared to their bare beam counterparts.

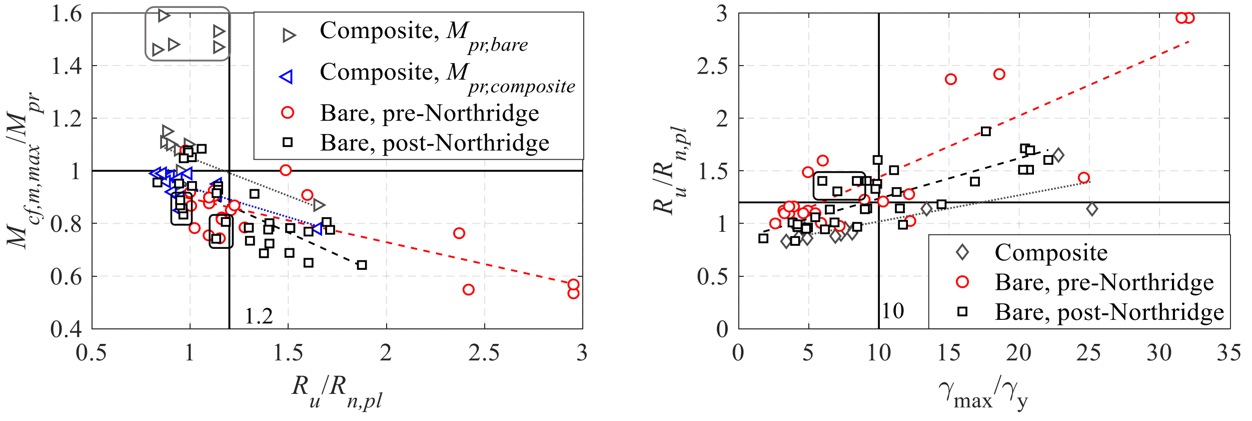

(a) (b)

Figure 2.16 (a) Normalized maximum attained beam end moment versus $R_u/R_{n,pl}$; and (b) $R_u/R_{n,pl}$ versus normalised maximum attained panel zone shear distortion.

2.6 High-fidelity continuum finite-element model validations

The digitized hysteretic responses that are made available may be utilized for CFE model validation purposes. Herein, such a validation is demonstrated with a full-scale interior subassembly [specimen SPEC-6, Ricles et al. (2004b)] that exhibited considerable panel zone inelastic distortions (approximately $12\gamma_y$). This test features deep members (W30x108 beams and a W24x131 column), continuity and doubler plates. From a modeling perspective, these are not trivial how to properly be integrated in a CFE model. For this reason, two CFE models are developed (noted as Model 1 and Model 2). One successfully reproduces the panel zone hysteretic behavior. The second one does not, due to the neglection of the panel zone transverse beam. The validated CFE model (Model 2) is made available through the Zenodo data repository together with the panel zone database (doi: http://www.doi.org/10.5281/zenodo.3689756, Skiadopoulos and Lignos 2020).

In brief, twenty-node quadratic brick elements (C3D20R) with reduced integration are employed in the CFE model; two per flange and web thickness. The element type and mesh size resulted from extensive sensitivity analysis on four element types (i.e., C3D20, C3D20R, C3D8, C3D8R). Local geometric imperfections in the beams are considered based on the recommendations by Elkady and Lignos (2018b). Residual stresses in the column and the beams are incorporated according to Young (1971). The doubler plate is modeled with additional perimetrical CJP welds and four plug welds with encastre boundary conditions. The continuity plates are also modelled as shown in Fig. 2.17. A multiaxial isotropic/kinematic hardening law (Lemaitre and Chaboche 1990) is incorporated in the CFE model within the J2 plasticity framework. The kinematic and isotropic material parameters employing two backstresses are derived based on the gradient-based optimization framework proposed by Sousa and Lignos (2018).

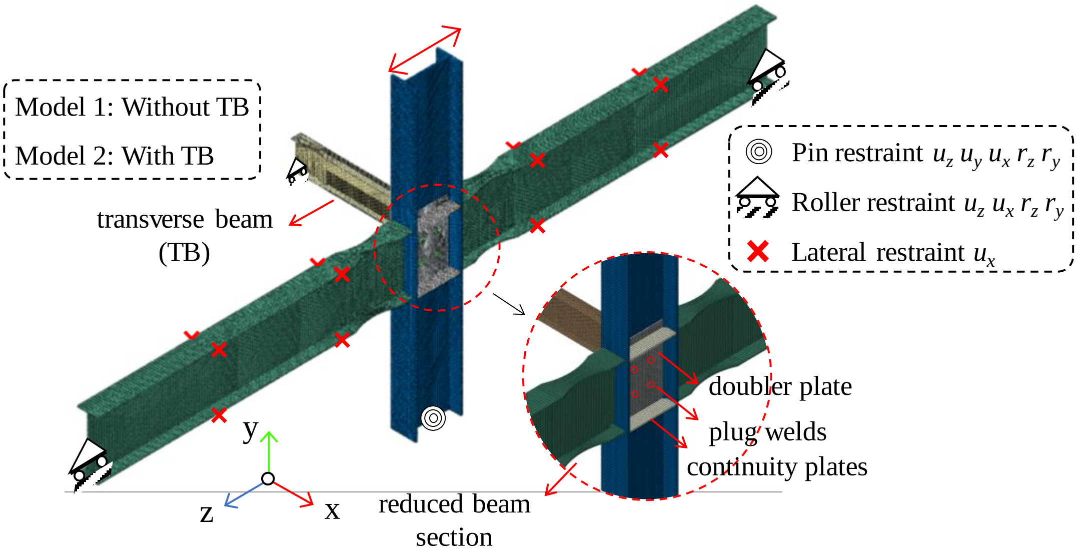
Model 1: Without TB
Model 2: With TB
transverse beam (TB)
Pin restraint $u_z\ u_y\ u_x\ r_z\ r_y$
Roller restraint $u_z\ u_x\ r_z\ r_y$
Lateral restraint u_x
doubler plate
plug welds
continuity plates
reduced beam section
y
z
x

Figure 2.17 Continuum finite element model schematics.

A simplified model (Model 1) that disregards the transverse beam (noted as TB in Fig. 2.17) is first considered. Figure 2.18 shows the comparison of the simulated and measured response in terms of global force-story drift ratio of the subassembly (see Fig. 2.18a) along with local response estimates (i.e., global force-beam rotation in Fig. 2.18b and global force-panel zone rotation in Fig. 2.18c). It is observed that Model 1 experiences strength degradation due to panel zone shear buckling, which did not occur in the experiment. As a result, the panel zone shear distortion angle is overestimated by almost 20%. Similarly, the beam's chord rotation is underestimated by 20%. During the experiment, a transverse beam was employed for lateral support at the panel zone location.

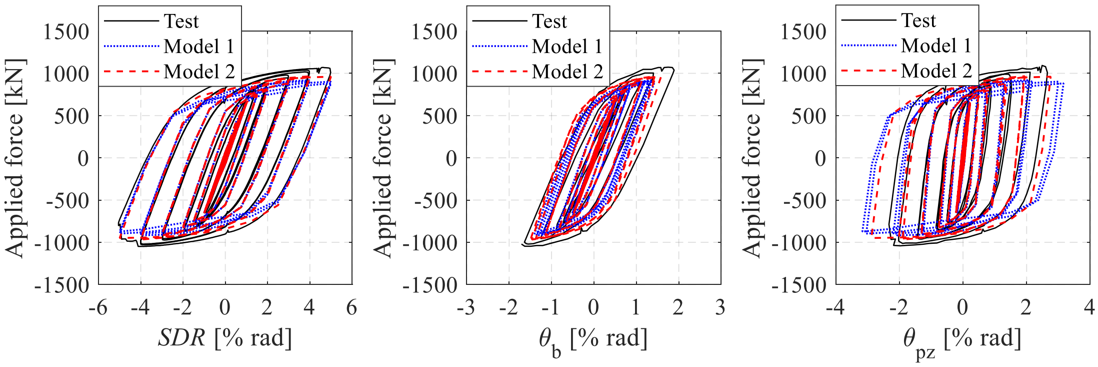

Figure 2.18 Comparison between CFE Model 1 and 2 prediction and test data of SPEC-6, Ricles et al. (2004b).

Since the transverse beam restricts the panel zone from out-of-plane deformations, a more refined CFE model (Model 2) that accounts for the transverse beam is also examined herein (see Fig. 2.17). As depicted in Fig. 2.18, Model 2 reproduces the experimental results with a noteworthy accuracy both at the global and local level. This CFE model could potentially inform fracture mechanics-based models [e.g., Kanvinde

(2017); Rice (1968)] for the evaluation of the fracture potential of beam-to-column connections with inelastic panel zone joints.

2.7 Summary and conclusions

This chapter discusses the development of a publicly available experimental database comprising 100 fully restrained beam-to-column connection physical tests. The collection process focuses on physical tests in which the panel zone experienced inelastic deformations. The collected data is provided in a consistent format and it includes; (a) material and geometric properties of the various subassemblies and their components; (b) metadata for beam-to-column connection performance assessment and (c) digitized global subassembly and local panel zone hysteretic responses for all the collected experiments. The adopted approach to digitize and document the assembled test data is thoroughly presented. The database facilitates the assessment of available panel zone models that are employed in current seismic design standards and system level nonlinear simulations. Aspects of balanced design are quantitatively discussed. Finally, the deduced digitized data support the validation process of high-fidelity CFE models.

The collected database suggests that typical pre-Northridge connections had a more than 50% probability of premature fracture given a modest inelastic panel zone demand (i.e. $4-6\gamma_y$) at a targeted SDR = 4%. If deep beams (d_b > 900mm) were employed, the variability in the cyclic performance of the connections was very large. On the other hand, typical unreinforced post-Northridge connections with bare or composite steel beams did not exhibit more than 10% probability of failure (i.e., fracture and/or 20% drop of the beam’s peak flexural resistance) at a lateral drift demand of 4%, while the panel zone demands reached $4-6\gamma_y$.

Available panel zone design models overestimate the elastic stiffness, K_e, by almost 30%, since the bending deformation mode of the panel zone is disregarded. The AISC (2016b) model overestimates the panel zone post-yield shear strength, V_p, by more than 30% for column cross sections with thick flanges (t_{cf} > 50mm), whereas, CEN (2005) underestimates V_p by the same amount. The above are major issues, from a design standpoint, in high-rise steel frame buildings in which steel columns with relatively thick cross sections are common.

Balanced inelastic deformations between the panel zone and the intersecting steel beam(s) may be achieved if the $R_u/R_{n,pl}$ ratio ranges from 1.1 to 1.4. In this case, panel zone shear distortions may reach up to about $10\gamma_y$, while the connection itself is not likely to experience premature fracture. The beam does not reach its probable moment, M_{pr}, in this case, thereby delaying the onset of local buckling. In composite steel beam subassemblies, the available data suggests that M_{pr} should be computed based on the composite steel beam’s flexural resistance, particularly for shallow beams with depths less than 500mm. Else, the corresponding inelastic shear distortion in the panel zone may be underestimated.

The digitized hysteretic responses of the gathered physical tests aid the validation process of high-fidelity CFE models mimicking the inelastic behavior of beam-to-column connections. Recommendations for rational beam-to-column connection modeling assumptions are validated by two model examples.

Chapter 3 Proposed panel zone model for seismic design of steel moment-resisting frames

Bibliographic details

This chapter presents the post-print version of the article with the following full bibliographic details:

Skiadopoulos, A., Elkady, A., and Lignos, D. G. (2021). "Proposed panel zone model for seismic design of steel moment-resisting frames." *Journal of Structural Engineering*, American Society of Civil Engineers, 147(4), 04021006. DOI: https://doi.org/10.1061/(ASCE)ST.1943-541X.0002935.

Author's contribution

Concerning the material presented in this chapter, Andronikos Skiadopoulos developed the proposed panel zone model, developed the continuum finite element (CFE) models, carried out the CFE simulations, analyzed the simulations results, created the figures, wrote the manuscript draft and revised the manuscript. The second author contributed in assisting with the CFE model development and training, and reviewing and editing the original manuscript draft. The third author contributed in developing the methodology presented in this chapter, supervising the work conducted by Andronikos Skiadopoulos, funding acquisition, and reviewing and editing the original and final manuscript drafts.

3.1 Introduction

In capacity-designed steel moment resisting frame (MRF) systems, a balanced beam-to-column connection design is promoted. In principle, the panel zone joint may experience limited inelastic behavior. A challenge to mobilize the panel zone in the seismic energy dissipation, is the increased potential of premature connection fracture, when improperly detailed (Chi et al. 1997; El-Tawil et al. 1999; Lu et al. 2000; Mao et al. 2001; Ricles et al. 2000, 2004b).

Experimental research (Kim and Lee 2017; Lee et al. 2005c; Shin and Engelhardt 2013b) indicates that a properly detailed fully restrained beam-to-column joint designed with controlled panel zone yielding may lead to an improved seismic performance compared to what is perceived as a "strong" panel zone design (where the panel zone remains elastic). In particular, data from assembled inelastic panel zone databases [http://resslabtools.epfl.ch; El Jisr et al. (2019); Skiadopoulos and Lignos (2021)] suggest that at story drift demands corresponding to 4% rad, modern fully restrained beam-to-column connections (AISC 2016c) do not experience premature weld fractures when their panel zone joints attain shear distortions up to $10\gamma_y$, (where γ_y is the panel zone yield shear distortion angle). Others (Chi and Uang 2002; Ricles et al. 2004b) found that when panel zones exhibit inelastic behavior within a steel MRF beam-to-column connection, the column twist demands due to beam plastic hinge formation become fairly minimal. This issue is prevalent in steel MRF designs featuring deep columns, which are prone to twisting (Elkady and Lignos 2018a; b; Ozkula et al. 2017). To reliably mobilize the inelastic behavior of a panel zone, its shear stiffness and strength should be accurately predicted during the steel MRF seismic design phase.

Models to simulate the inelastic panel zone behavior in terms of shear strength, V_{pz}, and shear distortion angle, γ, are available in the literature (Fielding and Huang 1971; Kato et al. 1988; Kim and Engelhardt 2002; Krawinkler 1978; Lee et al. 2005c; Wang 1988). Referring to Fig. 3.1 and Eq. (3.1), these models comprise a shear-dominated elastic stiffness, K_e, up to the yield shear strength, V_y [see Eq. (3.2)]. This is deduced by assuming a uniform shear stress distribution in the column web. An inelastic hardening branch with post-yield stiffness, K_p, defines the panel zone's post-yield behavior up to a shear strength, V_p [see Eq. (3.3)], at $4\gamma_y$. This strength accounts for the contribution of the surrounding elements (continuity plates and column flanges). Finally, a third branch, where the shear strength is assumed to stabilize, is typically accounted for with a post-γ_p slope that is expressed as percentage of the elastic stiffness, as discussed later on.

$$K_e = \frac{V_y}{\gamma_y} = 0.95 d_c \cdot t_{pz} \cdot G \tag{3.1}$$

$$V_y = \frac{f_y}{\sqrt{3}} \cdot 0.95 d_c \cdot t_{pz} \tag{3.2}$$

$$V_p = \mathrm{V_y} \cdot \left(1 + 3K_p/K_e\right) \tag{3.3}$$

In Eqs. (3.1)-(3.3), the panel zone thickness, $t_{pz} = t_{cw} + t_{dp}$ in case doubler plate(s) are present; t_{cw} is the thickness of the column web; t_{dp} is the total thickness of the doubler plates(s); d_c is the column depth; f_y is the steel material yield stress; G is the steel material modulus of rigidity. The bending deformation of the panel zone (see Fig. 3.1b) is neglected in this case.

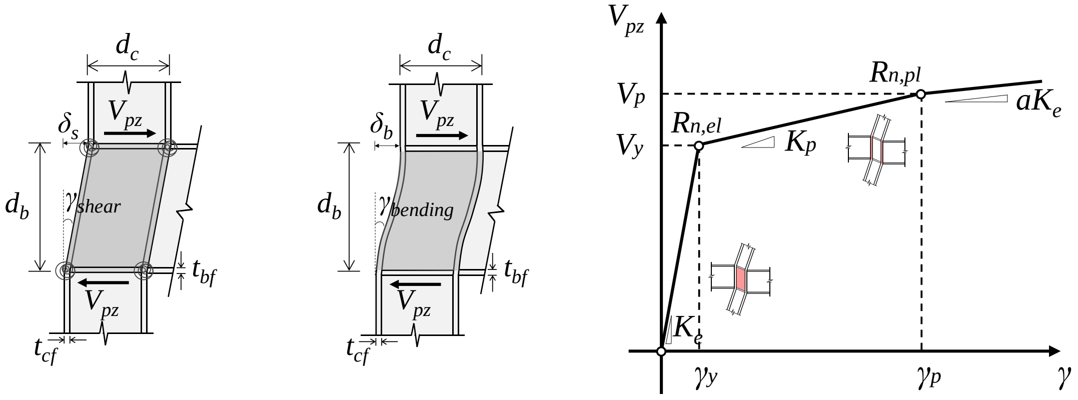

(a) panel zone shear deformation

(b) panel zone bending deformation

(c) typical trilinear panel zone model

Figure 3.1 Panel zone kinematics and mathematical model assumptions.

Krawinkler (1978) proposed the trilinear model (hereinafter referred as Krawinkler model) shown in Fig. 3.1c, which has been adopted in current design provisions with minor modifications throughout the years (AISC 2016b; CEN 2005). Once the panel zone yields uniformly at γ_y, the Krawinkler model assumes that the column web is not capable of withstanding any additional shear. Depending on the column cross section profile, its flanges and continuity plates (if installed) participate in resisting the post-yield panel zone shear demand. Referring to Fig. 3.1c, the post-yield stiffness, K_p, of the Krawinkler model was derived using the principle of virtual work for the panel zone kinking locations based on small-scale subassembly experiments (flange thickness between 10 and 24mm). Referring to Fig. 3.1c, the above model is valid up to $\gamma_p = 4\gamma_y$. Alternative γ_p values are proposed in literature by other researchers. For instance, Wang (1988) proposed a value of $3.5\gamma_y$ whereas Kim et al. (2015) related this value mathematically with the joint's geometric and material properties. The post-γ_p stiffness is usually taken as 3% of K_e (Gupta and Krawinkler 2000a; PEER/ATC 2010; Slutter 1981) acknowledging that the shear resistance is only attributed to material strain hardening. Krawinkler (1978) suggested that for joints comprising stocky columns (flanges thicker than 30 to 40mm), further experiments should be conducted to verify the predicted shear strength of his model.

Considering the assumptions and limitations of this model (Brandonisio et al. 2012; El-Tawil et al. 1999; Jin and El-Tawil 2005; Kim and Engelhardt 2002; Krawinkler 1978; Lee et al. 2005c; Qi et al. 2018; Soliman et al. 2018), several researchers attempted to propose more robust $V_{pz} - \gamma$ relations. In some of these studies (Castro et al. 2005; Chung et al. 2010; Han et al. 2007; Kim et al. 2015; Lee et al. 2005c), the resultant V_y

was more-or-less similar to that of the Krawinkler model [i.e., Eq. (3.2)] excluding distinct differences in the assumed effective shear area. The post-yield stiffness, K_p, was refined empirically based on available experimental data. Tsai and Popov (1988) showed that the average shear stress in the panel zone is 20% lower than the peak shear stress developed in the panel zone web center; thereby suggesting that the uniform shear distribution for calculating V_y is unjustifiable (Charney et al. 2005; Chung et al. 2010; Kim and Engelhardt 2002; Lin et al. 2000). Kim and Engelhardt (2002) and Lin et al. (2000) formulated the above findings in an empirical fashion based on limited experimental data featuring column flange thicknesses less than 35mm. Other studies leveraged the finite element method to examine the panel zone inelastic behavior (Hjelmstad and Haikal 2006; Krishnan and Hall 2006; Léger et al. 1991; Li and Goto 1998; Mulas 2004) without reaching to a consensus for an improved panel zone model to be used in the seismic design of steel MRFs.

From a design standpoint, panel zone joints may moderately participate in energy dissipation during an earthquake according to the North American provisions (AISC 2016a; CSA 2019). The code-based design shear strength (either the panel zone shear yield strength, $R_{n,el}$, or post-yield strength, $R_{n,pl}$) is computed based on the Krawinkler model (i.e., V_y and V_p, respectively). In Japan (AIJ 2012), the panel zone shear strength is computed as per $R_{n,el}$ (AISC 2016b), with the minor difference that AISC (2016b) rounds the shear yield stress to $0.6f_y$, while AIJ (2012) considers $1/\sqrt{3}$ instead. However, the panel zone shear demand imposed from beams is reduced by 25% to implicitly contemplate the neglected column shear force contribution and the disregarded panel zone post-yield strength. In Europe, CEN (2005) considers the contribution of the column web in a similar manner with $R_{n,el}$. If continuity plates are present, an additional term is included to compute the panel zone shear strength. This term is based on the plastic moment resistance of the column flanges at the kinking locations (see Fig. 3.1a).

Figure 3.2 depicts the analytically-derived elastic stiffness, K_e, of various panel zone geometries with/without doubler plates versus the measured one, $K_{e,m}$, from collected full-scale experiments (Skiadopoulos and Lignos 2021). In the case of test data without doubler plates, Fig. 3.2a suggests that common panel zone models (AISC 2016b; CEN 2005; Kim and Engelhardt 2002) overestimate K_e by up to 30%. This is attributed to the uniform yielding assumption at γ_y along with the depreciation of the panel zone bending deformation mode (see Fig. 3.1b) depending on the panel zone aspect ratio and column flange thickness.

Compelling issues with conflicting observations are also found in cases where doubler plates are utilized to reach a desirable panel zone shear strength. Depending on the weld details, the doubler plate efficiency (ratio of shear stresses in the doubler plate to those in the column web) does not exceed 50% (Kim and Engelhardt 2002); hence half of their thickness, at most, is participating in the connection stiffness and strength. For this reason, the panel zone model by CEN (2005) accounts only for one doubler plate even when two plates are required by design. Referring to Fig. 3.2b, the data suggests that K_e , based on CEN (2005), is underpredicted by nearly 20%. Lee et al. (2005c) found that fillet welded doubler plates to the column web, according to the AISC (2016a) provisions, allow for excellent stress compatibility between the plates and the column web. These conclusions are in line with earlier work on fillet-welded doubler plates (Bertero et al. 1973) and on complete joint penetration (CJP) welded plates (Ghobarah et al. 1992). More recently, Shirsat and Engelhardt (2012) showed that the stress compatibility between the column web and the doubler plate is lower for deep columns utilizing thick doubler plates (plate thicknesses, $t_{dp} \geq$ 26mm). Referring to Fig. 3.2b, the AISC panel zone model that accounts for both doubler plates (if applicable) generally overestimates K_e.

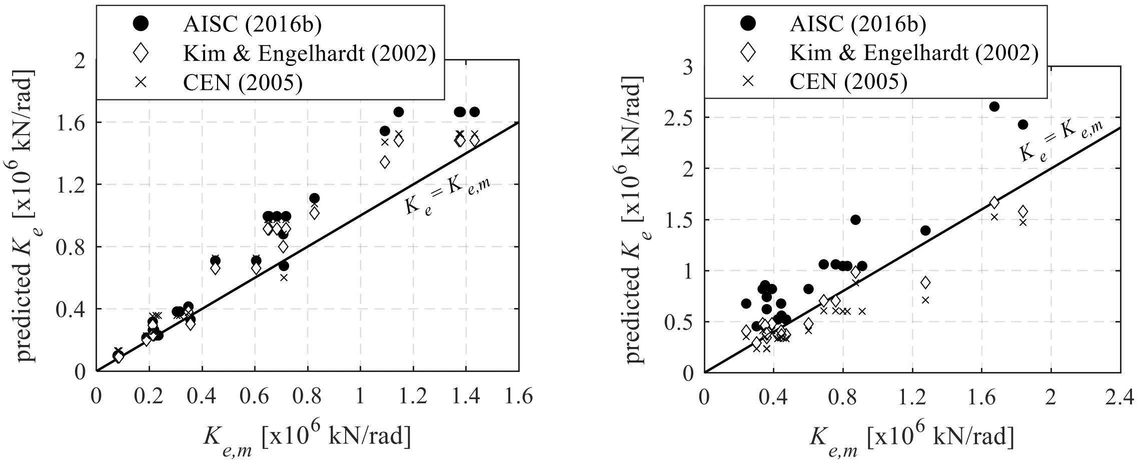

(a) test data without doubler plates

(b) test data with doubler plates

Figure 3.2 Comparison of analytically derived, K_e, and measured, $K_{e,m}$, panel zone elastic stiffness.

Figure 3.3a depicts the deviation of the analytically-predicted post-yield stiffness, K_p [as per AISC (2016b) and Lee et al. (2005c)], from the measured one, $K_{p,m}$ with respect to the column flange thickness, t_{cf}. For t_{cf} larger than 40mm, K_p, at a targeted shear distortion angle of $4\gamma_y$, is over-predicted by up to 40% as per the AISC (2016b) model. Referring to Fig. 3.3b, same observations hold true for V_p according to the AISC (2016b) panel zone model. Note that for the cyclic test data, the extraction of the panel zone measured parameters of interest is based on the average values of the positive and negative first cycle envelopes as shown in Fig. 3.3c. The panel zone measured strength at γ_y and $4\gamma_y$ is, then, determined and, as such, $K_{p,m}$ is defined based on these two reference points. The model by Lee et al. (2005c) consistently underestimates K_p (see Fig. 3.3a) since it was benchmarked with limited data from assemblies comprising columns with flange thicknesses less than 30mm. The Kim et al. (2015) model assumes that the post-yield panel zone response is controlled by the plastic column flange bending capacity under normal stresses. However, this assumption, which is the same with the CEN (2005) panel zone model, is unconservative for steel columns featuring thick flanges (i.e., t_{cf} > 50mm) (see Fig. 3.3b). These constitute a considerable amount (up to 40%) of the total shear force.

To capture the interaction of axial load and shear within the panel zone joint, a reduction factor $r = \sqrt{1 - n^2}$ has been proposed by Chung et al. (2006) and Krawinkler (1978) (where, $n = P/P_y$, P and P_y are the applied axial compressive load and axial yield strength of a steel column, respectively). This is based on the von Mises criterion (von Mises 1913). This is also consistent with the Japanese provisions (AIJ 2012). In the US, a panel zone shear strength reduction is employed according to a fit to the $r - n$ curve, when the panel zone is designed based on $R_{n,el}$ (AISC 2016b). Otherwise, if the design is based on $R_{n,pl}$, a reduction factor is applied to improbably high axial load demands ($n > 0.75$). This tends to overestimate the panel zone shear strength by nearly 15% for $n = 0.5$. In Europe, regardless of the axial demand-to-capacity ratio of the column, the shear resistance is accounted for through a constant reduction factor of 0.9 (Ciutina and Dubina 2003).

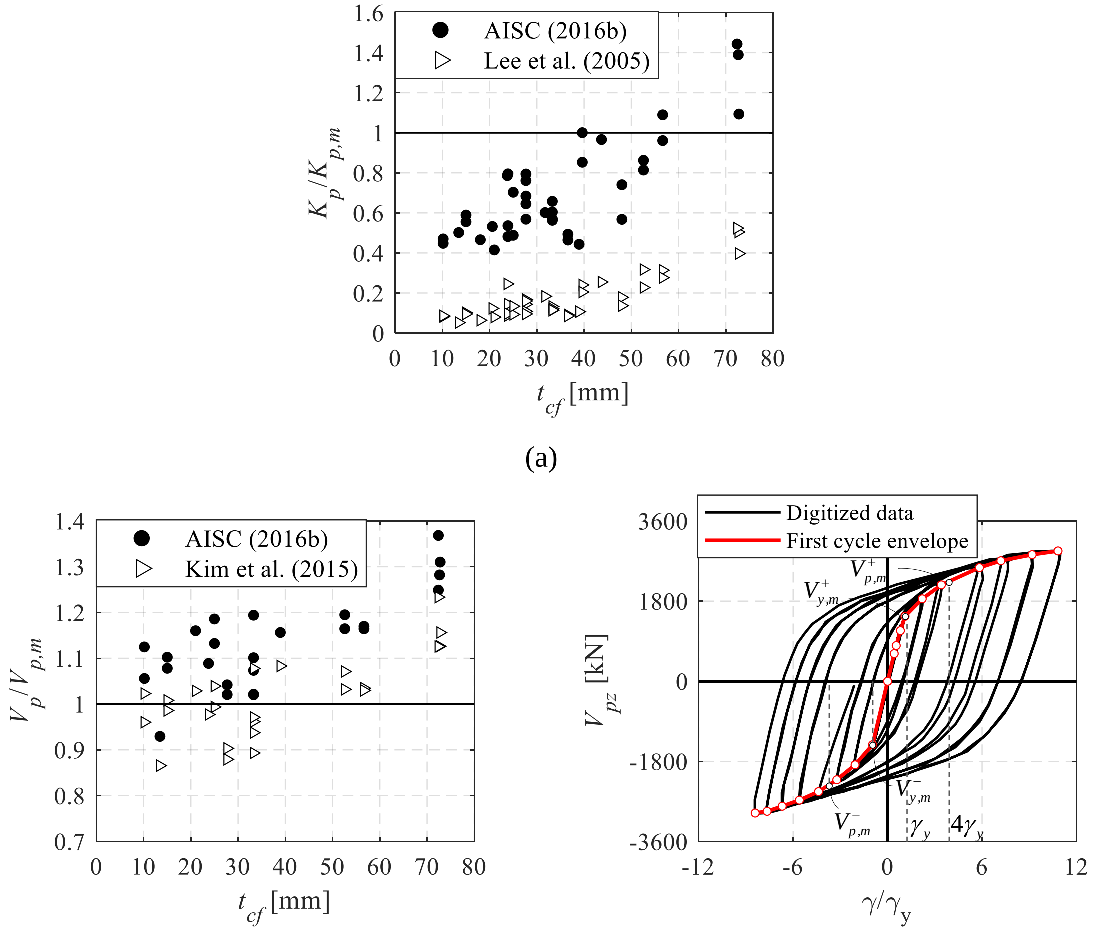

(a)

(b)

(c)

Figure 3.3 Comparison of inelastic panel zone test data without doubler plate: (a) $K_p/K_{p,m}$ versus t_{cf}; (b) $V_p/V_{p,m}$ versus t_{cf}; and (c) first cycle envelopes for panel zone measured shear stiffness and strength deduction (data extracted from Kim et al. (2015), specimen 3).

To address the above challenges, this chapter proposes a mechanics-based panel zone model that could be potentially used for the seismic design of steel MRF systems. This model is informed by continuum finite element (CFE) analyses validated to available experimental data. In the proposed model, panel zone joints are categorized according to the shear stress evolution in the column web and flanges. Moreover, improved panel zone shear strength equations that account for the realistic stress distributions within the web panel and column flanges at three levels of shear distortions (γ_y, $4\gamma_y$ and $6\gamma_y$) are proposed. The doubler plate stress compatibility with the column web is examined for panel zone configurations comprising CJP and fillet weld details according to today's construction practice. The axial load effect on the panel zone shear strength and stiffness is also examined for both interior and end columns within steel MRFs in an effort to generalize the proposed model.

3.2 Mechanics of panel zone behavior through CFE analysis

A CFE model is developed to examine the stress profile within a panel zone joint at various levels of inelastic shear distortion. The commercial finite element analysis software ABAQUS (version 6.14-1) (SIMULIA 2019) is used for this purpose. This section describes the CFE modeling approach and its validation along with the main panel zone parameters of interest. The CFE model validation is demonstrated with two full-scale beam-to-column connection tests. The first test [specimen UCB-PN3, FEMA (1997)] features an exterior subassembly with a stocky column (W14x257) and a 900mm deep beam (W36x150). The second test [specimen SPEC-6, Ricles et al. (2004b)] features an interior subassembly with deep members (W30x108 beams and a W24x131 column). All members were fabricated from Gr. 50 steel (nominal yield stress, $f_y =$ 345MPa).

3.2.1 Description and validation of CFE modeling approach

The CFE model, which is shown in Fig. 3.4a, constitutes twenty-node quadratic brick elements (C3D20R) with reduced integration and a maximum dimension of 20mm. These elements do not typically experience hourglassing and/or shear locking effects. To determine the optimum element type and mesh size, a mesh sensitivity analysis is conducted with four element types (i.e., C3D20, C3D20R, C3D8, C3D8R). Moreover, local imperfections in the beams are incorporated according to the first critical buckling eigenmode. Web imperfections are deemed critical and are tuned to an amplitude of $d_b/250$, which is consistent with prior related studies (Elkady and Lignos 2018b). Residual stresses according to Young (1971) are incorporated in the deep members. For the W14x257 column, the residual stress distribution by de Castro e Sousa and Lignos (2017) is adopted. The CFE model captures the steel material nonlinearity with a multiaxial combined isotropic/kinematic hardening law (Lemaitre and Chaboche 1990) within the J2 plasticity constitutive model (von Mises 1913). The input model parameters are based on prior work by de Castro e Sousa et al. (2020). Referring to Fig. 3.4b, the CJP welds along the perimeter of the doubler plate are modeled through tie constraints. However, in Section 3.5, the welds are modeled explicitly. Four plug welds are simulated with 15mm fasteners that constrain all six degrees-of-freedom. The continuity plates are tied in the column flanges and the doubler plate. Figure 3.5 shows comparisons between the measured and simulated results both at the global (load-story drift ratio response) and local level (panel zone shear force-shear distortion response). As for the UCB-PN3 specimen, the agreement of the simulated and measured data with regard to the global behavior is noteworthy (see Fig. 3.5a). In Fig. 3.5b, the simulated panel zone response agrees well with the test data up to an inelastic shear distortion of 0.5% rad (i.e., second to last loading cycle). After reviewing the experimental report (Popov et al. 1996), it is found that the reason for the observed discrepancy between the measured and simulated panel zone response is the occurrence of beam weld fracture in the second to last loading cycle. This was not simulated in the CFE model. After the occurrence of weld fracture, the shear demand in the panel zone reduced, thereby decreasing the associated inelastic shear distortion. This is confirmed from UCB-PN1 specimen, from the same test program, that involved a nominally identical subassembly with UCB-PN3. However, premature fracture occurred at a much later loading cycle.

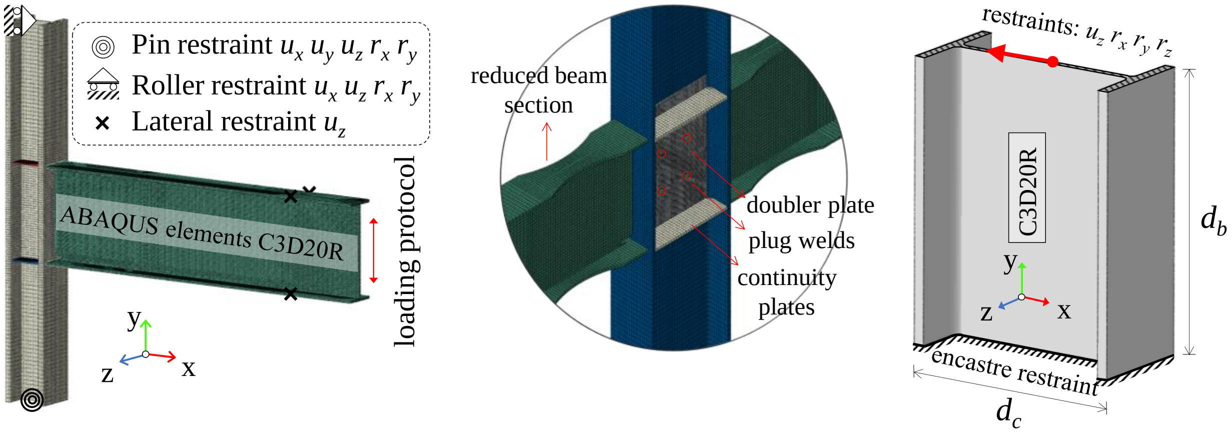

(a) detailed CFE model (b) doubler plate detailing (c) reduced-order CFE model

Figure 3.4 Detailed and reduced-order continuum finite element models.

In an effort to expedite the computations, a reduced-order panel zone CFE model is also developed as shown in Fig. 3.4c. This model does not include the continuity plates. Instead, a rigid body constraint is applied at the column’s top and bottom edges (i.e., at the locations of the beam flanges) to prevent stress concentrations during the imposed loading. According to the AISC (2016b) specifications, continuity plates are deemed necessary when the column cannot withstand the beam flange concentrated forces. Unlike slender column profiles, in stocky ones, the column itself is able to sustain the concentrated beam forces, hence continuity plates may be disregarded [see Section E3.6f, AISC (2016a)]. Besides, the panel zone strength and stiffness parameters would not be influenced by the presence of continuity plates. Accordingly, assuming fixed end boundaries is justifiable for both cases. Out-of-plane displacements and rotations as well as in plane rotations are restrained at the panel zone edges. Hence the panel zone joint behaves as a beam in contra-flexure. Referring to Figs. 3.5b and 3.5d, the simulated responses based on the detailed and reduced-order models are nearly identical for the examined subassemblies. Therefore, the reduced-order panel zone CFE model is adopted hereinafter.

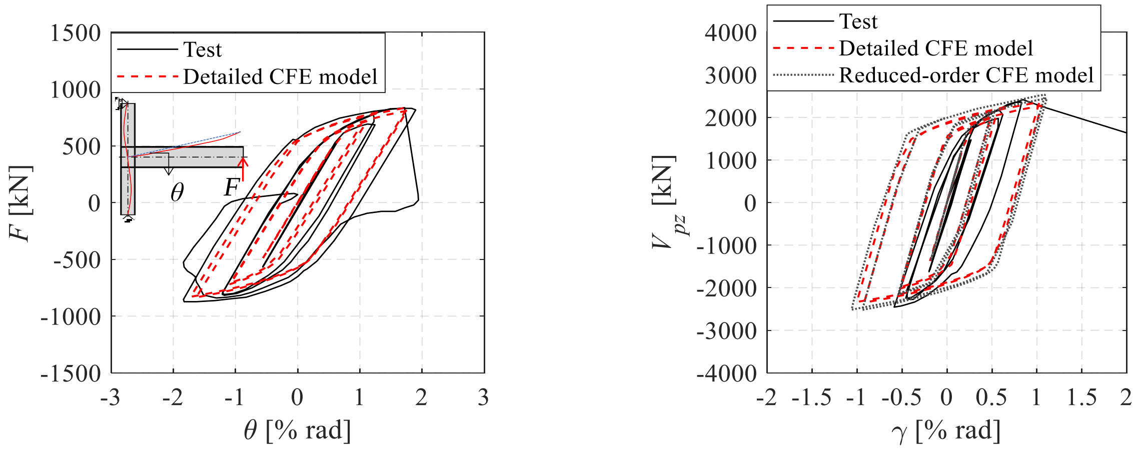

(a) load – story drift ratio

(b) load – panel zone shear distortion

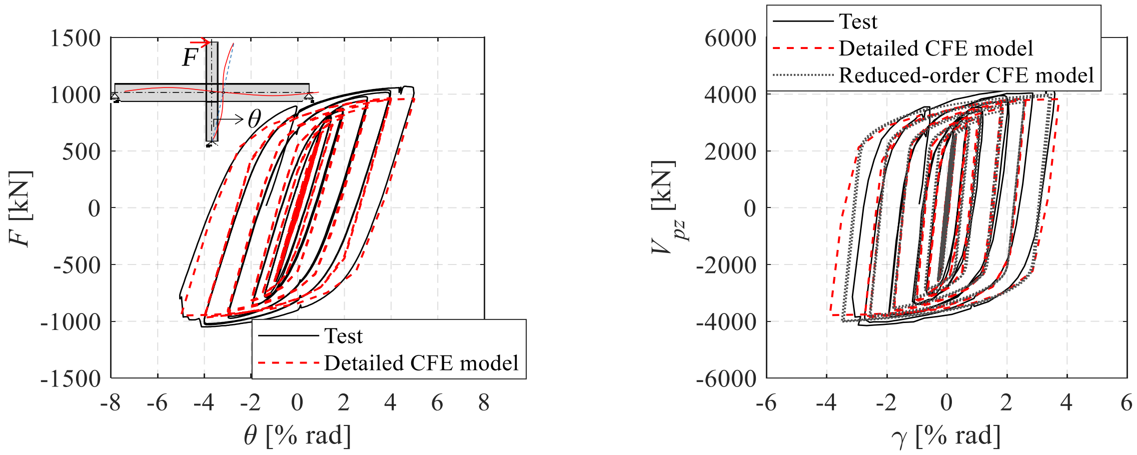

(c) load – story drift ratio

(d) load – panel zone shear distortion

Figure 3.5 Comparison between CFE model prediction and test data: (a)-(b) data reproduced from FEMA (1997); (c)-(d) data reproduced from Ricles et al. (2004b).

3.2.2 Deduced panel zone performance parameters

The simulation matrix comprises eight panel zone geometries. These are designed to have the same V_y with specimen UCB-PN3, i.e., the column web thickness and depth are kept constant. The varied geometric parameters are the panel zone aspect ratio, d_b/d_c, the column flange width, b_{cf}, and the column flange thickness, t_{cf}. The first two parameters are chosen to examine the effect of the bending deformation mode on K_e, whereas t_{cf} is chosen to examine the influence of the column flange thickness on the panel zone shear strength. The panel zone models are subjected to monotonic inelastic shear distortions up to $6\gamma_y$.

Figure 3.6 shows the primary panel zone performance parameters of interest. The elastic panel zone shear stiffness, K_e, is deduced from the elastic branch slope of the $V_{pz} - \gamma$ behavior. The yield strength, V_y, is deduced based on the yield initiation according to the von Mises criterion (von Mises 1913) in the panel zone center. Finally, the post-yield panel zone shear strength is deduced at two representative shear distortion levels, $4\gamma_y$ (V_p) and $6\gamma_y$ ($V_{6\gamma_y}$). The latter is considered, since there may be appreciable reserve shear strength attributed to the column flange contribution along with strain hardening due to column web shear yielding.

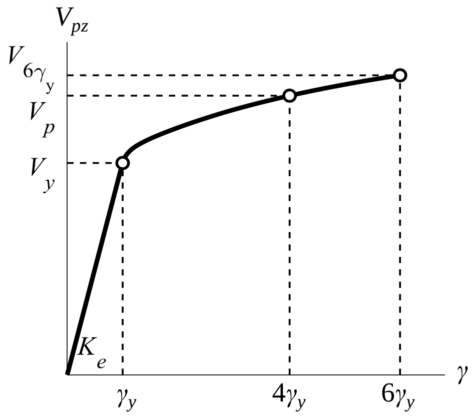

Figure 3.6 Deduced panel zone performance parameters.

3.3 Discussion

Figure 3.7 shows a comparison between representative CFE simulations for various panel zone aspect ratios, d_b/d_c and the predicted behavior according to the Krawinkler model. As expected, the figure suggests that the deviation of the predicted elastic stiffness, K_e [Eq. (3.1)], the yield strength, V_y [Eq. (3.2)] and post-yield strength, V_p [Eq. (3.3)] from the CFE results may be appreciable depending on the panel zone aspect ratio and the column flange thickness. Particularly, for slender panel zones (i.e., d_b/d_c=1.5 and t_{cf} =24mm) the measured elastic stiffness is about 30% lower than the predicted one since the Krawinkler model neglects the bending contribution (see Fig. 3.1b). However, for stocky and shallow panel zones with an aspect ratio of one and thick flanges ($t_{cf} \cong$ 50mm), where the shear deformation mode is dominant, the Krawinkler model predicts K_e reasonably well. Though, the panel zone stiffness is still underpredicted by 10-15% due to the assumed effective shear area (Charney et al. 2005). Same observations hold true for V_y. The Krawinkler model overestimates V_p by more than 20% for stocky and shallow panel zones. For the cross section range that the same model was calibrated for, the post-yield shear strength is only overestimated by up to 10%.

The above deviations can be justified by examining the stress distributions within the panel zone. Figure 3.8 shows the shear stress distributions for two characteristic panel zone geometries, normalized by the yield shear stress, τ_y ($\tau_y = f_y/\sqrt{3}$), at a shear distortion angle equal to γ_y, $4\gamma_y$ and $6\gamma_y$. The shear stress distributions are extracted from the column cross section corresponding to the beam centerline. Superimposed in the same figure are planes representing the average shear stress in the column web. Referring to Fig. 3.8a, the common assumption of a uniform shear distribution in the column web is not rational for slender panel zones, particularly at shear distortions near yielding, whereas the column flange contribution to shear yielding is indeed negligible.

Referring to Fig. 3.8b, stocky and shallow panel zones experience almost uniform shear stresses in their web regardless of the shear angle distortion. The contribution of the column flanges to the attained shear stresses (maximum of $4\%\tau_y$) may seem insignificant for shear distortion levels of γ_y. However, since the flange area of stocky cross sections outweighs that of their web, the resultant force is appreciable (15-40% of the total panel zone shear force, depending on the shear distortion level).

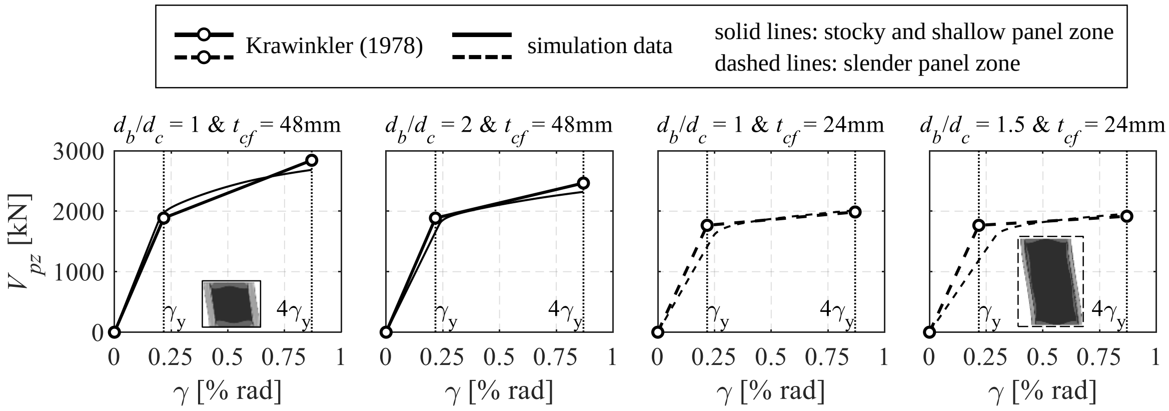

Figure 3.7 Representative continuum finite element analysis results with varying web panel zone aspect ratio and column flange thickness.

3.4 Proposed panel zone model

3.4.1 Panel zone elastic stiffness

The proposed panel zone elastic stiffness, K_e [see Eq. (3.4)], is derived based on both shear and bending deformation modes (see Fig. 3.1). The shear mode is accounted for based on Eq. (3.5). The bending mode is deduced based on the elastic stiffness (in terms of $V_{pz} - \gamma$ relation) of a beam in contra-flexure according to Eq. (3.6).

$$K_e = \frac{V_{pz}}{\gamma} = \frac{K_s \cdot K_b}{K_s + K_b} \tag{3.4}$$

$$K_s = A_v \cdot G = t_{pz} \cdot (d_c - t_{cf}) \cdot G \tag{3.5}$$

$$K_b = \frac{12 \cdot E \cdot I}{d_b^3} \cdot d_b \tag{3.6}$$

The proposed model assumes a panel zone shear strength equilibrium instead of shear deformation compatibility. Therefore, the proposed panel zone stiffness is computed based on Eq. (3.4) by considering the two deformation modes in series (i.e., $\gamma = \gamma_{shear} + \gamma_{bending}$) (see Fig. 3.1). In Eqs. (3.4) to (3.6), I is the second moment of area of the column cross section (including the doubler plate(s) thickness, if any) with respect to the column's strong-axis; and A_v is the effective shear area according to Charney et al. (2005). Although other panel zone models (AISC 2016b; Fielding and Huang 1971; Kato et al. 1988; Lui and Chen 1986; Mulas 2004) assume an effective depth, $d_{eff} = d_c$, the panel zone shear stiffness (and strength) tends to be overestimated by about 10% for stocky column cross sections (t_{cf} > 40mm) based on the above assumption. Note here that the second moment of area, I, refers to that of the full column cross section. Other researchers that attempted to address the bending deformation mode issue (Kim et al. 2015), accounted for the column flange deformation mode independently from the column web.

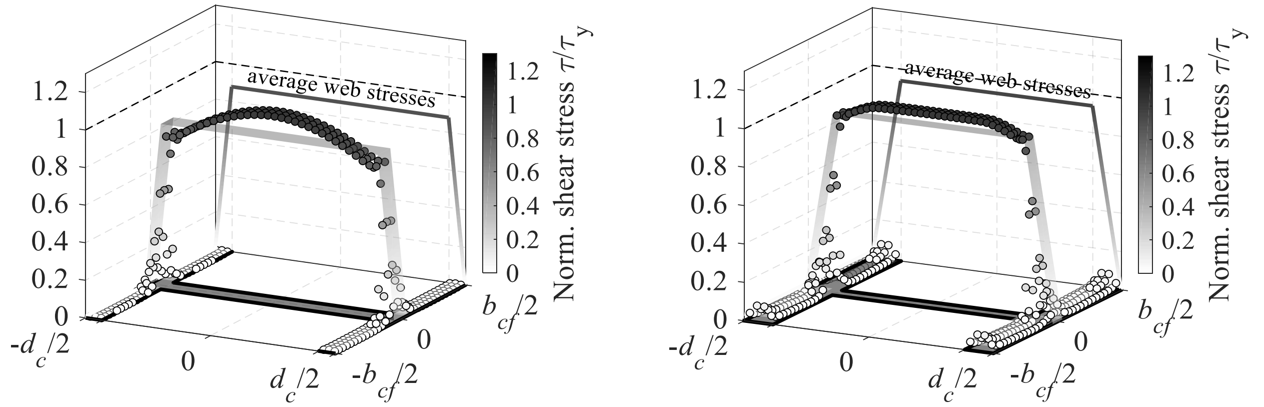

shear stress distribution at γ_y

shear stress distribution at γ_y

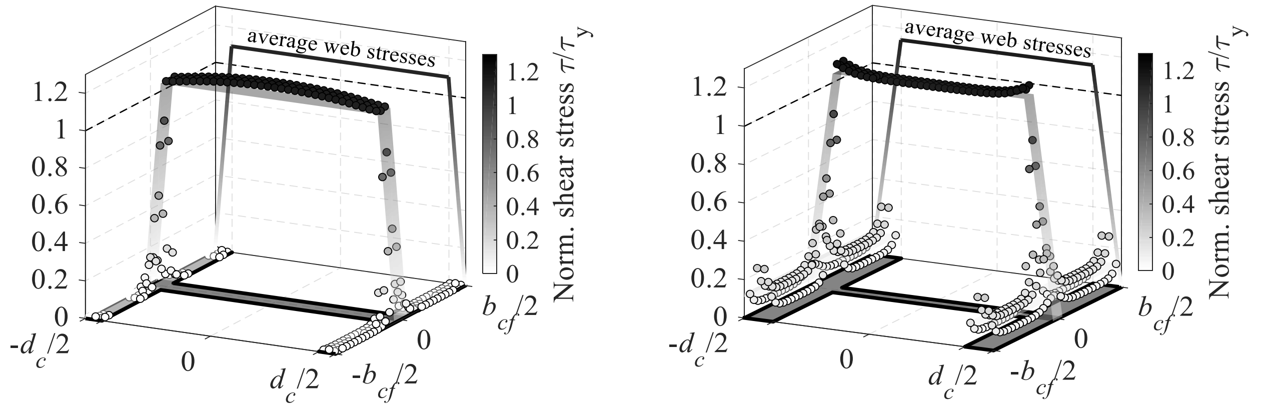

shear stress distribution at $4\gamma_y$

shear stress distribution at $4\gamma_y$

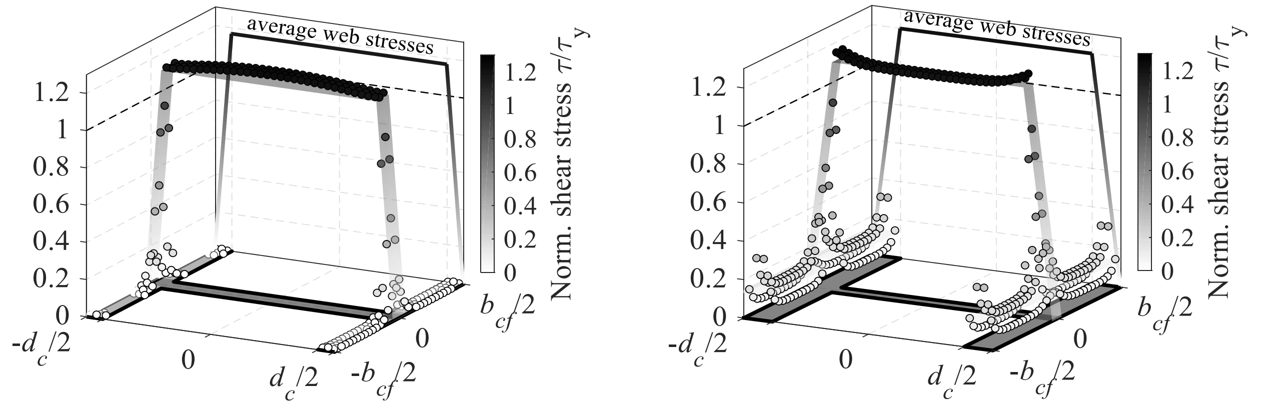

shear stress distribution at $6\gamma_y$

shear stress distribution at $6\gamma_y$

(a) slender panel zone (i.e., d_b/d_c = 1.5 and t_{cf} = 25mm)

(b) stocky and shallow panel zone (i.e., d_b/d_c = 1.0 and t_{cf} = 50mm)

Figure 3.8 Shear stress distributions at γ_y, $4\gamma_y$ and $6\gamma_y$: (a) slender; and (b) stocky and shallow panel zones.

3.4.2 Panel zone shear strength

To predict a realistic yield and post-yield panel zone shear strength, the shear stress distributions in the panel zone from Fig. 3.8 are employed. The panel zone shear force, V_{pz}, at a distortion, γ, may be approximated by Eq. (3.7) where, V_f is the shear force resisted by a single column flange; V_w is the shear force resisted by the column web. In turn, V_f may be assumed to be proportional to the ratio of the column flange stiffness, K_f, to the panel zone's elastic stiffness, K_e, according to Eq. (3.8). The column flange stiffness may be computed using Eq. (3.9) by considering both shear and bending deformation modes as depicted by Eqs. (3.10) and (3.11), respectively.

$$V_{pz} = 2V_f + V_w \tag{3.7}$$

$$V_f = (K_f/K_e) \cdot V_{pz} \tag{3.8}$$

Equation (3.10) assumes a uniform shear stress distribution in the column flanges, while Eq. (3.11) assumes contra-flexure deformation with respect to the weak-axis of the column flanges.

$$K_f = \frac{K_{sf} \cdot K_{bf}}{K_{sf} + K_{bf}} \tag{3.9}$$

$$K_{sf} = 2 \cdot (t_{cf} \cdot b_{cf} \cdot G) \tag{3.10}$$

$$K_{bf} = 2 \cdot \left[\frac{12E(b_{cf} \cdot t_{cf}^3/12)}{d_b^3} \cdot d_b\right] \tag{3.11}$$

In the above equations, the K_f/K_e ratio provides an estimate of the panel zone shear force resisted by the column flanges. Particularly, Fig. 3.9a shows how K_f/K_e influences the deduced K_e for the examined panel zone geometries discussed earlier. In the vertical axis, these parameters are either predicted by the proposed or the Krawinkler model. The predicted stiffness, K_e, is normalized by the $K_{e,m}$, deduced from the CFE results. The dashed line at an abscissa value of 1.0 represents the ideal agreement between the virtual tests and the analytical model predictions.

Referring to Fig. 3.9a, the proposed panel zone stiffness from Eq. (3.4) shows improved accuracy over the Krawinkler model particularly for slender panel zone geometries (K_f/K_e < 0.02). For stocky and shallow panel zone geometries (K_f/K_e > 0.07), the effective area limitation as per Charney et al. (2005) leads to at least the same accuracy as the Krawinkler model since the bending deformation mode is negligible.

Figure 3.9b shows the normalized post-yield panel zone stiffness, K_{γ_i}, at various shear distortions (i.e., $4\gamma_y$, $5\gamma_y$ and $6\gamma_y$), with respect to K_f/K_e. The K_{γ_i} is deduced from the tangential slope of the $V_{pz} - \gamma$ relation. Note that beyond $4\gamma_y$, the tangent stiffness is used to provide a consistent comparison with the constant $0.03K_e$ post-$4\gamma_y$ that has been historically assumed in literature (Gupta and Krawinkler 2000a; Slutter 1981). This figure suggests that at $4\gamma_y$, the post-yield panel zone stiffness reaches $0.07K_e$, whereas at $6\gamma_y$ attains

$0.04K_e$. The K_{γ_i}/K_e, at $4\gamma_y$, of stocky and shallow panel zones (K_f/K_e > 0.07) becomes double compared to slender ones. Consequently, the empirical post-$4\gamma_y$ stiffness of $0.03K_e$ (Gupta and Krawinkler 2000a; PEER/ATC 2010; Slutter 1981) is irrational for most panel zone geometries. Instead, the panel zone shear strength at a shear distortion angle of $6\gamma_y$ should be used with V_p to define the respective slope. This may also be more effective for optimal balanced design of beam-to-column joints in capacity-designed steel MRFs. Large panel zone shear distortions may raise concerns regarding localized deformations, consequential implications on system level response and increased potential for weld fractures (Chi et al. 1997; El-Tawil et al. 1999; Lu et al. 2000; Mao et al. 2001; Ricles et al. 2000, 2004b). However, experimental data from recently compiled databases with over 100 post-Northridge bare steel and composite-steel beam-to-column connections (El Jisr et al. 2019; Skiadopoulos and Lignos 2021) that exhibited inelastic behavior in their web panels, did not experience premature fracture even at inelastic shear distortions up to $10\gamma_y$ as discussed earlier.

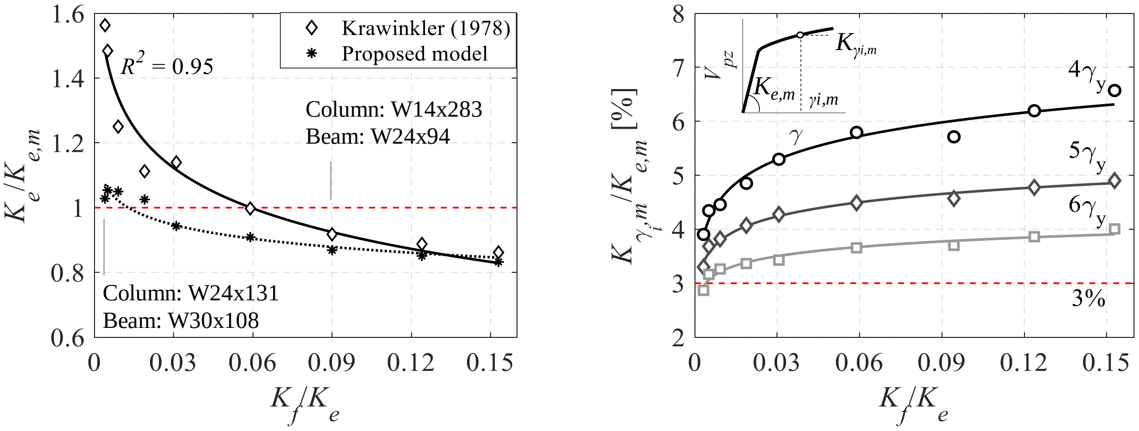

(a) (b)

Figure 3.9 (a) Deviation of predicted K_e from measured one, $K_{e,m}$, with respect to K_f/K_e; and (b) normalized panel zone stiffness at representative shear distortion levels with respect to K_f/K_e.

The panel zone shear strength can be generally computed using Eq. (3.12) by summing up the surface integral of the shear stresses along the panel zone's web and flange areas. A realistic shear stress distribution should be deduced at a given shear distortion level for this purpose. Given the discrete finite element mesh, the surface integral in Eq. (3.12) can be replaced by the double summation of the shear stresses as given by Eq. (3.13).

$$V_{pz} = \int_A \tau dA = \int_{A_w} \tau dA_w + 2\int_{A_f} \tau dA_f \tag{3.12}$$

The parameters a_w and a_f, introduced in Eq. (3.13), represent the shear stress of each element in the column web and each flange, respectively, normalized by the shear stress at yielding, τ_y. In these equations, the yield stress of the web and flanges is assumed to be the same. Since the column flanges and web element size was kept constant in the CFE model, Eq. (3.13) can be re-written as in Eq. (3.14).

$$V_{pz} = \frac{f_y}{\sqrt{3}} \cdot \sum_{-d_c/2}^{d_c/2} \sum_{-t_{cw}/2}^{t_{cw}/2} a_w(x,y)\delta_x\delta_y + \frac{f_y}{\sqrt{3}} \cdot 2 \sum_{-b_{cf}/2}^{b_{cf}/2} \sum_{-t_{cf}/2}^{t_{cf}/2} a_f(x,y)\delta_x\delta_y \tag{3.13}$$

$$V_{pz} = \frac{f_y}{\sqrt{3}} \cdot \frac{d_c \cdot t_{cw}}{N_w} \cdot \sum_{-d_c/2}^{d_c/2} \sum_{-t_{cw}/2}^{t_{cw}/2} a_w(x,y) + \frac{f_y}{\sqrt{3}} \cdot 2 \frac{(b_{cf} - t_{cw}) \cdot t_{cf}}{N_f} \cdot \sum_{-b_{cf}/2}^{b_{cf}/2} \sum_{-t_{cf}/2}^{t_{cf}/2} a_f(x,y) \tag{3.14}$$

Where, N_w and N_f are the number of finite elements of the web and each flange, respectively. Finally, as per Eq. (3.15), the panel zone shear strength can be expressed in terms of a_{eff} [see Eq. (3.16)], which is the average shear stress within the column flanges or web (i.e., sum of all stresses divided by number of elements in a given component), normalized by τ_y.

$$V_{pz} = a_{w,eff} \cdot \frac{f_y}{\sqrt{3}} \cdot \left(d_c - t_{cf}\right) \cdot t_{cw} + a_{f,eff} \cdot \frac{f_y}{\sqrt{3}} \cdot (b_{cf} - t_{cw}) \cdot 2t_{cf} \tag{3.15}$$

$$\begin{gathered} a_{w,eff} = \frac{\sum_{-\frac{d_c}{2}}^{\frac{d_c}{2}} \sum_{-\frac{t_{cw}}{2}}^{\frac{t_{cw}}{2}} \tau_w \delta x \delta y}{t_{cw} \cdot \left(d_c - t_{cf}\right) \cdot \tau_y} \\ a_{f,eff} = \frac{\sum_{-b_{cf}/2}^{b_{cf}/2} \sum_{-t_{cf}/2}^{t_{cf}/2} \tau_f \delta x \delta y}{t_{cf} \cdot b_{cf} \cdot \tau_y} \end{gathered} \tag{3.16}$$

Figure 3.10 illustrates the normalized average shear stresses of the column web and flanges from Eq. (3.16), as a function of K_f/K_e, at shear distortions of γ_y, $4\gamma_y$ and $6\gamma_y$. The linear regression curves for these relationships are superimposed in this figure and their statistical values (mean, standard deviation and coefficient of determination, R^2) are summarized in Table 3.1 for reference. Figure 3.10a suggests that in general, and even for high shear distortions ($\gamma = 6\gamma_y$), the influence of K_f/K_e on the column web stress contribution is not significant as inferred by the mild slope of the fitted trend lines. Quantitatively, this is expressed by the miniscule standard deviation values shown in Table 3.1 at $4\gamma_y$ and $6\gamma_y$. Accordingly, the average stress of the web at these distortions may be approximated by a single value regardless of the panel zone geometry. Referring to Fig. 3.10b, when $K_f/K_e > 0.07$ (stocky panel zones), the average stress of the column flange is appreciable for shear distortions larger than γ_y. In contrast, for slender panel zones ($K_f/K_e < 0.02$), the column flange average stress is negligible; hence, the column flange contribution to the panel zone shear strength is not important.

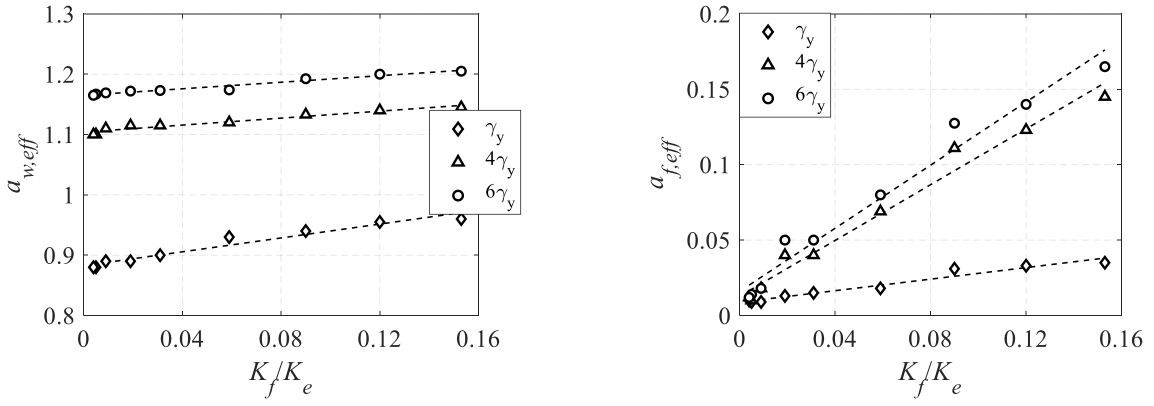

(a) (b)

Figure 3.10 Normalized average shear stress at γ_y, $4\gamma_y$ and $6\gamma_y$ for the: (a) web; and (b) flange.

Table 3.1 Statistical parameters for the linear regression curves of the $a_{eff} - K_f/K_e$ relationships.

Location	Web			Flange		
Distortion level	γ_y	$4\gamma_y$	$6\gamma_y$	γ_y	$4\gamma_y$	$6\gamma_y$
Mean	0.91	1.1	1.2	0.019	0.063	0.073
Standard deviation	0.032	0.016	0.015	0.011	0.051	0.058
R2	0.95	0.94	0.96	0.95	0.98	0.97

A set of panel zone shear strength equations at γ_y (i.e., V_y), $4\gamma_y$ (i.e., V_p) and $6\gamma_y$ (noted as $V_{6\gamma_y}$) are proposed in support of contemporary seismic design of steel MRFs. According to Eq. (3.17), the proposed, V_y, is as follows:

$$V_y = \frac{\left[0.58\left(K_f/K_e\right)+0.88\right]\cdot\frac{f_y}{\sqrt{3}}\cdot\left(d_c-t_{cf}\right)\cdot t_{pz}}{1-K_f/K_e} = \frac{f_y}{\sqrt{3}}\cdot a_y\cdot\left(d_c-t_{cf}\right)\cdot t_{pz} \qquad (3.17)$$

where $a_y = 0.9$ and 1.0 for slender and stocky panel zones, respectively. Note that for stocky panel zones, Eq. (3.17) matches the V_y of the Krawinkler model.

The proposed panel zone shear strength for V_p and $V_{6\gamma_y}$ is given by Eq. (3.18) along with recommended values for $a_{w,eff}$ and $a_{f,eff}$ in Table 3.2 directly extracted from representative shear stress profiles of panel zone geometries. Interpolation may be used for the corresponding a_{eff} values when the panel zone geometry is neither slender nor stocky (i.e., $K_f/K_e = 0.02$ to 0.07). For panel zone shear distortions higher than $6\gamma_y$, the panel zone stiffness equals the proposed $4\gamma_y - 6\gamma_y$ one.

$$V_{pz} = \frac{f_y}{\sqrt{3}}\cdot\left[a_{w,eff}\cdot\left(d_c-t_{cf}\right)\cdot t_{pz} + a_{f,eff}\cdot\left(b_{cf}-t_{cw}\right)\cdot 2t_{cf}\right] \qquad (3.18)$$

Table 3.2 Normalized average shear stress values and expressions in the web and the flanges, based on the proposed model.

Equation		Web ($a_{w,eff}$)		Flange ($a_{f,eff}$)	
		$4\gamma_y$ (V_p)	$6\gamma_y$ ($V_{6\gamma_y}$)	$4\gamma_y$ (V_p)	$6\gamma_y$ ($V_{6\gamma_y}$)
General case		1.1	1.15	$0.93(K_f/K_e)+0.015$	$1.05(K_f/K_e)+0.02$
Simplified case	Slender panel zone			0.02	0.03
	Stocky panel zone			0.1	0.1

3.4.3 Proposed panel zone model validation

Figure 3.11 shows a comparison of the panel zone's hysteretic response from characteristic full-scale tests (Ricles et al. 2004b; Shin 2017) and the predicted envelope curve based on the proposed model. For reference, the AISC (2016b) model is superimposed in the same figure. The additional third branch slope of $0.03K_e$ is also considered beyond V_p (Gupta and Krawinkler 2000a; PEER/ATC 2010; Slutter 1981). The comparisons highlight the superior accuracy of the proposed model in predicting the panel zone's shear strength and stiffness over the AISC model, which consistently overestimates the same quantities by nearly 30%. Moreover, the assumed $0.03K_e$ stiffness in the third branch is not justifiable for slender panel zones as discussed earlier (see Fig. 3.11a).

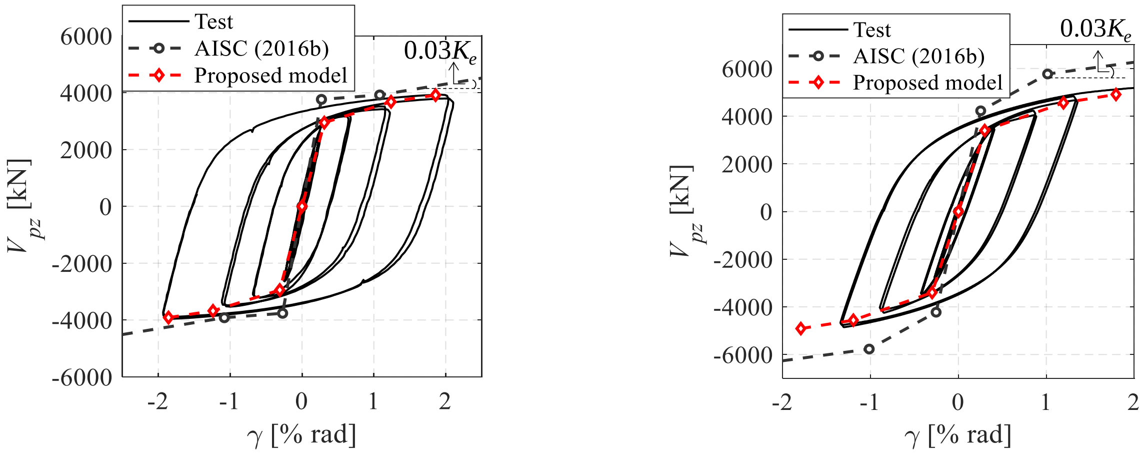

(a) slender panel zone, $K_f/K_e = 0.003$ [Beam: W30x108, Column: W24x131, data reproduced from Ricles et al. (2004b)]

(b) stocky panel zone, $K_f/K_e = 0.07$ [Beam: W36x150, Column: W14x398, data reproduced from Shin (2017)]

Figure 3.11 Comparison of measured and predicted panel zone hysteretic responses.

An assembled inelastic panel zone database (Skiadopoulos and Lignos 2021) comprising specimens without doubler plates in the panel zone is also used to further validate the accuracy of the proposed panel zone stiffness and Eq. (3.18) for both V_p and $V_{6\gamma_y}$. Referring to Fig. 3.12a, the proposed panel zone stiffness matches the experimental data relatively well. The maximum error is up to 15% and for only two cases. Referring to Fig. 3.12b, while the AISC (2016b) panel zone model does not depict the influence of column flange thickness, t_{cf}, on V_p, the proposed model is sufficient regardless of the panel zone geometry. Referring to Fig. 3.12c, same trends hold true for $V_{6\gamma_y}$. Notably, for cross sections with $t_{cf} > 40$mm, the proposed model is remarkably better than the current state of the seismic design practice.

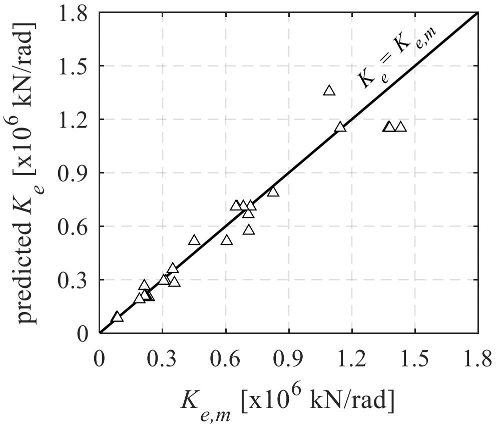

(a) $K_e/K_{e,m}$

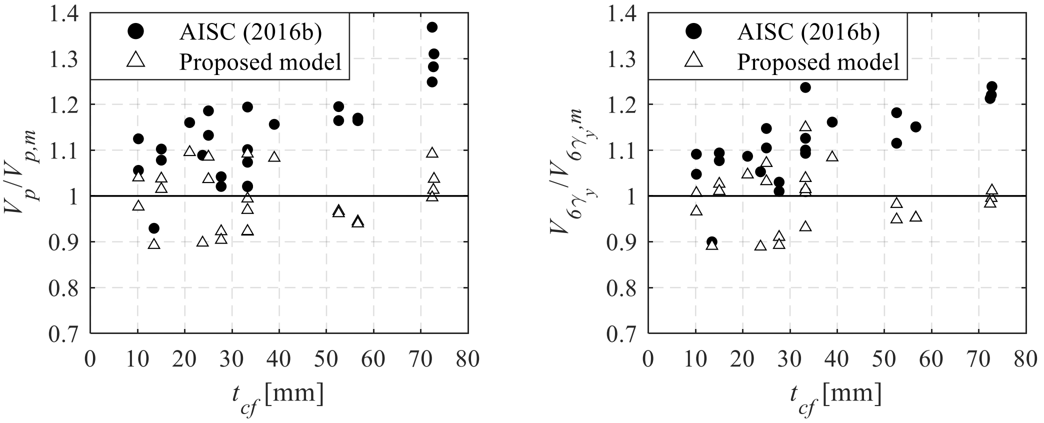

(b) $V_p/V_{p,m}$

(c) $V_{6\gamma_y}/V_{6\gamma_{y,m}}$

Figure 3.12 Comparison of the proposed panel zone stiffness and shear strength at $4\gamma_y$ and $6\gamma_y$ versus the measured ones from inelastic panel zone test data without doubler plates.

3.5 Effect of doubler plates

The impact of utilizing doubler plates, and their influence on the proposed model sufficiency is examined by means of supplemental CFE simulations featuring shallow and stocky (W14x398) as well as deep (W24x131) column cross sections with a one-sided thick doubler plate ($t_{dp} > 40$mm). Table 3.3 summarizes the virtual test matrix. It is comprised of panel zones in which the doubler plates are either welded with CJP or fillets to the respective column. The respective details are shown schematically in Figs. 3.13a and 3.13b. Note that the examined welded configurations are consistent with the current practice (AISC 2016a; AWS 2016). The shallow and stocky column (W14x398) does not necessitate the presence of continuity plates according to the AISC (2016a) provisions. The doubler plate thickness is determined by the fillet radii of the column cross section to avoid welding in its k-area (Lee et al. 2005c). Since for both cross sections the fillet radii, r, used for detailing equals to 33 mm, this leads to a doubler plate thickness of t_{dp} = 35mm (1-3/8" in). The respective fillet welds have a leg thickness of t_w = 48 mm by assuming that the filler metal classification strength, $F_{EXX} = 1.2F_{ycw}$ (F_{ycw}: yield stress of the column web base material). The calculated fillet weld material thickness satisfies the AISC (2016a) provisions. The doubler plate yield stress is assumed to be $F_{ydp} = 1.1F_{ycw}$. Neither plug welding nor horizontal welding on top and bottom of the doubler plates is necessary for the examined cases according to AISC (2016a). Either way, the above weld details would have increased the shear stress compatibility between the doubler plate and the column web. The column region is modelled with the same procedures discussed earlier. The doubler plate, which extends by $0.5d_b$ from the beam flanges, is modelled with quadratic brick elements with reduced integration (C3D20R). These are used to better capture the stress distribution through thickness of the doubler plate. Hard contact, that allows separation but not penetration, is employed between the doubler plate and the column web. In turn, the double plate is tied with the welding material, which was modeled explicitly as shown in Fig. 3.13.

Table 3.3 Virtual test matrix for the examination of doubler plate effectiveness.

Column	Beam	Doubler plate thickness [mm]	Welding type	Loading protocol
W14x398	W36x150	35	CJP	Cyclic symmetric
			Fillet	Monotonic
				Cyclic symmetric
				Collapse-consistent
W24x131	W30x108		CJP	Cyclic symmetric
			Fillet	Monotonic
				Cyclic symmetric
				Collapse-consistent

Three loading histories are employed: a monotonic, a ramped cyclic symmetric (AISC 2016a) and a collapse-consistent loading protocol (Suzuki and Lignos 2020) to account for potential accumulation of doubler plate shear stress incompatibility throughout the loading history. The shear stress incompatibility between the doubler plate and the column web is quantified based the relative difference between the average shear stresses in the column web, $\bar{\tau}_{cw}$, and doubler plates, $\bar{\tau}_{dp}$; that is $(\bar{\tau}_{cw} - \bar{\tau}_{dp})/\bar{\tau}_{dp}$.

Figures 3.14a and 3.14b show the above metric with respect to the accumulated panel zone shear distortion, $\Sigma\gamma$, for deep (W24x131) as well as shallow and stocky (W14x398) columns, respectively. Prior to panel zone yielding (i.e., γ_y), the stresses in the column web are higher than those in the doubler plate by 10 to 30%, depending on the cross section and the weld specification. However, once both the doubler plate and the column web yield, the relative difference of their shear stress demand is not more than -10%. This is attributed to the fact that the yield stress of the doubler plate is purposely assumed to be 10% higher than that of the column web. This indicates no evident stress incompatibility between the doubler plate and the column web.

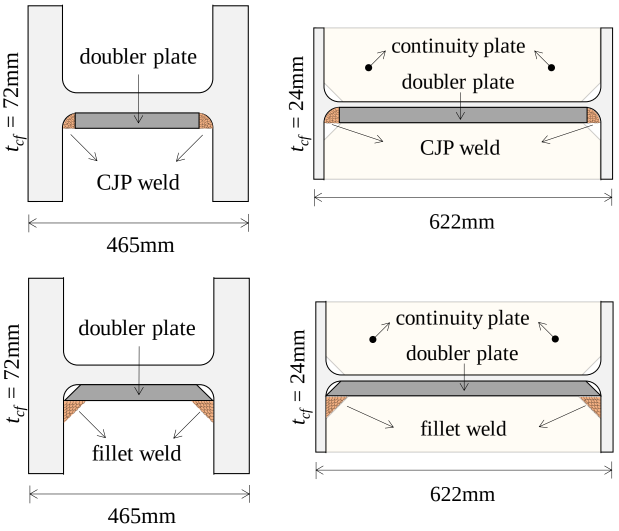
doubler plate
CJP weld
t_{cf} = 72mm
465mm
continuity plate
doubler plate
CJP weld
t_{cf} = 24mm
622mm
doubler plate
fillet weld
t_{cf} = 72mm
465mm
continuity plate
doubler plate
fillet weld
t_{cf} = 24mm
622mm

(a) column: W14x398 (b) column: W24x131

Figure 3.13 Continuum finite element model CJP and fillet weld details.

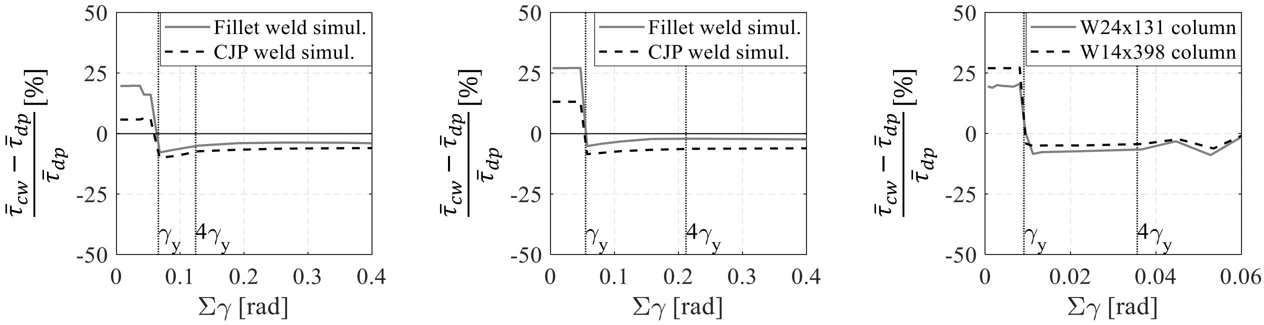

(a) column: W24x131 – symmetric cyclic protocol

(b) column: W14x398 – symmetric cyclic protocol

(c) collapse-consistent protocol

Figure 3.14 Relative difference in the average shear stresses between the doubler plate and the column web versus accumulated panel zone shear distortion.

Referring to Figs. 3.14a and 3.14b, the use of a CJP weld provides higher shear stress compatibility (more than 90%) compared to fillet welded doubler plates (70-80% at shear distortions lower than γ_y). It is also observed that the relative difference is initially higher for stocky and shallow columns compared to deep ones. However, after panel zone yielding, this difference diminishes. This is more apparent in Fig. 3.14c under the collapse-consistent loading protocol regardless of the examined column cross section. In brief, Fig. 3.14 suggests that the doubler plate ineffectiveness is not an issue for beam-to-column connections detailed according to AISC (2016a) and AWS (2016). For thick fillet-welded doubler plates, if the requirement for considerably thick fillet welds (so that the stresses impending from the column are properly attained by the doubler plate) is met, the doubler plate(s) and the column web attain fairly similar shear stresses. Therefore, the total panel zone thickness, including the double plate(s) (i.e., $t_{pz} = t_{cw} + t_{dp}$), may be directly employed in Eqs. (3.4), (3.17) and (3.18). Figure 3.15 illustrates indicative comparisons between the proposed model and data from full-scale beam-to-column joints with doubler plates retrieved from the analyzed inelastic panel zone cases.

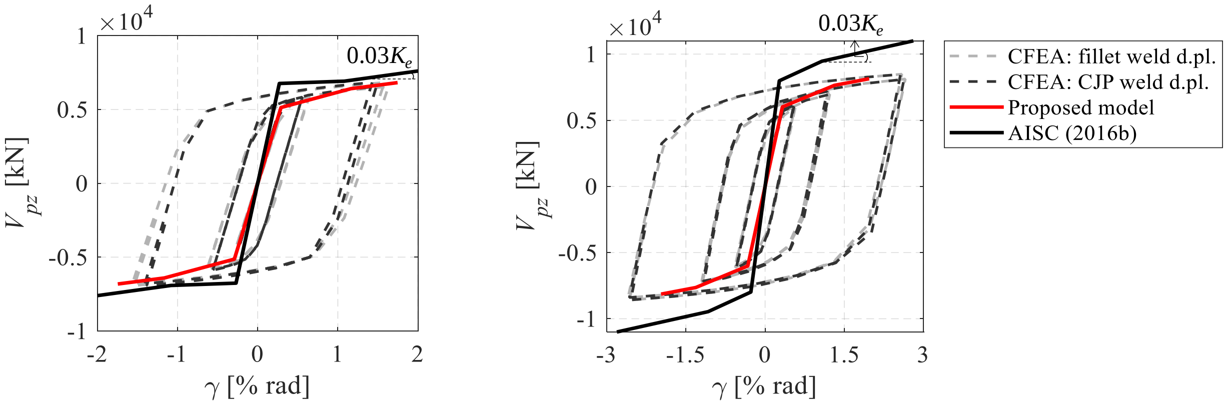

(a) W24x141 column

(b) W14x398 column

Figure 3.15 Comparison of measured and predicted response of panel zones with fillet- and CJP-welded doubler plates.

The authors are of the opinion that the doubler plate-to-column web shear-stress incompatibility, which was mostly highlighted in prior studies on pre-Northridge beam-to-column connections (Slutter 1981), is attributed to the uncertainty of the welding material and the weld specifications that were employed at that time. Differences in material properties between doubler plates (e.g., use of A36 plates) and the respective column (e.g., A992 or A572 Gr. 50) could have attributed to some of the reported differences.

3.6 Effect of axial load

This section examines how the axial load should be considered within the proposed model to design/model inelastic panel zones in end (exterior) and interior steel MRF beam-to-column connections. In the former, columns experience axial load variations due to the transient axial load component. Doubler plates are omitted in these simulations since this effect was separately examined in the previous section. Table 3.4 summarizes the virtual test matrix that was examined in this case. In brief, a gravity load ratio, P_g/P_y, of 15%, 30% and 50% is considered for interior columns, whereas $P_g/P_y = 15\%$ is assumed for end columns. The first two values are deemed reasonable based on nonlinear response history analyses of representative 4- and 8-story steel MRF designs (Elkady and Lignos 2014, 2015) according to current design specifications. The last gravity load ratio may be representative in existing high-rise steel MRF buildings designed prior to the 1994 Northridge earthquake (Bech et al. 2015). The axial load demand variation in end columns is depicted based on representative loading histories developed for experimental testing of steel MRF columns (Suzuki and

Lignos 2020). In particular, the imposed axial load demand, P/P_y, varies from -10% (tension) to 40% (compression) for the 8-story and from 5% to 25% for the 4-story MRF as retrieved from Suzuki and Lignos (2020). This is coupled with the imposed same shear distortion demand as the interior columns.

Table 3.4 Virtual test matrix for the examination of the axial load effect.

Column	Beam	Number of stories	Joint location	P_g/P_y
W14x398	W36x150	-	interior	15%
				30%
				50%
		4	end	15%
		8		
W24x131	W30x108	-	interior	15%
				30%
				50%
		4	end	15%

According to the AISC (2016b) specifications, no reduction in the panel zone shear strength would be introduced if it was designed to attain inelastic deformations (i.e., $n < 0.75$). If the panel zone was designed to remain elastic [based on $R_{n,el}$ from AISC (2016b) specifications], then a reduction based on the von Mises criterion (von Mises 1913) would be employed. In prior work by Kim et al. (2015), it was assumed that the axial load is only sustained by the column flanges. However, this does not hold true because the present study suggests that the column web contribution in sustaining the axial load demand may be up to 40%. As such, in the proposed model, n, accounts for the full column cross section with regard to the axial yield strength calculation. The relative difference between the panel zone shear resistance with/without the applied axial load throughout the loading history is computed as $(V_{pz}^{n=0} - V_{pz}^{n>0})/V_{pz}^{n=0}$, to evaluate the influence of the axial load.

3.6.1 Interior columns

Figure 3.16 shows the relative difference of interest versus the accumulated panel zone shear distortion, $\sum\gamma$, for the examined interior columns. In the same figure, a line is superimposed representing the relative difference according to AIJ (2012). The two plots of this figure are not schematically comparable, since the panel zone shear distortion history differs in both cases. Moreover, due to the imposed cyclic loading history, the relative difference attains zero when the panel zone shear strength attains zero as well. It is observed that the von Mises criterion, which is adopted by AIJ (2012) and AISC (2016b) for elastic panel zone design, corresponds well with the results regardless of the $\sum\gamma$ level. However, for inelastic panel zone design that no reduction in strength would be applied according to AISC (2016b), the panel zone shear resistance is overestimated by more than 10% for $P_g/P_y > 30\%$, depending on the cross section. However, the above gravity load ratio range is uncommon in contemporary steel MRF designs (Elkady and Lignos 2014, 2015; Suzuki and Lignos 2020).

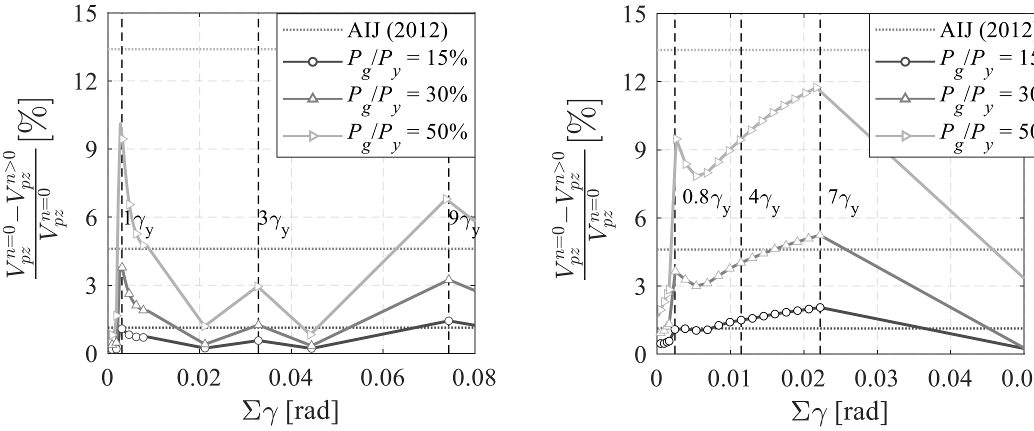

(a) W24x131 column (b) W14x398 column

Figure 3.16 Panel zone relative difference between the panel zone shear strength with/without applied axial load versus accumulated panel zone shear distortion for interior columns.

3.6.2 End columns

Figure 3.17 depicts the reduction in shear strength for both interior and end column panel zones for an 8-story MRF. It is observed that applying the von Mises criterion only for the applied gravity load leads to marginally unconservative results (~10%). Therefore, the panel zone shear strength reduction should be applied for the absolute peak load ratio P/P_y including the transient axial load component. For a 4-story MRF, the panel zone shear strength reduction is negligible (less than 4%) due to the decreased axial load variation in end columns.

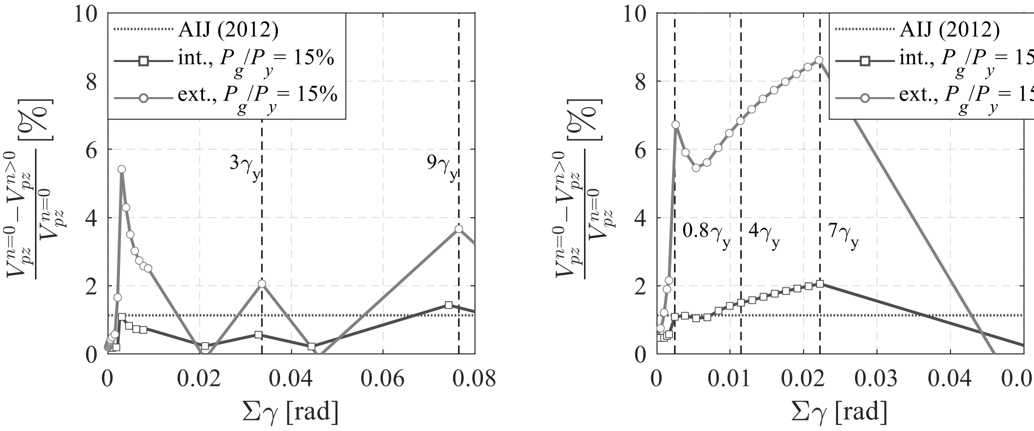

(a) W24x131 column (b) W14x398 column

Figure 3.17 Panel zone relative reduction due to axial force versus accumulated panel zone shear distortion for both interior and exterior columns (8-story steel MRF).

3.7 Limitations of the present study

The proposed panel zone model neglects the influence of the composite action on the panel zone behavior. This is an important aspect to be considered (Castro et al. 2005; El Jisr et al. 2019; Elkady and Lignos 2014; Kim and Engelhardt 2002). On the other hand, practical methods to decouple the slab from the steel column/panel zone are available (Chaudhari et al. 2019; Tremblay et al. 1997). While the effect of cyclic hardening on the panel zone shear strength was disregarded, during design-basis earthquakes, capacity-designed steel MRFs are likely to experience modest lateral drift demands (i.e., 2%); therefore, the panel zone is likely to experience shear distortions of nearly $4\gamma_y$, depending on the panel zone-to-beam relative strength ratio. Cyclic hardening is fairly minor for this range of shear distortions; thus, the proposed model should predict fairly well the panel zone shear strength. Moreover, at seismic intensities associated with low probability of occurrence seismic events (i.e., 2% in 50 years) the steel MRF behavior is expected to be asymmetric due to ratcheting (Lignos et al. 2011, 2013). Shake table collapse experiments (Lignos et al. 2013; Suita et al. 2008) suggest that the panel zone inelastic behavior is fairly similar with that depicted by the examined collapse-consistent loading protocol. Moreover, the use of A36 doubler plates with A992 Gr. 50 steel columns was not investigated. While this practice appeared to be a default choice in pre-Northridge steel MRF designs, the use of A572 Gr. 50 doubler plates with A992 Gr. 50 steel columns appears to be the current practice in modern seismic-resistant steel MRFs. Finally, the proposed model should be further validated for beam-to-column connections comprising hollow structural columns.

3.8 Summary and conclusions

This chapter presents a new panel zone model for the seismic design and analysis of beam-to-column panel zone joints in capacity-designed moment-resisting frames (MRFs). The proposed model, which is developed on the basis of structural mechanics, reflects the realistic stress distributions within a panel zone joint geometry. These distributions are extracted from continuum finite element (CFE) models, which are thoroughly validated to available experimental data from pre- and post-Northridge interior and exterior subassemblies. We propose improved equations to predict the panel zone stiffness and shear strength at discrete levels of panel zone shear distortion pertinent to the balanced design of steel MRF beam-to-column joints according to current seismic provisions.

The CFE simulation results underscore that the commonly used assumption of uniform shear yielding is only valid in panel zone geometries featuring stocky and shallow column cross sections regardless of the inelastic shear distortion level.

The elastic stiffness, K_e [see Eq. (3.4)], of the proposed panel zone model considers both shear and bending deformations based on shear strength equilibrium within the panel zone. Hence, its performance in predicting the elastic stiffness of slender panel zones (beam-to-column depth ratios, $d_b/d_c \geq 1.5$) is superior compared to available models in the literature as well as the ones available in current seismic provisions.

The proposed equation [see Eq. (3.17)] for the panel zone shear strength at yield, V_y (i.e., shear distortion of γ_y), matches that of the Krawinkler (1978) model for panel zones that are shear deformation-dominant (i.e., stocky cases) but performs much better in cases that the bending contribution is appreciable.

Comparisons with available full-scale test data suggest that the proposed model predicts the panel zone shear strength, V_p, [see Eq. (3.18) and Table 3.2] at a shear distortion of $4\gamma_y$ with a noteworthy accuracy even when panel zones feature columns with relatively thick flanges (i.e., $t_{cf} \geq 40\text{mm}$). The current model in the AISC (2016b) seismic specifications overpredicts V_p by 20% to 50% depending on the panel zone geometry. In that respect, the proposed model addresses a well-known limitation of available models in the literature.

The CFE simulations reveal that the commonly assumed value of $0.03K_e$ for the stiffness beyond $4\gamma_y$ shear distortions is not justifiable in most panel zone geometries. This is due to the increased column flange contribution to the panel zone strength at large inelastic shear distortions ($\gamma > 4\gamma_y$). For this reason, we propose an expression to predict the panel zone shear strength, $V_{6\gamma_y}$ [see Eq. (3.18) and Table 3.2], at a shear distortion of $6\gamma_y$. Beyond $6\gamma_y$, the panel zone is assumed to have the same stiffness with the proposed $4\gamma_y - 6\gamma_y$ branch.

Based on the examined cases, it is also found that the doubler plate to column web shear stress incompatibility does not appear to be an issue for beam-to-column connections, which are detailed according to current seismic provisions and detailing criteria (AISC 2016a; AWS 2016). Consequently, neither fillet nor CJP welded doubler plates should be treated differently either by reducing their strength or by intentionally accounting for one of the two doubler plates [i.e., CEN (2005)]. The authors are of the opinion that the doubler plate ineffectiveness reported in the literature is mostly attributed to weld specifications and construction practices prior to the 1994 Northridge earthquake.

Supplemental CFE simulations suggest that the von Mises criterion (von Mises 1913) may still be used to reduce the predicted panel zone shear strength for both interior and end columns in steel MRFs regardless of the employed lateral loading history. The shear strength reduction should always be based on the peak axial compressive load imposed to the respective column including the transient axial component due to dynamic overturning effects.

3.9 Dedication

This chapter is dedicated to the memory of Professor Helmut Krawinkler, former professor at Stanford University, who was among the first to identify the importance of the panel zone on the seismic behavior of steel MRFs in the early 1970s. This study builds upon his outstanding contribution and would not have been possible without it.

Chapter 4 Proposed backing bar detail in welded beam-to-column connections for seismic applications

Bibliographic details

This chapter presents the pre-print (accepted) version of the article with the following full bibliographic details:

Skiadopoulos, A., and Lignos, D. G. (2022). "Proposed backing bar detail in welded beam-to-column connections for seismic applications (accepted)." *Journal of Structural Engineering*, American Society of Civil Engineers. DOI: https://doi.org/10.1061/(ASCE)ST.1943-541X.0003374.

Author's contribution

Concerning the material presented in this chapter, Andronikos Skiadopoulos developed the proposed backing bar geometry, developed the continuum finite element (CFE) models, carried out the CFE simulations, analyzed the simulations results, created the figures, wrote the manuscript draft and revised the manuscript. The co-author contributed in developing the methodology presented in this chapter, supervising the work conducted by Andronikos Skiadopoulos, funding acquisition, and reviewing and editing the original and final manuscript drafts.

4.1 Introduction

Comprehensive evaluations in field-welded steel moment-resisting frame (MRF) buildings prior to 2000 (FEMA 2000b) and corroborating experimental studies after the 1994 Northridge earthquake (FEMA 2000a) highlighted a number of issues with regard to the, admittedly, poor seismic performance of field-welded unreinforced flange-bolted web (WUF-B) beam-to-column connections (FEMA 2000a; b). This connection is shown in Fig. 4.1a. Particular emphasis was placed in the bottom beam flange-to-column flange groove welded portion, which is shown schematically in Fig. 4.1b.

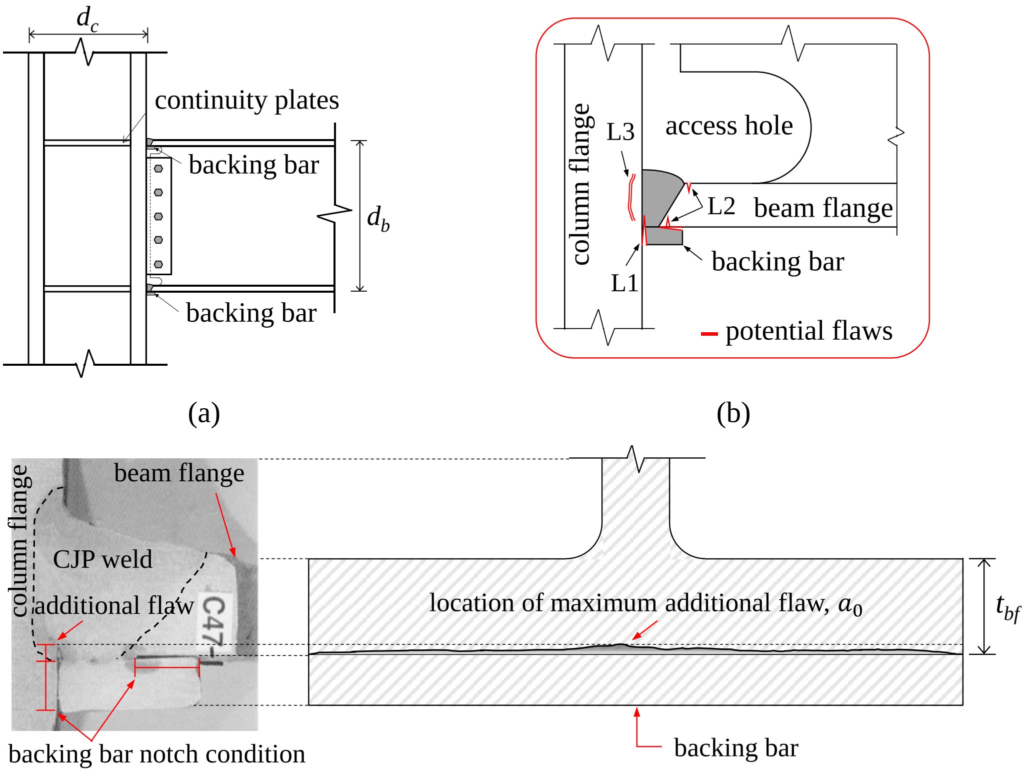
d_c
continuity plates
backing bar
d_b
backing bar
column flange
L3
access hole
L2
beam flange
backing bar
L1
potential flaws
column flange
beam flange
CJP weld
additional flaw
C47-1
backing bar notch condition
location of maximum additional flaw, a_0
t_{bf}
backing bar

(a) (b)

(c)

Figure 4.1 Welded unreinforced flange-bolted web (WUF-B) pre-Northridge connection: (a) typical configuration; (b) potential locations for crack initiation; and (c) typical bottom beam flange-to-column flange connection detail [adopted from (Paret 2000a), credit: Prof. J. Fisher] and schematic of additional flaw profile along the beam flange width.

In typical pre-Northridge WUF-B connections, the backing bars of rectangular shape were often left in place after completing the beam-to-column complete joint penetration (CJP) groove welds (FEMA 2000a). These welds were usually realized with self-shielded flux-cored arc welding (FCAW-SS) with a low toughness weld electrode E70T-4. Referring to Fig. 4.1c, the backing bar imposed a notch condition within the column and/or the beam flanges. Moreover, an additional crack-like flaw, a_0, often penetrated through the CJP weld root. The depth of this flaw was not uniform along the beam flange width as shown schematically in Fig. 4.1c. It maximized in the beam web centerline, where the welding process was interrupted. The presence of backing bars restricted weld inspections for potential flaws that were deemed critical in low toughness groove welds at the time. Kaufmann and Fisher (1996) found that a_0 varied between 3 and 10mm. The backing bar-to-column flange notch condition (noted as location "L1" hereinafter as per Fig. 4.1b), together with the high strain demands in the outer beam bottom flange fiber and the increased triaxial stresses due to the column web restraint, often triggered crack initiation and fracture at the same location (Mahin 1998; Miller 1998; Yang and Popov 1995). Figure 4.2 highlights a WUF-B connection where the particular fracture pattern initiated from the bottom backing bar at L1 and penetrated through the CJP weld material.

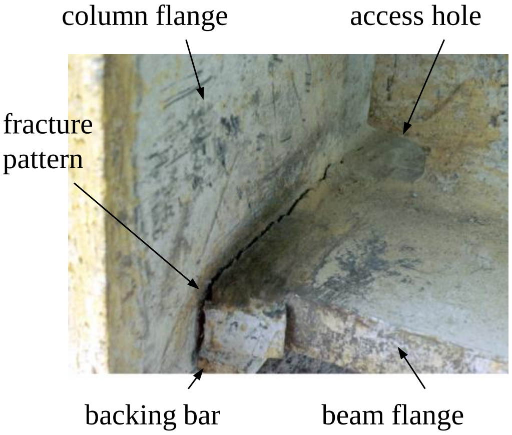

Figure 4.2 Fracture pattern observed during the 1994 Northridge earthquake in a welded unreinforced flange, bolted-web connection (photo courtesy: Professor Michael Engelhardt).

Referring to Fig. 4.1b, discontinuities adjacent to the beam flange-to-column flange CJP weld of pre-Northridge WUF-B connections often turned into crack-like flaws during the shrinkage of the weld material that was restrained by the surrounding base metal. These flaws, which are usually situated in the heat affected zone (HAZ), may be located either at the outer and/or the inner flange fiber (denoted as location "L2" hereinafter). Depending on the accuracy of the non-destructive inspection method, the depth of these crack-like flaws usually ranges from 0.1 to 0.5mm (ASTM 2015, 2017, 2018b). The increased fracture potential due to the presence of the above crack-like flaws together with the inferior base and weld material toughness requirements of pre-Northridge connections often lead to fracture that initiated at L2 and propagated through the CJP weld or the base metal of the beam flange. However, advancements in welding procedures (AWS 2010) and electrode specifications for demand critical welds (AISC 2016a) in pre-qualified beam-to-column connections reduce considerably the fracture potential at L2.

Krawinkler (1995) found that the inferior through-thickness steel material properties often lead to fracture due to lamellar tearing in pre-Northridge connections (denoted as location "L3" hereinafter) when steel columns featured relatively thick flanges (t_{cf} > 38mm). This reflects current practice requirements for non-destructive testing evaluation (AISC 2016a). The inferior through-thickness steel material properties result from the hot rolling process that transforms the metal inclusions to thin and long discontinuities parallel to the base metal longitudinal direction (Miller 2017). These can separate at a certain amplitude of imposed strain demands, thereby compromising the overall ductility of the connection. However, structural steel materials with through-thickness strength and toughness properties, which are equivalent to those in the longitudinal one, are currently available (Kanno 2016; Miki et al. 2002). For instance, in Europe, the through-thickness Z-direction demand, Z_{Ed}, determines the Z-direction material resistance, Z_{Rd}, to be utilized (CEN 2004b). In the US, the use of A913 Gr. 50 or 65 steel is an interesting alternative (Bouchard and Axmann 2000). Therefore, divot fracture at L3 is unlikely to occur in today’s connections provided that the above material requirements are respected.

Finally, the weld access hole geometry of the WUF-B connection often triggered crack initiation near the toe of the weld access hole. While there is no apparent initial sharp crack-like flaw in this area, microvoid nucleation, growth and coalescence (Kanvinde 2017) often lead to fracture initiation and propagation due to the concentration of high plastic strain demands and triaxial stresses. However, this crack type is stable, and it is not considered to compromise the overall connection ductility under cyclic loading (Suzuki and Lignos 2021).

The aforementioned considerations have been articulated in current standards (AISC 2016c; AWS 2010) and other concerted efforts (Landolfo et al. 2018) to enhance the seismic ductility of pre-qualified field-welded beam-to-column connections. Referring to Fig. 4.3, an improved weld access hole geometry is utilized based on rigorous finite element analysis studies (El-Tawil et al. 2000; Ricles et al. 2002a). This geometry minimizes the strain localization at the toe of the bottom beam flange weld access hole. Detailed surveys from prior testing in pre-qualified field welded connections suggests that fracture initiation at this location is unlikely to occur at lateral drift demands prior to 6% rads (Skiadopoulos and Lignos 2021). Moreover, the use of welded-web attachments in pre-qualified welded unreinforced flange-welded web (WUF-W) beam-to-column connections (see Fig. 4.3), which is the primary focus of this chapter, is imperative in an effort to reduce the, arguably large, seismic shear transfer and its prying effects into the beam flanges (Richard 2003).

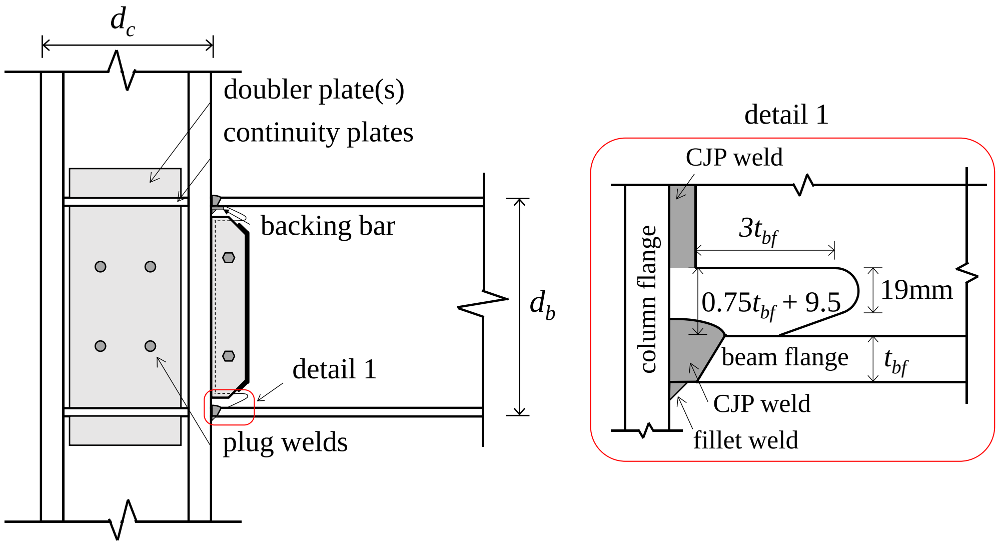

Figure 4.3 Typical welded unreinforced flange-welded web (WUF-W) pre-qualified connection detailing.

In today’s WUF-W connections, the bottom beam flange backing bar should be removed after the completion of the CJP welds. Weld root back gouging and fillet reinforcement (see Fig. 4.3) is necessary. Albeit this connection detailing minimizes the fracture potential (Chi et al. 2000), its fabrication is time consuming, thereby leading to increased fabrication costs (FEMA 2000a; Miller 2017; Popov et al. 1998). With today’s toughness requirements for demand-critical CJP welds, which are commonly used in pre-qualified beam-to-column connections (AISC 2016a), possible built-in flaws do not necessarily lead to brittle fracture (Shaw et al. 2015). A thorough review of available experimental data in post-Northridge connections (Skiadopoulos and Lignos 2021), suggests that fracture at L2 is unlikely to occur prior to 5-6% lateral drift demands. Therefore, cost-effective simplifications during fabrication of WUF-W connections for seismic applications may be possible. For the same reason, similar simplifications have been proposed for welded base plate connections (Myers et al. 2009) as well as welded column splices (Shaw et al. 2015; Stillmaker et al. 2016).

In prior work (Chi et al. 2000; Wang et al. 2010; Yang et al. 2019), alternative backing bar configurations were explored in an effort to reduce the fracture potential at the bottom beam flanges of WUF-B connections. The general consensus from these studies was that modified backing bar details may somewhat reduce the fracture potential relative to that from the use of conventional backing bar geometries. However, the above studies shared a number of limiting features. Particularly, these included (a) a single beam-to-column geometry; and (b) the use of two-dimensional (2-D) finite element models, that generally underpredicted the fracture potential at the bottom beam flange by about 40% (Chi et al. 2000). Particularly, 2-D finite element models do not properly depict the increased restraint at the center of the beam-flange-to-column flange joint, which increases the triaxiality and generally leads to nearly two times higher fracture potential in this location than that of the beam flange tip (Chi et al. 2000).

Motivated by the above, this chapter revisits, through simulation-assisted engineering, the commonly used practice in field-welded beam-to-column connections for seismic applications, aiming to propose potential fabrication detailing simplifications with emphasis on weld backing bar details. The proposed methodology, which features traditional fracture mechanics informed by 3-D continuum finite element (CFE) analyses, is validated by available pre-Northridge WUF-B connection full-scale experiments. A customized backing bar detail is then proposed that, although it is not removed after the completion of the CJP groove welds, decreases appreciably the fracture potential in both pre- and post-Northridge field-welded connections. In order to substantiate the findings, several parameters are interrogated, including the panel zone design distortions, the beam depth, as well as the thickness of the beam and column flanges. Limitations as well as directions for future work are discussed.

4.2 Methodology

While the focus of this chapter is to advance the seismic performance of post-Northridge WUF-W connections, knowledge and data acquired from prior work on pre-Northridge WUF-B connections is also of interest. The emphasis is on how to minimize the fracture potential at location L1. The current weld toughness requirements and weld practice (AISC 2016a; AWS 2016) for demand critical welds, the non-destructive testing evaluation (AWS 2010) along with the updated weld access hole geometries (AISC 2016c) and the current base metal technology (Kanno 2016; Miki et al. 2002) ensure a minimum fracture potential at L2 and L3 and at the toe of the access hole as discussed earlier. The type of fracture at L1 dictates the pertinent fracture mechanics method to be employed, which is informed by CFE analyses. These comprise beam-to-column subassembly global models that do not include backing bar and sharp crack-like built-in flaws in the locations of high fracture potential. These are explicitly considered in carefully developed and validated submodels, which are informed by the global connection models. The subsequent sections discuss the primary features of the employed methodology.

4.3 Employed fracture mechanics methods, primary assumptions and sensitivity analyses

The apparent sharp crack-like flaw (referred to as crack hereinafter) at L1 prohibits the applicability of micromechanics-based models (Jia and Kuwamura 2014; Kanvinde 2017). Instead, traditional fracture mechanics methods (Irwin 1961; Rice 1968; Wells 1961) should be employed. Location L1 is likely to experience relatively high stress and strain demands, regardless of the relative strength of the beam with respect to the column panel zone. For panel zone joints exhibiting highly inelastic shear distortions (e.g., $\gamma > 10$ to $12\gamma_y$, where γ_y is the panel zone shear distortion angle at yield), kinking in the panel zone edges may occur (Krawinkler 1978). The plastic zone is not bounded within the validity region of linear elastic fracture mechanics; thus, elastic-plastic fracture mechanics methods reflect a more realistic computation of the fracture potential at L1 (Kanvinde et al. 2008; Stillmaker et al. 2016). The same holds true for beam-to-column connections featuring a strong panel zone design.

In elastic-plastic fracture mechanics, there are two well established fracture metrics; the crack tip opening displacement ($CTOD$), which was originally proposed by Wells (1961) and the J-integral (Rice 1968). Fracture initiation occurs once the computed $CTOD$ or J-integral demand exceeds the respective material toughness ($CTOD_C$ and J_C, respectively). Referring to Fig. 4.4a, the J-integral (also called as the nonlinear energy release rate of a body) is defined by the change of the potential energy, Π, due to the extension, da, of a crack. The potential energy of a body is defined as the difference between the strain energy of the deformation and the potential energy of the tractions. Therefore, it can be proven that the J-integral is given by Eq. (4.1) for the two-dimensional x-y space:

$$J = \int_{\Gamma} \left(w dy - T_i \frac{\partial u_i}{\partial x} ds \right) \tag{4.1}$$

where, w is the strain energy density; T_i are the components of the boundary tractions vector; u_i are the components of the displacement vector; and ds is the increment along a contour Γ.

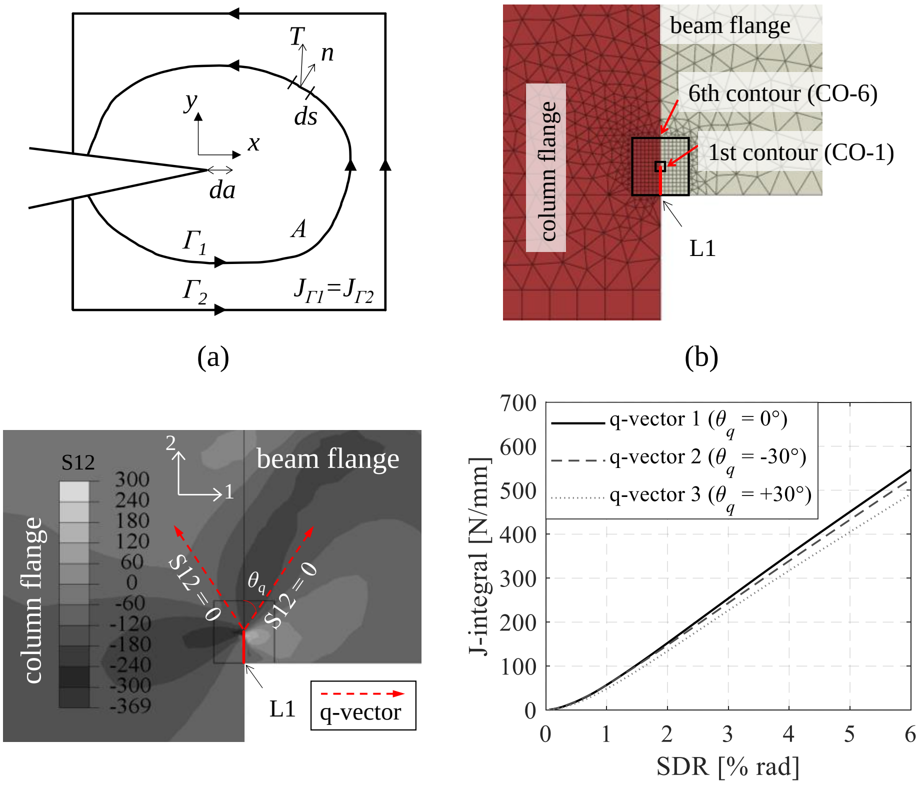

(a) (b)

(c) (d)

Figure 4.4 J-integral computation specifics for a typical beam flange-to-column flange connection: (a) contours for J-integral computation; (b) continuum finite element model contours for the L1 crack; (c) shear stress field of the L1 crack and respective q-vector definitions; and (d) J-integral versus story drift ratio for different q-vector definitions.

Referring to Fig. 4.4a, arbitrarily selected contours $\Gamma_1$and Γ_2 do not influence the J-integral computation. The J-integral is applicable to hyperelastic materials (i.e., deformation theory of plasticity), while it is not valid in materials experiencing irreversible plastic deformations (i.e., incremental theory of plasticity). However, the commercial finite element analysis software ABAQUS (version 6.14-1) (SIMULIA 2019) idealizes a steel material undergoing plastic deformations with an equivalent hyperelastic material; hence, the simulation results are deemed reasonable for monotonic loading regardless of the employed constitutive material law. These considerations hold true for both two- and three-dimensional problems that include J-integral computations (Bakker 1984; Brocks and Scheider 2001).

Several pre-Northridge WUF-B connections experienced fracture at L1 prior to the first ground motion reversal (FEMA 1997); hence the preceding small loading cycles did not practically influence the connection behavior. Moreover, shake table testing of steel MRFs with emphasis at collapse (Lignos et al. 2011, 2013) as well as tests that quantified the influence of loading history on the hysteretic behavior of steel connections

(Yu et al. 2000) and their members (Suzuki and Lignos 2021) suggest that the use of monotonic loading is indicative when ground shaking in the forward directivity region of a fault rupture is characterized by a large pulse early in the ground motion history. However, it is recognized that this is not generalizable in cases where the seismic hazard is characterized by other types of ground motion.

While the stress-strain field in the crack vicinity may not be accurately represented by CFE analyses, the advantage of using the J-integral is that the integration along a path, which does not include that region, provides legitimate results (Brocks and Scheider 2001). Referring to Fig. 4.4b, at L1, the J-integral is accurately computed by a contour that is far away from the crack vicinity (i.e., CO-6 instead of CO-1). Mesh and contour sensitivity analyses are, thus, imperative. Unlike the J-integral, the $CTOD$ necessitates a much finer mesh to accurately estimate the displacement field in the crack vicinity. Consequently, the J-integral metric is employed in the subsequent analyses.

The employed CFE software (ABAQUS) utilizes the virtual crack extension method (deLorenzi 1982; Parks 1977) for the J-integral computation; hence, the potential crack extension direction (i.e., q-vector) should be defined. According to Erdogan and Sih (1963), the crack propagates in the direction of the principal plane. Assuming that the stress flow is perpendicular to the potential crack at L1, the q-vector is parallel to the column longitudinal direction; hence, it represents the mode I fracture mechanism. In reality, the shear stresses near the crack tip do not lead to principal planes that are parallel to the crack. Referring to Fig. 4.4c for a representative crack at L1, the principal plane deviates by about 30° (shown as θ_q) from the beam flange-to-column flange interface plane. As such, in principle, the q-vector should be defined based on these planes. Figure 4.4d compares the J-integral evolution at L1 with respect to the story drift ratio (SDR) for the employed q-vector (i.e., θ_q = 0°) and those corresponding to the principal plane angle (i.e., θ_q = ±30°). The insignificant difference between the J-integral computations of the examined cases suggests that θ_q = 0° can be assumed in the CFE.

In welded connections, cracks may form at interfaces between different materials (e.g., in locations L1 and L2). This poses a challenge regarding the J-integral path independence at the interface (Brocks and Scheider 2001). Kolednik et al. (2005) and Simha et al. (2003) showed that if the bi-material interface plane is parallel to the crack plane, the J-integral path independence is respected, assuming that the contours along which the J-integral is computed are perpendicular to the interface (Smelser and Curtin 1977). This condition is respected for the bi-material interface between the beam and column flanges as shown in Fig. 4.4b.

4.4 Continuum finite element modeling for informing fracture mechanics methods

To reduce the associated computational cost in the CFE analyses, the node-based submodeling technique of ABAQUS (version 6.14-1) (SIMULIA 2019) is employed. A global model of a beam-to-column connection is initially loaded monotonically. Once the analysis is conducted, nodal deformations of the global model at all degrees of freedom are applied as boundary conditions in the selected submodel nodes, which are common to the global model. The presence of cracks and weld backing bars influences the deformation field at the crack vicinity, while their far field effect is miniscule. This implies that the crack at L1 and the backing bars can be neglected from the global model, whereas they can be explicitly considered in the submodel. Consequently, the submodel mesh is much finer than that of the global model.

In this section, the basic features of the two models are highlighted. Particularly, a representative global model is shown in Fig. 4.5, together with three submodel variants (noted as submodels 1, 2 and 3). The primary difference between the three submodels is associated with their boundary conditions. One of the three is selected based on a sensitivity analysis that is discussed later on in this section.

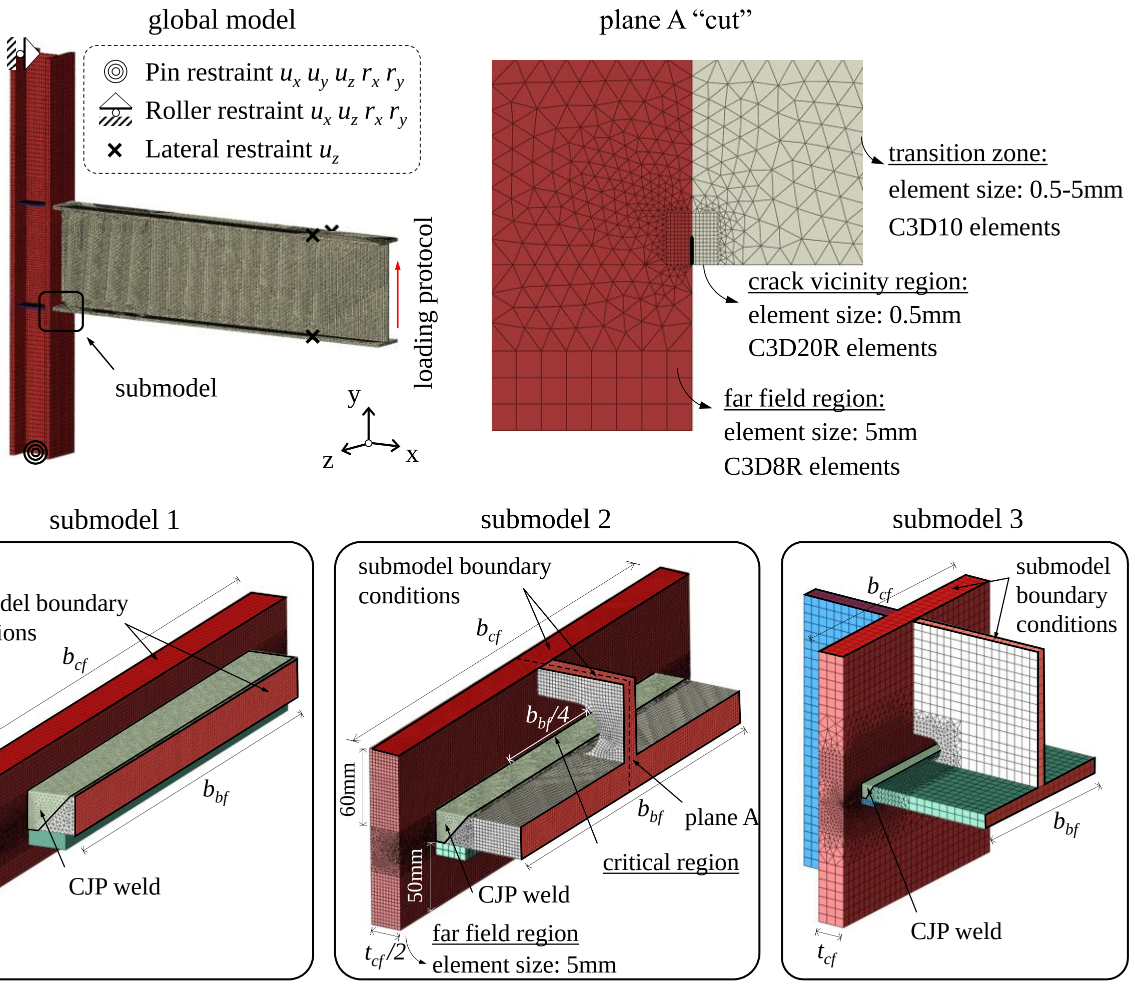
global model
Pin restraint $u_x\ u_y\ u_z\ r_x\ r_y$
Roller restraint $u_x\ u_z\ r_x\ r_y$
Lateral restraint u_z
loading protocol
submodel
y
z
x
plane A "cut"
transition zone:
element size: 0.5-5mm
C3D10 elements
crack vicinity region:
element size: 0.5mm
C3D20R elements
far field region:
element size: 5mm
C3D8R elements
submodel 1
submodel boundary conditions
b_{cf}
b_{bf}
CJP weld
$t_{cf}/2$
submodel 2
submodel boundary conditions
b_{cf}
$b_{bf}/4$
60mm
50mm
b_{bf}
plane A
critical region
CJP weld
far field region
element size: 5mm
$t_{cf}/2$
submodel 3
b_{cf}
submodel boundary conditions
b_{bf}
CJP weld
t_{cf}

Figure 4.5 Continuum finite element model of a beam-to-column connection; global model and submodel variants.

The global model utilizes twenty-node quadratic elements with reduced integration (C3D20R) with a characteristic element size of 15mm. Local initial geometric imperfections are accounted for in the steel beams to properly trigger local buckling, according to modeling recommendations by Elkady and Lignos (2018b). The CFE model employs a combined isotropic/kinematic hardening law (Lemaitre and Chaboche 1990) with consistent input material model parameters for cyclic metal plasticity as proposed by de Castro e Sousa et al. (2020) for A992 Gr. 50 steel (i.e., nominal yield stress, f_y = 345MPa). Prior studies on the fracture potential of beam-to-column connections (Chi et al. 2000) have shown that the role of residual stresses is negligible; hence, they are disregarded in the context of the present study. The CFE modeling assumptions for the global CFE model have been thoroughly summarized and validated in prior studies by Skiadopoulos et al. (2021).

The examined submodels constitute twenty-node quadratic elements with reduced integration (C3D20R). The characteristic size for the J-integral contours near the crack vicinity in the critical region is 0.5mm (see Fig. 4.5). The mesh is chosen to be finer over a width of $b_{cf}/4$ near the beam web centerline, because the J-integral becomes maximum at this location. The far field region employs eight-node quadratic elements with reduced integration (C3D8R) and a characteristic size of 5 mm. The submodels consider cracks of constant depth, a_0, throughout the beam flange width, which is a fairly conservative assumption (see Fig. 4.1c). Two crack depths are assumed: 3mm and 6mm (Chi et al. 2000; Wang et al. 2010). The gradual transition from the very fine crack tip mesh to the coarser far field mesh is achieved by ten-node tetrahedral elements (C3D10) as shown in the plane A "cut" of Fig. 4.5. The element sizes were determined by a sensitivity analysis in which the relative difference between simulation results was no more than 1%. These results are not presented herein due to brevity.

Figure 4.6a depicts the variation of the J-integral with respect to SDR under monotonic loading for six different contours (CO-1 to CO-6) near the crack tip. The number of utilized elements for the computation of the J-integral at each contour is shown in parenthesis. For instance, the most approximate to the crack tip contour (i.e., CO-1), incorporates only four elements in the computations, whereas contour CO-6, which leads to more accurate J-integral calculations, incorporates 144 elements. For the selected element types and mesh size, the results convergence according to the fifth contour. Hereinafter, the reported results are always extracted from the sixth contour.

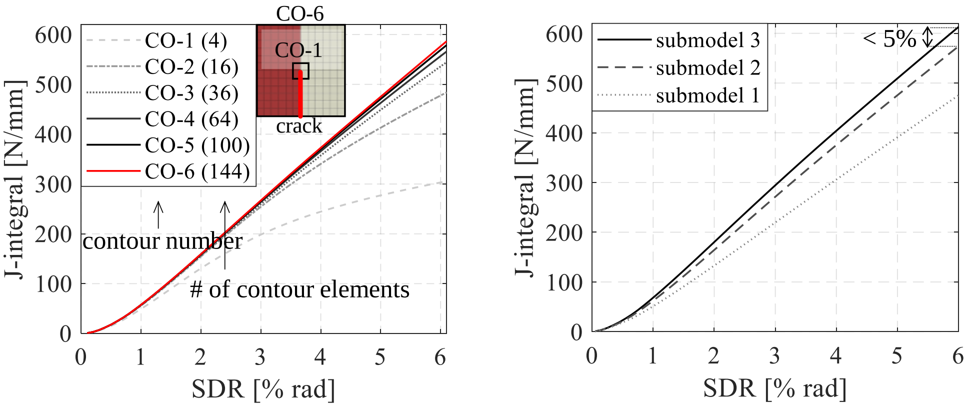

(a) (b)

Figure 4.6 Continuum finite element sensitivity analyses results: (a) contour number sensitivity analysis; and (b) submodel geometric sensitivity analysis.

Qualitatively, the global model underestimates the displacement field nearby the crack vicinity, because it neglects the crack at L1. This may underestimate the J-integral computations of the submodel if its boundary conditions are chosen such that they are close to the crack vicinity. Consequently, a submodel geometric sensitivity analysis is conducted. Figure 4.6b shows the variation of the J-integral with respect to SDR at the beam web centerline based on the three submodels. Submodel 1, which is considered to be the simplest one, underestimates the J-integral by about 30% for SDRs higher than 2% rads. On the other hand, submodel 2 provides nearly identical results with submodel 3, which is the most accurate one. As such, the geometry of submodel 2 is utilized for the analyses discussed hereinafter.

4.5 Overview and scope of fracture analysis

In the upcoming sections, the fracture potential of welded connections is examined based on the methodology discussed earlier. The primary scope is to demonstrate that simpler fabrication detailing suffices to minimize the fracture potential of both pre- and post-Northridge beam-to-column connections. Of particular interest is to revisit if removal of the bottom backing bar is deemed necessary after the completion of the CJP groove welds between the bottom beam flange-to-column flange. Referring to Fig. 4.7a, a conventional backing bar is first considered. While this is not expected to lead to superior results, it is considered as a reference case. A beveled backing bar (see Fig. 4.7b) is also examined. The premise in this case is to allow for the stress flow to pass through the backing bar, due to its attachment to the column flange. The beveled angle, θ_b, can be optimized through CFE analyses. The angle of the normal stress flow is varied so as the fracture potential at L1 (see Fig. 4.1b) is minimized. All the examined beveled angles, θ_b, and crack depths are summarized in Table 4.1. All the examined backing bar geometries conform to AWS (2016).

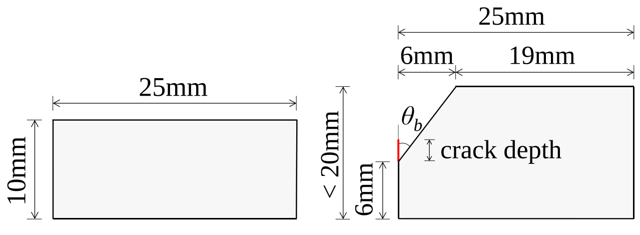

(a) (b)

Figure 4.7 Backing bar geometry: (a) conventional detail; and (b) beveled detail.

Table 4.1 CFE analyses beveled backing bar geometry characteristics.

θ_b	crack depth	θ_b	crack depth	θ_b	crack depth	θ_b	crack depth
35°	0 mm	25°	3 mm	-	-	-	-
35°	0 mm	30°	3 mm	25°	6 mm	-	-
45°	0 mm	35°	3 mm	30°	6 mm	25°	9 mm
60°	0 mm	45°	3 mm	35°	6 mm	30°	9 mm
∞	0 mm	60°	3 mm	45°	6 mm	35°	9 mm

The fracture analysis is mainly conducted on connection geometries featuring deep steel beams (i.e., W36x150) and web panel zones exhibiting inelastic shear distortions above $4\gamma_y$. The above criteria are intentionally selected because they can significantly compromise the ductility of welded connections (Chi et al. 1997; El-Tawil et al. 1999; FEMA 2000a; Lu et al. 2000; Mao et al. 2001; Ricles et al. 2002a, 2004b).

4.6 Assessment of pre-Northridge WUF-B connections

The chosen characteristic connection configuration to assess the differences between the two backing bar geometries in pre-Northridge WUF-B connections is the exterior subassembly UCB-PN3, which was tested by Yang and Popov (1995) at full scale as part of the SAC program (FEMA 1997). This specimen features a W36x150 deep beam and a W14x257 column. The beam-to-column web panel exhibited an inelastic shear distortion of $15\gamma_y$. The selected subassembly experienced fracture at the bottom beam flange CJP weld (at L1) prior to an SDR of 2% rads.

A 6mm weld toe with a 45° angle CJP weld is assumed as per AWS (2010). The web and flange measured material properties for the beams and the column are considered as per FEMA (1997) and for the weld metal as per Kanvinde et al. (2008). Figure 4.8 depicts the examined beam flange-to-column flange connections, together with the respective CFE submodels with a_0 = 3mm. Three different connection details are examined. In Fig. 4.8a, the model utilizes a conventional unreinforced backing bar. This has two potential crack tips; C1, that is adjacent to the backing bar and the column flange; and C2, that is adjacent to the backing bar and the beam flange. In Fig. 4.8b, the WUF-B connection is analyzed without the presence of the backing bar. Finally, Fig. 4.8c illustrates the pre-Northridge WUF-B connection with a beveled backing bar left in place after the completion of the CJP groove weld. In this case, crack tips C1 and C2 are explicitly considered.

Figure 4.9a shows the J-integral demand in the most critical location of the beam web centerline with respect to the SDR for all the analyzed cases. To put the results into perspective, the lower and upper bounds of the J-integral resistance (noted as J_{IC}) for the ASTM A572, Gr. 50 (i.e., f_y = 345MPa, where f_y is the nominal material yield stress) base metal of the column are superimposed in the same figure. These are computed according to Eq. (4.2):

$$J_{IC} = \lambda \cdot f_y \cdot CTOC_C \qquad (4.2)$$

where λ is a dimensionless factor, which is related to the stress state and the material properties and may be empirically assumed equal to 1.2 (Chi et al. 2000); $CTOD_C$ is the critical $CTOD$ and may be taken equal to 0.17mm (Chi et al. 1997). The lower bound of J_{IC} is determined based on the nominal yield stress of the steel base material (i.e., f_y = 345MPa), whereas the upper bound is based on its expected yield stress ($R_y f_y$ = 380MPa) as per AISC (2016a). The upper bound (J_{IC} = 78N/mm) matches that of the Grade 480 E70T7 low toughness filler metal, which was characteristic in pre-Northridge WUF-B connections (Kanvinde et al. 2008).

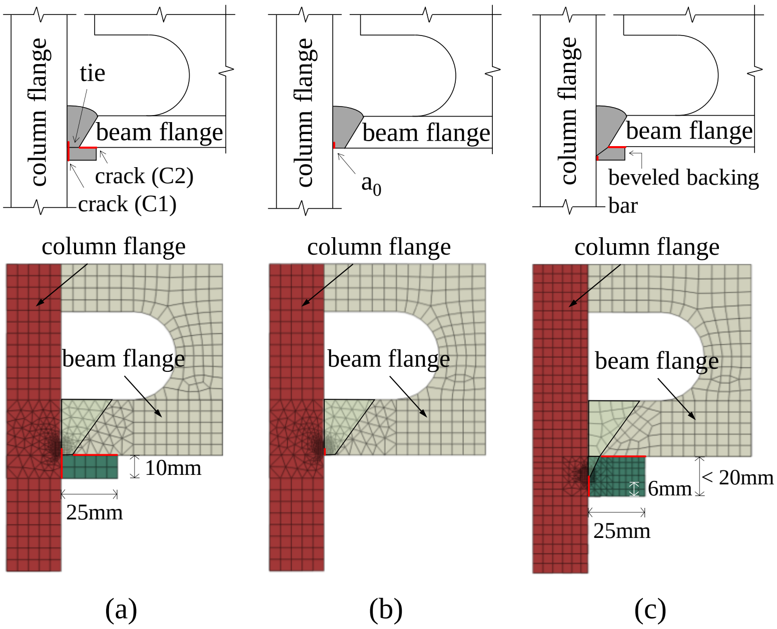
column flange
tie
beam flange
crack (C2)
crack (C1)
column flange
beam flange
a0
column flange
beam flange
beveled backing bar
column flange
beam flange
10mm
25mm
column flange
beam flange
column flange
beam flange
6mm
< 20mm
25mm
(a)
(b)
(c)

Figure 4.8 Bottom beam flange-to-column flange weld detail along with their respective continuum finite element submodels: (a) conventional backing bar; (b) no backing bar; and (c) beveled backing bar-C1 crack tip.

Referring to Fig. 4.9a, when the crack depth is 6-mm, the fracture potential is 40% higher than that of a 3-mm one when the conventional backing bar is not removed after the completion of the groove weld. In the former, the stress concentration near the crack is higher than that in the latter. Note that the depicted J-integral is based on calculations on crack tip C1 (see Fig. 4.8a). The J-integral demand at crack tip C2 is nearly zero, because the backing bar is not attached to the column flange to let the stress flow pass through the backing bar.

The CFE submodel with conventional backing bars exhibits fracture well before an SDR of 2% rads. This is consistent with the experimental findings (FEMA 1997). However, it should be noted that bolt slipping was not considered in the CFE analysis. Bolt slipping would increase the beam flange strain demands and subsequently the fracture potential at the same location (FEMA 2000a; Han et al. 2007). The fracture potential of the conventional and the ‘no backing bar’ models is nearly identical. The reason is that the backing bar remains practically unstressed during loading because it is solely attached to the beam flange. This agrees with prior work by Chi et al. (2000). Therefore, there is no benefit from removing the backing bar if the edge crack is not reinforced with a fillet weld in this case.

Interestingly, Fig. 4.9a suggests that the same pre-Northridge WUF-B connection with a beveled backing bar detailing (θ_b = 35°) is able to achieve an SDR of 4-6% rads prior to fracture for the same low toughness weld electrode (i.e., E70T7). Noteworthy stating that the fracture potential at L1 is lower than that at L2 for an assumed crack depth a_0 equal to 0.5mm in the HAZ. This was assumed to extend 3mm away from the weld toe (Ibrahim et al. 2019; Myers et al. 2009).

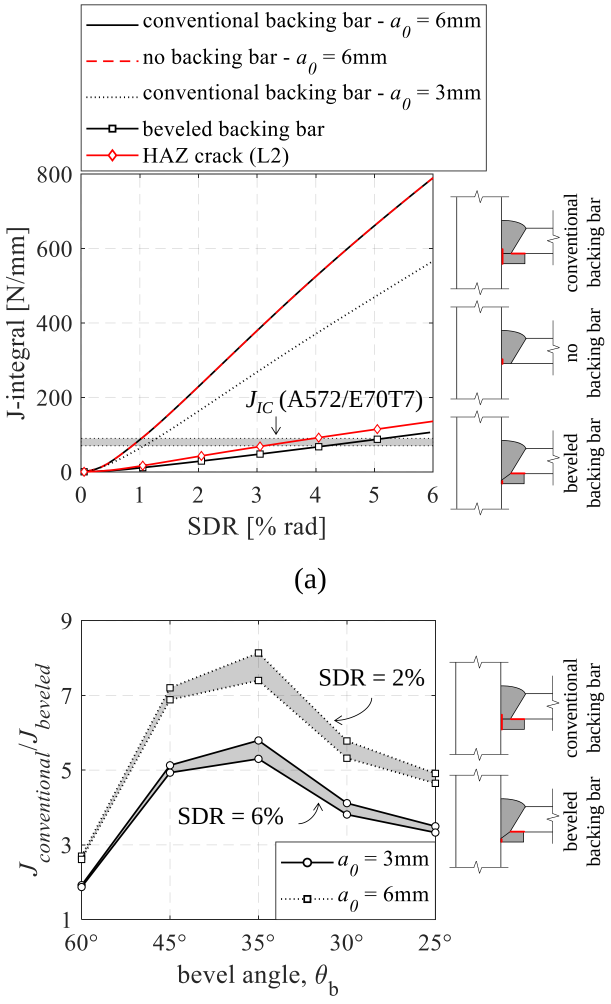

(a)

(b)

Figure 4.9 J-integral comparisons for a typical pre-Northridge WUF-B connection and its model variants: (a) J-integral versus story drift ratio; and (b) effect of bevel angle, θ_b, on J-integral.

Figure 4.9b compares the normalized J-integral demand with respect to the assumed bevel angle, θ_b. Particularly, the J-integral demand from the model with the conventional backing bar is normalized with respect to that from the model with the beveled backing bar. From the same figure, the largest (θ_b = 60°) and the smallest (θ_b = 25°) bevel angle lead to the highest fracture potential. Qualitatively, in the former the crack tip is situated near the beam flange, thereby causing high stress concentrations. In the latter, the smallest bevel angle has the crack tip away from the critical beam flange; thus, the J-integral is nearly zero at C1. Interestingly, in this case C2 becomes critical, because the stress flow passes through that crack tip. From a deformation compatibility perspective, once the backing bar attachment to the column flange increases (i.e., smallest bevel angle), C2 becomes critical. The optimal bevel angle is the one that imposes the same J-integral demand at both C1 and C2 crack tips. For the analyzed connection, this corresponds to θ_b = 35°. In this case the fracture potential is reduced by five to eight times relative to that with the conventional backing bar, depending on the assumed crack depth, a_0 and the SDR of interest. A significant decrease.

4.6.1 Effect of fillet weld reinforcement on J-integral demand

It is generally known that a fillet weld reinforcement can reduce the fracture potential of welded connections due to the closure of potential mode I cracks (Chi et al. 2000; Wang et al. 2010; Yang et al. 2019). Indeed, a closed crack has a decreased displacement field when contrasted with an open crack under the same loading conditions.

In this section, we investigate the possibility of reducing the fracture potential of crack tips at C1 and C2, with a fillet weld reinforcement either between the backing bar and the column flange (noted as fillet weld 1 in Fig. 4.10a) or between the backing bar and the beam flange (noted as fillet weld 2 in Fig. 4.10b), respectively. Referring to Fig. 4.10c, fillet welds 1 and 2 are also applied simultaneously.

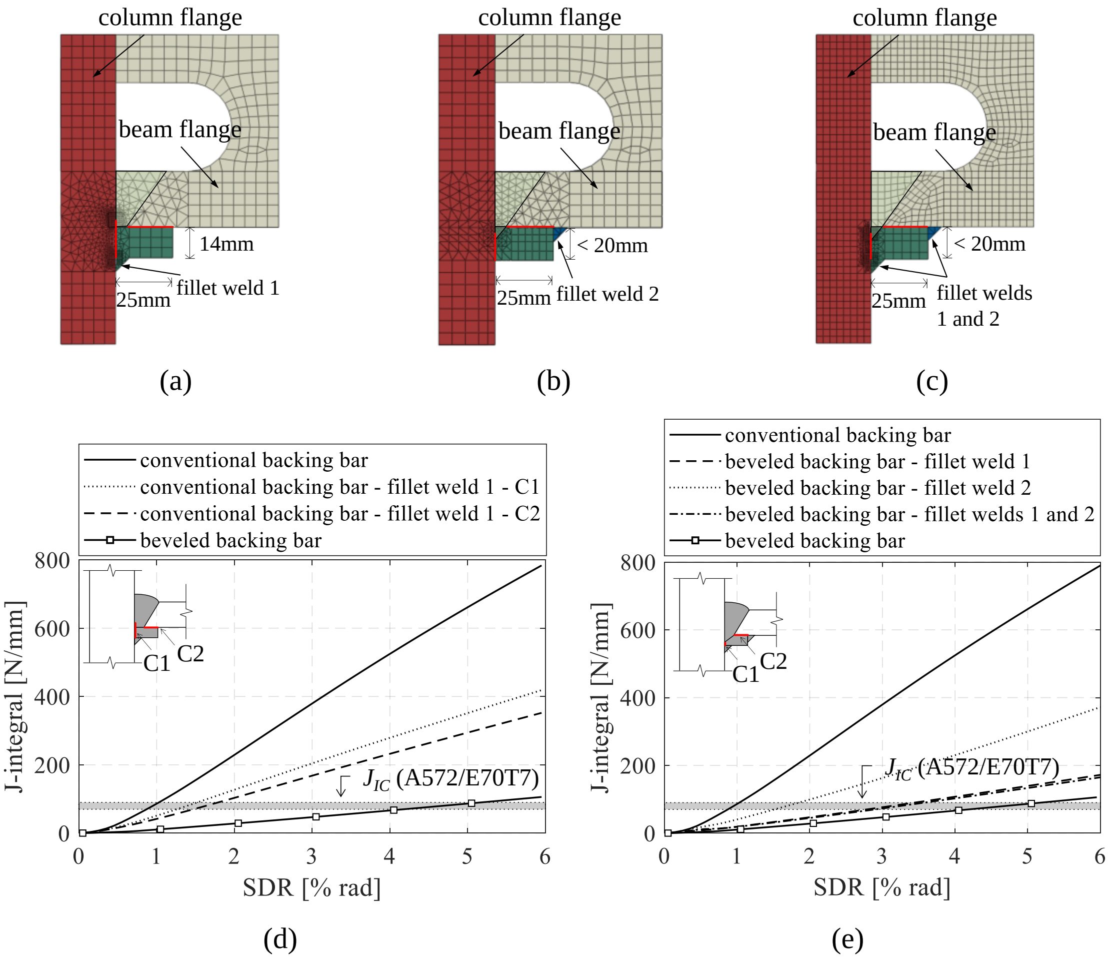

(a) (b) (c)

(d) (e)

Figure 4.10 Effect of fillet weld reinforcement on J-integral for pre-Northridge WUF-B connection detailing depending on the assumed continuum finite element submodel: (a) fillet weld 1 reinforced conventional backing bar; (b) fillet weld 2 reinforced beveled backing bar; (c) fillet weld 1 and 2 reinforced beveled backing bar; (d) fillet weld reinforced conventional backing bar effect on J-integral; and (e) fillet weld reinforced beveled backing bar effect on J-integral.

Figure 4.10d illustrates the effect of the fillet weld 1 reinforcement on the J-integral demand of the conventional backing bar detail with a_0 = 6mm (i.e., deepest crack-like flaw). In the same figure, the results are contrasted with those from the optimal beveled backing bar detail (i.e., θ_b = 35°) discussed earlier. While a fillet weld reinforcement does reduce the fracture potential at C1, interestingly, the corresponding fracture potential is almost four times higher than that with the beveled backing bar configuration. Albeit the fillet weld 1 reinforcement closes the edge crack C1, this is deemed to be more critical than the open crack C2. Therefore, the rest of the fillet weld reinforcement combinations are not examined because they would increase the J-integral at C1 and decrease it at C2.

The effect of fillet weld reinforcement is also examined for the pre-Northridge connection with a beveled backing bar in Fig. 4.10e. By welding the backing bar to the bottom beam flange (i.e., fillet weld 2), the stress flow in the backing bar increases, thereby compromising the J-integral at this location. Same findings hold true for fillet weld 1. The optimal beveled backing bar configuration (i.e., θ_b = 35°) balances the fracture potential between C1 and C2. Consequently, tack welds and fillet weld reinforcement between the beveled backing bar and the beam or column flanges outside the weld joint should be prohibited to achieve the highest connection ductility.

4.6.2 Effect of axial load on J-integral demand

End columns in steel MRFs may experience tensile excursions due to dynamic overturning effects (Suzuki and Lignos 2020). The applied axial load within the panel zone decreases its strength due to the axial-to-shear load interaction. Therefore, the likelihood of fracture due to kinking at C1 location increases. Youssef et al. (1995) highlighted fractures mainly in end columns that had increased axial load demands due to transient loading. To investigate this aspect, a tensile axial load ratio P/P_y = 10% (where P is the applied axial load and P_y is the axial yield strength of the column based on measured material properties) is applied to the steel column of the same connection examined earlier. Figure 4.11 shows the J-integral demand with respect to SDR when the two examined backing bars (see Fig. 4.7) are considered. The results are contrasted to the respective cases with no axial load demands. Overall the analyses suggest that the tensile axial load does not practically affect the J-integral demands regardless of the examined backing bar detail. However, it should be stated that this should be further verified when beam-to-column connections are under cyclic loading.

The general consensus from the CFE analyses presented in this section is that the proposed beveled backing bar configuration would have considerably delayed premature fractures in typical pre-Northridge WUF-B connections at location L1. Therefore, it is worth investigating the fracture potential of post-Northridge WUF-W connections when a beveled backing bar is intentionally left in place after the completion of demand-critical CJP welds at the bottom flange of the steel beam with filler weld electrodes according to AISC (2016a).

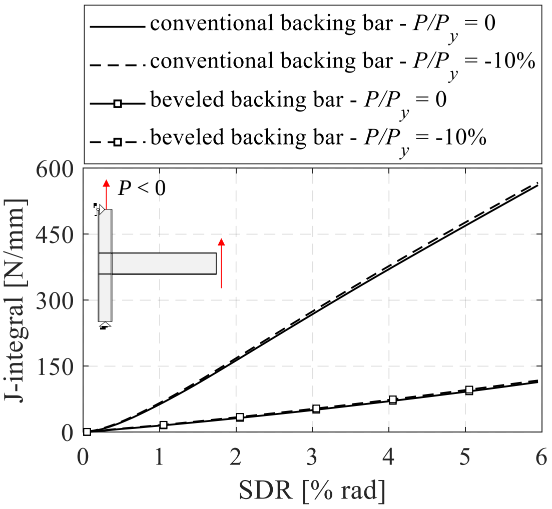

Figure 4.11 Effect of column tensile axial force on J-integral for pre-Northridge WUF-B connections.

4.7 Assessment of post-Northridge WUF-W connections

Pre-qualified WUF-W connections, necessitate bottom beam flange backing bar removal, weld root back gouging, fillet weld reinforcement and inspection of potential defects (AISC 2016c). These specifications practically provide zero fracture potential at the outer beam flange-to-column interface. Instead, fracture near the HAZ becomes critical. With the beveled backing bar configuration, potential defects in the weld root are positioned away from the beam flange, thus minimizing the fracture potential at the beam flange-to-column interface. The same holds true in cases where the bottom of the bevel may not be penetrated by the weld. However, referring to Fig. 4.9a, the simulation results suggest that the beveled backing bar, pushes the fracture-critical location to be near the HAZ, which is consistent with the current state of pre-qualified WUF-W connections.

A series of parametric analyses is conducted to examine the fracture potential of pre-qualified WUF-W connections when a beveled backing bar geometry is employed and, contrary to AISC (2016c), is not removed from the bottom flange of the steel beam. The analysis matrix, which is summarized in Table 4.2, includes the interior subassembly UT04 (denoted as Case 1), tested by Shin (2017), and the equivalent exterior one (denoted as Case 2). This subassembly features W36x150 beams and a W14x398 column. The rest of the analyzed cases (identified as Cases 3-6) conform to the current seismic design and fabrication standards (AISC 2016c; a; b; AWS 2010, 2016). In brief, the interior subassemblies comprise deep beams and columns (i.e., the panel zone aspect ratio is nearly equal to one). The beam and column depths range from 500-1000mm, while their flange thicknesses range from 19-44mm (¾ - 1¾ in.) and from 34-74mm (1⅜ - 2⅞ in.), respectively. The analyzed cases are within the design space of typical seismic designs of steel MRFs in North America (Elkady and Lignos 2014; NIST 2015). Nominally identical material properties are considered for the yield regions of the steel beams and columns in all cases.

Table 4.2 Post-Northridge subassembly CFE analysis matrix.

Specimen ID	Beam cross section	Column cross section	Beam depth, d_b [mm]	Column depth, d_c [mm]	Beam flange thickness, t_{bf} [mm]	Column flange thickness, t_{cf} [mm]	R_u/R_n	Expected γ_{max}/γ_y
Case 1	W36X150	W14X398	911.9	464.8	23.9	72.4	0.50	22.0
Case 2	W36X150	W14X398	911.9	464.8	23.9	72.4	0.99	4.3
Case 3	W21X73	W24X176	538.5	640.1	18.8	34.0	0.53	23.8
Case 4	W30X116	W33X263	762.0	876.3	21.6	39.9	0.56	28.5
Case 5	W36X150	W36X256	911.9	950.0	23.9	43.9	0.54	28.5
Case 6	W36X256	W36X529	950.0	1,010.9	43.9	73.9	0.56	28.6

The panel zone strength-to-resistance ratio, R_u/R_n, does not respect intentionally the requirements of AISC (2016b) to inhibit inelastic panel zone shear distortions. The panel zone strength, R_u, is computed according to the Skiadopoulos et al. (2021) design model, which is an improved representation of the AISC (2016b) panel zone model. The expected maximum panel zone inelastic shear distortions range from 20-25γ_y.

In all examined cases, continuity plates with a thickness equal to that of the beam flange are deemed to be imperative. The CFE modeling approach is consistent with that presented earlier. The fracture potential of the examined cases is compared for three beveled backing bar geometries (bevel angles of 45°, 35° and 30°).

Figure 4.12 depicts the lateral strength, F, versus SDR and the panel zone shear distortion, γ, versus SDR relations for all the examined cases. Referring to Fig. 4.12a, the examined subassemblies provide a wide range of lateral strength due to the selection of the beam and column cross sections. Figure 4.12b suggests that the panel zone shear distortion is appreciable in most subassemblies at modest lateral drift demands (i.e., 2% rads) as well as at 4% rads.

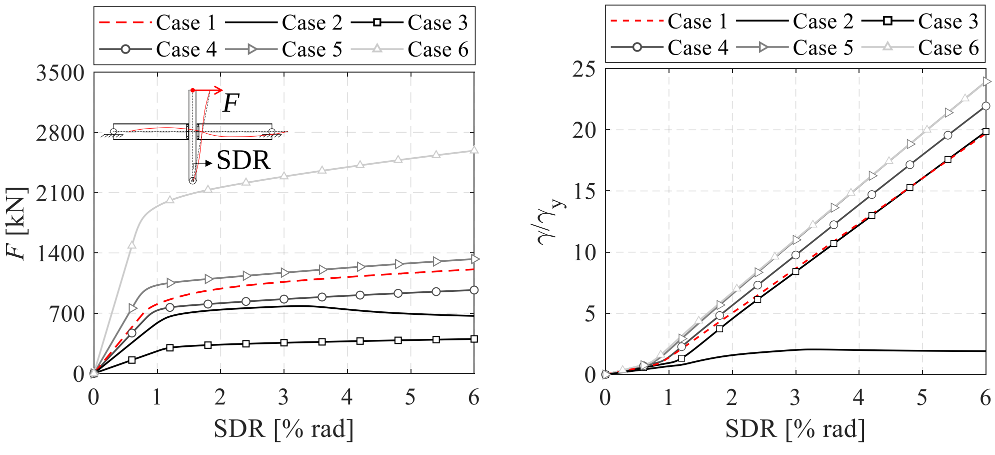

(a)

(b)

Figure 4.12 Pre-qualified WUF-W connection: (a) applied force versus story drift ratio; and (b) normalized panel zone shear distortion versus story drift ratio.

4.7.1 Effect of panel zone design distortions

Cases 1 (weak panel zone) and 2 (strong panel zone) are employed to assess the influence of panel zone design distortions on the connection performance. Because of the modified [AISC (2016c); AWS (2010)] weld access hole in post-Northridge WUF-W connections (see Fig. 4.3), the stress flow near the backing bar is altered compared to that in their pre-Northridge WUF-B counterparts. Figure 4.13a depicts the J-integral ratio between the conventional and the beveled backing bar with respect to the bevel angle for the models with a_0 = 6mm. The results indicate that the fracture potential of WUF-W connections with beveled backing bars reduces by 7 to 5 times at lateral drift demands of 2% and 6% rads compared to the equivalent cases with conventional backing bars left in place after welding. Moreover, the optimal bevel angle is 45°, regardless of the panel zone strength.

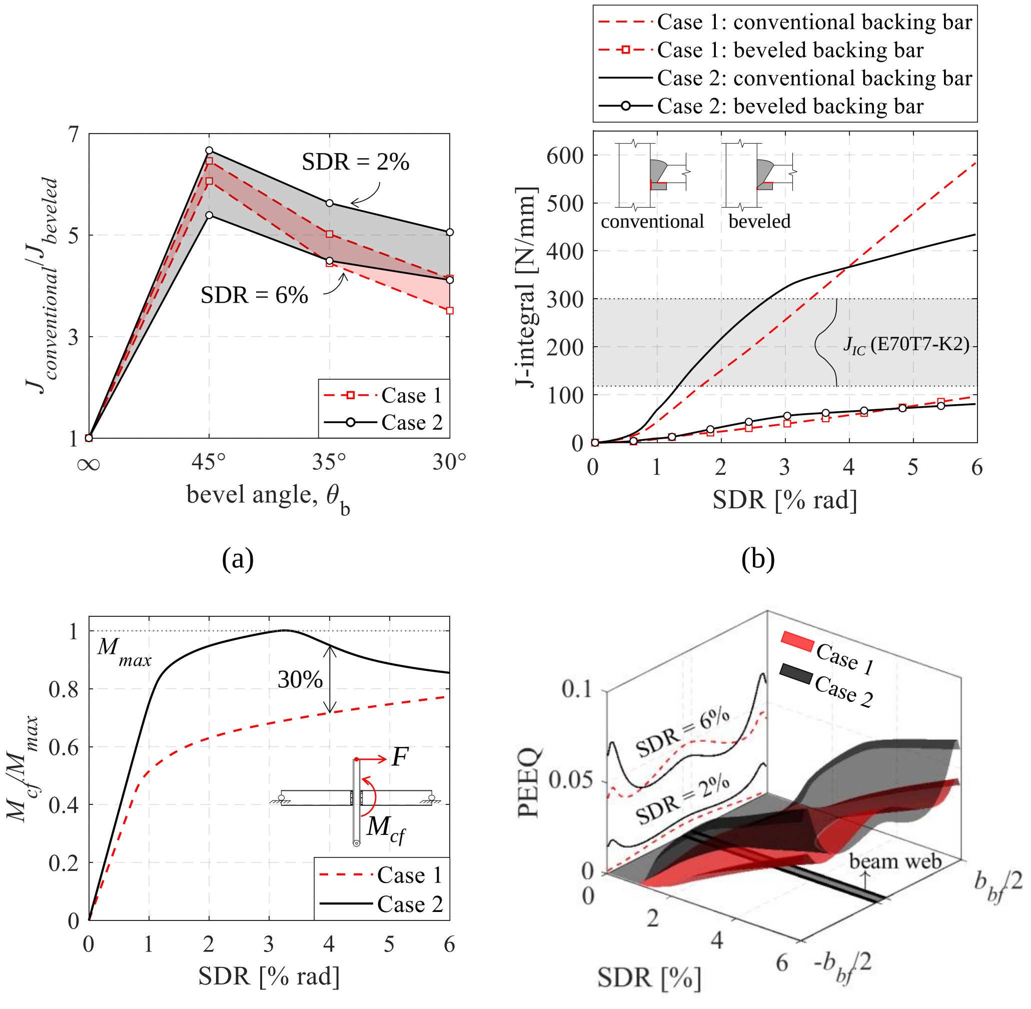

(a) (b)

(c) (d)

Figure 4.13 Pre-qualified WUF-W connections with weak and strong panel zones: (a) J-integral for conventional and beveled backing bars; (b) J-integral versus story drift ratio; (c) normalized moment at the column face versus story drift ratio; and (d) PEEQ distribution within the bottom beam flange versus story drift ratio.

Figure 4.13b depicts the J-integral versus SDR relation for WUF-W connections with a conventional (a_0 = 6mm) and the optimal beveled (i.e., θ_b = 45°) backing bar configurations. Moreover, the J-integral demands are compared with the J-integral resistance of the E70T7-K2 weld electrode (Grade 480) that satisfies the minimum criteria for demand critical welds (AISC 2016a) for pre-qualified beam-to-column connections. The median J_{IC} is equal to 208N/mm, while the 5th and 95th percentiles are equal to 118N/mm and 300N/mm, respectively, based on prior pertinent work (Gomez et al. 2008; Kanvinde et al. 2008). Referring to Fig. 4.13b, the conventional backing bar configuration leads to connection fractures prior to an SDR of 3-4% rads; hence its removal is justifiable. Conversely, the same connection with the optimal beveled backing bar configuration exceeds an SDR of 6% rads even when comparing with the 5th percentile of the weld electrode toughness.

Referring to Fig. 4.13b, the fracture potential of WUF-W connections featuring a weak panel zone is 1.4 times higher than that of the strong one only when SDRs exceed 4% rads. Conversely, prior to 4% rads, WUF-W connections with a strong panel zone possess almost 30-50% higher fracture potential compared to those with a weak one. To explain this, Fig. 4.13c depicts the moment demand at the column face, M_{cf}, (normalized to the maximum attained moment, M_{max}) versus SDR. When the panel zone is designed to remain elastic (Case 2), the flexural demand at the column face of the WUF-W connection is at least 30% higher than that of its weak panel zone counterpart. Once local buckling occurs in the steel beam (i.e., SDR of about 3% rads), the flexural moment demand is capped in the strong panel zone case. Conversely, local buckling does not occur in cases where panel zones exhibit highly inelastic deformations (i.e., γ > $20\gamma_y$) even at lateral drift demands higher than 6% rads.

Figure 4.13d compares the cumulative equivalent plastic strain (PEEQ) of the outer beam flange fiber versus SDR for Cases 1 (weak panel zone) and 2 (strong panel zone). The distributions are extracted along the beam flange width from positions adjacent to the respective backing bar. Characteristic 2-D projections are illustrated in the same figure at an SDR of 2% and 6% rads. Prior to an SDR of 4% rads, in the weak panel zone case, M_{cf} is 30% smaller than that in its strong panel zone counterpart. As such, the PEEQ is higher in the latter than that in the former. After the onset of steel beam local buckling in the strong panel zone case, the PEEQ caps, due to the high plastic concentration within the buckled region of the steel beam. Conversely, the weak panel zone attains relatively high inelastic deformations; hence, the PEEQ in the critical web centerline region becomes 1.4 times higher than that of the strong panel zone case.

4.7.2 Beam depth effect

Referring to Table 4.2, Cases 3 to 5 feature beams with depths ranging from 500 to about 900mm. The variation of the beam and column flange thickness and the panel zone design distortions is fairly minor in these models. Figure 4.14a depicts the J-integral evolution with respect to SDR for the optimal beveled backing bar configuration (i.e., θ_b = 45°). The shallower beam (i.e., d_b = 540mm) possesses almost 1.3 times lower fracture potential compared to the deeper one (i.e., d_b = 910mm). This is attributed to the increased strain demand in deep beams (El-Tawil et al. 1999). However, fracture is only expected at lateral drift demands exceeding 6% rads, and by only assuming the 5th percentile of the E70T7-K2 weld electrode toughness, which is a fairly conservative assumption.

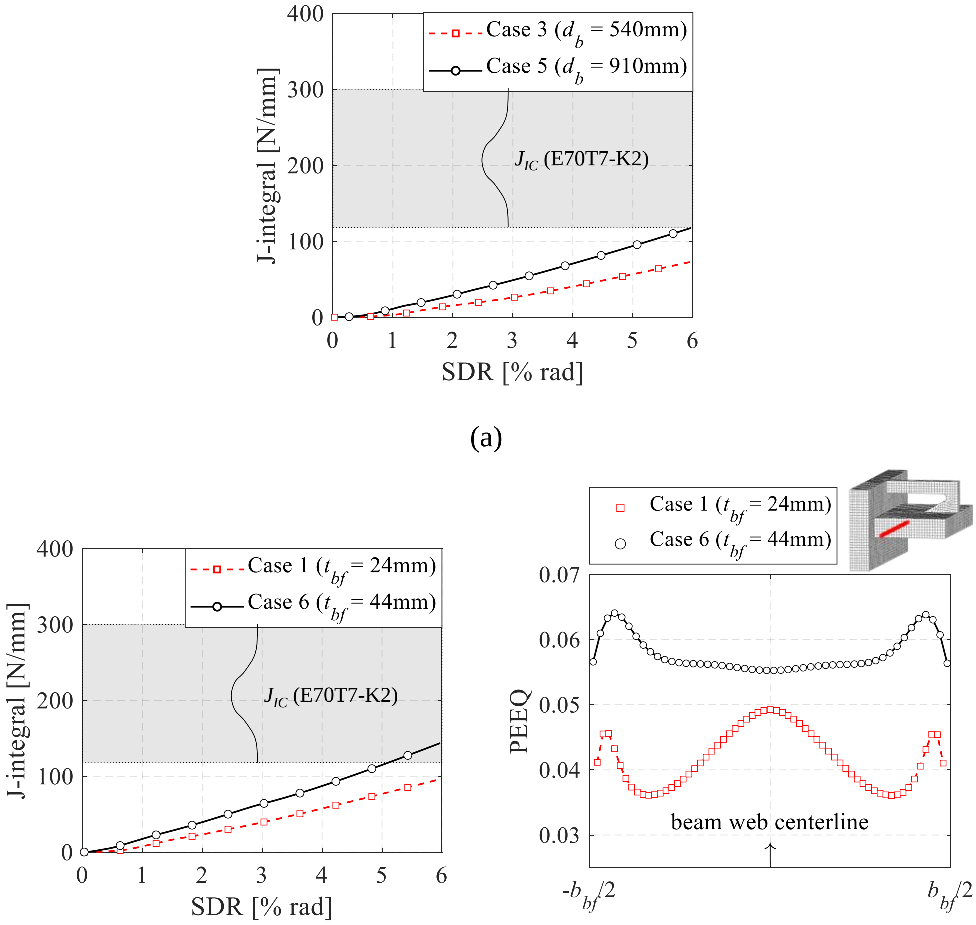

(a)

(b)

(c)

Figure 4.14 Fracture assessment of pre-qualified WUF-W connections with a beveled backing bar: (a) effect of varying beam depth on J-integral; (b) effect of varying beam flange thickness on J-integral; and (c) PEEQ distribution along the beam flange width at 6% SDR for different beam flange thicknesses.

4.7.3 Beam flange thickness effect

The beam flange thickness effect on the fracture potential of post-Northridge WUF-W connections is demonstrated by comparing Cases 1 and 6 (see Table 4.2). The former features a 24mm beam flange thickness, while the latter a 44mm beam flange thickness. Figure 4.14b depicts the J-integral evolution over SDR for the optimal beveled backing bar configuration. The beam with the thicker flange (i.e., beam flange thickness, t_{bf} = 44mm) possesses a 20% higher fracture potential than that of the beam with a flange thickness, t_{bf} of 24mm. Noteworthy stating that fracture initiation only occurs at lateral drift demands larger than 5% rads regardless of the beam flange thickness.

The increased J-integral demand in the thicker beam flanges, which is highlighted in Fig. 4.14b, may be explained by Fig. 4.14c, which depicts the PEEQ along the beam flange width at and SDR of 6% rads. For the thicker beam flange, the plastic strains are increased in the web centerline location by almost 10%. This increase in the plastic strains is associated with a higher-pressure index (i.e., ratio of hydrostatic stress over the yield stress) in beams with thicker flanges (El-Tawil et al. 1998).

4.7.4 Column flange thickness effect

Referring to Table 4.2, we can quantify the effect of the column flange thickness on the fracture potential of WUF-W connections by comparing the results from Cases 1 (column flange thickness, t_{cf} = 72mm) and 5 (t_{cf} = 44mm). Referring to Figs. 4.14a and 4.14b the fracture potential of the connection with thicker column flanges (i.e., Case 1) reduces by nearly 10% compared to that of the thinner column flange counterpart (i.e., Case 5) at SDRs ranging from 2-6% rads. Qualitatively, the kinking effect is more eminent in the thinner column flange element at inelastic panel zone distortions of 20-25γ_y. This, subsequently, leads to the J-integral increase. However, this only occurs at relatively large lateral drift demands (i.e., larger than 5% rads).

4.7.5 Weld toe size effect

The preceding analyses assumed a 6mm weld toe size for the beam flange-to-column CJP weld. According to AWS (2010), a 10mm weld toe size is also permissible; hence, this effect was also investigated. While the weld toe size does not affect the fracture potential of the connections with a beveled backing bar, the analyses suggest that a 45° and a 50° bevel angle are optimal for the 6mm and 10mm weld toe, respectively, assuming a built-in crack of a_0 = 3mm. The results are not presented herein due to brevity.

4.8 Limitations

This chapter focuses on the fracture potential of field-welded connections subjected to monotonic loading. Pre-qualified beam-to-column connections in capacity-designed steel MRFs experience inelastic cyclic drift demands, which cannot be assessed with the present methodology and employed fracture mechanics methods. On the other hand, in the present study, a uniform crack of two different depths (i.e., a_0 = 3mm and a_0 = 6mm) was assumed, which is deemed to be a conservative assumption (see Fig. 4.1c).

Fracture due to lamellar tearing in the column's through thickness flange was disregarded by assuming that the toughness requirements in the Z-direction of the column flange are sufficient. This issue deserves more attention in connection geometries featuring thick column flange thicknesses (i.e., larger than 38mm).

Another critical aspect relates to the role of the slab on the fracture potential of WUF-W connections. Prior investigations after the 1994 Northridge and 1995 Kobe earthquakes (FEMA 2000a; Mahin 1998; Nakashima et al. 2007) have demonstrated that when the slab is in fully composite or partially composite action with the floor beams, the neutral axis shifts towards the concrete slab, thereby increasing the inelastic strain demand at the beam's bottom flange welds when the slab is in compression (Nakashima et al. 2007; Ricles et al. 2002b). The increased strain demand may be prevented by isolating the slab from the steel column (Hobbs 2014; Tremblay et al. 1997).

Considering all above, the findings of the present study should be substantiated by full-scale physical testing of WUF-W beam-to-column connections under reversed cyclic loading. Beveled backing bars with the optimal geometry (i.e., bevel angle of 45°) may be used and left in place after the completion of demand-critical CJP groove welds between the beam and column flanges to examine their effectiveness in reducing the fracture potential in WUF-W connections. Such investigations are currently underway by the authors.

4.9 Summary and conclusions

This chapter revisits concepts in pre-qualified field-welded connections aiming to identify fabrication simplifications by means of simulation-based engineering design. For this purpose, this chapter explores the potential of keeping the bottom beam flange backing bar in place, after executing the complete joint penetration (CJP) groove welds at this location. To reduce the associated fracture potential at this location, a customized beveled backing bar is proposed. The employed methodology for such an endeavor features traditional fracture mechanics informed by three-dimensional continuum finite element (CFE) analyses. The CFE approach is validated to available test data from typical welded unreinforced flange-bolted web (WUF-B) pre-Northridge connections. Several backing bar geometry details are examined with and without fillet weld reinforcements. These are compared with the proposed one. The connection performance is assessed by means of parametric studies on pre-qualified welded unreinforced flange-welded web (WUF-W) connections.

Based on the CFE simulations, WUF-B pre-Northridge connections can sustain a lateral drift demand of 4 to 6% rads prior to fracture when the customized beveled backing bar is employed, even when the low-toughness E70T7 filler metal is utilized for completing the beam flange-to-column flange CJP weld. The reason is that with the beveled backing bar the crack tip is situated away from the critical beam flange location. The peak lateral drift capacity prior to fracture in this case is improved by more than four times relative to that with a conventional backing bar.

The CFE results suggest that the optimal backing bar bevel angle, θ_b, for typical pre-Northridge WUF-B connections, is 35°. When θ_b decreases, the backing bar-to-beam flange crack tip C2 becomes critical; hence the fracture potential at crack tips C1 and C2 is identical for the optimal bevel angle.

The fillet weld reinforcement in conventional backing bars closes the edge cracks and reduces the fracture potential of field-welded connections by up to two times. However, connections with the beveled backing bar still possess a fracture potential, which is one fourth compared with that of fillet weld reinforced conventional backing bar.

The simulation studies reveal that the fracture potential of field-welded connections is practically not influenced by the tensile and/or compressive column axial load demands regardless of the employed backing bar geometry. This is attributed to the fact that the column axial load does not affect the beam moment demand, which strongly influences the connection ductility under lateral loading.

Contrary to WUF-B pre-Northridge connections, in pre-qualified WUF-W connections, the optimal beveled angle, θ_b, is found to be 45°. This is due to the modified weld access hole geometry that is adopted in WUF-W connections. The CFE results suggest that pre-qualified WUF-W connections with a beveled backing bar left in place after welding sustain lateral drift demands of at least 6% rads prior to fracture regardless of the panel zone strength, the beam depth, as well as the thickness of the beam and column flanges, given that the minimum criteria for demand critical groove welds according to AISC (2016a) are respected.

Pre-qualified WUF-W connections featuring weak panel zones with $\gamma > 20\gamma_y$ possess nearly 1.5 times higher fracture potential compared to their strong panel zone counterparts at lateral drift demands above 4% rads. Interestingly, at SDRs less than 4% rads, the fracture potential of WUF-W connections with strong panel zones is nearly 1.5 higher than that of their weak panel zone counterparts. In the former, the moment at the column face is about 30% higher than that in the latter. However, in the strong panel zone case, the onset of local buckling in the beam caps the strain demands due to flexure at lateral drift demands of about 4% rads. On the other hand, at this drift range, panel zone kinking prevails in cases where the panel zone shear distortion is larger than $12\gamma_y$.

The fracture potential of WUF-W connections comprising shallow beams (e.g., d_b ~ 550mm) is about 30% less compared to that in connections with deeper beams (e.g., d_b ~ 900mm). Similarly, beams with thick flanges (e.g., t_{bf} > 40mm) possess about 10% higher fracture potential compared to beams with thinner flanges (e.g., t_{bf} < 25mm) due to the higher pressure index and the associated plastic strains in the former. On the other hand, steel columns with relatively thick flanges (e.g., t_{cf} > 70mm) possess about 10% lower fracture potential compared to columns with thinner flanges (e.g., t_{cf} < 45mm). This is attributed to the kinking effect, which is more eminent in the latter case.

Chapter 5 Full-scale experiments of cyclically loaded welded moment connections with highly dissipative panel zones and simplified weld details

5.1 Introduction

Steel moment resisting frames (MRFs) are widely used lateral load-resisting systems in seismic regions. The seismic stability of capacity-designed steel MRFs relies on the anticipated seismic performance of their fully restrained beam-to-column connections. The AISC 341-16 (AISC 2016a) seismic design provisions limit the participation of the beam-to-column web panel zones (referred as panel zones hereinafter) into the energy dissipation of cyclically loaded steel MRF beam-to-column connections. Depending on the targeted panel zone shear strength-to-demand ratio, the permissible level of panel zone distortions may be up to $4\gamma_y$ (where γ_y is the panel zone shear distortion at yield).

The current state-of-the-art in prequalified fully restrained welded beam-to-column connections as described in AISC (2016c) has been influenced by research, which was mostly conducted after the 1994 Northridge earthquake (Mahin et al. 2002; Malley 1998). At that time, common deficiencies that compromised the cyclic behavior of welded connections were: (a) the non-optimized access hole geometry (Lu et al. 2000; Mao et al. 2001; Ricles et al. 2002a, 2003); (b) the inadequate weld material toughness requirements (Chi et al. 2000); (c) the inferior base material quality control and through-thickness properties (Krawinkler 1995; Tremblay et al. 1995), and; (d) the presence of the weld backing bar in the bottom beam flange-to-column connection after the execution of the complete joint penetration (CJP) groove welds at this location. The notch at the bottom beam flange backing bar together with additional flaws that may result from the interruption of the welding process at the beam web location led to high strain demands at the backing bar-to-column face weld root location. These were enlarged particularly in connection geometries that featured deep beams and/or inelastic panel zone designs (Chi et al. 1997; El-Tawil 2000; El-Tawil et al. 1999; Whittaker et al. 1998). The role of the concrete slab on the observed behavior of welded connections was also stressed (Hajjar et al. 1998; Leon et al. 1998).

Follow-up experimental studies on welded unreinforced flange-bolted web connections with improved material and connection details (Han et al. 2007; Stojadinović et al. 2000) demonstrated the need for welding part of the beam's web to the shear tab, which lead to the development of the welded unreinforced flange-welded web (WUF-W) connections, which is the primary focus of the present study.

The typical WUF-W connection, which is shown in Fig. 5.1, features improved weld specifications (Chi et al. 1997), an optimized access hole geometry (Lu et al. 2000; Mao et al. 2001; Ricles et al. 2000, 2002a; b, 2003), continuity plates, when necessary, to transfer the beam flange forces due to flexure in the beam, and doubler plates to satisfy the targeted panel zone design requirements (Lee et al. 2005c; b). Moreover, after completing the CJP groove weld at the bottom beam flange-to-column face, it is imperative to remove the backing bar, while the weld root should be back-gouged. Fillet weld reinforcement should be placed at the same location to close potential defects in the beam flange outer fiber. Prequalified WUF-W connections should also be inspected with nondestructive ultrasonic testing (UT) in accordance with AWS (2016). While necessary, this is deemed to be time and resource consuming (FEMA 2000a; Miller 2017; Popov et al. 1998).

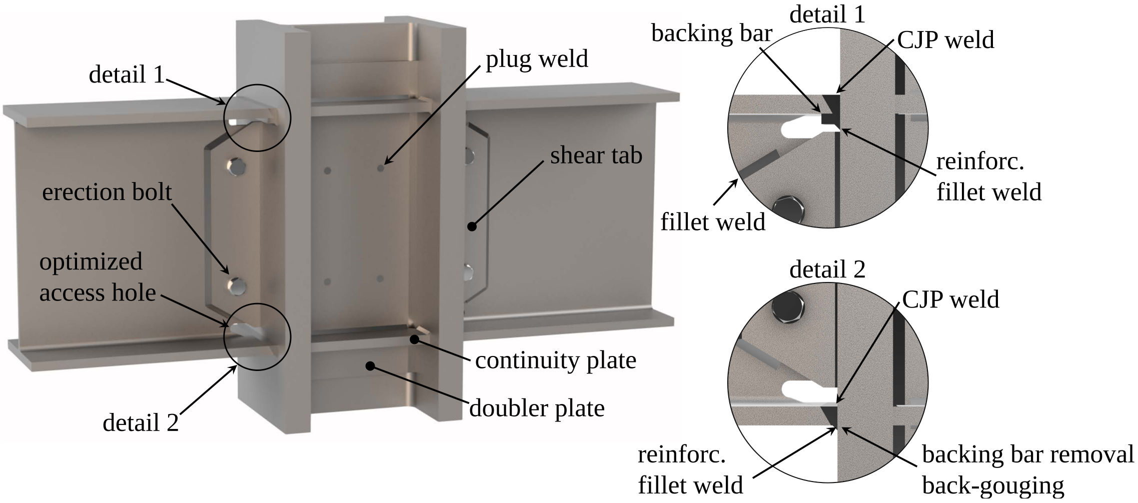

Figure 5.1 Illustration of typical welded unreinforced flange-welded web connection detailing.

Structural detailing simplifications for column splices (Shaw et al. 2015; Stillmaker et al. 2016) and for continuity and doubler plate weld details of WUF-W connections (Reynolds and Uang 2022) have emerged. These rely on advancements in weld specifications and practice as well as today's quality control in fabrication. Motivated by the above, Skiadopoulos and Lignos (2022a) proposed a customized beveled backing bar configuration for WUF-W connections by enabling finite element simulation-assisted design. The advantage of the beveled backing bar is that its removal is not imperative after the completion of the CJP groove welds at the beam flange-to-column flange location. Continuum finite element analyses by Skiadopoulos and Lignos (2022a) demonstrated that the beveled backing bar configuration shifts the fracture-critical location away from the backing bar location. However, these simulations were primarily based on monotonic loading and the proposed configuration has not been validated by means of cyclic experiments.

Experimental research (Engelhardt et al. 2000; Lee et al. 2005b; Ricles et al. 2002b; Shin 2017; Zhang and Ricles 2006) has shown that fully restrained welded beam-to-column connections generally meet the prequalification requirements as per AISC 341-16 (AISC 2016a) when inelastic deformations concentrate in the steel beams. Figure 5.2a shows such an example where the inelastic panel zone shear distortion did not exceed $2\gamma_y$ (Shin 2017). On the other hand, structural repairs are deemed imperative in this case due to inelastic local buckling near the beam ends (see Fig. 5.2b) even at modest lateral drift demands, particularly when the beam profiles are near the limits for highly ductile members (Uang and Bruneau 2018). This may also result in increased column twist demands when deep columns are utilized in the seismic design of steel MRFs (Chi and Uang 2002; Ricles et al. 2004b).

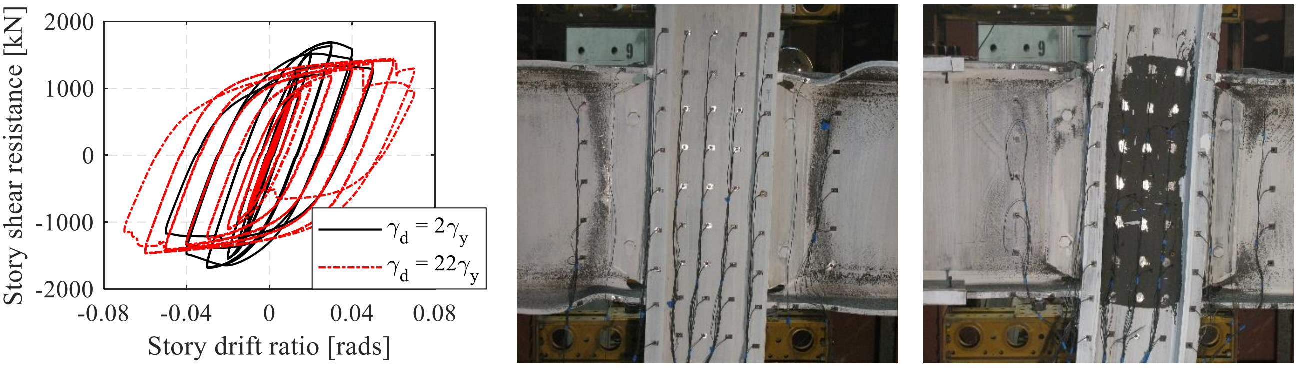

(a) (b) (c)

Figure 5.2 (a) Hysteretic responses of welded unreinforced flange-welded web beam-to-column connections with variable design panel zone distortions, γ_d; deformed shapes for the (b) $2\gamma_y$ (at 3% rad lateral drift demand); and the (c) $22\gamma_y$ (at 6% rad lateral drift demand) cases [source: Shin (2017)].

When balancing inelastic deformations between the beam ends and the panel zone in welded connections, nonlinear geometric instabilities do not occur prior to large lateral drift demands (Kim and Lee 2017; Lee et al. 2005b; Rahiminia and Namba 2013; Ricles et al. 2002b; Shin 2017). For instance, Fig. 5.2a illustrates the cyclic response of a WUF-W connection, which was designed with a targeted inelastic shear distortion of more than $20\gamma_y$ (Shin 2017). In this case, the use of doubler plates was not imperative, which reduced the associated fabrication costs. Moreover, Fig. 5.2c suggests that the WUF-W connection exhibits a stable hysteretic response up until a lateral drift of 6% rad. Arguably, at this drift level, the global stability of steel MRFs is governed by P-Δ effects (Elkady and Lignos 2015; Gupta and Krawinkler 2000a). Therefore, the connection performance at lateral drift demands of 6% rad or higher is not likely to influence the seismic stability of a steel MRF.

Despite the superior connection performance when leveraging the beneficial aspects of shear yielding in a panel zone, specific attention should be given on structural detailing of welded connections so as they are able to withstand the increased strain demands due to panel zone kinking (Krawinkler et al. 1971; Lee et al. 2005c). In cases where the columns are subjected to highly inelastic strain demands due to panel zone kinking, stricter flange through-thickness (i.e., Z-direction) material requirements are imperative so as lamellar tearing and/or divot fracture are prevented. Such fracture types, which are mostly common in columns with thick flanges [i.e., higher than 38 mm, as per AISC (2016a)], have even been reported in post-Northridge WUF-W connection tests (Lin et al. 2000). According to the European steel practice, CEN (2004b) requires increased Z-direction quality class steel materials for the above reasons. The same applies for columns with flange thicknesses larger than 38 mm (AISC 2016a). Such toughness requirements in North America may be respected by enabling A913 steels (Bouchard and Axmann 2000).

Motivated by the above, this chapter proposes simplified WUF-W beam-to-column connections that defy the current design paradigm of prequalified welded connections. The novelty of the proposed connections is threefold. First, beveled backing bars are employed and intentionally left in place after the completion of CJP groove welds; second, the connection design allows for highly dissipative panel zones; and third, steel columns are designed with minimum through thickness properties to avoid premature failure modes, such as divot fracture. Moreover, continuity and doubler plates are omitted from the seismic design of the welded connections. The hysteretic behavior of the proposed design concept is characterized by means of full-scale physical testing of two interior beam-to-column subassemblies. The effect of loading history on the global and local performance criteria is quantified. Implications on prospective seismic design of steel MRFs along with limitations and suggestions for future work are also discussed.

5.2 Test objectives and anticipated seismic performance

The proposed connection design exploits the beneficial aspects of shear yielding in a beam-to-column web panel zone by assuming a panel zone resistance-to demand ratio, $R_{n,pl}/R_u$ that equals 0.8 [$R_{n,pl}$ calculated as per Skiadopoulos et al. (2021)]. For this design value, at a design-basis earthquake (i.e., 10% probability of exceedance over 50 years), the steel beams are expected to exhibit flexural yielding but no geometric instabilities, while the panel zone distortions are expected to be less than $8\gamma_y$ (Skiadopoulos and Lignos 2022b). During a maximum-considered earthquake (i.e., 2% probability of exceedance over 50 years) it is anticipated that panel zone distortions should be up to $15\gamma_y$, whereas local buckling should not occur in the steel beams. With the above performance targets in mind, the overarching goal for the welded connection is to achieve a non-degrading hysteretic response up to a lateral drift demand of at least 5% rad. Within such a context, structural repairs at the connection level would be minimized in the aftermath of design-basis earthquakes. Moreover, such a connection design would guarantee a sufficient reserve capacity of a steel MRF in a typical mainshock/aftershock earthquake series.

Further economic benefits of the proposed design are anticipated through the use of a beveled backing bar (Skiadopoulos and Lignos 2022a). The anticipated inelastic panel zone response is expected to provide increased strain demands at this location due to kinking especially when connections feature deep beams (i.e., depths larger than 500 mm). To prevent divot fracture due to the expected high strain demands in the column through-thickness direction, a high notch toughness material in the Z-direction is enabled for the steel column material. The envisioned seismic performance of the above connection has also been explored and benchmarked in Skiadopoulos and Lignos (2022b) by means of system-level nonlinear response history analyses.

5.3 Overview of the test program

5.3.1 Test specimens

Figure 5.3 provides an overview of the examined interior WUF-W connections. The test configuration comprises two nominally identical beam-loaded test specimens. These feature HY650x300x16x25 steel beams (equivalent to a W24x131 in North America) with web and flange local slenderness ratios, $h/t_w = 35.9$, and $b/2t_f = 6$, respectively (where h is the clear flange distance minus the fillet radii, t_w is the web thickness, b is the flange width, and t_f is the flange thickness of the cross section). This profile meets the requirements for highly ductile members according to AISC 341-16 as well as Class 1 sections according to EN 1993-1-1:2005 (CEN 2004d). The steel columns feature a H498x432x45/70 (i.e., $h/t_w = 7.0$, and $b/2t_f = 3.1$), which is equivalent to a stocky W14x398 in North America. The flange thickness of the selected column equals 70 mm. For welded connections with highly dissipative panel zones and such thick column flanges, through-thickness toughness requirements should be imposed to avoid lamellar tearing and/or divot fracture. The above member sizes and the connection geometry reflect the current seismic design practice in North America (Elkady and Lignos 2015; NIST 2010; Skiadopoulos and Lignos 2022b).

The measured dimensions of both specimens are summarized in Table 5.1, where L_r is the actuator-to-actuator and the pin-to-pin centerline distances for the beams and the column, respectively. The cross-sectional dimensions are extracted from five locations per beam and column. The average values of these measurements are reported in Table 5.1 together with the nominal values per cross section. From this table, a good agreement is observed between the measured and the nominal dimensions in all cases. The steel beams are made of SN490B and the columns are made of SM490A, while both of which have a nominal yield stress, $f_y = 325$ MPa. The selected columns are from the same steel heat. The same applies for the steel beams.

The beam-to-column connection designs intentionally violate the doubler plate requirements and the beam flange-to-column face weld detail. The former is violated to allow for a balanced inelastic deformation design between the steel beams and the panel zone. Due to lab limitations, L_c/d equals 5.8 (where L_C equals 3751 mm as per Fig. 5.3), whereas AISC 358-16 (AISC 2016c) requires that $L_c/d = 7$ for special moment frames. This is a conservative consideration for the objectives of the present study. For the adopted span-to-depth ratio, increased shear strain demands are expected in the examined backing bar location. AISC (2016a) suggests that continuity plates are not imperative in the connection design because the column flange and web thicknesses are thick enough to accommodate the concentrated beam flange force demands. The strong column-weak beam ratio is larger than two. Therefore, the column is expected to remain elastic throughout the loading history.

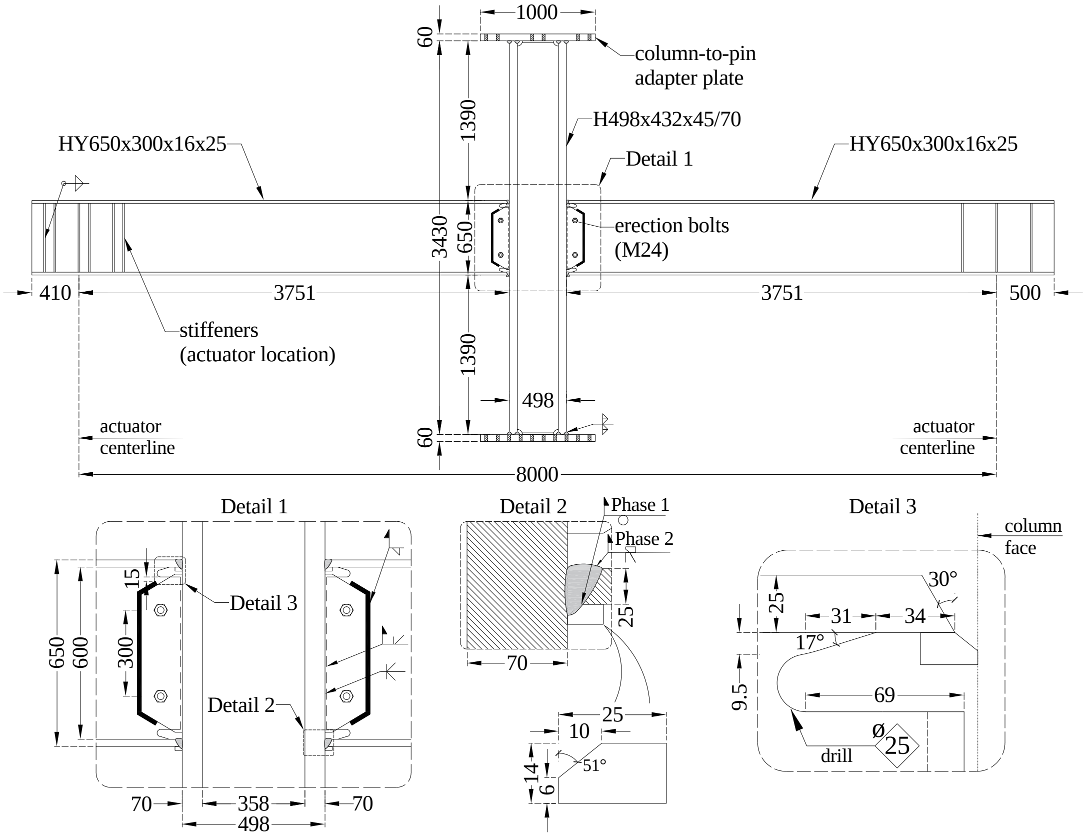
1000
60
column-to-pin adapter plate
1390
H498x432x45/70
HY650x300x16x25
Detail 1
HY650x300x16x25
3430
650
erection bolts (M24)
410
3751
3751
500
stiffeners (actuator location)
1390
498
60
actuator centerline
actuator centerline
8000
Detail 1
15
Detail 3
650
600
300
Detail 2
70
358
70
498
Detail 2
Phase 1
Phase 2
25
70
25
10
14
6
51°
Detail 3
column face
30°
25
31
34
17°
9.5
69
ø25
drill

Figure 5.3 Overview of the beam-to-column connection (unit: millimeters).

Table 5.1 Measured dimensions of the test specimens.

Section	ID	d (mm)	b (mm)	t_w (mm)	t_f (mm)	L_r (mm)
Beam (HY650x300x16x25)	Specimen 1	651.47	300.38	16.27	25.83	8,000
	Specimen 2	651.36	300.62	16.36	25.78	8,000
	Nominal dim.	650.00	300.00	16.00	25.00	8,000
Column (H498x432x45/70)	Specimen 1	498.90	431.61	45.63	69.88	4,549
	Specimen 2	498.53	431.41	45.53	69.72	4,551
	Nominal dim.	498.00	432.00	45.00	70.00	4,550

Two erection bolts, M24, of F10T material (equivalent to 10.9 grade in Europe and A490 in the US) are utilized to temporarily hold the steel beams in position prior to welding. The shear tab is shop-welded to the column face with double bevel CJP weld of YGW-18 weld electrode (see Fig. 5.3, Detail 1). Beveled backing bars were utilized for the top and bottom beam flanges. The geometry of the backing bars, which is shown in Fig. 5.3 (see Detail 2), is designed according to the recommendations by Skiadopoulos and Lignos (2022a). The beveled backing bars were tack-welded in the beam flange groove location (see Fig. 5.3, Detail 2) prior to the CJP welding. After completing it, the beveled backing bars were kept in place, while no fillet weld reinforcement was performed.

The beam flanges and web were CJP-field-welded to the column face by using YGW-18 and T49J0T1-1CA-UH5 weld electrodes, respectively (see Fig. 5.3, Detail 1). The above electrodes satisfy the requirements for demand critical welds in accordance with AISC (2016a). Ultrasonic testing was performed for all demand critical welds (AISC 2016a; AWS 2016). Fillet field weld reinforcement was placed in the shear tab, by using a T49J0T1-1CA-UH5 weld electrode, as per AISC (2016c). The access hole geometry (see Detail 3 of Fig. 5.3) respects the current design specifications (AISC 2016c; AWS 2016).

5.3.2 Specimen fabrication

The fabrication process of the test specimens aimed at simulating realistic field weld conditions. For this purpose, the construction sequence was performed with the test specimens in the upright position, as shown in Fig. 5.4. The shear tabs, with the aid of the pre-stressed erection bolts (AISC 2016a; b), served for positioning the steel beams in place and for satisfying a perpendicular alignment between the beams and the column (see Fig. 5.5a). The beveled backing bars were tack-welded at the top and bottom beam flanges, together with runoff tabs to satisfy a smooth start and termination of the welding process (see Figs. 5.5a-b). Prior to the CJP weld execution, a preheat was applied at 50°C in accordance with AIJ (2007). The CJP welds were, then, performed for both the top and bottom beam flanges as shown in Figs. 5.6a-b and for the beam web (see Fig. 5.6c). The maximum heat input was 30-40kJ/cm and the maximum permissible temperature between passes was 250-350°C. The runoff tabs were removed and grinded to ensure a smooth surface, according to AISC 358-16 (AISC 2016c), as shown in Fig. 5.7. The shear tabs were, then, fillet-weld reinforced. After the completion of welding, UT was performed in all CJP welds to ensure that potential discontinuities were below the established limits of current practice (AIJ 2018).

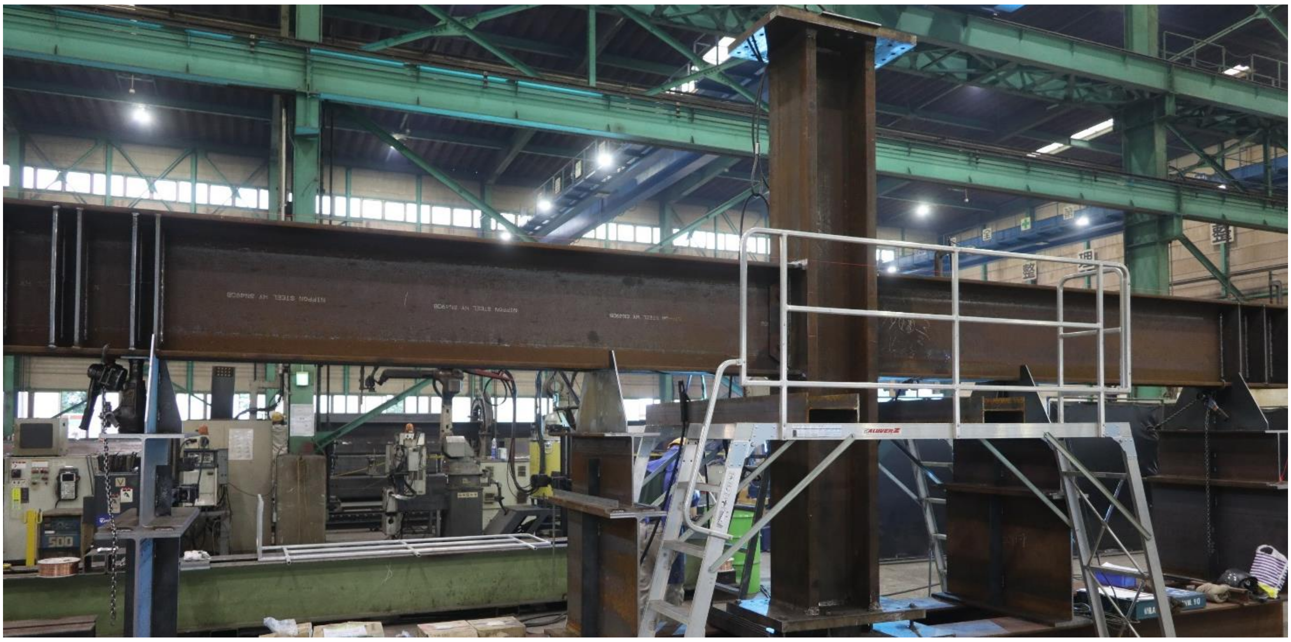

Figure 5.4 Fabrication of test specimen – welding preparation in the upright position.

The UT confirmed that Specimen 1 had no traceable discontinuities outside the accuracy of the inspection method (ASTM 2017). On the other hand, Specimen 2 had two discontinuities at the west beam flange-to-column face connection. These are illustrated in Fig. 5.8 in scale. The former was found at the shear tab-to-column weld mid-height location, adjacent to the shear tab. This discontinuity was 2 mm deep and 10 mm long. The latter was found at the bottom beam flange CJP weld, adjacent to the beam flange and was positioned at the beam web centerline, where the welding process was interrupted at the access hole location. This discontinuity was 1 mm deep and 10 mm long. The above discontinuities were within the allowable limits of AIJ (2018); therefore, no weld repairs were executed.

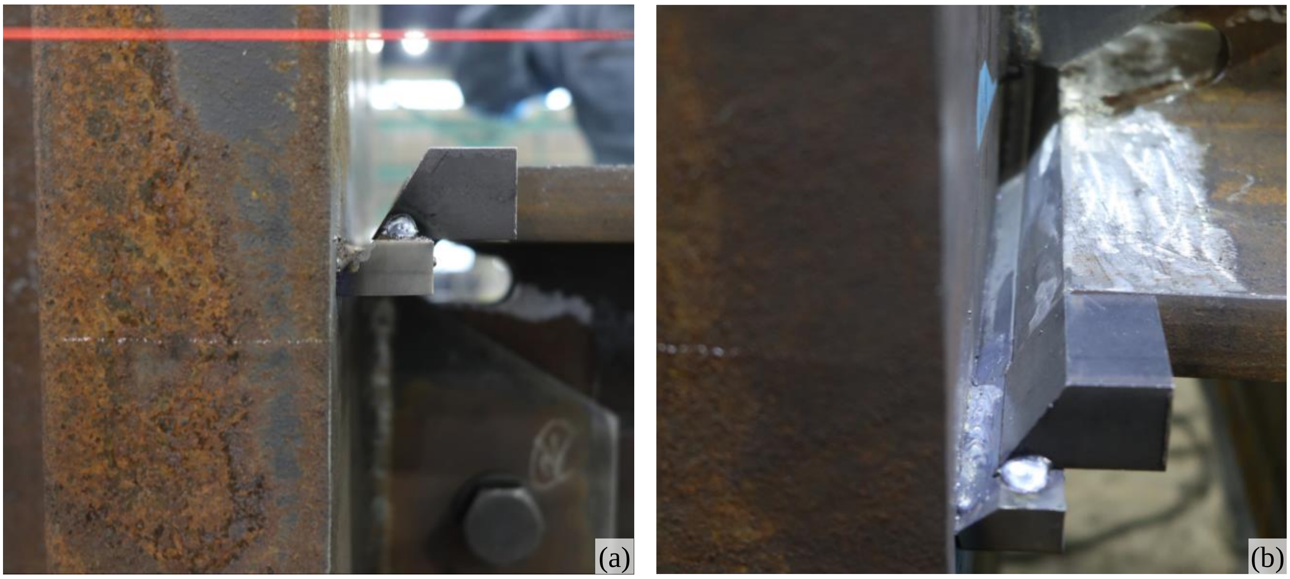

Figure 5.5 Fabrication of the beam-to-column connection – beveled backing bar details.

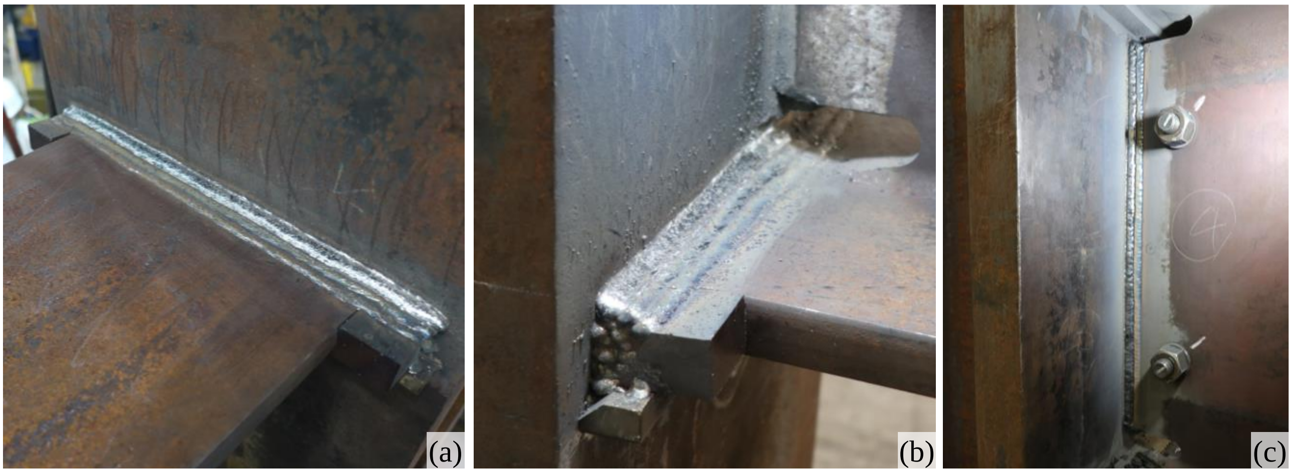

Figure 5.6 Fabrication of the beam-to-column connection – completion of CJP welding details.

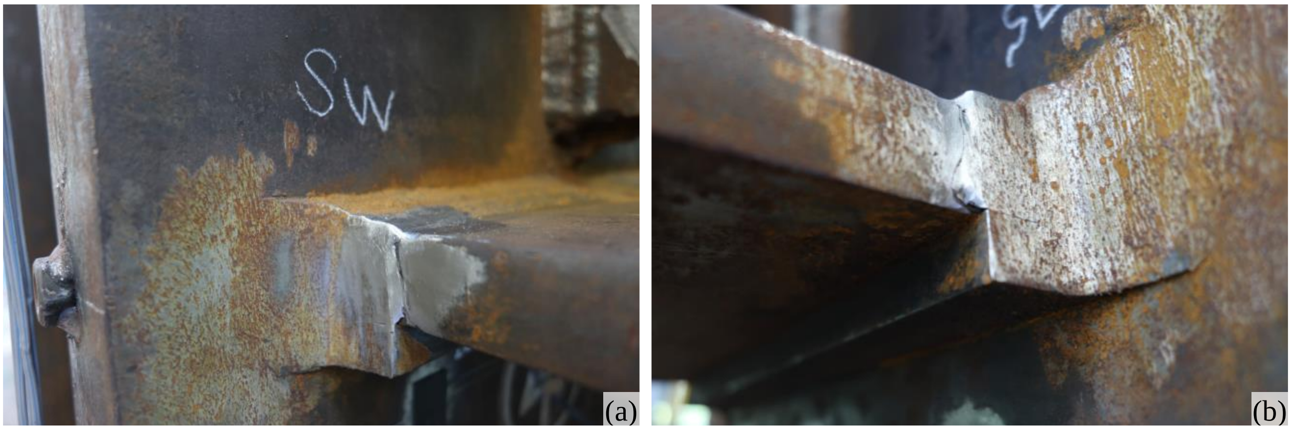

Figure 5.7 Fabrication of the beam-to-column connection – removal of weld runoff tabs.

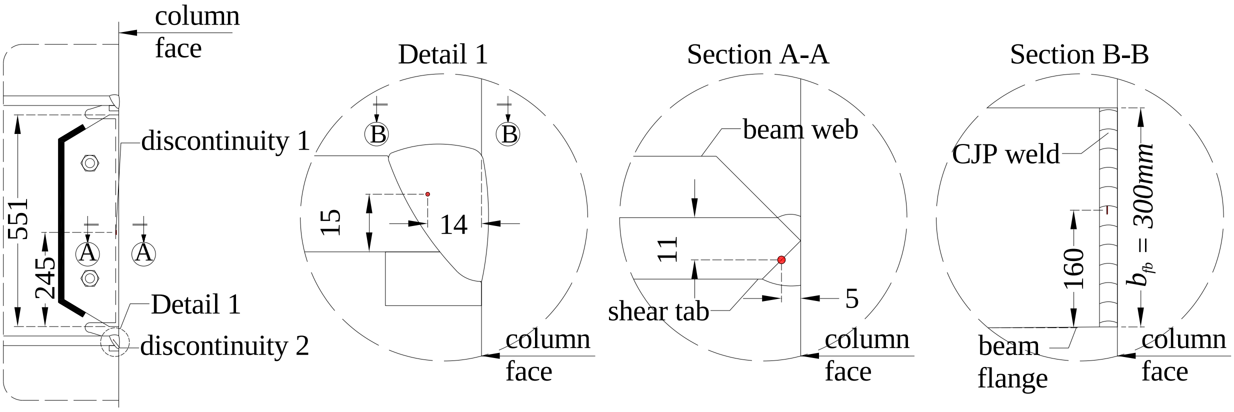
column face
discontinuity 1
551
245
A
A
Detail 1
discontinuity 2
Detail 1
B
B
15
14
column face
Section A-A
beam web
11
shear tab
5
column face
Section B-B
CJP weld
160
b_{fb} = 300mm
beam flange
column face

Figure 5.8 Identified locations of weld discontinuities after ultrasoning testing for Specimen 2 (unit: millimeters).

5.3.3 Test apparatus

Figure 5.9 illustrates the test apparatus after the installation of the first specimen. Two 5,000 kN displacement-controlled servo hydraulic actuators impose lateral loading to the steel beams. These actuators transfer the load from the test specimen to the reaction wall through a spreader steel beam. Each actuator is attached to the beam ends through adapter plates and 16 pretensioned rods to avoid slippage. Stiffeners are positioned at the beam loading points to prevent localized deformations in this region. A pinned connection is realized in the column north end, while the shear and axial reaction forces are transferred to the reaction wall through the spreader beam.

The axial force in the column is applied through a 10,000 kN servo hydraulic actuator in force control. Therefore, a roller connection in the north-south direction is realized. The movement in the west-east direction is restrained by a rigid support beam that reacts in the reaction wall through a spreader beam. A lateral support system is designed to restrain the connection movement in the out-of-plane direction. The lateral bracing requirements according to AISC (2016a; b) were adopted for this purpose. A pantograph is placed

1000 mm away from the actuators' centerlines. The pantographs are clamped to the steel beams to provide them with a lateral restraint. An additional lateral support system is designed and placed near the beam-to-column joint. This lateral support system consists of a pair of C10x90x300 beams and a four L19x150x150-column configuration, as illustrated in Fig. 5.9.

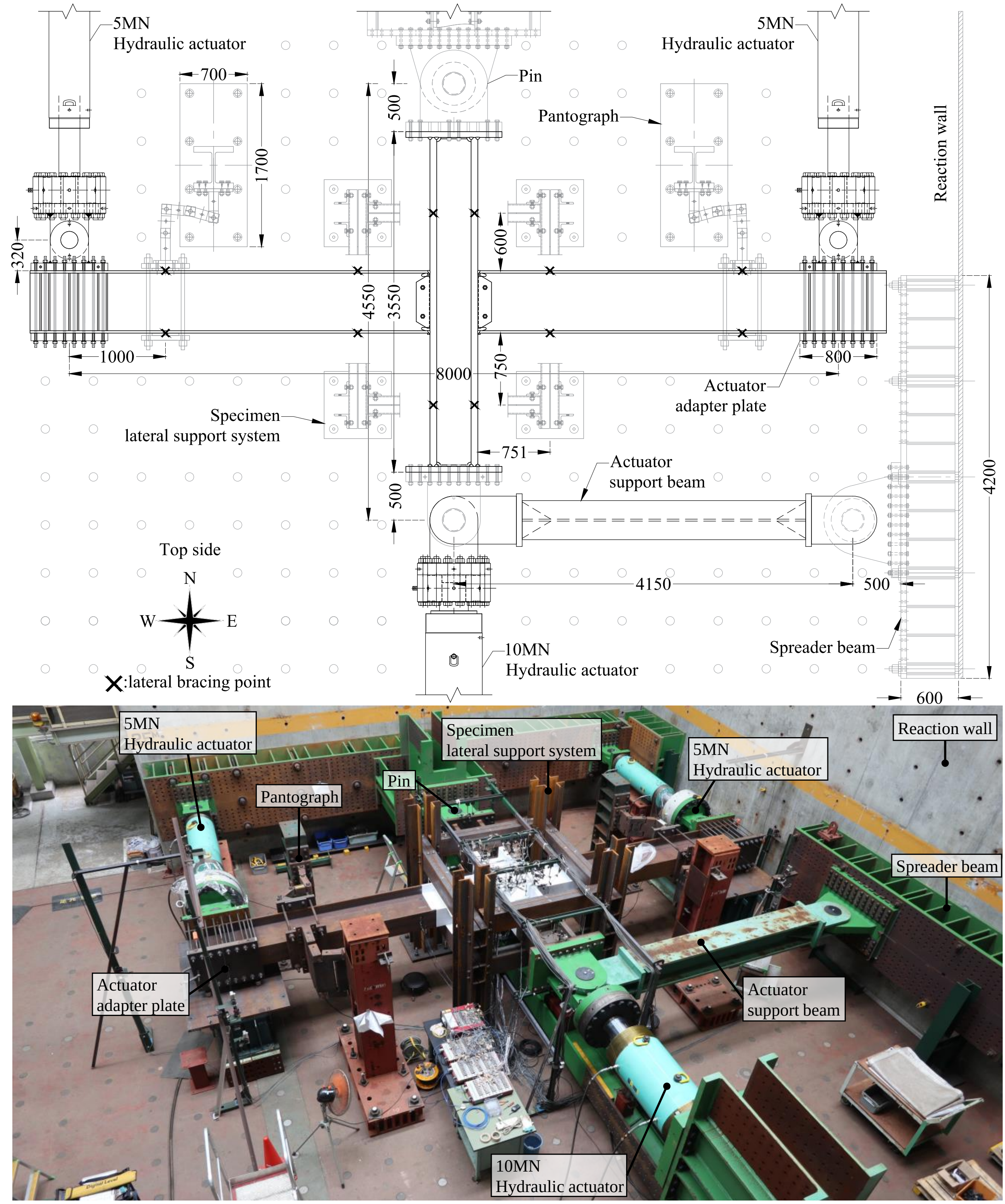
5MN
Hydraulic actuator
700
1700
Pin
500
Pantograph
5MN
Hydraulic actuator
Reaction wall
320
600
4550
3550
1000
8000
750
800
Actuator
adapter plate
Specimen
lateral support system
751
Actuator
support beam
500
4200
Top side
N
W
E
S
✕:lateral bracing point
4150
500
10MN
Hydraulic actuator
Spreader beam
600
5MN
Hydraulic actuator
Specimen
lateral support system
Pin
Pantograph
5MN
Hydraulic actuator
Reaction wall
Spreader beam
Actuator
adapter plate
Actuator
support beam
10MN
Hydraulic actuator

Figure 5.9 Overview of the test setup (unit: millimeters).

5.3.4 Instrumentation plan and deduced measurements

Each test specimen employed 171 channels of instrumentation in total. These comprised 72 strain gauges in the beams and the columns, five rosette gauges in the panel zone and four near the access hole region, 58 linear variable differential transformers (LVDTs) in the panel zone and the pinned connections, four potentiometers in the panel zone kinking locations and 10 string potentiometers at the actuator locations, as characteristically illustrated in Figs. 5.10a-e. The instrumentation, right before starting the test, is depicted in Figs. 5.10f-g for the panel zone top and bottom sides, respectively.

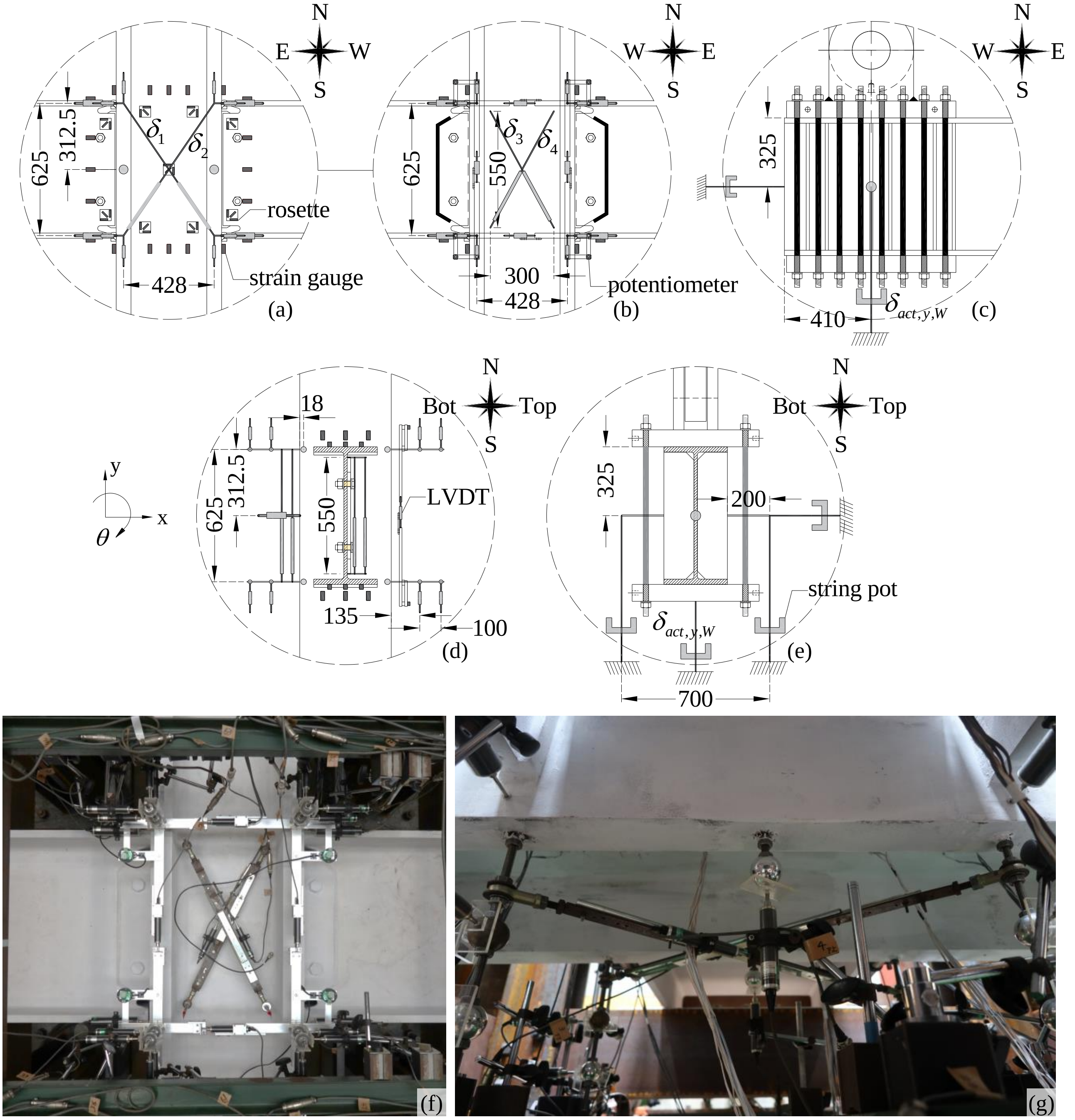
N
E
W
S
312.5
625
δ_1
δ_2
rosette
428
strain gauge
(a)
N
W
E
S
625
550
δ_3
δ_4
300
428
potentiometer
(b)
N
W
E
S
325
410
$\delta_{act,y,W}$
(c)
y
x
θ
N
Bot
Top
S
18
625
312.5
550
LVDT
135
100
(d)
N
Bot
Top
S
325
200
string pot
$\delta_{act,y,W}$
700
(e)
(f)
(g)

Figure 5.10 Instrumentation plan at the panel zone and the load application locations (unit: millimeters).

The story drift ratio, θ_{tot} is calculated by considering a correction due to rigid body motion rotation, θ_{RB}, as per Eq. (5.1) and Fig. 5.11:

$$\begin{gathered}\theta_{tot} = \frac{\delta_{act,y,W} - \delta_{act,y,E}}{L_b} - \theta_{RB} \\ \theta_{RB} = \frac{\delta_{RB,x,N} - \delta_{RB,x,S}}{H_{c,RB}}\end{gathered} \tag{5.1}$$

where $\delta_{act,y,W}$ and $\delta_{act,y,E}$ are the west and east actuator displacements in the y-direction (see Figs. 5.10c and 5.10e), $\delta_{RB,x,N}$ and $\delta_{RB,x,S}$ are the LVDT displacements in the x-direction at the north and south column ends at the adapter plate mid-height location, respectively, $H_{c,RB}$ is the distance between these LVDTs, which equals 3,490 mm (see Fig. 5.3), and L_b is the distance between the displacement-control actuator centerlines, which equals 8,000 mm.

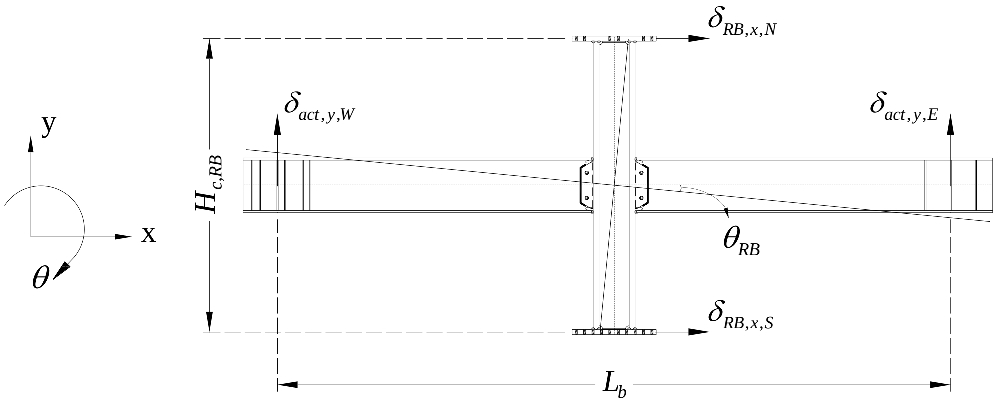

Figure 5.11 Illustration of the rigid body motion rotation.

Vis-a-vis the above details, the panel zone shear distortion, γ, which is the primary measurement in this testing program, is calculated according to three different ways for redundancy. These are based on: (a) the displacements of the diagonal pair of LVDTs that are mounted at the column flanges (see Fig. 5.10a, δ_1 and δ_2), (b) the LVDTs positioned in the column web (see Fig. 5.10b, δ_3 and δ_4), and (c) the average of the rotations given by the four potentiometers (see Fig. 5.10b). The panel zone shear distortion is calculated according to Eq. (5.2):

$$\gamma = \frac{(\delta_i - \delta_{i+1}) \cdot \sqrt{b_{pz}^2 + d_{pz}^2}}{2 \cdot b_{pz} \cdot d_{pz}} \tag{5.2}$$

where i is either 1 or 2 for the first and second ways of calculating γ, accordingly, b_{pz} and d_{pz} is the width and the depth of the panel zone as defined by the points the LVDTs are attached to (i.e., for $i = 1$, $b_{pz} =$ 428 mm and $d_{pz} = 625$ mm as per Fig. 5.10a). During the tests, the three methods were found to provide fairly similar results. Hereinafter, the first method is utilized for all computations.

The chord rotations of the beams, θ_b' and the column, θ_c', are calculated based on the LVDT readings at the panel zone corners. At each corner, the absolute displacements are provided by three LVDTs, one pair attached to the column flanges and single LVDTs that are attached to the column face, as depicted in Fig. 5.10d. In the calculations of θ_b', and θ_c', the LVDT, which is attached to the column face, is utilized in the x-direction displacements and the pair LVDTs in the y-direction ones, as per Eqs. (5.3) and (5.4), respectively:

$$\theta_b' = \frac{2 \cdot \delta_{act,y}}{L_b - d_c - t_{fc}} + \frac{\delta_{pz,y,W} - \delta_{pz,y,E}}{L_b - d_c - t_{fc}} + \frac{\delta_{pz,x,N} - \delta_{pz,y,S}}{d_b - t_{fb}} \tag{5.3}$$

$$\theta_c' = \frac{\delta_{pz,y,W} - \delta_{pz,y,E}}{d_c - t_{fc}} + \frac{\delta_{pz,x,N} - \delta_{pz,y,S}}{H_c - d_b - t_{fb}} - \theta_{RB} \tag{5.4}$$

where, $\delta_{act,y}$ is the displacement of the west or the east actuator, depending on which chord rotation (i.e., east or west) is computed, d_c is the column depth, t_{fc} and t_{fb} are the column and beam flange thicknesses, $\delta_{pz,y,W}$ and $\delta_{pz,y,E}$ are the panel zone west and east side y-direction displacements, $\delta_{pz,x,N}$ and $\delta_{pz,x,S}$ are the panel zone north and south x-direction displacements. For the computation of θ_b', these are extracted from the west or east panel zone sides, depending on the beam of interest, while for the computation of θ_c', west and east side average values are assumed.

5.3.5 Ancillary tests

A number of ancillary tests were performed to infer the material properties of the steel beams and columns. The yield stress, $f_{y,m}$, the ultimate stress, $f_{u,m}$ and the elongation at fracture were determined according to standard tensile coupon testing (ASTM 2016). The average values based on five coupons with thickness, t, are reported in Table 5.2 for the web and flange plates. The specified minimum yield, f_y, and ultimate stresses, f_u, are 325 MPa and 490 MPa, respectively, for the beam and column materials. As for JIS-G3136, SN490B, the results indicate that the measured-to-nominal yield strength ratio, $f_{y,m}/f_y = 1.13$ and the measure-to-nominal ultimate strength ratio $f_{u,m}/f_u = 1.08$, on average. Similar values are found for JIS-G3106, SM490A. These values are consistent with prior reports on relevant Japanese materials (Fujisawa et al. 2013) and correspond to similar values for A992 Gr. 50 steel as per AISC 341-16 (AISC 2016a).

Table 5.2 Measured and nominal material properties of the test specimens.

Section	t (mm)	Measured material properties			Nominal material properties	$\frac{f_{y,m}}{f_y}$	$\frac{f_{u,m}}{f_u}$
		$f_{y,m}$ (MPa)	$f_{u,m}$ (MPa)	Elongation (%)			
Beam	25	Flange: 363	Flange: 509	Flange: 31.4		1.13	1.08
JIS-G3136 SN490B	16	Web: 398	Web: 525	Web: 26.6	$f_y = 325$ MPa	1.12	1.08
Column	70	Flange: 368	Flange: 531	Flange: 36.0	$f_u = 490$ MPa	1.12	1.04
JIS-G3106 SM490A	45	Web: 363	Web: 528	Web: 33.7		1.22	1.07

Uniaxial cyclic round coupon testing was also conducted to manifest other properties of interest (e.g., cyclic hardening, Bauschinger effect) for the steel materials. The testing procedures according to de Castro e Sousa et al. (2020) were employed, involving 10 strain-based uniaxial loading protocols. Characteristic test results for the column web plate are shown in Fig. 5.12. The simulation results are superimposed for reference by employing the multiaxial constitutive law proposed by Hartloper et al. (2021), based on two backstresses. The calibrated material model parameters are shown in Table 5.3 for the column and beam flanges and webs, where E is the Young's modulus, $\sigma_{y,0}$ is the equivalent yield stress at zero plastic strain, Q_∞ and b are the maximum and the rate of expansion of the yield surface, accordingly, D_∞ and a are the magnitude and rate of decrease in the initial yield stress, accordingly, C_k and γ_k are parameters that describe the magnitude and rate of the yield surface translation of the backstress component k. The deduced input model parameters are consistent with those reported in de Castro e Sousa et al. (2020) for A992 Gr. 50 steel.

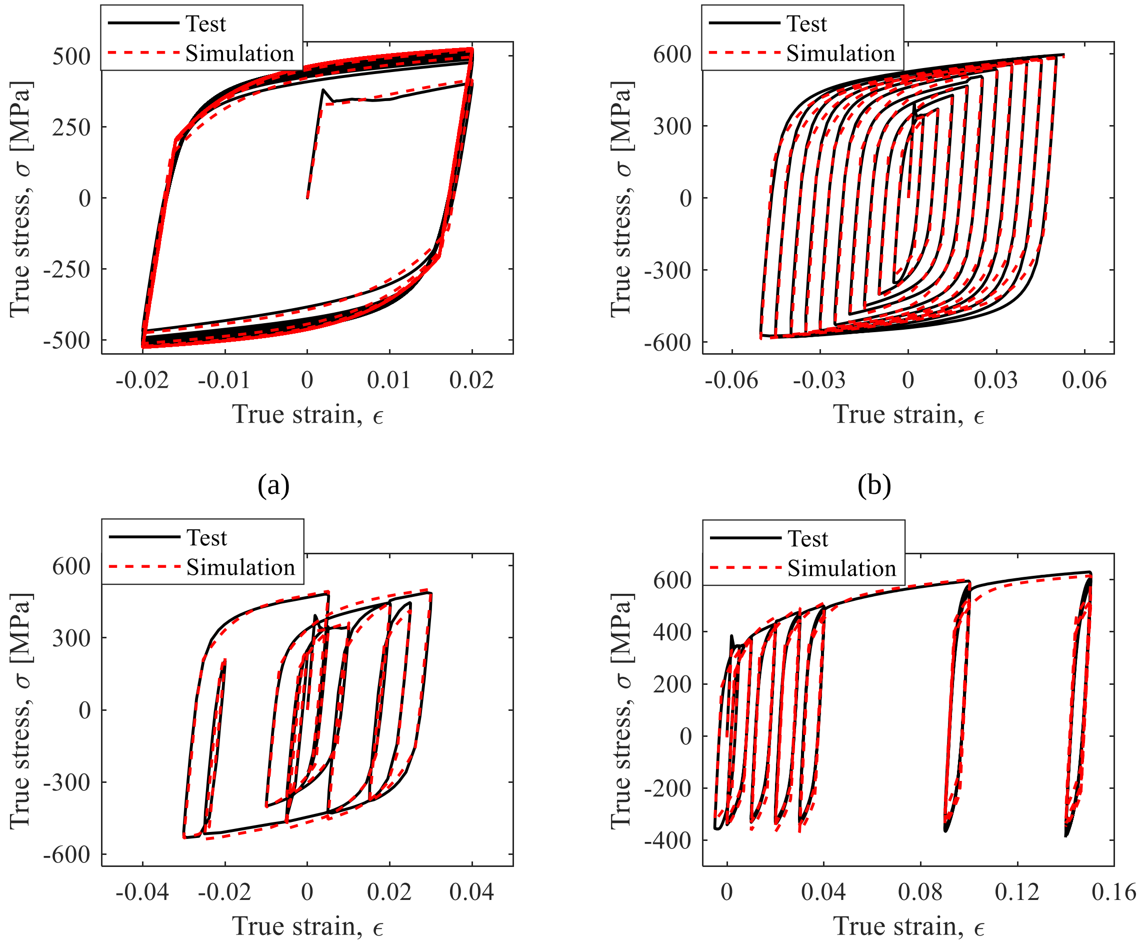

(a) (b)

(c) (d)

Figure 5.12 Cyclic true stress-strain behavior of representative uniaxial loading protocols in the column web: (a) loading protocol 5; (b) loading protocol 6; (c) loading protocol 9; and (d) loading protocol 10.

The chemical composition of the beam and column steel materials is summarized in Table 5.4. The carbon equivalent (CEV) that is a function of the chemical composition of steels (AWS 2010) is also reported. The CEV values indicate that the structural steel employed in the test specimens provides good weldability; hence, there is decreased potential for cracking near the heat affected zone (AWS 2010). According to Table 5.4, the sulfur content (denoted as "S") for the column is 0.004% of the total mass. For this level of sulfur content, the brittleness decreases, the weldability increases and the steel anisotropy is practically eliminated (ASTM 2018a; Miller 2017). Therefore, the through-thickness material strength and toughness are expected to be similar to those in the longitudinal direction (ASTM 2018a). The above were also confirmed with conventional CVN tests according to ASTM (2021).

Table 5.3 Calibrated parameters of multiaxial constitutive law for the steel material of columns and beams.

Parameter	E (MPa)	$\sigma_{y,0}$ (MPa)	Q_∞ (MPa)	b	D_∞ (MPa)	a	C_1 (MPa)	γ_1	C_2 (MPa)	γ_2
Column flange	182459	324.7	144.6	16.6	95.8	280.2	21872.5	185.0	2586.2	15.3
Column web	182120	329.0	144.1	18.6	107.2	227.8	19457.9	158.6	2270.4	12.4
Beam flange	181105	358.1	141.4	21.1	148.2	138.5	16047.8	130.2	1498.9	7.7
Beam web	172061	385.6	120.9	19.1	143.5	145.7	16984.2	132.5	1835.5	9.2

Table 5.4 Chemical composition of steel materials.

Material	Chemical composition (% mass)														CEV
	C	Si	Mn	P	S	Cu	Ni	Cr	V	Nb	Mo	Ti	Al	N	
Beam JIS-G3136 SN490B	0.18	0.34	1.07	0.019	0.008	NR	0.01	0.05	0.000	NR	0.010	NR	0.016	NR	0.37
Column JIS-G3106 SM490A	0.16	0.30	1.40	0.017	0.004	NR	NR	NR	NR	NR	NR	NR	0.032	NR	0.41

5.3.6 Applied loading protocols

Specimen 1 is subjected to a standard cyclic symmetric loading protocol (AISC 2016a; Clark et al. 1997), as per Fig. 5.13a. This protocol is considered so that the connection performance is compared with the prequalification requirements as per AISC 341-16. Moreover, since this loading protocol is commonly used in standard cruciform beam-to-column connection testing, the experimental results will form a basis of performance comparison with prior test programs on welded connections.

For Specimen 2, three loading phases are implemented as per Fig. 5.13b. Phase 1 consists of the SAC near-fault asymmetric loading protocol (Krawinkler et al. 2000), while phase 2 comprises the collapse-consistent loading protocol (Suzuki and Lignos 2020). In phase 3, the specimen is loaded cyclically at ±10% rad drift ratio cyclic intervals. The first loading phase is considered, since pulse-like near-fault ground motions with forward directivity are found to be considerably damaging compared with ordinary ground motions (Alavi and Krawinkler 2004). The second phase is considered to acquire representative experimental data at large deformations associated with global collapse of steel MRFs; thus, the loading protocol replicates the ratcheting behavior of MRFs prior to sidesway collapse (Lignos et al. 2011; Suzuki and Lignos 2021). The third phase was employed until the loss of at least 50% of the lateral load carrying capacity of the test specimen so as its ultimate failure mode is also characterized experimentally and compared with that of Specimen 1.

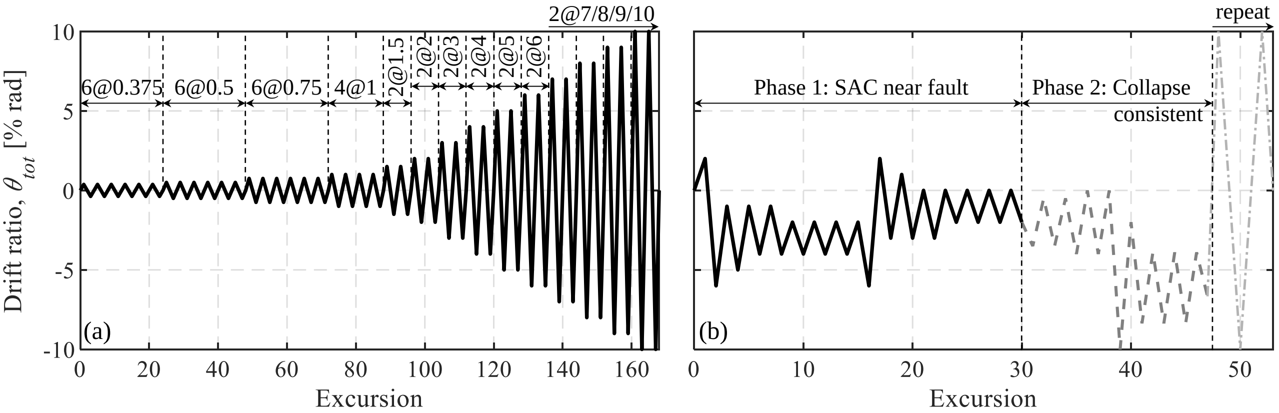

Figure 5.13 Loading protocols for the beam-to-column connection test specimens: (a) Specimen 1; and (b) Specimen 2.

Prior to the imposition of the above-mentioned loading protocols, a compressive axial load was applied to the steel column of each test specimen. This load was kept constant throughout the imposed cyclic loading histories. The magnitude of the applied axial force is $P_c = 5000$ kN, which corresponds to $0.2P_{y,n}$ ($P_{y,n}$ is the column axial yield strength, based on the nominal material properties), as per Skiadopoulos and Lignos (2022b).

5.4 Experimental results and discussion

5.4.1 Qualitative summary of experimental behavior

In this section, the results from both experiments are discussed in a qualitative manner. Emphasis is given on the story shear resistance, V_{col}, versus story drift ratio, θ_{tot}, and on the panel zone shear force, V_{pz}, versus panel zone normalized shear distortions, γ/γ_y, of both test specimens. Both V_{col} and V_{pz} are obtained based on equilibrium of forces in the statically determinate test specimen. The story drift ratio, θ_{tot}, is calculated as per Eq. (5.1), while γ as per Eq. (5.2). The discussion hereinafter is also facilitated with a number of informative illustrations, which demonstrate the overall performance of the welded connections.

Figure 5.14 shows the hysteretic responses of Specimens 1 (see Fig. 5.14a) and 2 (see Fig. 5.14b). Superimposed in the same figure are key damage states, which were identified during testing. Both test specimens remained elastic until 0.75-1% rad lateral drift demand, where the onset of panel zone yielding occurred. That was identified by the flaking of the whitewash paint near the panel zone area and by the plastic strain readings in the central panel zone rosette (see Fig. 5.10a). The panel zone yielding at a lateral drift demand of 1% rad is also evident in Fig. 5.15 that shows the panel zone hysteretic responses of both test specimens. In this case, the results are reported until the deduction of γ was deemed accurate based on the LVDT readings (i.e., 8% rad for Specimen 1 and the 50th loading excursion for Specimen 2). The lateral elastic stiffness of both test specimens is almost identical and equals 8.34×10^4 kN/rad. At a lateral drift demand of 2% rad, the beams of both test specimens yielded as identified by the strain gauge measurements near the CJP welds (see Fig. 5.10a). The panel zones at this point reached $4\gamma_y$ shear distortions. The deformed test specimens at 2% rad are shown in Figs. 5.16a-b for Specimen 1 and in Figs. 5.17a-b for Specimen 2, respectively, with the focus being on the beam bottom flange. It is observed that for this level of lateral drift demand, which is representative of a design-basis earthquake (DBE), the beam-to-column connections do not practically indicate any sign of visual damage.

Regarding Specimen 1, at a lateral drift demand of 3% rad, flexural yielding in the beams and panel zone progressed without any indication of local buckling (see Figs. 5.16c-d). The panel zone shear distortions reached $8\gamma_y$. Referring to Fig. 5.14a, strength stabilization occurred at about 4% rad. At this lateral story drift demand, that is representative of a maximum considered earthquake (MCE), there was no indication of beam localized deformations (see Fig. 5.16e), while the backing bar region did not exhibit any visual damage (see Fig. 5.16f). The panel zone shear distortions at this drift amplitude were nearly $10\gamma_y$. Referring to Fig. 5.18a, at 4% rad the panel zones exhibited localized yielding in the inside of the column flanges at the kinking locations. The yielding zone at these locations increased at higher lateral drift demands, while it progressed more near the column web centerline, as discussed in the subsequent sections. Similar observations hold true at the outside of the column flange, near the backing bar region, where the yielding zone progresses in an elliptical manner and maximized near the column web centerline (see Fig. 5.19). The stress and strain demands near this critical location are quantified in the subsequent sections.

Upon further loading (i.e., 5-6% rad), the onset of local buckling became evident in the beam flanges and the panel zone distortion design target (i.e., $15\gamma_y$) was reached at 6% rad. Therefore, the contribution of the panel zone to the total story drift ratio capped at about 4-5% rad. After the onset of local buckling, the contribution of the steel beams to the total story drift ratio increased. Yielding in the inside of the column flanges became more evident at this point (see Figs. 5.18b-c). At the first loading excursion of the 6% rad amplitude, a ductile crack was observed at the east beam top flange near the shear tab end that was under tension (see Fig. 5.14a for θ_{tot} sign convention), which is depicted in Fig. 5.20a. During the next loading excursion of the same amplitude, the beam-to-column connection reached the maximum negative story shear resistance (i.e., 1249 kN). At this lateral drift demand amplitude, beam local buckling was not prominent, while the bottom beam flange backing bar did not exhibit any visible damage (see Figs. 5.16g-h). At the first loading excursion of the 7% rad lateral drift amplitude, the story shear resistance maximized at 1265 kN.

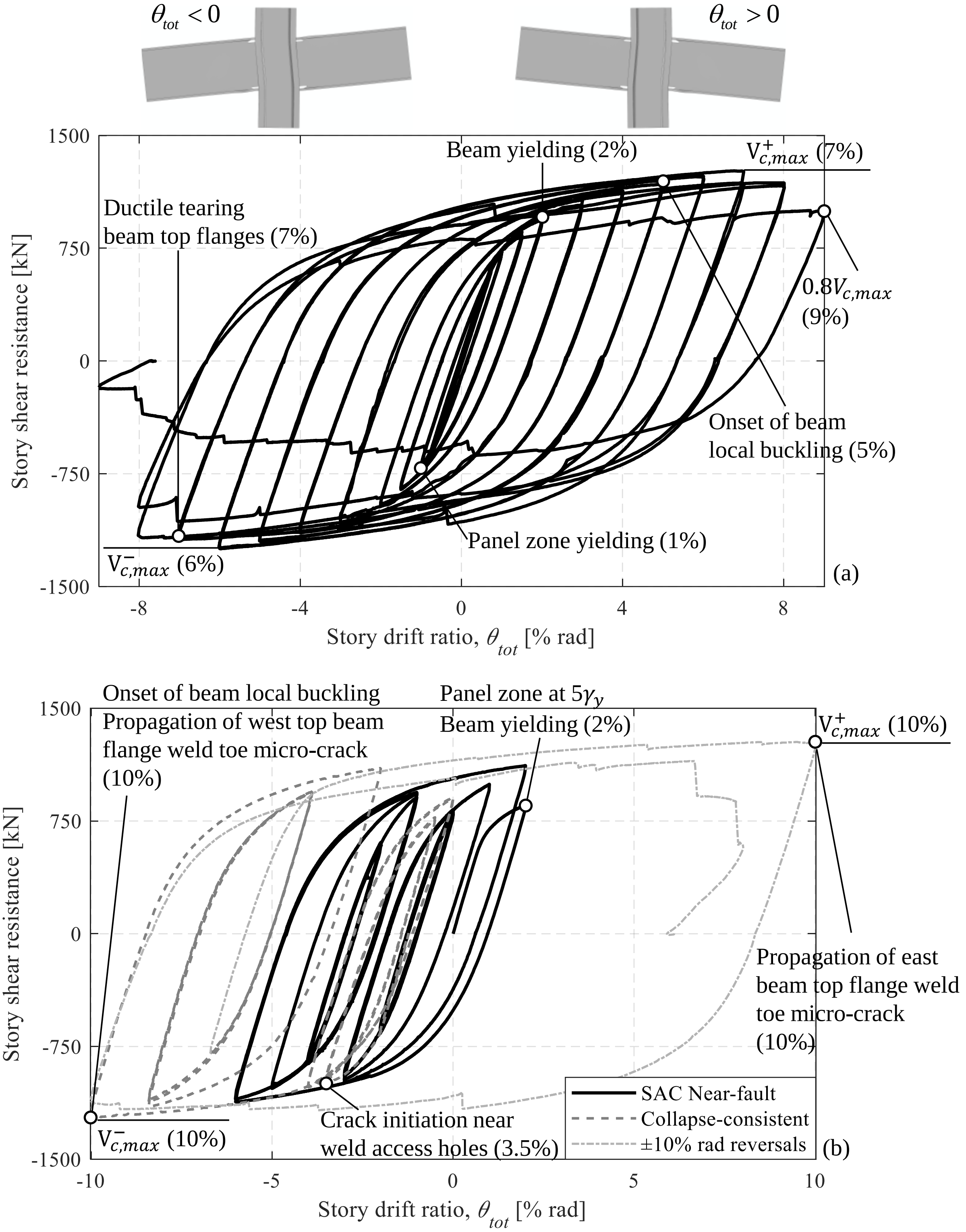

Figure 5.14 Story shear resistance versus story drift ratio: (a) Specimen 1; and (b) Specimen 2.

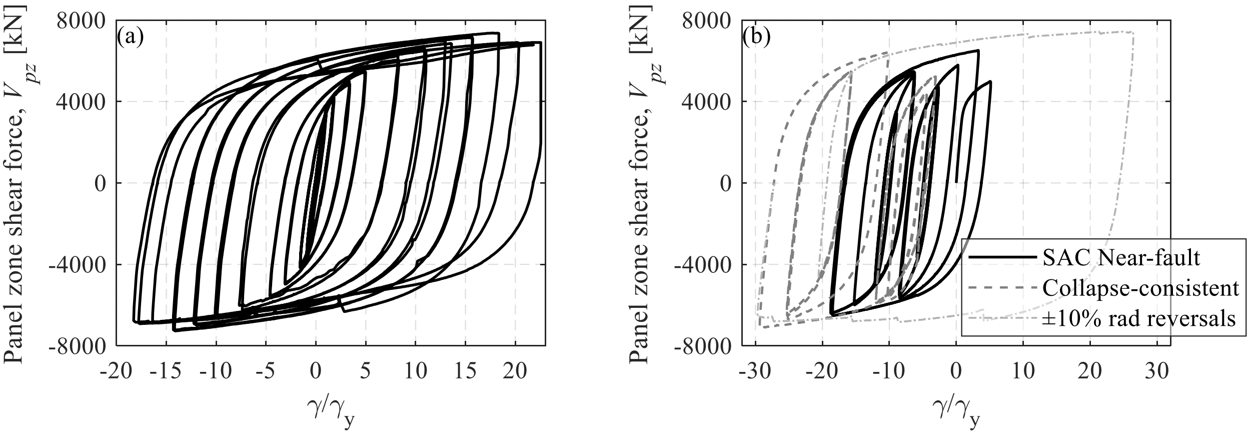

Figure 5.15 Panel zone shear force versus normalized panel zone shear distortion: (a) Specimen 1; and (b) Specimen 2.

During the last cycle of 7% rad, ductile tearing propagated slightly through the thickness of the column flange at the CJP weld toe of the west and east beam top flanges, as depicted in Figs. 5.20b-c, accordingly. Up until this lateral drift amplitude, Specimen 1 did not attain a negative stiffness (see Fig. 5.14a). Moreover, Specimen 1 did not exhibit cyclic deterioration in the story shear resistance due to local buckling in the steel beams and/or crack initiation and propagation in the column. At the last cycle of the 7% rad amplitude, a minor panel zone waving perpendicular to its compressive strut was observed, thereby indicating mild shear buckling. The amplitude of the waving did not increase up until the end of the test. At the first negative loading excursion of 8% rad, localized inelastic deformations at the west beam bottom flange were prominent. This effect, in combination with the ductile tearing initiation at the shear tab top flange position (similarly to the east beam, Fig. 5.20a), lead to about 20% reduction in the story shear resistance of the same specimen. Moreover, at the east beam bottom flange, a ductile crack initiated at the weld root between the backing bar and the column flange (see Fig. 5.20d). At this lateral drift demand, panel zone yielding at the inside and outside of the column flange progressed to the full column flange width in a zone of nearly 100 mm height (see Figs. 5.18d and 5.19b). At the positive excursion of 9% rad, a 20% loss of the maximum achieved story shear resistance was observed due to the propagation of the existing ductile cracks. At the negative excursion of the same lateral drift amplitude, the beam-to-column connection lost more than 80% of its lateral load resistance due to ultra-low cycle fatigue in the west top and east bottom beam flanges and the test was terminated with the panel zone reaching $23\gamma_y$ (see Fig. 5.15a). More details on the crack propagation modes and the ultimate failure modes are found in the subsequent sections.

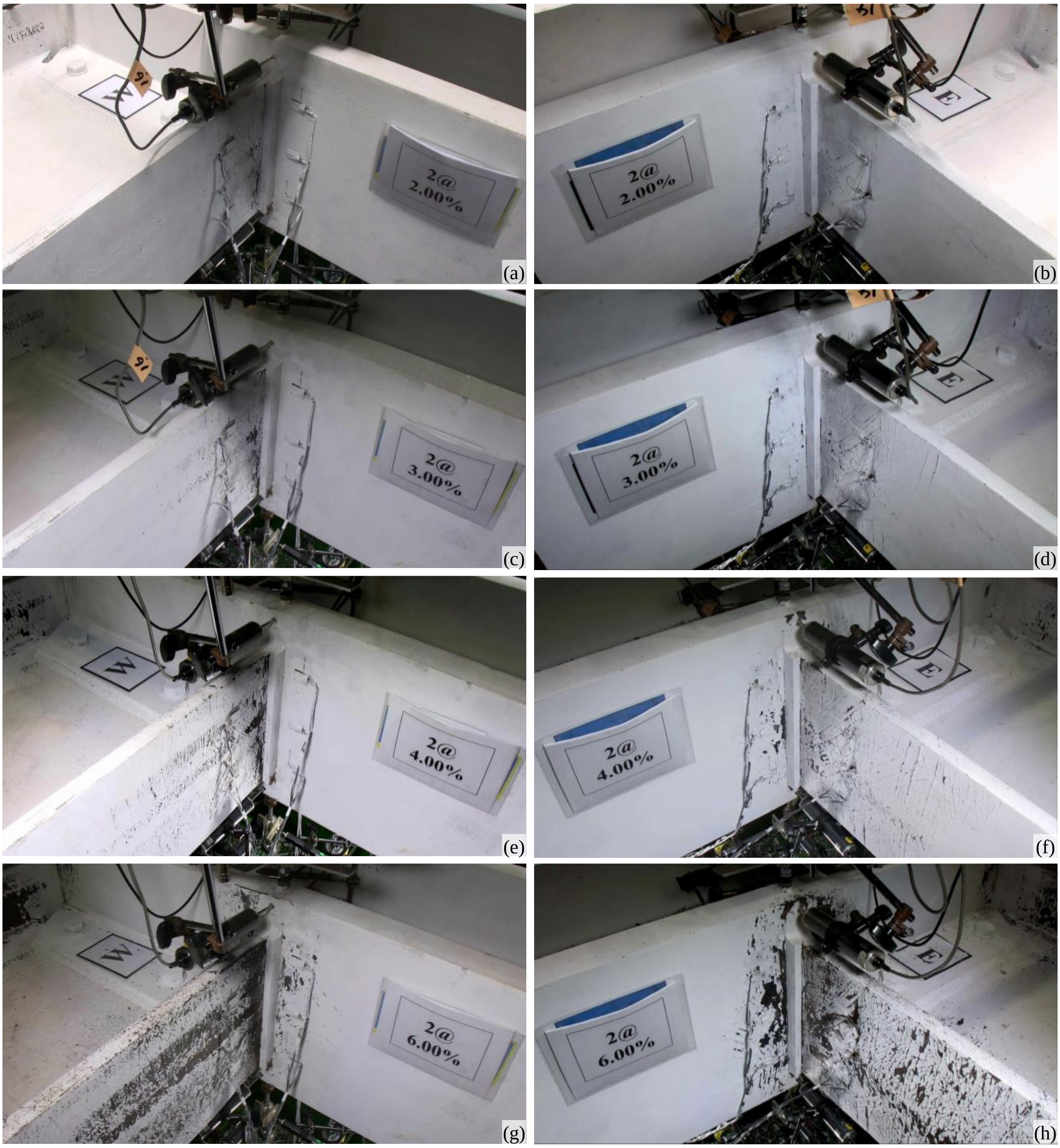
W
2@
2.00%
(a)
E
2@
2.00%
(b)
W
2@
3.00%
(c)
E
2@
3.00%
(d)
W
2@
4.00%
(e)
E
2@
4.00%
(f)
W
2@
6.00%
(g)
E
2@
6.00%
(h)

Figure 5.16 Specimen 1 bottom beam flanges at characteristic loading excursions (left: west beam, right: east beam).

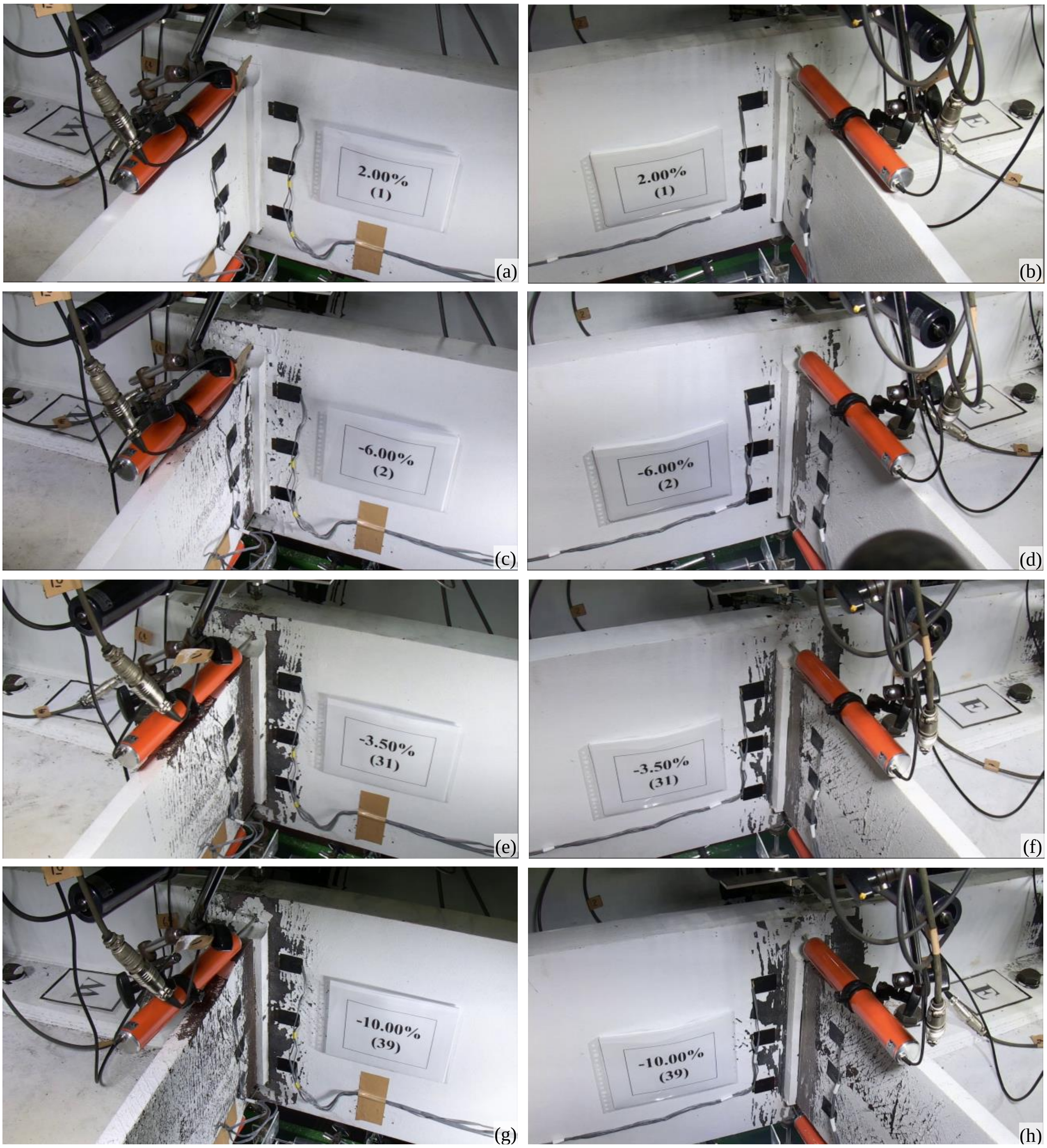
2.00%
(1)
(a)
2.00%
(1)
(b)
-6.00%
(2)
(c)
-6.00%
(2)
(d)
-3.50%
(31)
(e)
-3.50%
(31)
(f)
-10.00%
(39)
(g)
-10.00%
(39)
(h)

Figure 5.17 Specimen 2 bottom beam flanges at characteristic loading excursions (left: west beam, right: east beam).

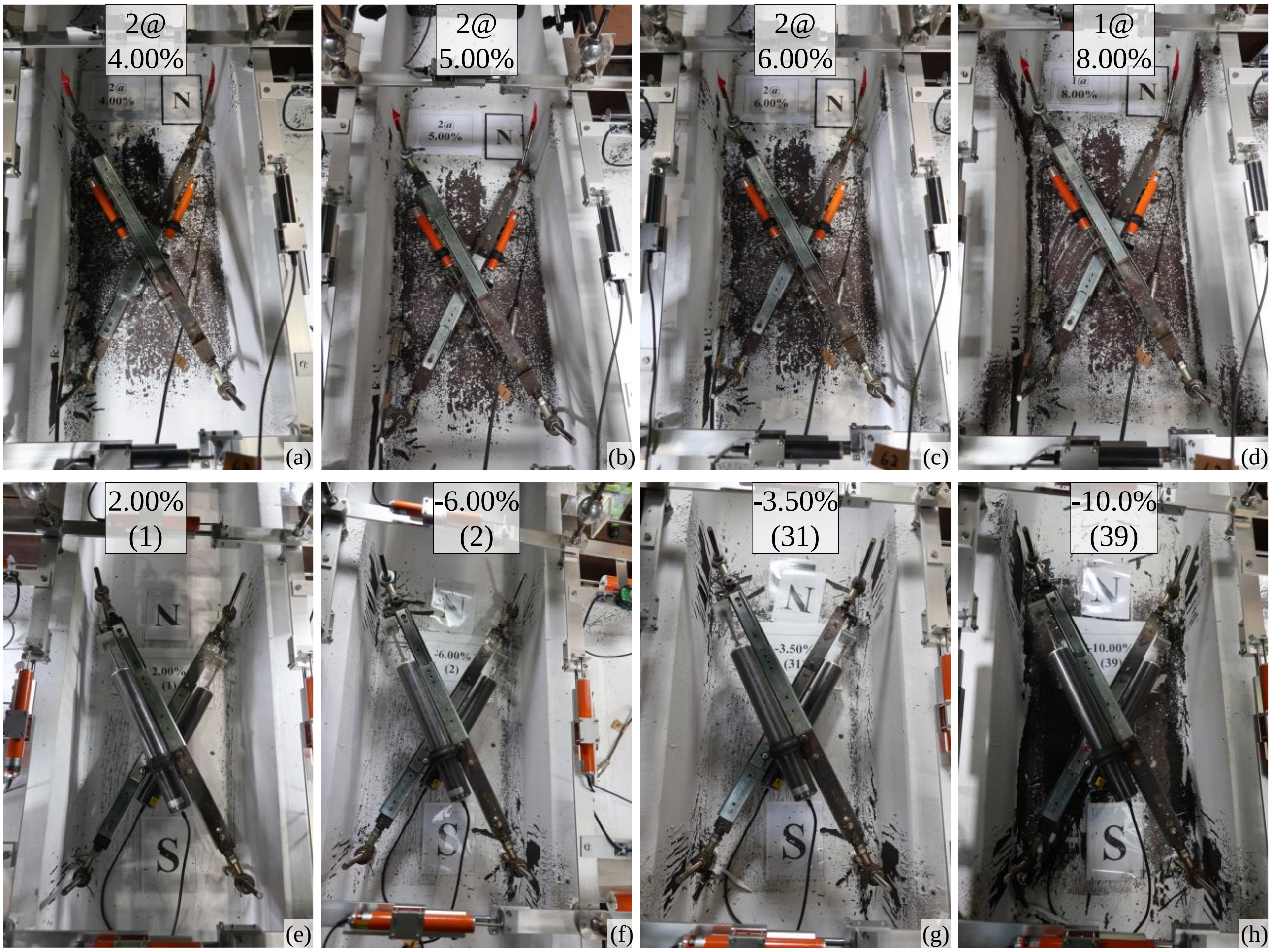
2@
4.00%
(a)
2@
5.00%
(b)
2@
6.00%
(c)
1@
8.00%
(d)
2.00%
(1)
(e)
-6.00%
(2)
(f)
-3.50%
(31)
(g)
-10.0%
(39)
(h)
N
S

Figure 5.18 Panel zone deformation at characteristic loading excursions (top: Specimen 1, bottom: Specimen 2).

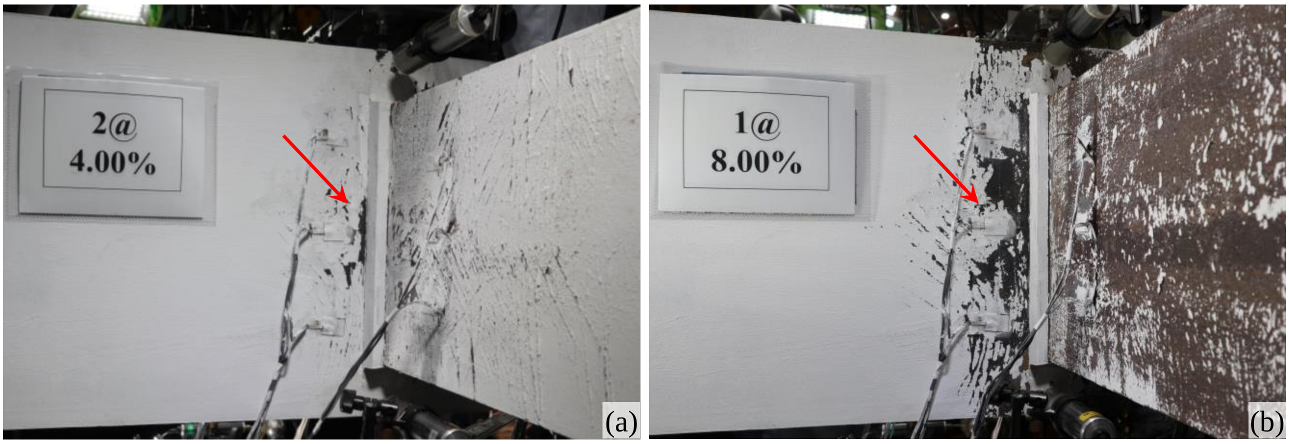
2@
4.00%
(a)
1@
8.00%
(b)

Figure 5.19 Yield pattern around the beveled backing bar of the bottom flange of the steel beam (Specimen 1).

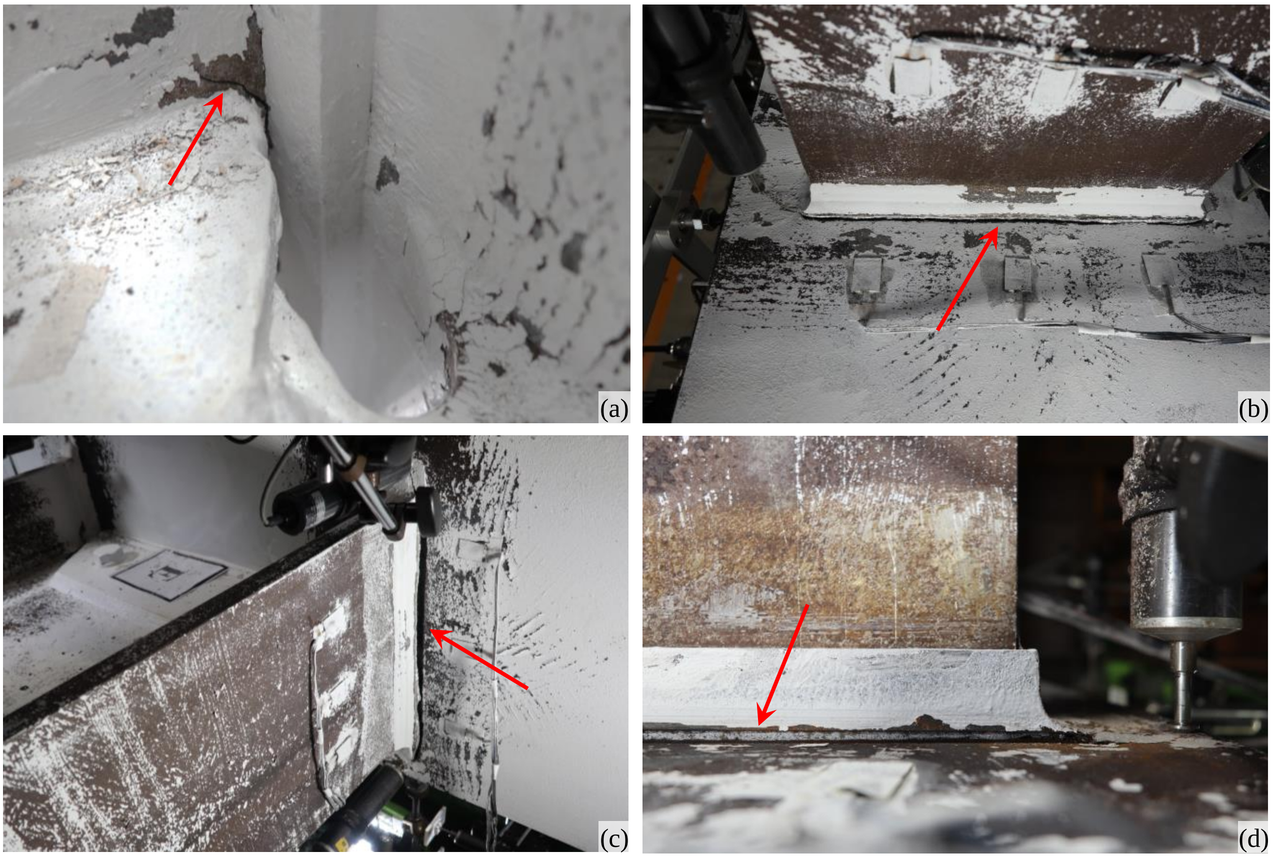

Figure 5.20 Specimen 1 crack patterns at characteristic lateral drift demands of: (a) +6% rad; (b) -7% rad; (c) +7% rad; and (d) -8% rad.

Regarding Specimen 2 (see Figs. 5.14b and 5.17), at the second peak lateral drift amplitude of the near-fault protocol (-6% rad) flexural yielding in the beams and shear yielding in the panel zone progressed. Visual inspection of the steel beams and the beveled backing bars did not reveal any noticeable damage (see Figs. 5.17c-d). Figure 5.15b suggests that the panel zone inelastic shear distortion reached about $18\gamma_y$. Shear yielding in the panel zone was more evident due to the whitewash flaking (see Figs. 5.18e-f). Cyclic hardening in the steel beams increased the moment demands and the resultant shear demand in the panel zone; hence, the design target of $15\gamma_y$ was slightly exceeded at 6% rad. Upon further loading, ductile cracks became visible at the west top flange weld toe adjacent to the column flange surface and at the west beam bottom side shear tab near the access hole. These were consistent with those seen in Specimen 1. During the 18th loading excursion (-3% rad), the same crack types were observed at the east beam top flange. At the 22nd excursion (-3% rad), mild out of plane flange deformations were observed near the beam plastic hinge region at the flanges under compression. At the end of the near-fault loading protocol, the panel zone peak shear distortion remained at $18\gamma_y$ (see Fig. 5.15b). Noteworthy stating that the overall hysteretic behavior of the welded connection was stable due to the absence of nonlinear geometric instabilities in the steel beams.

During the first loading excursion of the collapse-consistent protocol (31st excursion of the loading protocol, at -3.5% rad), a crack was observed at the east beam bottom side shear tab weld fusion near the access hole, which was similar to the one seen at the west beam. The one observed on the east beam propagated more compared to the one on the west beam, since the east beam bottom flange was mainly in tension during the near-fault loading protocol. Referring to Figs. 5.17e-f, both steel beams experienced flexural yielding, which propagated over 300 mm length in their flanges. The panel zone yielding at the kinking locations further progressed compared to the 2nd excursion (see Figs. 5.18f-g). At the peak lateral drift excursion of the collapse-consistent protocol (-10% rad), the cracks of the shear tab (see Fig. 5.21a) and top beam flange weld fusion (see Fig. 5.21b) propagated towards the column width and thickness direction. At this excursion, the beam-to-column connection reached its negative maximum story shear resistance, that equals -1223 kN. All the above-mentioned cracks were deemed to be stable considering that (a) they propagated slowly and (b) did not compromise the overall hysteretic behavior of the welded connection (see Fig. 5.14b). Moreover, the panel zone shear distortion reached $30\gamma_y$ (see Fig. 5.15b). At this shear distortion, the kinking effect at the column flanges was prominent as shown in Fig. 5.18h. The beam local deformations did not progress (see Fig. 5.17g), whereas the region near the bottom backing bar exhibited yielding (see Fig. 5.17h). Despite the crack initiation at the above-mentioned locations, as the imposed story drift increased up to 10% rad, Specimen 2 exhibited a stable hysteretic response until the end of the collapse-consistent loading protocol. The overall response was dominated by cyclic hardening of the steel material. From a collapse assessment standpoint, lateral drift demands above 5% rad are usually considered indicative of dynamic instability of steel MRFs due to global P-Δ effects (FEMA 2009a; Gupta and Krawinkler 2000a; NIST 2010).

From this point forward, lateral drift reversals of ±10% rad were performed. While lateral drift reversals of this amplitude are very unlikely during an actual earthquake, these were still conducted to determine the ultimate failure mode of the beam-to-column connection. During the first excursion of this loading phase, a crack initiated at the east beam top side of the shear tab and propagated in the column flange width direction. The crack propagation stopped about 50 mm away from the column flange edge (see Fig. 5.21c). At the west beam top flange weld toe, a ductile crack initiated, which was consistent with those seen at similar locations in Specimen 1 (e.g., see Figs. 5.20b and 5.21b). These ductile cracks led to nearly 5% loss of the lateral load resisting capacity of Specimen 2. During the next loading excursion, the ductile crack of the west beam top flange propagated through the column flange thickness (see Fig. 5.21d), thereby indicating a consistent failure mode between test specimens regardless of the employed loading history. The test was terminated once Specimen 2 lost at least 50% of its story shear resistance due to ultra-low cycle fatigue. The ultimate failure modes are described in the subsequent sections.

The stable beam-to-column hysteretic response until large lateral drift demands is partially attributable to the balanced design of the inelastic deformations between the beams and the panel zone and the beneficial aspects of the panel zone shear yielding, which is a stable damage mechanism. The targeted panel zone shear distortions were exceeded in both test specimens at about 6% rad lateral drift demand. Therefore, the established performance objectives of the targeted welded connection design were met. Specimen 2 reached higher levels of panel zone inelastic shear distortions compared to Specimen 1, since the cyclic symmetric loading protocol triggered beam local buckling at lower lateral drift demands compared to the non-symmetric loading protocols of Specimen 2. The experimental program demonstrates that the proposed beam-to-column connection detailing can sustain panel zone shear distortions that are substantially higher than the targeted values. Therefore, regardless of the material uncertainty and the employed loading history, the overall connection performance is not impaired given the proposed detailing simplifications and the panel zone design recommendations by Skiadopoulos et al. (2021).

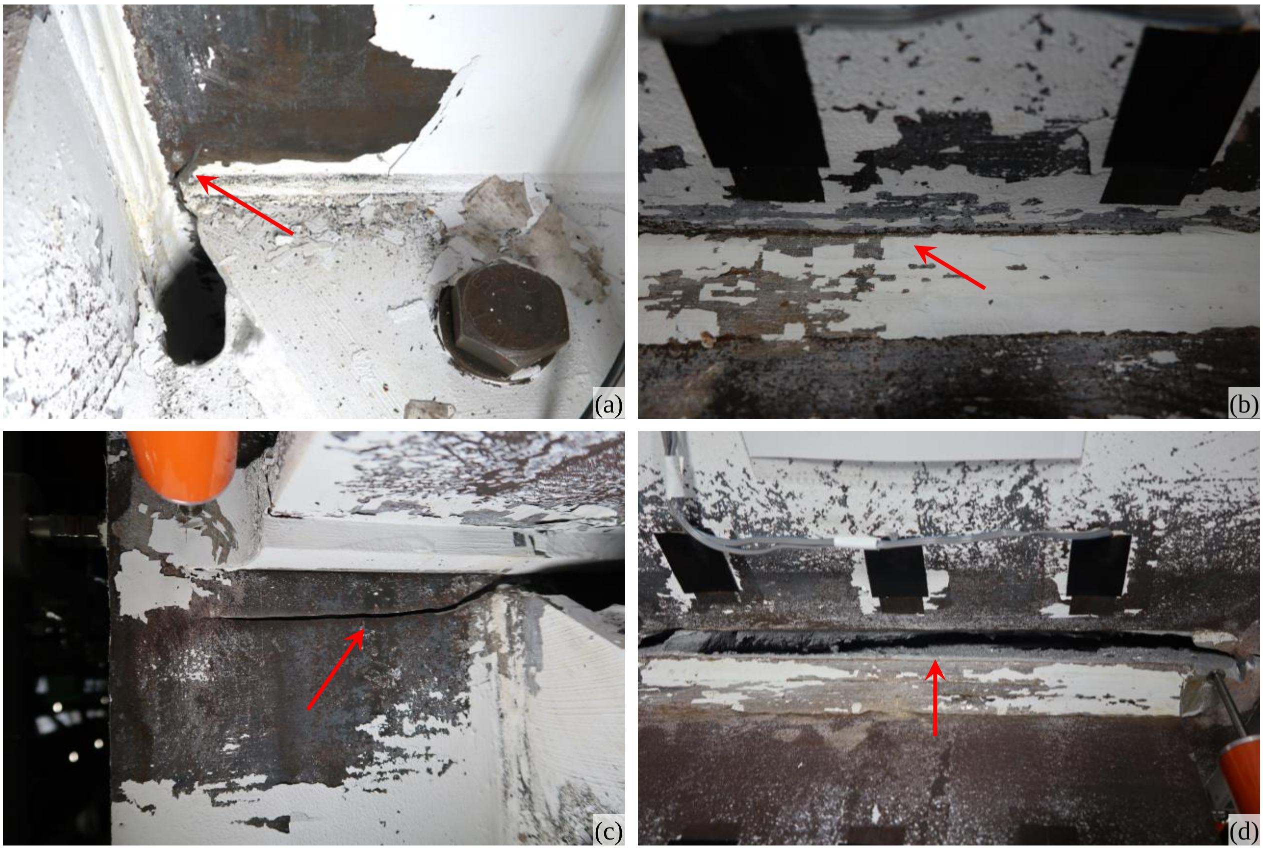

Figure 5.21 Specimen 2 crack patterns at characteristic loading excursions: (a-b) 39th (-10.0% rad); (c) 48th (+10.0% rad); and (d) 50th (-10% rad).

5.4.1.1 Performance of beveled backing bars

In this section, the performance of the beveled backing bars is discussed for both test specimens. Current prequalification requirements (AISC 2016c) allow for top flange backing bars to remain in place. The test results confirmed that this location did not experience any notable damage at lateral drift demands associated with both design-basis and maximum considered earthquakes. Similar observations hold true for the bottom beam flange beveled backing bars. The beveled backing bars achieve an optimal fracture potential between the backing bar-to-column face and the backing bar-to-beam flange notch tips (Skiadopoulos and Lignos 2022a). These notches are characteristically depicted in Fig. 5.22 at a lateral drift demand of 10% rad for Specimen 2. Therefore, if the backing bar was fillet-weld reinforced to the beam or column flange, the stress flow in the backing bar would have increased, thereby compromising the optimal fracture potential in the beveled backing bar notch tips.

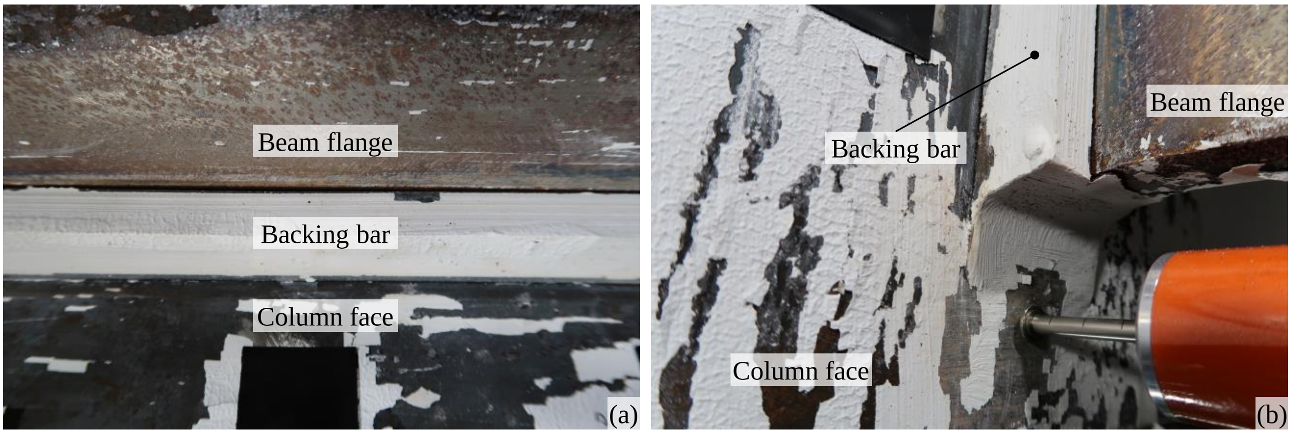

Figure 5.22 Backing bar deformations (Specimen 2, at a 10% rad lateral drift demand).

5.4.1.2 Ultimate failure modes

In this section, the ultimate failure modes of both test specimens are discussed. Figure 5.23 shows the ultimate failure modes of the beams' top and the east beam's bottom flanges of Specimen 1. In all cases, the cracks initiated after 7% rad lateral drift demand and are attributed to ultra-low cycle fatigue. Referring to Figs. 5.23a-b, the cracks at the beam top flanges initiated at the column flange, near the beam top flange-to-column face CJP weld fusion at the beam web centerline. On the other hand, the crack at the bottom flange of the east beam initiated nearly 100 mm away from the beam web centerline. In all cases, the cracks propagated towards the column thickness and longitudinal direction. During the crack propagation face, Specimen 1 was able to dissipate one third of the total absorbed energy. The test results did not reveal any signs of cracks/fracture at the bottom flange of the west beam of Specimen 1.

Figure 5.24 shows the ultimate failure modes for Specimen 2. In all cases, the crack initiation is also attributed to ultra-low-cycle fatigue. Figure 5.24b depicts the fracture modes of the column flange near the top flange of the west and east beams, respectively. Qualitatively, the cracks in both cases initiated near the centerline of the beam web and propagated along the flange width. Referring to Fig. 5.24b, the crack initiated from the weld fusion of the shear tab end. The crack then extended towards the column flange and in part through the column web. As far as the beams' bottom flange-to-column flange interfaces, these did not experience any visible cracks as shown in Fig. 5.24c. Figure 5.25 demonstrates the deformed shape of Specimens 1 and 2 after the end of testing and the removal of the instrumentation.

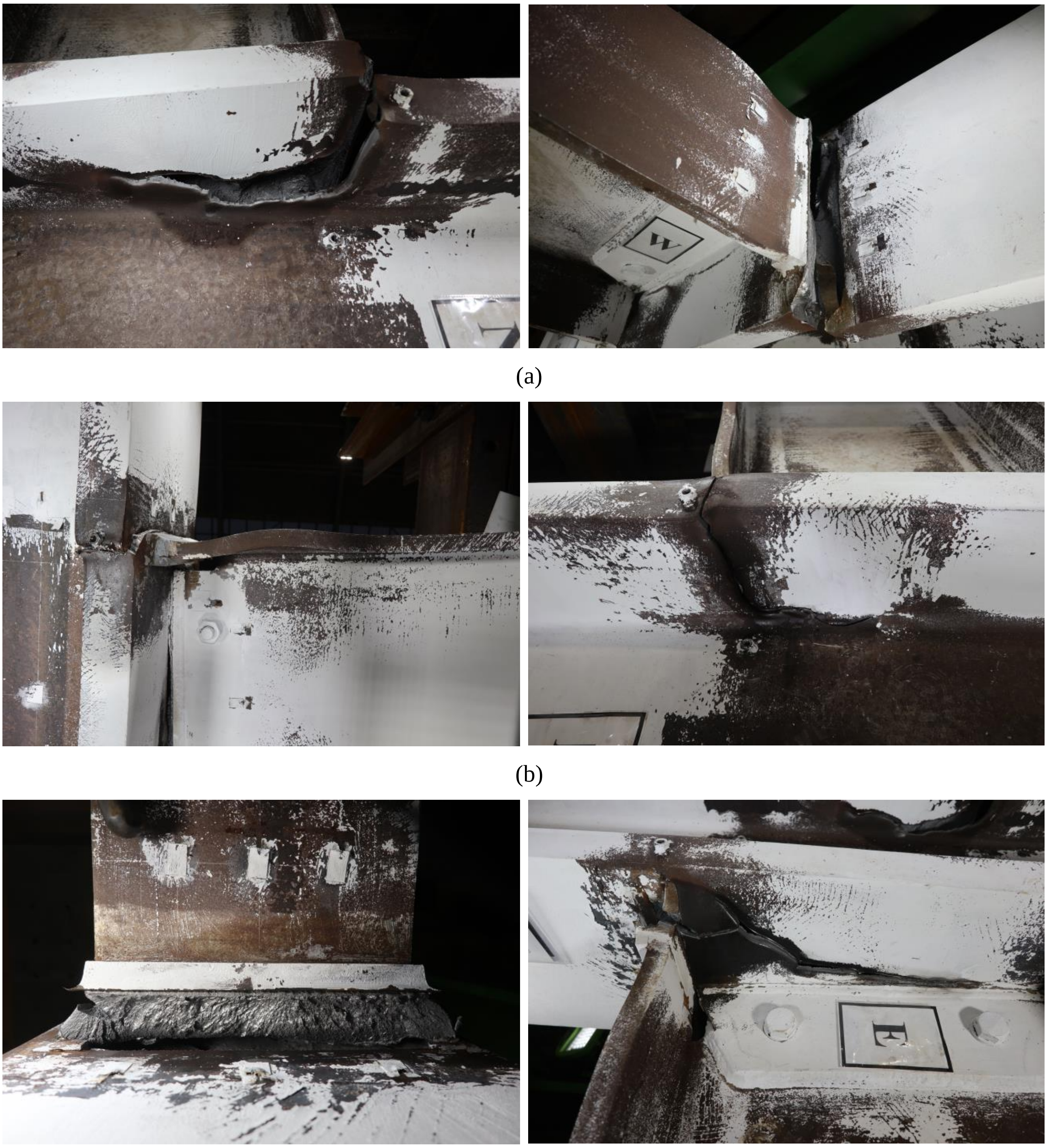

(a)

(b)

(c)

Figure 5.23 Ultimate failure modes of Specimen 1 after the test completion: (a) west beam top flange; (b) east beam top flange; and (c) east beam bottom flange.

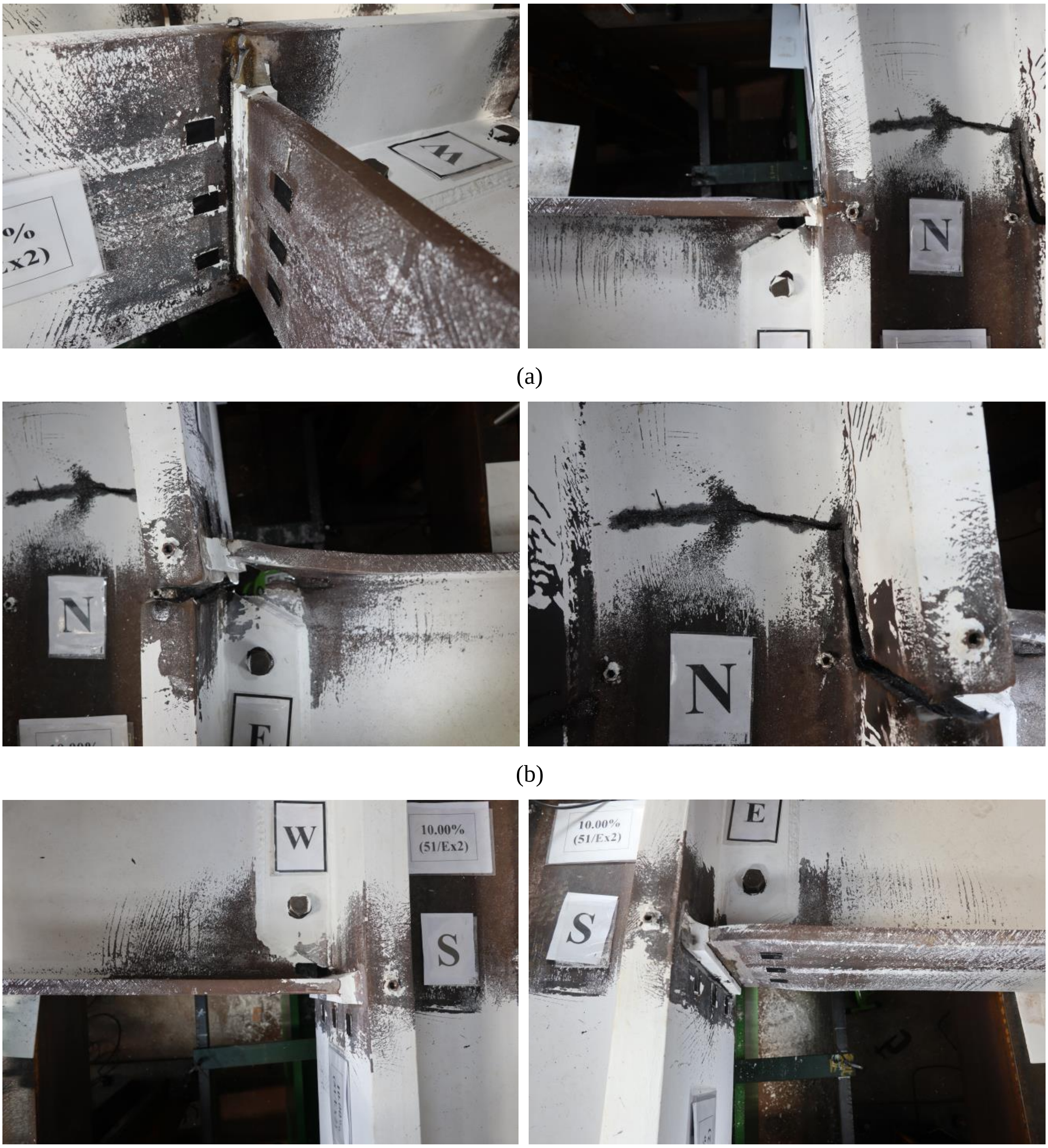

(a)

(b)

(c)

Figure 5.24 Ultimate failure modes of Specimen 2 after the test completion: (a) west beam top flange; (b) east beam top flange; and (c) west and east beam bottom flanges.

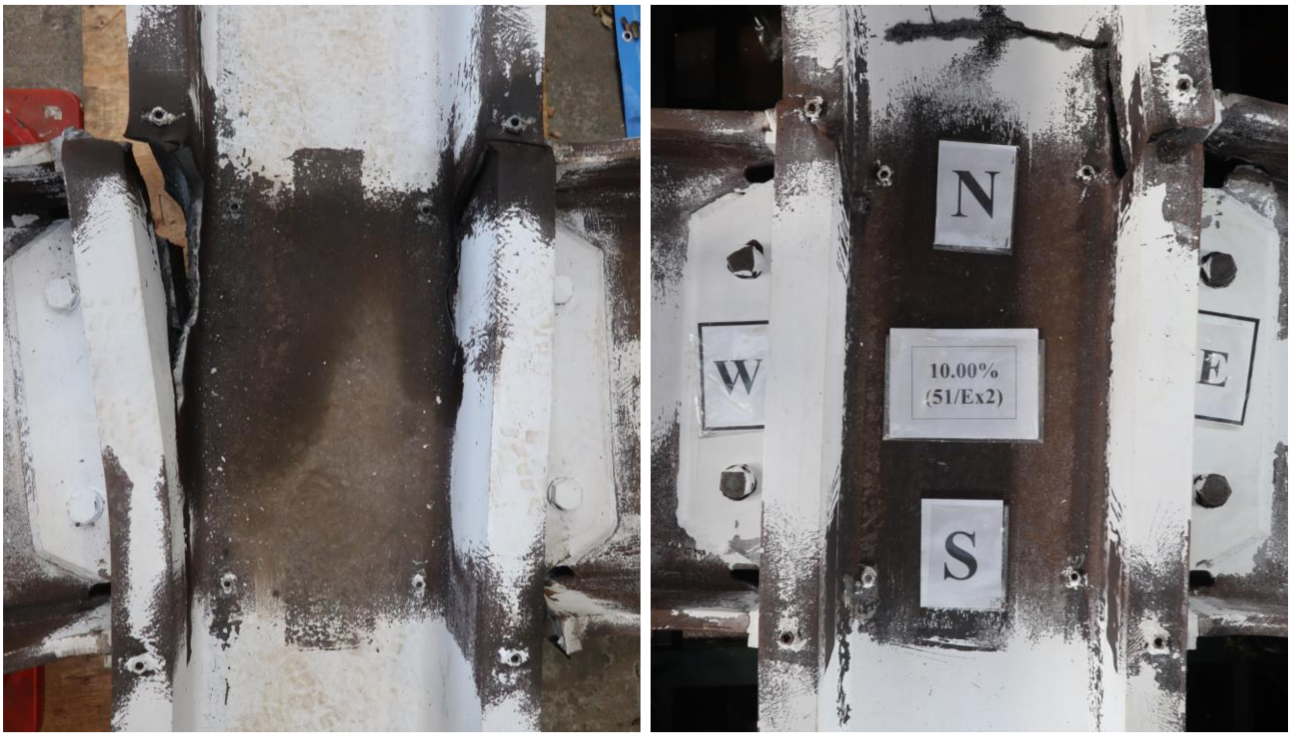

Figure 5.25 Deformation pattern of the test specimens after the completion of the test program (left: Specimen 1, right: Specimen 2).

Vis-a-vis the above discussion, the experimental observations reveal that the observed ultimate failure modes were fairly consistent in both specimens. While cracks did initiate due to ultra-low cycle fatigue, they were deemed to be stable and did not compromise the overall stability of the welded connections till large amplitude lateral drift demands (i.e., above 7% rad). Evidently, from the theoretical point of crack initiation to the point of loss of at least 50% of the lateral load carrying capacity of both connections, these dissipated about one third of the total dissipated energy.

5.4.2 Quantitative assessment of test results

This section discusses in a quantitative manner the experimental results of both test specimens. Their performance is first assessed based on the AISC (2016a) beam-to-column connection prequalification criteria. The discussion also focuses on other performance indicators, such as the column twist demands, column flange localized deformations and strain demands at selected locations. The influence of loading history is also discussed.

5.4.2.1 Prequalification limits

According to AISC 341-16 (AISC 2016a), beam-to-column connections under symmetric cyclic loading histories should sustain beam end moment demands higher than $0.8M_{pl}$ (M_{pl} is the beam plastic moment resistance based on the nominal material properties) during both loading cycles of a lateral drift demand of 4% rad.

Referring to Figs. 5.26a-b, the west and east beam moments at the column face are depicted for Specimen 1, respectively. The beam end moments at the column face are normalized with respect to M_{pl} and are compared with the AISC (2016a) limit of $0.8M_{pl}$. Both beams resisted nearly $1.4M_{pl}$ during the two loading cycles of 8% rad. Therefore, the prequalification criteria are satisfied. In fact, the cyclic performance of the connection was superior. Similar comparisons are shown for Specimen 2 (see Figs. 5.26c-d), which was subjected to asymmetric lateral drift demands.

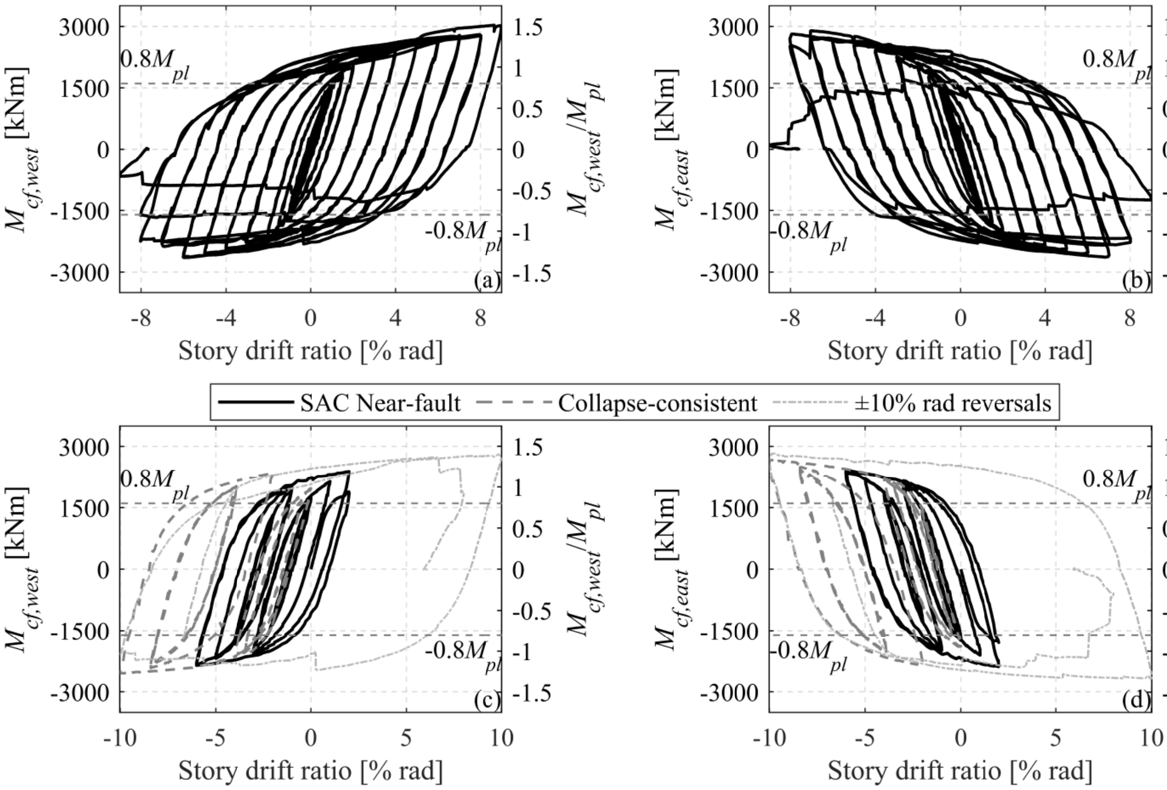

Figure 5.26 Beam moment at the column face versus story drift ratio: (a) Specimen 1, west beam; (b) Specimen 1, east beam; (c) Specimen 2, west beam; and (d) Specimen 2, east beam.

According to AISC 358-16, the beam-to-column web panel zones should be designed based on M_{pr}. The peak connection strength factor, C_{pr}, is taken equal to 1.4 for WUF-W connections (AISC 2016c). The computed C_{pr} equals 1.22 and 1.23 for Specimens 1 and 2, respectively. Therefore, the C_{pr} value of AISC (2016c) overestimates the influence of strain hardening on WUF-W connections. This finding corroborates with those from prior work (Lee et al. 2005b; Shin 2017). Collectively, this has also been confirmed after assessing the results from nearly 100 connection tests with dissipative panel zones (Skiadopoulos and Lignos 2021).

5.4.2.2 Decomposition of inelastic deformations and assessment of balanced design

Figure 5.27 shows the moments at the beam ends at the column face location versus the beam chord rotations and the moments at the column at the panel zone top horizontal edge location versus the column chord rotations, for both test specimens. The associated chord rotations are calculated over the beam cantilever length (i.e., from the column face to the load application point) and over the column cantilever length (i.e., from the panel zone top edge to the pin location), respectively. The results are reported until the last loading excursion for which the decomposition of deflections was deemed accurate (i.e., 6% rad for Specimen 1 and 49th excursion for Specimen 2). Regarding Specimen 1, the beam chord rotations reached nearly 3% rad, while at lateral drift demands representative of an MCE, beam chord rotations did not exceed 1.5% rad. Regarding Specimen 2, after the end of the near-fault loading protocol, beam chord rotations reached up to 2% rad, while at the end of the collapse-consistent loading protocol, they reached 4% rad. The columns remained elastic in both test specimens (see Figs. 5.27c and 5.27f).

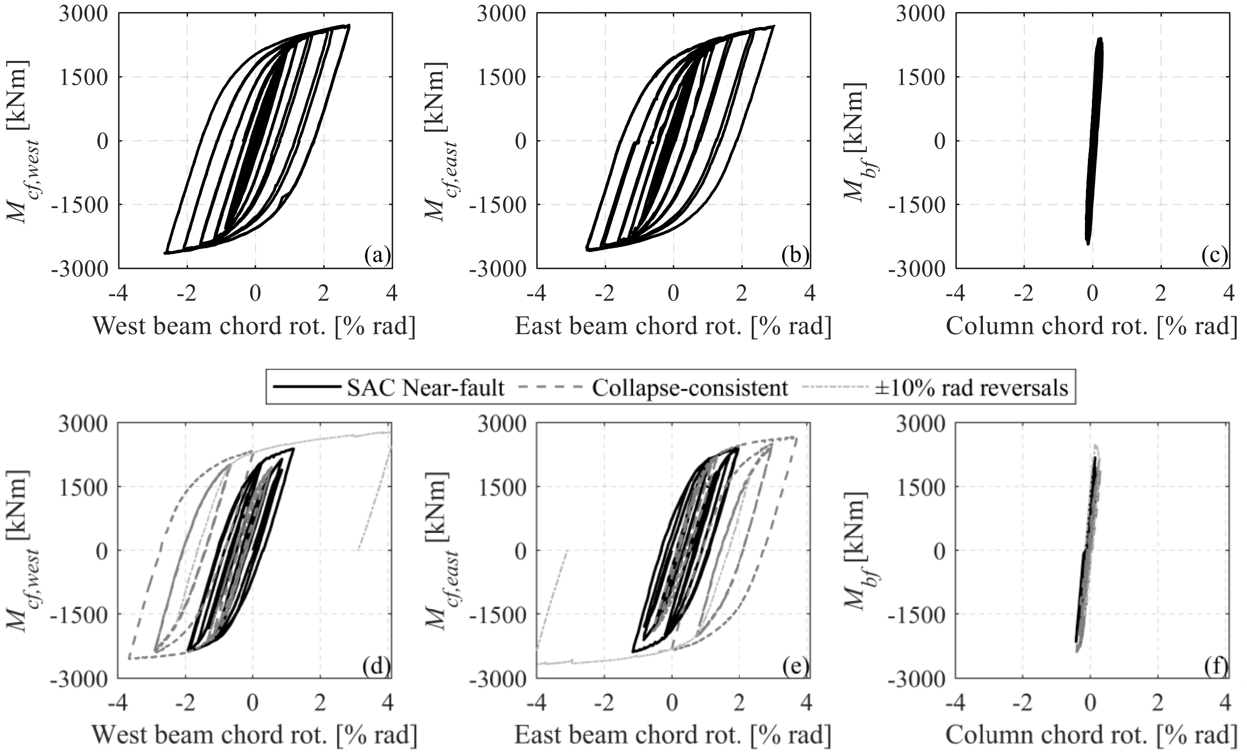

Figure 5.27 Moments at the beam ends at the column face location versus beam chord rotations and moments at the column at the panel zone top horizontal edge location versus column chord rotations: (a-c) Specimen 1; and (d-f) Specimen 2.

Figure 5.28 depicts the contribution of the beams, the panel zone and the column to the story drift ratio, θ_{tot}. The connection behavior of Specimen 1 was elastic up until a lateral drift demand of 1% rad. Referring to Fig. 5.28a, the panel zone contributed nearly 40%, the beams nearly 50% and the column 10% to θ_{tot} at 1% rad. From the same figure, once inelastic deformations concentrated in the panel zone, its contribution increased up to 50% and stabilized up until the onset of mild flange local buckling in the beams (i.e., 5% rad). From this point onwards, the contribution of the beams increased compared to that of the panel zone. Referring to Fig. 5.28b, the contribution of the panel zone and the beams to θ_{tot} was nearly 60% and 30%, respectively, throughout the imposed loading history of Specimen 2.

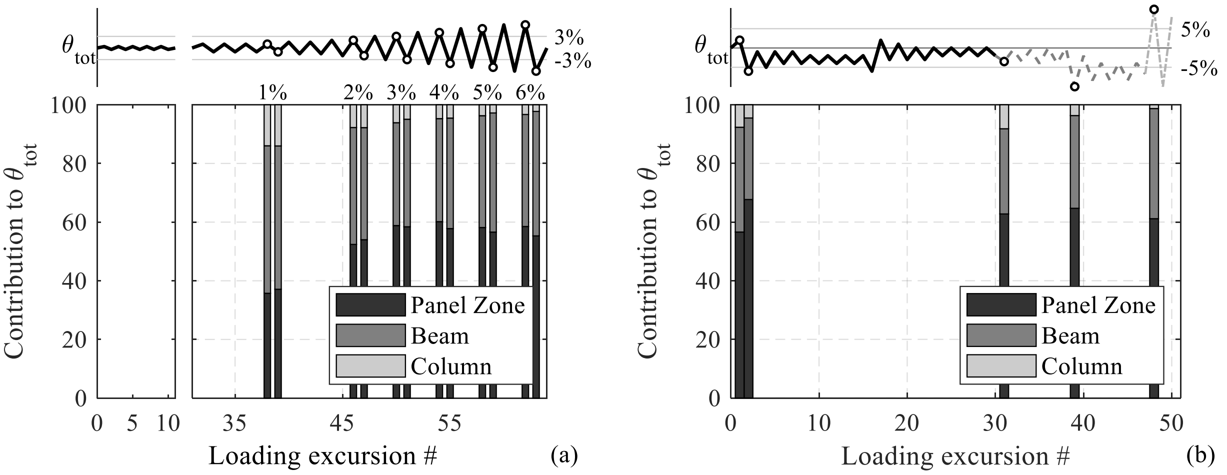

Figure 5.28 Contributions of the panel zone, the beams and the column to the story drift ratio at characteristic lateral loading excursions: (a) Specimen 1; and (b) Specimen 2.

The general consensus from the above findings is that the overall connection design was fairly well balanced between the panel zone and the steel beams, regardless of the employed loading history.

5.4.2.3 Twist demands in the column

Figure 5.29a shows a definition of the column twist rotation demand, $\theta_{c,twist}$. This is calculated according to Eq. (5.5), by using the LVDTs, which are positioned at the column flange centerline, at the column mid-height (see Fig. 5.10a). Accordingly:

$$\theta_{c,twist} = \frac{\delta_{c,twist,W} - \delta_{c,twist,E}}{L_{c,twist}} \tag{5.5}$$

The column twist demands are shown in Figs. 5.29b-c at characteristic lateral drift demands for both test specimens. Referring to Specimen 1, the column twist demands do not exceed 0.1% rad up until a lateral drift demand of 6% rad. Once beam local buckling becomes prominent, $\theta_{c,twist}$ reaches 0.4% rad at a lateral drift demand of 8% rad. Referring to Specimen 2 (see Fig. 5.29b), $\theta_{c,twist}$ does not exceed 0.25% rad even at a lateral drift demand of 10% rad. The insignificant column twist demands are attributable to two reasons. The first relates to the high torsional stiffness of the employed column cross section. The second one is indicative of the well-balanced inelastic deformations between the steel beams and the panel zone, which agrees with previous test findings on beam-to-column subassemblies (Chi and Uang 2002; Engelhardt et al. 2000; Lee et al. 2005a; Ricles et al. 2004b). This aspect becomes important when deep columns (i.e., depths larger than 400 mm) are employed in the seismic design of steel MRFs. Elkady and Lignos (2018a) reported twist angles for 600 mm deep columns on the order of 3% rad at a lateral drift demand of 4% rad. These members are prone to coupled instabilities and their overall stability may be compromised once local buckling forms within the anticipated beam plastic hinge. The column out-of-plane deformations at the column mid-height location did not exceed 1 mm and 2 mm for Specimens 1 and 2, respectively. This confirms that the lateral support system design requirements of AISC (2016a; b) were effective in both tests.

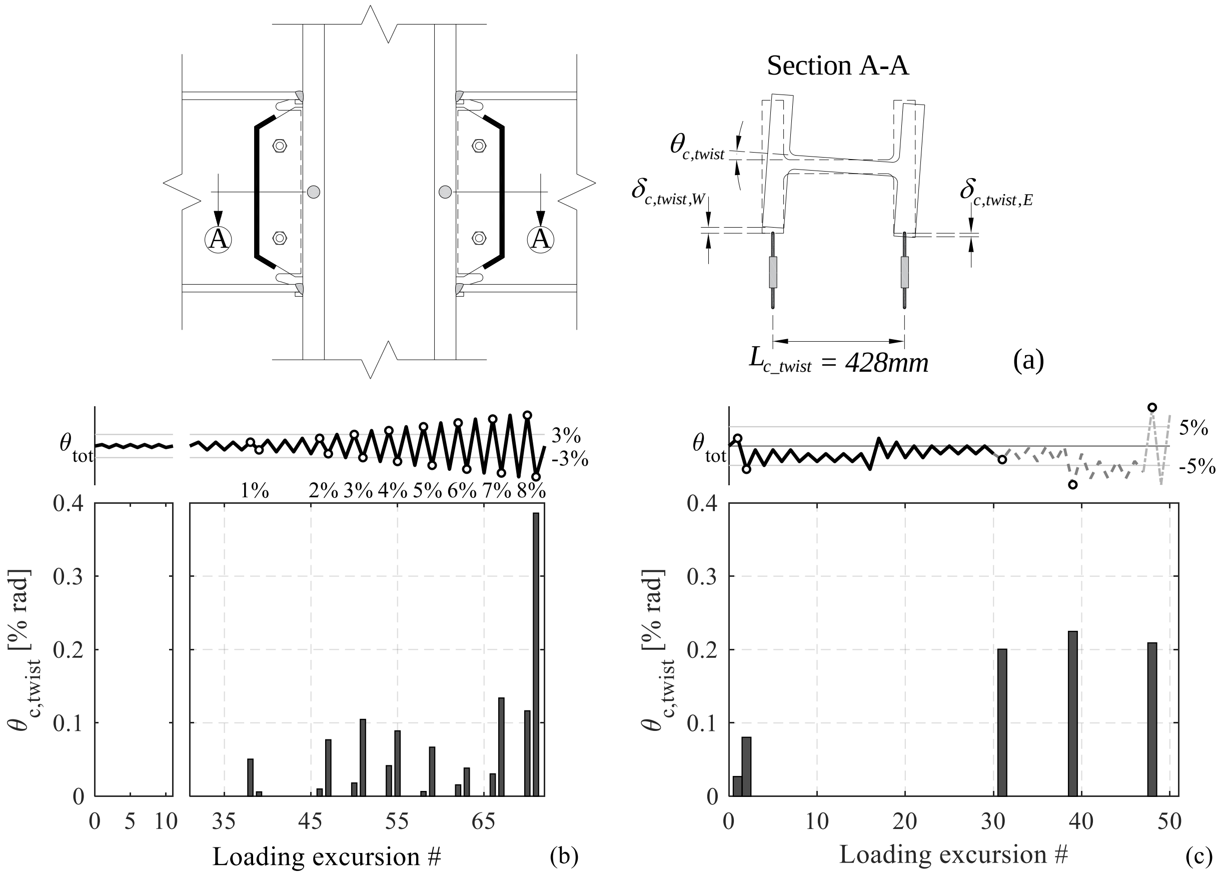

Figure 5.29 Column twist demands at characteristic lateral loading excursions: (a) schematic illustration of column twist angle; (b) Specimen 1; and (c) Specimen 2.

5.4.2.4 Column flange local deformations

Figure 5.30a depicts the column flange local deformations in the beam flange-to-column face locations. According to the AISC 360-16 provisions, the use of continuity plates is not imperative for the selected connection geometry. From the same figure, the cantilever-like deformation mode caused column flange localized yielding, which initiated near the column web at the panel zone kinking locations (see Fig. 5.31). El-Tawil (2000) found that similar deformations may increase the fracture potential of a beam-to-column connection.

To quantify the column flange local deformations, the horizontal pair LVDTs that were placed at each kinking location (see Fig. 5.10d) are utilized. The column flange tangential rotation at the flange extremity, $\theta_{cf,local}$, is then calculated (see Fig. 5.30a). Moreover, the displacement at the panel zone kinking locations, $\delta_{cf,local}$ (see Fig. 5.30a), is deduced from $\theta_{cf,local}$, by conservatively assuming that the column flange cantilever is under uniform load. However, this is not the case considering that the flange near the k-area of the cross section has a higher rigidity than at the tip of the column flange(s).

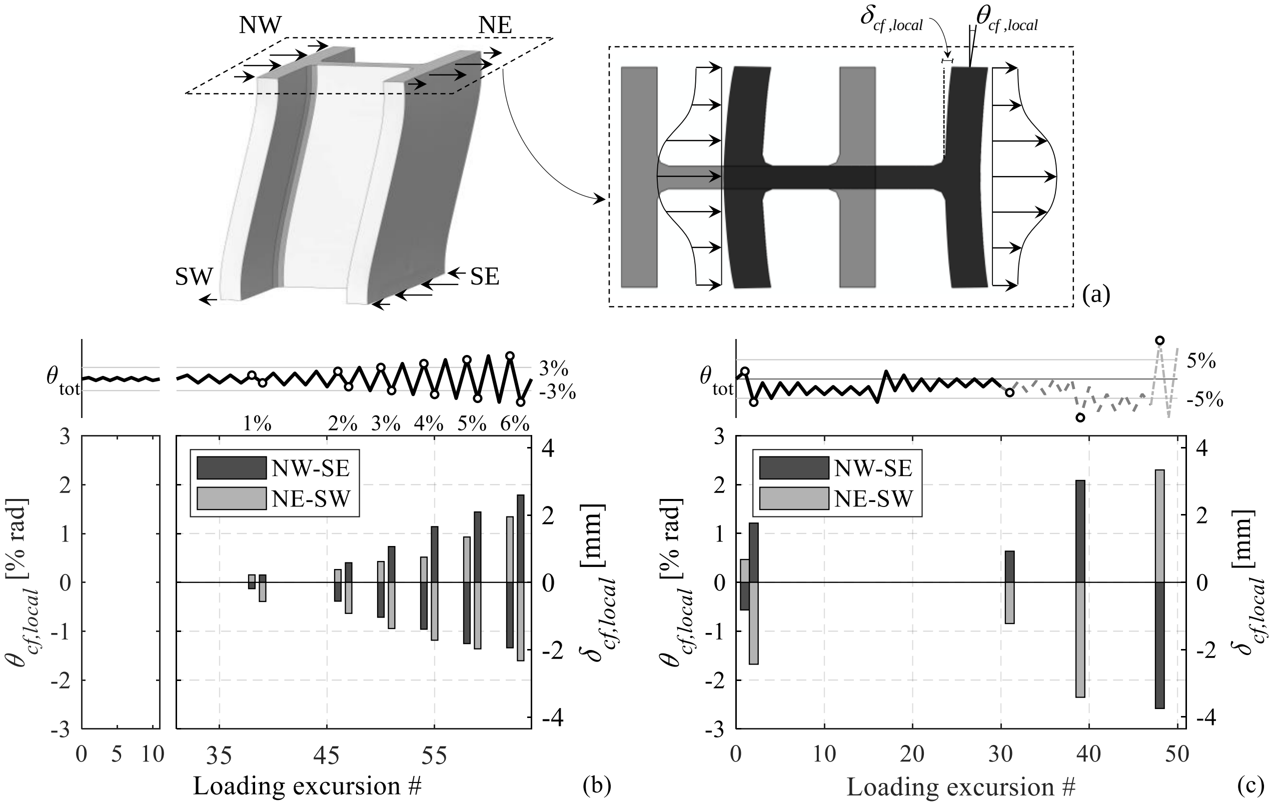

Figure 5.30 Column flange local deformations at characteristic lateral loading excursions: (a) schematic illustration of beam flange local deformations; (b) Specimen 1; and (c) Specimen 2.

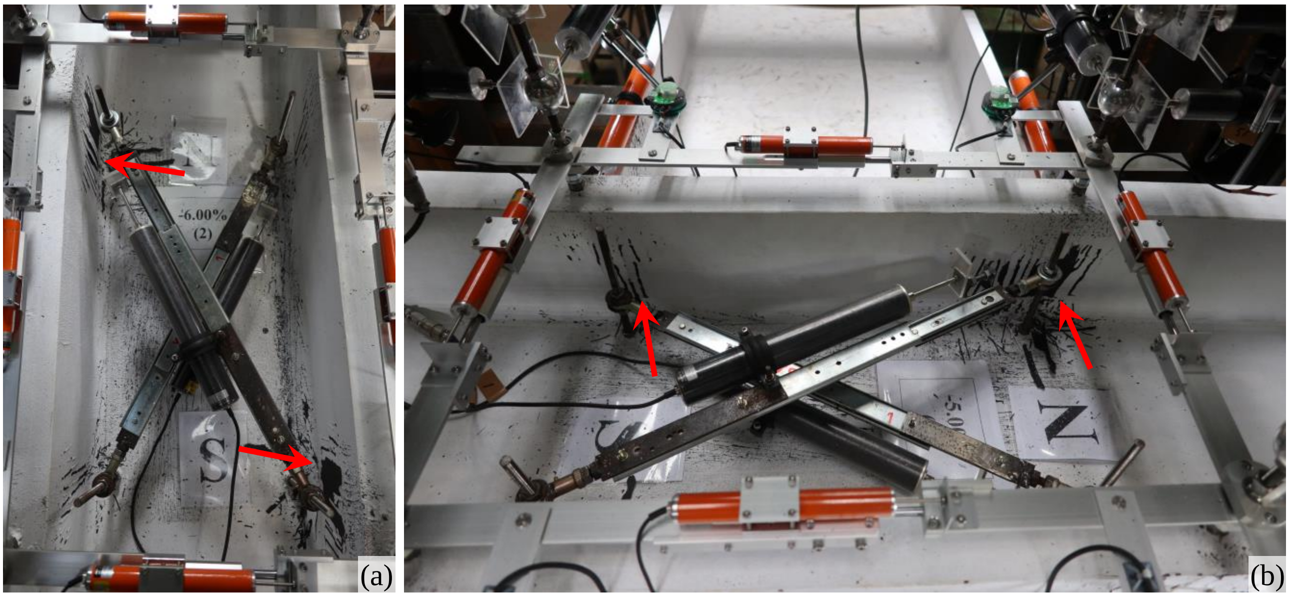

Figure 5.31 Yield pattern at the panel zone kinking locations due to column flange local deformations at characteristic lateral drift demands of Specimen 2.

Figures 5.30b-c depict the computed $\theta_{cf,local}$ and $\delta_{cf,local}$ at characteristic loading excursions for Specimens 1 and 2, respectively. Due to symmetry, the north-west and south-east panel zone kinking locations provided nearly identical results. Similar findings hold true for the north-east (NE) and south-west (SW) locations. Therefore, the peak values of these pairs are shown herein (i.e., NW-SE and NE-SW, accordingly). The average of the top and bottom test specimen side (see Fig. 5.10d) rotations is considered in the computations, while the column twist rotation component is subtracted from the computations. Positive values of $\theta_{cf,local}$ and $\delta_{cf,local}$ correspond to column flanges being “pulled” by the adjacent beams (i.e., NE-SW in Fig. 5.30a).

Referring to Fig. 5.30, the column flange local deformations are fairly consistent at both NW-SE and NE-SW locations, while their amplitude is, qualitatively, proportional to the imposed lateral drift demands. At 2% rad and 4% rad lateral drift demands, $\theta_{cf,local}$ equals nearly 0.5% rad and 1.0% rad, accordingly for both test specimens. As for Specimen 2 (see Fig. 5.30c), $\theta_{cf,local}$ reaches nearly 2.5% rad at 10% rad lateral drift demand. At this drift level, $\delta_{cf,local}$ equals 3 mm. The results confirm that the relatively minor column flange local deformations are attributable to the thick column flanges (i.e., $t_{cf} = 70$ mm) of the employed column cross section; hence the AISC 360-16 requirements for continuity plates are deemed to be satisfactory.

5.4.2.5 Strain demands at critical locations

Figure 5.32 illustrates the true stress and true strain demands at the panel zone bottom kinking location. The engineering strains are first extracted from the nine strain gauges positioned at this location for both test specimens. The true strain histories extracted from Specimen 1 and Specimen 2 at the east side mid-flange strain gauges are applied in cyclic coupons to extract the true stresses, as depicted in Figs. 5.32a-b (denoted as “Test”). In the same figures we have superimposed the simulated response with the Hartloper et al. (2021) constitutive material law at the same locations based on the calibrated material parameters of Table 5.3. The agreement between the measured and simulated quantities is noteworthy. Therefore, the same constitutive model may be used to predict the corresponding stress demands at selected locations for a given uniaxial strain history.

Based on the above methodology, the true stress-strain histories of the column 50 mm below the panel zone are shown in Figs. 5.32c-f for both test specimens. The yield stress and strains are superimposed with dashed lines for reference. Referring to Specimen 1 (see Figs. 5.32c-d), the results of the last cycle of the 1-6% rad amplitudes are highlighted for the last positive and the last negative loading excursions, with the emphasis being on the last, negative, excursion. At a lateral drift demand of 3% rad, localized yielding in the column at the kinking locations initiated. At a lateral drift demand of 6% rad, the longitudinal strain demands reached 1.2%, while the stresses capped at nearly 440 MPa. Referring to Specimen 2 (see Figs. 5.32e-f), the strain demands confirm that yielding at the panel zone kinking locations initiated after 2% rad. At a lateral drift demand of 6% rad, the strain demands reached 1%, while the stresses reached 360 MPa. Moreover, at the end of the test values of 2% and 470 MPa, respectively, are reported.

The experimental results confirm that the panel zone kinking effect causes some localized yielding near the panel zone edges, which initiates at a lateral drift demand of about 3% rad. However, this effect does not compromise the column stability or the overall stability of the welded connections.

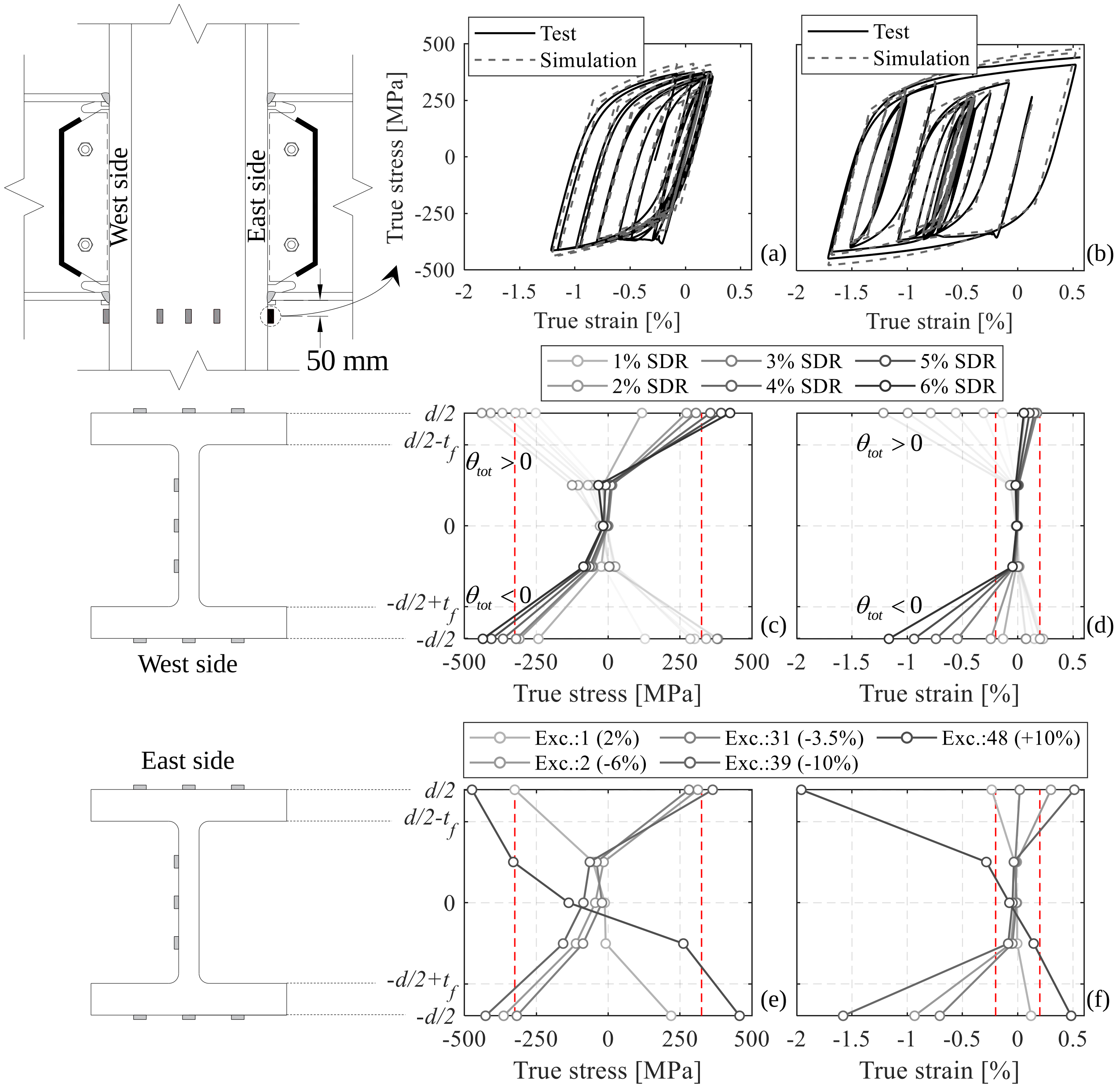

Figure 5.32 Stress and strain demands 50 mm away from the bottom panel zone kinking location for Specimens 1 and 2.

5.4.3 Effect of loading history and implications on structural collapse and predictive modeling

Prior work (FEMA 2009b; Krawinkler 1996, 2009; Lignos et al. 2011) has stressed the influence of loading history on the evaluation of seismic demand and capacities of structural components. The same issue has also been stressed regarding the future development of acceptance criteria for collapse prevention (Maison and Speicher 2016; Suzuki and Lignos 2020, 2021). While the AISC symmetric cyclic loading protocol is generally conservative for structural component qualification at lateral drift demands higher than 2% rad (Krawinkler 2009), the experimental results suggest that the welded connections tested herein satisfy the prequalification requirements established by AISC 360-16. In fact, Figs. 5.14a and 5.26a-b demonstrate that the connection exhibits a stable hysteretic response up until a lateral drift demand of about 8% rad. While local buckling did occur in the steel beams at lateral drift demands of 6% rad, it was fairly mild and did not result in softening (i.e., negative stiffness) for both test specimens.

It is generally known that the seismic performance of steel MRFs during low-probability of occurrence earthquakes tends to become asymmetric due to ratcheting prior to structural collapse (Ibarra and Krawinkler 2005; Lignos et al. 2011). Within such a context, cyclic deterioration in flexural strength, attributable to nonlinear geometric instabilities and P-Δ effects dominate the dynamic behavior of a steel MRF near collapse (Zareian et al. 2009). In formal collapse risk assessment methodologies [e.g., FEMA (2009b)] as well as system level simulation studies, it has been shown that a steel MRF's dynamic stability is governed by global P-Δ effects at lateral drift demands of 5% rad and above. The experimental findings (see Figs. 5.14b and 5.26c-d) suggest that even in cases where seismic demands become asymmetric due to ratcheting of a steel MRF prior to sidesway collapse, the response of the welded connection exhibits a stable and non-degrading hysteretic behavior even at a lateral drift demand of 10% rad.

Ibarra and Krawinkler (2005) pointed out the role of strength and post-peak strength deterioration (i.e., softening) on the earthquake-induced collapse risk of MRFs. In that respect, the testing program demonstrates that the welded connections remain stable throughout the employed loading histories. Therefore, unlike steel MRFs with elastic panel zone designs, the global collapse of steel MRFs featuring welded connections with highly dissipative panel zones is mostly controlled by the destabilizing effects of the gravity load and not by component deterioration. In that respect, Fig. 5.27 implies that simple bilinear models may suffice for simulating the steel beam behavior even at large lateral drift demands associated with collapse; hence, modeling uncertainties in component modeling at large deformations, where the validity of available deterioration models [e.g., Ibarra et al. (2005)] may be questionable (Krawinkler and Deierlein 2013), are eliminated. This issue is further elaborated in the subsequent section.

5.5 Predictive models and implications on collapse safety

In this section, the deduced experimental results are compared with continuum finite element (CFE) predictions. Implications on the seismic design of steel MRFs are also discussed. The CFE modeling assumptions presented in Chapters 2 and 3 are employed into the CFE models of Specimens 1 and 2. The global response comparisons are shown in Figs. 5.33a and 5.33c, while the panel zone response comparisons in Figs. 5.33b and 5.33d. The comparisons suggest a nearly identical match both at the global as well as the local response parameters. The CFE simulation results demonstrate the benefit of utilizing an instability-free beam-to-column connection design with regards to the modeling accuracy. In such case, the connection response is insensitive to initial beam imperfections due to hot rolling and/or fabrication.

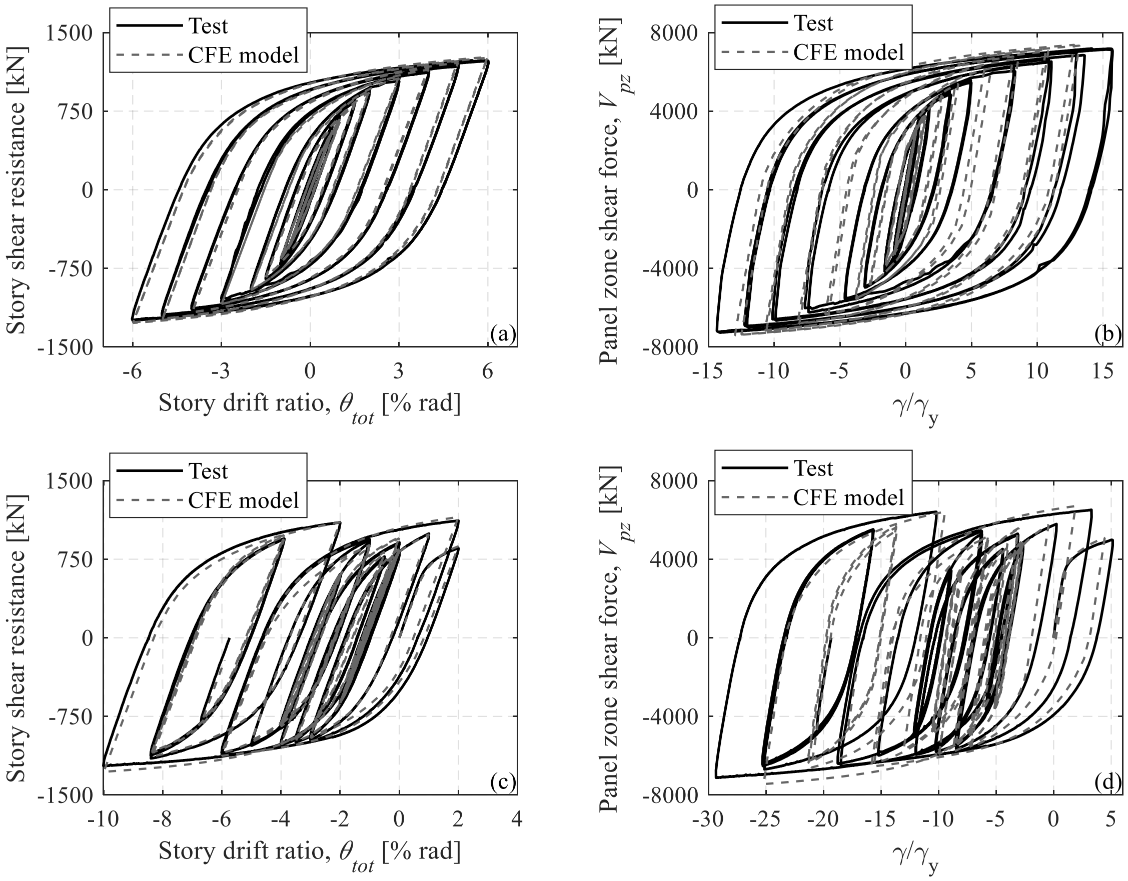

Figure 5.33 Comparisons of simulated versus experimental results: (a) global response of Specimen 1; (b) panel zone response of Specimen 1; (c) global response of Specimen 2; and (d) panel zone response of Specimen 2.

Conversely, beam-to-column connections with elastic panel zone designs may experience nonlinear geometric instabilities in the dissipative zone of a beam at modest lateral drift demands, depending on its cross-sectional local slenderness ratios. Figure 5.34 shows indicative comparisons between the welded connections with highly dissipative panel zone test results (i.e., $\gamma_d = 15\gamma_y$) and their counterparts with elastic panel zone designs (i.e., $\gamma_d = \gamma_y$). The imposed loading protocols of Specimens 1 and 2 are used (see Figs. 5.34a-b and 5.34c-d, respectively). Referring to Fig. 5.34a, the beam-to-column connection with highly dissipative panel zone design is instability-free, whereas the elastic panel zone design triggers beam local buckling at lateral drift demands of 3-4% rad. This is attributable to the minimal participation of the panel zone to the story drift ratio (see Fig. 5.34b). On the other hand, the issue of repairability of structural components in the aftermath of earthquakes may be challenging depending on the extent of local buckling within a dissipative zone of steel MRF beams. Another important issue is the collapse safety of a steel MRF in a regular mainshock/aftershock sequence depending on the extent of inelastic local buckling within its steel beams.

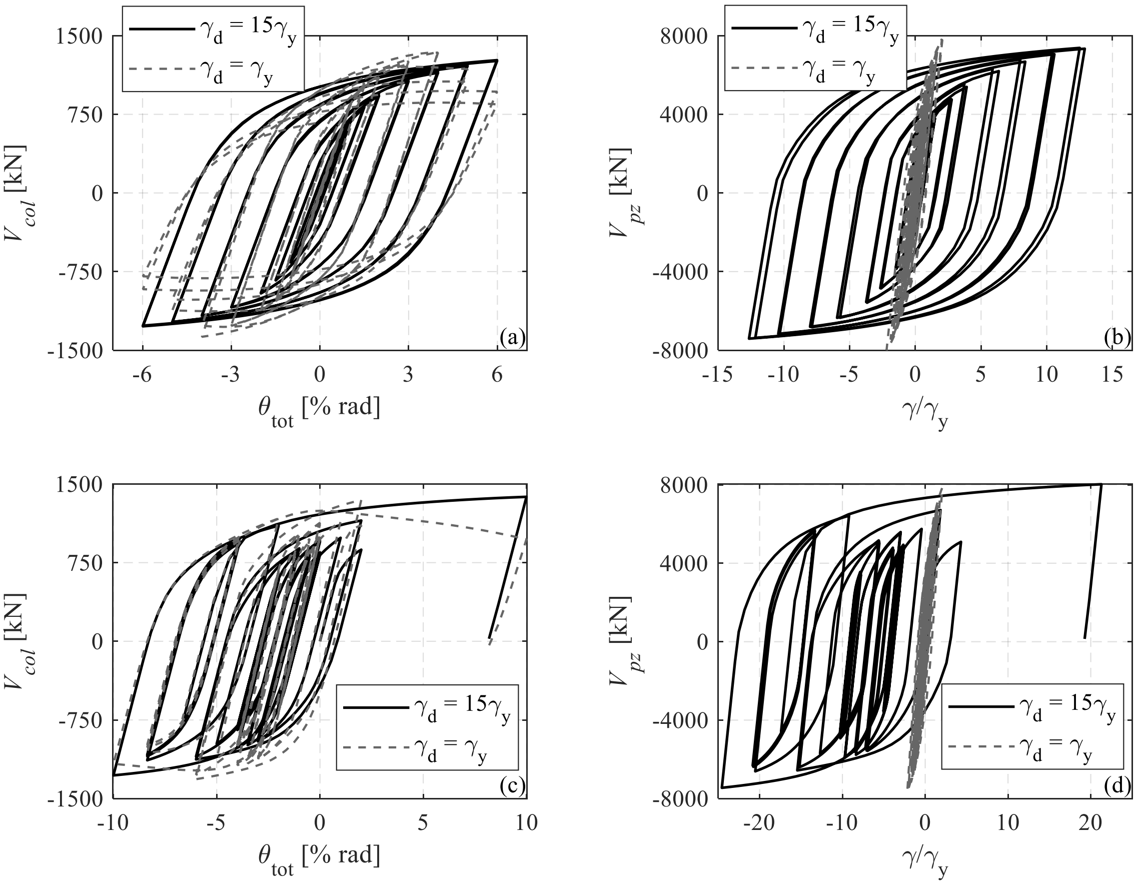

Figure 5.34 Response comparisons of welded connections with elastic and highly dissipative panel zones: (a) global response of Specimen 1 protocol; (b) panel zone response of Specimen 1 protocol; (c) global response of Specimen 2 protocol; and (d) panel zone response of Specimen 2 protocol.

5.6 Limitations of the present study

In the experimental program of the present study, the beam composite action effect on the beam-to-column connection performance was not considered. The composite action would increase the strain demands on the bottom beam flange, thereby increasing the fracture potential at the beam flange-to-column face welded connection (Hajjar et al. 1998; Kim and Lee 2017; Leon et al. 1998). To achieve the designed panel zone and beam deformation balancing, the panel zone demand shall be calculated based on the maximum probable moment of the composite beam. In this case, the panel zone and beam deformation objectives would be met.

In the present study, all welds were performed based on the gas metal arc welding (GMAW) process. This welding process, that is similar in nature with gas-shielded flux-cored arc welding (FCAW-G), is sensitive to the wind speed under which the welds are performed. Under windy conditions, porosity in the welded joint may occur. Therefore, such welding processes are more typical for shop welds, since they are prohibited for wind speeds above 5km/h (AWS 2016). A more typical welding process for field welds is self-shielded flux-cored arc welding (FCAW-S), which is found to provide decreased arc action compared to the FCAW-G.

The investigation of the beam-to-column connection performance with beveled backing bars under such welding processes should be examined in future studies.

Referring to the utilized weld electrode, the present study utilized an electrode with diameter of 1.2 mm, regardless of the weld detail and weld pass. Even though this weld electrode diameter lies in the upper bound of available electrode diameters, the relatively tight welded joint between the beveled backing bars and the column face intersection was filled with the molten metal without any trace of discontinuity. Therefore, the proposed backing bar detail is insensitive to the electrode diameter to be utilized.

Another issue to be stressed is the existent challenge tracing discontinuities through ultrasonic testing in welded joints with backing bars in presence, especially in the beam web centerline location (FEMA 2000a; Paret 2000b). Inspection of potential discontinuities in beam flange-to-column face joints with backing bars in presence, may be more uncertain compared to joints without backing bars. However, the finite element study of Chapter 4 showed that uncertainty in potential weld root discontinuities would not compromise the connection performance in this case.

Finally, in the present study, the geometric tolerances in beam and column alignment, beam flange groove angles, and backing bar geometry, were respected. In reality, the backing bar groove angle may not coincide precisely with the groove angle of the beam flange. This issue should be considered in future work.

5.7 Summary and conclusions

In this chapter, the cyclic performance of a welded connection with highly dissipative panel zones and simplified weld details was investigated through two full-scale cyclic experiments. The novel aspects of the explored welded connection were: (a) a beveled backing bar configuration that was intentionally kept in place after the completion of the top and bottom beam flange-to-column face complete joint penetration (CJP) welds, (b) the exploitation of the stable hysteretic response of panel zones in an effort to delay the onset of nonlinear geometric instabilities in the connection till a lateral drift demand of at least 5% rad, and (c) the utilization of a column steel material with minimum toughness requirements in the through-thickness direction so as to prevent divot fracture in the column flange. Two nominally identical welded connections were tested. The first one was subjected to a reversed cyclic symmetric loading protocol (AISC 2016a). The second experiment was conducted with a near-fault loading protocol (Krawinkler et al. 2000), which was followed by a collapse-consistent protocol (Suzuki and Lignos 2020) to benchmark the seismic performance of the welded connection at incipient collapse. The main findings are summarized as follows:

- At seismic demands representative of a design-basis earthquake event (i.e., lateral drift demands of 2% rad), the welded connections experienced shear yielding in the panel zone and flexural yielding in the beams. No visual signs of structural damage were observed in the beam-to-column connections in this case. The panel zone shear distortions reached $4\gamma_y$ at 2% rad, as intended.

- At lateral drift demands representative of a maximum-considered earthquake event (i.e., 3-4% rad), the panel zone shear distortions remained below $10\gamma_y$. Panel zone kinking led to mild localized yielding in the column flanges near the panel zone corners. Moreover, the welded connections did not exhibit strength and stiffness degradation. The test results confirmed that the prequalification requirements of AISC (2016a) were satisfied. From a repairability standpoint, no visual structural damage was observed in the welded connection at the same drift amplitude, regardless of the employed loading protocol.
- Local buckling in the steel beams became visible after 6% rad under a symmetric cyclic loading protocol. At the same lateral drift amplitude, the panel zones reached their targeted inelastic shear distortions (i.e., $15\gamma_y$). The onset of local buckling in the steel beams did not cause in-cycle strength/stiffness deterioration in the connection. Local buckling in the steel beams was further delayed in the case of non-symmetric lateral loading history. Despite the severity of the symmetric cyclic loading history, at a lateral drift ratio of 6% rad, no cracks were observed in the welded connections.
- The experimental results suggest that the ultimate failure modes were fairly consistent in both test specimens, regardless of the employed loading protocol. At 7-10% rad lateral drift demands, ductile cracks initiated due to ultra-low cycle fatigue at two primary locations: (a) at the column face, near the beam flange CJP weld root, and (b) at the shear tab end at the weld fusion. The first crack mostly controlled the cyclic behavior of the connections. These were able to withstand nearly 30% of the total energy dissipated from the point where crack initiation occurred up until 50% loss of the load-carrying capacity of the connection, which occurred at lateral drift demands higher than 9% rad.
- The beveled backing bars did not exhibit any visible sign of structural damage, even at lateral drift demands exceeding 9% rad. This is attributable to the optimal bevel angle design that minimized the fracture potential near the backing bar notches. Another reason is that the notch tip was kept away from the beam flanges. The experimental results highlighted that fillet-weld reinforcement between the backing bars and the column and beam flanges are not effective in the examined cases.
- For the panel zone demand-to-resistance design ratio, $R_{n,pl}/R_u = 0.8$, the panel zone and the beams participated nearly equally to the energy dissipation of the welded connections throughout the imposed lateral load history. The experimental program demonstrated that, at a lateral drift amplitude of 10% rad, the welded connection can sustain panel zone shear distortions of nearly $30\gamma_y$.
- The experimental results revealed that the delay of local buckling in the beam(s) in combination with the stocky cross section of the column, led to minimal column twist demands. The measured out-of-plane deformations at the panel zone location did not exceed 2mm at lateral drift demands of 10% rad. Therefore, the lateral bracing design requirements of AISC (2016a; b) are deemed to be satisfactory.
- The experiments suggest that the absence of the continuity plates did not lead to accountable column flange local deformations due to the concentrated beam flange load. It was demonstrated that the column cross section with 70 mm flange thickness did not allow for column flange relative deformations higher than 2-4 mm at 10% rad lateral drift demands.

- Comparisons of the test results with simulations from continuum finite element (CFE) models showed a remarkable agreement up until the point of crack initiation. The delay of the onset of local buckling in the steel beams due to panel zone shear yielding minimizes the influence of modeling uncertainties regarding the proper tuning of local instability modes for triggering local buckling. While the capabilities of the predictive CFE model may still be impaired by the steel material uncertainty, this can be easily incorporated in simulation studies to benchmark the system seismic behavior of steel MRFs with highly dissipative panel zones.

Chapter 6 Seismic demands of steel moment resisting frames with inelastic beam-to-column web panel zones

Bibliographic details

This chapter presents the pre-print (accepted) version of the article with the following full bibliographic details:

Skiadopoulos, A., and Lignos, D. G. (2022). “Seismic demands of steel moment resisting frames with inelastic beam-to-column web panel zones (accepted).” *Earthquake Engineering & Structural Dynamics*, Wiley.

DOI: https://doi.org/10.1002/eqe.3629

Author’s contribution

Concerning the material presented in this chapter, Andronikos Skiadopoulos developed the proposed panel zone modeling approaches, designed the archetype steel buildings, carried out the nonlinear system level simulations, analyzed the results, conducted the seismic risk assessment of the steel moment resisting frames, created the figures, wrote the manuscript draft and revised the manuscript. The co-author contributed in developing the methodology presented in this chapter, supervising the work conducted by Andronikos Skiadopoulos, funding acquisition, and reviewing and editing the original and final manuscript drafts.

6.1 Introduction

In capacity-designed steel moment resisting frames (MRFs), the inelastic deformations in the beam-to-column web panel zones are usually limited (AISC 2016b; CEN 2005). Instead, dissipative zones are situated near the beam ends and at the base of first story columns. While steel beams usually comprise seismically compact but slender cross sections near the current seismic compactness limits, local buckling is likely to occur even at modest lateral drift demands. Prior studies have shown that nonlinear geometric instabilities, such as local buckling, compromise a member's flexural resistance and subsequently increase the collapse risk of steel MRFs during seismic events with a relatively low probability of occurrence (Elkady and Lignos 2014; Ibarra et al. 2005). Although the annualized collapse risk of modern steel MRF buildings (Elkady and Lignos 2015) is within established limits of modern seismic standards (ASCE 2017), structural repairs may be deemed necessary depending on the extent of local buckling within a steel MRF's dissipative zone. A potential way to limit structural damage near the beam ends is to allow for some participation of the beam-to-column web panel zone joints in the inelastic response of the respective beam-to-column connections. However, following the 1994 Northridge and 1995 Kobe earthquakes, it was found that steel MRF connections that featured inadequate base and weld material toughness requirements had a high fracture potential when their panel zones exhibited inelastic shear distortions higher than $4\gamma_y$ (FEMA 1997, 2000a) (where γ_y is the panel zone shear distortion at yield).

Recent test findings (Engelhardt et al. 2000; Lee et al. 2002; Rahiminia and Namba 2013; Ricles et al. 2000, 2004b; Shin and Engelhardt 2013a) suggest that pre-qualified welded unreinforced flange-welded web (WUF-W) connections with highly inelastic panel zones (i.e., shear distortions up to $25\gamma_y$) are not susceptible to fractures at the beam flange-to-column flange region even at lateral drift demands of 4% rads. This is attributed to today's improvements in weld specifications and fabrication practices (AISC 2016c; AWS 2010, 2016; Ricles et al. 2000). Noteworthy stating that for beam-to-column connections in multi-bay and space steel MRFs that feature beams with depths up to 500mm, the fracture potential is usually less than that in connections with deeper beams (Chi et al. 1997; El-Tawil et al. 1999; Ricles et al. 2000).

Figure 6.1 shows the hysteretic response of pre-qualified WUF-W connections from recent experiments (Shin and Engelhardt 2013a) with limited ($2\gamma_y$) and high ($12\gamma_y$) inelastic panel zone shear distortion designs, γ_d. While both subassemblies featured the same cross sections, the fabrication cost in the second one was reduced because of the absence of doubler plates. Moreover, fabrication problems associated with welding near the k-area of steel columns are not a concern in this case. From the same figure, when inelastic deformations concentrate in the steel beams (see Fig. 6.1a), cyclic deterioration in flexural strength is evident at lateral drift demands of 3% rads. Conversely, WUF-W connections that exhibit inelastic deformations in their panel zones (see Fig. 6.1b) do not exhibit local instabilities prior to 5% story drift ratio (SDR). Prior work (Elkady and Lignos 2014; Gupta and Krawinkler 2000b; NIST 2010) has shown that at these lateral deformation demands, the global stability of steel MRFs is controlled by P-Delta effects. Another aspect to be considered is that panel zone yielding within fully restrained beam-to-column connections relaxes the column twist demands due to the beam instability in its dissipative zone. This may be a concerning issue in designs that feature wide flange steel columns with deep cross sections (i.e., $d_b > 500$mm) (Ricles et al. 2004a).

A handful of studies highlighted that inelastic panel zones increase the lateral drift demands in steel MRFs by up to 30% and decrease their base shear capacity by 30% (Krawinkler and Mohasseb 1987; Liew and Chen 1995; Schneider and Amidi 1998). Conversely, research (Biddah and Heidebrecht 1998; Challa and Hall 1994) suggests that steel MRFs that exhibit some inelastic behavior in their panel zone joints enjoy a higher seismic collapse capacity than their elastic panel zone counterparts. Moreover, beam local buckling is delayed (Castro et al. 2008). However, the above studies utilized simplified modeling approaches and disregarded the likelihood of fracture within the beam-to-column connection attributable to panel zone kinking. Other studies investigated the influence of connection fractures on the seismic response of steel MRFs with pre-Northridge beam-to-column connections (Foutch and Yun 2002; Luco and Cornell 2000; Song and Ellingwood 1999a; b). However, these studies did not consider explicitly the effects of the panel zone inelastic deformation on the seismic response of the analyzed steel MRFs. To the best of our knowledge, there has not been a comprehensive study to benchmark the seismic demands of steel MRFs with inelastic panel zones from the onset of damage to structural collapse On the other hand, there is a perception (Castro et al. 2005; Tsai and Popov 1990) that steel MRFs exhibiting inelastic deformations in their panel zones are susceptible to collapse.

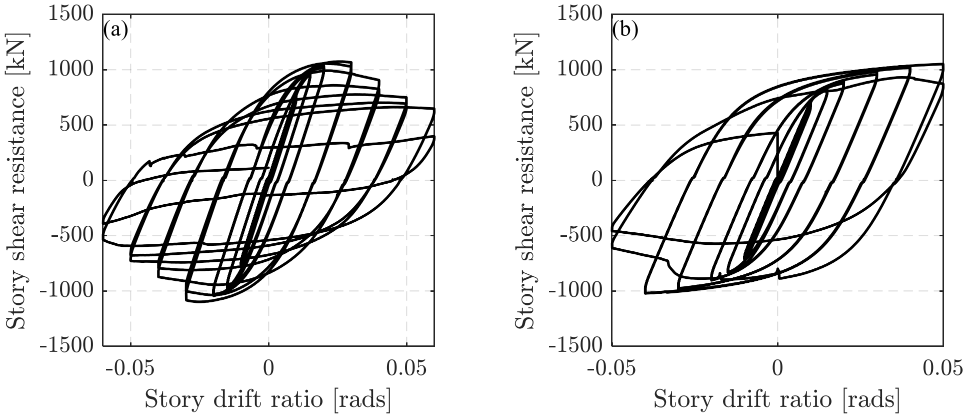

Figure 6.1 Hysteretic response of subassemblies with variable panel zone inelastic shear distortions: (a) $\gamma_d = 2\gamma_y$; and (b) $\gamma_d = 12\gamma_y$ [data from Shin and Engelhardt (2013a)].

This chapter proposes a new panel zone modeling approach that can be incorporated into system-level simulations without compromising important features of the panel zone and overall beam-to-column connection response. The seismic demands of archetype steel buildings with MRFs are then quantified by means of nonlinear static and dynamic analyses procedures. Several design parameters are interrogated, including the steel

MRFs' number of stories and bays as well as the 'allowable' level of panel zone inelastic distortions. The collapse risk of the examined steel MRFs is quantified in the context of performance-based earthquake engineering. Hazard curves for global as well as local engineering demand parameters (EDPs) are developed to examine the influence of inelastic panel zone distortions on the seismic stability of steel MRFs at seismic intensities of interest to the engineering profession.

6.2 Proposed modeling approach for beam-to-column connections with inelastic panel zones

6.2.1 Behavioral insights

Seminal studies (Krawinkler 1978) at the University of California at Berkeley in the 1970s demonstrated that beam-to-column web panel zone joints experience shear yielding, which is a stable damage mechanism, under cyclic loading. Referring to Fig. 6.1a, the kinematics of the panel zone joint essentially imply that the top and bottom edges of the panel zone remain plain under lateral loading, whereas the column web and flanges exhibit shear and flexural modes of deformation, respectively, depending on the panel zone geometry. Moreover, the evolution of shear yielding, the cyclic hardening, and the axial-to-shear load interaction are important considerations in the overall hysteretic behavior of panel zones. Two modeling approaches are proposed in the subsequent sections to preserve some of the above characteristics within a frame analysis nonlinear finite element program. Both approaches are made publicly available (https://github.com/RESSLab-Team).

6.2.2 Shell element modeling approach

Figure 6.1b depicts schematically the proposed modeling approach for a typical panel zone geometry that is comprised of a steel beam and column with depths d_b and d_c, respectively. Plane stress conditions are assumed for the column web and flanges. These are modeled with shell elements with a thickness equal to the column web, t_{cw}, and the column flange width, b_{cf}, respectively. A high fidelity four-node shell element is first developed and implemented in the Open System for Earthquake Engineering Simulation (OpenSees) (McKenna 1997) platform for this purpose. The developed element (so-called *FourNodeQuad2D3DOF*), which is suitable for two dimensional (2D) nonlinear analyses, considers both the translational and rotational degrees-of-freedom (DOFs). The proposed element employs a combined isotropic and kinematic hardening constitutive law within the framework of J2 plasticity (Hartloper et al. 2021). In order to satisfy the panel zone kinematics, rigid links are employed between the column top and bottom nodes and the panel zone top and bottom edge nodes, respectively (see Fig. 6.1b). These links constrain the translational and the rotational DOFs for this purpose. The proposed modeling approach captures the panel zone bending and shear deformation modes. This is achieved by connecting the beam ends with a pin directly to the column's rigid link corner nodes, without imposing any constraints to the shell element nodes of the panel zone. The beam moment is transferred as a force couple, V_{pz}, through beam rigid links as shown in Fig. 6.1b. The translational and rotational DOFs are constrained for the rigid links between the beam end nodes and the bottom panel zone corners. Between the top panel zone corners and the beam end nodes, the translational DOF in the y direction is released so as the axial force passes through the panel zone shell elements. Therefore, the axial-to-shear load interaction in the panel zone is explicitly considered.

The proposed modeling approach is facilitated through an automatic mesh generator. This considers the input panel zone geometry and the desired elements per web and flange thickness. Based on a sensitivity analysis that was conducted as part of the present chapter, it was found that one element per flange thickness and eight elements per web thickness provide superior results.

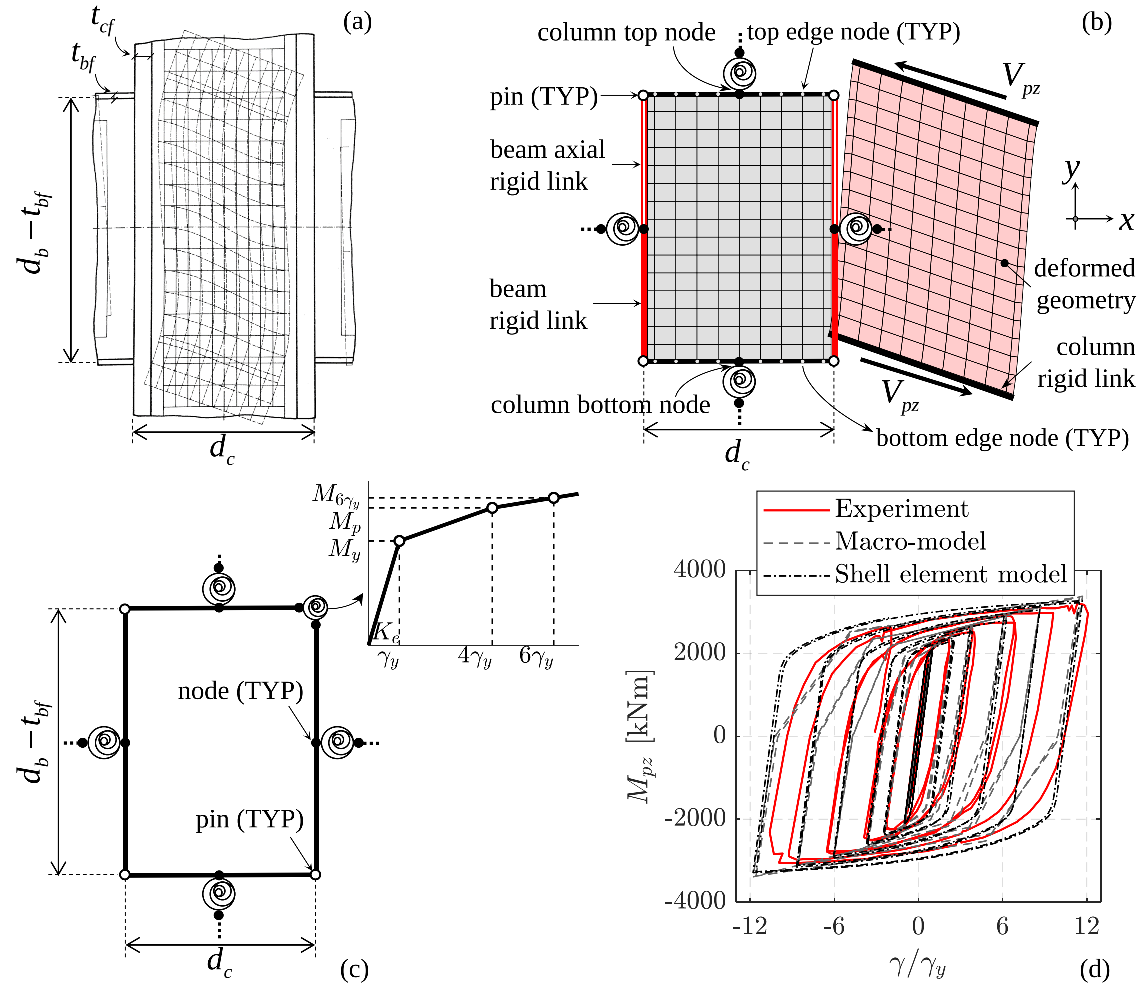
t_{cf}
t_{bf}
(a)
$d_b - t_{bf}$
d_c
column top node
top edge node (TYP)
(b)
V_{pz}
pin (TYP)
beam axial rigid link
y
x
deformed geometry
beam rigid link
column rigid link
column bottom node
V_{pz}
bottom edge node (TYP)
$d_b - t_{bf}$
d_c
$M_{6\gamma_y}$
M_p
M_y
K_e
γ_y
$4\gamma_y$
$6\gamma_y$
node (TYP)
pin (TYP)
$d_b - t_{bf}$
d_c
(c)
Experiment
Macro-model
Shell element model
4000
2000
0
-2000
-4000
M_{pz} [kNm]
-12
-6
0
6
12
γ/γ_y
(d)

Figure 6.2 Schematic representation of panel zone modeling approaches: (a) kinematics of the panel zone joint [image adopted from Krawinkler (1978)]; (b) shell element model; (c) macro-model; and (d) modeling approach validation.

6.2.3 Macro-model approach

In this case, the proposed modeling approach is motivated by the parallelogram model, which was originally proposed by Gupta and Krawinkler (1999). This model is illustrated in Fig. 6.1c. The proposed modeling approach retains simplicity and computational efficiency within a frame analysis nonlinear finite element program. Rigid links are assumed for the panel zone edges and pinned connections at three of the panel zone corners. The hysteretic behavior of the panel zone is preserved in a rotational spring, which is located at one of the panel zone corners as shown in Fig. 6.1c. This spring is assigned a trilinear panel zone moment, M_{pz}, versus panel zone shear distortion, γ, relationship. While the parallelogram model does not account explicitly for the bending deformation mode of a panel zone, this is implicitly considered based on the recently proposed model by Skiadopoulos et al. (2021). In particular, the panel zone elastic stiffness, K_e, is computed based on Eqs. (6.1)-(6.3):

$$K_e = \frac{M_{pz}}{\gamma} = \frac{K_S \cdot K_b}{K_s + K_b} \tag{6.1}$$

$$K_s = \frac{A_v \cdot G}{d_b - t_{bf}} = \frac{t_{pz} \cdot \left(d_c - t_{cf}\right) \cdot G}{d_b - t_{bf}} \tag{6.2}$$

$$K_b = \frac{12 \cdot E \cdot I_c}{d_b - t_{bf}} \tag{6.3}$$

where K_s and K_b are the elastic stiffnesses corresponding to the shear and bending mode of deformation of the panel zone, respectively; A_v is the panel zone shear area; G is the shear modulus of the steel material; t_{pz} is the panel zone thickness, including the column web and doubler plate(s) thicknesses, if any; d_c is the depth of the column cross section; t_{cf} is the thickness of the column flange; E is the Young's modulus of the steel material; I_c is the second moment of area of the column cross section (including the doubler plate thickness, if any) with respect to the strong axis of the column's cross section.

Referring to Fig. 6.1c, the moment resistance of the panel zone is defined at γ_y, $4\gamma_y$ and $6\gamma_y$, according to Eq. (6.4) (Skiadopoulos et al. 2021):

$$M_{pz} = \frac{f_y}{\sqrt{3}} \cdot \left[a_{w,eff} \cdot \left(d_c - t_{cf}\right) \cdot t_{cw} + a_{f,eff} \cdot \left(b_{cf} - t_{cw}\right) \cdot 2t_{cf}\right] \cdot \left(d_b - t_{bf}\right) \tag{6.4}$$

where f_y is the steel material yield stress; $a_{w,eff}$ and $a_{f,eff}$ are shear stress coefficients for the web and the flanges, respectively, that depend on the level of inelastic shear distortion within the panel zone. These coefficients can be estimated according to Skiadopoulos et al. (2021). This model depicts well the contribution of the column flanges to the overall shear resistance of the panel zone, especially in designs that feature stocky column cross sections. It should be noted that, unlike the first approach, the macro-model discussed herein does not capture the cyclic hardening and shear-to-axial load interaction within the panel zone.

6.2.4 Validation and comparison with system level behavior

Figure 6.1d shows indicative comparisons between the simulated and measured panel zone moment versus shear distortion relationships from prior experimental work (Ricles et al. 2004b). The panel zone shear distortion reached up to $12\gamma_y$ in this case. The proposed shell element model provides a remarkable accuracy in predicting the panel zone behavior, including the onset of shear yielding and the cyclic hardening. The simulated response based on the macro-model is a modest representation of the experimental data. Same observations hold true for validations with a rich set of collected experimental data (Skiadopoulos and Lignos 2021), which are not shown herein due to brevity.

To quantify the impact of the different panel zone modeling approaches on the structural response of steel MRF buildings, a four-story, three-bay steel MRF is analyzed with both modeling approaches. The evaluation was conducted with nonlinear response history analysis based on the set of 44 far-field ground motions from FEMA P695 (NIST 2010). The plan view and the modeling assumptions of prior studies (Elkady and Lignos 2014, 2015; NIST 2010) are employed for WUF-W connections. In this case, $\gamma_d = 10\gamma_y$ is considered. Figure 6.3 depicts the median values of the peak SDR and of the peak normalized panel zone distortions, γ/γ_y along the steel MRF height. The 16th and 84th percentiles are also superimposed in the same graph. Both panel zone modeling approaches lead to nearly identical distributions for the above mentioned EDPs of interest. Similar observations hold true for the beam and column responses, the absolute floor accelerations and the residual SDR distributions along the steel MRF height. Therefore, to expedite the nonlinear analyses, which are discussed in the subsequent sections, the macro-model approach is adopted.

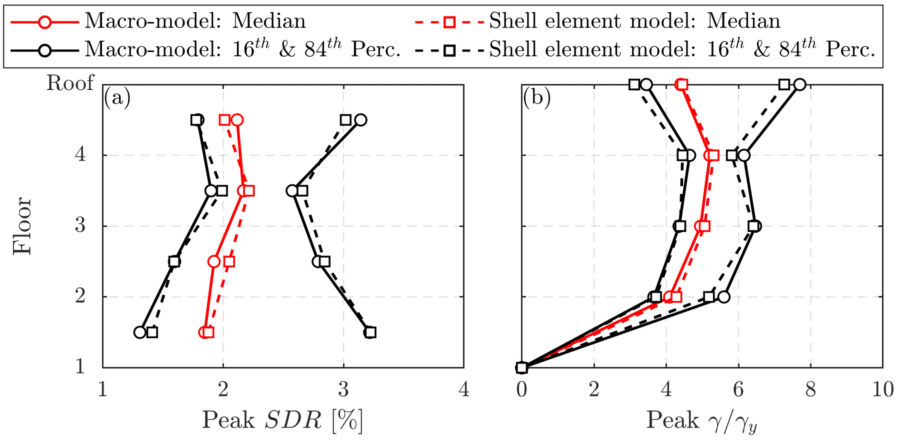

Figure 6.3 Panel zone shell element model versus macro-model for the DBE-scaled FEMA P695 far-field ground motion set: (a) peak story drift ratio distributions; and (b) peak γ/γ_y distributions.

6.2.5 Modeling of beam flange fracture

In this section, a methodology is formulated to consider the fracture potential in WUF-W beam-to-column connections with highly inelastic panel zone joints. The model updating technique of OpenSees (McKenna 1997) is utilized for this purpose. Figure 6.4 shows a schematic illustration of the adopted workflow. In brief, at each analysis time step, k, the SDR_{ik}, at floor i and the normalized shear distortion, $\gamma_{ijk}/\gamma_{y,ij}$, for each panel zone ij are computed. For the given SDR_{ik} and $\gamma_{ijk}/\gamma_{y,ij}$, the probability of fracture P_{ijk} is computed for adjoining steel beams with their bottom flange in tension (denoted as Beam ij in Fig. 6.4). It is assumed that beam fracture is evident at this location, because the top flange is considered to be restrained by the concrete slab of the floor system. The computed P_{ijk} is based on bivariate log-normal distributions for WUF-W post-Northridge connections (Skiadopoulos and Lignos 2021) with input predictor variables the SDR_{ik} and $\gamma_{ijk}/\gamma_{y,ij}$ as shown in Fig. 6.4. To claim fracture in Beam ij at time k, the P_{ijk} should be greater or equal to a targeted threshold, P_{max}. In this case, model updating is applied at the rotational zero-length element that represents the response of the Beam ij end. The flexural resistance of the steel beam is set equal to zero at this step, k, as shown in Fig. 6.4. This is consistent with prior experimental work (Engelhardt et al. 2000; Ricles et al. 2000, 2004b; Shin and Engelhardt 2013a).

A sensitivity analysis was conducted to determine the influence of the assumed P_{max} value to the steel MRF's seismic response. Three threshold values were explored, for $P_{max} = [25, 50, 100]\%$. For all EDPs of interest, at DBE, the simulations confirmed that there were no connection fractures regardless of the P_{max} value. At MCE, only the $P_{max} = 25\%$ showed beam end fractures in the steel MRFs with highly inelastic panel zones (i.e., $\gamma_d = 15\gamma_y$). However, these fractures do not practically affect any of the local and global EDPs of interest. In the subsequent nonlinear building simulations, $P_{max} = 50\%$ is conservatively assumed.

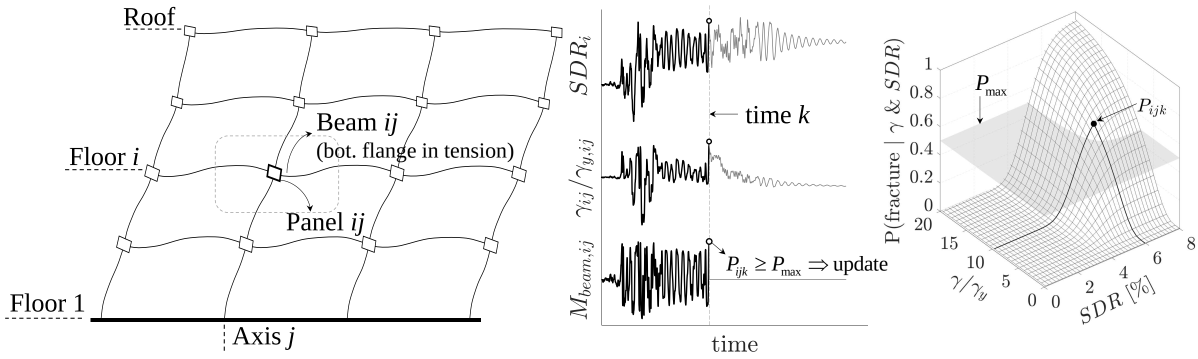

Figure 6.4 Schematic illustration of workflow for modeling of beam flange fracture during nonlinear response history analysis.

6.3 Archetype steel buildings

Thirty-two archetype steel office buildings are designed according to AISC (2016b; c; a); ASCE (2017). The design location is assumed to be in urban California (coordinates: 33.996°N, -118.162°W). A soil class D and risk category II are assumed as per ASCE/SEI 7-16 (ASCE 2017). The steel buildings consist of two perimeter steel MRFs, two orthogonal concentrically braced frames (CBFs), and a gravity frame system as shown in Fig. 6.5a. Four-, eight-, 12- and 20-story steel buildings are considered. The steel MRFs in the East-West loading direction have either three or five bays as shown in Fig. 6.5b and are designed as steel special moment frames. The typical story height is 4m in all examined cases. The first story height is 4.3m for the four-story steel MRF. The rest of the steel MRFs have a first story height of 4.2m. Beams and columns are made of A992, Gr. 50 (i.e., nominal yield stress, $f_y = 345MPa$) with a 100mm thick slab that rests on a 90mm thick steel deck. Pre-qualified WUF-W beam-to-column connections (AISC 2016c) are considered. Four steel MRF designs are conducted. The beam-to-column web panel zones are designed with the following targeted panel zone distortions, $\gamma_d = [1, 4, 10, 15]\gamma_y$. The first two values comply with AISC 360-16 (AISC 2016b), whereas the last two design variations do not. The panel zone shear resistance, R_n (AISC 2016b), over the panel zone shear demand, R_u (AISC 2016a), values are reported in Table 6.1 for all the designs. Column splices are positioned at the mid-height of every other story.

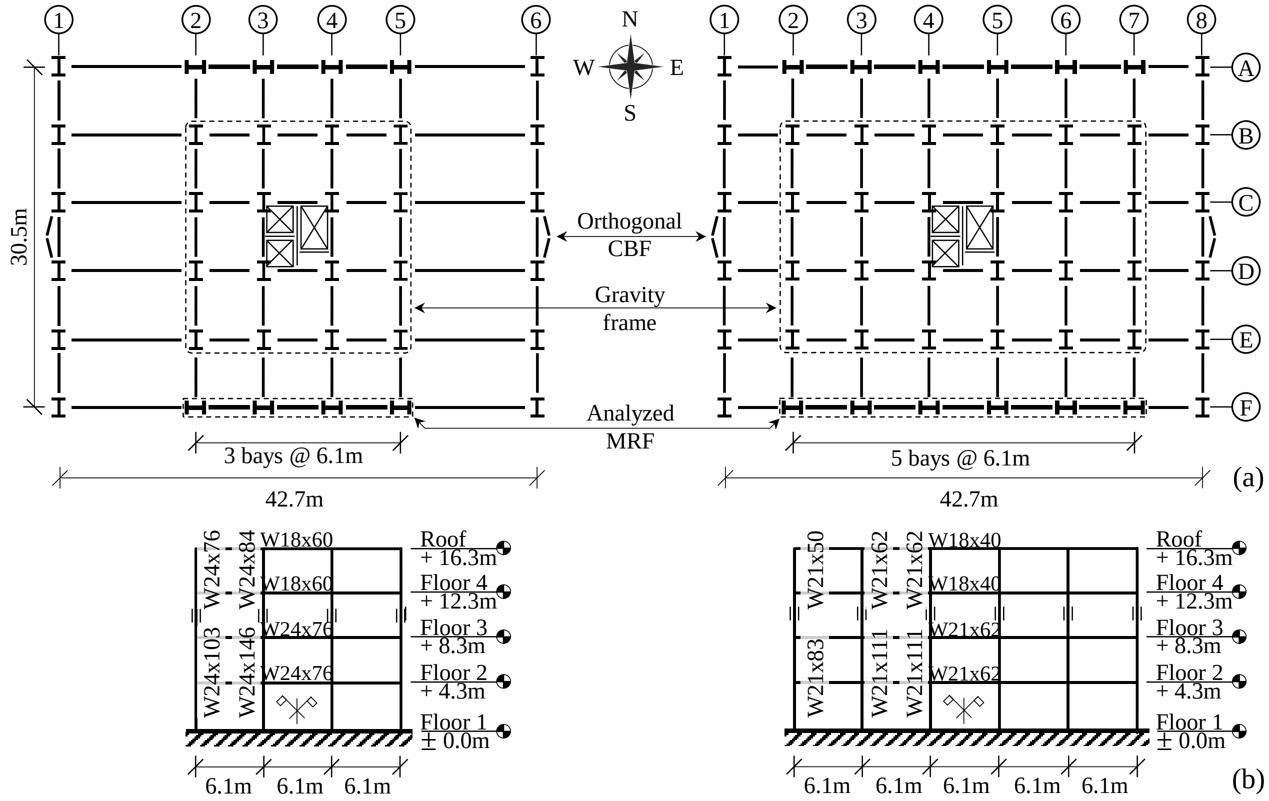
①
②
③
④
⑤
⑥
N
W
E
S
①
②
③
④
⑤
⑥
⑦
⑧
Ⓐ
Ⓑ
Ⓒ
Ⓓ
Ⓔ
Ⓕ
30.5m
Orthogonal CBF
Gravity frame
Analyzed MRF
3 bays @ 6.1m
5 bays @ 6.1m
42.7m
42.7m
(a)
W24x76
W24x84
W24x103
W24x146
W18x60
W18x60
W24x76
W24x76
Roof
+ 16.3m
Floor 4
+ 12.3m
Floor 3
+ 8.3m
Floor 2
+ 4.3m
Floor 1
± 0.0m
6.1m
6.1m
6.1m
W21x50
W21x62
W21x62
W21x83
W21x111
W21x111
W18x40
W18x40
W21x62
W21x62
Roof
+ 16.3m
Floor 4
+ 12.3m
Floor 3
+ 8.3m
Floor 2
+ 4.3m
Floor 1
± 0.0m
6.1m
6.1m
6.1m
6.1m
6.1m
(b)

Figure 6.5 Three- and five-bay, four-story steel buildings: (a) typical plan views; and (b) elevation views of the analyzed MRFs.

The archetype steel buildings are designed based on response spectrum analysis. The first mode periods, T_1, of the buildings in the East-West direction are also summarized in Table 6.1 for comparison purposes. For the same structural height, the first mode period is fairly similar between buildings regardless of the targeted panel zone strength and the number of bays. This is attributed to the fact that the steel MRFs are drift-controlled. Referring to the same table, the range of the strong-column/weak-beam (SCWB) ratios is fairly similar between designs. The panel zone contribution to the MRF lateral deformations is considered as part of the design process. In steel MRF designs where panel zones were designed to attain 10 or $15\gamma_y$, doubler plates were either not deemed to be necessary or they featured thicknesses up to 13mm. The above reduce the anticipated fabrication costs due to weld savings. A summary of the complete designs of the 32 MRFs presented herein are made publicly available from https://www.doi.org/10.5281/zenodo.5962407.

Table 6.1 Archetype steel MRF first mode periods and global performance factors.

		γ_d	R_n/R_u	T_1 (s)	SCWB ratio	Ω	μ_T	μ_{Sa_C}	$\sigma_{\ln Sa_C}$
4-story	3-bay	γ_y	1.25	1.28	1.4-2.2	2.30	3.98	1.65	0.42
		$4\gamma_y$	1.03	1.29		2.28	4.21	1.70	0.42
		$10\gamma_y$	0.82	1.31		2.21	4.85	1.67	0.39
		$15\gamma_y$	0.79	1.32		2.17	5.23	1.78	0.37
	5-bay	γ_y	1.26	1.28	1.4-2.0	2.60	3.70	1.55	0.37
		$4\gamma_y$	1.04	1.29		2.58	3.89	1.64	0.41
		$10\gamma_y$	0.85	1.31		2.52	4.34	1.74	0.36
		$15\gamma_y$	0.75	1.32		2.45	4.86	1.89	0.35
8-story	3-bay	γ_y	1.22	2.04	1.2-2.3	2.56	3.35	0.96	0.36
		$4\gamma_y$	1.00	2.08		2.52	3.57	0.99	0.35
		$10\gamma_y$	0.85	2.11		2.45	4.08	1.04	0.34
		$15\gamma_y$	0.77	2.13		2.39	4.50	1.09	0.33
	5-bay	γ_y	1.23	2.06	1.1-2.2	2.77	3.03	0.96	0.36
		$4\gamma_y$	0.98	2.09		2.73	3.18	0.99	0.35
		$10\gamma_y$	0.84	2.12		2.65	3.53	1.04	0.34
		$15\gamma_y$	0.74	2.14		2.59	3.83	1.09	0.33
12-story	3-bay	γ_y	1.23	2.41	1.1-2.1	3.46	2.92	0.93	0.36
		$4\gamma_y$	0.97	2.45		3.41	3.06	0.91	0.35
		$10\gamma_y$	0.81	2.49		3.34	3.35	1.00	0.35
		$15\gamma_y$	0.75	2.50		3.27	3.64	1.04	0.34
	5-bay	γ_y	1.21	2.47	1.1-2.7	3.68	2.69	0.92	0.37
		$4\gamma_y$	0.99	2.51		3.61	2.90	0.91	0.35
		$10\gamma_y$	0.84	2.55		3.48	3.45	0.99	0.35
		$15\gamma_y$	0.76	2.57		3.37	3.87	1.03	0.34
20-story	3-bay	γ_y	1.24	3.91	1.1-2.1	2.98	1.57	0.50	0.32
		$4\gamma_y$	0.99	3.95		2.94	1.63	0.52	0.32
		$10\gamma_y$	0.83	3.98		2.89	1.73	0.52	0.31
		$15\gamma_y$	0.74	4.00		2.81	1.91	0.51	0.31
	5-bay	γ_y	1.23	3.86	1.1-2.2	3.16	1.65	0.50	0.32
		$4\gamma_y$	0.97	3.91		3.09	1.75	0.52	0.32
		$10\gamma_y$	0.85	3.94		3.01	1.91	0.52	0.31
		$15\gamma_y$	0.75	3.97		2.92	2.14	0.51	0.31

6.4 Nonlinear building models

Two-dimensional models of the steel buildings are developed in OpenSees (McKenna 1997). The steel members of the perimeter steel MRFs shown in Fig. 6.5b are idealized with elastic beam-column elements and concentrated plasticity elements at their ends. The modified Ibarra-Medina-Krawinkler deterioration model (Ibarra et al. 2005) is considered to model cyclic deterioration in flexural strength and stiffness of the respective steel beams and columns. For this purpose, the modeling recommendations by Lignos and Krawinkler (2011) and Lignos et al. (2019) are employed, respectively. The panel zones are modeled as explained in Chapter 6.2 based on the macro-model approach.

The nonlinear geometric effects are explicitly considered during the nonlinear analyses of the considered models with the P-Delta geometric transformation. The destabilizing effects of the gravity load are considered through a leaning column, which is connected to the steel MRF through axially rigid links. The axial load assigned to the leaning column equals half the gravity load, excluding that assigned directly to the steel MRF columns based on their tributary area. Two percent damping ratio is assigned at the first and third modes of the steel MRFs. Viscous damping is considered with the Rayleigh model based on the procedures discussed in Zareian and Medina (2010). While prior studies (Elkady and Lignos 2015; Flores et al. 2014; Gupta and Krawinkler 1999) have emphasized on the beneficial effects of the gravity framing system on the seismic stability of steel frame buildings, herein, the lateral stiffness and strength of the gravity framing system is, conservatively, neglected. While the prototype frames in this study are designed by disregarding the composition action, this may be considered according to prior related studies (El Jisr et al. 2022; Elkady and Lignos 2014).

6.5 Nonlinear static analysis

Nonlinear static analysis (referred to as *pushover* analysis hereinafter) based on a first mode lateral load pattern of each steel MRF is conducted to quantify the effect of the targeted panel zone distortions, γ_d, on the static overstrength factor, Ω, and the period-based ductility factor, μ_T. These parameters, which are shown in Fig. 6.6a for the four-story, three-bay steel MRFs, are defined according to FEMA P-695 (NIST 2010). In this figure, the base shear, V, is normalized with respect to the seismic weight, W; the roof drift ratio, δ_r/H, is computed based on the roof displacement, δ_r, over the total height, H, of the steel building. Superimposed in the same figure is the normalized design base shear, V_d/W, which is identical in all design cases shown in the figure. The results suggest that the elastic stiffness and the base shear capacity (noted as V_{max} in Fig. 6.6a) are nearly the same in all cases.

Referring to Fig. 6.6a, the static overstrength, Ω, and the period-based ductility, μ_T, are summarized in Table 6.1 for all the examined MRFs. The variation of both parameters between the three- and the five-bay MRFs is insignificant. Except for a few MRF designs, Ω appears to be lower than the minimum overstrength factor for special moment frames, i.e., $\Omega_d = 3$, as specified in ASCE/SEI 7-16 (ASCE 2017). However, this is because the stabilizing effects of the gravity framing system have been neglected (Elkady and Lignos 2015). Interestingly, Table 6.1 suggests that Ω is practically not influenced by the targeted panel zone shear distortion designs. The μ_T generally decreases while the structural height increases. In taller MRFs, their primary collapse mechanism involves lesser stories due to the shear mode of deformation. Moreover, the μ_T of steel MRFs increases by 20 to 30% when their panel zone design intentionally exceeds the current seismic design requirements (i.e., $\gamma_d \leq 4\gamma_y$) due to the delay of the onset of local buckling in beam ends.

Figure 6.6b shows the normalized floor displacements along the building heights for the 4-story steel MRF designs. The floor displacements, δ_i, are normalized with respect to the building heights, H. The results suggest that the collapse mechanisms of the employed designs are not sensitive to the targeted panel zone shear distortions even at roof drift ratios of 6% rads. Figure 6.6c depicts the maximum (among all bays) plastic rotations, $\theta_{pl.}$, of the first story columns at the base and at the floor beams along the building height at a roof drift ratio of 3% rads. In the same figure, we have superimposed the pre-capping plastic rotations, θ_p, of the same members according to Lignos et al. (2019); Lignos and Krawinkler (2011). These values indicate the onset of local buckling within the dissipative zone of the respective member(s). Interestingly, in steel MRF designs with $\gamma_d \geq 10\gamma_y$, although flexural yielding occurs in the steel beam ends, these do not experience local buckling. Conversely, designs with $\gamma_d \leq 4\gamma_y$ experience local buckling within the dissipative zones of steel beams, particularly in the first two stories of the steel MRF. This comparison demonstrates the value of balancing the panel zone strength with respect to that of the adjoining steel beam(s).

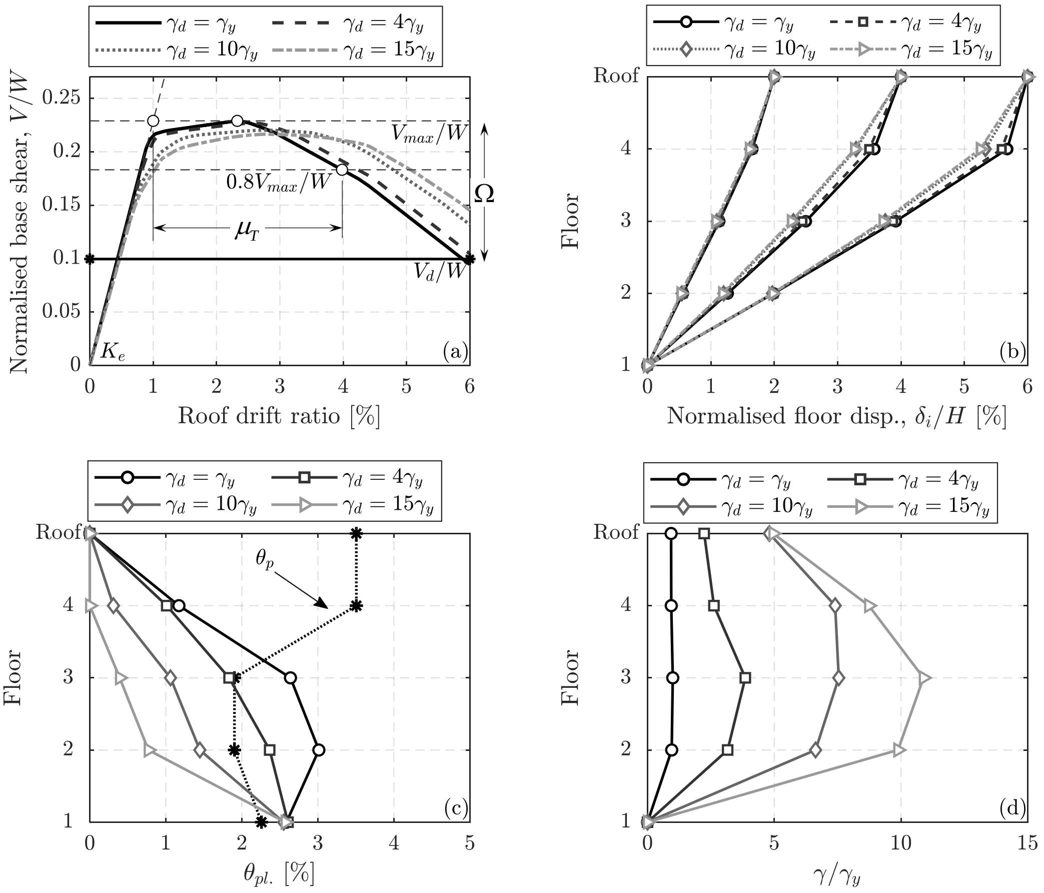

Figure 6.6 Pushover analysis results for the four-story, three-bay MRF: (a) normalized base shear versus roof drift ratio; (b) normalized floor displacement distributions; (c) plastic rotation distributions; and (d) γ/γ_y distributions.

Figure 6.6d depicts the normalized panel zone shear distortions, γ/γ_y, along the building height at a targeted roof drift ratio of 3% rads, i.e., characteristic of an MCE with a 2% probability of exceedance over a 50-year building life expectancy. It is observed that for the designs with $\gamma_d \leq 4\gamma_y$, the panel zones reach the targeted distortion, since beams reach their capping moment at the targeted roof drift ratio. Conversely, in designs where $\gamma_d \geq 10\gamma_y$, the targeted inelastic shear distortions are not attained. This explains the increased μ_T values in the latter case. Same findings hold true for the rest of the designs but the results are not shown herein due to brevity.

Observations from nonlinear static analyses suggest that when inelastic deformations are more balanced between the steel beams and the beam-to-column web panel zone, local buckling is not pronounced even at lateral drifts associated with an MCE, thereby minimizing the need for structural repairs in the aftermath of earthquakes. Due to well-known limitations of pushover analysis (Krawinkler and Seneviratna 1998), nonlinear response history analyses are carried out in the subsequent section for quantifying both local and global EDPs of interest for all the examined steel MRFs.

6.6 Nonlinear response history analysis

6.6.1 Collapse risk evaluation

This section summarizes the effect of the targeted panel zone inelastic shear distortions on the collapse risk of the examined steel MRFs. Incremental dynamic analysis (IDA) (Vamvatsikos and Cornell 2002) is conducted for the set of 44 far-field ground motions of FEMA-P695 (NIST 2010). For a given ground motion, its seismic intensity is scaled till a single story or a number of stories displaces laterally by more than 15% rads and the corresponding story shear resistance becomes zero. This definition of sidesway collapse is consistent with measurements from shake table collapse experiments on steel MRFs (Lignos et al. 2011). The adopted intensity measure (IM) for the ground motion scaling is the first mode, 5% damped spectral acceleration, $S_a(T_1, 5\%)$. Although more efficient and sufficient IMs exist (Eads et al. 2015), at this time, the lack of available seismic hazard curves as a function of these IMs hinders their adaptation in the present study. The seismic hazard curves of the 4-, 8-, 12-, and 20-story, three-bay steel MRFs at the design location are shown in Fig. 6.7. These are adopted from the United States Geological Survey (USGS) online tool (USGS 2014).

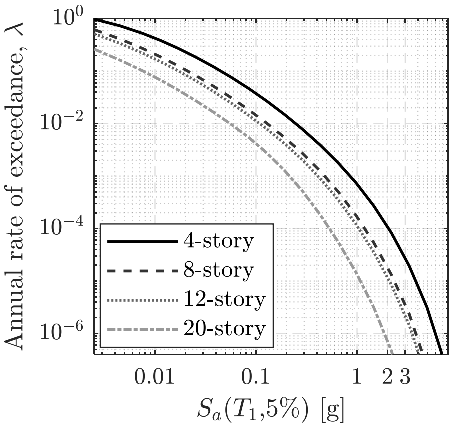

Figure 6.7 Seismic hazard curves for the three-bay moment resisting frames.

Figure 6.8a shows representative IDA curves for the three-bay, four-story steel MRF with $\gamma_d = 10\gamma_y$. The median, the 16th and 84th percentiles of the IDA curves are superimposed for reference based on counted statistics. The peak SDR at which structural collapse occurs ranges from 6 to 11% rads. Figure 6.8b shows the IDA curves with respect to the peak γ/γ_y along the height of the steel MRF. The results suggest that when $S_a(T_1, 5\%)$ is larger than 1.2g (i.e., at MCE), the peak panel zone inelastic shear distortions are capped at about $10\gamma_y$. This is because the adjacent steel beams attain their capping moment at the same lateral drift demands, as intended. From the same figure, the peak γ ranges between $8\gamma_y$ and $14\gamma_y$.

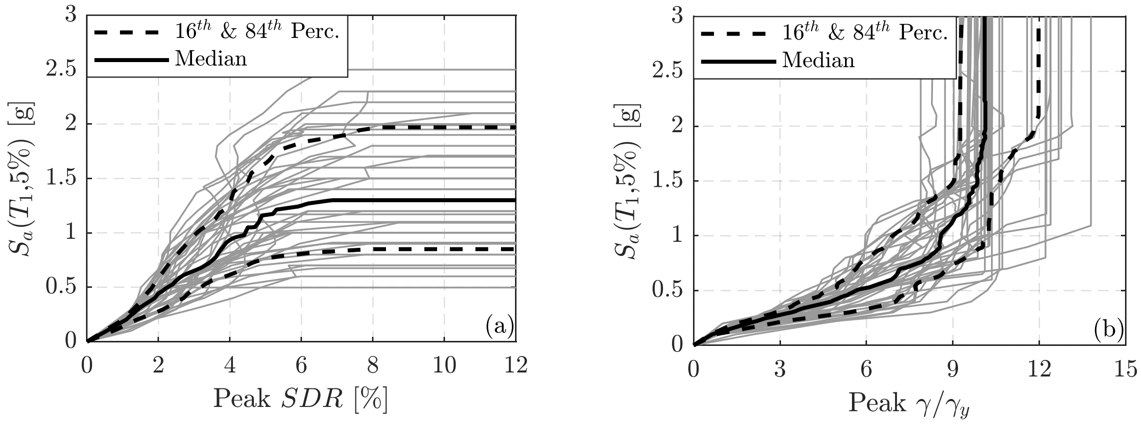

Figure 6.8 IDA curves for the three-bay, four-story steel MRF with $\gamma_d = 10\gamma_y$: (a) $S_a(T_1, 5\%)$ versus peak story drift ratio; and (b) $S_a(T_1, 5\%)$ versus peak γ/γ_y.

Figures 6.9a-b compare the fitted log-normal collapse fragility curves of the $\gamma_d = \gamma_y$ and $\gamma_d = 10\gamma_y$ design cases for the 4-story, three- and five-bay steel MRFs. In the collapse fragility computations, spectral shape effects that were disregarded from the ground motion selection are considered through an adjustment of epsilon as per Haselton et al. (2011). Noteworthy stating that the median collapse intensity of all steel MRFs with inelastic panel zone designs is almost 10-20% higher than that of their elastic panel zone design counterparts. Because all designs are drift-controlled, the collapse fragility curves are not practically affected by the number of the steel MRF bays. Similar trends hold true for the rest of the MRF designs. This can also be seen in Table 6.1 from the tabulated median, $\mu_{Sa,C}$ and the logarithmic standard deviation, $\sigma_{lnSa,C}$, of the collapse intensities of the respective steel MRFs. Interestingly, the $\sigma_{lnSa,C}$ values for the examined steel MRFs are not practically influenced by the extent of the panel zone inelastic shear distortion. The seismic collapse risk of the steel MRFs is evaluated by computing the mean annual frequency of collapse, λ_c. To compute λ_c, the collapse fragility curves of the steel MRFs are numerically integrated over the seismic hazard curve that corresponds to the design location (Zareian et al. 2009), as per Eq. (6.5). For a given intensity, im, the probability of collapse, $P(C|im)$, is computed based on the empirical cumulative probability distribution. The term $d\lambda(im)/d(im)$ is then computed from the slope of the hazard curve at the given im, while $d(im)$ is the increment over which the numerical integration is applied as per Eads et al. (2013). By assuming that earthquakes follow a Poisson distribution, the probability of collapse over 50 years, $P_c\ (50\ years)$ is then computed in Figs 6.9c-d for the three- and five-bay steel MRF, respectively.

$$\lambda_c = \int_0^\infty P(C|im)\cdot\left|\frac{d\lambda(im)}{d(im)}\right|\cdot d(im) \tag{6.5}$$

The results suggest that the earthquake-induced collapse risk is practically not influenced by the number of the steel MRF bays. This is attributed to the fact that the steel MRF designs are drift-controlled as discussed earlier; hence P-Delta effects dominate their seismic stability (Christoph et al. 2004; NIST 2010). The collapse risk tends to decrease while the number of stories increases because the seismic hazard is typically lower for long-period structures (see Fig. 6.7). The 1% limit of the probability of collapse over 50 years of ASCE/SEI 7-16 (ASCE 2017) is superimposed for reference in Figs. 6.9c-d. While steel MRFs with elastic panel zone designs do not respect the above limit, it should be stressed that the stabilizing effects of the gravity framing have been neglected in the collapse simulations (Elkady and Lignos 2015).

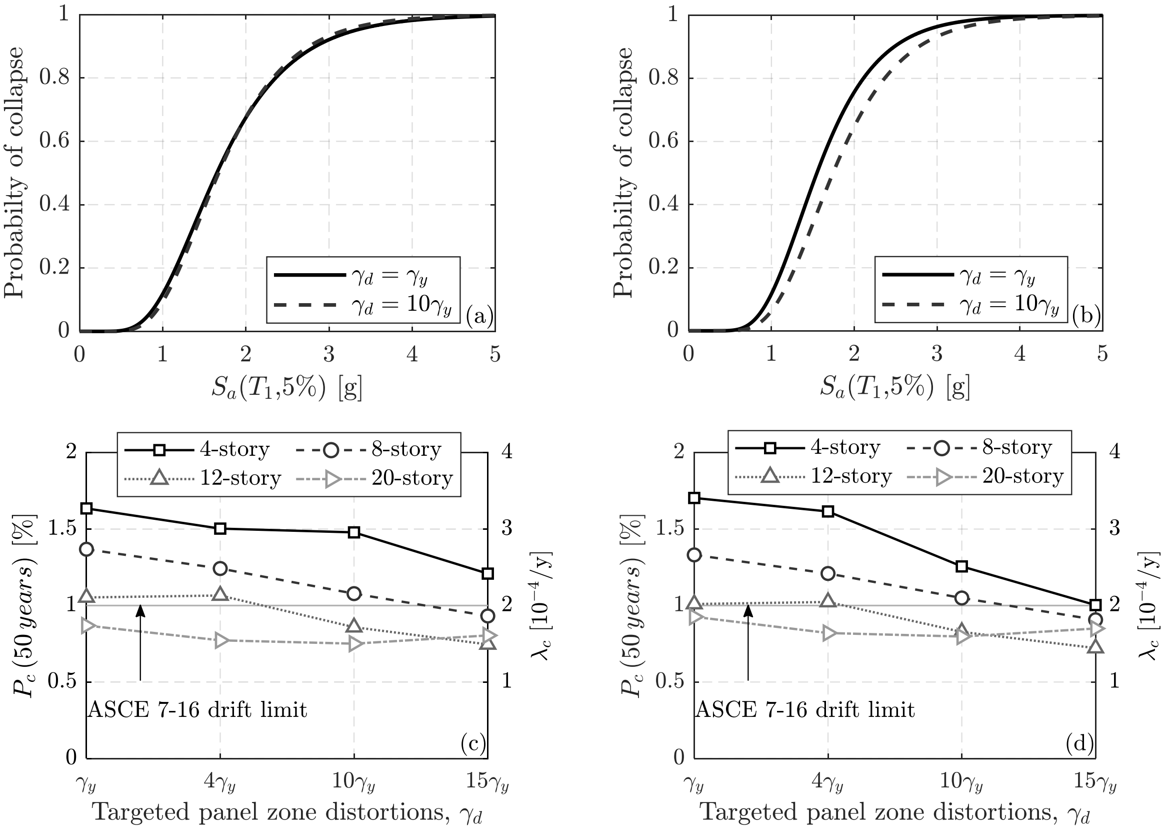

Figure 6.9 Collapse fragility curves for the four-story steel MRFs: (a) three-bay steel MRFs; and (b) five-bay steel MRFs. Probabilities of collapse in 50 years and mean annual frequency of collapse for the four-story steel MRFs: (c) three-bay steel MRFs; and (d) five-bay steel MRFs.

Interestingly, steel MRFs with panel zones attaining $10-15\gamma_y$ have smaller or equal collapse risk with code-compliant steel MRFs. For instance, for the four-story, three-bay steel MRF, the collapse risk decreases by more than 30% when panel zones are designed to attain $15\gamma_y$ contrary to the design with $\gamma_d = \gamma_y$. Moreover, the findings suggest that steel MRFs exhibiting inelastic panel zone deformations are not necessarily prone to soft story collapse mechanisms. This is further substantiated in Fig. 6.10 that shows the median peak SDRs along the steel MRF heights at the last stable point of each IDA curve for the three-bay steel MRFs. The peak SDR distributions along the building heights are nearly the same regardless of the targeted panel zone inelastic shear distortion.

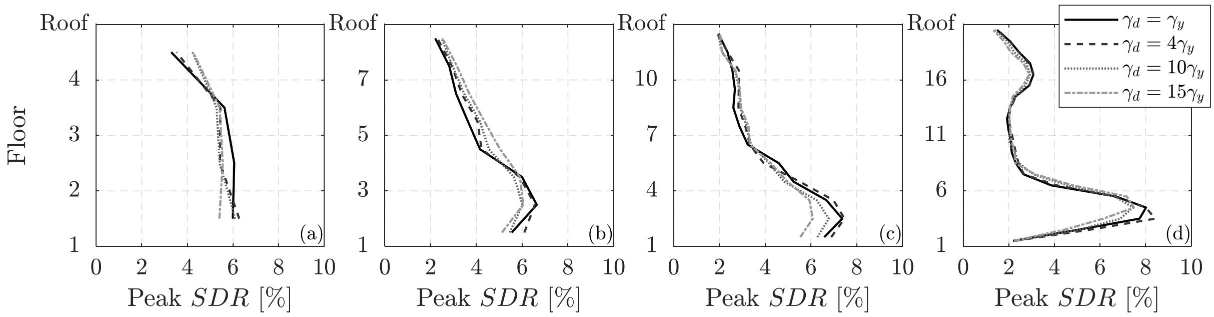

Figure 6.10 Peak story drift ratio distributions near collapse for the three-bay MRFs: (a) 4-story; (b) 8-story; (c) 12-story; and (d) 20-story.

6.6.2 Seismic demands at discrete seismic intensities of interest

This section quantifies the seismic demands of the examined steel MRFs at two seismic intensities of interest, namely DBE and MCE. The focus is on global EDPs, such as the peak $SDRs$ and the residual $SDRs$ along the steel MRF heights. Moreover, of interest are local EDPs, such as the peak panel zone inelastic shear distortions, the peak plastic rotations of the steel beams as well as the number of potential beam bottom flange fractures. Among other reasons, the above EDPs are strongly related to structural repairs in steel MRFs in the aftermath of earthquakes.

Figure 6.11 shows comparisons of the EDPs of interest between the $\gamma_d = \gamma_y$ and the $\gamma_d = 10\gamma_y$ cases. The median and the 84th percentiles of the four-story, three-bay MRFs are shown for reference. The peak SDR demands are somewhat reduced in cases where steel MRFs are designed with highly inelastic panel zones (i.e., $\gamma_d = 10\gamma_y$) relative to their elastic panel zone counterparts. These reductions are more pronounced at MCE (see Figs 6.11a and 6.11e).

Figures 6.11b and 6.11f suggest that the residual $SDRs$ are reduced by 50-100% in steel MRFs with inelastic panel zones compared to those in their elastic panel zone counterparts. Prior studies (Elkady et al. 2020; Hwang and Lignos 2017; Ramirez and Miranda 2012) have highlighted the impact of residual SDR on economic losses of MRF buildings due to demolition. Noteworthy stating that at DBE, steel MRF designs with $\gamma_d = 10\gamma_y$ do not exhibit residual SDR values of more than 0.4% rads, on average, contrary to 0.6% rads for the designs with $\gamma_d = \gamma_y$. At MCE, the same designs attain, on average, about 0.8% and 1.2% residual

$SDRs$, respectively. Interestingly, the 84th percentile of the analyzed cases at MCE suggests that the residual SDR is 2% or less along the steel MRF height when panel zones are designed to exhibit inelastic shear distortions of $10\gamma_y$. Conversely, steel MRFs with elastic panel zones are likely to experience a residual SDR in the order of 4% at an MCE. While in both cases building demolition is likely, in the latter the likelihood of structural collapse is high in a typical mainshock-aftershock seismic event series (Li et al. 2014; Shokrabadi et al. 2018). The general consensus from the above findings is that leveraging the beneficial stable hysteretic behavior of beam-to-column web panel zones greatly reduces the anticipated residual $SDRs$ in steel MRFs after a low probability-of-occurrence earthquake. This is further substantiated from the local EDP responses of the examined steel MRFs.

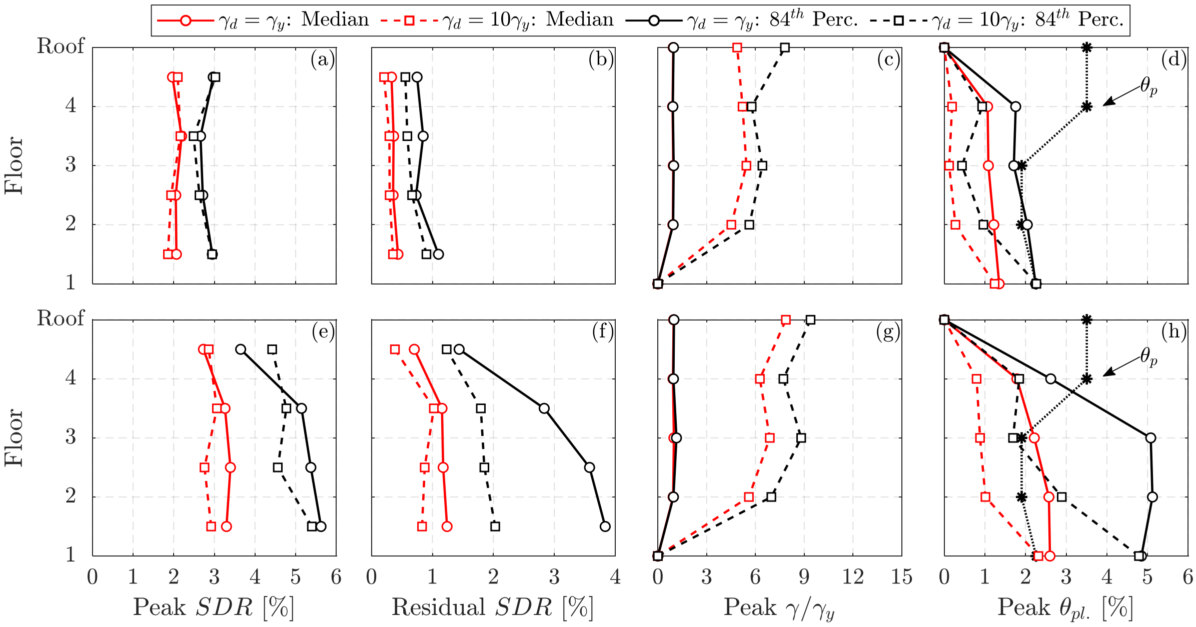

Figure 6.11 Effect of targeted panel zone distortion on engineering demand parameters of interest for the four-story, three-bay MRF [top figures (a)-(d) refer to DBE and bottom figures (e)-(h) refer to MCE].

Figures 6.11c and 6.11g suggest that in steel MRFs with $\gamma_d = 10\gamma_y$, the panel zones contribute 5 to 15 times more to the SDR for the DBE and the MCE, respectively, compared to steel MRFs with elastic panel zones. Steel MRF panel zones designed with $\gamma_d = 10{-}15\gamma_y$ do not experience, on average, more than $6 - 9\gamma_y$, respectively. This suggests that fracture due to kinking is highly unlikely (El Jisr et al. 2019; Skiadopoulos and Lignos 2021), given that the fabrication of beam-to-column connections follows the current practice (AISC 2016b; c; a; AWS 2010, 2016).

Figures 6.11d and 6.11h depict the median and 84th percentiles of the peak plastic rotation demands along the height of the steel MRFs with elastic and inelastic panel zones at DBE and MCE, respectively. Superimposed in the same figures are the rotation demands at which the onset of local buckling at the beam ends is anticipated. The results suggest that steel MRFs designed with elastic panel zones are likely to experience local buckling at their beam ends even at modest lateral drift demands associated with DBE seismic events.

Conversely, steel MRFs with a balanced beam-to-column connection design are only expected to experience flexural yielding at their beam ends even at an MCE seismic event, thereby minimizing the likelihood of structural repairs for the same intensity. However, one aspect to be evaluated is the likelihood of fractures at the bottom flanges of steel beams due to panel zone kinking (Krawinkler 1978).

At DBE seismic intensities, the simulation results confirm that none of the steel MRFs experienced beam fractures regardless of the targeted panel zone inelastic shear distortion demands and the associated number of steel MRF bays. Therefore, our focus hereinafter is at seismic intensities associated with a 2% probability of exceedance earthquakes. Naturally, steel MRFs with a lesser number of bays feature deeper beams to achieve the targeted lateral drift requirements by current seismic standards. It is generally known that beam-to-column connections featuring deep beams (i.e., depths larger than 500mm) are more prone to beam flange fractures (El-Tawil et al. 1999; Ricles et al. 2000). Figure 6.12 shows the likelihood of having one or more beam end fractures per MRF (noted as “fractures” hereinafter) for variable degrees of inelasticity in the panel zone joints (see Fig. 6.12a) and MRF heights (see Fig. 6.12b). Figure 6.12a underscores that for the MCE, no beam fractures are anticipated for panel zone designs that respect the current specifications (AISC 2016b). For highly inelastic panel zone designs, the chance of getting up to four fractures is less than 20% for the four-story steel MRF. On the other hand, Fig. 6.11h suggests that at least half of the steel beams of the MRF with elastic panel zone designs will experience local buckling within their dissipative zones. Similar observations hold true for the 8- and the 12-story MRFs (see Fig. 6.12b). From the same figure, taller steel MRFs experience significantly less beam fractures compared to the low-rise ones.

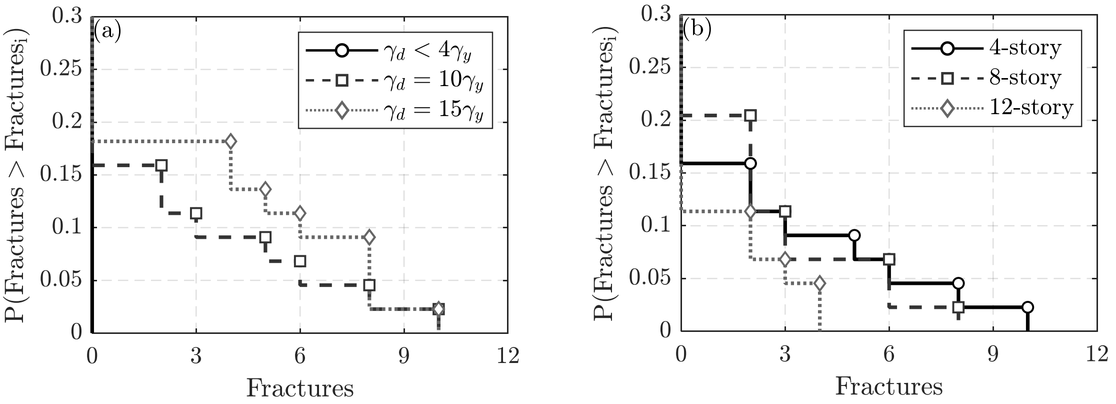

Figure 6.12 Exceedance functions for the number of beam end fractures per MRF at MCE: (a) four-story, three-bay MRFs with varying γ_d; and (b) three-bay MRFs with $\gamma_d = 10\gamma_y$ and variable number of stories.

6.6.3 Engineering demand parameter hazard curves

To further explore the potential benefits of panel zone shear yielding on the seismic response of steel MRFs, in this section, global and local EDP hazard curves are developed within the methodological framework of Performance-based Earthquake Engineering (FEMA 2012). The EDP hazard curves are computed according to Eq. (6.6). To compute the annual rate of exceeding a certain EDP value, EDP_i, the EDP_i fragility curves are numerically integrated over the hazard curve at $d\lambda(im)$ increments. The EDP_i fragility curves are then developed according to Eq. (6.7):

$$\lambda_{EDP}(EDP_i) = \int_0^{\infty} P[EDP > EDP_i|im] \cdot |d\lambda(im)| \tag{6.6}$$

$$P[EDP > EDP_i|im] = \begin{cases} P[EDP > EDP_i|NC, im] \cdot (1 - P[C|im]) + P[C|im] \; (a) \\ \sum [EDP > EDP_i|im]/Nr\_GMs \; (b) \end{cases} \tag{6.7}$$

where $P[EDP > EDP_i|NC, im]$ is the probability of exceeding EDP_i given no collapse at a targeted im, which is calculated by assuming the empirical cumulative distribution; and Nr_GMs is the number of considered ground motions.

Equation (6.7)a assumes that the probability of exceeding EDP_i at collapse equals one, meaning $P[EDP > EDP_i|C, im] = 1$. This assumption holds true for EDPs that reach 'infinite' values when a steel MRF collapses. However, this is not the case for other EDPs, such as the absolute accelerations that saturate once steel MRFs exhibit inelastic behavior. The same holds true for the peak γ/γ_y EDP (see Figs. 6.8b and 6.13); hence in these cases, Eq. (6.7)b is utilized. This is illustrated in Fig. 6.13b, where the number of ground motions that lead to peak γ/γ_y higher than (peak $\gamma/\gamma_y)_i$ are divided by the total number of ground motions for each im.

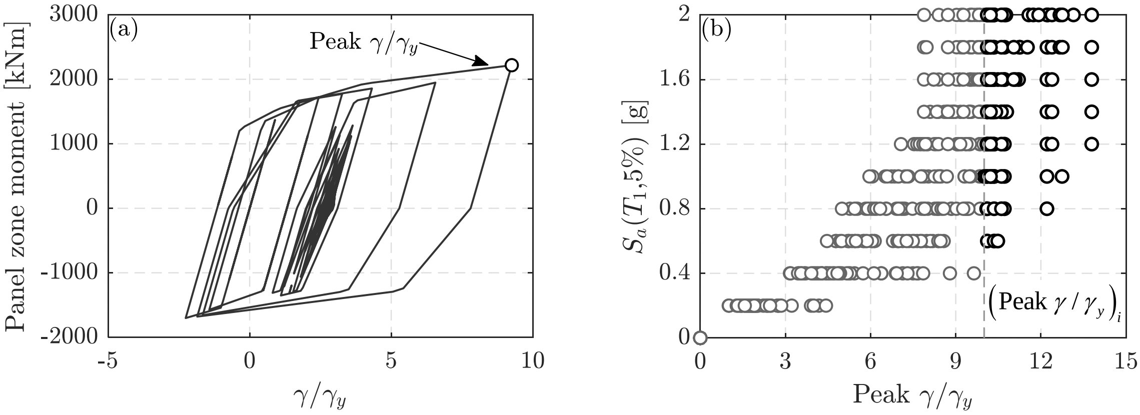

Figure 6.13 (a) Peak γ/γ_y for the most critical panel zone along the building height for the four-story, 3-bay, MRF with $\gamma_d = 10\gamma_y$; and (b) distribution of peak γ/γ_y for selected seismic intensities.

Figure 6.14 shows the computed EDP hazard curves of the four-story, three-bay steel MRFs. The EDPs of interest are the residual $SDRs$ (see Fig. 6.14a), the peak γ/γ_y (see Fig. 6.14b), the number of beam end fractures (see Fig. 6.14c) and the number of beam end local buckles (see Fig. 6.14d) per steel MRF. The mean annual frequency of the DBE, λ_{DBE}, and that of the MCE, λ_{MCE}, are superimposed as a reference in these figures based on a 475year and 2475year return periods, respectively. Referring to Fig. 6.14a, steel MRF designs with panel zones achieving $10\gamma_y$ to $15\gamma_y$ experience at least 50% less residual SDR than their code-compliant counterparts. Figure 6.14b suggests that, at DBE, steel MRFs reach the anticipated γ_d only when elastic panel zones are employed. Conversely, steel MRF designs with inelastic panel zones do not generally exceed inelastic distortions of more than $7 - 8\gamma_y$. The improved seismic performance of MRFs designed with panel zones reaching $10 - 15\gamma_y$ is highlighted in the above discussion. For panel zone design targets of $10\gamma_y$, even when the beam-to-column relative expected strength is not as anticipated due to the material variability of the adjoining steel members, the structural performance is not impaired. Therefore, some variability in the steel material properties of the respective members is not considered to be detrimental to the overall beam-to-column connection performance under seismic loading.

At this level of inelastic shear distortions there are no documented fractures in prequalified beam-to-column connections (Skiadopoulos and Lignos 2021), as highlighted in Fig. 6.14c. At MCE, panel zones reach distortions close to their design targets. In this case, up to two beam bottom flange fractures per MRF may be expected. Noteworthy stating that at DBE, steel MRF designs with $\gamma_d = \gamma_y$ lead to local buckles within the beam ends, whereas this is not the case for steel MRF designs with inelastic panel zones. At MCE, the number of beam end local buckles is nearly half when steel MRF panel zones feature $\gamma_d = 15\gamma_y$ designs compared to those for steel MRFs with $\gamma_d = \gamma_y$.

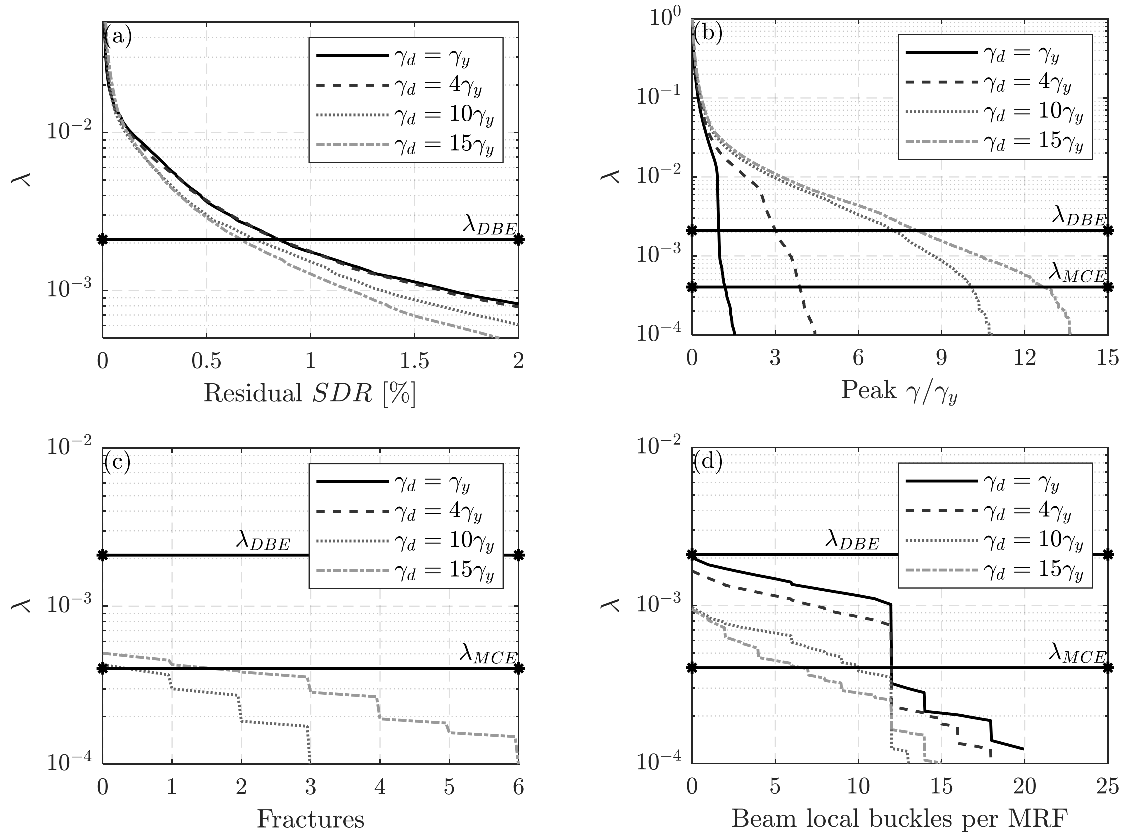

Figure 6.14 Hazard curves for engineering demand parameters of interest for the four-story, three-bay MRFs: (a) residual story drift ratio; (b) peak γ/γ_y; (c) beam end fractures per MRF; and (d) beam local buckles per MRF.

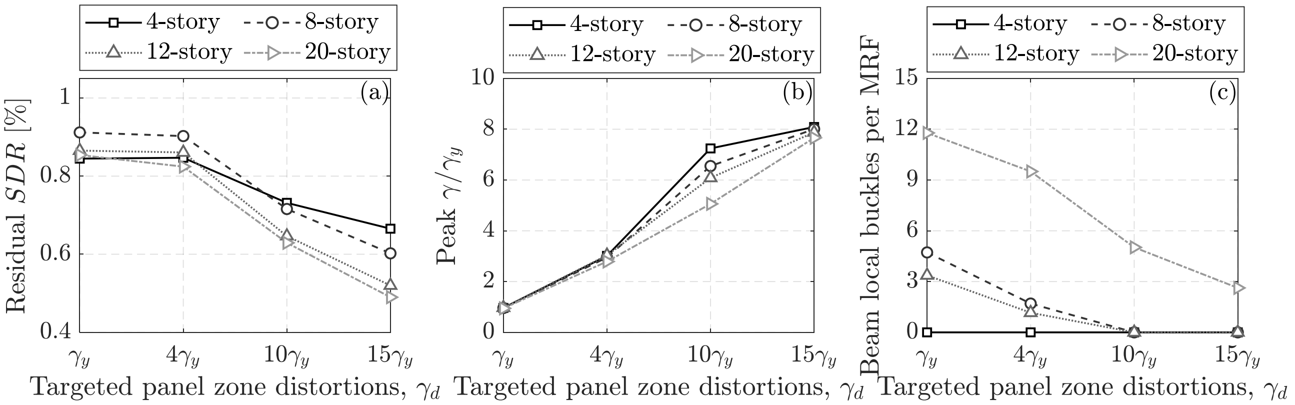

Figure 6.15 Expected global and local engineering demand parameters at DBE for the three-bay MRFs: (a) residual story drift ratio; (b) peak γ/γ_y; and (c) beam local buckles per MRF.

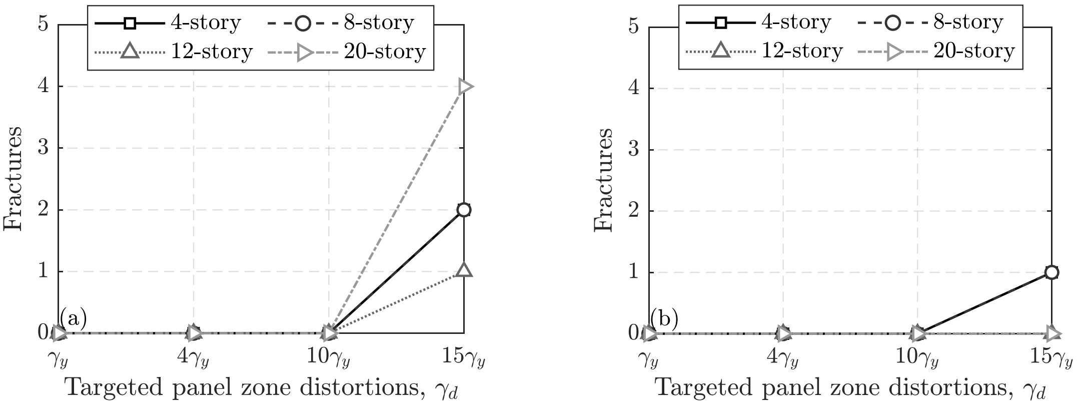

Figure 6.16 Expected number of beam end fractures per MRF at MCE: (a) three-bay; and (b) five-bay.

Figure 6.15 summarizes expected global and local EDPs of interest at DBE for the three-bay MRFs, as extracted from the developed EDP hazard curves. The results suggest that residual $SDRs$ decrease in steel MRFs with inelastic panel zones regardless of the steel MRF height (see Fig. 6.15a). For instance, in steel MRF designs with $\gamma_d = 10 - 15\gamma_y$, there is at least a 50% reduction in residual $SDRs$ compared to their counterparts with $\gamma_d \leq 4\gamma_y$. According to Fig. 6.15b, code-compliant panel zone designs (i.e., $\gamma_d \leq 4\gamma_y$) are likely to achieve γ_d at DBE. However, steel MRFs with panel zones designed to attain $\gamma_d = 10 - 15\gamma_y$ reach distortions of up to $5 - 8\gamma_y$. These findings hold true for all the examined steel MRFs regardless of their height. Moreover, beam flange fractures are unlikely to occur at DBE for all the examined steel MRFs. On the other hand, designs where panel zones are designed to remain elastic exhibit local buckling in 3-10 beam-to-column connections (see Fig. 6.15c), thereby increasing the anticipated repair costs and potential downtime in the aftermath of earthquakes.

Figure 6.16 compares the expected number of fractures at the bottom beam flange of the steel MRF connections at MCE for the three- and the five-bay steel MRFs. The designs with $\gamma_d \leq 10\gamma_y$ do not experience any fractures, regardless of the number of bays in the steel MRFs. The three-bay designs with $\gamma_d = 15\gamma_y$ experience one to four beam flange fractures per steel MRF. Fractures practically do not occur for the five-bay MRFs, due to the utilization of beams with smaller depths (d_b ranges from 450 to 750mm).

6.7 Summary and conclusions

This chapter provides quantitative knowledge on important seismic response characteristics of steel frame buildings with moment resisting frames (MRFs) with inelastic panel zone joints. For this reason, two beam-to-column connection modeling approaches are proposed for simulating the hysteretic response of steel MRF beam-to-column web panel zone joints. The first approach involves shell elements, whereas the second one features a macro-model. The former captures the panel zone yielding evolution, the cyclic hardening, and the axial-to-shear load interaction. The latter utilizes an improved tri-linear backbone curve to simulate the panel zone response (Skiadopoulos et al. 2021) and assumes an effective panel zone uniform yielding, while it disregards the cyclic hardening phenomena and the shear-to-axial load interaction. Both models consider the shear and bending panel zone deformation modes, which is a limitation of available panel zone models in the literature. Validations with available experimental data suggest that both modeling approaches accurately represent the panel zone hysteretic response in steel MRFs. Moreover, the seismic response of steel MRFs is not practically affected by the employed modeling approach. A methodology is also proposed to consider the fracture potential in steel MRF beam-to-column connections with highly inelastic panel zones (i.e., shear distortions higher than $10\gamma_y$, where γ_y is the panel zone distortion at yield).

Nonlinear static and dynamic analyses are conducted to evaluate the seismic demands and the collapse risk of prototype steel buildings with moment resisting frames (MRFs) as their primary lateral load resisting system. The archetype steel buildings feature welded beam-to-column connections with variable targeted inelastic shear distortions. Geometric parameters that are examined involve the number of stories as well as number of bays in steel MRFs. The prototype buildings are designed based on ASCE/SEI 7-16 (ASCE 2017) and AISC (2016b; c; a), except for the panel zones that comprise code-compliant as well as highly inelastic panel zone design distortions (i.e., $10 - 15\gamma_y$). The seismic demands of the examined steel MRFs are quantified from the onset of structural damage through structural collapse. Local as well as global engineering demand parameter (EDP) hazard curves are developed in the context of performance-based earthquake engineering to interpret the simulation results for risk-targeted seismic performance. The primary findings of this study are summarized as follows:

- Nonlinear static analyses demonstrate that the static overstrength factor of steel MRFs is not practically influenced by the level of inelastic deformations within the panel zone joints. Designs with highly inelastic panel zones (i.e., inelastic shear distortions of $10 - 15\gamma_y$) generally increase the period-based ductility of steel MRFs by 20-30% relative to their elastic panel zone counterparts.
- Low-rise steel MRFs with highly dissipative panel zones (i.e., $10 - 15\gamma_y$) demonstrate up to 30% lower collapse risk than that of conventionally designed steel MRFs ($\gamma \leq 4\gamma_y$). On the other hand, the collapse

risk of mid- to high-rise steel MRFs remains practically unchanged regardless of the panel zone design. This is because the global stability of these MRFs is generally sensitive to the destabilizing effects of the gravity load. The collapse mechanism is consistent between steel MRFs of the same height regardless of the examined levels of inelastic deformations in the MRF panel zones. Moreover, there is no indication of soft-story collapse mechanisms even in cases that γ_d ranges from 10 to $15\gamma_y$.

- At seismic intensities associated with a design-basis earthquake, the expected residual story drift ratios ($SDRs$) are reduced by nearly 50% for steel MRFs with highly inelastic panel zones ($10 - 15\gamma_y$). The results suggest that the number of beam end local buckles per MRF is minimal in this case, contrary to those in steel MRFs featuring elastic panel zone designs. In steel MRFs with inelastic panel zones, these attain $7 - 8\gamma_y$ even when the design targets $10 - 15\gamma_y$, because the respective beams do not reach their capping moment at a design-basis earthquake. None of the examined steel MRFs exhibited any connection fractures at the same seismic intensity.
- At seismic intensities associated with a maximum considered earthquake, the expected residual $SDRs$ range from 1-2% rads for steel MRF designs with highly inelastic panel zones, which are two times lower than corresponding results with code-compliant steel MRFs (i.e., $\gamma \leq 4\gamma_y$). The above findings are important when considering the collapse risk during mainshock-aftershock earthquake series.
- The simulation results reveal that beam-to-column connections that provide well balance between the inelastic deformations occurring in the panel zone and the adjoining steel beams, these do not experience local buckling, contrary to the elastic panel zone designs. It is also found that the number of beam flange fractures is zero even for steel MRF designs with targeted inelastic panel zone shear distortions of $10\gamma_y$ even for a low probability of occurrence seismic event (2% probability of exceedance over 50 years).
- While at rare seismic events (return periods higher than 2475 years), it is probable that the number of beam-to-column connection fractures increases for highly inelastic panel zone designs, at this level of lateral drift demands (6% rads and above), the steel MRF seismic stability is governed by P-Delta effects.

The above findings, which apply in the examined cases and for the assumed nonlinear modeling conditions described herein, suggest that structural repairs due to beam end local buckling are less likely when steel MRFs are designed with panel zones attaining inelastic shear distortions on the order of $10\gamma_y$. At this level of inelastic shear distortions, the system-level simulations conducted herein do not reveal any connection fractures even at seismic intensities with a low probability of occurrence (i.e., 2% in 50 years) regardless of the steel MRF height and number of bays. The above findings are substantiated by a comprehensive review (El Jisr et al. 2019; Skiadopoulos and Lignos 2021) of over 100 experiments on bare and composite beam-to-column connections where their panel zones exhibited similar inelastic shear distortions under cyclic loading.

Chapter 7 Conclusions and future work

7.1 Summary

This doctoral thesis advanced the state of knowledge regarding the seismic design and behavior of steel moment-resisting frames (MRFs) with highly dissipative panel zones. A key contribution of this thesis was the development of a new panel zone design model that addresses the primary limitations of all available models in the literature to this date. The model was systematically validated with available experiments on beam-to-column connections with inelastic panel zones and can be effectively used to achieve balanced design of fully restrained beam-to-column connections.

The second primary contribution of this thesis was the development of an optimized beveled backing bar for welded connections through simulation-assisted design. The proposed backing bar defies the current paradigm in prequalified welded connections where backing bars shall be removed after the completion of complete joint penetration (CJP) groove welds at the bottom beam flange-to-column face joints. Instead, the beveled backing bar, which is not imperative to be removed, minimizes the fracture potential at this location. The findings are substantiated by means of detailed continuum finite element (CFE) analysis that leverage traditional fracture mechanics along with full-scale experiments of cyclically loaded welded connections that adopted the simplified weld detail. The physical experiments demonstrate a superior hysteretic performance of the welded connections, which were designed to leverage the beneficial aspect of shear yielding in the panel zones. Consequently, structural repairs due to beam local buckling are circumvented even at lateral drift demands of 7% rad. As such, the seismic stability of steel MRFs is only governed by global P-Delta effects at large deformations since component deterioration under cyclic loading is not prevailing.

Nonlinear system-level dynamic simulations highlighted that steel MRFs with highly dissipative panel zone designs enjoy up to 30% reduced collapse risk, depending on their height, compared to their counterparts with elastic panel zone designs. Moreover, residual story drift ratios along the steel MRF's height are reduced by up to two times and beam local buckling is not evident for low probability of occurrence earthquakes.

7.2 Conclusions

7.2.1 Proposed panel zone model for the seismic design of fully restrained beam-to-column connections

To potentially mobilize the beneficial aspects of the stable hysteretic response of the panel zones, a robust panel zone design model is necessary. The accuracy of available panel zone design models was assessed based on comparisons with nearly 100 available experiments of beam-to-column connections with inelastic panel zones. The assembled data from these tests were made publicly available. The comparisons reveal that the AISC (2016b) panel zone model overestimates the panel zone elastic stiffness, K_e, by nearly 30%. This is attributed to the fact that this model neglects the panel zone bending deformation mode, which is found to be important in panel zone geometries with d_b/d_c larger than 1.5 (i.e., typical in North American designs). The same model overestimates the panel zone strength at yield, V_y, by more than 10% due to the assumption of uniform shear stresses at yield. The panel zone shear strength, V_p, at $4\gamma_y$ (where γ_y is the panel zone shear distortions at yield), is overestimated by more than than 40% when column cross sections feature thick flanges ($t_{cf} > 40$ mm). Similar limitations hold true for other pane zone models (CEN 2005; Kim et al. 2015; Kim and Engelhardt 2002; Krawinkler 1978; Lee et al. 2005c; Lin et al. 2000).

To overcome the above shortcomings, a new panel zone model was developed. The model relies on mechanics first principles and realistic panel zone shear stresses, which are extracted from representative panel zone geometries. The panel zone shear distributions are informed by CFE analyses for a broad range of panel zone geometries. The CFE analyses revealed that the panel zone bending deformation modes are prominent for slender panel zone geometries (beam-to-column depth ratios, $d_b/d_c \geq 1.5$). Therefore, the proposed model accounts for both shear and bending deformations modes on the calculation of K_e. Moreover, the proposed model assumes realistic shear stress distributions at yield for the calculation of V_y, which is particularly important for slender panel zone geometries, since the shear distributions on the web are not uniform in this case. Regarding V_p, a distinction is made in the shear stresses resisted by the column web and flanges, depending on the panel zone geometry. For stocky and shallow panel zone geometries (e.g., $d_b/d_c = 1.0$ and $t_{cf} = 50$ mm), where the contribution of the flanges in the panel zone shear strength may reach 40%, the flange contributes five times more compared to that in slender panel zone geometries.

Available panel zone models assume a post-$4\gamma_y$ stiffness that equals $0.03K_e$. The CFE analysis simulations demonstrate that this assumption is not justifiable after $4\gamma_y$ due to the increased contribution of the column flanges in resisting the panel zone shear demand. Instead, the panel zone shear strength at $6\gamma_y$ is proposed and utilized to predict the panel zone stiffness at shear distortions higher than $4\gamma_y$. Comparisons of the proposed panel zone model with about 100 experiments highlight the superior accuracy in predicting both the panel zone stiffness and strength at $4-6\gamma_y$, especially when panel zones feature columns with thick flanges ($t_{cf} > 40$ mm), which was a known limitation in literature since the 1970s.

The compatibility of shear stresses between the column web and potential doubler plates was examined. Simulation results on both fillet- and CJP-welded doubler plates revealed the compatibility in the shear stresses between doubler plates and the column web, provided that the current seismic provisions and detailing criteria are respected (AISC 2016a; AWS 2016). Therefore, doubler plates should not be treated differently either by reducing the total panel zone thickness (i.e., thickness of the web plus the total doubler plate thickness) or by accounting only for one out of the potentially two doubler plates (CEN 2005).

The effect of column axial load in reducing the panel zone strength was also examined. The CFE analyses demonstrated that the commonly used von Mises criterion (von Mises 1913) suffices to describe the shear force-to-axial load interaction within the panel zone. This holds true for both interior and end columns in steel MRFs, regardless of the applied lateral loading history. Particularly for end columns, the peak axial compressive load should be considered, including the gravity and the transient axial components due to dynamic overturning effects.

7.2.2 Hysteretic behavior of welded connections with highly dissipative panel zones and simplified weld details

A welded beam-to-column connection detail simplification for seismic applications was explored by keeping the beam flange-to-column face weld backing bars in place after the completion of the CJP weld at the beam flange-to-column face joint. The concept development was informed by CFE analyses. Several configurations were investigated including beveled backing bars, with and without fillet weld reinforcement for a broad range of monotonically-loaded beam-to-column connection geometries. The assessment was based on traditional fracture mechanics to quantify the fracture potential of the proposed configuration.

The simulation results highlighted the superior connection performance of optimally designed beveled backing bars that are kept in place after the execution of the CJP welds, contrary to the current practice with conventional backing bars. Notably, pre-Northridge welded beam-to-column connections with the customized beveled backing bars could withstand at least 4-6% rad prior to fracture. This is attributable to the optimized beveled backing bar configuration that pushes the crack tip away from the critical beam flange-to-column face location. From a wide range of examined bevel angles, the optimal one (i.e., 35° for pre-Northridge connections) increases the peak lateral drift capacity by at least 4 times compared to that with conventional backing bars. Fillet-weld reinforcement in the backing bars was found to depreciate the optimal fracture potential of the proposed beveled backing bars. This is attributable to the fact that fillet-weld reinforcement impairs the optimal backing bar stress flow that is achieved by the proposed beveled backing bar configuration.

Post-Northridge welded connections with weld electrodes of improved fracture toughness can sustain lateral drift demands of at least 6% rad based on the proposed customized beveled backing bar (i.e., 45° bevel angle). At these lateral drift demands, welded connections with panel zones exhibiting highly inelastic shear distortions (i.e., higher than $15\gamma_y$) possess 50% higher fracture potential compared to their elastic panel zone counterparts. However, at lateral drift demands associated with a design-basis (2% probability of exceedance over 50 years) or a maximum considered earthquake event (2% probability of exceedance over 50 years), the panel zone kinking effect is not prominent. Therefore, elastic panel zone designs possess 50% higher fracture potential in this case compared to inelastic panel zone connection designs. The beam depth was found to affect the fracture potential of welded connections the most. For instance, connections with beam depths less than 600mm possess 30% lower fracture potential compared to those with beam depths of 900mm.

The seismic performance of fully restrained welded beam-to-column connections that utilize the developed beveled backing bar was validated through two full-scale experiments on welded unreinforced flange-welded web connections. The connection design featured highly dissipative panel zones to exploit their stable hysteretic response, deep beams of 650mm depth and minimum toughness requirements for the column material to avoid divot fracture. The experimental results highlighted the superior performance of the proposed beam-to-column connection design. Regardless of the applied lateral loading protocol, the test specimens sustained lateral drift demands of at least 9% rad before losing more than 20% of their peak story shear resistance.

At seismic intensities corresponding to design-basis and maximum considered earthquake events (i.e., lateral drift demands of 2% and 3-4% rad, respectively), there was no visual damage in the form of beam local deformations or crack initiation in the beam-to-column connections. The onset of beam yielding occurred at 2% rad, while the panel zones reached distortions of $4\gamma_y$ and $10\gamma_y$, respectively. At 4% rad, there was no sign of in-cycle strength or stiffness deterioration in the test specimens. Therefore, the prequalification requirements of AISC (2016a) were safely met. The panel zone kinking effect started being visible in the form of column flange localized yielding at the panel zone corners for lateral drift demands of 4% rad and higher. At 6% rad, the panel zone shear distortion became $15\gamma_y$, as targeted by the connection design.

The ultimate failure modes were fairly consistent in both test specimens. These involved ductile cracks due to ultra-low-cycle fatigue. The cracks initiated at lateral drift demands of 7-10% rad depending on the employed loading protocol. The initiation locations were at the column, near the beam flange CJP weld root and at the shear tab end at the weld fusion. These cracks propagated in a ductile manner in the column thickness and in the longitudinal direction. From the crack initiation to the loss of more than 50% of the load-carrying capacity of the test specimens, these were able to dissipate at least 30% of their total dissipated energy throughout the loading history.

The experimental results demonstrated that the proposed beveled backing bars did not induce fracture, even at lateral drift demands exceeding 9% rad. Noteworthy stating that at this lateral drift demand, panel zone shear distortions reached $30\gamma_y$.

The panel zone demand-to-resistance design ratio, $R_{n,pl}/R_u = 0.8$, led to a well-balanced contribution of the steel beams and panel zone to the total story drift ratio. The delayed onset of beam local instabilities in combination with the stocky column cross section was associated with minimal column twist demands and out-of-plane deformations. The lateral support system design requirements of AISC (2016a; b) were found to be adequate. Moreover, regardless of the absence of continuity plates in the design, the column flange local deformations did not exceed 2-4mm at 10% rad lateral drift demands.

The stable hysteretic response of the welded connections until very large lateral drift demands was captured with remarkable accuracy by CFE analyses up until the crack initiation. This is attributable to the exploitation of the stable hysteretic response of panel zones that delays the onset of beam local buckling, which is a considerable source of modeling uncertainty in CFE simulations.

7.2.3 Seismic demands of steel moment resisting frames with inelastic beam-to-column web panel zones

The role of inelastic panel zones on the seismic demands of steel MRFs was quantified through nonlinear static and dynamic analyses on 32 steel buildings with variable number of bays, storeys and panel zone targeted distortions. To assist the simulations, two panel zone modeling approaches were developed: (a) a spring-based approach that involves a tri-linear backbone curves as proposed by Skiadopoulos et al. (2021), and (b) a shell element approach that employs a recently developed multiaxial plasticity formulation for structural steels (Hartloper et al. 2021). Both approaches were validated with experimental data. The former is computationally more effective in system-level simulations, while the latter captures with higher accuracy the onset and evolution of panel zone yielding, the cyclic hardening phenomena and the shear-to-axial load interaction within the panel zone. The fracture potential of highly dissipative panel zones was explicitly considered in the modeling approach through model updating during the nonlinear building simulations.

Results of nonlinear static analyses highlighted that the static overstrength factor of steel MRFs is not practically affected by the extent of inelasticity within the panel zone(s). On the other hand, for highly inelastic panel zones (i.e., $\gamma_d = 10 - 15\gamma_y$, where γ_d are the panel zone design distortions), the period-based ductility of steel MRFs may increase by up to 30% relative to their elastic panel zone design counterparts. Steel MRFs with highly inelastic panel zones show up to 30% lower collapse risk compared to their counterparts with elastic panel zones, while the collapse mechanism is insensitive to the extent of panel zone yielding.

For seismic intensities associated with design-basis earthquake events, a 50% reduction in the residual story drift ratios was observed when highly dissipative panel zones were employed in the steel MRF designs. Beam local buckling in this case was not evident, contrary to that in connections that featured elastic panel zone designs. Panel zones did not exceed $8\gamma_y$ and there were no fracture incidents. At seismic intensities associated with the maximum considered earthquake, residual story drift ratios decreased by two times when highly inelastic panel zones were utilized in the seismic design of steel MRFs.

For steel MRF designs featuring panel zones with a targeted shear distortion of $10\gamma_y$, no fractures are likely to occur for seismic events with a 2% probability of exceedance over 50 years. While steel MRF designs with panel zones reaching or exceeding $15\gamma_y$ may experience a handful of connection fractures, at this level of lateral drift demands (i.e., above 6% rad), the steel MRF seismic stability is mostly governed by global P-Delta effects.

The system level simulations revealed that by targeting $10\gamma_y$ panel zone shear distortions, steel MRF panel zones do not exceed $7\gamma_y$ and $10\gamma_y$ for the 10% and 2% probability of exceedance over 50 years earthquake event, respectively. Such a design is associated with delayed beam local buckles and reduction of residual story drift ratios due to the exploitation of the stable panel zone hysteretic response. For such panel zone shear distortions, available experiments in the literature, which are all summarized in Chapter 2, showed that welded moment connections are not prone to fractures at lateral drift demands lower than 4% rad. The developed welded connections with highly inelastic panel zones and improved details ensure a superior hysteretic behavior during earthquake loading at the above connection performance targets. Therefore, a connection design with a targeted panel zone shear distortion of $10\gamma_y$ is proposed for ductile welded connections that incorporate beveled backing bars.

7.3 Recommendations for future research

Building upon the contributions of this doctoral thesis, the following topics are few of those proposed for future research:

- The focus of this doctoral thesis was mainly on welded connections with steel wide flange columns. The proposed beveled backing bar configuration should be explored for welded hollow steel column moment connections. In such a context, a panel zone model for hollow structural cross sections should be developed.
- The proposed beam-to-column connection design was validated experimentally by utilizing bare steel beams of a certain depth. The proposed concepts should be explored in cases where deeper beams may be of interest. Moreover, the role of the composite slab on the overall connection performance should be carefully examined.
- The simulation results suggest a remarkable accuracy up until the point that cracks initiate due to ultra-low-cycle fatigue. The development of reliable fracture models that simulate the crack initiation as well as the propagation phase should be further developed and validated to explore the beneficial aspects of the developed concepts presented herein.

Appendix A. Design drawings of test specimens

Description

This appendix includes the design drawings of the test specimens described in Chapter 5.

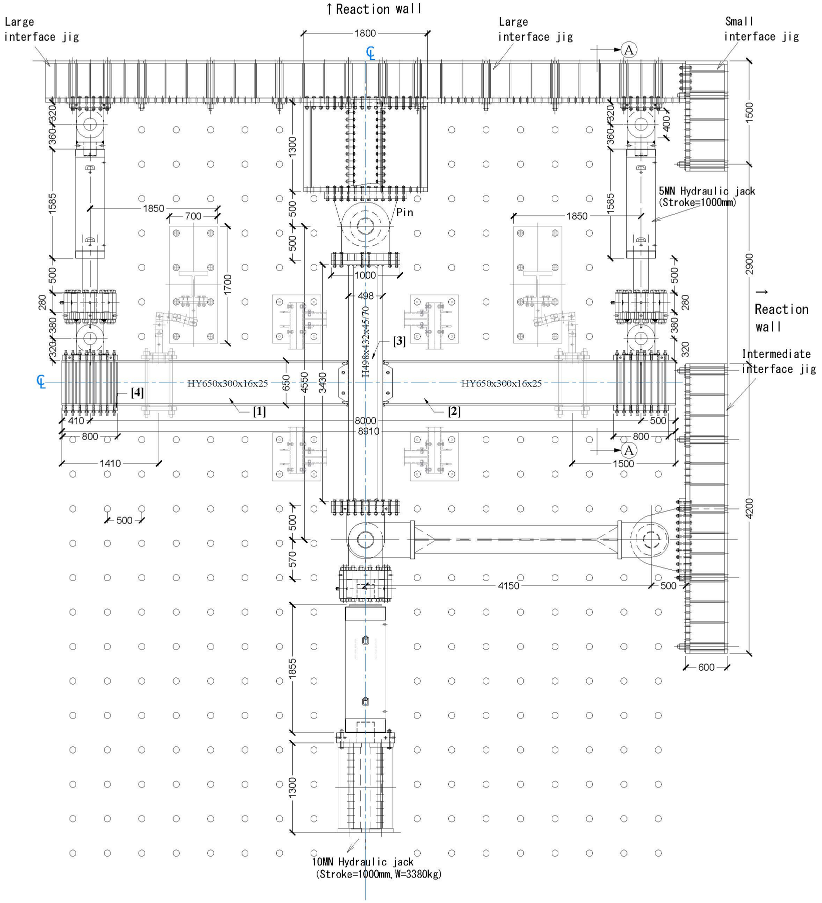
Reaction wall
Large interface jig
Large interface jig
Small interface jig
1800
℄
A
1500
1300
360
320
400
1585
1850
700
1700
500
Pin
1850
5MN Hydraulic jack
(Stroke=1000mm)
1585
2900
Reaction wall
Intermediate interface jig
1000
498
H498x432x45/70
[3]
280
380
320
℄
HY650x300x16x25
HY650x300x16x25
[4]
[1]
[2]
650
4550
3430
410
800
8000
8910
500
800
A
1410
1500
500
4200
500
570
4150
500
600
1855
1300
10MN Hydraulic jack
(Stroke=1000mm, W=3380kg)

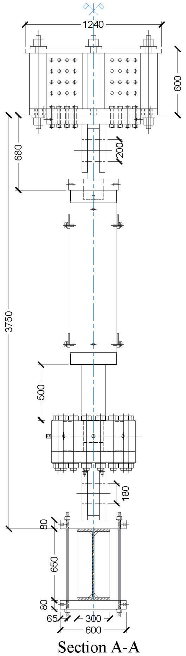
1240
600
680
200
3750
500
180
80
650
80
65
300
600

Section A-A
Scale (1:25)

PROJECT	EXTRA No.	DRAWING Nr.
RESSLab-NSC		0

General Plan

Resilient Steel Structures Laboratory (RESSLab)
School of Architecture, Civil, and Environmental Engineering,
École Polytechnique Fédérale de Lausanne (EPFL)
Adresse: GC B3 485 (Bâtiment GC) Station 18 CH-1015 Lausanne
Attention to: Prof. Dimitrios Lignos, Andronikos Skiadopoulos
email: dimitrios.lignos@epfl.ch

DATE	REV.	DIM	SCALE	PAPER SIZE
29/01/2021	2	mm	1:40	A2

SUBASSEMBLY DRAWINGS

ID	DESCRIPTION	DRAWING
1	Subassembly	1
2	Beam-to-column connection (Details A, B, C)	2

COMPONENT LIST

ID	DESCRIPTION	PIECE	QUAN	DRAWING
3	West beam	HY650x300x16x25	2	3
4	East beam	HY650x300x16x25	2	4
5a	Column	H498x432x45/70	2	5a
5b	Column - Details	H498x432x45/70	-	5b
6	Actuator adapter plate	800x600x80	2	6
7	List of bolts and rods	-	-	7

COUPON DRAWINGS

8	HY650x300x16x25 coupon specimen overview	8
9	HY650x300x16x25 coupon specimen drawings	9
10	H498x432x45x70 coupon specimen overview	10
11	H498x432x45x70 coupon specimen drawings	11

Figure A.1 Test specimen general plan drawings.

PROJECT		EXTRA No.		DRAWING Nr.
RESSLab-NSC				1
Subassembly				
Resilient Steel Structures Laboratory (RESSLab) School of Architecture, Civil, and Environmental Engineering, École Polytechnique Fédérale de Lausanne (EPFL) Adresse: GC B3 485 (Bâtiment GC) Station 18 CH-1015 Lausanne Attention to: Prof. Dimitrios Lignos, Andronikos Skiadopoulos email: dimitrios.lignos@epfl.ch				
DATE 29/01/2021	**REV.** 2	**DIM** mm	**SCALE** 1:25	**PAPER SIZE** A2

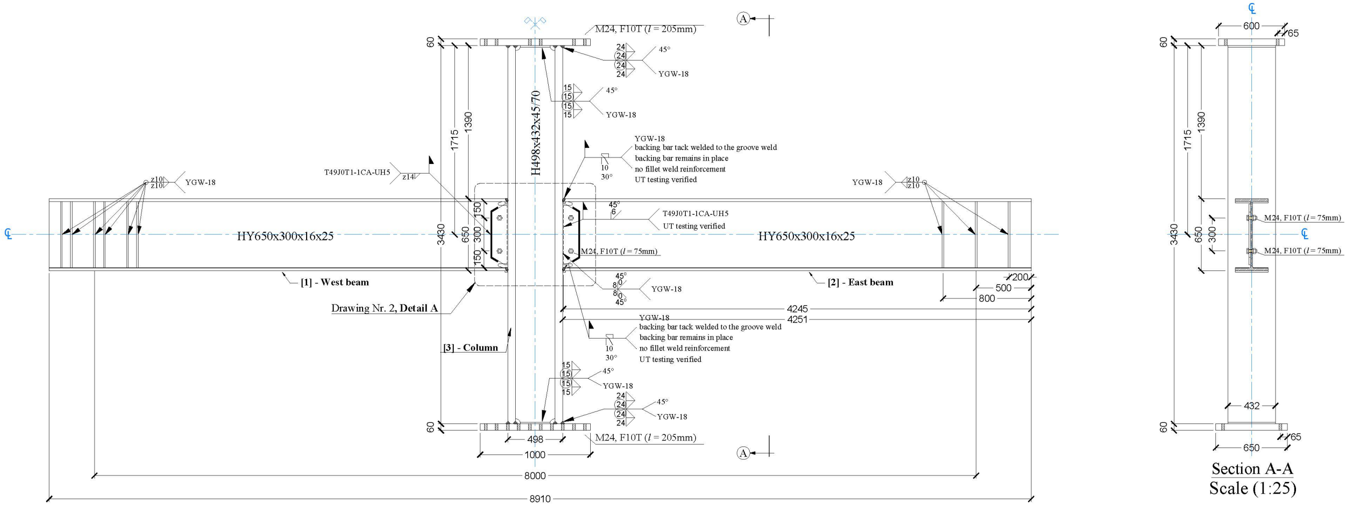
M24, F10T (l = 205mm)
A
24
24
24
24
45°
YGW-18
15
15
15
15
45°
YGW-18
H498x432x45/70
60
1715
1390
3430
650
300
150
150
YGW-18
backing bar tack welded to the groove weld
backing bar remains in place
no fillet weld reinforcement
UT testing verified
10
30°
T49J0T1-1CA-UH5
z14
z10
z10
YGW-18
45°
6
T49J0T1-1CA-UH5
UT testing verified
HY650x300x16x25
HY650x300x16x25
M24, F10T (l = 75mm)
[1] - West beam
[2] - East beam
Drawing Nr. 2, Detail A
[3] - Column
45°
8
0
8
0
45°
YGW-18
200
500
800
4245
4251
498
1000
8000
8910
M24, F10T (l = 205mm)
600
65
M24, F10T (l = 75mm)
M24, F10T (l = 75mm)
432
650
65
Section A-A
Scale (1:25)

Note:
Due to a fabrication problem, the west beam had to be cut 90mm shorter than the specified length. Since the initially specified stiffeners were already welded before the fabrication problem, new stiffeners were positioned in symmetry with the actuator position, like for the east beam.
This difference in the beam lengths does not affect the beam cantilever specified length, which is 4000mm from the column centerline to the actuator centerline.

Figure A.2 Test specimen detailed drawings.

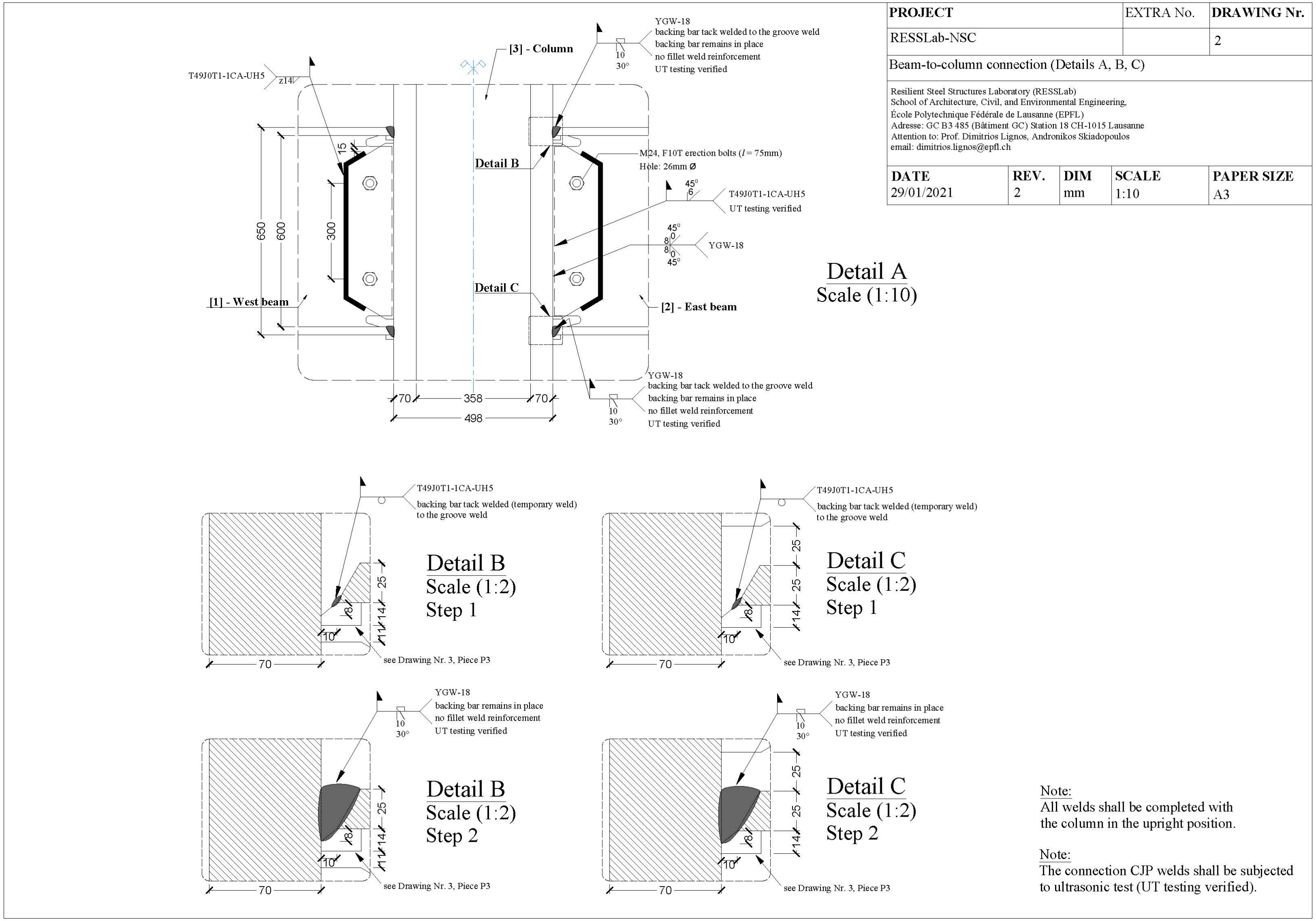
YGW-18
backing bar tack welded to the groove weld
backing bar remains in place
no fillet weld reinforcement
UT testing verified
10
30°
[3] - Column
T49J0T1-1CA-UH5
z14
15
Detail B
M24, F10T erection bolts (l = 75mm)
Hole: 26mm Ø
45°
6
T49J0T1-1CA-UH5
UT testing verified
45°
0
8
8
0
45°
YGW-18
650
600
300
Detail C
[1] - West beam
[2] - East beam
Detail A
Scale (1:10)
70
358
70
498
T49J0T1-1CA-UH5
backing bar tack welded (temporary weld) to the groove weld
Detail B
Scale (1:2)
Step 1
25
8
14
11
10
70
see Drawing Nr. 3, Piece P3
Detail C
Scale (1:2)
Step 1
25
25
14
Detail B
Scale (1:2)
Step 2
Detail C
Scale (1:2)
Step 2

PROJECT	EXTRA No.	DRAWING Nr.
RESSLab-NSC		2
Beam-to-column connection (Details A, B, C)		
Resilient Steel Structures Laboratory (RESSLab) School of Architecture, Civil, and Environmental Engineering, École Polytechnique Fédérale de Lausanne (EPFL) Adresse: GC B3 485 (Bâtiment GC) Station 18 CH-1015 Lausanne Attention to: Prof. Dimitrios Lignos, Andronikos Skiadopoulos email: dimitrios.lignos@epfl.ch		

DATE	REV.	DIM	SCALE	PAPER SIZE
29/01/2021	2	mm	1:10	A3

Note:
All welds shall be completed with
the column in the upright position.

Note:
The connection CJP welds shall be subjected
to ultrasonic test (UT testing verified).

Figure A.3 Beam-to-column connection drawings.

ITEM	QUAN	DESCRIPTION	LENGTH [mm]	WEIGHT [kg]	REMARKS	MATERIAL
P1	2	HY650x300x16x25	4155	824		SN490B
P2	24	600x142x16	-	11		SN490A
P3	4	25x14x300	-	1		SN490A

PROJECT	EXTRA No.	DRAWING Nr.
RESSLab-NSC		3

West beam [1]

Resilient Steel Structures Laboratory (RESSLab)
School of Architecture, Civil, and Environmental Engineering,
École Polytechnique Fédérale de Lausanne (EPFL)
Adresse: GC B3 485 (Bâtiment GC) Station 18 CH-1015 Lausanne
Attention to: Prof. Dimitrios Lignos, Andronikos Skiadopoulos
email: dimitrios.lignos@epfl.ch

DATE	REV.	DIM	SCALE	PAPER SIZE
29/01/2021	2	mm	1:25	A3

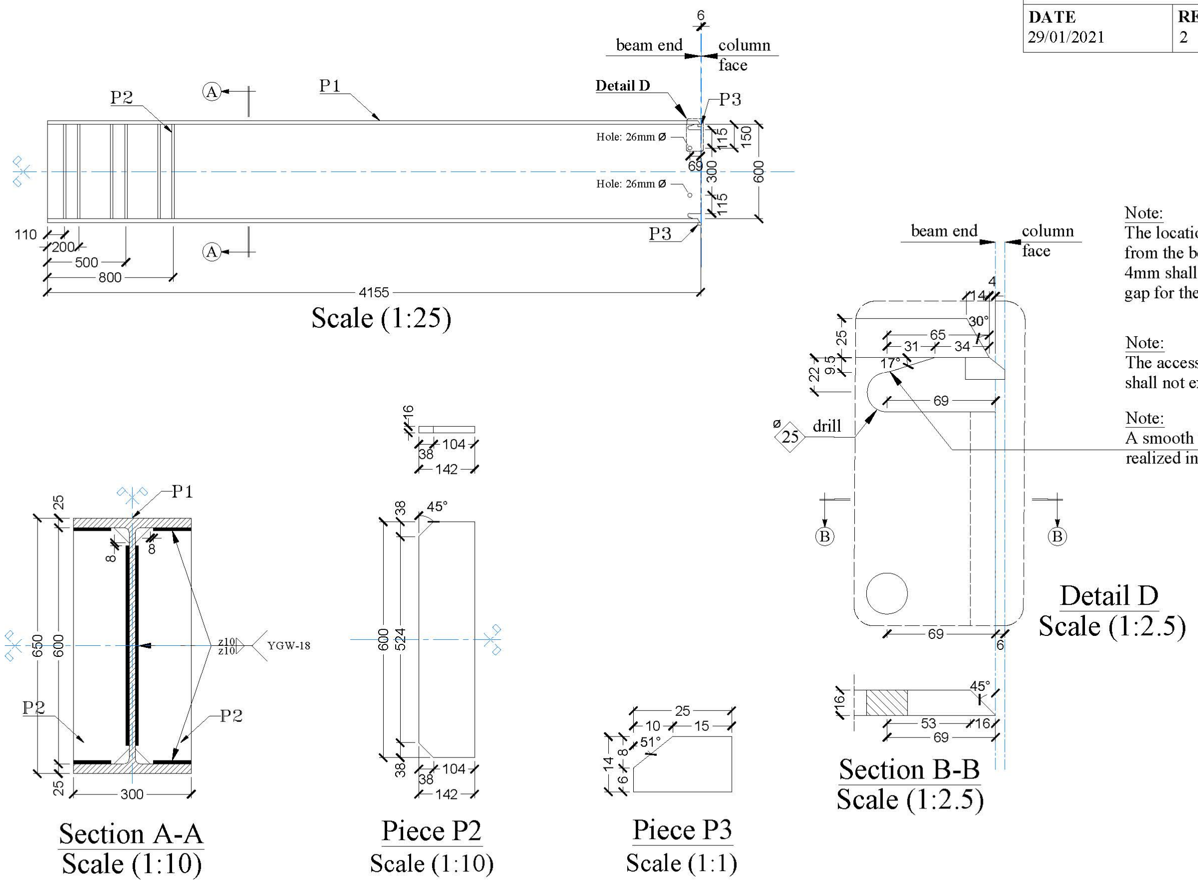
6
beam end
column face
Detail D
P3
P2
A
P1
Hole: 26mm Ø
Hole: 26mm Ø
69
115
150
300
600
115
P3
110
200
500
800
4155
Scale (1:25)
beam end
column face
4
14
30°
25
65
31
34
17°
22
9.5
69
ø 25
drill
B
B
69
6
Detail D
Scale (1:2.5)
16
45°
53
16
69
Section B-B
Scale (1:2.5)
16
104
38
142
P1
25
8
8
650
600
z10
z10
YGW-18
P2
P2
25
300
Section A-A
Scale (1:10)
38
45°
600
524
38
104
38
142
Piece P2
Scale (1:10)
25
10
15
51°
14
8
6
Piece P3
Scale (1:1)

Note:
The location of the bolt holes is such that a 6mm gap is kept from the beam web to the column face. As such, additional 4mm shall be cut from the beam flanges to have the 10mm gap for the groove weld.

Note:
The access hole surface roughness shall not exceed 13μm.

Note:
A smooth transition shall be realized in the indicated corner

Figure A.4 Test specimen west beam drawings.

ITEM	QUAN	DESCRIPTION	LENGTH [mm]	WEIGHT [kg]	REMARKS	MATERIAL
P1	2	HY650x300x16x25	4245	824		SN490B
P2	12	600x142x16	-	11		SN490A
P3	4	25x14x300	-	1		SN490A

PROJECT		EXTRA No.		**DRAWING Nr.**
RESSLab-NSC				4
East beam [2]				
Resilient Steel Structures Laboratory (RESSLab) School of Architecture, Civil, and Environmental Engineering, École Polytechnique Fédérale de Lausanne (EPFL) Adresse: GC B3 485 (Bâtiment GC) Station 18 CH-1015 Lausanne Attention to: Prof. Dimitrios Lignos, Andronikos Skiadopoulos email: dimitrios.lignos@epfl.ch				
DATE 29/01/2021	**REV.** 2	**DIM** mm	**SCALE** 1:25	**PAPER SIZE** A3

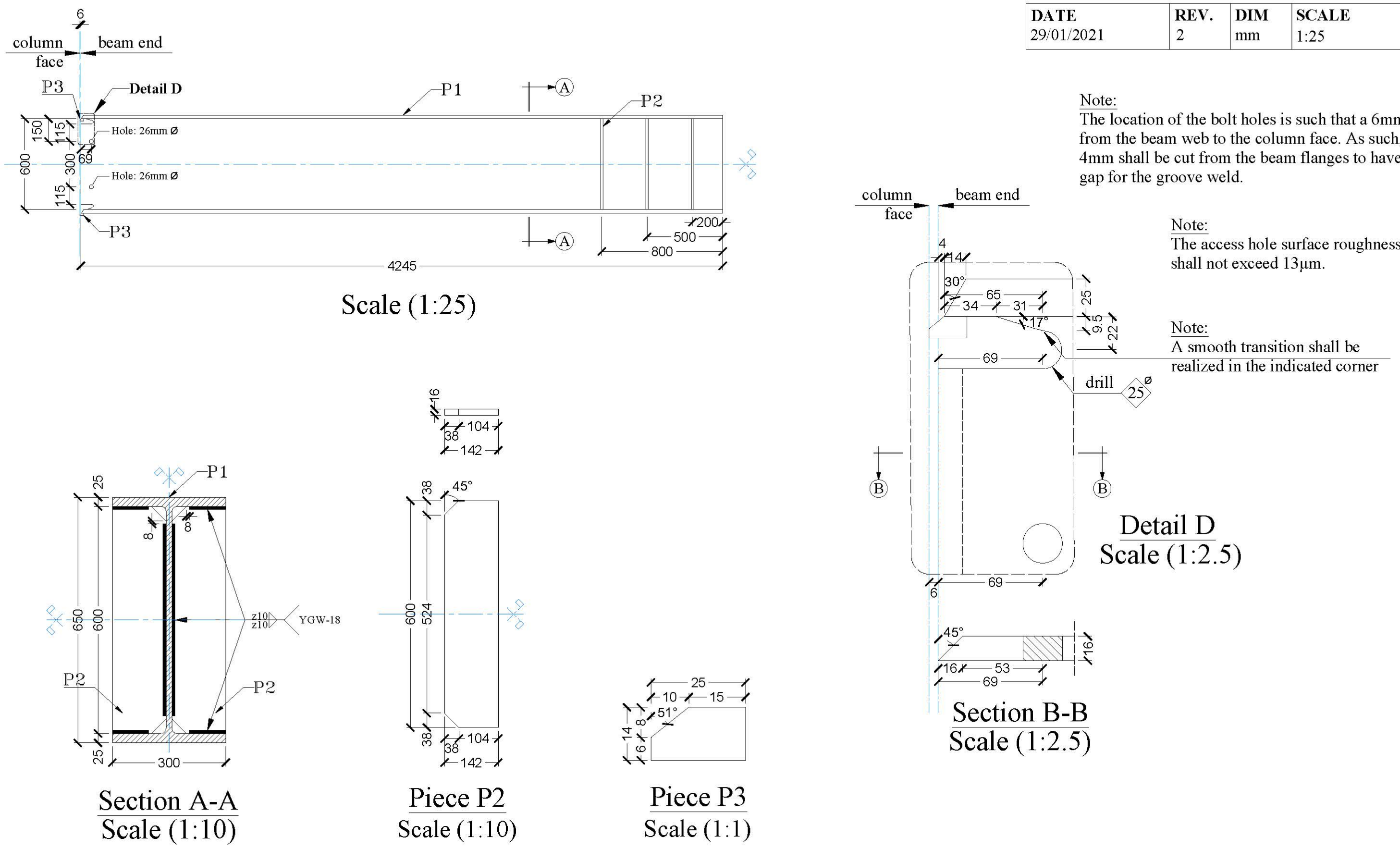

6
column face
beam end
P3
Detail D
P1
A
P2
Hole: 26mm Ø
Hole: 26mm Ø
150
115
600
300
69
115
P3
200
500
800
4245
Scale (1:25)
column face
beam end
4
14
30°
65
34
31
17°
25
9.5
22
69
drill
25 Ø
B
B
Detail D
Scale (1:2.5)
69
6
45°
16
53
69
16
Section B-B
Scale (1:2.5)
16
104
38
142
P1
25
8
8
650
600
z10
z10
YGW-18
P2
P2
25
300
Section A-A
Scale (1:10)
38
45°
600
524
38
104
38
142
Piece P2
Scale (1:10)
25
10
15
51°
8
14
6
Piece P3
Scale (1:1)

Note:
The location of the bolt holes is such that a 6mm gap is kept from the beam web to the column face. As such, additional 4mm shall be cut from the beam flanges to have the 10mm gap for the groove weld.

Note:
The access hole surface roughness shall not exceed 13µm.

Note:
A smooth transition shall be realized in the indicated corner

Figure A.5 Test specimen east beam drawings.

ITEM	QUAN	DESCRIPTION	LENGTH [mm]	WEIGHT [kg]	REMARKS	MATERIAL
P1	2	H498x432x45/70	3350	2027		SM490A
P2	4	551x142.5x16	-	10		SN490A
P3	2	1000x600x60	-	284		SN490A
P4	2	1000x650x60	-	308		SN490A

PROJECT	EXTRA No.	**DRAWING Nr.**
RESSLab-NSC		5a

Column [3]

Resilient Steel Structures Laboratory (RESSLab)
School of Architecture, Civil, and Environmental Engineering,
École Polytechnique Fédérale de Lausanne (EPFL)
Adresse: GC B3 485 (Bâtiment GC) Station 18 CH-1015 Lausanne
Attention to: Prof. Dimitrios Lignos, Andronikos Skiadopoulos
email: dimitrios.lignos@epfl.ch

DATE	**REV.**	**DIM**	**SCALE**	**PAPER SIZE**
29/01/2021	2	mm	1:25	A3

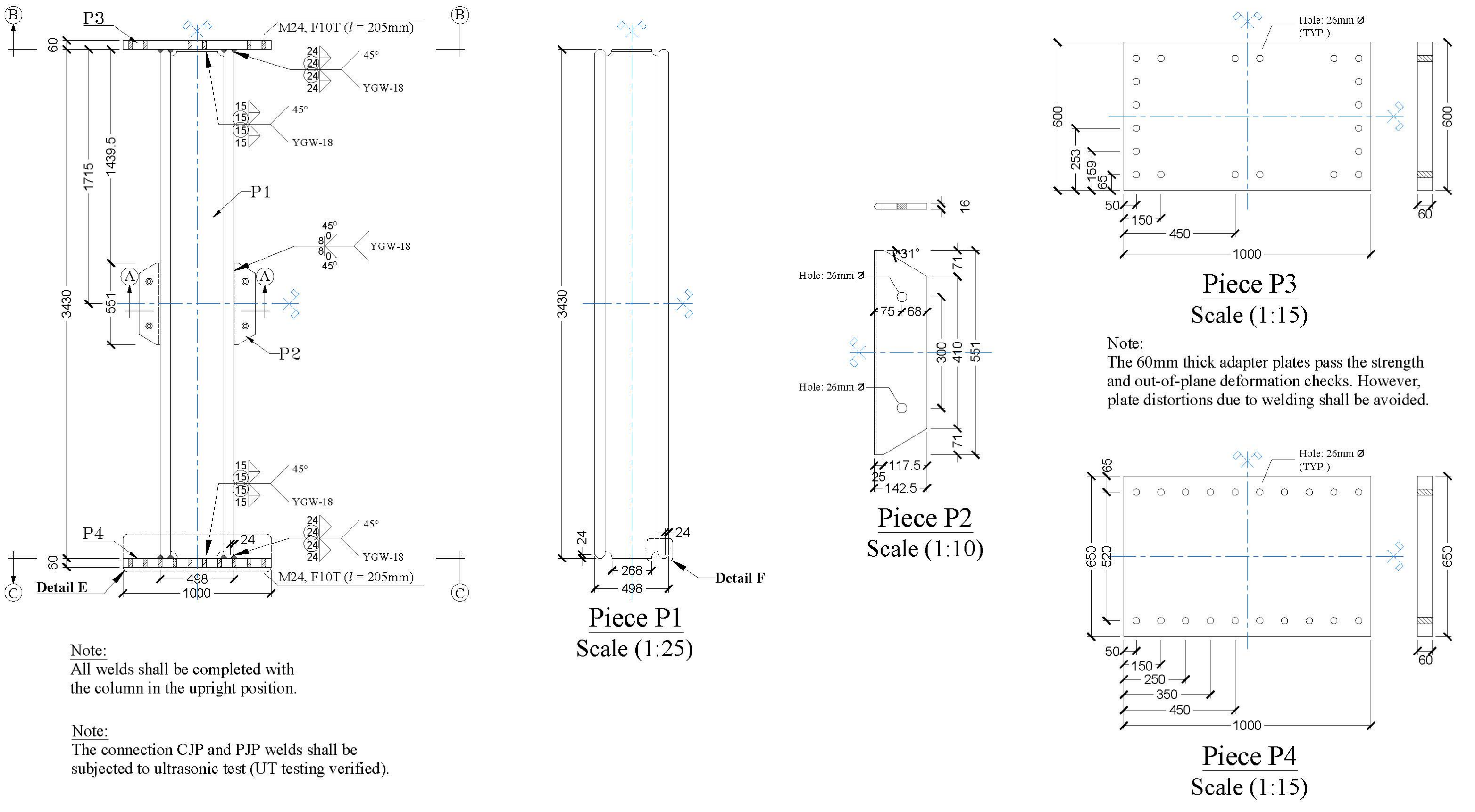
B
P3
M24, F10T (l = 205mm)
60
24
24
24
24
45°
YGW-18
15
15
15
15
45°
YGW-18
1715
1439.5
P1
45°
8
0
8
0
45°
YGW-18
A
A
3430
551
P2
15
15
15
15
45°
YGW-18
P4
24
24
24
24
45°
YGW-18
24
60
498
1000
M24, F10T (l = 205mm)
Detail E
C
C
3430
24
24
268
498
Detail F
Piece P1
Scale (1:25)
16
31°
Hole: 26mm Ø
75
68
71
300
410
551
Hole: 26mm Ø
71
117.5
25
142.5
Piece P2
Scale (1:10)
Hole: 26mm Ø
(TYP.)
600
253
159
65
50
150
450
1000
600
60
Piece P3
Scale (1:15)
Hole: 26mm Ø
(TYP.)
65
650
520
50
150
250
350
450
1000
650
60
Piece P4
Scale (1:15)

Note:
All welds shall be completed with the column in the upright position.

Note:
The connection CJP and PJP welds shall be subjected to ultrasonic test (UT testing verified).

Note:
The 60mm thick adapter plates pass the strength and out-of-plane deformation checks. However, plate distortions due to welding shall be avoided.

Figure A.6 Test specimen column drawings.

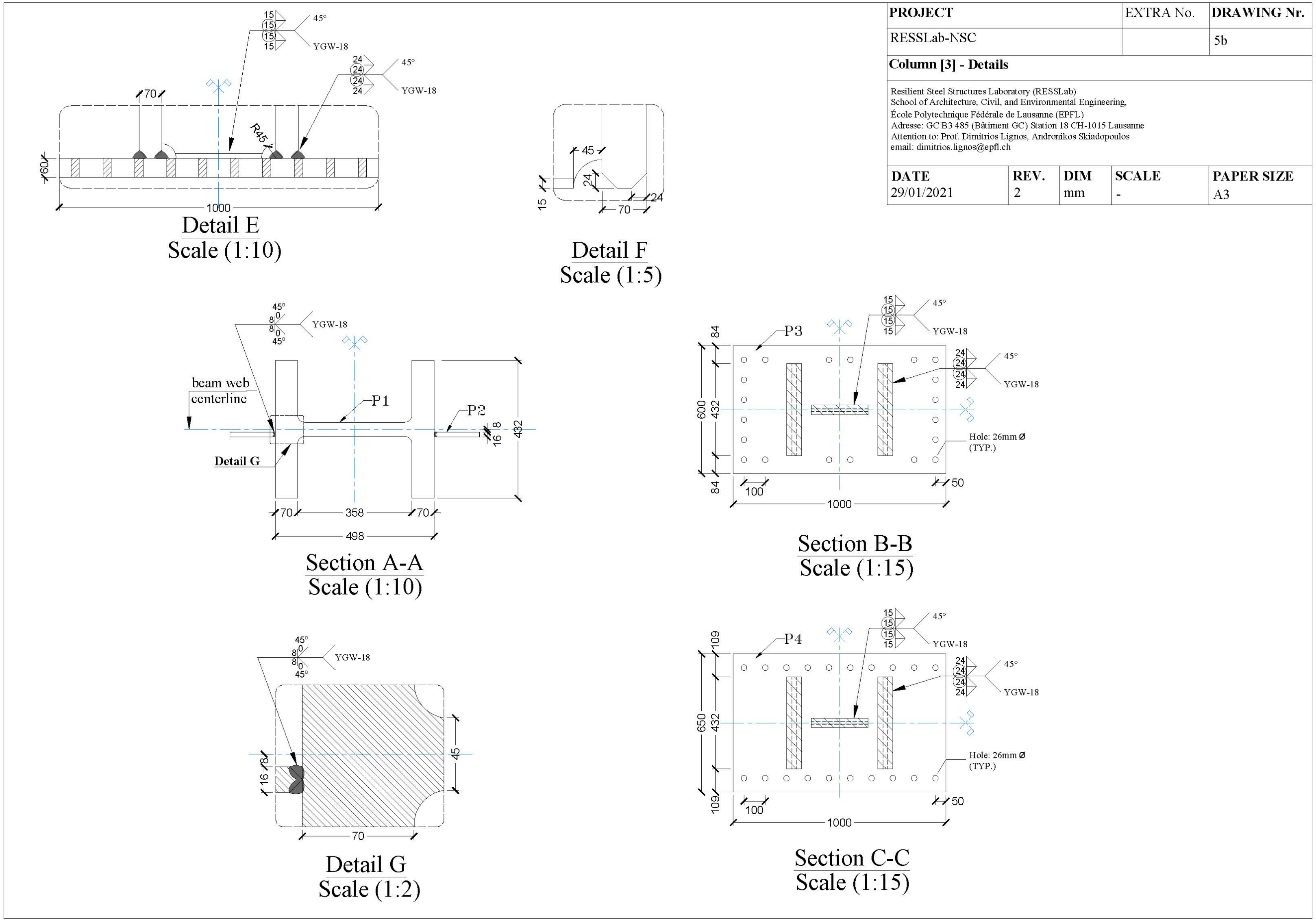

PROJECT	EXTRA No.	DRAWING Nr.
RESSLab-NSC		5b
Column [3] - Details		

Resilient Steel Structures Laboratory (RESSLab)
School of Architecture, Civil, and Environmental Engineering,
École Polytechnique Fédérale de Lausanne (EPFL)
Adresse: GC B3 485 (Bâtiment GC) Station 18 CH-1015 Lausanne
Attention to: Prof. Dimitrios Lignos, Andronikos Skiadopoulos
email: dimitrios.lignos@epfl.ch

DATE	REV.	DIM	SCALE	PAPER SIZE
29/01/2021	2	mm	-	A3

Detail E
Scale (1:10)
15
15
15
15
45°
YGW-18
24
24
24
24
45°
YGW-18
70
R45
60
1000
Detail F
Scale (1:5)
45
24
15
70
24
Section A-A
Scale (1:10)
45°
8
0
8
0
45°
YGW-18
beam web
centerline
P1
P2
Detail G
16
8
432
70
358
70
498
Section B-B
Scale (1:15)
P3
84
600
432
84
100
1000
50
Hole: 26mm Ø
(TYP.)
Detail G
Scale (1:2)
45
16
8
70
Section C-C
Scale (1:15)
P4
109
650
432
109
100
1000
50
Hole: 26mm Ø
(TYP.)

Figure A.7 Test specimen column weld drawings.

ITEM	QUAN	DESCRIPTION	LENGTH [mm]	WEIGHT [kg]	REMARKS	MATERIAL
P1	2	800x600x80	-	304	To be used for both specimens	SN490A

PROJECT	EXTRA No.	DRAWING Nr.
RESSLab-NSC		6

Actuator adapter plate [4]

Resilient Steel Structures Laboratory (RESSLab)
School of Architecture, Civil, and Environmental Engineering,
École Polytechnique Fédérale de Lausanne (EPFL)
Adresse: GC B3 485 (Bâtiment GC) Station 18 CH-1015 Lausanne
Attention to: Prof. Dimitrios Lignos, Andronikos Skiadopoulos
email: dimitrios.lignos@epfl.ch

DATE	REV.	DIM	SCALE	PAPER SIZE
29/01/2021	2	mm	1:15	A3

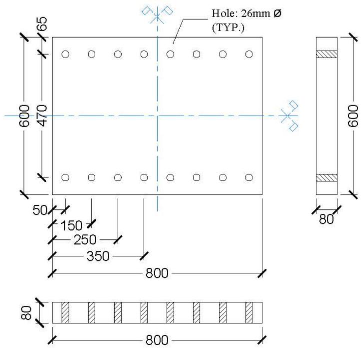

Piece P1
Scale (1:15)

Figure A.8 Test specimen actuator adapter plate drawings.

LIST OF BOLTS

QUAN	TYPE x Length - Class	Threaded length (mm)	Remarks	Comments	Use
8	M24 x 75mm - F10T	45 TYP.	1 Nut + 2 Washers per bolt		erection bolts
40	M24 x 205mm - F10T	45 TYP.	1 Nut + 2 Washers per bolt	To be used for both specimens	column adapter plate-to-pin

LIST OF RODS

QUAN	diameter x Length - Class	Remarks	Comments	Use
32	24mm x 950mm - F10T	2 Nuts + 2 Washers per rod	To be used for both specimens	actuator clamping rods

PROJECT		EXTRA No.		**DRAWING Nr.**
RESSLab-NSC				7
List of bolts and rods				
Resilient Steel Structures Laboratory (RESSLab) School of Architecture, Civil, and Environmental Engineering, École Polytechnique Fédérale de Lausanne (EPFL) Adresse: GC B3 485 (Bâtiment GC) Station 18 CH-1015 Lausanne Attention to: Prof. Dimitrios Lignos, Andronikos Skiadopoulos email: dimitrios.lignos@epfl.ch				
DATE 29/01/2021	**REV.** 2			**PAPER SIZE** A3

Figure A.9 Test specimen list of bolts and rods.

Appendix B. Design drawings of the test specimen lateral support system

Description

This appendix includes the design drawings of the test specimen lateral support system described in Chapter 5.

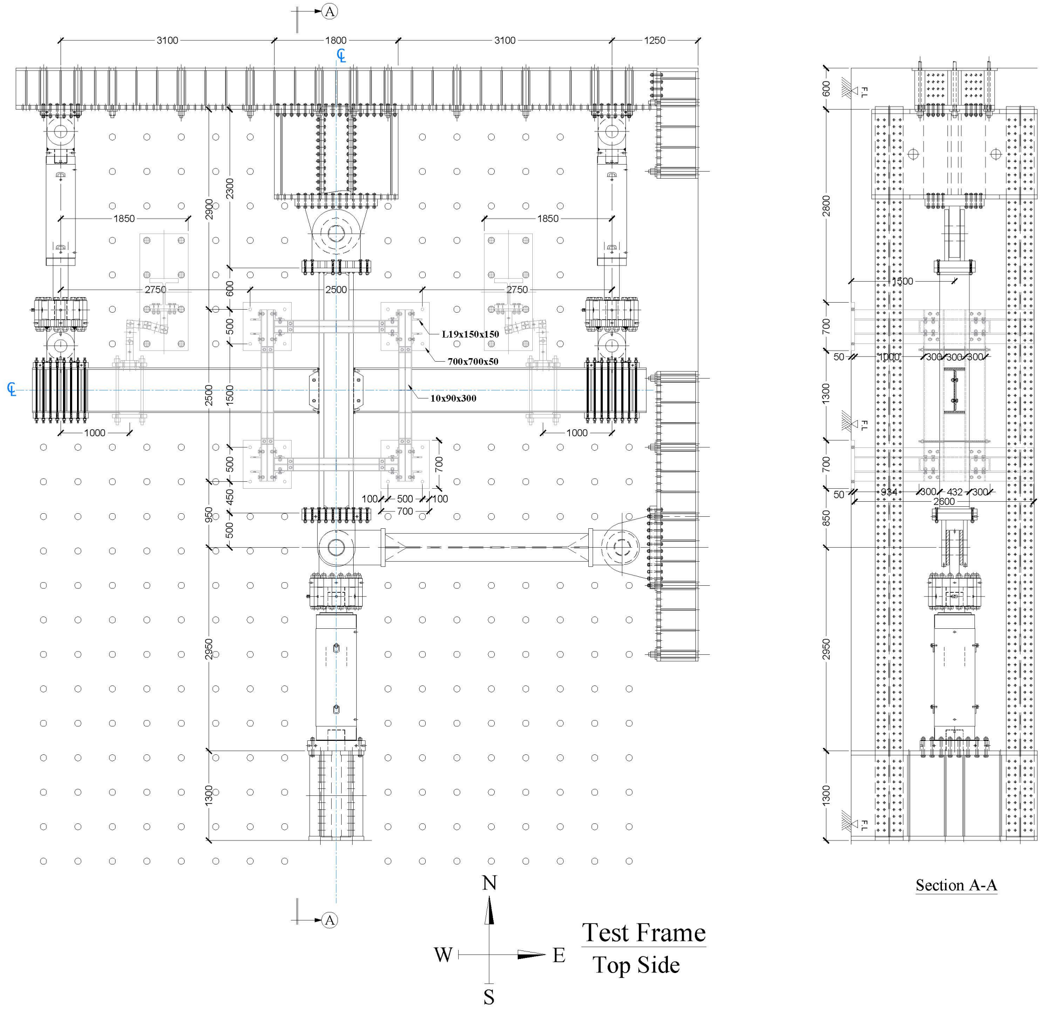
A
3100
1800
3100
1250
℄
2900
2300
1850
1850
2750
2500
2750
600
500
L19x150x150
700x700x50
10x90x300
2500
1500
1000
1000
500
450
700
100
500
100
700
950
500
2950
1300
A
N
W
E
S
Test Frame
Top Side
600
F.L.
2800
1500
700
50
1000
300
300
300
1300
F.L.
700
50
934
300
432
300
2600
850
2950
1300
F.L.
Section A-A

PROJECT	EXTRA No.	DRAWING Nr.
RESSLab-NSC		0

Lateral Support System - General Plan

Resilient Steel Structures Laboratory (RESSLab)
School of Architecture, Civil, and Environmental Engineering,
École Polytechnique Fédérale de Lausanne (EPFL)
Adresse: GC B3 485 (Bâtiment GC) Station 18 CH-1015 Lausanne
Attention to: Prof. Dimitrios Lignos, Andronikos Skiadopoulos
email: dimitrios.lignos@epfl.ch

DATE	REV.	DIM	SCALE	PAPER SIZE
26/02/2021	2	mm	1:40	A2

DRAWINGS

ID	DESCRIPTION	DRAWING
0	Lateral Support System - General Plan	0
1	Lateral Support System - Overview	1
2	Lateral Support System - Piece Locations	2
3	Lateral Support System - Angle Overview	3
4	Lateral Support System - Angle P1	4
5	Lateral Support System - Angle P2	5
6	Lateral Support System - Angle P3	6
7	Lateral Support System - Beam P4	7
8	Lateral Support System - Beam P5	8
9	List of bolts and rods	9

Figure B.1 Lateral support system general plan drawings.

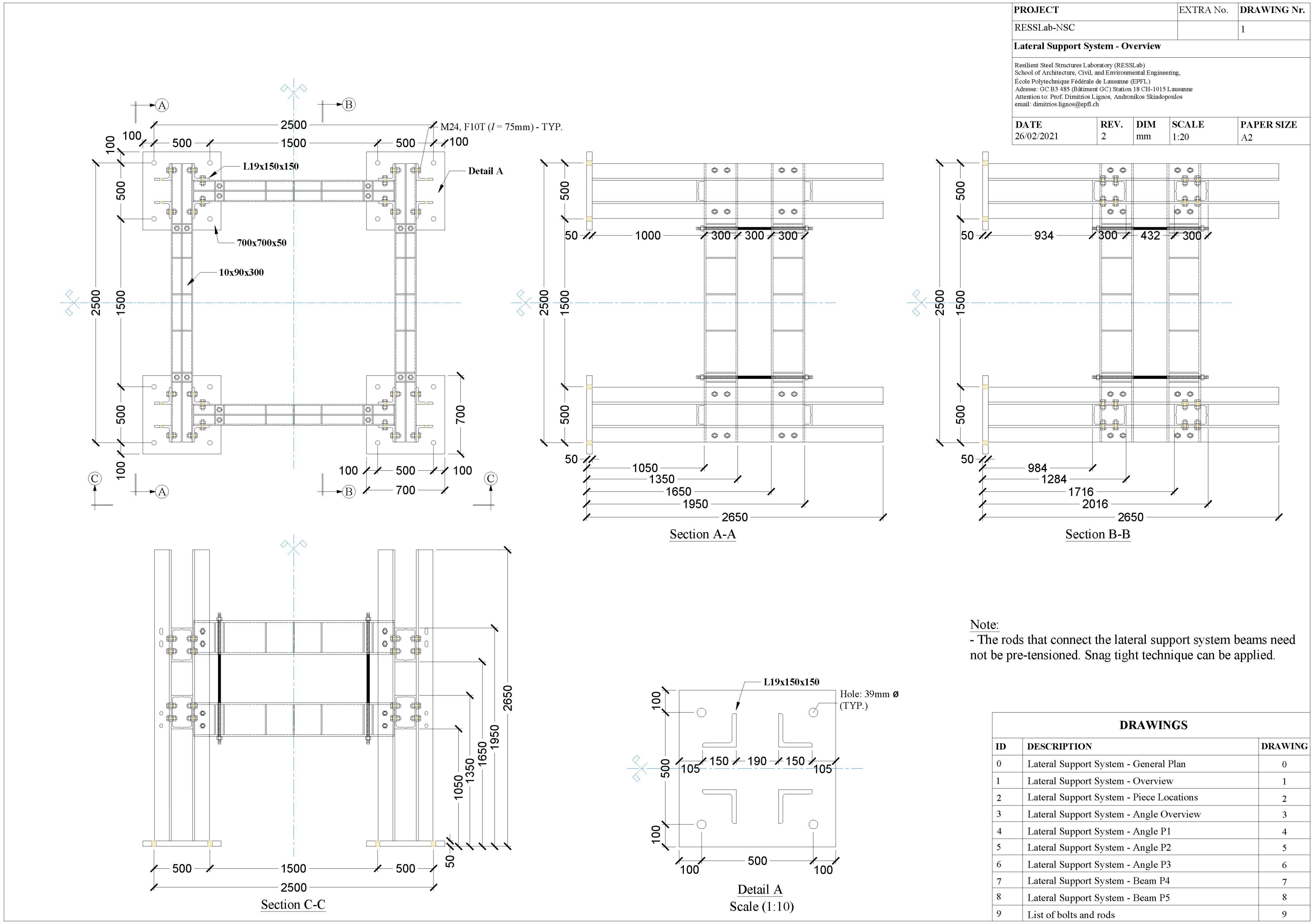
A
B
C
2500
100
500
1500
500
100
M24, F10T (*l* = 75mm) - TYP.
L19x150x150
Detail A
700x700x50
10x90x300
700
1000
300
934
432
50
1050
1350
1650
1950
2650
984
1284
1716
2016
Section A-A
Section B-B
Section C-C
Hole: 39mm ø (TYP.)
105
150
190
Detail A
Scale (1:10)

PROJECT	EXTRA No.	DRAWING Nr.
RESSLab-NSC		1

Lateral Support System - Overview

Resilient Steel Structures Laboratory (RESSLab)
School of Architecture, Civil, and Environmental Engineering,
École Polytechnique Fédérale de Lausanne (EPFL)
Adresse: GC B3 485 (Bâtiment GC) Station 18 CH-1015 Lausanne
Attention to: Prof. Dimitrios Lignos, Andronikos Skiadopoulos
email: dimitrios.lignos@epfl.ch

DATE	REV.	DIM	SCALE	PAPER SIZE
26/02/2021	2	mm	1:20	A2

Note:
- The rods that connect the lateral support system beams need not be pre-tensioned. Snag tight technique can be applied.

DRAWINGS

ID	DESCRIPTION	DRAWING
0	Lateral Support System - General Plan	0
1	Lateral Support System - Overview	1
2	Lateral Support System - Piece Locations	2
3	Lateral Support System - Angle Overview	3
4	Lateral Support System - Angle P1	4
5	Lateral Support System - Angle P2	5
6	Lateral Support System - Angle P3	6
7	Lateral Support System - Beam P4	7
8	Lateral Support System - Beam P5	8
9	List of bolts and rods	9

Figure B.2 Lateral support system overview drawings.

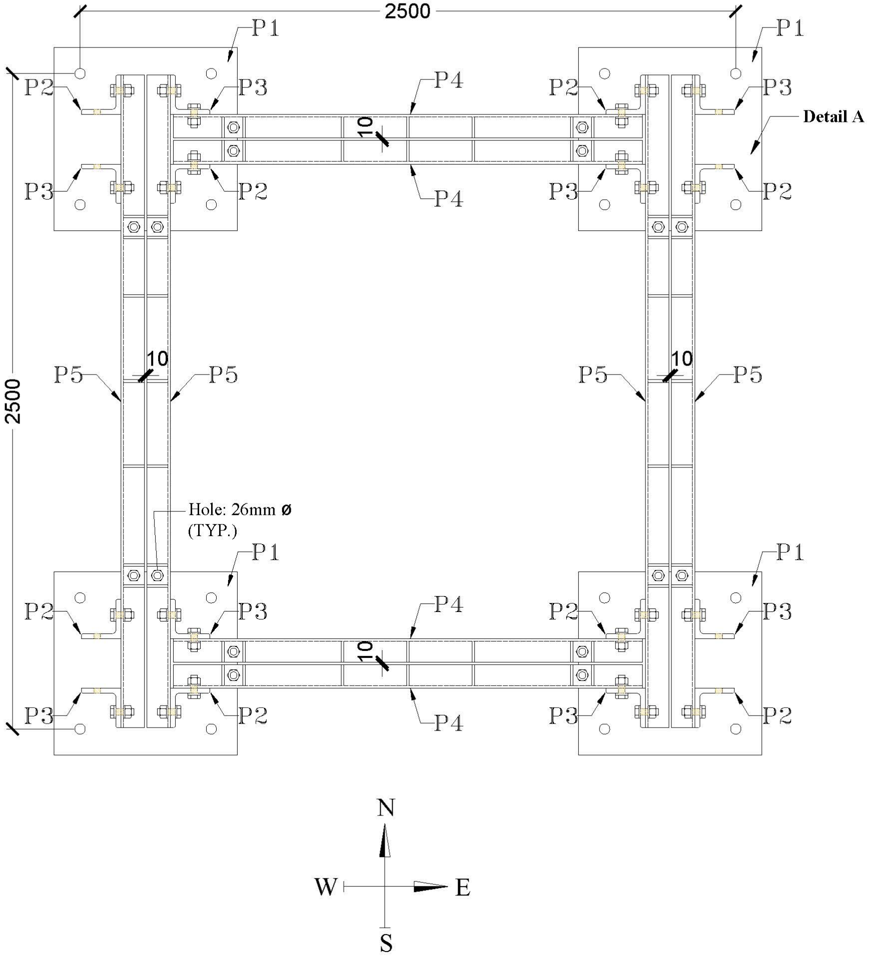

PROJECT	EXTRA No.	**DRAWING Nr.**
RESSLab-NSC		2

Lateral Support System - Piece Locations

Resilient Steel Structures Laboratory (RESSLab)
School of Architecture, Civil, and Environmental Engineering,
École Polytechnique Fédérale de Lausanne (EPFL)
Adresse: GC B3 485 (Bâtiment GC) Station 18 CH-1015 Lausanne
Attention to: Prof. Dimitrios Lignos, Andronikos Skiadopoulos
email: dimitrios.lignos@epfl.ch

DATE	**REV.**	**DIM**	**SCALE**	**PAPER SIZE**
26/02/2021	2	mm	1:15	A3

DRAWINGS

ID	**DESCRIPTION**	**DRAWING**
0	Lateral Support System - General Plan	0
1	Lateral Support System - Overview	1
2	Lateral Support System - Piece Locations	2
3	Lateral Support System - Angle Overview	3
4	Lateral Support System - Angle P1	4
5	Lateral Support System - Angle P2	5
6	Lateral Support System - Angle P3	6
7	Lateral Support System - Beam P4	7
8	Lateral Support System - Beam P5	8
9	List of bolts and rods	9

Figure B.3 Lateral support system piece location drawings.

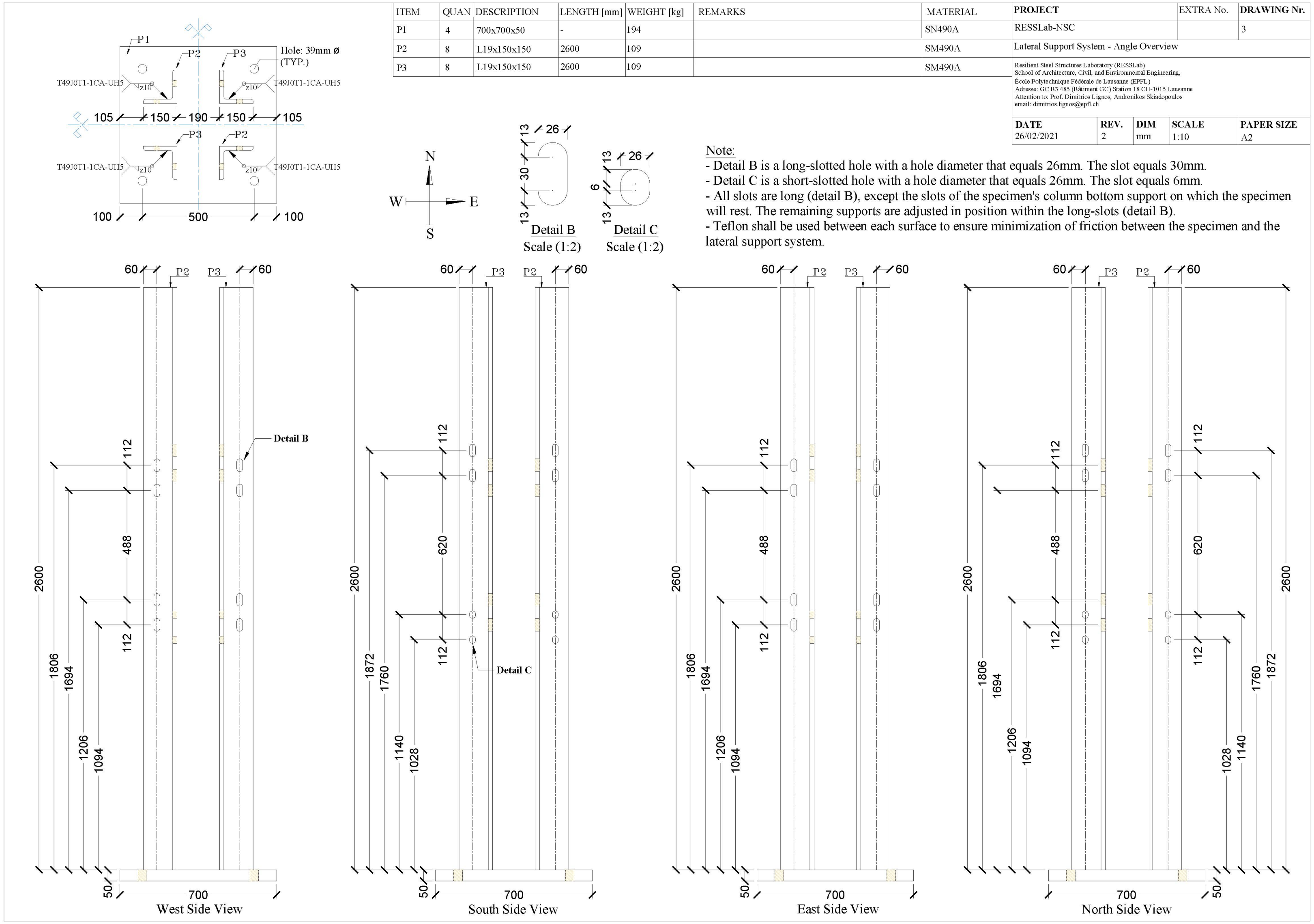

ITEM	QUAN	DESCRIPTION	LENGTH [mm]	WEIGHT [kg]	REMARKS	MATERIAL
P1	4	700x700x50	-	194		SN490A
P2	8	L19x150x150	2600	109		SM490A
P3	8	L19x150x150	2600	109		SM490A

PROJECT	EXTRA No.	**DRAWING Nr.**
RESSLab-NSC		3

Lateral Support System - Angle Overview

Resilient Steel Structures Laboratory (RESSLab)
School of Architecture, Civil, and Environmental Engineering,
École Polytechnique Fédérale de Lausanne (EPFL)
Adresse: GC B3 485 (Bâtiment GC) Station 18 CH-1015 Lausanne
Attention to: Prof. Dimitrios Lignos, Andronikos Skiadopoulos
email: dimitrios.lignos@epfl.ch

DATE	**REV.**	**DIM**	**SCALE**	**PAPER SIZE**
26/02/2021	2	mm	1:10	A2

Note:
- Detail B is a long-slotted hole with a hole diameter that equals 26mm. The slot equals 30mm.
- Detail C is a short-slotted hole with a hole diameter that equals 26mm. The slot equals 6mm.
- All slots are long (detail B), except the slots of the specimen's column bottom support on which the specimen will rest. The remaining supports are adjusted in position within the long-slots (detail B).
- Teflon shall be used between each surface to ensure minimization of friction between the specimen and the lateral support system.

P1
P2
P3
Hole: 39mm ø
(TYP.)
T49J0T1-1CA-UH5
z10
105
150
190
150
105
100
500
100
N
W
E
S
13
26
30
Detail B
Scale (1:2)
6
Detail C
Scale (1:2)
60
2600
1806
1694
1206
1094
112
488
620
1872
1760
1140
1028
50
700
West Side View
South Side View
East Side View
North Side View

Figure B.4 Lateral support system angle overview drawings.

ITEM	QUAN	DESCRIPTION	LENGTH [mm]	WEIGHT [kg]	REMARKS	MATERIAL
P1	4	700x700x50	-	194		SN490A

PROJECT	EXTRA No.	DRAWING Nr.
RESSLab-NSC		4

Lateral Support System - Angle P1

Resilient Steel Structures Laboratory (RESSLab)
School of Architecture, Civil, and Environmental Engineering,
École Polytechnique Fédérale de Lausanne (EPFL)
Adresse: GC B3 485 (Bâtiment GC) Station 18 CH-1015 Lausanne
Attention to: Prof. Dimitrios Lignos, Andronikos Skiadopoulos
email: dimitrios.lignos@epfl.ch

DATE	REV.	DIM	SCALE	PAPER SIZE
26/02/2021	2	mm	1:10	A3

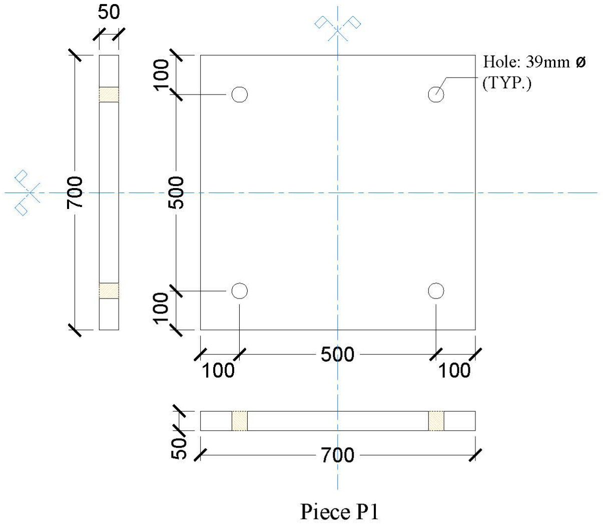

Figure B.5 Lateral support system angle P1 drawings.

ITEM	QUAN	DESCRIPTION	LENGTH [mm]	WEIGHT [kg]	REMARKS	MATERIAL
P2	8	L19x150x150	2600	109		SM490A

PROJECT	EXTRA No.	**DRAWING Nr.**
RESSLab-NSC		5

Lateral Support System - Angle P2

Resilient Steel Structures Laboratory (RESSLab)
School of Architecture, Civil, and Environmental Engineering,
École Polytechnique Fédérale de Lausanne (EPFL)
Adresse: GC B3 485 (Bâtiment GC) Station 18 CH-1015 Lausanne
Attention to: Prof. Dimitrios Lignos, Andronikos Skiadopoulos
email: dimitrios.lignos@epfl.ch

DATE	**REV.**	**DIM**	**SCALE**	**PAPER SIZE**
26/02/2021	2	mm	1:10	A3

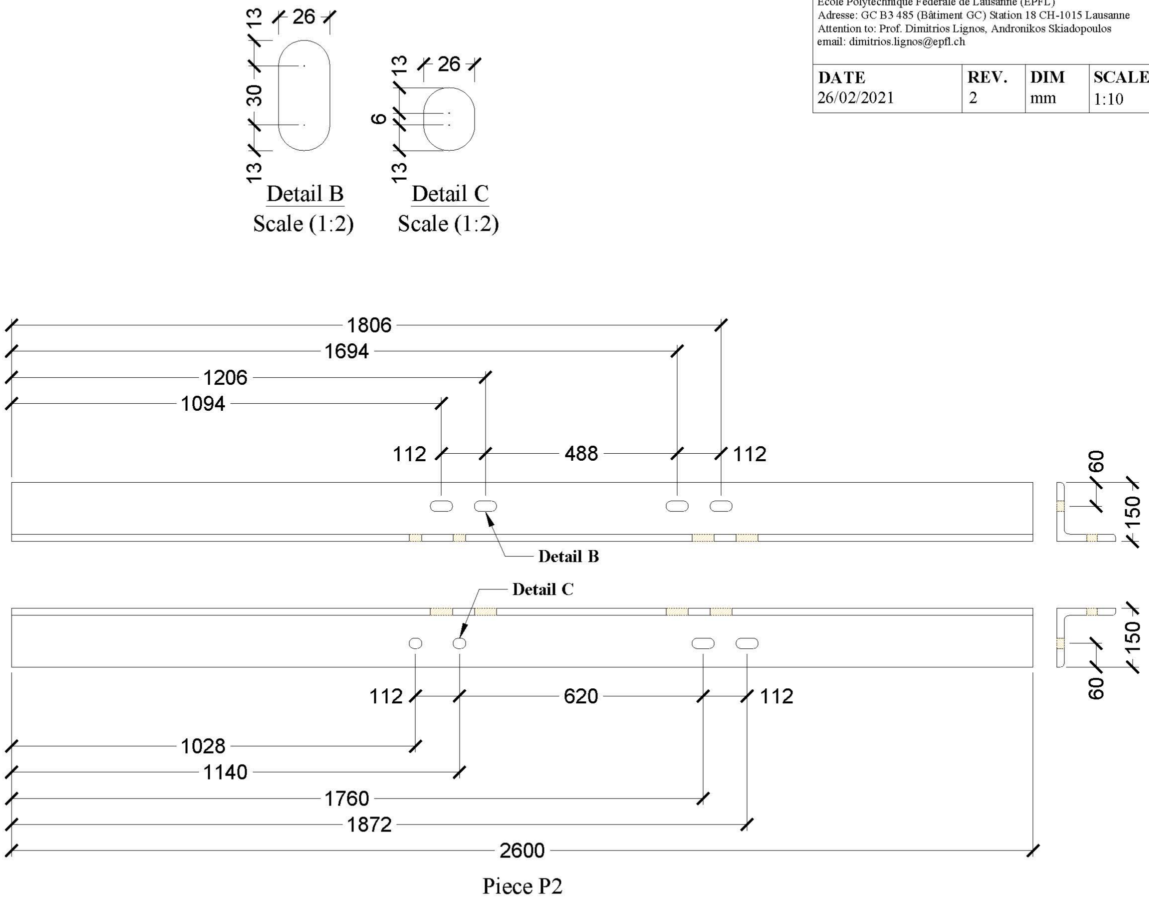
13
26
30
13
Detail B
Scale (1:2)
13
26
6
13
Detail C
Scale (1:2)
1806
1694
1206
1094
112
488
112
60
150
Detail B
Detail C
150
60
112
620
112
1028
1140
1760
1872
2600
Piece P2

Figure B.6 Lateral support system angle P2 drawings.

ITEM	QUAN	DESCRIPTION	LENGTH [mm]	WEIGHT [kg]	REMARKS	MATERIAL
P3	8	L19x150x150	2600	109		SM490A

PROJECT	EXTRA No.	DRAWING Nr.
RESSLab-NSC		6

Lateral Support System - Angle P3

Resilient Steel Structures Laboratory (RESSLab)
School of Architecture, Civil, and Environmental Engineering,
École Polytechnique Fédérale de Lausanne (EPFL)
Adresse: GC B3 485 (Bâtiment GC) Station 18 CH-1015 Lausanne
Attention to: Prof. Dimitrios Lignos, Andronikos Skiadopoulos
email: dimitrios.lignos@epfl.ch

DATE	REV.	DIM	SCALE	PAPER SIZE
26/02/2021	2	mm	1:10	A3

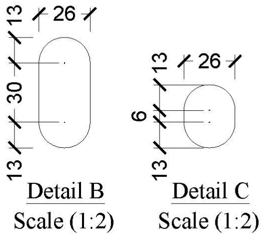
13
26
30
13
Detail B
Scale (1:2)
13
26
6
13
Detail C
Scale (1:2)

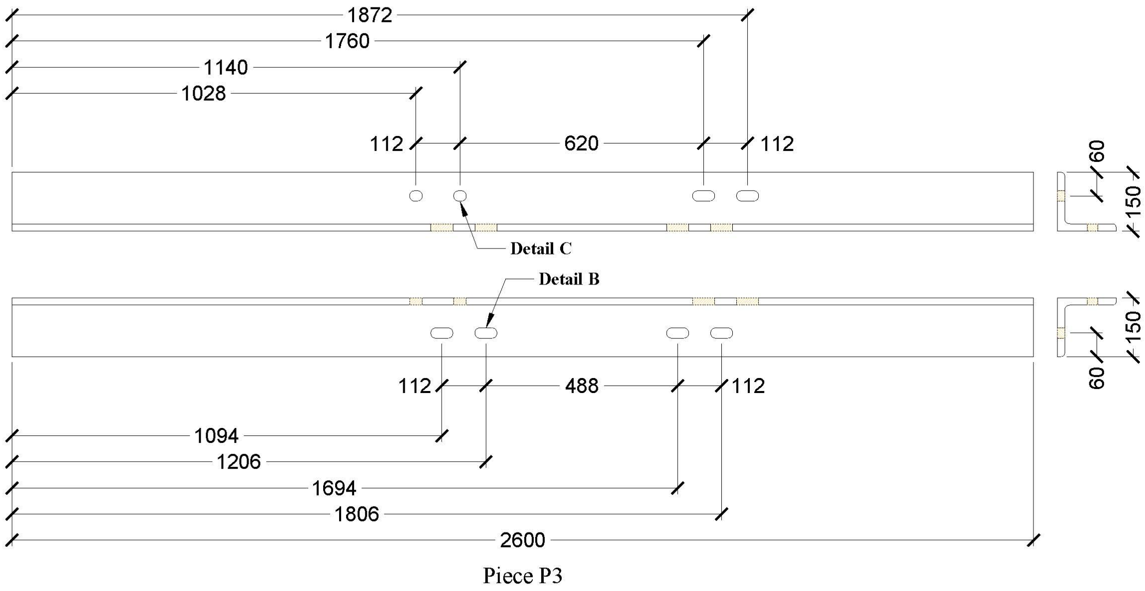
1872
1760
1140
1028
112
620
112
60
150
Detail C
Detail B
150
60
112
488
112
1094
1206
1694
1806
2600
Piece P3

Figure B.7 Lateral support system angle P3 drawings.

ITEM	QUAN	DESCRIPTION	LENGTH [mm]	WEIGHT [kg]	REMARKS	MATERIAL
P4	8	10x90x300	1790	79		SM490A
P6	112	10x71x269	-	2	Four stiffeners per P4 are needed (7*8 = 56) and four per P5 (56+56 = 112 in total)	SN490A

PROJECT	EXTRA No.	DRAWING Nr.
RESSLab-NSC		7
Lateral Support System - Beam P4		

Resilient Steel Structures Laboratory (RESSLab)
School of Architecture, Civil, and Environmental Engineering,
École Polytechnique Fédérale de Lausanne (EPFL)
Adresse: GC B3 485 (Bâtiment GC) Station 18 CH-1015 Lausanne
Attention to: Prof. Dimitrios Lignos, Andronikos Skiadopoulos
email: dimitrios.lignos@epfl.ch

DATE	REV.	DIM	SCALE	PAPER SIZE
26/02/2021	2	mm	1:10	A3

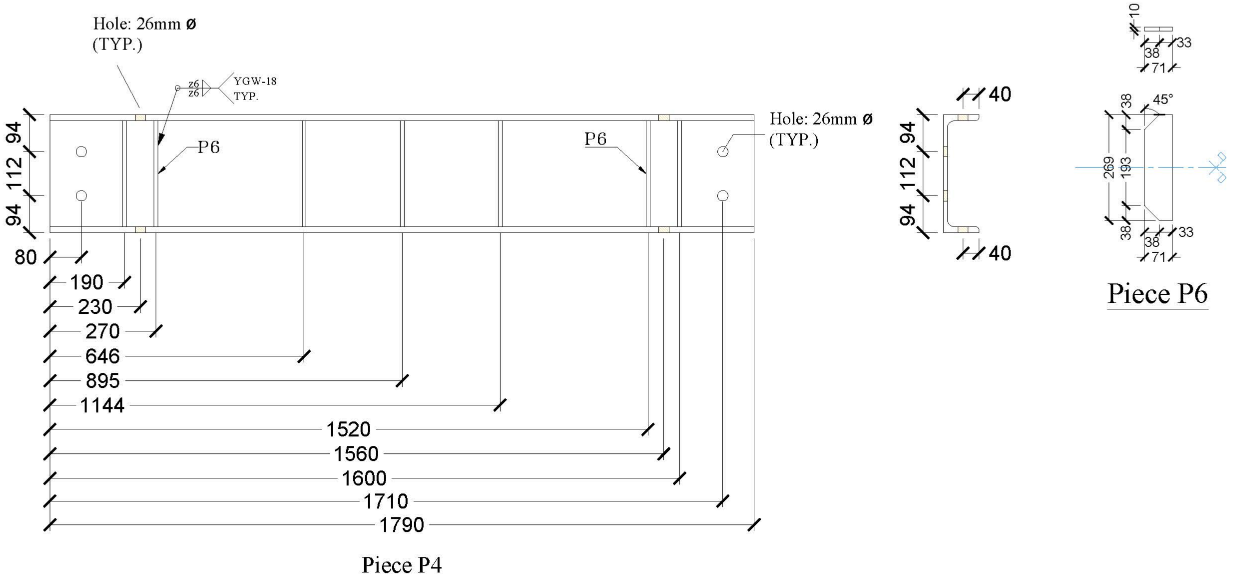
Hole: 26mm ø
(TYP.)
z6
z6
YGW-18
TYP.
P6
P6
Hole: 26mm ø
(TYP.)
94
112
94
80
190
230
270
646
895
1144
1520
1560
1600
1710
1790
Piece P4
40
94
112
94
40
10
38
33
71
38
45°
269
193
38
38
33
71
Piece P6

Figure B.8 Lateral support system beam P4 drawings.

ITEM	QUAN	DESCRIPTION	LENGTH [mm]	WEIGHT [kg]	REMARKS	MATERIAL
P5	8	10x90x300	2490	109		SM490A
P6	112	10x71x269	-	2	Four stiffeners per P4 are needed (7*8 = 56) and four per P5 (56+56 = 112 in total)	SN490A

PROJECT				EXTRA No.	DRAWING Nr.
RESSLab-NSC					8
Lateral Support System - Beam P5					

Resilient Steel Structures Laboratory (RESSLab)
School of Architecture, Civil, and Environmental Engineering,
École Polytechnique Fédérale de Lausanne (EPFL)
Adresse: GC B3 485 (Bâtiment GC) Station 18 CH-1015 Lausanne
Attention to: Prof. Dimitrios Lignos, Andronikos Skiadopoulos
email: dimitrios.lignos@epfl.ch

DATE	REV.	DIM	SCALE	PAPER SIZE
26/02/2021	2	mm	1:10	A3

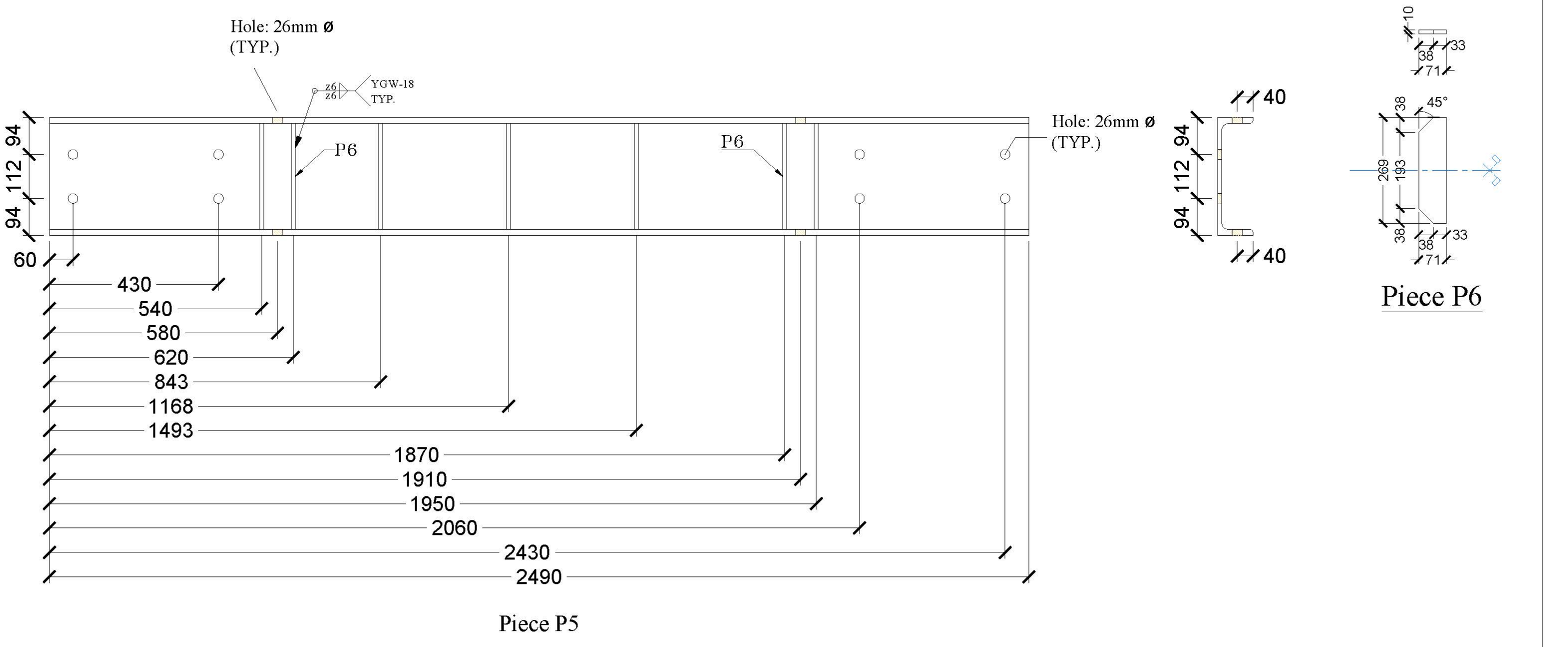
Hole: 26mm ø
(TYP.)
z6
z6
YGW-18
TYP.
P6
P6
Hole: 26mm ø
(TYP.)
94
112
94
60
430
540
580
620
843
1168
1493
1870
1910
1950
2060
2430
2490
Piece P5
40
94
112
94
40
10
33
38
71
38
45°
269
193
38
33
38
71
Piece P6

Figure B.9 Lateral support system beam P5 drawings.

LIST OF BOLTS

QUAN	TYPE x Length - Class	Threaded length (mm)	Remarks	Comments	Use
96	M24 x 75mm - F10T	45 TYP.	1 Nut + 2 Washers per bolt	To be used for both specimens	lateral support system bolts

LIST OF RODS

QUAN	diameter x Length - Class	Remarks	Comments	Use
8	24mm diameter - F10T (1040mm)	2 Nuts + 2 Washers per rod	To be used for both specimens	clamping rods
8	24mm diameter - F10T (1170mm)	2 Nuts + 2 Washers per rod	To be used for both specimens	clamping rods
16	36mm diameter - F10T	2 Nuts + 2 Washers per rod	To be used for both specimens	plate-to-ground connection

The length of the rods to be determined by NSC based on
the floor depth and the 50mm lateral support system plate.

PROJECT	EXTRA No.	**DRAWING Nr.**
RESSLab-NSC		9

List of bolts and rods

Resilient Steel Structures Laboratory (RESSLab)
School of Architecture, Civil, and Environmental Engineering,
École Polytechnique Fédérale de Lausanne (EPFL)
Adresse: GC B3 485 (Bâtiment GC) Station 18 CH-1015 Lausanne
Attention to: Prof. Dimitrios Lignos, Andronikos Skiadopoulos
email: dimitrios.lignos@epfl.ch

DATE	**REV.**			**PAPER SIZE**
26/02/2021	2			A3

Figure B.10 Lateral support system list of bolts and rods.

Appendix C. Detailed instrumentation plan

Description

This appendix includes the drawings of the instrumentation plan described in Chapter 5.

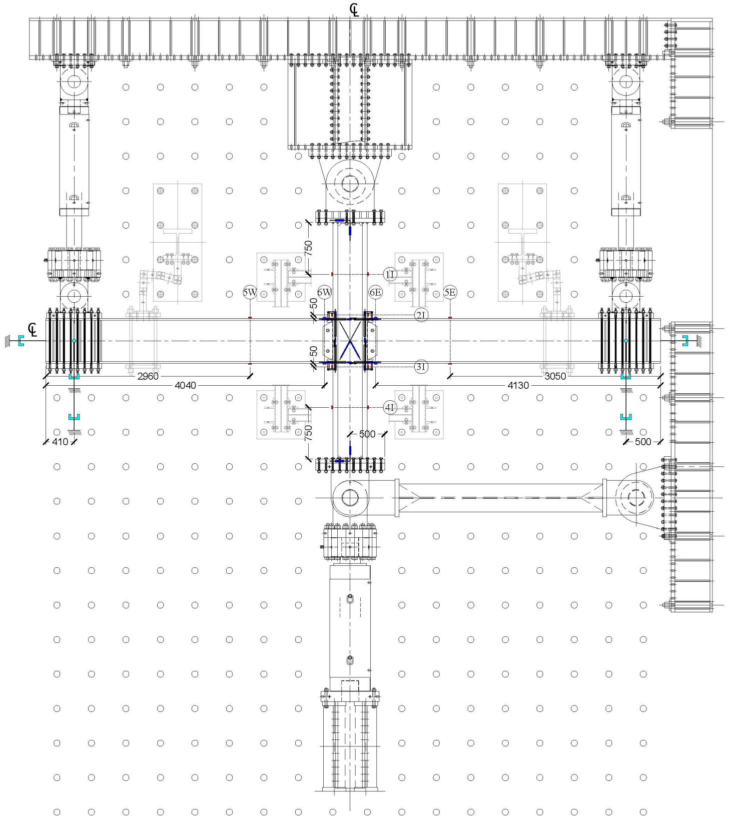

SYMBOL	DEFINITION
● or ⊏—	String Pot
▬	Strain Gauge
● or —●—	Potentiometer
▨	Rosette
● or ▬	LVDT

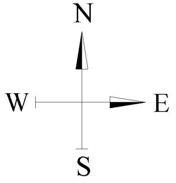

SUBASSEMBLY DRAWINGS	
DESCRIPTION	DRAWING
Strain Gauges - Column	1
Strain Gauges - West Beam	2
Strain Gauges - East Beam	3
Instrumentation - LVDTs (Part A)	4
Instrumentation - LVDTs (Part B)	5
Instrumentation - LVDTs (Part C)	6
Instrumentation - Rosette/Potentiometers	7
Instrumentation - Beam Ends	8

Test Frame
Top Side

PROJECT	EXTRA No.	DRAWING Nr.
RESSLab-NSC		0a

General Plan - Top Side

Resilient Steel Structures Laboratory (RESSLab)
School of Architecture, Civil, and Environmental Engineering,
École Polytechnique Fédérale de Lausanne (EPFL)
Adresse: GC B3 485 (Bâtiment GC) Station 18 CH-1015 Lausanne
Attention to: Prof. Dimitrios Lignos, Andronikos Skiadopoulos
email: dimitrios.lignos@epfl.ch

DATE	REV.	DIM	SCALE	PAPER SIZE
10/10/2021	3	mm	1:40	A2

Figure C.1 Instrumentation plan – top side general plan drawings.

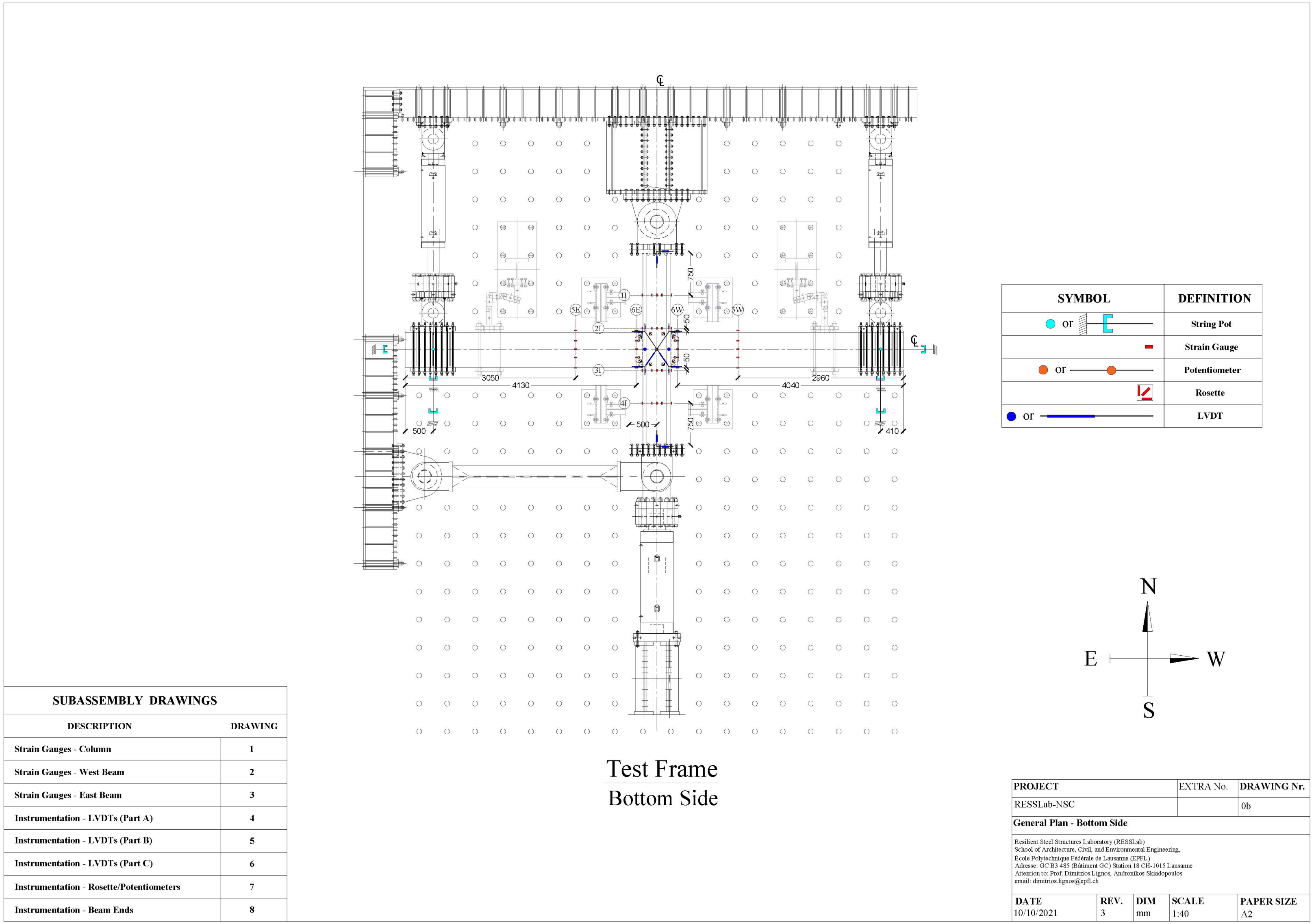

SYMBOL	DEFINITION
● or	String Pot
▬	Strain Gauge
● or	Potentiometer
	Rosette
● or	LVDT

SUBASSEMBLY DRAWINGS

DESCRIPTION	DRAWING
Strain Gauges - Column	1
Strain Gauges - West Beam	2
Strain Gauges - East Beam	3
Instrumentation - LVDTs (Part A)	4
Instrumentation - LVDTs (Part B)	5
Instrumentation - LVDTs (Part C)	6
Instrumentation - Rosette/Potentiometers	7
Instrumentation - Beam Ends	8

PROJECT	EXTRA No.	DRAWING Nr.
RESSLab-NSC		0b

General Plan - Bottom Side

Resilient Steel Structures Laboratory (RESSLab)
School of Architecture, Civil, and Environmental Engineering,
École Polytechnique Fédérale de Lausanne (EPFL)
Adresse: GC B3 485 (Bâtiment GC) Station 18 CH-1015 Lausanne
Attention to: Prof. Dimitrios Lignos, Andronikos Skiadopoulos
email: dimitrios.lignos@epfl.ch

DATE	REV.	DIM	SCALE	PAPER SIZE
10/10/2021	3	mm	1:40	A2

Figure C.2 Instrumentation plan – bottom side general plan drawings.

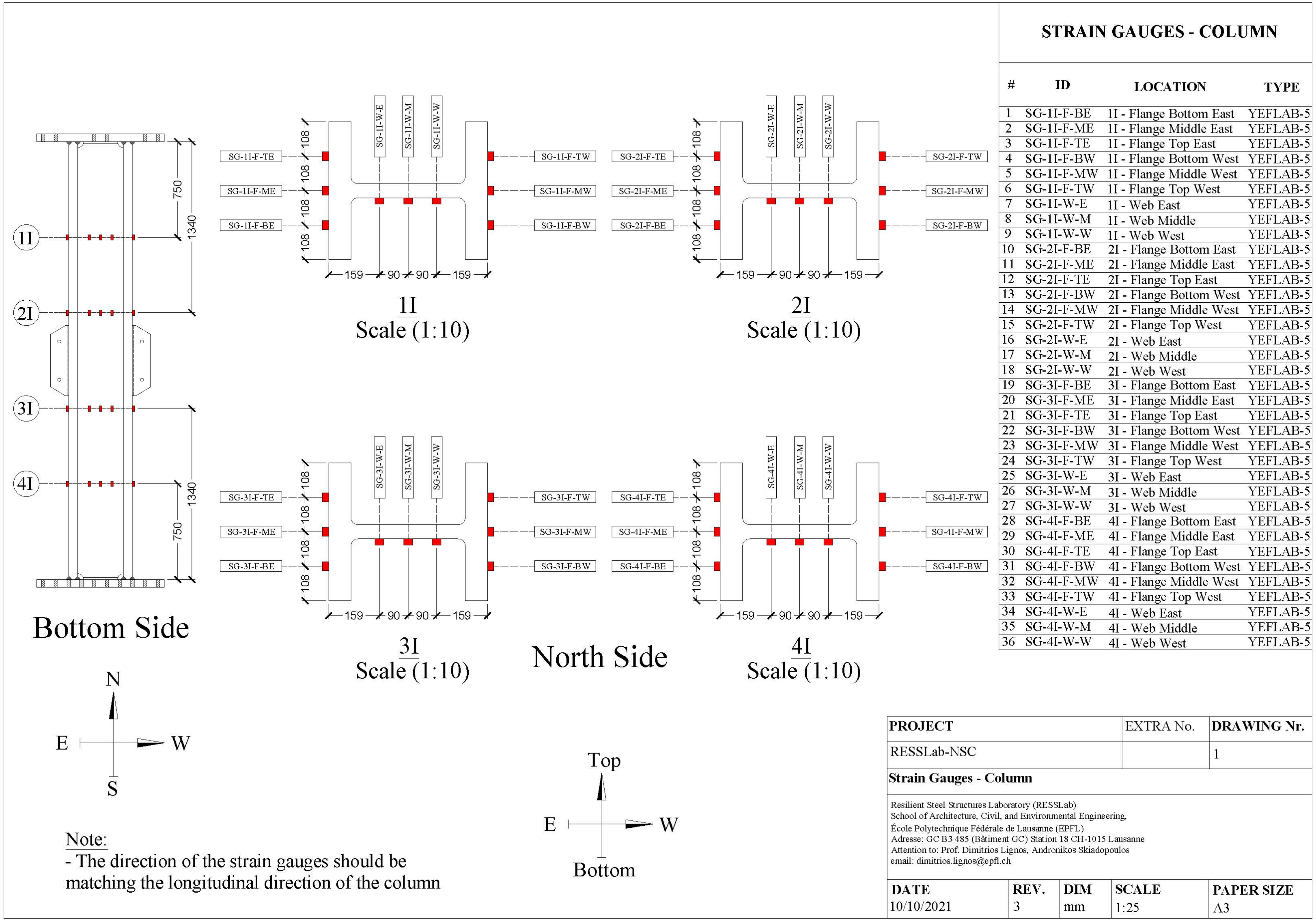
SG-1I-W-E
SG-1I-W-M
SG-1I-W-W
SG-1I-F-TE
SG-1I-F-ME
SG-1I-F-BE
SG-1I-F-TW
SG-1I-F-MW
SG-1I-F-BW
108
108
108
108
159
90
90
159
1I
Scale (1:10)
SG-2I-W-E
SG-2I-W-M
SG-2I-W-W
SG-2I-F-TE
SG-2I-F-ME
SG-2I-F-BE
SG-2I-F-TW
SG-2I-F-MW
SG-2I-F-BW
2I
Scale (1:10)
1I
2I
3I
4I
750
1340
1340
750
Bottom Side
SG-3I-W-E
SG-3I-W-M
SG-3I-W-W
SG-3I-F-TE
SG-3I-F-ME
SG-3I-F-BE
SG-3I-F-TW
SG-3I-F-MW
SG-3I-F-BW
3I
Scale (1:10)
North Side
SG-4I-W-E
SG-4I-W-M
SG-4I-W-W
SG-4I-F-TE
SG-4I-F-ME
SG-4I-F-BE
SG-4I-F-TW
SG-4I-F-MW
SG-4I-F-BW
4I
Scale (1:10)
N
E
W
S
Top
E
W
Bottom

Note:
- The direction of the strain gauges should be matching the longitudinal direction of the column

STRAIN GAUGES - COLUMN

#	ID	LOCATION	TYPE
1	SG-1I-F-BE	1I - Flange Bottom East	YEFLAB-5
2	SG-1I-F-ME	1I - Flange Middle East	YEFLAB-5
3	SG-1I-F-TE	1I - Flange Top East	YEFLAB-5
4	SG-1I-F-BW	1I - Flange Bottom West	YEFLAB-5
5	SG-1I-F-MW	1I - Flange Middle West	YEFLAB-5
6	SG-1I-F-TW	1I - Flange Top West	YEFLAB-5
7	SG-1I-W-E	1I - Web East	YEFLAB-5
8	SG-1I-W-M	1I - Web Middle	YEFLAB-5
9	SG-1I-W-W	1I - Web West	YEFLAB-5
10	SG-2I-F-BE	2I - Flange Bottom East	YEFLAB-5
11	SG-2I-F-ME	2I - Flange Middle East	YEFLAB-5
12	SG-2I-F-TE	2I - Flange Top East	YEFLAB-5
13	SG-2I-F-BW	2I - Flange Bottom West	YEFLAB-5
14	SG-2I-F-MW	2I - Flange Middle West	YEFLAB-5
15	SG-2I-F-TW	2I - Flange Top West	YEFLAB-5
16	SG-2I-W-E	2I - Web East	YEFLAB-5
17	SG-2I-W-M	2I - Web Middle	YEFLAB-5
18	SG-2I-W-W	2I - Web West	YEFLAB-5
19	SG-3I-F-BE	3I - Flange Bottom East	YEFLAB-5
20	SG-3I-F-ME	3I - Flange Middle East	YEFLAB-5
21	SG-3I-F-TE	3I - Flange Top East	YEFLAB-5
22	SG-3I-F-BW	3I - Flange Bottom West	YEFLAB-5
23	SG-3I-F-MW	3I - Flange Middle West	YEFLAB-5
24	SG-3I-F-TW	3I - Flange Top West	YEFLAB-5
25	SG-3I-W-E	3I - Web East	YEFLAB-5
26	SG-3I-W-M	3I - Web Middle	YEFLAB-5
27	SG-3I-W-W	3I - Web West	YEFLAB-5
28	SG-4I-F-BE	4I - Flange Bottom East	YEFLAB-5
29	SG-4I-F-ME	4I - Flange Middle East	YEFLAB-5
30	SG-4I-F-TE	4I - Flange Top East	YEFLAB-5
31	SG-4I-F-BW	4I - Flange Bottom West	YEFLAB-5
32	SG-4I-F-MW	4I - Flange Middle West	YEFLAB-5
33	SG-4I-F-TW	4I - Flange Top West	YEFLAB-5
34	SG-4I-W-E	4I - Web East	YEFLAB-5
35	SG-4I-W-M	4I - Web Middle	YEFLAB-5
36	SG-4I-W-W	4I - Web West	YEFLAB-5

PROJECT	EXTRA No.	**DRAWING Nr.**
RESSLab-NSC		1

Strain Gauges - Column

Resilient Steel Structures Laboratory (RESSLab)
School of Architecture, Civil, and Environmental Engineering,
École Polytechnique Fédérale de Lausanne (EPFL)
Adresse: GC B3 485 (Bâtiment GC) Station 18 CH-1015 Lausanne
Attention to: Prof. Dimitrios Lignos, Andronikos Skiadopoulos
email: dimitrios.lignos@epfl.ch

DATE	**REV.**	**DIM**	**SCALE**	**PAPER SIZE**
10/10/2021	3	mm	1:25	A3

Figure C.3 Instrumentation plan – column strain gauge drawings.

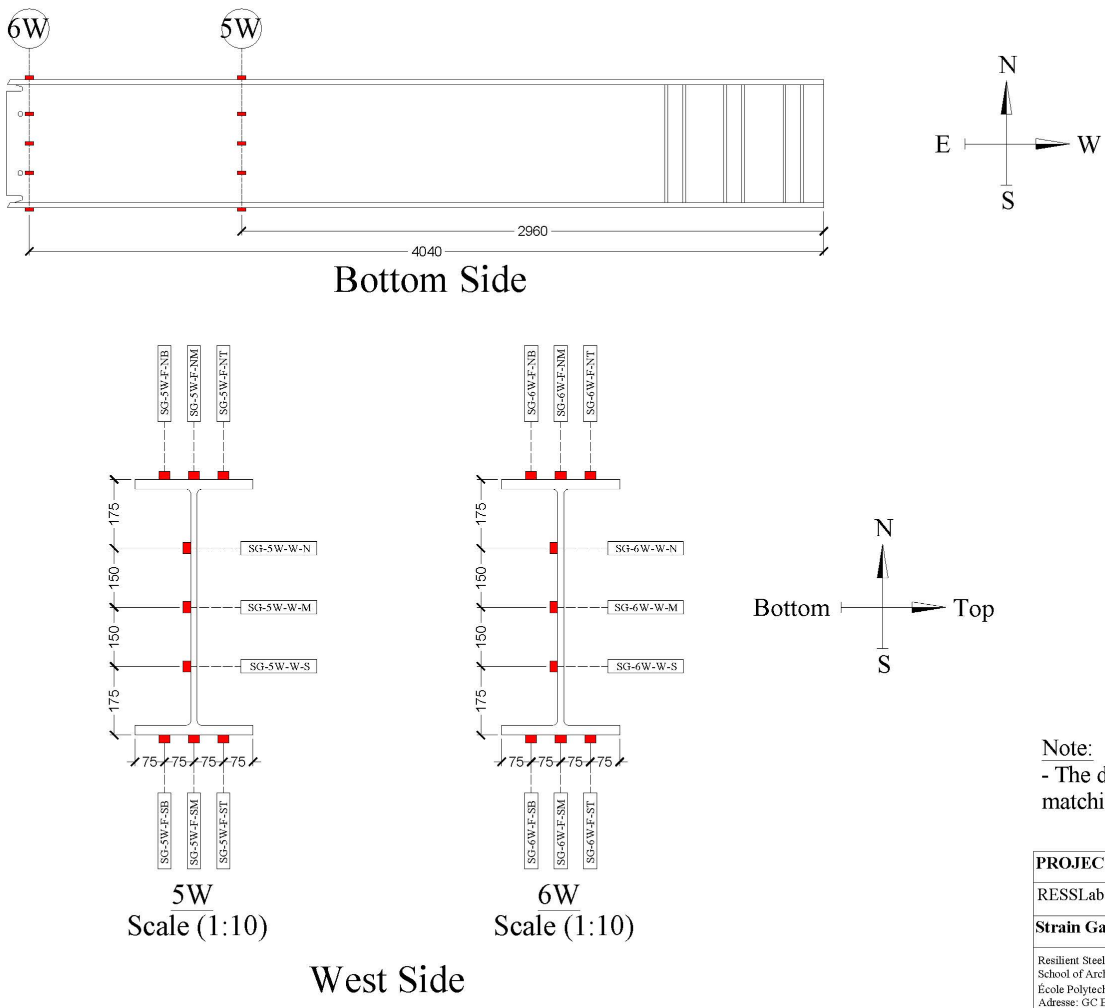
6W
5W
2960
4040
Bottom Side
N
E
W
S
SG-5W-F-NB
SG-5W-F-NM
SG-5W-F-NT
SG-6W-F-NB
SG-6W-F-NM
SG-6W-F-NT
175
150
150
175
SG-5W-W-N
SG-5W-W-M
SG-5W-W-S
SG-6W-W-N
SG-6W-W-M
SG-6W-W-S
75 75 75 75
SG-5W-F-SB
SG-5W-F-SM
SG-5W-F-ST
SG-6W-F-SB
SG-6W-F-SM
SG-6W-F-ST
5W
Scale (1:10)
6W
Scale (1:10)
West Side
N
Bottom
Top
S

STRAIN GAUGES - WEST BEAM

#	ID	LOCATION	TYPE
1	SG-5W-F-NB	5W - Flange North Bottom	YEFLAB-5
2	SG-5W-F-NM	5W - Flange North Middle	YEFLAB-5
3	SG-5W-F-NT	5W - Flange North Top	YEFLAB-5
4	SG-5W-F-SB	5W - Flange South Bottom	YEFLAB-5
5	SG-5W-F-SM	5W - Flange South Middle	YEFLAB-5
6	SG-5W-F-ST	5W - Flange South Top	YEFLAB-5
7	SG-5W-W-N	5W - Web North	YEFLAB-5
8	SG-5W-W-M	5W - Web Middle	YEFLAB-5
9	SG-5W-W-S	5W - Web South	YEFLAB-5
10	SG-6W-F-NB	6W - Flange North Bottom	YEFLAB-5
11	SG-6W-F-NM	6W - Flange North Middle	YEFLAB-5
12	SG-6W-F-NT	6W - Flange North Top	YEFLAB-5
13	SG-6W-F-SB	6W - Flange South Bottom	YEFLAB-5
14	SG-6W-F-SM	6W - Flange South Middle	YEFLAB-5
15	SG-6W-F-ST	6W - Flange South Top	YEFLAB-5
16	SG-6W-W-N	6W - Web North	YEFLAB-5
17	SG-6W-W-M	6W - Web Middle	YEFLAB-5
18	SG-6W-W-S	6W - Web South	YEFLAB-5

Note:
- The direction of the strain gauges should be matching the longitudinal direction of the beam

PROJECT	EXTRA No.	**DRAWING Nr.**
RESSLab-NSC		2

Strain Gauges - West Beam

Resilient Steel Structures Laboratory (RESSLab)
School of Architecture, Civil, and Environmental Engineering,
École Polytechnique Fédérale de Lausanne (EPFL)
Adresse: GC B3 485 (Bâtiment GC) Station 18 CH-1015 Lausanne
Attention to: Prof. Dimitrios Lignos, Andronikos Skiadopoulos
email: dimitrios.lignos@epfl.ch

DATE	**REV.**	**DIM**	**SCALE**	**PAPER SIZE**
10/10/2021	3	mm	1:20	A3

Figure C.4 Instrumentation plan – west beam strain gauge drawings.

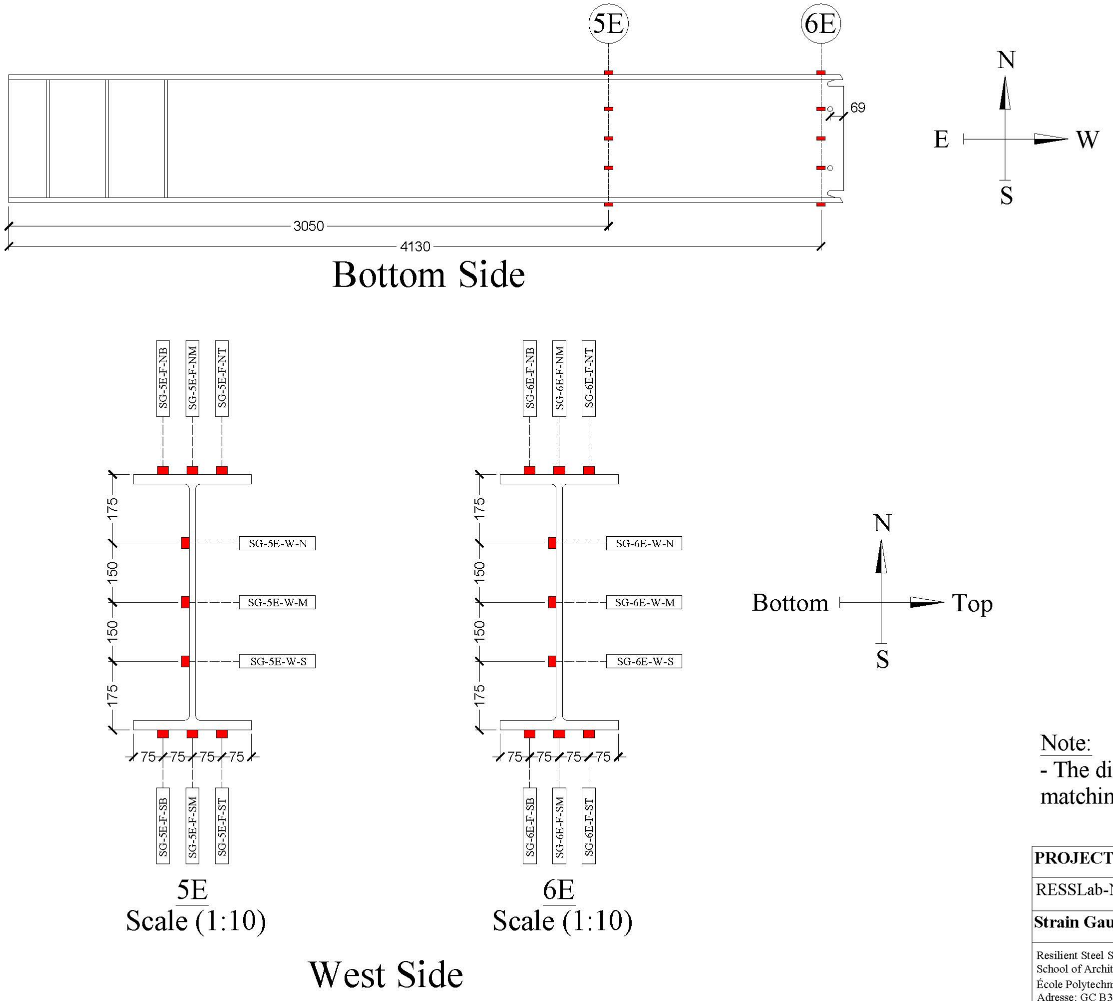
5E
6E
69
3050
4130
Bottom Side
N
E
W
S
SG-5E-F-NB
SG-5E-F-NM
SG-5E-F-NT
SG-6E-F-NB
SG-6E-F-NM
SG-6E-F-NT
175
150
150
175
SG-5E-W-N
SG-5E-W-M
SG-5E-W-S
SG-6E-W-N
SG-6E-W-M
SG-6E-W-S
75
75
75
75
SG-5E-F-SB
SG-5E-F-SM
SG-5E-F-ST
SG-6E-F-SB
SG-6E-F-SM
SG-6E-F-ST
5E
Scale (1:10)
6E
Scale (1:10)
West Side
N
Bottom
Top
S

STRAIN GAUGES - EAST BEAM

#	ID	LOCATION	TYPE
1	SG-5E-F-NB	5E - Flange North Bottom	YEFLAB-5
2	SG-5E-F-NM	5E - Flange North Middle	YEFLAB-5
3	SG-5E-F-NT	5E - Flange North Top	YEFLAB-5
4	SG-5E-F-SB	5E - Flange South Bottom	YEFLAB-5
5	SG-5E-F-SM	5E - Flange South Middle	YEFLAB-5
6	SG-5E-F-ST	5E - Flange South Top	YEFLAB-5
7	SG-5E-W-N	5E - Web North	YEFLAB-5
8	SG-5E-W-M	5E - Web Middle	YEFLAB-5
9	SG-5E-W-S	5E - Web South	YEFLAB-5
10	SG-6E-F-NB	6E - Flange North Bottom	YEFLAB-5
11	SG-6E-F-NM	6E - Flange North Middle	YEFLAB-5
12	SG-6E-F-NT	6E - Flange North Top	YEFLAB-5
13	SG-6E-F-SB	6E - Flange South Bottom	YEFLAB-5
14	SG-6E-F-SM	6E - Flange South Middle	YEFLAB-5
15	SG-6E-F-ST	6E - Flange South Top	YEFLAB-5
16	SG-6E-W-N	6E - Web North	YEFLAB-5
17	SG-6E-W-M	6E - Web Middle	YEFLAB-5
18	SG-6E-W-S	6E - Web South	YEFLAB-5

Note:
- The direction of the strain gauges should be matching the longitudinal direction of the beam

PROJECT	EXTRA No.	**DRAWING Nr.**
RESSLab-NSC		3

Strain Gauges - East Beam

Resilient Steel Structures Laboratory (RESSLab)
School of Architecture, Civil, and Environmental Engineering,
École Polytechnique Fédérale de Lausanne (EPFL)
Adresse: GC B3 485 (Bâtiment GC) Station 18 CH-1015 Lausanne
Attention to: Prof. Dimitrios Lignos, Andronikos Skiadopoulos
email: dimitrios.lignos@epfl.ch

DATE	**REV.**	**DIM**	**SCALE**	**PAPER SIZE**
10/10/2021	3	mm	1:20	A3

Figure C.5 Instrumentation plan – east beam strain gauge drawings.

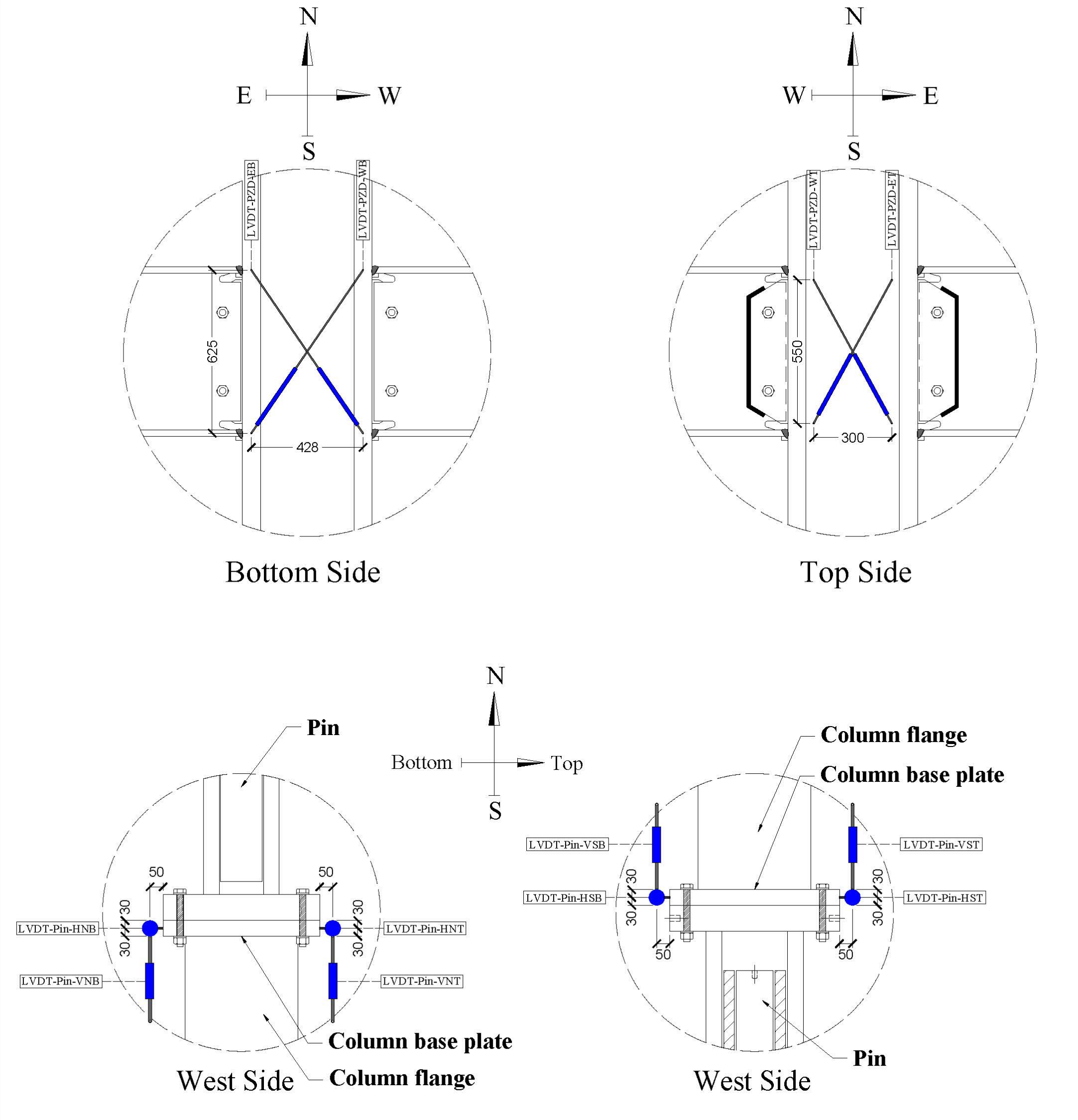
N
E
W
S
LVDT-PZD-EB
LVDT-PZD-WB
625
428
Bottom Side
N
W
E
S
LVDT-PZD-WT
LVDT-PZD-ET
550
300
Top Side
Pin
N
Bottom
Top
S
50
50
30
30
30
30
LVDT-Pin-HNB
LVDT-Pin-VNB
LVDT-Pin-HNT
LVDT-Pin-VNT
Column base plate
West Side
Column flange
Column flange
Column base plate
LVDT-Pin-VSB
LVDT-Pin-HSB
LVDT-Pin-VST
LVDT-Pin-HST
30
30
30
30
50
50
Pin
West Side

INSTRUMENTATION
LVDTs

#	ID	LOCATION	TYPE
1	LVDT-PZD-ET	Panel Zone Diag. East - Top	CDP-50M
2	LVDT-PZD-WT	Panel Zone Diag. West - Top	CDP-50M
3	LVDT-PZD-EB	Panel Zone Diag. East - Bottom	CDP-100
4	LVDT-PZD-WB	Panel Zone Diag. West - Bottom	CDP-100
5	LVDT-Pin-HNT	Pin Horizontal North - Top	CDP-25
6	LVDT-Pin-HST	Pin Horizontal South - Top	CDP-25
7	LVDT-Pin-HNB	Pin Horizontal North - Bottom	CDP-25
8	LVDT-Pin-HSB	Pin Horizontal South - Bottom	CDP-25
9	LVDT-Pin-VNT	Pin Vertical North - Top	CDP-25
10	LVDT-Pin-VST	Pin Vertical South - Top	CDP-25
11	LVDT-Pin-VNB	Pin Vertical North - Bottom	CDP-25
12	LVDT-Pin-VSB	Pin Vertical South - Bottom	CDP-25

PROJECT	EXTRA No.	**DRAWING Nr.**
RESSLab-NSC		4

Instrumentation - LVDTs (Part A)

Resilient Steel Structures Laboratory (RESSLab)
School of Architecture, Civil, and Environmental Engineering,
École Polytechnique Fédérale de Lausanne (EPFL)
Adresse: GC B3 485 (Bâtiment GC) Station 18 CH-1015 Lausanne
Attention to: Prof. Dimitrios Lignos, Andronikos Skiadopoulos
email: dimitrios.lignos@epfl.ch

DATE	**REV.**	**DIM**	**SCALE**	**PAPER SIZE**
10/10/2021	3	mm	1:15	A3

Figure C.6 Instrumentation plan – LVDT (Part A) drawings.

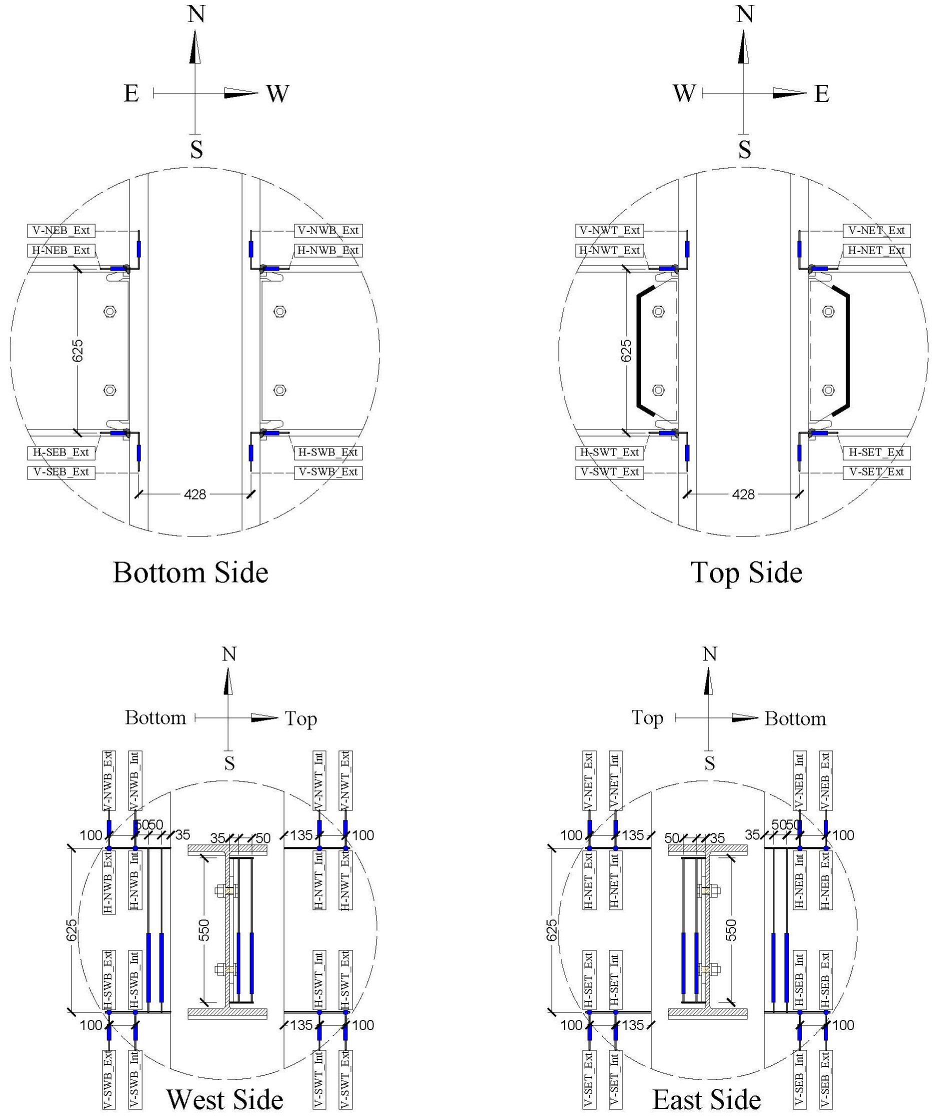
N
E
W
S
V-NEB_Ext
H-NEB_Ext
V-NWB_Ext
H-NWB_Ext
625
H-SEB_Ext
V-SEB_Ext
H-SWB_Ext
V-SWB_Ext
428
Bottom Side
N
W
E
S
V-NWT_Ext
H-NWT_Ext
V-NET_Ext
H-NET_Ext
625
H-SWT_Ext
V-SWT_Ext
H-SET_Ext
V-SET_Ext
428
Top Side
N
Bottom
Top
S
V-NWB_Ext
V-NWB_Int
V-NWT_Int
V-NWT_Ext
100
50
50
35
35
50
135
100
H-NWB_Ext
H-NWB_Int
H-NWT_Int
H-NWT_Ext
625
550
H-SWB_Ext
H-SWB_Int
H-SWT_Int
H-SWT_Ext
100
135
100
V-SWB_Ext
V-SWB_Int
V-SWT_Int
V-SWT_Ext
West Side
N
Top
Bottom
S
V-NET_Ext
V-NET_Int
V-NEB_Int
V-NEB_Ext
100
135
50
35
35
50
50
100
H-NET_Ext
H-NET_Int
H-NEB_Int
H-NEB_Ext
625
550
H-SET_Ext
H-SET_Int
H-SEB_Int
H-SEB_Ext
100
135
100
V-SET_Ext
V-SET_Int
V-SEB_Int
V-SEB_Ext
East Side

INSTRUMENTATION
LVDTs

#	ID	LOCATION	TYPE
1	LVDT-CFlPairsH-NET-Ext	NETop-Exterior	CDP-100
2	LVDT-CFlPairsH-NET-Int	NETop-Interior	CDP-100
3	LVDT-CFlPairsH-NEB-Ext	NEBot-Exterior	CDP-100
4	LVDT-CFlPairsH-NEB-Int	NEBot-Interior	CDP-100
5	LVDT-CFlPairsH-SET-Ext	SETop-Exterior	CDP-100
6	LVDT-CFlPairsH-SET-Int	SETop-Interior	CDP-100
7	LVDT-CFlPairsH-SEB-Ext	SEBot-Exterior	CDP-100
8	LVDT-CFlPairsH-SEB-Int	SEBot-Interior	CDP-100
9	LVDT-CFlPairsH-NWT-Ext	NWTop-Exterior	CDP-100
10	LVDT-CFlPairsH-NWT-Int	NWTop-Interior	CDP-100
11	LVDT-CFlPairsH-NWB-Ext	NWBot-Exterior	CDP-100
12	LVDT-CFlPairsH-NWB-Int	NWBot-Interior	CDP-100
13	LVDT-CFlPairsH-SWT-Ext	SWTop-Exterior	CDP-100
14	LVDT-CFlPairsH-SWT-Int	SWTop-Interior	CDP-100
15	LVDT-CFlPairsH-SWB-Ext	SWBot-Exterior	CDP-100
16	LVDT-CFlPairsH-SWB-Int	SWBot-Interior	CDP-100
17	LVDT-CFlPairsV-NET-Ext	NETop-Exterior	CDP-25
18	LVDT-CFlPairsV-NET-Int	NETop-Interior	CDP-25
19	LVDT-CFlPairsV-NEB-Ext	NEBot-Exterior	CDP-25
20	LVDT-CFlPairsV-NEB-Int	NEBot-Interior	CDP-25
21	LVDT-CFlPairsV-SET-Ext	SETop-Exterior	CDP-25
22	LVDT-CFlPairsV-SET-Int	SETop-Interior	CDP-25
23	LVDT-CFlPairsV-SEB-Ext	SEBot-Exterior	CDP-25
24	LVDT-CFlPairsV-SEB-Int	SEBot-Interior	CDP-25
25	LVDT-CFlPairsV-NWT-Ext	NWTop-Exterior	CDP-25
26	LVDT-CFlPairsV-NWT-Int	NWTop-Interior	CDP-25
27	LVDT-CFlPairsV-NWB-Ext	NWBot-Exterior	CDP-25
28	LVDT-CFlPairsV-NWB-Int	NWBot-Interior	CDP-25
29	LVDT-CFlPairsV-SWT-Ext	SWTop-Exterior	CDP-25
30	LVDT-CFlPairsV-SWT-Int	SWTop-Interior	CDP-25
31	LVDT-CFlPairsV-SWB-Ext	SWBot-Exterior	CDP-25
32	LVDT-CFlPairsV-SWB-Int	SWBot-Interior	CDP-25

PROJECT	EXTRA No.	**DRAWING Nr.**
RESSLab-NSC		5

Instrumentation - LVDTs (Part B)

Resilient Steel Structures Laboratory (RESSLab)
School of Architecture, Civil, and Environmental Engineering,
École Polytechnique Fédérale de Lausanne (EPFL)
Adresse: GC B3 485 (Bâtiment GC) Station 18 CH-1015 Lausanne
Attention to: Prof. Dimitrios Lignos, Andronikos Skiadopoulos
email: dimitrios.lignos@epfl.ch

DATE	**REV.**	**DIM**	**SCALE**	**PAPER SIZE**
10/10/2021	3	mm	1:15	A3

Figure C.7 Instrumentation plan – LVDT (Part B) drawings.

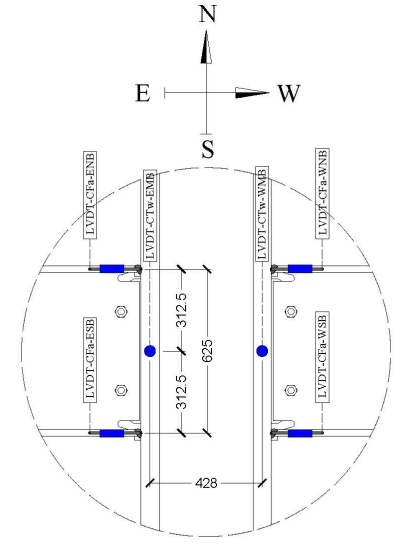
N
E
W
S
LVDT-CFa-ENB
LVDT-CTw-EMB
LVDT-CTw-WMB
LVDT-CFa-WNB
LVDT-CFa-ESB
LVDT-CFa-WSB
312.5
625
312.5
428

Bottom Side

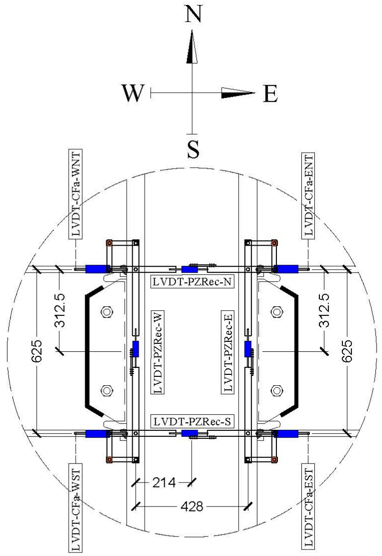
N
W
E
S
LVDT-CFa-WNT
LVDT-CFa-ENT
LVDT-PZRec-N
LVDT-PZRec-W
LVDT-PZRec-E
LVDT-PZRec-S
625
312.5
312.5
625
214
428
LVDT-CFa-WST
LVDT-CFa-EST

Top Side

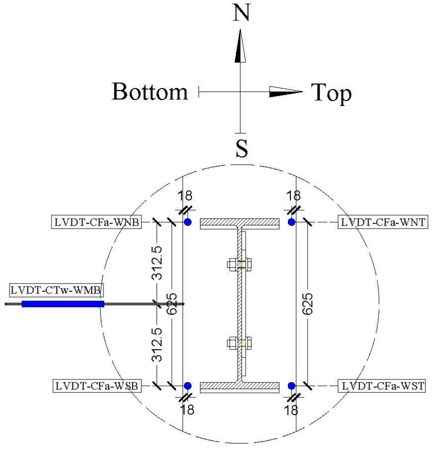
N
Bottom
Top
S
18
18
LVDT-CFa-WNB
LVDT-CFa-WNT
LVDT-CTw-WMB
312.5
625
312.5
625
LVDT-CFa-WSB
LVDT-CFa-WST
18
18

West Side

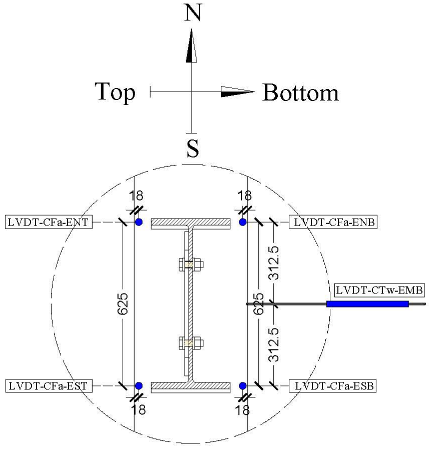
N
Top
Bottom
S
18
18
LVDT-CFa-ENT
LVDT-CFa-ENB
LVDT-CTw-EMB
625
312.5
625
312.5
LVDT-CFa-EST
LVDT-CFa-ESB
18
18

East Side

INSTRUMENTATION
LVDTs

#	ID	LOCATION	RANGE [MM]
1	LVDT-CFa-ENT	Col. Face East North - Top	CDP-100M
2	LVDT-CFa-EST	Col. Face East South - Top	CDP-100M
3	LVDT-CFa-WNT	Col. Face West North - Top	CDP-100M
4	LVDT-CFa-WST	Col. Face West South - Top	CDP-100M
5	LVDT-CFa-ENB	Col. Face East North - Bottom	CDP-100M
6	LVDT-CFa-ESB	Col. Face East South - Bottom	CDP-100M
7	LVDT-CFa-WNB	Col. Face West North - Bottom	CDP-100M
8	LVDT-CFa-WSB	Col. Face West South - Bottom	CDP-100M
9	LVDT-CTw-EMB	Col. Twist East Middle - Bottom	CDP-10
10	LVDT-CTw-WMB	Col. Twist West Middle - Bottom	CDP-10
11	LVDT-PZRec-S	Panel Zone Rec. - South	CDP-25
12	LVDT-PZRec-N	Panel Zone Rec. - North	CDP-25
13	LVDT-PZRec-E	Panel Zone Rec. - East	CDP-25
14	LVDT-PZRec-W	Panel Zone Rec. - West	CDP-25

PROJECT	EXTRA No.	**DRAWING Nr.**
RESSLab-NSC		6

Instrumentation - LVDTs (Part C)

Resilient Steel Structures Laboratory (RESSLab)
School of Architecture, Civil, and Environmental Engineering,
École Polytechnique Fédérale de Lausanne (EPFL)
Adresse: GC B3 485 (Bâtiment GC) Station 18 CH-1015 Lausanne
Attention to: Prof. Dimitrios Lignos, Andronikos Skiadopoulos
email: dimitrios.lignos@epfl.ch

DATE	**REV.**	**DIM**	**SCALE**	**PAPER SIZE**
10/10/2021	3	mm	1:15	A3

Figure C.8 Instrumentation plan – LVDT (Part C) drawings.

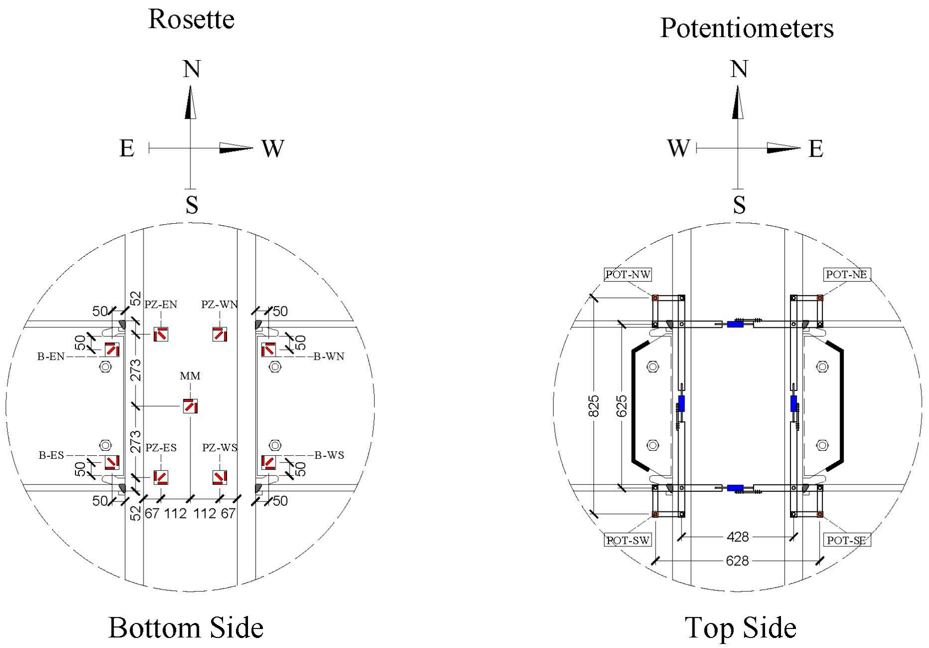
Rosette
N
E
W
S
PZ-EN
PZ-WN
MM
PZ-ES
PZ-WS
B-EN
B-WN
B-ES
B-WS
50
52
273
273
52
67 112 112 67
Bottom Side
Potentiometers
N
W
E
S
POT-NW
POT-NE
POT-SW
POT-SE
825
625
428
628
Top Side

INSTRUMENTATION
Rosette

#	ID	LOCATION	TYPE
1	ROS-PZ-EN	Panel Zone - East North	YEFRAB-5
2	ROS-PZ-WN	Panel Zone - West North	YEFRAB-5
3	ROS-PZ-MM	Panel Zone - Middle Middle	YEFRAB-5
4	ROS-PZ-ES	Panel Zone - East South	YEFRAB-5
5	ROS-PZ-WS	Panel Zone - West South	YEFRAB-5
6	ROS-B-WN	Beam - West North	YEFRAB-5
7	ROS-B-WS	Beam - West South	YEFRAB-5
8	ROS-B-EN	Beam - East North	YEFRAB-5
9	ROS-B-ES	Beam - East South	YEFRAB-5

INSTRUMENTATION
Potentiometers

#	ID	LOCATION	RANGE [degrees]
1	POT-NE	North East	±2
2	POT-NW	North West	±2
3	POT-SE	South East	±4
4	POT-SW	South West	±4

Note:
- The potentiometers are attached to aluminum plates. The aluminum plates shall be attached to threaded studs allowing rotation. The threaded studs shall be mounted to the column flanges with tack welds.

PROJECT	EXTRA No.	DRAWING Nr.
RESSLab-NSC		7

Instrumentation - Rosette/Potentiometers

Resilient Steel Structures Laboratory (RESSLab)
School of Architecture, Civil, and Environmental Engineering,
École Polytechnique Fédérale de Lausanne (EPFL)
Adresse: GC B3 485 (Bâtiment GC) Station 18 CH-1015 Lausanne
Attention to: Prof. Dimitrios Lignos, Andronikos Skiadopoulos
email: dimitrios.lignos@epfl.ch

DATE	REV.	DIM	SCALE	PAPER SIZE
10/10/2021	3	mm	1:15	A3

Figure C.9 Instrumentation plan – Rosette and potentiometer drawings.

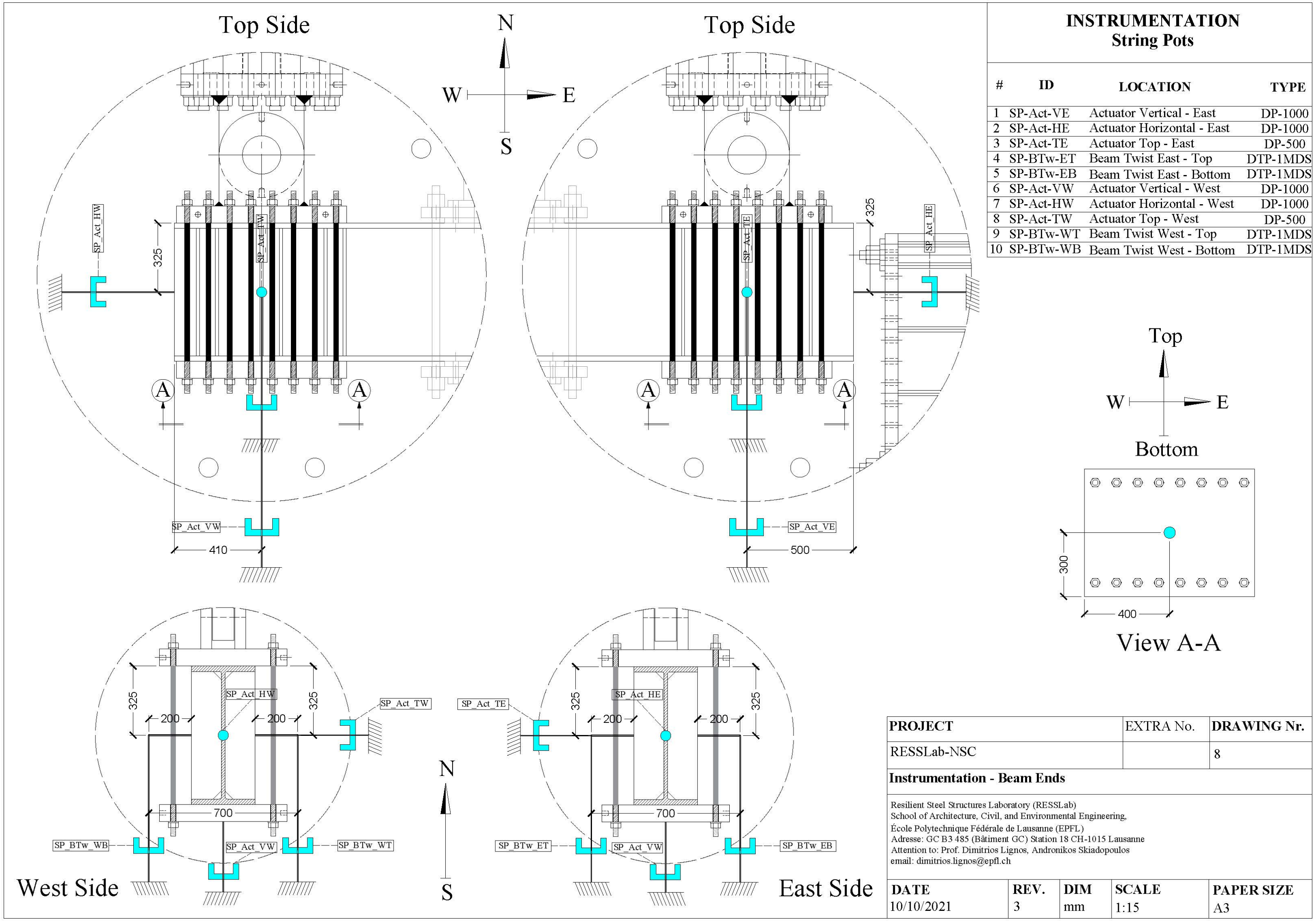
Top Side
N
W
E
S
Top Side
SP_Act_HW
325
SP_Act_TW
A
A
SP_Act_VW
410
SP_Act_TE
325
SP_Act_HE
A
A
SP_Act_VE
500
Top
W
E
Bottom
300
400
View A-A
325
200
SP_Act_HW
200
325
SP_Act_TW
700
SP_BTw_WB
SP_Act_VW
SP_BTw_WT
West Side
N
S
SP_Act_TE
325
200
SP_Act_HE
200
325
700
SP_BTw_ET
SP_Act_VW
SP_BTw_EB
East Side

INSTRUMENTATION
String Pots

#	ID	LOCATION	TYPE
1	SP-Act-VE	Actuator Vertical - East	DP-1000
2	SP-Act-HE	Actuator Horizontal - East	DP-1000
3	SP-Act-TE	Actuator Top - East	DP-500
4	SP-BTw-ET	Beam Twist East - Top	DTP-1MDS
5	SP-BTw-EB	Beam Twist East - Bottom	DTP-1MDS
6	SP-Act-VW	Actuator Vertical - West	DP-1000
7	SP-Act-HW	Actuator Horizontal - West	DP-1000
8	SP-Act-TW	Actuator Top - West	DP-500
9	SP-BTw-WT	Beam Twist West - Top	DTP-1MDS
10	SP-BTw-WB	Beam Twist West - Bottom	DTP-1MDS

PROJECT	EXTRA No.	**DRAWING Nr.**
RESSLab-NSC		8

Instrumentation - Beam Ends

Resilient Steel Structures Laboratory (RESSLab)
School of Architecture, Civil, and Environmental Engineering,
École Polytechnique Fédérale de Lausanne (EPFL)
Adresse: GC B3 485 (Bâtiment GC) Station 18 CH-1015 Lausanne
Attention to: Prof. Dimitrios Lignos, Andronikos Skiadopoulos
email: dimitrios.lignos@epfl.ch

DATE	**REV.**	**DIM**	**SCALE**	**PAPER SIZE**
10/10/2021	3	mm	1:15	A3

Figure C.10 Instrumentation plan – beam end string pot drawings.

Appendix D. Welding procedure specifications and ultrasonic test results

Description

This appendix includes the weld electrode mill certificates, the welding procedure specifications and the ultrasonic test results of all weld details of the test specimens described in Chapter 5.

Contributors of the specimen fabrication:

The fabricator of the test specimens was Techno Steel Daishin.
The welder of the beam-to-column connections was Mr. Kenta Yoshiba.
The ultrasonic testing was performed by Mr. Shun Ri.
The weld electrodes were provided by Nippon Steel Welding & Engineering Co., Ltd.

D.1 Weld electrode mill certificates

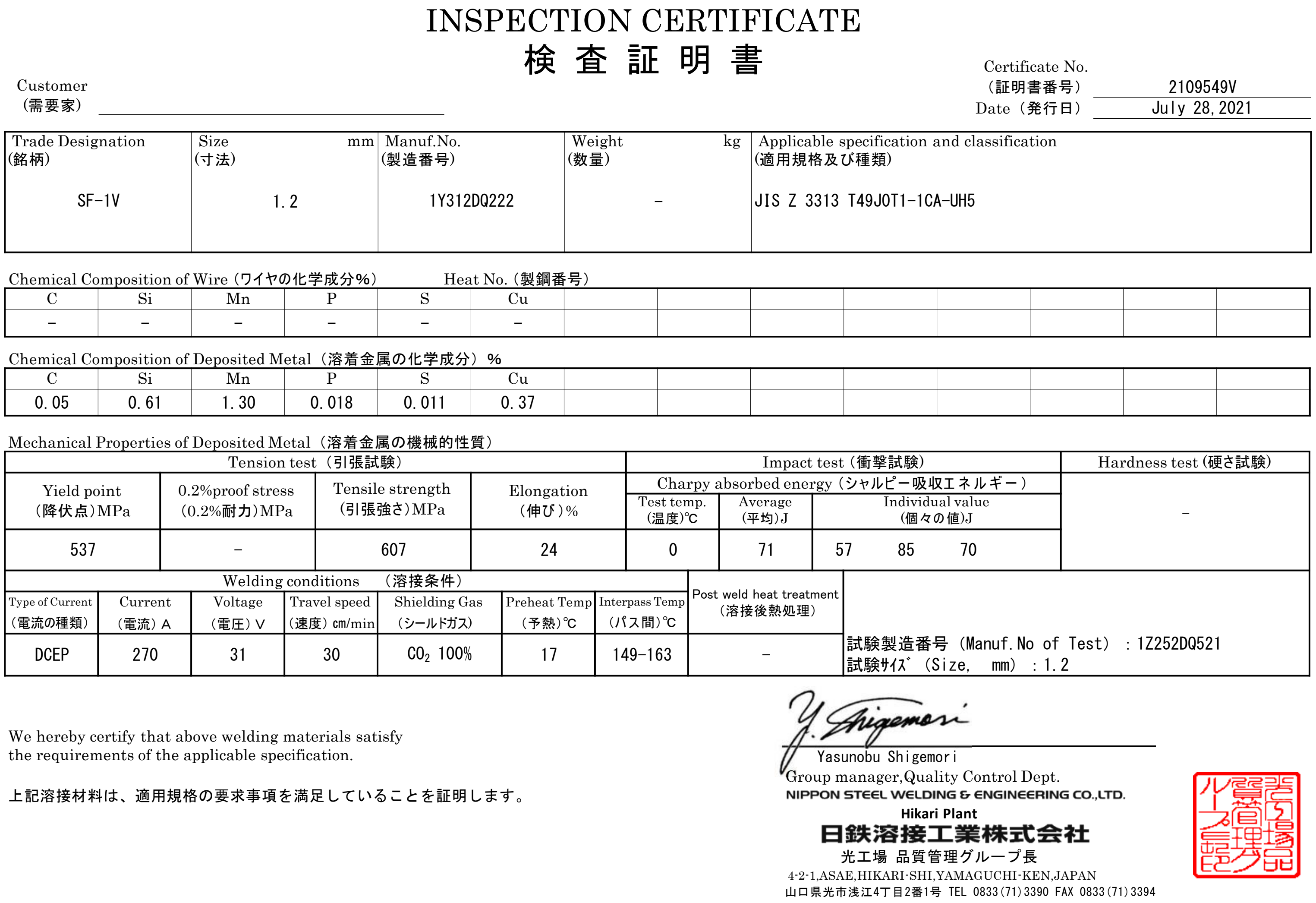

INSPECTION CERTIFICATE

検 査 証 明 書

Customer
（需要家）

Certificate No.
（証明書番号） 2109549V
Date（発行日） July 28, 2021

Trade Designation (銘柄)	Size mm (寸法)	Manuf.No. (製造番号)	Weight kg (数量)	Applicable specification and classification (適用規格及び種類)
SF-1V	1.2	1Y312DQ222	-	JIS Z 3313 T49J0T1-1CA-UH5

Chemical Composition of Wire（ワイヤの化学成分%） Heat No.（製鋼番号）

C	Si	Mn	P	S	Cu								
-	-	-	-	-	-								

Chemical Composition of Deposited Metal（溶着金属の化学成分）%

C	Si	Mn	P	S	Cu								
0.05	0.61	1.30	0.018	0.011	0.37								

Mechanical Properties of Deposited Metal（溶着金属の機械的性質）

Tension test（引張試験）				Impact test（衝撃試験）			Hardness test（硬さ試験）
				Charpy absorbed energy（シャルピー吸収エネルギー）			
Yield point (降伏点)MPa	0.2%proof stress (0.2%耐力)MPa	Tensile strength (引張強さ)MPa	Elongation (伸び)%	Test temp. (温度)℃	Average (平均)J	Individual value (個々の値)J	
537	-	607	24	0	71	57 85 70	-

Welding conditions（溶接条件）							Post weld heat treatment（溶接後熱処理）	
Type of Current (電流の種類)	Current (電流) A	Voltage (電圧) V	Travel speed (速度) cm/min	Shielding Gas (シールドガス)	Preheat Temp (予熱)℃	Interpass Temp (パス間)℃		
DCEP	270	31	30	CO_2 100%	17	149-163	-	試験製造番号（Manuf.No of Test）：1Z252DQ521 試験ｻｲｽﾞ（Size, mm）：1.2

We hereby certify that above welding materials satisfy
the requirements of the applicable specification.

上記溶接材料は、適用規格の要求事項を満足していることを証明します。

Y. Shigemori
Yasunobu Shigemori
Group manager,Quality Control Dept.
NIPPON STEEL WELDING & ENGINEERING CO.,LTD.
Hikari Plant
日鉄溶接工業株式会社
光工場 品質管理グループ長
4-2-1,ASAE,HIKARI-SHI,YAMAGUCHI-KEN,JAPAN
山口県光市浅江4丁目2番1号 TEL 0833(71)3390 FAX 0833(71)3394

Figure D.1 Mill certificate of the T49J0T1-1CA-UH5 weld electrode.

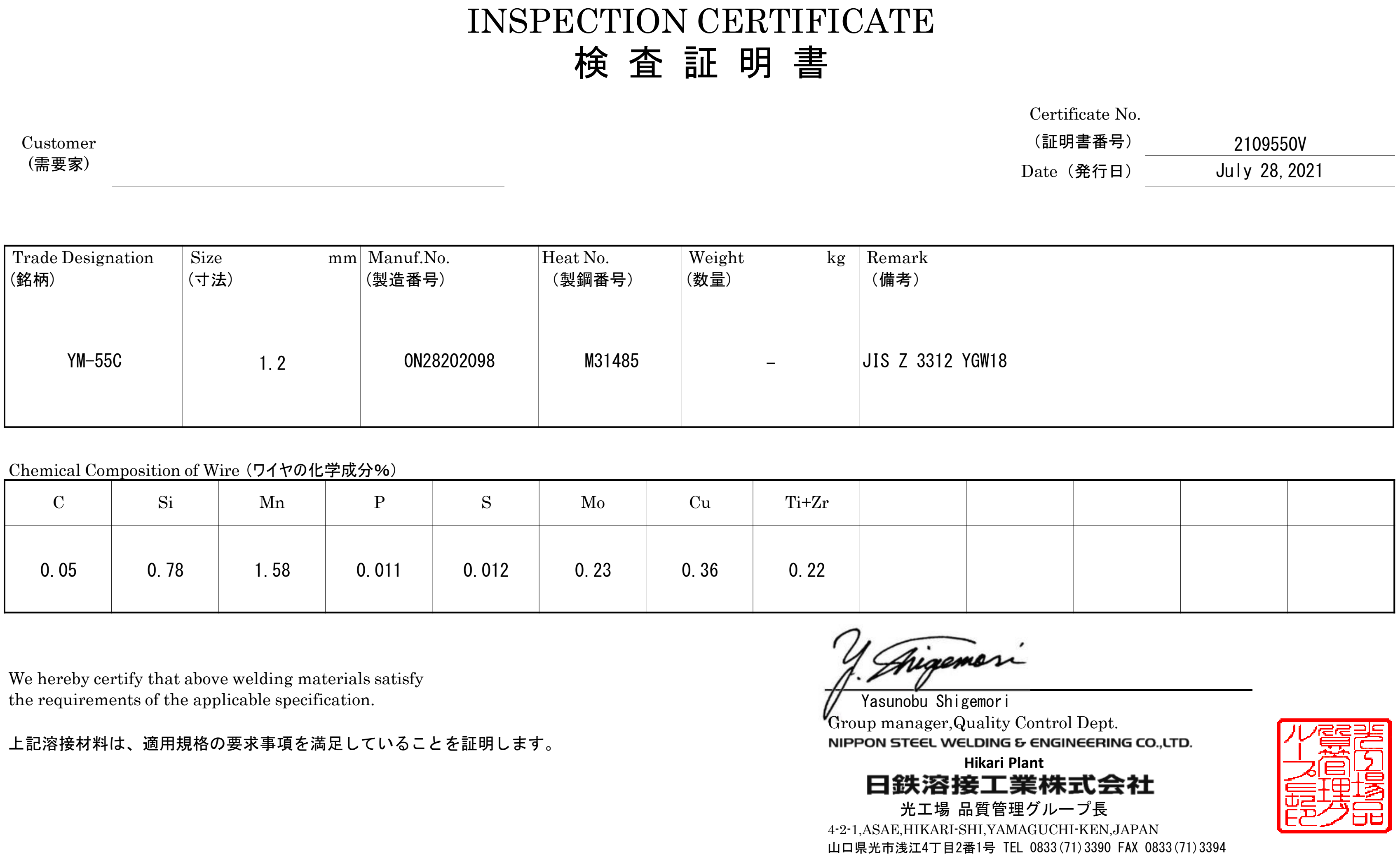

INSPECTION CERTIFICATE
検 査 証 明 書

Certificate No.
（証明書番号） 2109550V
Date（発行日） July 28, 2021

Customer
（需要家）

Trade Designation （銘柄）	Size mm （寸法）	Manuf.No. （製造番号）	Heat No. （製鋼番号）	Weight kg （数量）	Remark （備考）
YM-55C	1.2	ON28202098	M31485	-	JIS Z 3312 YGW18

Chemical Composition of Wire（ワイヤの化学成分%）

C	Si	Mn	P	S	Mo	Cu	Ti+Zr					
0.05	0.78	1.58	0.011	0.012	0.23	0.36	0.22					

We hereby certify that above welding materials satisfy the requirements of the applicable specification.

上記溶接材料は、適用規格の要求事項を満足していることを証明します。

Y. Shigemori
Yasunobu Shigemori
Group manager,Quality Control Dept.
NIPPON STEEL WELDING & ENGINEERING CO.,LTD.
Hikari Plant
日鉄溶接工業株式会社
光工場 品質管理グループ長
4-2-1,ASAE,HIKARI-SHI,YAMAGUCHI-KEN,JAPAN
山口県光市浅江4丁目2番1号 TEL 0833(71)3390 FAX 0833(71)3394

Figure D.2 Mill certificate of the YGW-18 weld electrode.

D.2 Welding procedure specifications

Table D.1 Overview of the weld procedure specifications of both test specimens.

Order of loading test	Symbol of specimen		Location on loading setup	Part	Bevel angle	Root gap (Nominal)	Date of welding	Sheets	Discontinuities found
2nd	A	①	East	Shear-tab to column	45, dual	0	13-May-21	2(A)-1	✔
				Top flange to column	30, single	10	30-Jun-21	2(A)-2	
				Bottom flange to column (Right)	30, single	10	1-Jul-21	2(A)-4	
				Bottom flange to column (Left)	30, single	10	1-Jul-21	2(A)-5	
				Web to column	45, single	6	1-Jul-21	2(A)-3	
		②	West	Shear-tab to column	45, dual	0	13-May-21	2(A)-6	
				Top flange to column	30, single	10	30-Jun-21	2(A)-7	
				Bottom flange to column (Right)	30, single	10	30-Jun-21	2(A)-9	✔
				Bottom flange to column (Left)	30, single	10	1-Jul-21	2(A)-10	✔
				Web to column	45, single	6	1-Jul-21	2(A)-8	
1st	B	③	East	Shear-tab to column	45, dual	0	13-May-21	1(B)-1	
				Top flange to column	30, single	10	24-Jun-21	1(B)-2	
				Bottom flange to column (Right)	30, single	10	24-Jun-21	1(B)-4	
				Bottom flange to column (Left)	30, single	10	24-Jun-21	1(B)-5	
				Web to column	45, single	6	24-Jun-21	1(B)-3	
		④	West	Shear-tab to column	45, dual	0	13-May-21	1(B)-6	
				Top flange to column	30, single	10	23-Jun-21	1(B)-7	
				Bottom flange to column (Right)	30, single	10	23-Jun-21	1(B)-9	
				Bottom flange to column (Left)	30, single	10	23-Jun-21	1(B)-10	
				Web to column	45, single	6	23-Jun-21	1(B)-8	

Project		H-Beam to H-Column Connection Interior Joint Specimen				Date	May 13, 2021	Weather	Cloudy
Specimen		Grade:	SN490B	No.:	1 (Shear Tab)	Temperature	16°C	Humidity	61%
(Base Metal)		Thickness:	16mm	Width:	550mm	Welder's Name		Yoshiba	
Groove Design		Bevel Angle:	45°	Root Gap:	0mm	Recorder's Name		Huy	
Welding Process		Gas Metal Arc Welding (Semi-Automatic Welding)				Welding Sequence 5 layers 6 passes		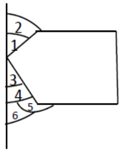	
		Welding Positio	Flat Position	Shielding Gas:	CO$_2$ (100%)				
Welding Wire		Manufacturer:	Kobe Steel, ltd.	Classification:	YGW18 (JIS)				
		Product Name:	MG-56	Wire Diameter:	1.2mm				
Maximum Heat Input		30kJ/cm	Maximum Interpass Temperatur		250°C				
Measuring Instrument		Adachi HD1200K				Initial Temperature(°C): 86			
Pass No.	Current (A)	Voltage (V)	Arcing Time (sec)	Travel Speed (cm/min)	Heat Input (kJ/cm)	Post-Weld Temperature (°C)	Interpass Temperature (°C)	Interval Time (sec)	Remarks
1	292	35.0	89	37.2	16.50	283	97	145	●▲
2	294	35.0	118	27.9	22.11	240	53	Back Gouging	●▲
3	284	35.0	99	33.3	17.89	226	100	144	●▲
4	288	35.0	120	27.5	21.99	260	112	134	●▲
5	294	35.0	96	34.4	17.96	277	141	132	●▲
6	282	35.0	86	38.5	15.40	193	—	—	
Notes:	●···Slag Removal	▲···Nozzle Cleaning							

Figure D.3 Shear tab-to-column face welding procedure specification of Specimen 1 east beam.

Project		H-Beam to H-Column Connection Interior Joint Specimen				Date	June 30, 2021	Weather	Cloudy
Specimen (Base Metal)		Grade:	SN490B	No.:	1 (Top Flange)	Temperature	24.4°C	Humidity	61%
		Thickness:	25mm	Width:	375mm	Welder's Name		Yoshiba	
Groove Design		Bevel Angle:	30°	Root Gap:	12mm	Recorder's Name		Ueno	
Welding Process		Gas Metal Arc Welding (Semi-Automatic Welding)				Welding Sequence 9 layers 22 passes 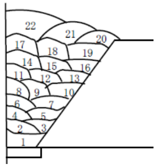 Initial Temperature(°C): 54			
		Welding Positio	Flat Position	Shielding Gas:	CO_2 (100%)				
Welding Wire		Manufacturer:	Nippon Steel Welding & Engineering co.,ltd.	Classification:	YGW18 (JIS)				
		Product Name:	YM-55C	Wire Diameter:	1.2mm				
Maximum Heat Input		30kJ/cm	Maximum Interpass Temperatur		250°C				
Measuring Instrument		Adachi HD1200K							
Pass No.	Current (A)	Voltage (V)	Arcing Time (sec)	Travel Speed (cm/min)	Heat Input (kJ/cm)	Post-Weld Temperature (°C)	Interpass Temperature (°C)	Interval Time (sec)	Remarks
1	236	33.2	88	25.5	18.43	66	62	108	●▲
2	252	33.4	45	50.0	10.10	72	70	65	●▲
3	236	33.2	79	28.4	16.55	124	108	73	●▲
4	246	33.4	58	38.7	12.75	114	110	67	●▲
5	248	33.2	58	38.7	12.78	152	142	70	●▲
6	252	33.4	74	30.5	16.56	151	145	45	●▲
7	258	33.2	70	32.1	16.04	179	171	57	●▲
8	246	33.4	56	40.3	12.23	175	169	46	●▲
9	238	33.4	45	50.0	9.54	170	160	65	●▲
10	254	33.4	61	36.8	13.85	195	185	60	●▲
11	242	33.6	59	38.3	12.75	197	190	44	●▲
12	240	32.8	53	42.6	11.08	195	187	44	●▲
13	248	33.2	59	38.3	12.91	200	188	44	●▲
14	246	33.4	65	34.7	14.20	190	174	78	●▲
15	252	33.6	61	36.8	13.82	191	179	47	●▲
16	240	33.2	66	34.1	14.02	212	198	79	●▲
17	254	33.4	73	30.7	16.56	180	170	49	●▲
18	240	33.6	72	31.3	15.48	201	189	45	●▲
19	234	33.2	47	48.1	9.69	212	190	96	●▲
20	242	33.4	53	42.6	11.38	228	209	33	●▲
21	234	33.2	76	29.5	15.78	225	198	46	●▲
22	238	33.2	58	38.7	12.26	210	—	—	
Notes:	●・・・Slag Removal	▲・・・Nozzle Cleaning							

Figure D.4 Top beam flange-to-column face welding procedure specification of Specimen 1 east beam.

Project	H-Beam to H-Column Connection Interior Joint Specimen				Date	July 1, 2021	Weather	Cloudy
Specimen	Grade:	SN490B	No.:	1 (Bottom Flange Right)	Temperature	21.6°C	Humidity	69%
(Base Metal)	Thickness:	25mm	Width:	195mm	Welder's Name		Yoshiba	
Groove Design	Bevel Angle:	30°	Root Gap:	12mm	Recorder's Name		Huy	
Welding Process	Gas Metal Arc Welding (Semi-Automatic Welding)				Welding Sequence 9 layers 21 passes 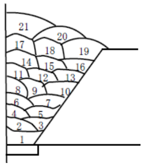			
	Welding Positio	Flat Position	Shielding Gas:	CO_2 (100%)				
Welding Wire	Manufacturer:	Nippon Steel Welding & Engineering co.,ltd.	Classification:	YGW18 (JIS)				
	Product Name:	YM-55C	Wire Diameter:	1.2mm				
Maximum Heat Input	30kJ/cm	Maximum Interpass Temperatur		250°C				
Measuring Instrument	Adachi HD1200K				Initial Temperature(°C): 52			

Pass No.	Current (A)	Voltage (V)	Arcing Time (sec)	Travel Speed (cm/min)	Heat Input (kJ/cm)	Post-Weld Temperature (°C)	Interpass Temperature (°C)	Interval Time (sec)	Remarks
1	232	34.4	41	28.7	16.70	64	68	50	●▲
2	234	34.2	24	48.8	9.85	75	72	80	●▲
3	258	34.2	34	34.2	15.48	137	137	56	●▲
4	232	34.2	37	31.5	15.14	159	149	55	●▲
5	234	34.2	35	33.6	14.28	154	147	56	●▲
6	240	34.2	39	30.0	16.42	173	166	80	●▲
7	242	34.2	36	32.5	15.28	222	210	75	●▲
8	246	34.2	26	45.4	11.13	194	198	50	●▲
9	242	34.2	24	48.8	10.19	201	213	65	●▲
10	252	34.2	27	43.3	11.93	273	187	150	●▲
11	242	34.4	36	32.5	15.37	172	184	90	●▲
12	226	34.2	31	37.5	12.37	208	160	180	●▲
13	238	34.0	31	37.5	12.95	230	224	85	●▲
14	222	34.2	37	31.5	14.48	216	206	75	●▲
15	238	34.0	31	37.5	12.95	248	231	58	●▲
16	226	34.0	33	35.5	13.01	269	233	154	●▲
17	224	34.2	42	27.9	16.50	221	218	45	●▲
18	222	34.2	38	31.0	14.72	261	229	86	●▲
19	224	33.8	40	29.1	15.61	250	186	290	●▲
20	232	34.0	37	31.5	15.05	196	182	110	●▲
21	216	34.2	49	23.8	18.64	179	—	—	

Notes: ●・・・Slag Removal ▲・・・Nozzle Cleaning

Figure D.5 Bottom right beam flange-to-column face welding procedure specification of Specimen 1 east beam.

Project		H-Beam to H-Column Connection Interior Joint Specimen				Date	July 1, 2021	Weather	Cloudy
Specimen (Base Metal)		Grade:	SN490B	No.:	1 (Bottom Flange Left)	Temperature	21.6°C	Humidity	69%
		Thickness:	25mm	Width:	187mm	Welder's Name		Yoshiba	
Groove Design		Bevel Angle:	30°	Root Gap:	12mm	Recorder's Name		Huy	
Welding Process		Gas Metal Arc Welding (Semi-Automatic Welding)				Welding Sequence 9 layers 21 passes 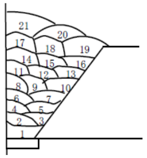 21 20 17 18 19 14 15 16 11 12 13 8 9 10 6 7 4 5 2 3 1 Initial Temperature(°C): 60			
		Welding Positio	Flat Position	Shielding Gas:	CO$_2$ (100%)				
Welding Wire		Manufacturer:	Nippon Steel Welding & Engineering co.,ltd.	Classification:	YGW18 (JIS)				
		Product Name:	YM-55C	Wire Diameter:	1.2mm				
Maximum Heat Input		30kJ/cm	Maximum Interpass Temperatur		250°C				
Measuring Instrument		Adachi HD1200K							
Pass No.	Current (A)	Voltage (V)	Arcing Time (sec)	Travel Speed (cm/min)	Heat Input (kJ/cm)	Post-Weld Temperature (°C)	Interpass Temperature (°C)	Interval Time (sec)	Remarks
1	236	33.4	47	24.0	19.73	64	62	55	●▲
2	242	33.4	35	32.2	15.04	72	74	65	●▲
3	248	33.2	33	34.0	14.53	127	128	50	●▲
4	250	33.4	39	28.8	17.41	139	146	42	●▲
5	224	33.6	36	31.2	14.49	182	169	90	●▲
6	222	33.2	41	27.5	16.08	157	175	50	●▲
7	222	33.4	37	30.2	14.75	218	215	50	●▲
8	232	33.6	33	34.0	13.76	190	184	55	●▲
9	242	33.2	26	43.5	11.08	199	188	72	●▲
10	236	33.4	33	34.0	13.91	216	192	68	●▲
11	246	33.6	39	28.8	17.24	191	169	80	●▲
12	224	33.2	31	36.0	12.41	186	179	60	●▲
13	232	33.4	36	31.2	14.92	236	203	90	●▲
14	236	33.3	41	27.5	17.15	191	191	55	●▲
15	224	33.4	34	32.8	13.68	231	218	60	●▲
16	226	33.4	31	36.0	12.59	228	200	100	●▲
17	230	33.4	30	37.4	12.32	197	190	47	●▲
18	226	33.2	30	37.4	12.04	205	213	50	●▲
19	224	33.4	36	31.2	14.40	255	205	70	●▲
20	238	33.2	30	37.4	12.68	229	219	55	●▲
21	216	33.2	32	35.3	12.20	213	—	—	
Notes: ●・・・Slag Removal ▲・・・Nozzle Cleaning									

Figure D.6 Bottom left beam flange-to-column face welding procedure specification of Specimen 1 east beam.

Project		H-Beam to H-Column Connection Interior Joint Specimen				Date	July 1, 2021	Weather	Cloudy
Specimen		Grade:	SN490B	No.:	1 (Web)	Temperature	21.6°C	Humidity	69%
(Base Metal)		Thickness:	16mm	Width:	530mm	Welder's Name		Yoshiba	
Groove Design		Bevel Angle:	45°	Root Gap:	9mm	Recorder's Name		Huy	
Welding Process		Gas Metal Arc Welding (Semi-Automatic Welding)				Welding Sequence 6 layers 11 passes 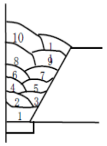 			
		Welding Positio	Vertical Positior	Shielding Gas:	CO_2 (100%)				
Welding Wire		Manufacturer:	Nippon Steel Welding & Engineering co.,ltd.	Classification:	A5.36 E71T1-C1A0-CS1 (AWS)				
		Product Name:	SF-1V	Wire Diameter:	1.2mm				
Maximum Heat Input		30kJ/cm	Maximum Interpass Temperatur		250°C				
Measuring Instrument		Adachi HD1200K				Initial Temperature(°C): 64			
Pass No.	Current (A)	Voltage (V)	Arcing Time (sec)	Travel Speed (cm/min)	Heat Input (kJ/cm)	Post-Weld Temperature (°C)	Interpass Temperature (°C)	Interval Time (sec)	Remarks
1	162	23.4	228	14.0	16.30	86	74	130	●▲
2	178	24.2	123	25.9	10.00	91	88	116	●▲
3	176	24.0	163	19.5	13.00	125	121	80	●▲
4	172	24.4	184	17.3	14.59	118	113	55	●▲
5	168	24.4	225	14.1	17.41	142	131	110	●▲
6	152	24.2	173	18.4	11.99	123	120	80	●▲
7	170	24.6	223	14.3	17.61	159	145	60	●▲
8	172	24.4	249	12.8	19.72	142	143	65	●▲
9	172	24.2	241	13.2	18.95	145	134	125	●▲
10	168	24.4	294	10.8	22.73	132	92	900	●▲
11	168	24.2	252	12.6	19.33	123	—	—	
Notes: ●···Slag Removal ▲···Nozzle Cleaning									

Figure D.7 Beam web-to-column face welding procedure specification of Specimen 1 east beam.

Project		H-Beam to H-Column Connection Interior Joint Specimen				Date	May 13, 2021	Weather	Cloudy
Specimen		Grade:	SN490B	No.:	2 (Shear Tab)	Temperature	16°C	Humidity	61%
(Base Metal)		Thickness:	16mm	Width:	550mm	Welder's Name		Yoshiba	
Groove Design		Bevel Angle:	45°	Root Gap:	0mm	Recorder's Name		Huy	
Welding Process		Gas Metal Arc Welding (Semi-Automatic Welding)				Welding Sequence 5 layers 6 passes		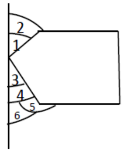	
		Welding Positio	Flat Position	Shielding Gas:	CO$_2$ (100%)				
Welding Wire		Manufacturer:	Kobe Steel, ltd.	Classification:	YGW18 (JIS)				
		Product Name:	MG-56	Wire Diameter:	1.2mm				
Maximum Heat Input		30kJ/cm	Maximum Interpass Temperatur		250°C				
Measuring Instrument		Adachi HD1200K				Initial Temperature(°C): 82			
Pass No.	Current (A)	Voltage (V)	Arcing Time (sec)	Travel Speed (cm/min)	Heat Input (kJ/cm)	Post-Weld Temperature (°C)	Interpass Temperature (°C)	Interval Time (sec)	Remarks
1	294	35.0	96	34.4	17.96	248	85	140	●▲
2	298	35.0	101	32.7	19.11	217	82	Back Gouging	●▲
3	280	30.0	134	24.7	20.44	202	105	132	●▲
4	270	30.0	128	25.8	18.82	218	138	89	●▲
5	252	30.0	88	37.4	12.13	185	129	100	●▲
6	256	30.0	92	36.0	12.82	146	―	―	
Notes:	●･･･Slag Removal	▲･･･Nozzle Cleaning							

Figure D.8 Shear tab-to-column face welding procedure specification of Specimen 1 west beam.

Project		H-Beam to H-Column Connection Interior Joint Specimen				Date	June 30, 2021	Weather	Cloudy
Specimen		Grade:	SN490B	No.:	2 (Top Flange)	Temperature	24.4°C	Humidity	59%
(Base Metal)		Thickness:	25mm	Width:	375mm	Welder's Name		Yoshiba	
Groove Design		Bevel Angle:	45°	Root Gap:	11mm	Recorder's Name		Ueno	
Welding Process		Gas Metal Arc Welding (Semi-Automatic Welding)				Welding Sequence 9 layers 19 passes 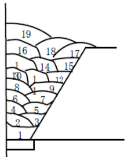 19 16 18 17 14 15 10 12 8 9 6 7 4 5 2 3 1 Initial Temperature(°C): 62.7			
		Welding Positio	Flat Position	Shielding Gas:	CO_2 (100%)				
Welding Wire		Manufacturer:	Nippon Steel Welding & Engineering co.,ltd.	Classification:	YGW18 (JIS)				
		Product Name:	YM-55C	Wire Diameter:	1.2mm				
Maximum Heat Input		30kJ/cm	Maximum Interpass Temperatur		250°C				
Measuring Instrument		Adachi HD1200K							
Pass No.	Current (A)	Voltage (V)	Arcing Time (sec)	Travel Speed (cm/min)	Heat Input (kJ/cm)	Post-Weld Temperature (°C)	Interpass Temperature (°C)	Interval Time (sec)	Remarks
1	242	33.6	94	23.9	20.42	78.3	75	92	●▲
2	236	33.6	58	38.7	12.31	87.7	86.8	84	●▲
3	252	33.8	55	40.8	12.54	144	127	88	●▲
4	242	33.8	68	33.2	14.79	141	129	95	●▲
5	262	33.4	67	33.5	15.68	187	157	144	●▲
6	254	33.8	77	29.3	17.58	166	154	60	●▲
7	256	33.4	84	26.8	19.15	226	172	124	●▲
8	258	33.6	70	32.1	16.23	179	168	103	●▲
9	252	33.4	90	25.0	20.20	241	185	127	●▲
10	254	33.8	67	33.5	15.39	189	172	81	●▲
11	262	33.8	55	40.8	13.04	192	188	75	●▲
12	254	33.6	59	38.3	13.38	246	195	90	●▲
13	248	33.8	73	30.7	16.36	207	178	101	●▲
14	252	33.4	74	30.5	16.56	213	199	91	●▲
15	242	33.6	69	32.6	14.96	222	191	124	●▲
16	246	33.8	49	45.7	10.91	197	165	122	●▲
17	272	33.8	64	35.1	15.74	130	120	95	●▲
18	264	33.2	83	27.2	19.36	192	177	86	●▲
19	246	33.4	80	28.2	17.48	193	—	—	
Notes:	●・・・Slag Removal	▲・・・Nozzle Cleaning							

Figure D.9 Top beam flange-to-column face welding procedure specification of Specimen 1 west beam.

Project		H-Beam to H-Column Connection Interior Joint Specimen				Date	June 30, 2021	Weather	Cloudy
Specimen (Base Metal)		Grade:	SN490B	No.:	2 (Bottom Flange Right)	Temperature	24.5°C	Humidity	61%
		Thickness:	25mm	Width:	185mm	Welder's Name		Yoshiba	
Groove Design		Bevel Angle:	30°	Root Gap:	11mm	Recorder's Name		Ueno	
Welding Process		Gas Metal Arc Welding (Semi-Automatic Welding)				Welding Sequence 9 layers 20 passes 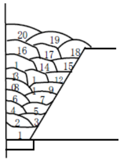 Initial Temperature(°C): 62			
		Welding Positio	Flat Position	Shielding Gas:	CO_2 (100%)				
Welding Wire		Manufacturer:	Nippon Steel Welding & Engineering co.,ltd.	Classification:	YGW18 (JIS)				
		Product Name:	YM-55C	Wire Diameter:	1.2mm				
Maximum Heat Input		30kJ/cm	Maximum Interpass Temperatur		250°C				
Measuring Instrument		Adachi HD1200K							
Pass No.	Current (A)	Voltage (V)	Arcing Time (sec)	Travel Speed (cm/min)	Heat Input (kJ/cm)	Post-Weld Temperature (°C)	Interpass Temperature (°C)	Interval Time (sec)	Remarks
1	226	33.6	47	23.7	19.21	72	69	88	●▲
2	234	33.8	34	32.5	14.62	76	70	79	●▲
3	242	33.4	34	32.5	14.94	124	121	85	●▲
4	232	33.4	36	30.8	15.08	138	130	67	●▲
5	238	33.4	38	29.4	16.24	190	175	73	●▲
6	256	33.4	44	25.3	20.25	195	176	88	●▲
7	242	33.4	39	28.5	17.04	224	180	101	●▲
8	254	33.8	48	23.1	22.27	196	171	86	●▲
9	236	33.4	39	28.5	16.62	207	194	85	●▲
10	256	33.4	37	29.8	17.19	201	192	64	●▲
11	246	33.6	28	39.4	12.60	216	200	69	●▲
12	262	33.6	28	39.4	13.42	263	218	71	●▲
13	258	33.4	37	29.8	17.33	207	190	101	●▲
14	254	33.6	29	38.5	13.29	230	183	90	●▲
15	262	33.4	30	37.0	14.19	252	189	107	●▲
16	254	33.4	36	30.8	16.51	201	180	85	●▲
17	248	33.2	30	37.0	13.35	222	199	77	●▲
18	224	33.2	42	26.4	16.88	264	211	91	●▲
19	248	33.4	29	38.5	12.90	215	212	70	●▲
20	242	33.4	35	31.9	15.20	206	—	—	
Notes:	●・・・Slag Removal	▲・・・Nozzle Cleaning							

Figure D.10 Bottom right beam flange-to-column face welding procedure specification of Specimen 1 west beam.

Project	H-Beam to H-Column Connection Interior Joint Specimen				Date	July 1, 2021	Weather	Cloudy
Specimen (Base Metal)	Grade:	SN490B	No.:	2 (Bottom Flange Left)	Temperature	21.6°C	Humidity	69%
	Thickness:	25mm	Width:	197mm	Welder's Name		Yoshiba	
Groove Design	Bevel Angle:	30°	Root Gap:	11mm	Recorder's Name		Huy	
Welding Process	Gas Metal Arc Welding (Semi-Automatic Welding)				Welding Sequence 9 layers 21 passes 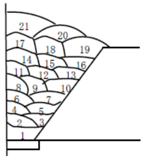 Initial Temperature(°C): 54			
	Welding Positio	Flat Position	Shielding Gas:	CO_2 (100%)				
Welding Wire	Manufacturer:	Nippon Steel Welding & Engineering co.,ltd.	Classification:	YGW18 (JIS)				
	Product Name:	YM-55C	Wire Diameter:	1.2mm				
Maximum Heat Input	30kJ/cm	Maximum Interpass Temperatur		250°C				
Measuring Instrument	Adachi HD1200K							

Pass No.	Current (A)	Voltage (V)	Arcing Time (sec)	Travel Speed (cm/min)	Heat Input (kJ/cm)	Post-Weld Temperature (°C)	Interpass Temperature (°C)	Interval Time (sec)	Remarks
1	226	33.4	44	27.0	16.78	61	63	60	●▲
2	242	33.8	25	46.9	10.46	72	60	46	●▲
3	240	33.4	32	37.2	12.94	111	126	55	●▲
4	236	33.6	35	34.0	14.01	141	145	55	●▲
5	238	33.6	37	31.8	15.10	194	155	100	●▲
6	226	33.6	42	28.1	16.19	174	165	60	●▲
7	238	33.6	39	30.3	15.83	224	185	85	●▲
8	234	33.2	29	41.0	11.36	188	186	45	●▲
9	232	33.6	22	53.2	8.78	204	199	40	●▲
10	240	33.8	30	39.4	12.35	273	208	80	●▲
11	224	33.6	37	31.8	14.21	211	151	312	●▲
12	226	33.4	33	35.8	12.64	179	173	50	●▲
13	220	34.2	30	39.4	11.46	256	164	113	●▲
14	224	33.8	42	28.1	16.14	187	186	40	●▲
15	228	33.8	34	34.6	13.38	225	211	56	●▲
16	226	33.8	27	43.8	10.47	276	196	100	●▲
17	230	33.8	28	41.9	11.13	202	190	38	●▲
18	232	33.6	30	39.4	11.87	238	223	45	●▲
19	230	33.8	38	31.3	14.92	271	226	95	●▲
20	212	34.0	33	35.8	12.07	248	208	80	●▲
21	210	34.0	40	29.4	14.57	221	—	—	

Notes: ●・・・Slag Removal ▲・・・Nozzle Cleaning

Figure D.11 Bottom left beam flange-to-column face welding procedure specification of Specimen 1 west beam.

Project		H-Beam to H-Column Connection Interior Joint Specimen				Date	July 1, 2021	Weather	Cloudy
Specimen		Grade:	SN490B	No.:	2 (Web)	Temperature	21.6°C	Humidity	69%
(Base Metal)		Thickness:	16mm	Width:	530mm	Welder's Name		Yoshiba	
Groove Design		Bevel Angle:	45°	Root Gap:	8mm	Recorder's Name		Huy	
Welding Process		Gas Metal Arc Welding (Semi-Automatic Welding)				Welding Sequence 6 layers 11 passes		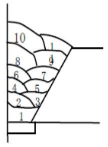	
		Welding Positio	Vertical Positior	Shielding Gas:	CO_2 (100%)				
Welding Wire		Manufacturer:	Nippon Steel Welding & Engineering co.,ltd.	Classification:	A5.36 E71T1-C1A0-CS1 (AWS)				
		Product Name:	SF-1V	Wire Diameter:	1.2mm				
Maximum Heat Input		30kJ/cm	Maximum Interpass Temperatur		250°C				
Measuring Instrument		Adachi HD1200K				Initial Temperature(°C): 58			
Pass No.	Current (A)	Voltage (V)	Arcing Time (sec)	Travel Speed (cm/min)	Heat Input (kJ/cm)	Post-Weld Temperature (°C)	Interpass Temperature (°C)	Interval Time (sec)	Remarks
1	176	24.2	141	22.6	11.33	78	78	35	●▲
2	176	24.4	132	24.1	10.70	89	83	30	●▲
3	178	24.6	144	22.1	11.90	114	104	70	●▲
4	180	24.4	147	21.6	12.18	109	100	52	●▲
5	166	24.0	161	19.8	12.08	135	130	44	●▲
6	178	24.2	179	17.8	14.53	123	112	66	●▲
7	176	23.6	176	18.1	13.78	153	142	62	●▲
8	176	23.8	206	15.5	16.27	129	122	50	●▲
9	178	23.8	210	15.1	16.79	138	121	137	●▲
10	178	24.0	272	11.7	21.91	119	111	75	●▲
11	176	23.6	288	11.0	22.57	134	—	—	
Notes:	●･･･Slag Removal	▲･･･Nozzle Cleaning							

Figure D.12 Beam web-to-column face welding procedure specification of Specimen 1 west beam.

Project		H-Beam to H-Column Connection Interior Joint Specimen				Date	May 13, 2021	Weather	Cloudy
Specimen		Grade:	SN490B	No.:	3 (Shear Tab)	Temperature	16°C	Humidity	61%
(Base Metal)		Thickness:	16mm	Width:	550mm	Welder's Name		Yoshiba	
Groove Design		Bevel Angle:	45°	Root Gap:	0mm	Recorder's Name		Huy	
Welding Process		Gas Metal Arc Welding (Semi-Automatic Welding)				Welding Sequence 6 layers 7 passes 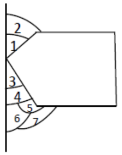 Initial Temperature(°C): 86			
		Welding Positio	Flat Position	Shielding Gas:	CO_2 (100%)				
Welding Wire		Manufacturer:	Kobe Steel, ltd.	Classification:	YGW18 (JIS)				
		Product Name:	MG-56	Wire Diameter:	1.2mm				
Maximum Heat Input		30kJ/cm	Maximum Interpass Temperatur		250°C				
Measuring Instrument		Adachi HD1200K							
Pass No.	Current (A)	Voltage (V)	Arcing Time (sec)	Travel Speed (cm/min)	Heat Input (kJ/cm)	Post-Weld Temperature (°C)	Interpass Temperature (°C)	Interval Time (sec)	Remarks
1	256	35.0	102	32.4	16.62	220	112	162	●▲
2	278	35.0	100	32.9	17.73	247	74	Back Gouging	●▲
3	264	30.0	129	25.6	18.58	183	96	151	●▲
4	276	33.0	136	24.2	22.55	236	129	137	●▲
5	240	33.0	75	44.0	10.80	236	134	39	●▲
6	270	33.0	93	35.5	15.07	184	127	130	●▲
7	242	33.0	102	32.4	14.81	256	–	–	
Notes: ●···Slag Removal ▲···Nozzle Cleaning									

Figure D.13 Shear tab-to-column face welding procedure specification of Specimen 2 east beam.

Project	H-Beam to H-Column Connection Interior Joint Specimen				Date	June 24, 2021	Weather	Cloudy
Specimen	Grade:	SN490B	No.:	3 (Top Flange)	Temperature	22°C	Humidity	58%
(Base Metal)	Thickness:	25mm	Width:	376mm	Welder's Name		Yoshiba	
Groove Design	Bevel Angle:	30°	Root Gap:	10mm	Recorder's Name		Ueno	
Welding Process	Gas Metal Arc Welding (Semi-Automatic Welding)				Welding Sequence 9 layers 16 passes 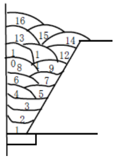 16 13 15 14 11 1 12 10 8 9 6 7 4 5 3 2 1 Initial Temperature(°C): 66			
	Welding Positio	Flat Position	Shielding Gas:	CO$_2$ (100%)				
Welding Wire	Manufacturer:	Nippon Steel Welding & Engineering co.,ltd.	Classification:	YGW18 (JIS)				
	Product Name:	YM-55C	Wire Diameter:	1.2mm				
Maximum Heat Input	30kJ/cm	Maximum Interpass Temperatur		250°C				
Measuring Instrument	Adachi HD1200K							

Pass No.	Current (A)	Voltage (V)	Arcing Time (sec)	Travel Speed (cm/min)	Heat Input (kJ/cm)	Post-Weld Temperature (°C)	Interpass Temperature (°C)	Interval Time (sec)	Remarks
1	226	33.2	88	25.6	17.60	79	73	75	●▲
2	222	33.4	111	20.3	21.89	146	120	100	●▲
3	234	33.4	114	19.8	23.70	149	139	105	●▲
4	232	33.6	57	39.6	11.82	138	140	75	●▲
5	234	33.6	72	31.3	15.06	178	126	195	●▲
6	246	33.2	85	26.5	18.51	146	147	70	●▲
7	246	33.2	70	32.1	15.25	182	138	158	●▲
8	252	33.6	82	27.5	18.51	158	164	65	●▲
9	246	33.8	87	25.9	19.24	208	182	90	●▲
10	248	33.6	80	28.3	17.69	148	174	55	●▲
11	234	33.6	50	45.3	10.41	184	169	70	●▲
12	262	33.6	60	37.6	14.05	213	188	205	●▲
13	232	33.8	53	42.7	11.01	168	169	50	●▲
14	224	33.8	55	40.9	11.12	196	169	120	●▲
15	224	33.6	76	29.6	15.25	198	191	70	●▲
16	264	33.6	70	32.1	16.56	187	—	—	

Notes: ●･･･Slag Removal ▲･･･Nozzle Cleaning

Figure D.14 Top beam flange-to-column face welding procedure specification of Specimen 2 east beam.

Project	H-Beam to H-Column Connection Interior Joint Specimen				Date	June 24, 2021	Weather	Cloudy
Specimen	Grade:	SN490B	No.:	3 (Bottom Flange Right)	Temperature	22°C	Humidity	58%
(Base Metal)	Thickness:	25mm	Width:	205mm	Welder's Name		Yoshiba	
Groove Design	Bevel Angle:	30°	Root Gap:	10mm	Recorder's Name		Ueno	
Welding Process	Gas Metal Arc Welding (Semi-Automatic Welding)				Welding Sequence 9 layers 20 passes 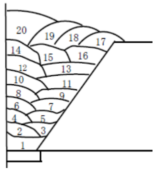 Initial Temperature(°C): 52			
	Welding Positio	Flat Position	Shielding Gas:	CO$_2$ (100%)				
Welding Wire	Manufacturer:	Nippon Steel Welding & Engineering co.,ltd.	Classification:	YGW18 (JIS)				
	Product Name:	YM-55C	Wire Diameter:	1.2mm				
Maximum Heat Input	30kJ/cm	Maximum Interpass Temperatur		250°C				
Measuring Instrument	Adachi HD1200K							

Pass No.	Current (A)	Voltage (V)	Arcing Time (sec)	Travel Speed (cm/min)	Heat Input (kJ/cm)	Post-Weld Temperature (°C)	Interpass Temperature (°C)	Interval Time (sec)	Remarks
1	232	33.8	42	29.3	16.06	62	65	80	●▲
2	246	33.6	25	48.8	10.16	72	73	85	●▲
3	246	33.4	30	41.0	12.02	125	122	70	●▲
4	242	33.4	34	36.0	13.49	142	136	105	●▲
5	242	33.4	31	39.4	12.30	166	162	65	●▲
6	258	33.6	30	41.0	12.69	154	163	55	●▲
7	236	33.8	35	35.3	13.54	203	196	80	●▲
8	232	33.6	34	36.0	13.01	197	184	76	●▲
9	232	33.6	37	33.1	14.15	218	206	84	●▲
10	250	33.6	39	31.5	15.98	209	194	78	●▲
11	226	33.6	35	35.3	12.89	232	195	105	●▲
12	236	33.6	44	28.1	16.94	213	186	90	●▲
13	234	33.4	39	31.5	14.87	247	176	161	●▲
14	248	33.8	31	39.4	12.76	168	163	60	●▲
15	252	33.6	28	43.6	11.65	194	177	75	●▲
16	248	33.2	30	41.0	12.05	206	184	75	●▲
17	242	33.2	32	38.7	12.46	235	208	75	●▲
18	222	33.4	35	35.3	12.59	223	218	60	●▲
19	242	33.2	35	35.3	13.64	208	168	110	●▲
20	246	33.4	34	36.0	13.71	183	—	—	

Notes: ●・・・Slag Removal ▲・・・Nozzle Cleaning

Figure D.15 Bottom right beam flange-to-column face welding procedure specification of Specimen 2 east beam.

Project		H-Beam to H-Column Connection Interior Joint Specimen				Date	June 24, 2021	Weather	Cloudy
Specimen (Base Metal)		Grade:	SN490B	No.:	3 (Bottom Flange Left)	Temperature	22°C	Humidity	58%
		Thickness:	25mm	Width:	185mm	Welder's Name		Yoshiba	
Groove Design		Bevel Angle:	30°	Root Gap:	10mm	Recorder's Name		Ueno	
Welding Process		Gas Metal Arc Welding (Semi-Automatic Welding)				Welding Sequence 8 layers 18 passes 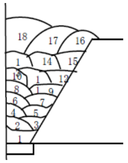 18 17 16 1 14 15 10 1 12 8 1 9 6 7 4 5 2 3 1 Initial Temperature(°C): 72			
		Welding Positio	Flat Position	Shielding Gas:	CO_2 (100%)				
Welding Wire		Manufacturer:	Nippon Steel Welding & Engineering co.,ltd.	Classification:	YGW18 (JIS)				
		Product Name:	YM-55C	Wire Diameter:	1.2mm				
Maximum Heat Input		30kJ/cm	Maximum Interpass Temperatur		250°C				
Measuring Instrument		Adachi HD1200K							
Pass No.	Current (A)	Voltage (V)	Arcing Time (sec)	Travel Speed (cm/min)	Heat Input (kJ/cm)	Post-Weld Temperature (°C)	Interpass Temperature (°C)	Interval Time (sec)	Remarks
1	222	33.6	43	25.7	17.42	78	79	45	●▲
2	232	33.6	23	48.7	9.61	79	82	55	●▲
3	234	33.6	32	34.9	13.51	132	151	56	●▲
4	240	33.6	33	33.6	14.38	154	161	50	●▲
5	246	33.4	30	37.0	13.32	202	206	55	●▲
6	248	33.6	36	30.8	16.22	190	176	115	●▲
7	248	33.6	36	30.8	16.22	222	179	110	●▲
8	240	33.6	37	29.8	16.21	178	192	56	●▲
9	236	33.2	40	27.6	17.03	261	189	200	●▲
10	222	33.4	34	32.5	13.71	193	189	70	●▲
11	238	33.6	22	50.0	9.60	204	198	50	●▲
12	252	33.4	27	41.1	12.28	252	179	200	●▲
13	246	33.4	36	30.8	15.99	191	188	57	●▲
14	246	33.4	30	37.0	13.32	212	206	48	●▲
15	242	33.4	29	38.5	12.58	272	189	150	●▲
16	232	33.2	32	34.9	13.24	218	206	130	●▲
17	254	33.2	30	37.0	13.67	222	207	60	●▲
18	234	33.0	35	31.9	14.52	204	—	—	
Notes: ●・・・Slag Removal ▲・・・Nozzle Cleaning									

Figure D.16 Bottom left beam flange-to-column face welding procedure specification of Specimen 2 east beam.

Project		H-Beam to H-Column Connection Interior Joint Specimen				Date	June 24, 2021	Weather	Cloudy
Specimen		Grade:	SN490B	No.:	3 (Web)	Temperature	22°C	Humidity	58%
(Base Metal)		Thickness:	16mm	Width:	530mm	Welder's Name		Yoshiba	
Groove Design		Bevel Angle:	45°	Root Gap:	10mm	Recorder's Name		Ueno	
Welding Process		Gas Metal Arc Welding (Semi-Automatic Welding)				Welding Sequence		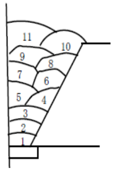	
		Welding Positio	Vertical Positio	Shielding Gas:	CO_2 (100%)	7 layers 11 passes			
Welding Wire		Manufacturer:	Nippon Steel Welding & Engineering co.,ltd.	Classification:	A5.36 E71T1-C1A0-CS1 (AWS)				
		Product Name:	SF-1V	Wire Diameter:	1.2mm				
Maximum Heat Input		30kJ/cm	Maximum Interpass Temperatur		250°C				
Measuring Instrument		Adachi HD1200K				Initial Temperature(°C): 53			
Pass No.	Current (A)	Voltage (V)	Arcing Time (sec)	Travel Speed (cm/min)	Heat Input (kJ/cm)	Post-Weld Temperature (°C)	Interpass Temperature (°C)	Interval Time (sec)	Remarks
1	164	24.6	170	18.7	12.92	87	78	100	●▲
2	164	24.8	190	16.7	14.60	106	93	70	●▲
3	162	24.8	218	14.6	16.51	116	112	55	●▲
4	172	24.6	140	22.8	11.16	134	118	105	●▲
5	178	24.8	165	19.3	13.74	135	119	100	●▲
6	166	24.8	178	17.9	13.84	144	126	140	●▲
7	174	24.2	155	20.5	12.30	128	116	170	●▲
8	170	25.0	173	18.4	13.86	129	118	72	●▲
9	164	25.4	172	18.5	13.53	119	114	130	●▲
10	162	25.4	170	18.7	13.18	122	120	70	●▲
11	172	24.6	182	17.5	14.52	126	—	—	
Notes:	●・・・Slag Removal	▲・・・Nozzle Cleaning							

Figure D.17 Beam web-to-column face welding procedure specification of Specimen 2 east beam.

Project		H-Beam to H-Column Connection Interior Joint Specimen				Date	May 13, 2021	Weather	Cloudy
Specimen		Grade:	SN490B	No.:	4 (Shear Tab)	Temperature	16°C	Humidity	61%
(Base Metal)		Thickness:	16mm	Width:	550mm	Welder's Name		Yoshiba	
Groove Design		Bevel Angle:	45°	Root Gap:	0mm	Recorder's Name		Huy	
Welding Process		Gas Metal Arc Welding (Semi-Automatic Welding)				Welding Sequence			
		Welding Positio	Flat Position	Shielding Gas:	CO_2 (100%)	6 layers 7 passes		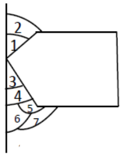	
Welding Wire		Manufacturer:	Kobe Steel, ltd.	Classification:	YGW18 (JIS)				
		Product Name:	MG-56	Wire Diameter:	1.2mm				
Maximum Heat Input		30kJ/cm	Maximum Interpass Temperatur		250°C				
Measuring Instrument		Adachi HD1200K				Initial Temperature(°C): 79			
Pass No.	Current (A)	Voltage (V)	Arcing Time (sec)	Travel Speed (cm/min)	Heat Input (kJ/cm)	Post-Weld Temperature (°C)	Interpass Temperature (°C)	Interval Time (sec)	Remarks
1	280	35.0	91	36.2	16.25	213	104	110	●▲
2	284	35.0	95	34.8	17.13	203	77	Back Gouging	●▲
3	242	33.0	112	29.4	16.29	166	94	198	●▲
4	256	33.0	132	25.0	20.28	241	122	127	●▲
5	240	32.0	86	38.5	11.98	220	142	97	●▲
6	252	33.0	99	33.3	14.97	175	160	55	●▲
7	252	32.0	103	32.0	15.13	246	—	—	
Notes:	●・・・Slag Removal	▲・・・Nozzle Cleaning							

Figure D.18 Shear tab-to-column face welding procedure specification of Specimen 2 west beam.

Project		H-Beam to H-Column Connection Interior Joint Specimen				Date	June 23, 2021	Weather	Cloudy
Specimen		Grade:	SN490B	No.:	4 (Top Flange)	Temperature	21.5°C	Humidity	58%
(Base Metal)		Thickness:	25mm	Width:	375mm	Welder's Name		Yoshiba	
Groove Design		Bevel Angle:	30°	Root Gap:	10mm	Recorder's Name		Ueno	
Welding Process		Gas Metal Arc Welding (Semi-Automatic Welding)				Welding Sequence 9 layers 15 passes		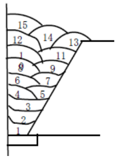 15 12 14 13 1 11 9 8 9 6 7 4 5 3 2 1	
		Welding Positio	Flat Position	Shielding Gas:	CO_2 (100%)				
Welding Wire		Manufacturer:	Nippon Steel Welding & Engineering co.,ltd.	Classification:	YGW18 (JIS)				
		Product Name:	YM-55C	Wire Diameter:	1.2mm				
Maximum Heat Input		30kJ/cm	Maximum Interpass Temperatur		250°C				
Measuring Instrument		Adachi HD1200K				Initial Temperature(°C): 61.2			
Pass No.	Current (A)	Voltage (V)	Arcing Time (sec)	Travel Speed (cm/min)	Heat Input (kJ/cm)	Post-Weld Temperature (°C)	Interpass Temperature (°C)	Interval Time (sec)	Remarks
1	234	34.0	85	26.4	18.07	73	71	80	●▲
2	236	34.8	112	20.1	24.58	151	115	135	●▲
3	250	34.6	101	22.3	23.25	166	125	156	●▲
4	252	35.0	55	40.8	12.98	140	133	53	●▲
5	248	34.8	56	40.3	12.84	187	152	100	●▲
6	250	35.0	60	37.5	14.00	166	139	105	●▲
7	252	34.8	71	31.8	16.56	209	147	159	●▲
8	246	34.6	67	33.5	15.25	174	136	124	●▲
9	234	34.6	91	24.7	19.69	214	159	135	●▲
10	240	34.6	87	25.9	19.27	185	158	120	●▲
11	242	34.6	94	23.9	21.03	228	184	125	●▲
12	230	34.8	78	28.9	16.65	179	142	180	●▲
13	220	35.0	67	33.5	13.80	183	133	180	●▲
14	286	34.2	63	35.7	16.43	205	161	100	●▲
15	240	34.6	74	30.5	16.34	163	—	—	
Notes:	●・・・Slag Removal	▲・・・Nozzle Cleaning							

Figure D.19 Top beam flange-to-column face welding procedure specification of Specimen 2 west beam.

Project		H-Beam to H-Column Connection Interior Joint Specimen				Date	June 23, 2021	Weather	Cloudy
Specimen (Base Metal)		Grade:	SN490B	No.:	4 (Bottom Flange Right)	Temperature	21.5°C	Humidity	58%
		Thickness:	25mm	Width:	185mm	Welder's Name		Yoshiba	
Groove Design		Bevel Angle:	30°	Root Gap:	10mm	Recorder's Name		Ueno	
Welding Process		Gas Metal Arc Welding (Semi-Automatic Welding)				Welding Sequence 9 layers 17 passes 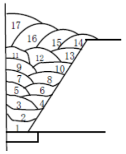 1 2 3 4 5 6 7 8 9 10 11 12 13 14 15 16 17 Initial Temperature(°C): 66			
		Welding Positio	Flat Position	Shielding Gas:	CO_2 (100%)				
Welding Wire		Manufacturer:	Nippon Steel Welding & Engineering co.,ltd.	Classification:	YGW18 (JIS)				
		Product Name:	YM-55C	Wire Diameter:	1.2mm				
Maximum Heat Input		30kJ/cm	Maximum Interpass Temperatur		250°C				
Measuring Instrument		Adachi HD1200K							
Pass No.	Current (A)	Voltage (V)	Arcing Time (sec)	Travel Speed (cm/min)	Heat Input (kJ/cm)	Post-Weld Temperature (°C)	Interpass Temperature (°C)	Interval Time (sec)	Remarks
1	234	34.6	40	27.6	17.59	76	74	45	●▲
2	230	34.8	57	19.5	24.67	146	128	120	●▲
3	233	35.0	29	38.5	12.70	136	128	80	●▲
4	272	34.6	30	37.0	15.26	192	146	120	●▲
5	234	34.8	31	35.6	13.73	156	149	85	●▲
6	254	34.8	36	30.8	17.20	209	148	140	●▲
7	246	34.6	41	27.2	18.77	174	165	85	●▲
8	234	34.6	41	27.2	17.85	215	171	105	●▲
9	250	34.6	42	26.4	19.64	198	180	70	●▲
10	252	34.6	42	26.4	19.79	257	176	155	●▲
11	250	34.6	36	30.8	16.83	178	186	65	●▲
12	256	34.6	25	44.1	12.06	220	184	110	●▲
13	276	34.8	26	43.0	13.40	240	190	150	●▲
14	252	34.8	27	41.1	12.80	223	190	96	●▲
15	248	34.8	30	37.0	14.00	200	180	120	●▲
16	272	34.8	23	48.7	11.67	212	186	77	●▲
17	254	34.6	31	35.6	14.82	194	—	—	
Notes:	●・・・Slag Removal	▲・・・Nozzle Cleaning							

Figure D.20 Bottom right beam flange-to-column face welding procedure specification of Specimen 2 west beam.

Project		H-Beam to H-Column Connection Interior Joint Specimen				Date	June 23, 2021	Weather	Cloudy
Specimen (Base Metal)		Grade:	SN490B	No.:	4 (Bottom Flange Left)	Temperature	21.5°C	Humidity	58%
		Thickness:	25mm	Width:	195mm	Welder's Name		Yoshiba	
Groove Design		Bevel Angle:	30°	Root Gap:	10mm	Recorder's Name		Ueno	
Welding Process		Gas Metal Arc Welding (Semi-Automatic Welding)				Welding Sequence 9 layers 17 passes 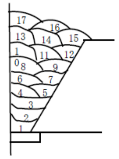 Initial Temperature(°C): 71			
		Welding Positio	Flat Position	Shielding Gas:	CO_2 (100%)				
Welding Wire		Manufacturer:	Nippon Steel Welding & Engineering co.,ltd.	Classification:	YGW18 (JIS)				
		Product Name:	YM-55C	Wire Diameter:	1.2mm				
Maximum Heat Input		30kJ/cm	Maximum Interpass Temperatur		250°C				
Measuring Instrument		Adachi HD1200K							
Pass No.	Current (A)	Voltage (V)	Arcing Time (sec)	Travel Speed (cm/min)	Heat Input (kJ/cm)	Post-Weld Temperature (°C)	Interpass Temperature (°C)	Interval Time (sec)	Remarks
1	240	34.6	40	29.1	17.12	78	84	60	●▲
2	230	34.4	43	27.1	17.53	145	122	140	●▲
3	232	34.6	43	27.1	17.79	165	163	60	●▲
4	240	34.4	31	37.5	13.21	162	169	66	●▲
5	248	34.4	32	36.8	13.91	212	207	70	●▲
6	240	34.4	44	26.7	18.55	201	194	75	●▲
7	252	33.8	36	32.5	15.72	249	169	150	●▲
8	258	34.4	36	32.5	16.38	194	168	94	●▲
9	236	34.2	39	30.0	16.14	219	214	96	●▲
10	234	34.6	29	40.6	11.96	209	185	66	●▲
11	254	34.4	22	52.7	9.95	205	189	70	●▲
12	242	34.0	30	39.0	12.66	279	192	126	●▲
13	246	34.4	29	40.6	12.50	210	190	102	●▲
14	242	34.2	23	51.3	9.68	213	187	96	●▲
15	240	34.4	35	33.6	14.73	251	227	70	●▲
16	262	34.2	28	41.5	12.96	239	228	50	●▲
17	232	34.6	35	33.6	14.33	221	–	–	
Notes: ●・・・Slag Removal ▲・・・Nozzle Cleaning									

Figure D.21 Bottom left beam flange-to-column face welding procedure specification of Specimen 2 west beam.

Project		H-Beam to H-Column Connection Interior Joint Specimen				Date	June 23, 2021	Weather	Cloudy
Specimen		Grade:	SN490B	No.:	4 (Web)	Temperature	21.5°C	Humidity	57%
(Base Metal)		Thickness:	16mm	Width:	530mm	Welder's Name		Yoshiba	
Groove Design		Bevel Angle:	45°	Root Gap:	10mm	Recorder's Name		Ueno	
Welding Process		Gas Metal Arc Welding (Semi-Automatic Welding)				Welding Sequence		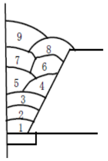	
		Welding Positio	Vertical Positior	Shielding Gas:	CO_2 (100%)	6 layers 9 passes			
Welding Wire		Manufacturer:	Nippon Steel Welding & Engineering co.,ltd.	Classification:	A5.36 E71T1-C1A0-CS1 (AWS)				
		Product Name:	SF-1V	Wire Diameter:	1.2mm				
Maximum Heat Input		30kJ/cm	Maximum Interpass Temperatur		250°C				
Measuring Instrument		Adachi HD1200K				Initial Temperature(°C): 51			
Pass No.	Current (A)	Voltage (V)	Arcing Time (sec)	Travel Speed (cm/min)	Heat Input (kJ/cm)	Post-Weld Temperature (°C)	Interpass Temperature (°C)	Interval Time (sec)	Remarks
1	162	26.6	174	18.3	14.14	93	75	130	●▲
2	154	25.4	207	15.4	15.28	105	76	240	●▲
3	170	26.0	204	15.6	17.01	120	95	198	●▲
4	170	26.0	143	22.3	11.91	140	105	130	●▲
5	174	26.0	153	20.8	13.06	132	107	135	●▲
6	174	25.8	164	19.4	13.88	253	116	135	●▲
7	176	26.0	159	21.4	12.85	134	107	165	●▲
8	174	26.6	210	15.1	18.34	157	108	220	●▲
9	170	26.4	179	17.8	15.14	135	—	—	
Notes:	●・・・Slag Removal ▲・・・Nozzle Cleaning								

Figure D.22 Beam web-to-column face welding procedure specification of Specimen 2 west beam.

D.3 Ultrasonic test results

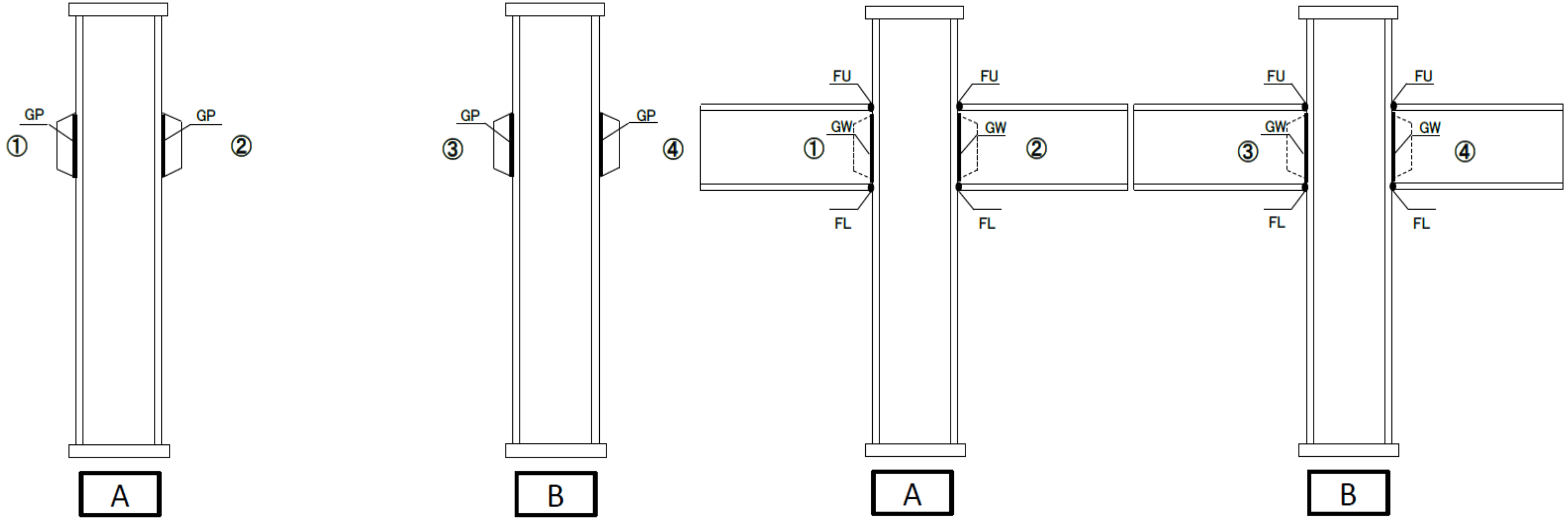
GP
GP
①
②
A
GP
GP
③
④
B
FU
FU
GW
GW
①
②
FL
FL
A
FU
FU
GW
GW
③
④
FL
FL
B

Figure D.23 Locations of welds subjected to ultrasonic test.

Table D.2 Overview of the ultrasonic test results of both test specimens.

	Weld identification	Number of Inspections	Number of Visual Inspections	Number of Failures	Acceptance Rate	Number of UT Inspections	Number of Failures	Acceptance Rate	Number of Acceptable Defects	Defect No.	Inspection Date
1	A1-GP (Shear Tab)	1	1	0	100%	1	0	100%	1	1	5/14/2021
2	A2-GP (Shear Tab)	1	1	0	100%	1	0	100%	0	—	5/14/2021
3	B3-GP (Shear Tab)	1	1	0	100%	1	0	100%	0	—	5/14/2021
4	B4-GP (Shear Tab)	1	1	0	100%	1	0	100%	0	—	5/14/2021
5	B3-FU (Top Flange)	1	1	0	100%	1	0	100%	0	—	6/24/2021
6	B3-FL (Bottom Flange)	1	1	0	100%	1	0	100%	0	—	6/24/2021
7	B3-GW (Web)	1	1	0	100%	1	0	100%	0	—	6/24/2021
8	B4-FU (Top Flange)	1	1	0	100%	1	0	100%	0	—	6/25/2021
9	B4-FL (Bottom Flange)	1	1	0	100%	1	0	100%	0	—	6/25/2021
10	B4-GW (Web)	1	1	0	100%	1	0	100%	0	—	6/25/2021
11	A1-FU (Top Flange)	1	1	0	100%	1	0	100%	0	—	7/2/2021
12	A1-FL (Bottom Flange)	1	1	0	100%	1	0	100%	0	—	7/2/2021
13	A1-GW (Web)	1	1	0	100%	1	0	100%	0	—	7/2/2021
14	A2-FU (Top Flange)	1	1	0	100%	1	0	100%	0	—	7/2/2021
15	A2-FL (Bottom Flange)	1	1	0	100%	1	0	100%	1	2	7/2/2021
16	A2-GW (Web)	1	1	0	100%	1	0	100%	0	—	7/2/2021
	Subtotal	16	16	0	100%	16	0	100%	2	1,2	

Defect No.	Acceptance / Rejection	Weld identification	Groove Design	Thickness of inspected plate (mm)	UT Length (mm)	Surface	Probe Angle (°)	Location (mm)					Region of echo height	Single Defect Length (mm)	Equivalent Single Defect Length (mm)	Summation (mm)	Threshold Length (mm)	Re-inspection
								X	Y	W	d	k						
1	Accept	A1-GP (Shear Tab)	K (Double Bevel Groove)	16	550	A	70	245	38	33	11	7	III	15	15	–	20	–
2	Accept	A2-FL (Bottom Flange)	レ (Single Bevel Groove)	25	300	B	70	160	40	28	15	14	III	15	15	–	25	–

	Location of Defect	
1	Location on the plane	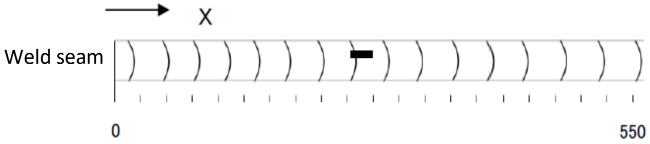 X Weld seam 0 550
	Location in cross section	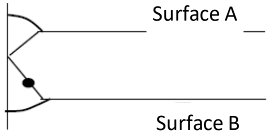 Surface A Surface B
2	Location on the plane	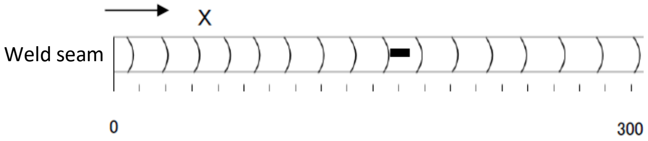 X Weld seam 0 300
	Location in cross section	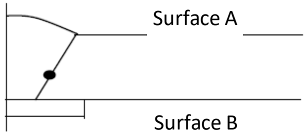 Surface A Surface B

Definitions:
X:Distance from left end of the weld seam to start of the defect
Y:Distance from reference line to probe
W:Ultrasonic transmission distance from probe to the defect
d:Depth from surfae to the defect
k:Y-direction distance from reference line to the defect
L:Single defect length

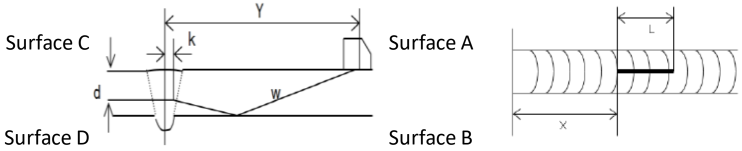
Y
Surface C
k
Surface A
d
W
Surface D
Surface B
L
X

Figure D.24 Ultrasonic test results.

Appendix E. Material test results

Description

This appendix includes material test results from coupons extracted from the web and flanges of the steel beams and columns of the test specimens described in Chapter 5.

E.1 Monotonic material test results

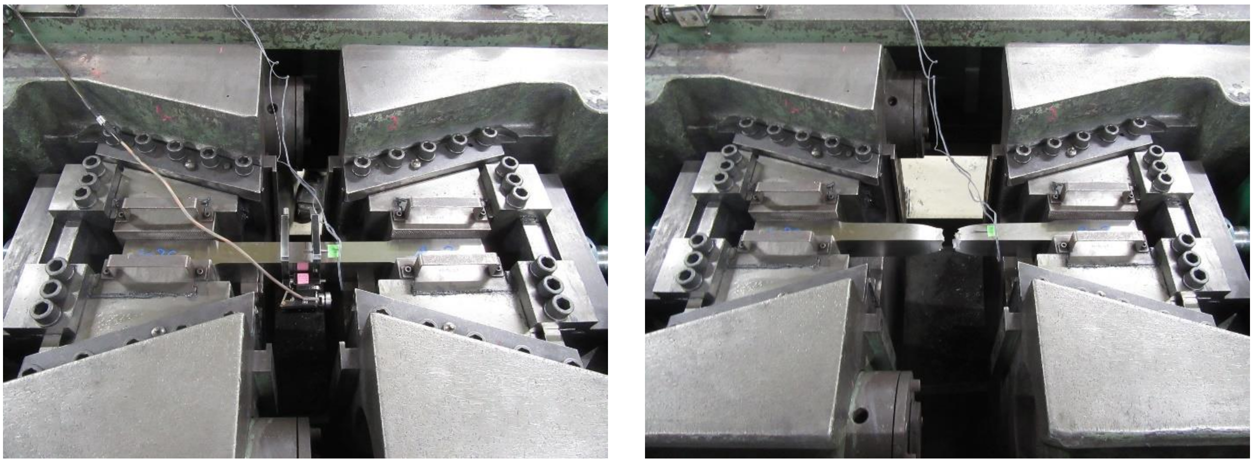

Figure E.1 Representative monotonic coupon test before and after test (Column flange, 2nd test).

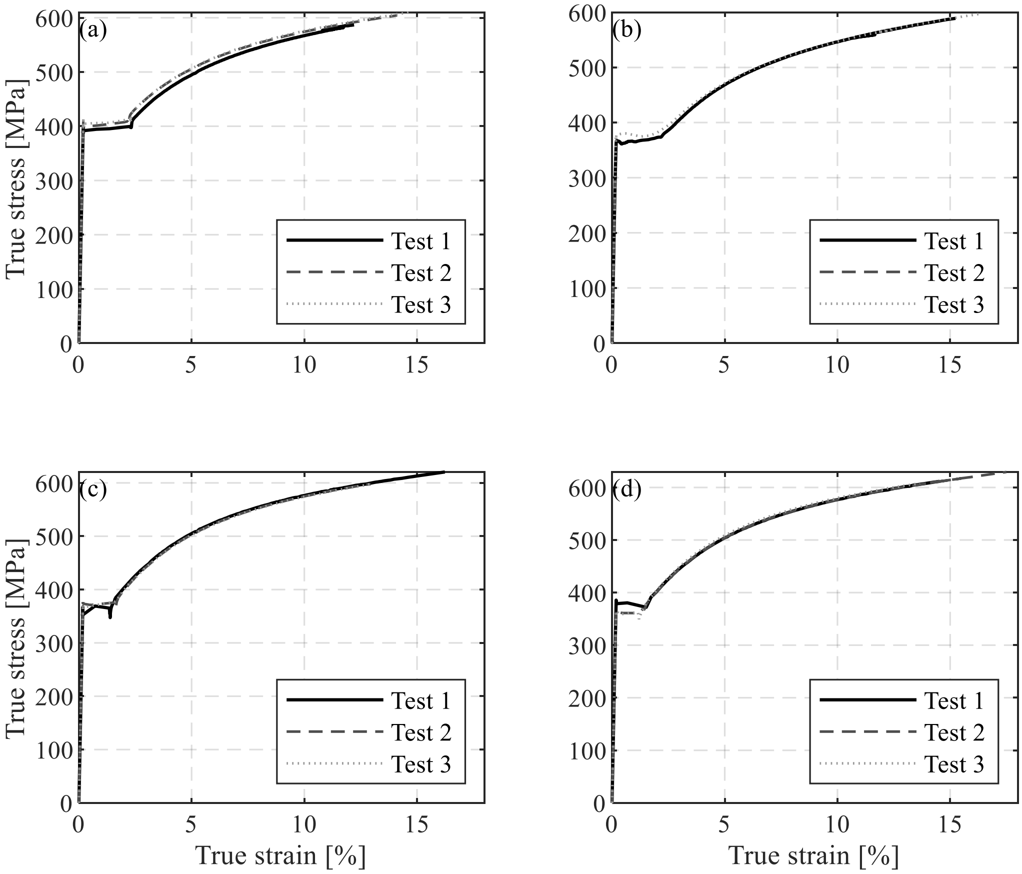

Figure E.2 Monotonic coupon test results: (a) beam web; (b) beam flange; (c) column web; and (d) column flange.

E.2 Cyclic material test results

The 10 strain-based uniaxial loading protocols based on the testing procedures of de Castro e Sousa et al. (2020) are described herein. The cyclic coupon test results are compared with the simulation results by employing the multiaxial constitutive law proposed by Hartloper et al. (2021), based on two backstresses. The calibrated material model parameters are shown in Table E.1 for the column and beam flanges and webs, where E is the Young's modulus, $\sigma_{y,0}$ is the equivalent yield stress at zero plastic strain, Q_∞ and b are the maximum and the rate of expansion of the yield surface, accordingly, D_∞ and a are the magnitude and rate of decrease in the initial yield stress, accordingly, C_k and γ_k are parameters that describe the magnitude and rate of the yield surface translation of the backstress component k.

Table E.1 Calibrated parameters of multiaxial constitutive law for the steel material of columns and beams.

Parameter	E (MPa)	$\sigma_{y,0}$ (MPa)	Q_∞ (MPa)	b	D_∞ (MPa)	a	C_1 (MPa)	γ_1	C_2 (MPa)	γ_2
Column flange	182459	324.7	144.6	16.6	95.8	280.2	21872.5	185.0	2586.2	15.3
Column web	182120	329.0	144.1	18.6	107.2	227.8	19457.9	158.6	2270.4	12.4
Beam flange	181105	358.1	141.4	21.1	148.2	138.5	16047.8	130.2	1498.9	7.7
Beam web	172061	385.6	120.9	19.1	143.5	145.7	16984.2	132.5	1835.5	9.2

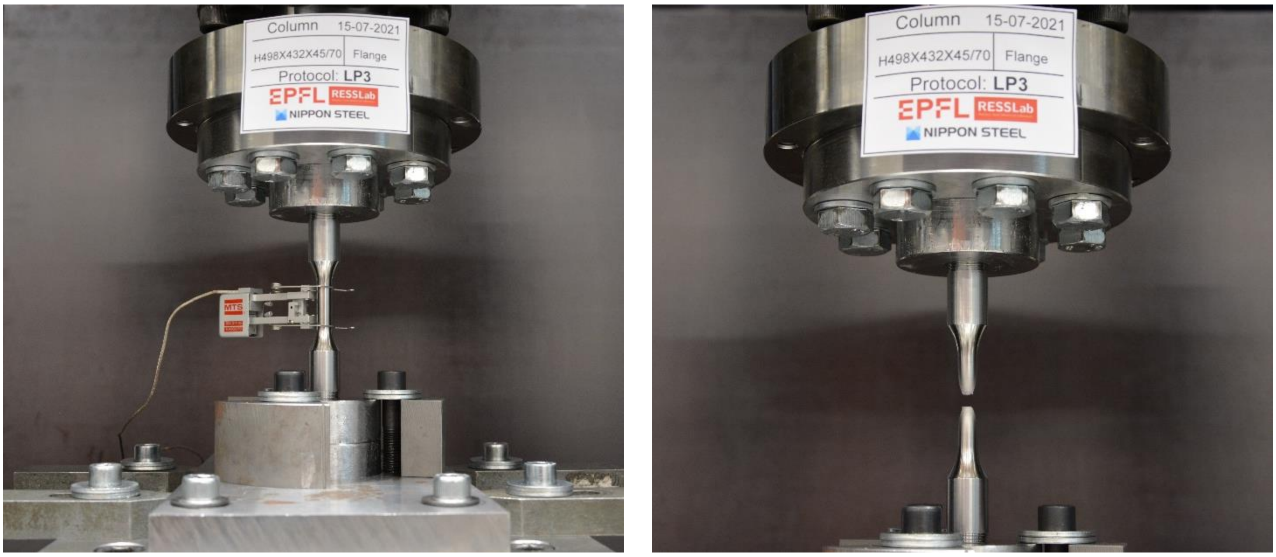
Column 15-07-2021
H498X432X45/70 Flange
Protocol: LP3
EPFL RESSLab
NIPPON STEEL
MTS
Column 15-07-2021
H498X432X45/70 Flange
Protocol: LP3
EPFL RESSLab
NIPPON STEEL

Figure E.3 Representative cyclic coupon test before and after test (Column flange, loading protocol 3).

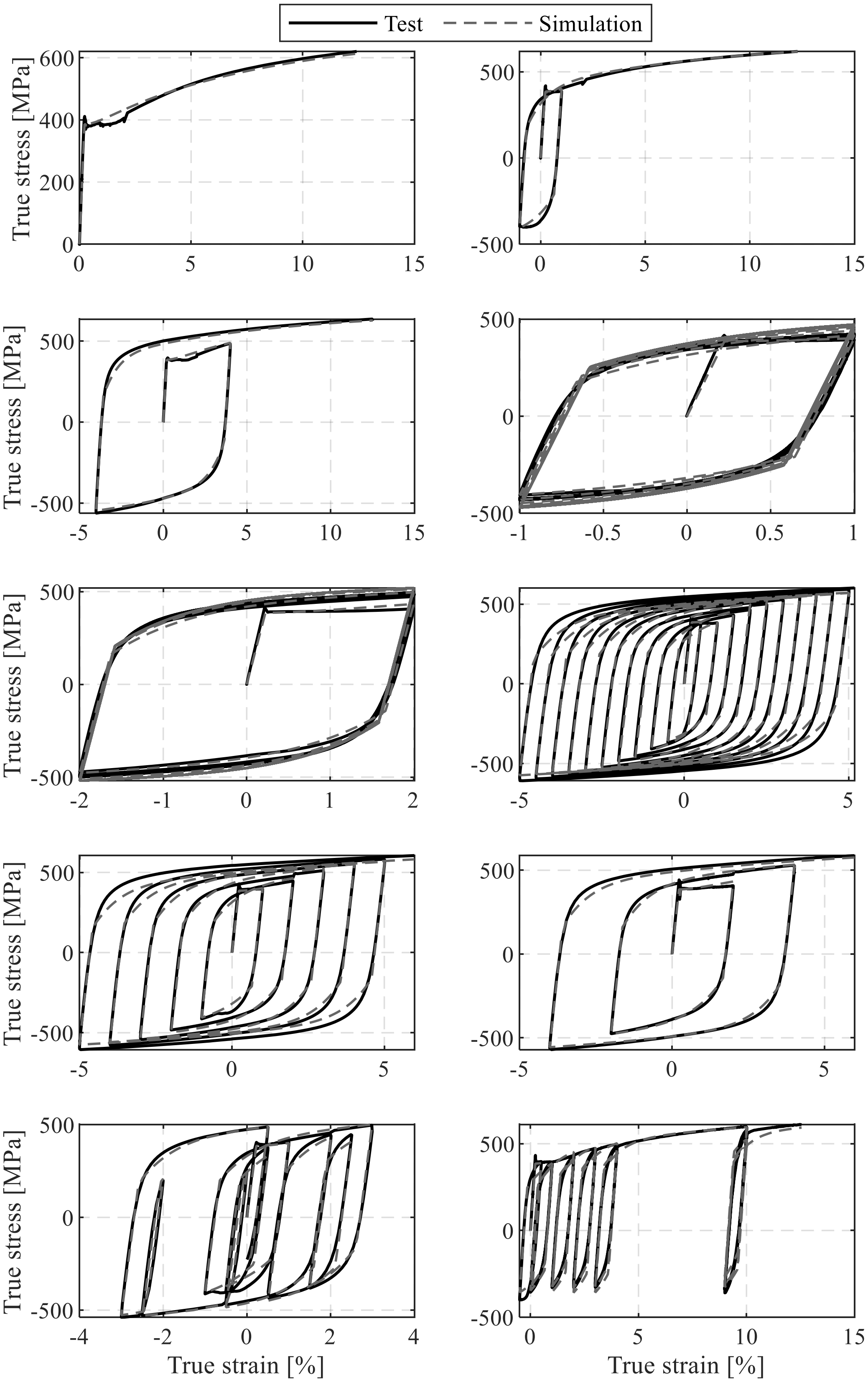

Figure E.4 Beam web coupon test and simulation results.

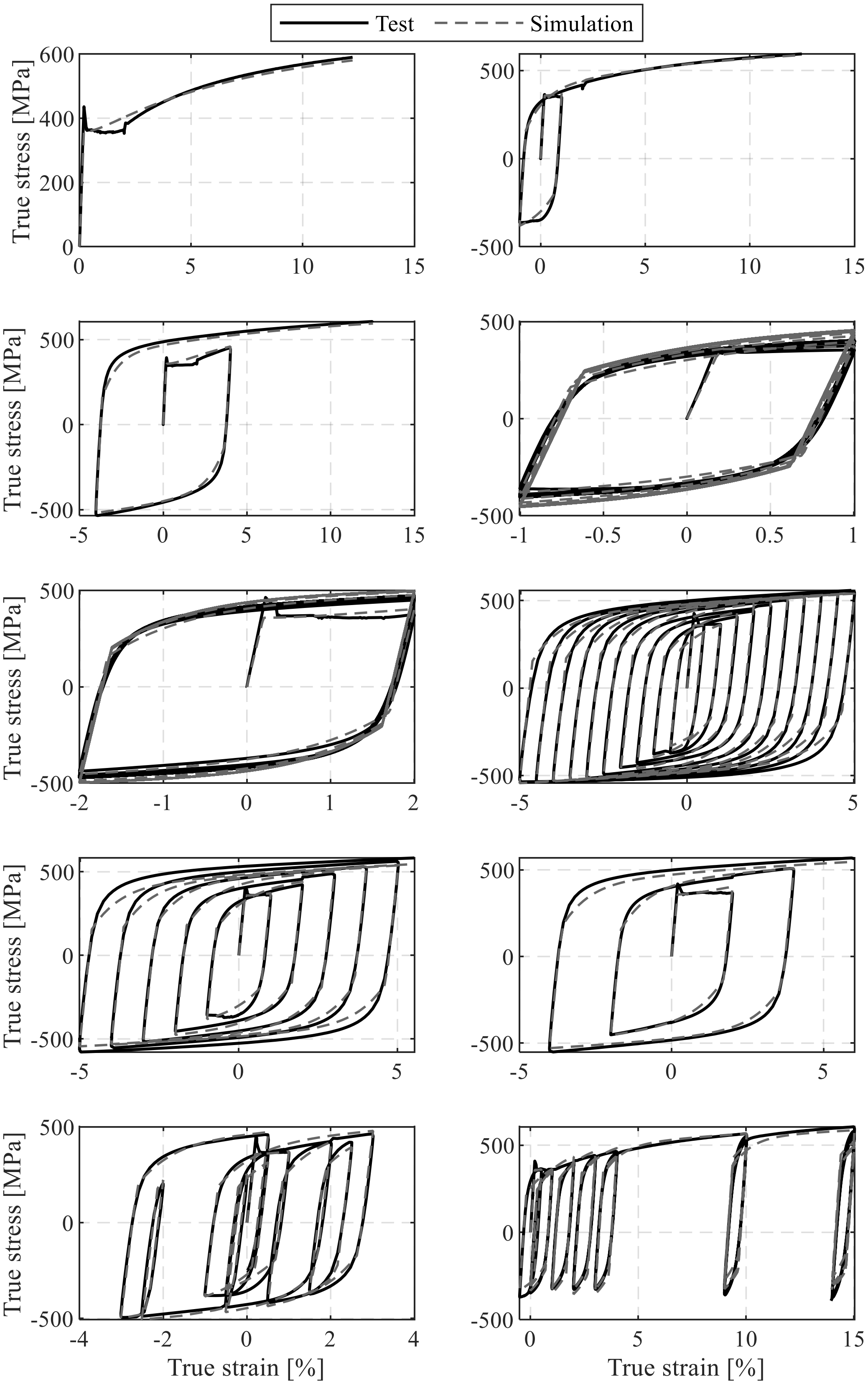

Figure E.5 Beam flange coupon test and simulation results.

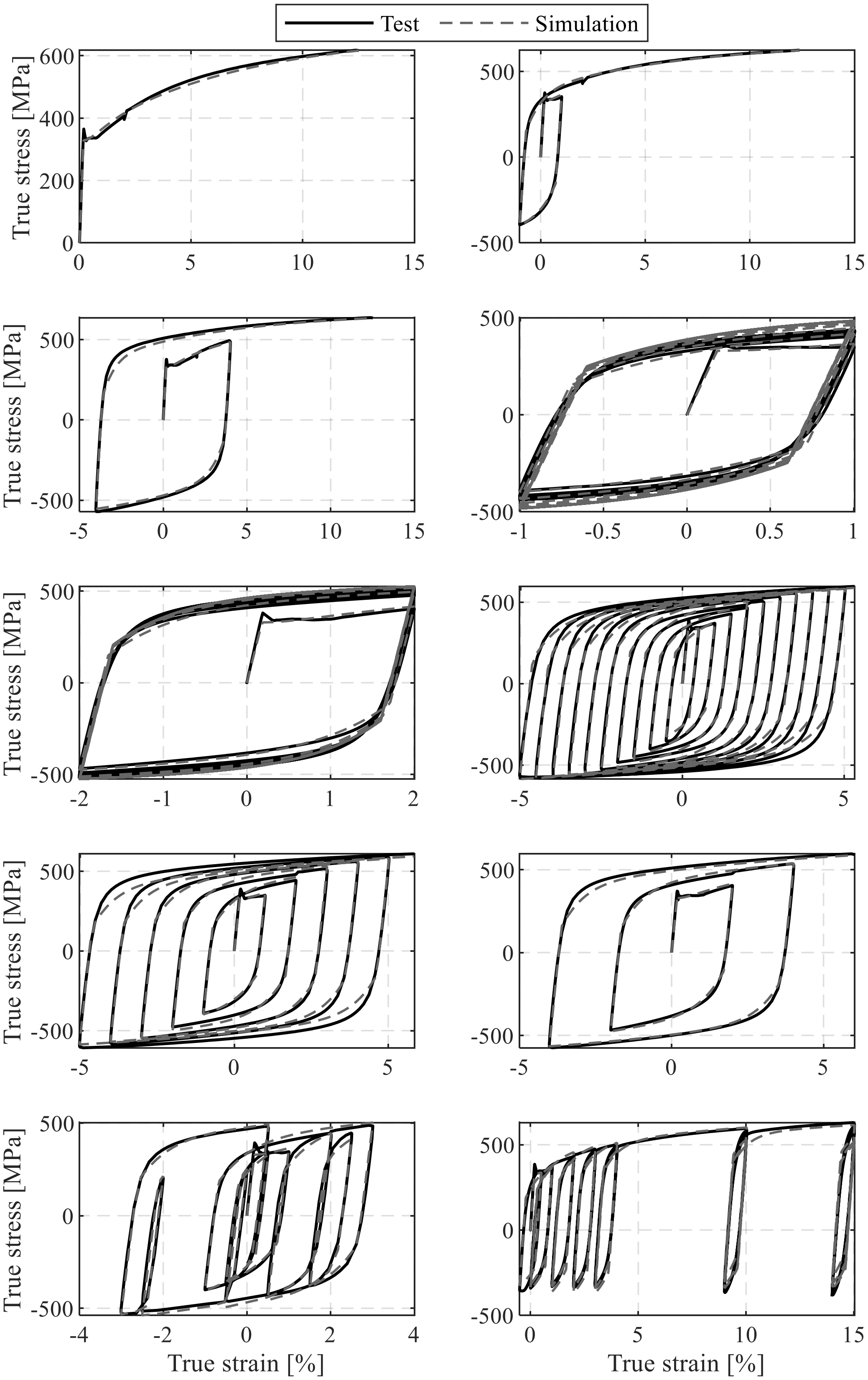

Figure E.6 Column web coupon test and simulation results.

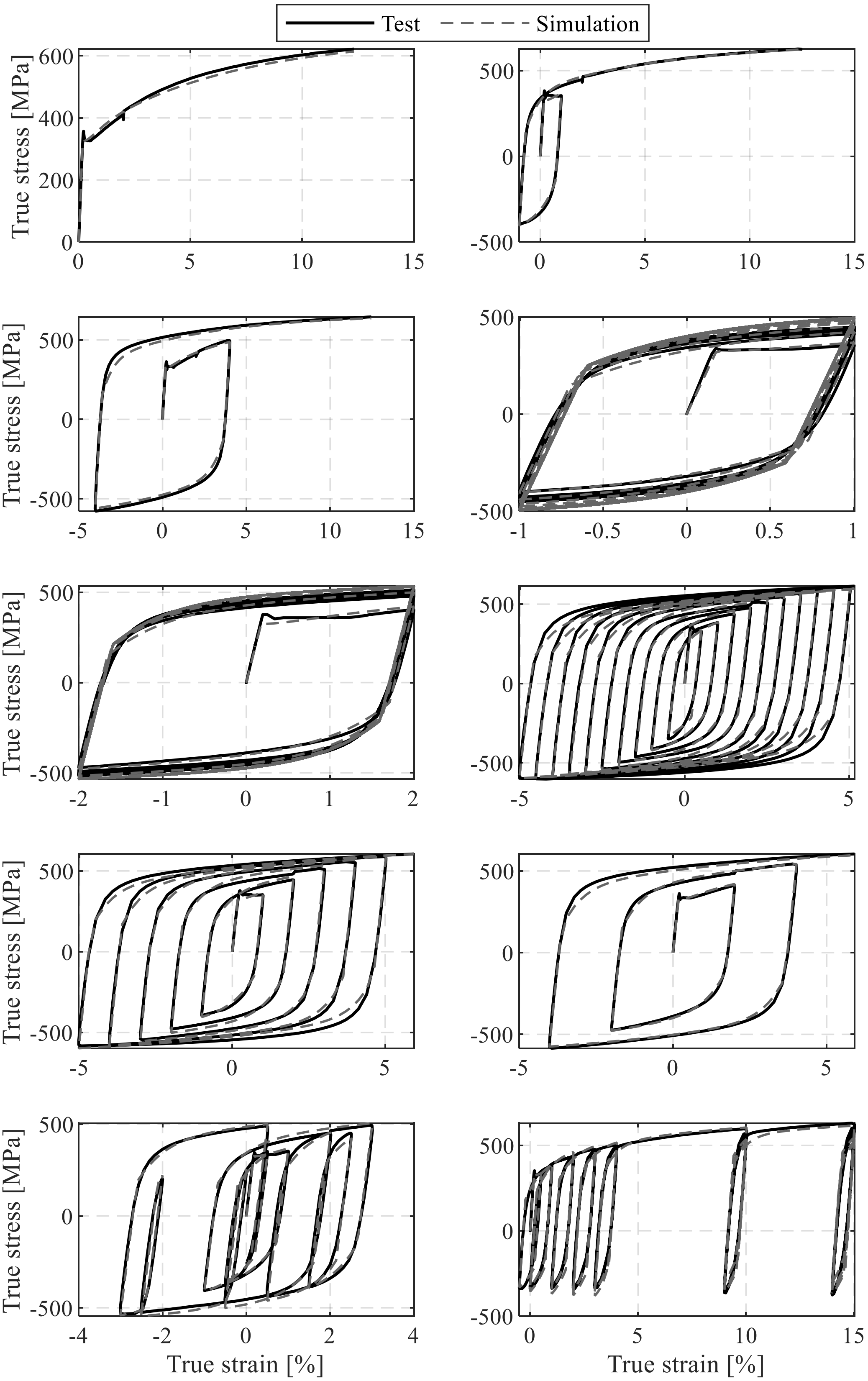

Figure E.7 Column flange coupon test and simulation results.

E.3 Material test results from measured experimental strain histories

The calibrated material model described in Chapter 5 is validated based on eight additional material tests based on realistic experimental strain histories. The applied strain histories come from the following critical test specimen locations (same locations for Specimen 1 and 2):

- Beam flange: west beam, south flange, middle strain gauge, plastic hinge region.
- Beam web: west beam, north side, horizontal rosette component, plastic hinge region.
- Column flange: west side, below panel zone, bottom side.
- Column web: panel zone centre, diagonal rosette component.

The applied strain gauge histories are shown in Fig. E.8 for Specimen 1 and in Fig. E.9 for Specimen 2.

The comparisons of the tested coupons with the calibrated material model (referred to as "Simulation") are shown in Figs. E.10-E.13.

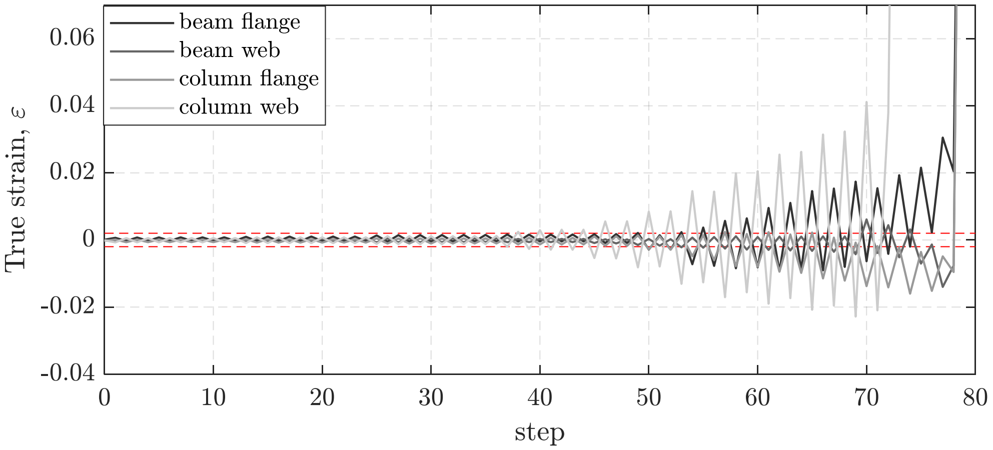

Figure E.8 Experimental strain histories: Specimen 1.

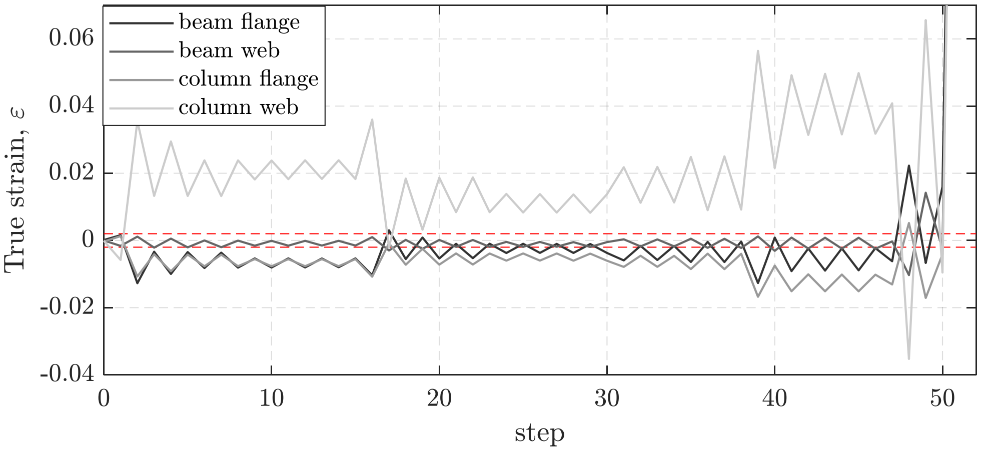

Figure E.9 Experimental strain histories: Specimen 2.

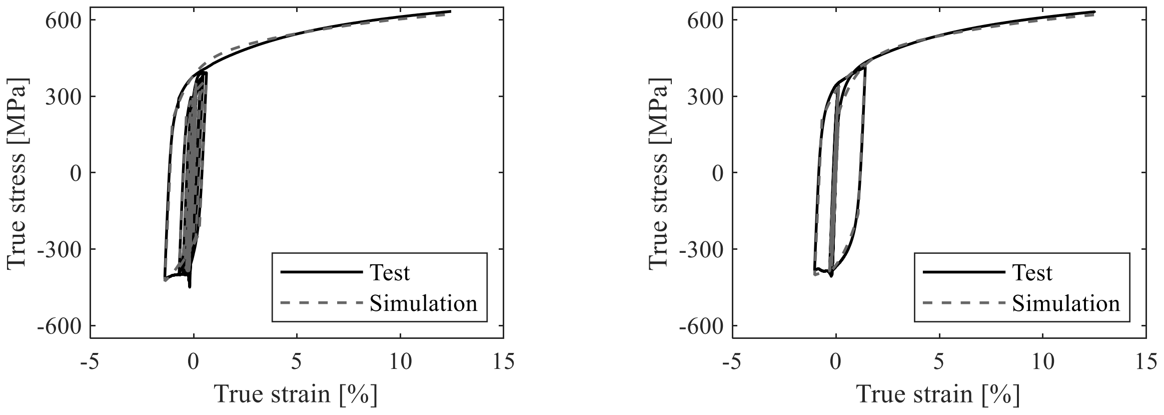

(a)

(b)

Figure E.10 Beam web coupon test and simulation results based on experimental strain histories: (a) Specimen 1; and (b) Specimen 2.

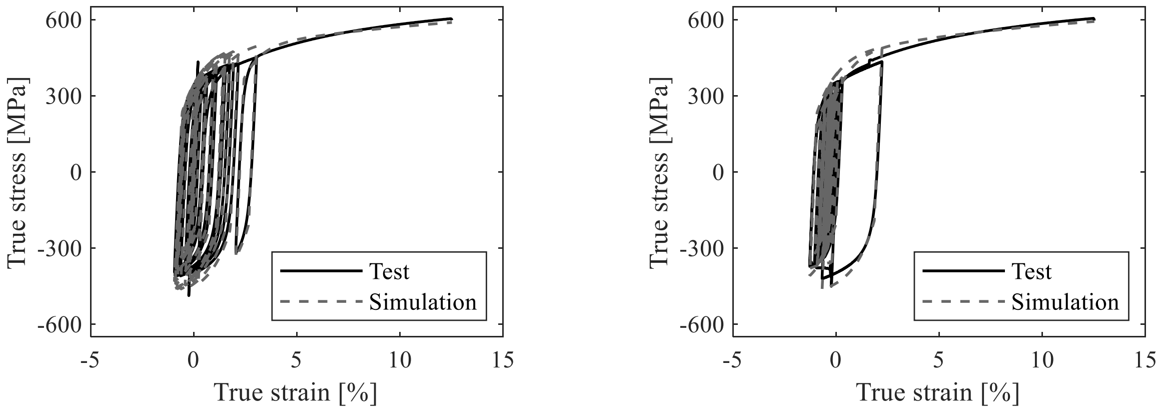

(a)

(b)

Figure E.11 Beam flange coupon test and simulation results based on experimental strain histories: (a) Specimen 1; and (b) Specimen 2.

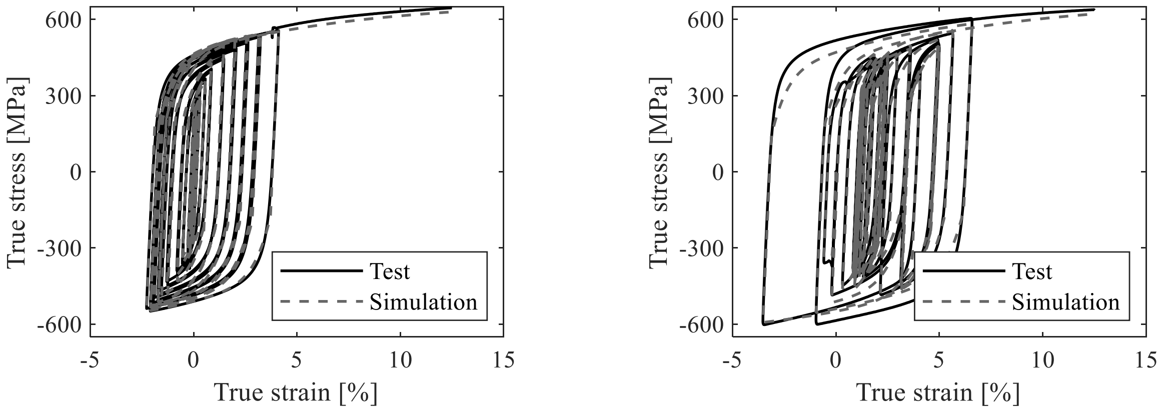

(a)

(b)

Figure E.12 Column web coupon test and simulation results based on experimental strain histories: (a) Specimen 1; and (b) Specimen 2.

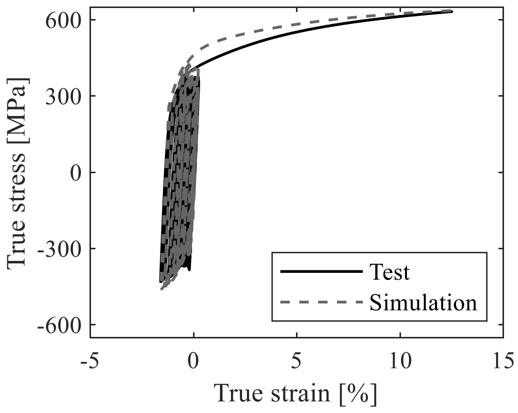

(a)

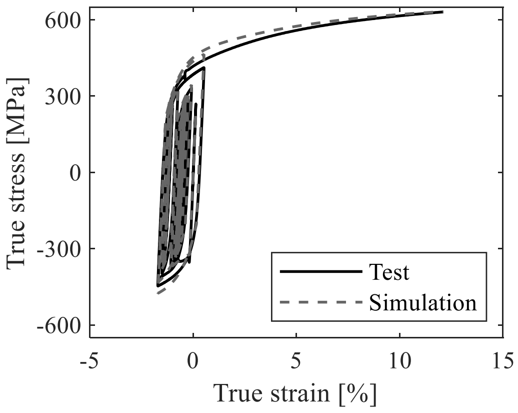

(b)

Figure E.13 Column flange coupon test and simulation results based on experimental strain histories: (a) Specimen 1; and (b) Specimen 2.

Appendix F. Detailing requirements and design procedure of the proposed welded connections and summary of experimental results of test specimens

Description

This appendix includes the design and detailing requirements for the test specimens described in Chapter 5, as well as a brief summary of the experimental results.

F.1 Detailing requirements and design procedure of the proposed welded connections

The proposed welded unreinforced flange-welded web (WUF-W) moment connection is described in this section, as illustrated in Fig. F.1. The connection features: (a) the beveled backing bars developed in Chapter 4 that are intentionally kept in place after the execution of the complete joint penetration (CJP) welds in the beam flange to column face connection, (b) a balanced participation of the panel zones and the adjoining beams in the energy dissipation, and (c) toughness requirements in the through-thickness direction of the column mild steel material. In this design context, the panel zones are designed to attain shear distortions of $10\gamma_y$ when the beams reach their capping moment, while beam local instabilities are expected for lateral drift demands exceeding 4% rad (associated with the 2475 return period earthquake event). The proposed targeted panel zone deformations are based on findings from Chapters 2 to 6.

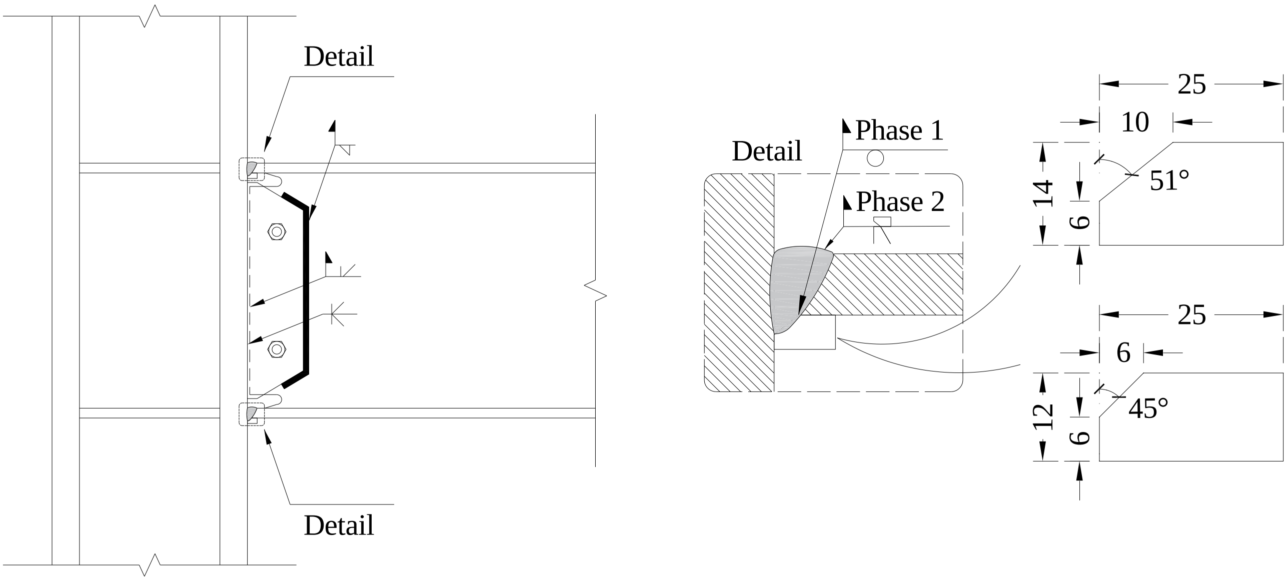

Figure F.1 Proposed welded unreinforced moment connection detailing.

F.1.1 Detailing requirements of the proposed welded connections

- The beams feature the access hole geometry of AWS D1.8/D1.8M:2016 (AWS 2016), Section 6.11.1.2.
- Continuity plates in the column may be deemed imperative, if any of the required flange local bending, web local yielding, web local crippling, web sidesway buckling and web compression buckling strengths exceed the available strengths, according to ANSI/AISC 360-16, Section J10.1-J10.5 (AISC 2016b). The continuity plate requirements should conform with ANSI/AISC 341-16, Section E3.6f (AISC 2016a).
- Doubler plates in the column may be deemed imperative to achieve the targeted panel zone design distortions. The doubler plate requirements should conform with ANSI/AISC 341-16, Section E3.6e.3 (AISC 2016a).

- The thickness of the column web and the doubler plates (if applicable) should conform with ANSI/AISC 341-16, Section E3.6e.2 (AISC 2016a) to prevent shear buckling.
- The shear tab is shop-welded to the column with double bevel CJP welds. The geometry of the shear tab complies with ANSI/AISC 358-16, Section 8.6 (AISC 2016c).
- The beams are positioned in place with the aid of erection bolts.
- The beveled weld backing bars shall be tack welded to the beam flanges at the interior of the beam flange groove angle (see “Detail” of Fig. F.1). Tack welds should not be executed in other locations. Depending on the root length of the beam flange-to-column face CJP welds (i.e., either 6mm or 10mm), the backing bar geometry is illustrated in Fig. F.1. Fillet weld reinforcement between the backing bar and the column face or the beam flanges shall be prohibited.
- To satisfy a smooth start and end of the CJP welding, runoff tabs shall be installed at the end of the beam flanges. After the execution of the CJP welds, runoff tabs should be removed according to ANSI/AISC 358-16, Section 3.4 (AISC 2016c).
- The beam flanges and beam web shall be connected to the column face using CJP welds (see Fig. F.1). The weld properties shall conform with the requirements of demand critical welds of ANSI/AISC 341-16 (AISC 2016a) and AWS D1.8/D1.8M:2016 (AWS 2016).
- The shear tab shall be connected to the beam web with fillet welds, according to ANSI/AISC 358-16, Section 8.6 (AISC 2016c).
- Nondestructive ultrasonic testing shall be performed in all demand critical welds to identify potential discontinuities, as per AWS D1.8/D1.8M:2016 (AWS 2016).
- The lateral bracing of the beams and the columns should conform to the requirements of ANSI/AISC 341-16 (AISC 2016a). No attachment of lateral bracing shall be placed between the column face and a distance d_b from it (where d_b is the beam depth), since this area is deemed to be a protected zone.

F.1.2 Design procedure of the proposed welded connections

Step 1: Compute the probable maximum beam end moment at the beam plastic hinge location according to Eq. (6.1).

$$M_{pr} = C_{pr} R_y F_y Z_e \tag{F.1}$$

$$C_{pr} = \frac{F_y + F_u}{2F_y} \leq 1.2 \tag{F.2}$$

Where C_{pr} is the factor to account for the peak connection strength as per Eq. (F.2); F_y is the specified minimum yield stress of the beam; F_u is the specified minimum tensile stress of the beam; R_y is the ratio of the expected to specified minimum yield stress as per ANSI/AISC 341-16 (AISC 2016a); Z_e is the effective plastic modulus of the beam within the assumed plastic hinge location.

The plastic hinge location is assumed at the column face location.

Step 2: Compute the panel zone available shear strength at $10\gamma_y$ shear distortions, which is the design target, according to Eq. (F.3). This is based on the panel zone strength model developed in Chapter 3, Eq. (3.18).

$$V_{10\gamma_y} = V_{6\gamma_y} + 2 \cdot (V_{6\gamma_y} - V_{4\gamma_y}) \tag{F.3}$$

Step 3: Compute the panel zone required shear strength according to Eq. (2.10).

$$R_u = \frac{aM_{pr}}{d_b - t_{bf}} \cdot \left(\frac{1 - \frac{ad_c}{2L_b} - \frac{d_b}{H_c}}{1 - \frac{ad_c}{2L_b}} \right) \tag{F.4}$$

Where $a = 1$ for exterior joints and $a = 2$ for interior joints; d_b is the beam depth; t_{bf} is the beam flange thickness; d_c is the column depth; L_b is the inflection point-to-inflection point beam length; H_c is the inflection point-to-inflection point column height.

Step 4: Compute the required doubler plate thickness, if applicable.

If $V_{10\gamma_y} \geq R_u$, then no doubler plates are needed.

If $V_{10\gamma_y} < R_u$, then doubler plates should be designed with a thickness such that $V_{10\gamma_y} \geq R_u$.

Step 5: Compute the shear force at the beam plastic hinge region, V_h, according to ANSI/AISC 358-16, Section 8.7. Step 3 (AISC 2016c). Based on V_h, compute the strong column weak beam ratio according to ANSI/AISC 358-16, Section 8.4.(2) (AISC 2016c) and check if the beam design shear strength is higher than V_h at both beam ends.

Step 6: Check for continuity plate requirements according to Section F.1.1 of this Ph.D. thesis.

F.2 Summary of experimental results of Specimen 1

F.2.1 Specimen 1 connection and test setup details

The experimental results of Specimen 1 of the testing program of Chapter 5 are summarized in this section. The testing program information is summarized in Table F.1. The welded beam-to-column connection is illustrated in Fig. F.2. A schematic of the test setup is illustrated in Fig. F.3. The material properties together with some connection detailing information are summarized in Table F.2.

Table F.1 Testing program information of Specimen 1.

Specimen IDs	Specimen 1
Keywords	Welded beam-to-column connections, inelastic panel zones, full-scale experiments, beveled weld backing bars, ductile tearing fracture
Test location	Hasaki Research and Development Center, Nippon Steel Corporation
Test date	17th August 2021
Principal investigators	A. Skiadopoulos, D. G. Lignos, M. Arita, S. Hiroshima
Reference	Skiadopoulos, A. (2022). “Welded moment connections with highly dissipative panel zones for enhanced seismic performance of steel moment frames.” PhD Thesis, School of Architecture, Civil and Environmental Engineering, École Polytechnique Fédérale de Lausanne (EPFL), Switzerland.
Funding source	Nippon Steel Corporation (NSC) École Polytechnique Fédérale de Lausanne (EPFL)

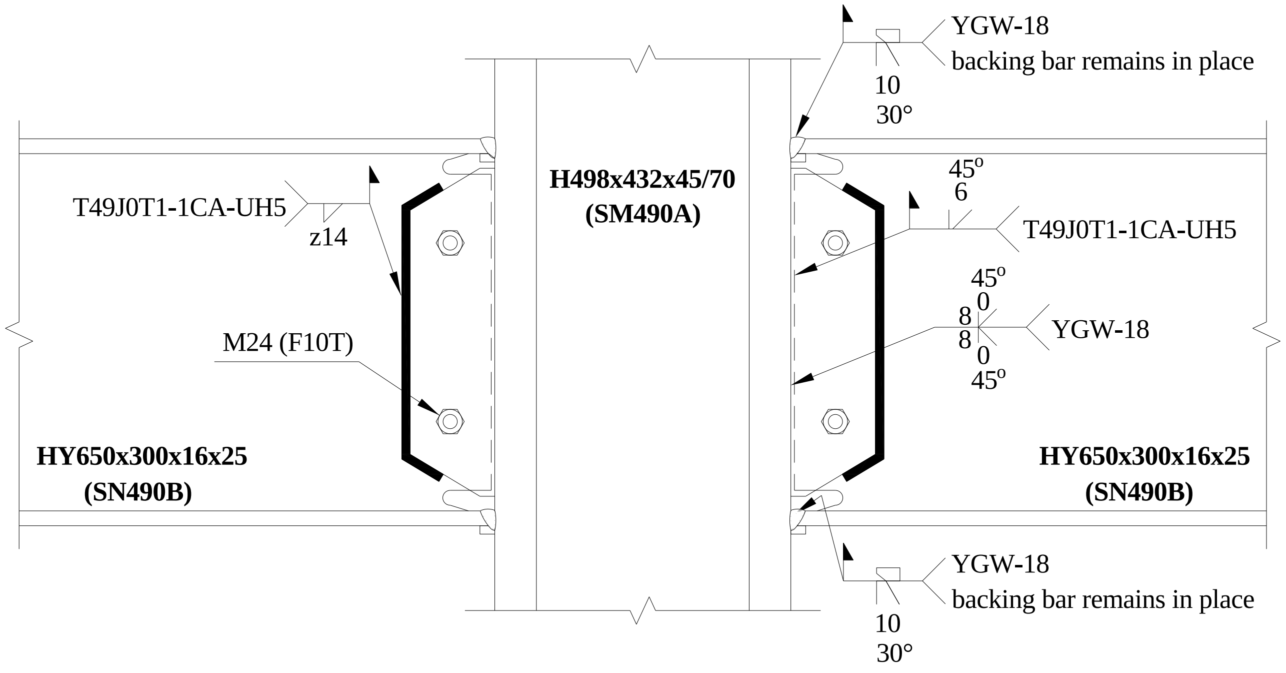
YGW-18
backing bar remains in place
10
30°
H498x432x45/70
(SM490A)
T49J0T1-1CA-UH5
z14
45°
6
T49J0T1-1CA-UH5
45°
0
8
8
0
45°
YGW-18
M24 (F10T)
HY650x300x16x25
(SN490B)
HY650x300x16x25
(SN490B)
YGW-18
backing bar remains in place
10
30°

Figure F.2 Beam-to-column connection detailing of Specimen 1.

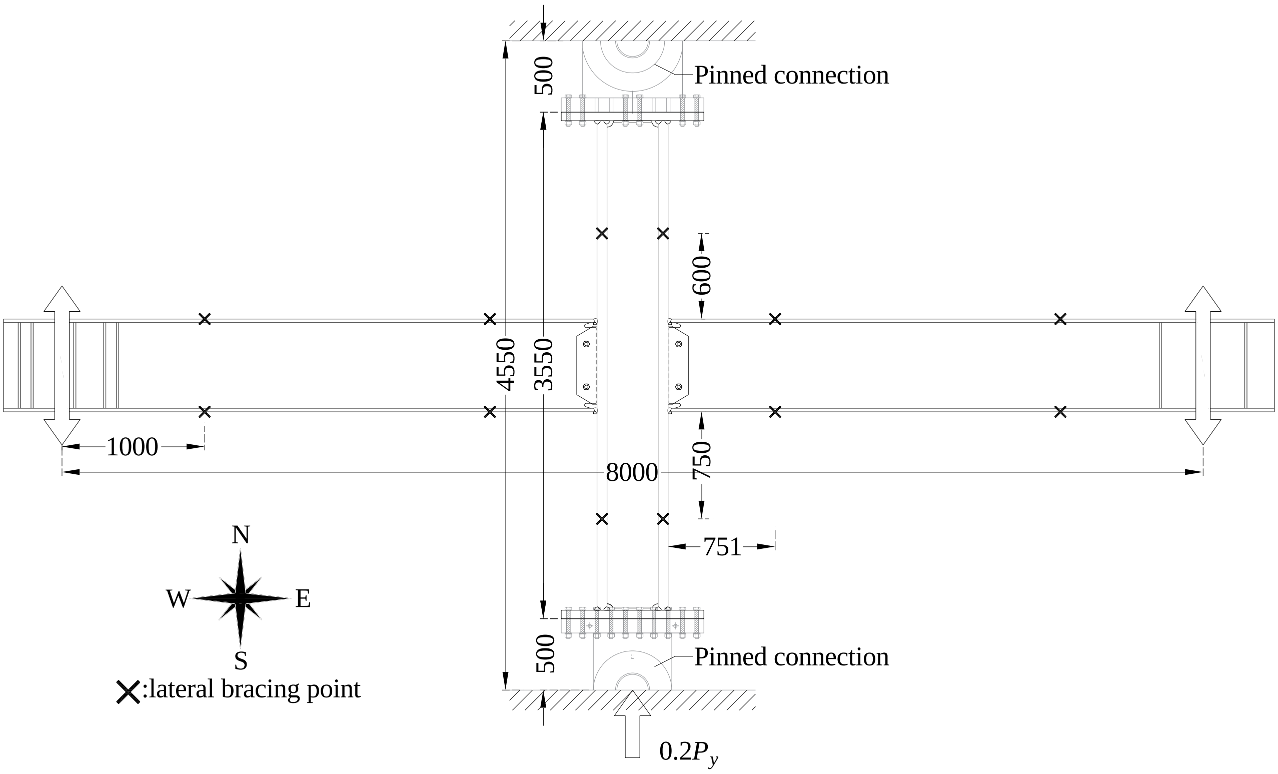

Figure F.3 Schematic of the test setup of Specimen 1.

Table F.2 Material properties and test specimen details of Specimen 1.

Member	Size	Grade	Yield stress (MPa)	Ultimate stress (MPa)
Beam	HY650x300x16x25	SN490B ($f_y = 325$ MPa)	Flange: 363 Web: 398	Flange: 509 Web: 525
Column	H498x432x45/70	SM490A ($f_y = 325$ MPa)	Flange: 368 Web: 363	Flange: 531 Web: 528

Welding details	All welds were performed as per the gas metal arc welding (GMAW) procedure The beam web and beam flange-to-column face complete joint penetration welds were designed as demand critical welds Ultrasonic testing was performed in these welds The diameter of the wire was 1.2 mm in all welds and all weld passes A preheat of 50°C was applied in all complete joint penetration welds Maximum heat input: 30-40 kJ/cm Maximum permissible temperature between passes: 250-350°C
Panel zone	No doubler and no continuity plates
Boundary conditions	Beam-loaded interior subassembly tested in horizontal position No beam composite action Constant compressive axial load applied at the column south location of magnitude $0.2P_y = 5000$ kN (P_y is the column axial yield strength)
Loading protocol	Standard cyclic symmetric loading protocol (AISC 2016a)
Other details	All field welds were performed with the column in the upright position

F.2.2 Specimen 1 experimental results

Specimen 1 was subjected to a standard cyclic symmetric loading protocol (AISC 2016a) so that the connection performance is compared with the prequalification requirements of AISC (2016b). The story shear resistance versus story drift ratio, the panel zone shear force versus normalized panel zone shear distortions, γ/γ_y, as well as the west and east beam end moments at the column face location versus beam chord rotations are shown in Fig. F.4. Key experimental observations of Specimen 1 are shown in Table F.3, while the experimental results of Specimen 1 are summarized in Table F.4. In Fig. F.5, characteristic views of the Specimen 1 are shown that correspond to points 2 to 5 of Table F.3.

At 4% rad lateral drift demands, Specimen 1 exhibited a stable hysteretic response and met the prequalification criteria of AISC (2016b). Specimen 1 showed a stable hysteretic response up until 7% rad, where ductile tearing cracks initiated at the weld root of the beam top flanges near the column face and propagated slightly through the thickness of the column flange. At 8% rad, ductile tearing crack initiated at the weld root between the bottom beam flange and the column face. At 9% rad, the beam-to-column connection lost its load carrying capacity.

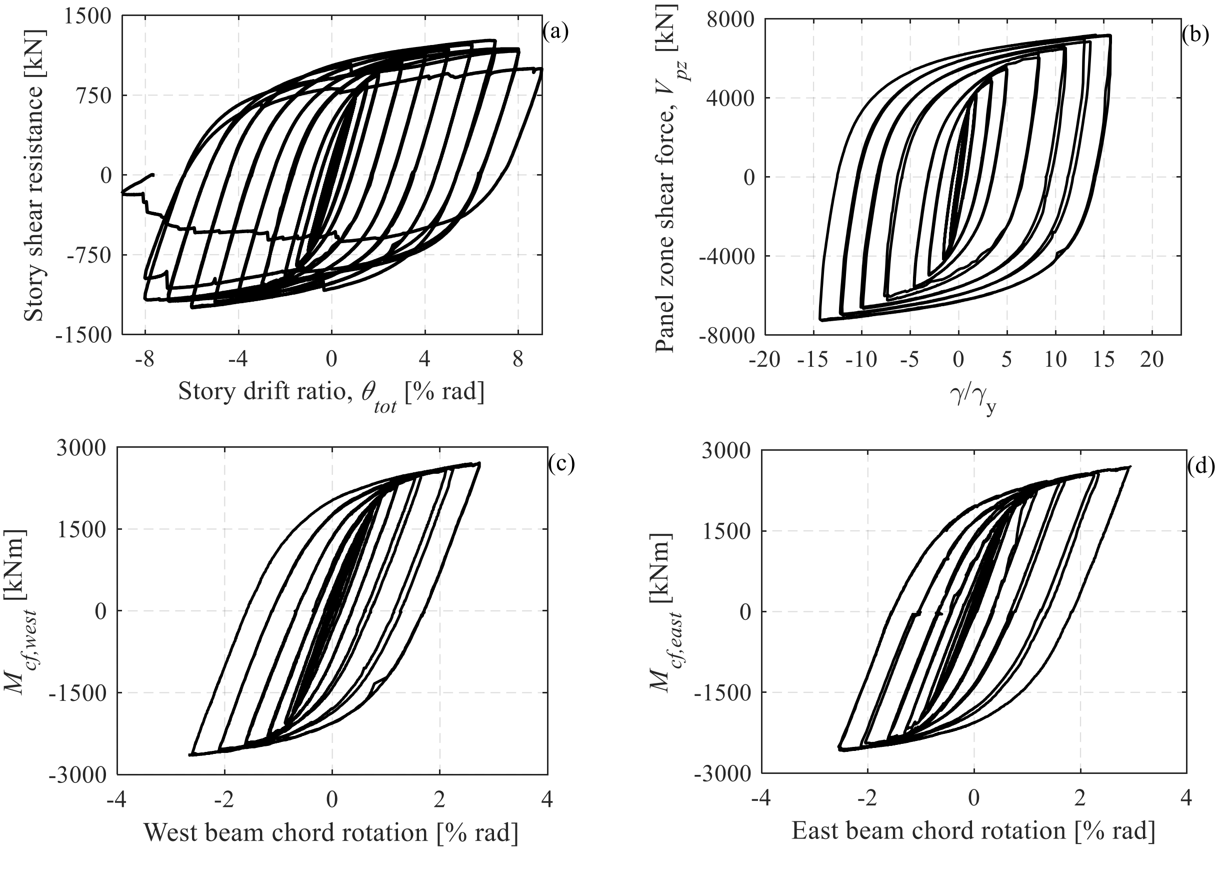

Figure F.4 Specimen 1 hysteretic responses of: (a) subassembly; (b) panel zone; (c) west beam; and (d) east beam.

Table F.3 Key experimental observations of Specimen 1.

Applied drift ratio	Point	Description
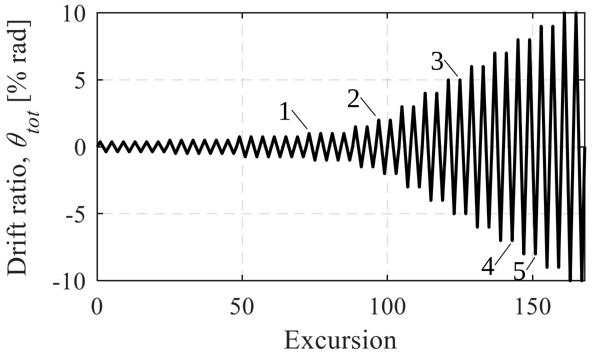	1	Onset of panel zone shear yielding
	2	Onset of beam flange yielding
	3	Onset of beam local buckling
	4	Ductile tearing cracks initiated at the weld root of the beam top flanges near the column face and propagated slightly through the thickness of the column flange
	5	Ductile tearing crack initiated at the weld root between the bottom beam flange and the column face

Table F.4 Summary of Specimen 1 experimental results.

Quantity		Maximum
Force/Deformation	Peak actuator force [kN] Beam tip displacement [mm]	1265 360
Rotation	Story drift ratio [% rad] Panel zone shear distortions [% rad] Beam chord rotation [% rad] Cumulative story drift ratio [% rad]	9.0 4.8 (16γ_y) 2.9 380
Cumulative energy dissipation	Beams [kNm] Panel zone [kNm] Column [kNm] Total [kNm]	3003 6424 0 9427

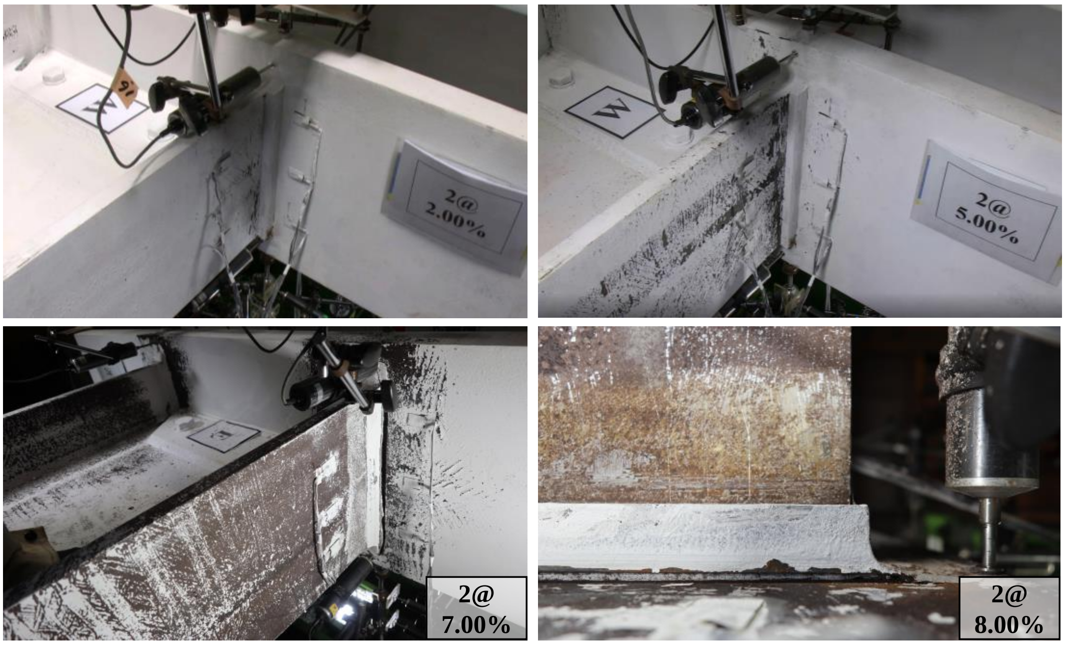

Figure F.5 Characteristic views of Specimen 1 during the experiment.

F.3 Summary of experimental results of Specimen 2

F.3.1 Specimen 2 connection and test setup details

The experimental results of Specimen 2 of the testing program of Chapter 5 are summarized in this section. The testing program information is summarized in Table F.5. The welded beam-to-column connection is illustrated in Fig. F.6. A schematic of the test setup is illustrated in Fig. F.7. The material properties together with some connection detailing information are summarized in Table F.6.

Table F.5 Testing program information of Specimen 2.

Specimen IDs	Specimen 2
Keywords	Welded beam-to-column connections, inelastic panel zones, full-scale experiments, beveled weld backing bars, ductile tearing fracture
Test location	Hasaki Research and Development Center, Nippon Steel Corporation
Test date	28th September 2021
Principal investigators	A. Skiadopoulos, D. G. Lignos, M. Arita, S. Hiroshima
Reference	Skiadopoulos, A. (2022). “Welded moment connections with highly dissipative panel zones for enhanced seismic performance of steel moment frames.” PhD Thesis, School of Architecture, Civil and Environmental Engineering, École Polytechnique Fédérale de Lausanne (EPFL), Switzerland.
Funding source	Nippon Steel Corporation (NSC) École Polytechnique Fédérale de Lausanne (EPFL)

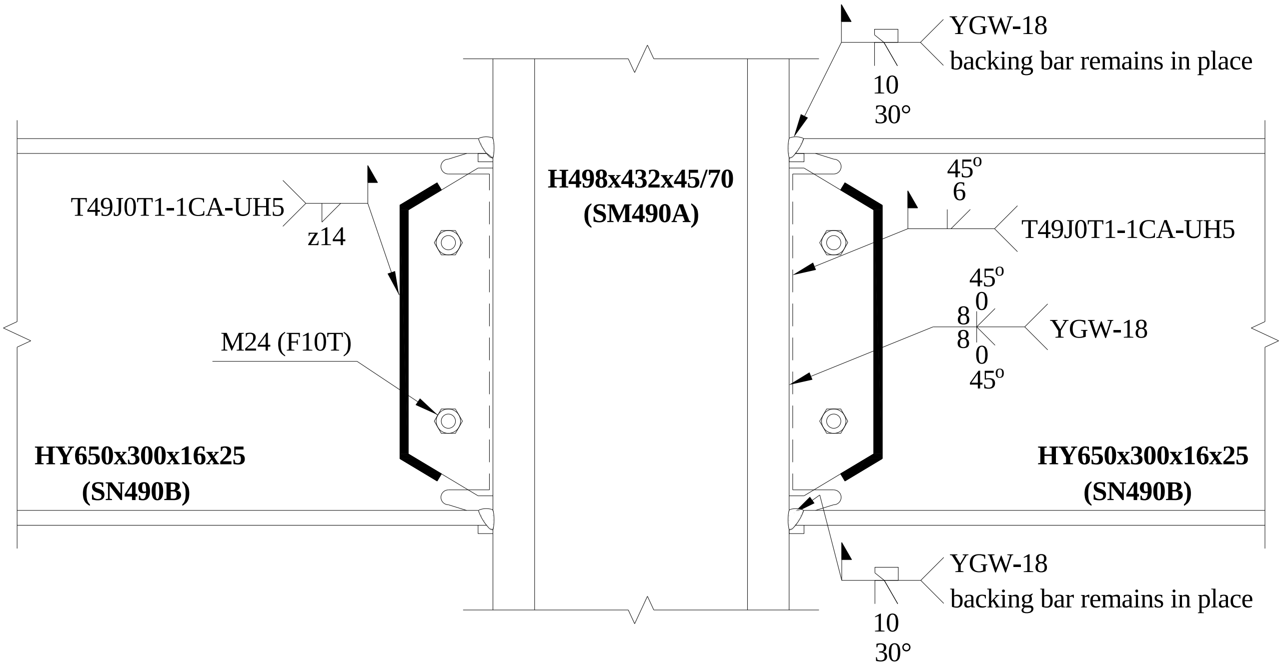
YGW-18
backing bar remains in place
10
30°
H498x432x45/70
(SM490A)
T49J0T1-1CA-UH5
z14
45°
6
T49J0T1-1CA-UH5
45°
0
8
8
0
45°
YGW-18
M24 (F10T)
HY650x300x16x25
(SN490B)
HY650x300x16x25
(SN490B)
YGW-18
backing bar remains in place
10
30°

Figure F.6 Beam-to-column connection detailing of Specimen 2.

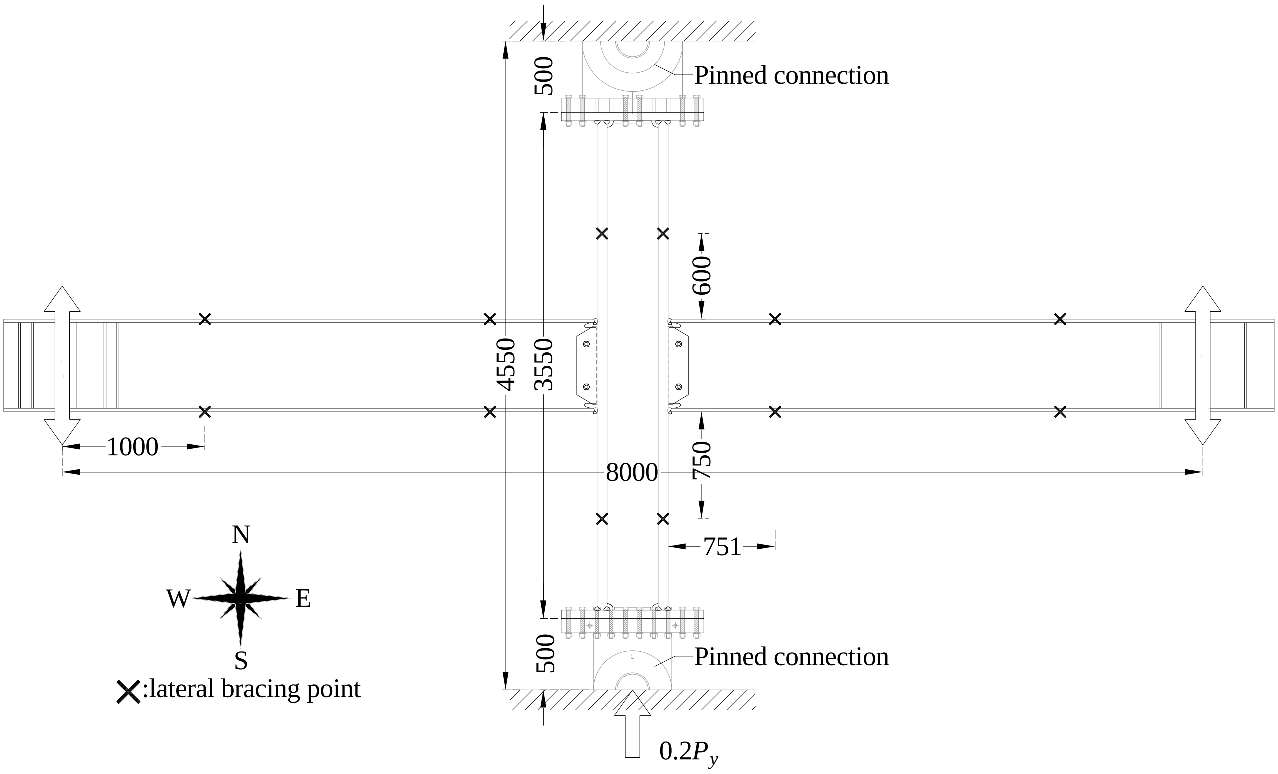

Figure F.7 Schematic of the test setup of Specimen 2.

Table F.6 Material properties and test specimen details of Specimen 2.

Member	Size	Grade	Yield stress (MPa)	Ultimate stress (MPa)
Beam	HY650x300x16x25	SN490B ($f_y = 325$ MPa)	Flange: 363 Web: 398	Flange: 509 Web: 525
Column	H498x432x45/70	SM490A ($f_y = 325$ MPa)	Flange: 368 Web: 363	Flange: 531 Web: 528

Welding details	All welds were performed as per the gas metal arc welding (GMAW) procedure The beam web and beam flange-to-column face complete joint penetration welds were designed as demand critical welds Ultrasonic testing was performed in these welds The diameter of the wire was 1.2 mm in all welds and all weld passes A preheat of 50°C was applied in all complete joint penetration welds Maximum heat input: 30-40 kJ/cm Maximum permissible temperature between passes: 250-350°C
Panel zone	No doubler and no continuity plates
Boundary conditions	Beam-loaded interior subassembly tested in horizontal position No beam composite action Constant compressive axial load applied at the column south location of magnitude $0.2P_y = 5000$ kN (P_y is the column axial yield strength)
Loading protocol	SAC Near fault (Krawinkler et al. 2000)/Collapse-consistent (Suzuki and Lignos 2020)/Cyclic intervals of ±10% rad drift ratio
Other details	All field welds were performed with the column in the upright position

F.3.2 Experimental results of Specimen 2

Specimen 2 was subjected to three loading protocols: (a) the SAC near-fault asymmetric loading protocol (Krawinkler et al. 2000); (b) the collapse-consistent loading protocol by Suzuki and Lignos (2020); and (c) cyclic intervals of ±10% rad drift ratio until loss of the load-carrying capacity. The story shear resistance versus story drift ratio, the panel zone shear force versus normalized panel zone shear distortions, γ/γ_y, as well as the west and east beam end moments at the column face location versus beam chord rotations are shown in Fig. F.8. Key experimental observations of Specimen 2 are shown in Table F.7, while the experimental results of Specimen 2 are summarized in Table F.8. In Fig. F.9, characteristic views of the Specimen 2 are shown that corresponds to points 1 to 4 of Table F.7.

Specimen 2 showed a stable hysteretic response until the end of the collapse-consistent loading protocol, even with the backing bars being present, the panel zone reaching $30\gamma_y$ shear distortions and the lateral drift demands reached 10% rad. During the third loading protocol, ductile tearing cracks propagated through the column thickness direction starting at the west beam top flange weld roots near the column face. Moreover, ductile tearing cracks propagated at the east beam top side near the shear tab end towards the column width direction. Macro-etching inspection results revealed no crack initiating from the beam flange backing bars.

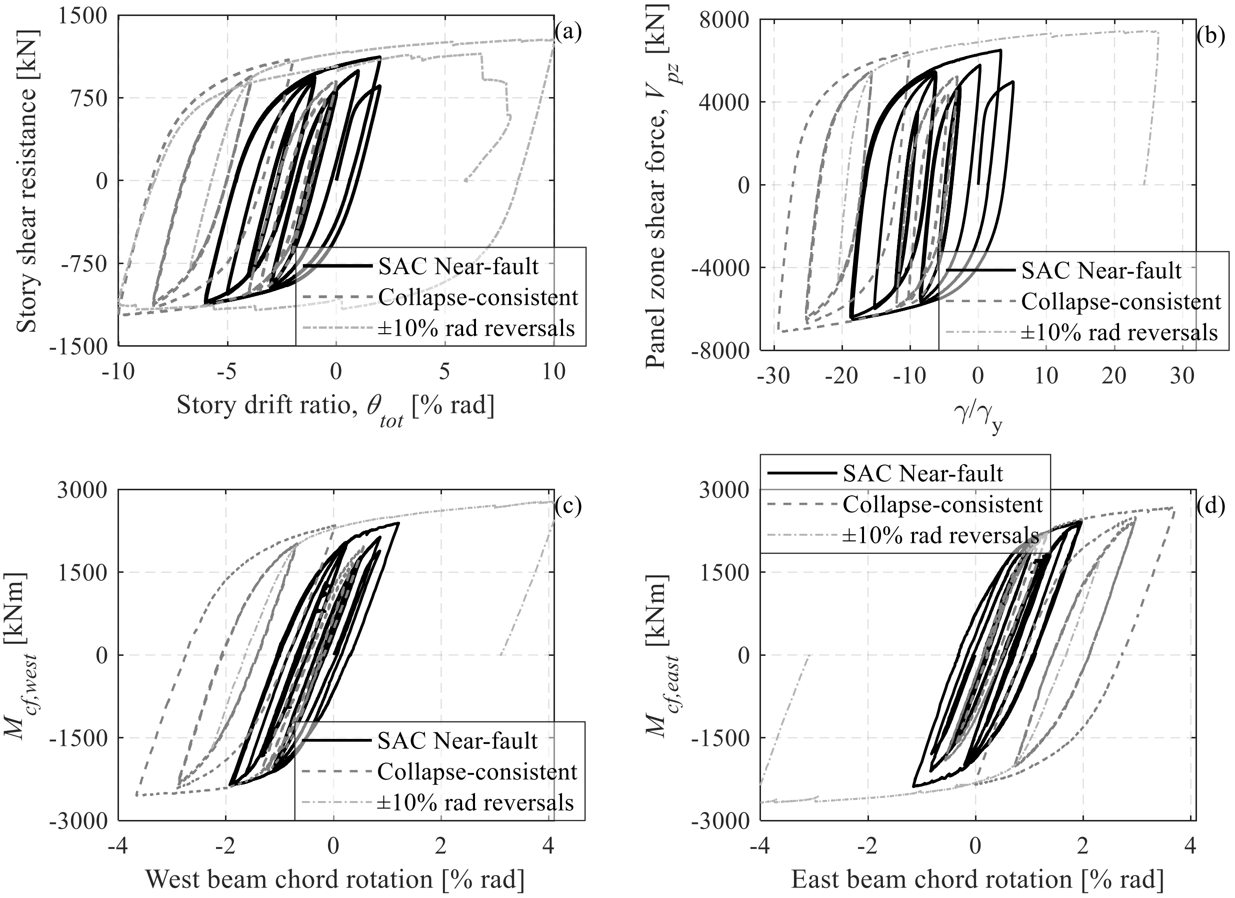

Figure F.8 Specimen 2 hysteretic responses of: (a) subassembly; (b) panel zone; (c) west beam; and (d) east beam.

Table F.7 Key experimental observations of Specimen 2.

Applied drift ratio	Point	Description
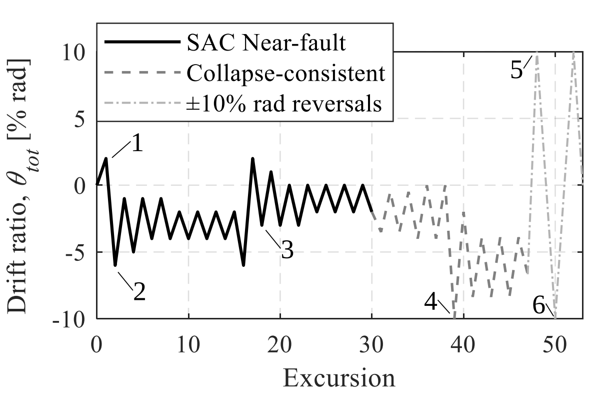	1	Onset of panel zone and beam flange yielding
	2	Panel zone reached $30\gamma_y$ shear distortions
	3	Ductile micro-cracks observed at the west beam top flange weld roots near the column face and near the access hole
	4	Propagation of west beam cracks towards the column width and longitudinal direction
	5	Ductile tearing crack propagated at the east beam top side near the shear tab end towards the column width direction
	6	Ductile tearing crack propagated at the weld fusion of the west beam top flange towards the column flange thickness

$* \gamma_y$: panel zone shear distortion at yield

Table F.8 Summary of Specimen 2 experimental results.

Quantity		Maximum
Force/Deformation	Peak actuator force [kN]	1278
	Beam tip displacement [mm]	400
Rotation	Story drift ratio [% rad]	10.0
	Panel zone shear distortions [% rad]	8.9 ($29\gamma_y$)
	Beam chord rotation [% rad]	4.2
	Cumulative story drift ratio [% rad]	235
Cumulative energy dissipation	Beams [kNm]	1154
	Panel zone [kNm]	3904
	Column [kNm]	0
	Total [kNm]	5058

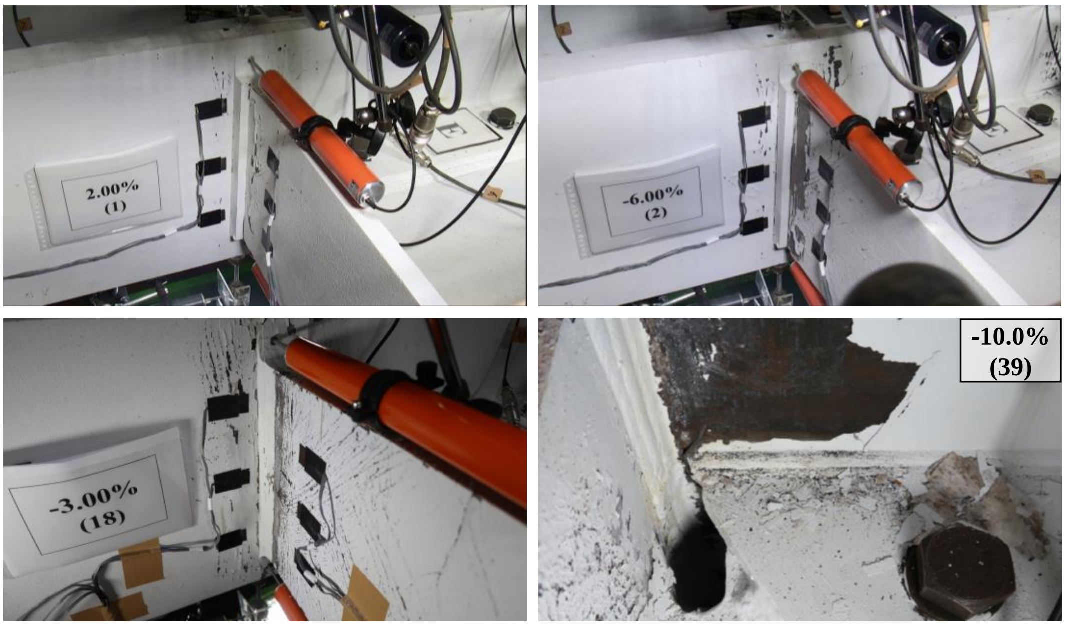

Figure F.9 Characteristic views of Specimen 2 during the experiment.

Appendix G. Design summaries of steel moment resisting frames with elastic and dissipative panel zones

Description

This appendix includes the design summaries of the 32 steel moment resisting frames with elastic and dissipative panel zone designs, described in Chapter 6.

In this appendix, the thirty-two (32) archetype steel office building designs examined in Chapter 6 are summarized. The designs are based on AISC (2016c; a; b); ASCE (2016). A soil class D and risk category II are assumed. The design location is urban California, and specifically Los Angeles, with (Latitude = 33.996° and Longitude = -118.162°). The design spectrum of the selected location in shown in Fig. G.1. The steel buildings comprise two perimeter steel MRFs, two orthogonal concentrically braced frames, and a gravity frame system, as depicted in the plan view in Fig. G.2. Four-, Eight-, 12- and 20-story steel buildings are considered. The typical story height is 4m in all examined cases. The first story height is 4.3m for the four-story steel MRF. The rest of the steel MRFs have a first story height of 4.2m. The elevation views of all MRFs are shown in Fig. G.3 (four-story), Fig. G.4 (eight-story), Fig. G.5 (twelve-story), and Fig. G.6 (twenty-story). Beams and columns are made of A992, Gr. 50 (i.e., nominal yield stress, $f_y = 345$ MPa) with a 100mm thick slab that rests on a 90mm thick steel deck. Pre-qualified WUF-W beam-to-column connections are considered.

The beam-to-column web panel zones are designed with the following targeted panel zone distortions, $\gamma_d = [1,\ 4, 10, 15] \cdot \gamma_y$, where γ_y is the panel zone shear distortions at yield. The last two values do not comply with AISC 360-16. The panel zone shear resistance, R_n (AISC 2016b), over the panel zone shear demand, R_u (AISC 2016a), values are reported in Table G.1 for all the designs. Column splices are positioned at the mid-height of every other story. The MRFs are designed with a response modification coefficient, $R = 8$, an overstrength factor, $\Omega_0 = 3$ and a deflection amplification factor, $C_d = 5.5$. From Table G.2 to Table G.9, the cross sections of the beams and the columns and the doubler plate thicknesses are shown for all the steel MRF designs.

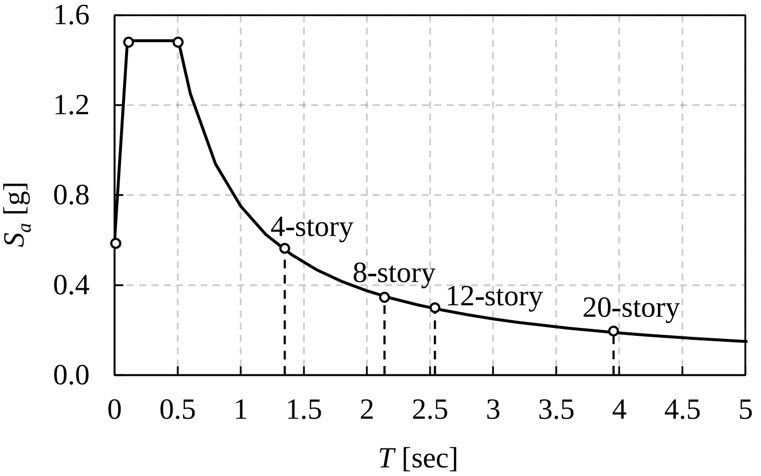

Figure G.1 Design spectrum and archetype MRF periods.

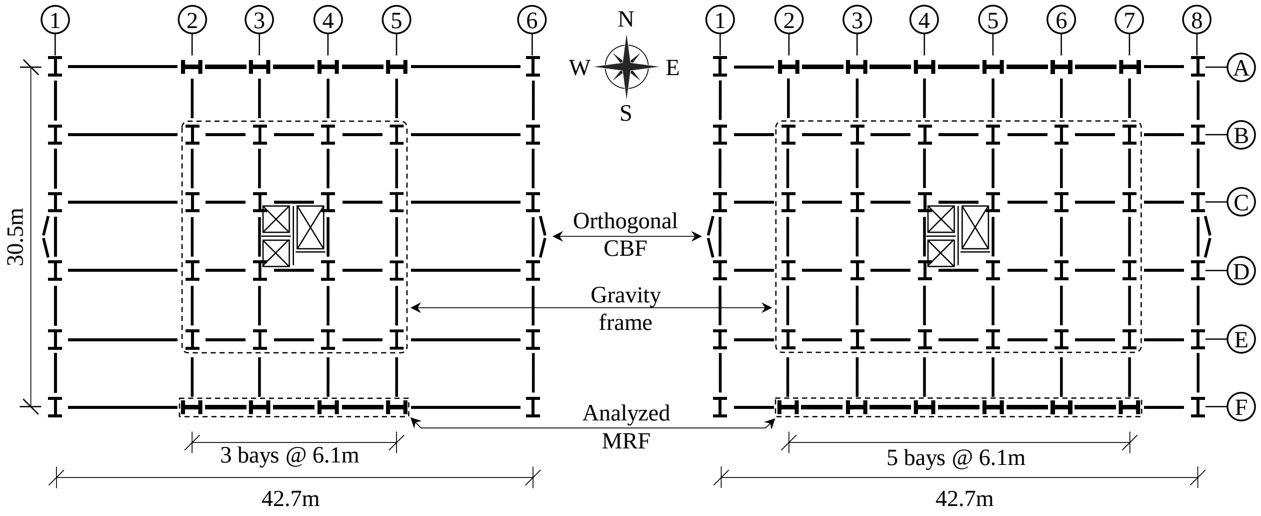
1
2
3
4
5
6
7
8
N
W
E
S
A
B
C
D
E
F
30.5m
Orthogonal CBF
Gravity frame
Analyzed MRF
3 bays @ 6.1m
5 bays @ 6.1m
42.7m
42.7m

Figure G.2 Plan view of the three- and five-bar steel MRFs.

The MRFs are designed by considering:

- P-Delta effects.
- The panel zone contribution to the MRF deformations.
- End beam offsets (physical dimensions of beams and columns).
- Response spectrum analysis (RSA).
- Wind design is neglected.

The loads for which the MRFs are designed are the following:

- Dead load: $4.3kN/m^2 (90psf)$.
- Live load floor: $2.4kN/m^2 (50psf)$.
- Dead load roof: $0.96kN/m^2 (20psf)$.
- Cladding: $1.2kN/m^2 (25psf)$.
- Earthquake load: design spectrum as shown in Fig. G.1.

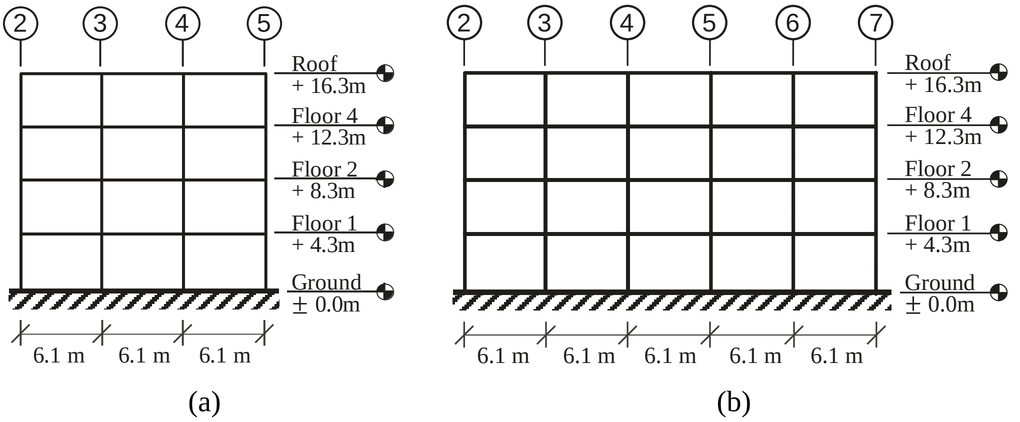
2
3
4
5
6
7
Roof
+ 16.3m
Floor 4
+ 12.3m
Floor 2
+ 8.3m
Floor 1
+ 4.3m
Ground
± 0.0m
6.1 m
(a)
(b)

Figure G.3 Elevation view of the four-story steel MRFs: (a) three-bay; and (b) five-bay.

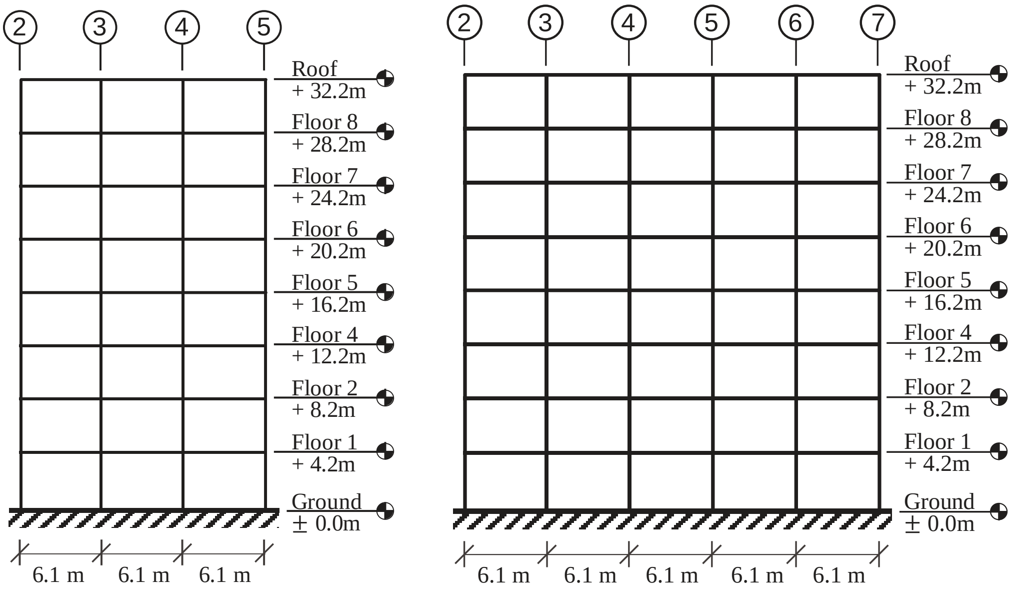
②
③
④
⑤
⑥
⑦
Roof
+ 32.2m
Floor 8
+ 28.2m
Floor 7
+ 24.2m
Floor 6
+ 20.2m
Floor 5
+ 16.2m
Floor 4
+ 12.2m
Floor 2
+ 8.2m
Floor 1
+ 4.2m
Ground
± 0.0m
6.1 m
6.1 m
6.1 m
6.1 m
6.1 m

(a)

(b)

Figure G.4 Elevation view of the eight-story steel MRFs: (a) three-bay; and (b) five-bay.

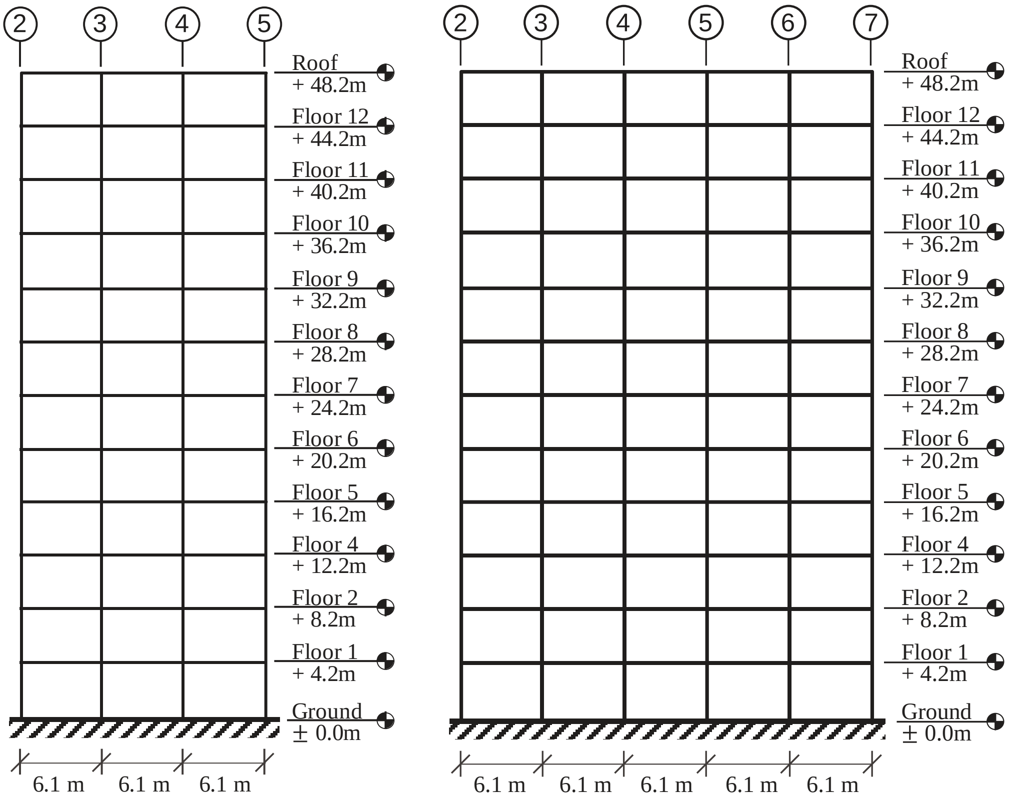
②
③
④
⑤
⑥
⑦
Roof
+ 48.2m
Floor 12
+ 44.2m
Floor 11
+ 40.2m
Floor 10
+ 36.2m
Floor 9
+ 32.2m
Floor 8
+ 28.2m
Floor 7
+ 24.2m
Floor 6
+ 20.2m
Floor 5
+ 16.2m
Floor 4
+ 12.2m
Floor 2
+ 8.2m
Floor 1
+ 4.2m
Ground
± 0.0m
6.1 m
6.1 m
6.1 m
6.1 m
6.1 m

(a)

(b)

Figure G.5 Elevation view of the twelve-story steel MRFs: (a) three-bay; and (b) five-bay.

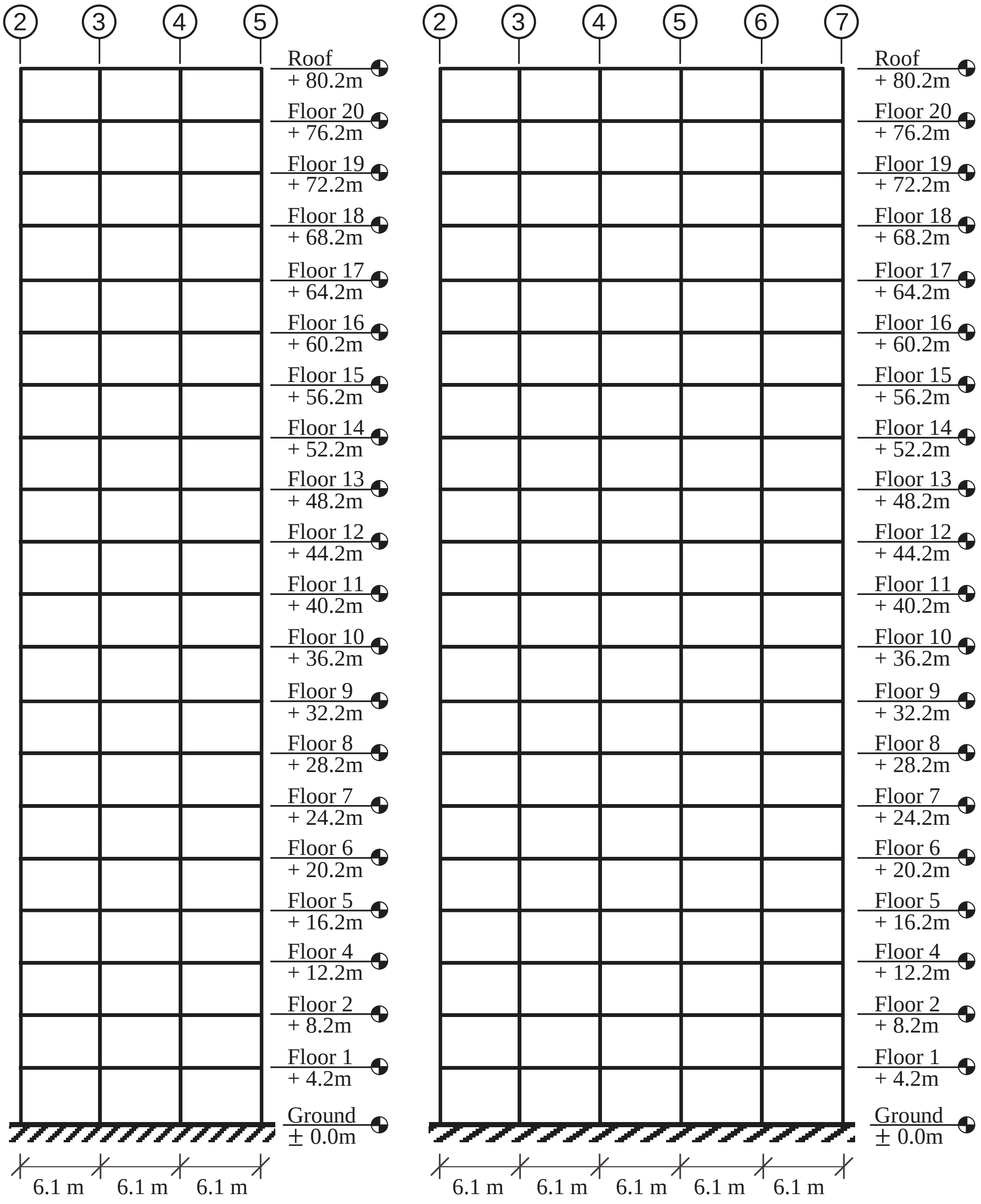
2
3
4
5
Roof
+ 80.2m
Floor 20
+ 76.2m
Floor 19
+ 72.2m
Floor 18
+ 68.2m
Floor 17
+ 64.2m
Floor 16
+ 60.2m
Floor 15
+ 56.2m
Floor 14
+ 52.2m
Floor 13
+ 48.2m
Floor 12
+ 44.2m
Floor 11
+ 40.2m
Floor 10
+ 36.2m
Floor 9
+ 32.2m
Floor 8
+ 28.2m
Floor 7
+ 24.2m
Floor 6
+ 20.2m
Floor 5
+ 16.2m
Floor 4
+ 12.2m
Floor 2
+ 8.2m
Floor 1
+ 4.2m
Ground
± 0.0m
6.1 m
6.1 m
6.1 m
2
3
4
5
6
7
Roof
+ 80.2m
Floor 20
+ 76.2m
Floor 19
+ 72.2m
Floor 18
+ 68.2m
Floor 17
+ 64.2m
Floor 16
+ 60.2m
Floor 15
+ 56.2m
Floor 14
+ 52.2m
Floor 13
+ 48.2m
Floor 12
+ 44.2m
Floor 11
+ 40.2m
Floor 10
+ 36.2m
Floor 9
+ 32.2m
Floor 8
+ 28.2m
Floor 7
+ 24.2m
Floor 6
+ 20.2m
Floor 5
+ 16.2m
Floor 4
+ 12.2m
Floor 2
+ 8.2m
Floor 1
+ 4.2m
Ground
± 0.0m
6.1 m
6.1 m
6.1 m
6.1 m
6.1 m

(a) (b)

Figure G.6 Elevation view of the twenty-story steel MRFs: (a) three-bay; and (b) five-bay.

Table G.1 Archetype steel MRF panel zone shear resistance over panel zone shear demand values and first mode periods.

		γ_d	R_n/R_u	T_1 (s)
4-story	3-bay	γ_y	1.25	1.28
		$4\gamma_y$	1.03	1.29
		$10\gamma_y$	0.82	1.31
		$15\gamma_y$	0.79	1.32
	5-bay	γ_y	1.26	1.28
		$4\gamma_y$	1.04	1.29
		$10\gamma_y$	0.85	1.31
		$15\gamma_y$	0.75	1.32
8-story	3-bay	γ_y	1.22	2.04
		$4\gamma_y$	1.00	2.08
		$10\gamma_y$	0.85	2.11
		$15\gamma_y$	0.77	2.13
	5-bay	γ_y	1.23	2.06
		$4\gamma_y$	0.98	2.09
		$10\gamma_y$	0.84	2.12
		$15\gamma_y$	0.74	2.14
12-story	3-bay	γ_y	1.23	2.41
		$4\gamma_y$	0.97	2.45
		$10\gamma_y$	0.81	2.49
		$15\gamma_y$	0.75	2.50
	5-bay	γ_y	1.21	2.47
		$4\gamma_y$	0.99	2.51
		$10\gamma_y$	0.84	2.55
		$15\gamma_y$	0.76	2.57
20-story	3-bay	γ_y	1.24	3.91
		$4\gamma_y$	0.99	3.95
		$10\gamma_y$	0.83	3.98
		$15\gamma_y$	0.74	4.00
	5-bay	γ_y	1.23	3.86
		$4\gamma_y$	0.97	3.91
		$10\gamma_y$	0.85	3.94
		$15\gamma_y$	0.75	3.97

Table G.2 Four-story, three-bay steel MRF design.

Story/Floor	Columns		Doubler plates (in)				Beam
	Exterior	Interior	$\gamma_d = \gamma_y$	$\gamma_d = 4\gamma_y$	$\gamma_d = 10\gamma_y$	$\gamma_d = 15\gamma_y$	
4/Roof	W24x76	W24x84	4/16, 14/16	2/16, 10/16	0, 7/16	0, 6/16	W18x60
3/4	W24x103, W24x76	W24x146, W24x84	4/16, 14/16	2/16, 10/16	0, 7/16	0, 6/16	W18x60
2/3	W24x103	W24x146	4/16, 15/16	2/16, 10/16	0, 7/16	0, 5/16	W24x76
1/2	W24x103	W24x146	4/16, 15/16	2/16, 10/16	0, 7/16	0, 5/16	W24x76

Table G.3 Four-story, five-bay steel MRF design.

Story/Floor	Columns		Doubler plates (in)				Beam
	Exterior	Interior	$\gamma_d = \gamma_y$	$\gamma_d = 4\gamma_y$	$\gamma_d = 10\gamma_y$	$\gamma_d = 15\gamma_y$	
4/Roof	W21x50	W21x62	2/16, 10/16	1/16, 7/16	0, 5/16	0, 3/16	W18x40
3/4	W21x83, W21x50	W21x111, W21x62	2/16, 10/16	1/16, 7/16	0, 5/16	0, 3/16	W18x40
2/3	W21x83	W21x111	4/16, 15/16	2/16, 11/16	0, 8/16	0, 6/16	W21x62
1/2	W21x83	W21x111	4/16, 16/16	2/16, 11/16	0, 8/16	0, 6/16	W21x62

Table G.4 Eight-story, three-bay MRF design.

Story/Floor	Columns		Doubler plates (in)				Beam
	Exterior	Interior	$\gamma_d = \gamma_y$	$\gamma_d = 4\gamma_y$	$\gamma_d = 10\gamma_y$	$\gamma_d = 15\gamma_y$	
8/Roof	W24x94	W24x94	4/16, 15/16	2/16, 11/16	0, 8/16	0, 6/16	W21x68
7/8	W24x103, W24x94	W24x131, W24x94	4/16, 15/16	2/16, 11/16	0, 8/16	0, 6/16	W21x68
6/7	W24x103	W24x131	4/16, 16/16	2/16, 11/16	0, 7/16	0, 6/16	W24x76
5/6	W24x131, W24x103	W24x176, W24x131	4/16, 16/16	2/16, 11/16	0, 7/16	0, 6/16	W24x76
4/5	W24x131	W24x176	6/16, 18/16	3/16, 12/16	1/16, 9/16	0, 7/16	W27x94
3/4	W24x162, W24x131	W24x192, W24x176	6/16, 18/16	3/16, 12/16	1/16, 9/16	0, 7/16	W27x94
2/3	W24x162	W24x192	5/16, 20/16	2/16, 13/16	0, 9/16	0, 7/16	W27x102
1/2	W24x162	W24x192	5/16, 20/16	2/16, 13/16	0, 10/16	0, 7/16	W27x102

Table G.5 Eight-story, five-bay MRF design.

Story/Floor	Columns		Doubler plates (in)				Beam
	Exterior	Interior	$\gamma_d = \gamma_y$	$\gamma_d = 4\gamma_y$	$\gamma_d = 10\gamma_y$	$\gamma_d = 15\gamma_y$	
8/Roof	W24x62	W24x84	3/16, 12/16	1/16, 9/16	0, 6/16	0, 4/16	W18x55
7/8	W24x84, W24x62	W24x94, W24x84	3/16, 12/16	1/16, 9/16	0, 6/16	0, 4/16	W18x55
6/7	W24x84	W24x94	3/16, 13/16	1/16, 9/16	0, 6/16	0, 5/16	W21x62
5/6	W24x103, W24x84	W24x103, W24x94	3/16, 13/16	1/16, 9/16	0, 6/16	0, 5/16	W21x62
4/5	W24x103	W24x103	4/16, 16/16	1/16, 12/16	0, 8/16	0, 6/16	W21x73
3/4	W24x131, W24x103	W24x131, W24x103	4/16, 16/16	1/16, 12/16	0, 8/16	0, 6/16	W21x73
2/3	W24x131	W24x131	3/16, 16/16	1/16, 11/16	0, 8/16	0, 6/16	W24x76
1/2	W24x131	W24x131	3/16, 16/16	1/16, 11/16	0, 8/16	0, 6/16	W24x76

Table G.6 Twelve-story, three-bay MRF design.

Story/Floor	Columns		Doubler plates (in)				Beam
	Exterior	Interior	$\gamma_d = \gamma_y$	$\gamma_d = 4\gamma_y$	$\gamma_d = 10\gamma_y$	$\gamma_d = 15\gamma_y$	
12/Roof	W27x94	W27x102	4/16, 15/16	2/16, 10/16	0, 7/16	0, 5/16	W24x76
11/12	W27x114, W27x94	W27x129, W27x102	4/16, 15/16	2/16, 10/16	0, 7/16	0, 5/16	W24x76
10/11	W27x114	W27x129	5/16, 17/16	2/16, 12/16	0, 9/16	0, 7/16	W27x94
9/10	W27x129, W27x114	W27x194, W27x129	5/16, 17/16	2/16, 12/16	0, 9/16	0, 7/16	W27x94
8/9	W27x129	W27x194	5/16, 17/16	2/16, 12/16	0, 8/16	0, 6/16	W30x108
7/8	W27x178, W27x129	W27x217, W27x194	5/16, 17/16	2/16, 12/16	0, 8/16	0, 6/16	W30x108
6/7	W27x178	W27x217	6/16, 21/16	2/16, 14/16	0, 10/16	0, 8/16	W30x124
5/6	W27x217, W27x178	W27x258, W27x217	6/16, 21/16	2/16, 14/16	0, 10/16	0, 8/16	W30x124
4/5	W27x217	W27x258	5/16, 21/16	1/16, 13/16	0, 9/16	0, 7/16	W30x132
3/4	W27x235, W27x217	W27x281, W27x258	5/16, 21/16	1/16, 13/16	0, 9/16	0, 7/16	W30x132
2/3	W27x235	W27x281	4/16, 18/16	0, 11/16	0, 8/16	0, 5/16	W30x132
1/2	W27x235	W27x281	4/16, 19/16	0, 12/16	0, 8/16	0, 6/16	W30x132

Table G.7 Twelve-story, five-bay MRF design.

Story/Floor	Columns		Doubler plates (in)				Beam
	Exterior	Interior	$\gamma_d = \gamma_y$	$\gamma_d = 4\gamma_y$	$\gamma_d = 10\gamma_y$	$\gamma_d = 15\gamma_y$	
12/Roof	W24x84	W24x84	4/16, 20/16	2/16, 10/16	0, 7/16	0, 6/16	W18x60
11/12	W24x94, W24x84	W24x94, W24x84	4/16, 20/16	2/16, 10/16	0, 7/16	0, 6/16	W18x60
10/11	W24x94	W24x94	4/16, 15/16	2/16, 11/16	0, 8/16	0, 6/16	W21x68
9/10	W24x103, W24x94	W24x131, W24x94	4/16, 15/16	2/16, 11/16	0, 8/16	0, 6/16	W21x68
8/9	W24x103	W24x131	4/16, 16/16	2/16, 11/16	0, 7/16	0, 6/16	W24x76
7/8	W24x131, W24x103	W24x146, W24x131	4/16, 16/16	2/16, 11/16	0, 7/16	0, 6/16	W24x76
6/7	W24x131	W24x146	6/16, 20/16	3/16, 14/16	1/16, 10/16	0, 8/16	W27x94
5/6	W24x146, W24x131	W24x176, W24x146	6/16, 20/16	3/16, 14/16	1/16, 10/16	0, 8/16	W27x94
4/5	W24x146	W24x176	5/16, 18/16	2/16, 12/16	0, 9/16	0, 7/16	W27x94
3/4	W24x162, W24x146	W24x192, W24x176	5/16, 18/16	2/16, 12/16	0, 9/16	0, 7/16	W27x94
2/3	W24x162	W24x192	5/16, 20/16	2/16, 13/16	0, 9/16	0, 7/16	W27x102
1/2	W24x162	W24x192	5/16, 20/16	2/16, 13/16	0, 9/16	0, 7/16	W27x102

Table G.8 Twenty-story, three-bay MRF design.

Story/Floor	Columns		Doubler plates (in)				Beam
	Exterior	Interior	$\gamma_d = \gamma_y$	$\gamma_d = 4\gamma_y$	$\gamma_d = 10\gamma_y$	$\gamma_d = 15\gamma_y$	
20/Roof	W33x130	W36x150	5/16, 15/16	2/16, 10/16	0, 7/16	0, 5/16	W27x114
19/20	W33x152, W33x130	W36x170, W36x150	5/16, 15/16	2/16, 10/16	0, 7/16	0, 5/16	W27x114
18/19	W33x152	W36x170	5/16, 17/16	2/16, 12/16	0, 8/16	0, 6/16	W30x132
17/18	W33x169, W33x152	W36x194, W36x170	5/16, 17/16	2/16, 12/16	0, 8/16	0, 6/16	W30x132
16/17	W33x169	W36x194	5/16, 16/16	2/16, 10/16	0, 7/16	0, 4/16	W30x132
15/16	W33x201, W33x169	W36x262, W36x194	5/16, 16/16	2/16, 10/16	0, 7/16	0, 4/16	W30x132
14/15	W33x201	W36x262	6/16, 18/16	2/16, 12/16	0, 8/16	0, 5/16	W33x152
13/14	W33x241, W33x201	W36x282, W36x262	6/16, 18/16	2/16, 12/16	0, 8/16	0, 5/16	W33x152
12/13	W33x241	W36x282	4/16, 17/16	1/16, 11/16	0, 7/16	0, 5/16	W36x160
11/12	W33x291, W33x241	W36x302, W36x282	4/16, 17/16	1/16, 11/16	0, 7/16	0, 5/16	W36x160
10/11	W33x291	W36x302	2/16, 16/16	0, 10/16	0, 7/16	0, 4/16	W36x160
9/10	W33x318, W33x291	W36x330, W36x302	2/16, 16/16	0, 10/16	0, 7/16	0, 4/16	W36x160
8/9	W33x318	W36x330	0, 15/16	0, 9/16	0, 5/16	0, 3/16	W36x160
7/8	W33x387, W33x318	W36x330	0, 15/16	0, 9/16	0, 5/16	0, 3/16	W36x160
6/7	W33x387	W36x330	0, 17/16	0, 10/16	0, 7/16	0, 4/16	W36x170
5/6	W36x441, W33x387	W36x361, W36x330	0, 17/16	0, 10/16	0, 7/16	0, 4/16	W36x170
4/5	W36x441	W36x361	0, 15/16	0, 8/16	0, 5/16	0, 3/16	W36x170
3/4	W36x487, W36x441	W36x395, W36x361	0, 15/16	0, 8/16	0, 5/16	0, 3/16	W36x170
2/3	W36x487	W36x395	0, 13/16	0, 7/16	0, 3/16	0, 1/16	W36x170
1/2	W36x487	W36x395	0, 13/16	0, 7/16	0, 3/16	0, 1/16	W36x170

Table G.9 Twenty-story, five-bay MRF design.

Story/Floor	Columns		Doubler plates (in)				Beam
	Exterior	Interior	$\gamma_d = \gamma_y$	$\gamma_d = 4\gamma_y$	$\gamma_d = 10\gamma_y$	$\gamma_d = 15\gamma_y$	
20/Roof	W27x94	W27x102	4/16, 15/16	2/16, 10/16	0, 7/16	0, 5/16	W24x76
19/20	W27x114, W27x94	W27x129, W27x102	4/16, 15/16	2/16, 10/16	0, 7/16	0, 5/16	W24x76
18/19	W27x114	W27x129	5/16, 17/16	2/16, 12/16	0, 9/16	0, 7/16	W27x94
17/18	W27x129, W27x114	W27x161, W27x129	5/16, 17/16	2/16, 12/16	0, 9/16	0, 7/16	W27x94
16/17	W27x129	W27x161	4/16, 17/16	1/16, 11/16	0, 8/16	0, 6/16	W27x94
15/16	W27x161, W27x129	W27x194, W27x161	4/16, 17/16	1/16, 11/16	0, 8/16	0, 6/16	W27x94
14/15	W27x161	W27x194	5/16, 17/16	2/16, 12/16	0, 8/16	0, 6/16	W30x108
13/14	W27x178, W27x161	W27x217, W27x194	5/16, 17/16	2/16, 12/16	0, 8/16	0, 6/16	W30x108
12/13	W27x178	W27x217	6/16, 21/16	2/16, 14/16	0, 10/16	0, 8/16	W30x124
11/12	W27x194, W27x178	W27x235, W27x217	6/16, 21/16	2/16, 14/16	0, 10/16	0, 8/16	W30x124
10/11	W27x194	W27x235	5/16, 19/16	2/16, 12/16	0, 9/16	0, 6/16	W30x124
9/10	W27x217, W27x194	W27x258, W27x235	5/16, 19/16	2/16, 12/16	0, 9/16	0, 6/16	W30x124
8/9	W27x217	W27x258	4/16, 18/16	0, 11/16	0, 7/16	0, 5/16	W30x124
7/8	W27x235, W27x217	W27x281, W27x258	4/16, 18/16	0, 11/16	0, 7/16	0, 5/16	W30x124
6/7	W27x235	W27x281	4/16, 18/16	0, 11/16	0, 8/16	0, 5/16	W30x132
5/6	W27x281, W27x235	W27x307, W27x281	4/16, 18/16	0, 11/16	0, 8/16	0, 5/16	W30x132
4/5	W27x281	W27x307	1/16, 17/16	0, 10/16	0, 6/16	0, 4/16	W30x132
3/4	W27x307, W27x281	W27x336, W27x307	1/16, 17/16	0, 10/16	0, 6/16	0, 4/16	W30x132
2/3	W27x307	W27x336	2/16, 19/16	0, 12/16	0, 7/16	0, 5/16	W30x148
1/2	W27x307	W27x336	2/16, 19/16	0, 12/16	0, 7/16	0, 5/16	W30x148

The above designs were controlled by the drift limit as per ASCE (2016), while all beam and column strength checks are respected. The drift check was performed for the $\gamma_d = 15\gamma_y$ cases, since deformations are higher in these cases. The drift stability coefficient checks are shown in Fig. F.7 and Fig. G.8 for the three- and the five-bay MRFs, respectively.

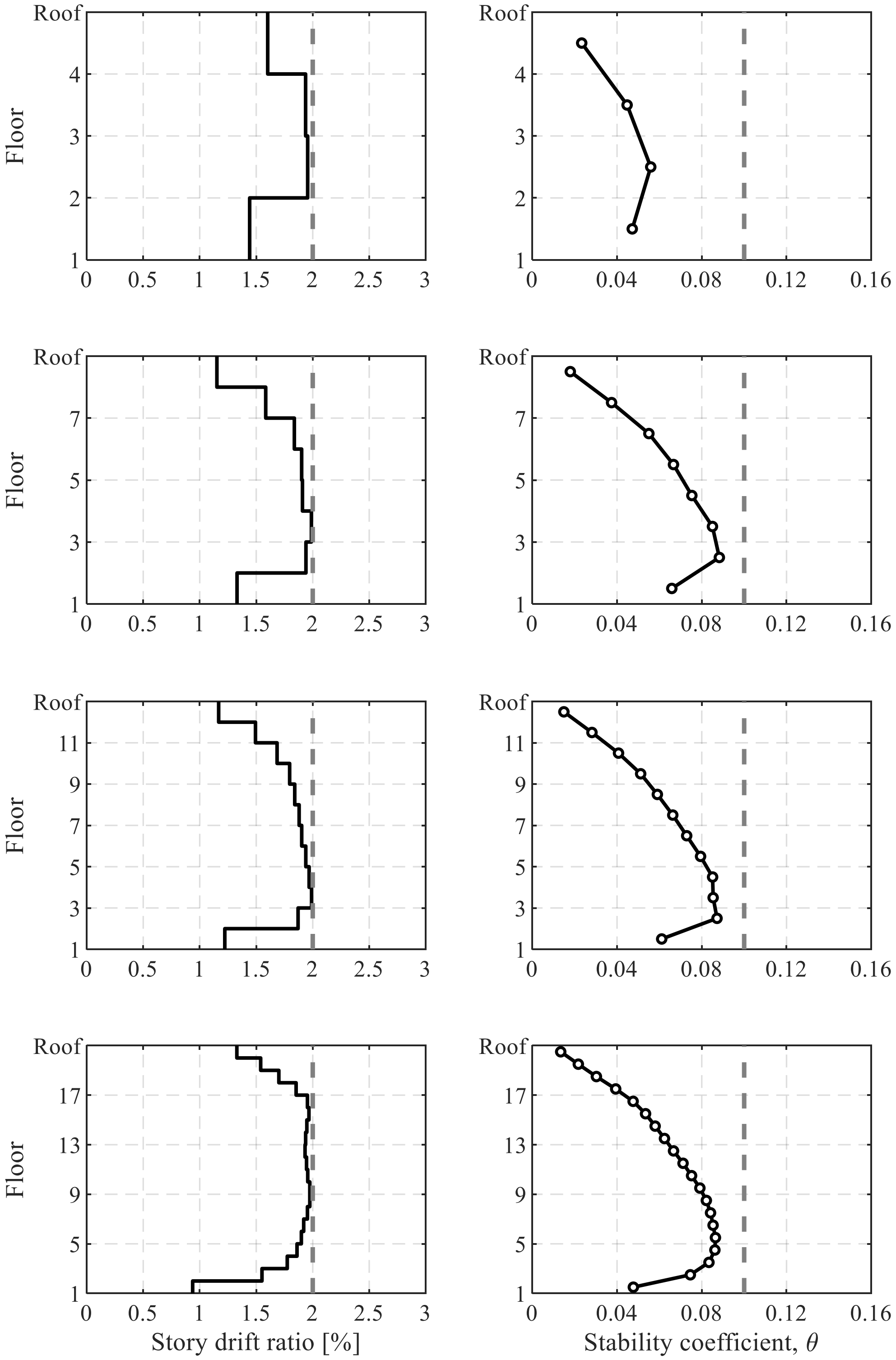

Figure G.7 Drift and stability coefficient checks for the four-, eight-, twelve- and twenty-story, three-bay MRFs.

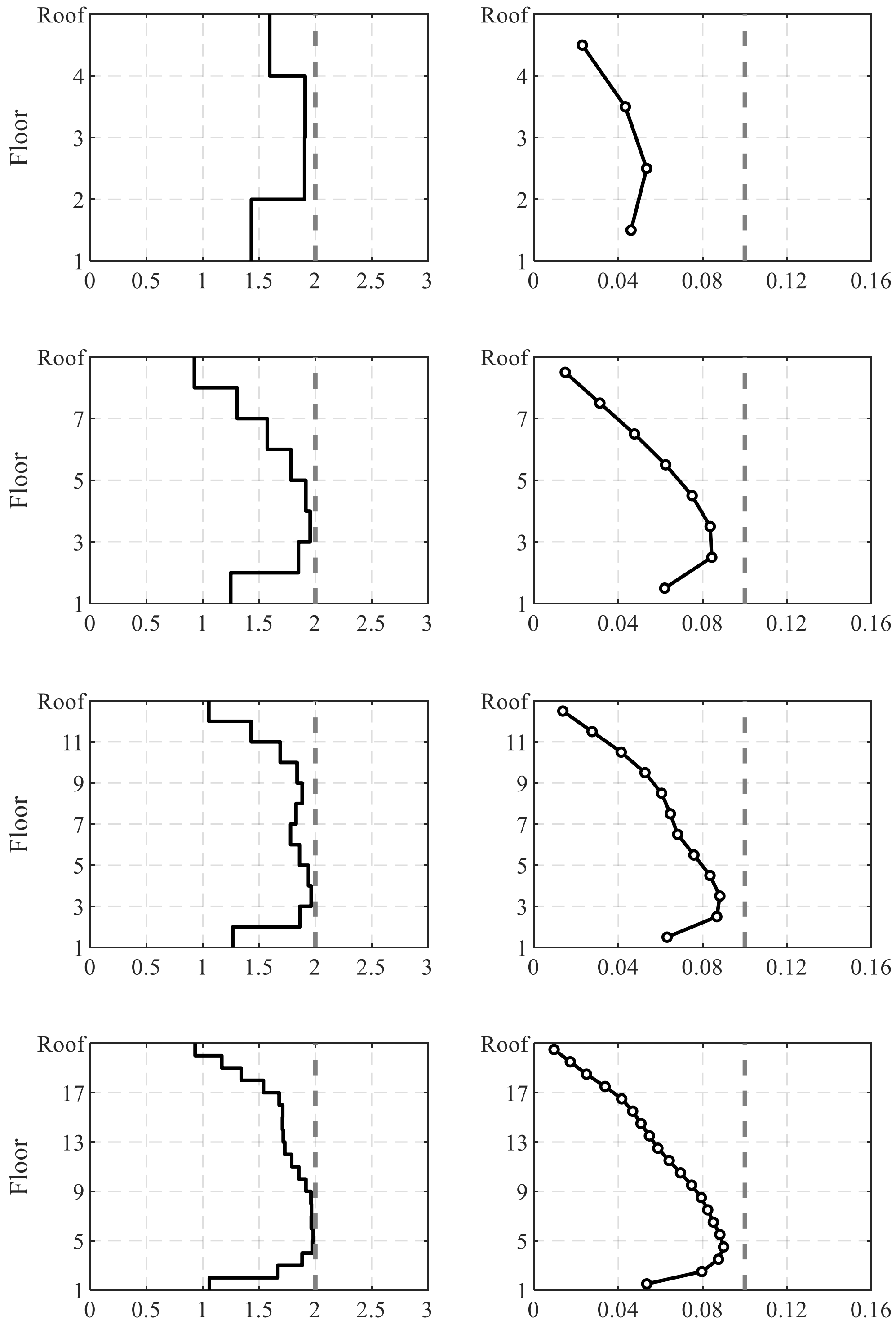

Figure G.8 Drift and stability coefficient checks for the four-, eight-, twelve- and twenty-story, five-bay MRFs.

The strong column weak beam (SCWB) check for all MRFs is respected and shown from Table G.10 to Table G.17.

Table G.10 SCWB ratio for the four-story, three-bay MRF

Story/Floor	Column 1	Column 2	Column 3	Column 4
4/Roof	1.2	0.7	0.7	1.2
3/4	2.2	1.4	1.4	2.2
2/3	1.8	1.7	1.7	1.8
1/2	1.5	1.6	1.6	1.5

Table G.11 SCWB ratio for the four-story, five-bay MRF

Story/Floor	Column 1	Column 2	Column 3	Column 4	Column 5	Column 6
4/Roof	1.1	0.7	0.7	0.7	0.7	1.1
3/4	2.0	1.4	1.4	1.4	1.4	2.0
2/3	1.9	1.5	1.5	1.5	1.5	1.9
1/2	1.6	1.5	1.5	1.5	1.5	1.6

Table G.12 SCWB ratio for the eight-story, three-bay MRF

Story/Floor	Column 1	Column 2	Column 3	Column 4
8/Roof	1.2	0.6	0.6	1.2
7/8	2.3	1.2	1.2	2.3
6/7	1.9	1.5	1.5	1.9
5/6	1.6	1.4	1.4	1.6
4/5	1.5	1.4	1.4	1.5
3/4	1.2	1.4	1.4	1.2
2/3	1.4	1.4	1.4	1.4
1/2	1.2	1.3	1.3	1.2

Table G.13 SCWB ratio for the eight-story, five-bay MRF

Story/Floor	Column 1	Column 2	Column 3	Column 4	Column 5	Column 6
8/Roof	1.0	0.8	0.8	0.8	0.8	1.0
7/8	2.0	1.5	1.5	1.5	1.5	2.0
6/7	2.2	1.3	1.3	1.3	1.3	2.2
5/6	1.9	1.3	1.3	1.3	1.3	1.9
4/5	1.9	1.2	1.2	1.2	1.2	1.9
3/4	1.7	1.1	1.1	1.1	1.1	1.7
2/3	1.9	1.3	1.3	1.3	1.3	1.9
1/2	1.7	1.3	1.3	1.3	1.3	1.7

Table G.14 SCWB ratio for the twelve-story, three-bay MRF

Story/Floor	Column 1	Column 2	Column 3	Column 4
12/Roof	1.1	0.6	0.6	1.1
11/12	2.1	1.2	1.2	2.1
10/11	1.7	1.1	1.1	1.7
9/10	1.5	1.1	1.1	1.5
8/9	1.3	1.4	1.4	1.3
7/8	1.1	1.4	1.4	1.1
6/7	1.5	1.3	1.3	1.5
5/6	1.3	1.2	1.2	1.3
4/5	1.6	1.4	1.4	1.6
3/4	1.3	1.4	1.4	1.3
2/3	1.4	1.5	1.5	1.4
1/2	1.2	1.5	1.5	1.2

Table G.15 SCWB ratio for the twelve-story, five-bay MRF

Story/Floor	Column 1	Column 2	Column 3	Column 4	Column 5	Column 6
12/Roof	1.4	0.7	0.7	0.7	0.7	1.4
11/12	2.7	1.4	1.4	1.4	1.4	2.7
10/11	2.3	1.2	1.2	1.2	1.2	2.3
9/10	2.1	1.1	1.2	1.2	1.1	2.1
8/9	1.7	1.4	1.4	1.4	1.4	1.7
7/8	1.6	1.3	1.4	1.4	1.3	1.6
6/7	1.5	1.1	1.1	1.1	1.1	1.5
5/6	1.4	1.0	1.1	1.1	1.0	1.4
4/5	1.5	1.3	1.3	1.3	1.3	1.5
3/4	1.3	1.2	1.3	1.3	1.2	1.3
2/3	1.3	1.2	1.3	1.3	1.2	1.3
1/2	1.1	1.2	1.3	1.3	1.2	1.1

Table G.16 SCWB ratio for the twenty-story, three-bay MRF

Story/Floor	Column 1	Column 2	Column 3	Column 4
20/Roof	1.1	0.7	0.7	1.1
19/20	2.1	1.3	1.3	2.1
18/19	1.8	1.2	1.2	1.8
17/18	1.7	1.1	1.1	1.7
16/17	1.7	1.3	1.3	1.7
15/16	1.5	1.2	1.2	1.5
14/15	1.4	1.4	1.4	1.4
13/14	1.2	1.4	1.4	1.2
12/13	1.4	1.3	1.3	1.4
11/12	1.2	1.3	1.3	1.2
10/11	1.6	1.4	1.4	1.6
9/10	1.3	1.3	1.3	1.3
8/9	1.4	1.4	1.4	1.4
7/8	1.2	1.4	1.4	1.2
6/7	1.6	1.3	1.3	1.6
5/6	1.4	1.3	1.3	1.4
4/5	1.8	1.4	1.4	1.8
3/4	1.5	1.4	1.4	1.5
2/3	1.7	1.6	1.6	1.7
1/2	1.4	1.6	1.6	1.4

Table G.17 SCWB ratio for the twenty-story, five-bay MRF

Story/Floor	Column 1	Column 2	Column 3	Column 4	Column 5	Column 6
20/Roof	1.1	0.6	0.6	0.6	0.6	1.1
19/20	2.2	1.2	1.2	1.2	1.2	2.2
18/19	1.8	1.1	1.1	1.1	1.1	1.8
17/18	1.7	1.0	1.1	1.1	1.0	1.7
16/17	1.9	1.4	1.4	1.4	1.4	1.9
15/16	1.7	1.3	1.4	1.4	1.3	1.7
14/15	1.8	1.3	1.4	1.4	1.3	1.8
13/14	1.7	1.3	1.4	1.4	1.3	1.7
12/13	1.5	1.2	1.3	1.3	1.2	1.5
11/12	1.4	1.1	1.3	1.3	1.1	1.4
10/11	1.5	1.2	1.4	1.4	1.2	1.5
9/10	1.3	1.2	1.3	1.3	1.2	1.3
8/9	1.5	1.3	1.5	1.5	1.3	1.5
7/8	1.3	1.3	1.5	1.5	1.3	1.3
6/7	1.3	1.3	1.5	1.5	1.3	1.3
5/6	1.1	1.3	1.5	1.5	1.3	1.1
4/5	1.5	1.4	1.6	1.6	1.4	1.5
3/4	1.3	1.4	1.6	1.6	1.4	1.3
2/3	1.2	1.4	1.6	1.6	1.4	1.2
1/2	1.1	1.3	1.5	1.5	1.3	1.1

References

AIJ. (2007). *Japanese architectural standard specification*. 2nd edn, JASS 6, Steel Work: Architectural Institute of Japan, Tokyo (in Japanese).

AIJ. (2010). *Recommendation for limit state design of steel structures*. 3rd edn, Architectural Institute of Japan, Tokyo (in Japanese).

AIJ. (2012). *Recommendations for design of connections in steel structures*. Architectural Institute of Japan, Tokyo (in Japanese).

AIJ. (2018). *Standard for the ultrasonic inspection of weld defects in steel structures*. Architectural Institute of Japan, Tokyo (in Japanese).

AISC. (2016a). *Seismic provisions for structural steel buildings, ANSI/AISC 341-16*. Chicago, IL: American Institute for Steel Construction.

AISC. (2016b). *Specification for structural steel buildings, ANSI/AISC 360-16*. Chicago, IL: American Institute for Steel Construction.

AISC. (2016c). *Prequalified connections for special and intermediate steel moment frames for seismic applications, ANSI/AISC 358-16*. Chicago, IL: American Institute for Steel Construction.

Alavi, B., and Krawinkler, H. (2004). "Behavior of moment-resisting frame structures subjected to near-fault ground motions." *Earthquake Engineering & Structural Dynamics*, 33(6), 687–706. https://doi.org/10.1002/eqe.369.

ASCE. (2016). *Minimum design loads and associated criteria for buildings and other structures*. ASCE/SEI 7-10, American Society of Civil Engineers, Reston, VA, USA. https://doi.org/10.1061/9780784412916.

ASCE. (2017). *Minimum design loads and associated criteria for buildings and other structures*. ASCE/SEI 7-16, American Society of Civil Engineers, Reston, VA, USA. https://doi.org/10.1061/9780784414248.

Aslani, H., and Miranda, E. (2005). *Probabilistic earthquake loss estimation and loss disaggregation in buildings*. Report No. 157, The John A. Blume Earthquake Engineering Research Center, Department of Civil Engineering, Stanford University, Stanford, CA, USA.

ASTM. (2015). *Standard guide for magnetic particle testing*. ASTM E709 − 15, American Society for Testing and Materials, West Conshohocken, PA, USA. https://doi.org/10.1520/E0709-15.

ASTM. (2016). *Standard test methods for tension testing of metallic materials*. ASTM E8 / E8M-16a, American Society for Testing and Materials, West Conshohocken, PA, USA. https://doi.org/10.1520/E0008_E0008M-16AE01.

ASTM. (2017). *Standard specification for straight beam ultrasonic examination of rolled steel structural shapes*. ASTM A898/A898M − 17, American Society for Testing and Materials, West Conshohocken, PA, USA. https://doi.org/10.1520/A0898_A0898M-17.

ASTM. (2018a). *Standard specification for through-thickness tension testing of steel plates for special applications*. A770/A770M − 03 (Reapproved 2018), American Society for Testing and Materials, West Conshohocken, PA, USA. https://doi.org/10.1520/A0770_A0770M-03R18.

ASTM. (2018b). *Standard practice for liquid penetrant examination for general industry*. ASTM E165/E165M − 18, American Society for Testing and Materials, West Conshohocken, PA, USA. https://doi.org/10.1520/E0165_E0165M-18.

ASTM. (2021). *Standard test methods and definitions for mechanical testing of steel products*. ASTM A370-21, American Society for Testing and Materials, West Conshohocken, PA, USA. https://doi.org/10.1520/A0370-21.

AWS. (2010). *Structural welding code—steel*. ANSI/AWS D1.1:2010, American Welding Society, Miami, FL, USA.

AWS. (2016). *Structural welding code-seismic supplement*. AWS D1.8/D1.8M:2016, American Welding Society, Miami, FL, USA.

Bakker, A. (1984). *The three-dimensional J-Integral*. Report No. WTHD 167, Delft University of Technology (The Netherlands).

Barsom, J. M., Johnson, M., and Mohr, B. (2000). *Evaluation of mechanical properties in full-scale connections and recommended minimum weld toughness for moment resisting frames*. SAC Background Documents, Report No. SAC/ BD-00/14, SAC Joint Venture, Sacramento, CA, USA.

Barsom, J. M., and Korvink, S. A. (1998). “Through-thickness properties of structural steels.” *Journal of Structural Engineering*, American Society of Civil Engineers, 124(7), 727–735. https://doi.org/10.1061/(ASCE)0733-9445(1998)124:7(727).

Barsom, J. M., and Pellegrino, J. V. (2000). *Failure analysis of a column k-Area fracture*. SAC Background Documents, Report No. SAC/BD-00/28, SAC Joint Venture, Sacramento, CA, USA.

BCJ. (2016). *Building standard law of Japan*. Building Center of Japan, Tokyo, Japan.

Bech, D., Tremayne, B., and Houston, J. (2015). “Proposed changes to steel column evaluation criteria for existing buildings.” *2nd ATC-SEI Conf. on Improving the Seismic Performance of Existing Buildings and Other Structures*, Earthquake Engineering Research Institute, San Francisco, 255–272. https://doi.org/10.1061/9780784479728.022.

Bertero, V., Krawinkler, H., and Popov, E. P. (1973). *Further studies on seismic behavior of steel beam-column subassemblages*. Report No. EERC-73/27, Earthquake Engineering Research Center, University of California, Berkeley, California.

Biddah, A., and Heidebrecht, A. C. (1998). “Seismic performance of moment-resisting steel frame structures designed for different levels of seismic hazard.” *Earthquake Spectra*, 14(4), 597–627. https://doi.org/10.1193/1.1586018.

Bonowitz, D. (2009). “Resilience criteria for seismic evaluation of existing buildings: A proposal to supplement ASCE 31 for intermediate performance objectives.” *Improving the Seismic Performance of Existing Buildings and Other Structures*, San Francisco, California, United States: American Society of Civil Engineers, 477–488. https://doi.org/10.1061/41084(364)44.

Bouchard, S., and Axmann, G. (2000). “ASTM A913 grades 50 and 65: Steels for seismic applications.” *In Proc., 3rd International Conference on Behavior of Steel Structures in Seismic Areas (STESSA)*, Montreal, Canada: CRC Press, 11–17.

Braconi, A., Finetto, M., and Degee, H. (2013). *Optimising the seismic performance of steel and steel-concrete structures by standardising material quality control (OPUS)*. European Commission, Luxembourg.

Brandonisio, G., De Luca, A., and Mele, E. (2012). “Shear strength of panel zone in beam-to-column connections.” *Journal of Constructional Steel Research*, 71(1), 129–142. https://doi.org/10.1016/j.jcsr.2011.11.004.

Brocks, W., and Scheider, I. (2001). *Numerical aspects of the path-dependence of the J-integral in incremental plasticity: How to calculate reliable J-values in FE analysis*. GKSS-Forschungszentrum, Geesthacht, Germany.

de Castro e Sousa, A., and Lignos, D. G. (2017). *Residual stress measurements of European hot-rolled I-shaped steel profiles*. Technical Rep. No. 231302, Ecole Polytechnique Federale de Lausanne, Lausanne.

de Castro e Sousa, A., Suzuki, Y., and Lignos, D. (2020). “Consistency in solving the inverse problem of the Voce-Chaboche constitutive model for plastic straining.” *Journal of Engineering Mechanics*, American Society of Civil Engineers, 146(9), 04020097. https://doi.org/10.1061/(ASCE)EM.1943-7889.0001839.

Castro, J. M., Dávila-Arbona, F. J., and Elghazouli, A. Y. (2008). “Seismic design approaches for panel zones in steel moment frames.” *Journal of Earthquake Engineering*, 12(1), 34–51. https://doi.org/10.1080/13632460801922712.

Castro, J. M., Elghazouli, A. Y., and Izzuddin, B. A. (2005). “Modelling of the panel zone in steel and composite moment frames.” *Engineering Structures*, 27(1), 129–144. https://doi.org/10.1016/j.engstruct.2004.09.008.

CEN. (2004a). *EN 1998-1: Eurocode 8: Design of structures for earthquake resistance – Part 1: General rules, seismic actions and rules for buildings*. Brussels, Belgium: European Committee for Standardization.

CEN. (2004b). *EN 1993-1-10: Eurocode 3: Design of steel structures - Part 10: Material toughness and through-thickness properties*. Brussels, Belgium: European Committee for Standardization.

CEN. (2004c). *EN 1994-1-1: Eurocode 4: Design of composite steel and concrete structures – Part 1-1: General rules and rules for buildings*. Brussels, Belgium: European Committee for Standardization.

CEN. (2004d). *EN 1993-1-1: Eurocode 3: Design of steel structures - Part 1-1: General rules and rules for buildings*. Brussels, Belgium: European Committee for Standardization.

CEN. (2005). *EN 1993-1-8: Eurocode 3: Design of steel structures – Part 1-8: Design of joints*. European Committee for Standardization, Brussels, Belgium.

Challa, V. R. M., and Hall, J. F. (1994). "Earthquake collapse analysis of steel frames." *Earthquake Engineering & Structural Dynamics*, 23(11), 1199–1218. https://doi.org/10.1002/eqe.4290231104.

Charney, F. A., Iyer, H., and Spears, P. W. (2005). "Computation of major axis shear deformations in wide flange steel girders and columns." *Journal of Constructional Steel Research*, 61(11), 1525–1558. https://doi.org/10.1016/j.jcsr.2005.04.002.

Chaudhari, T., MacRae, G., Bull, D., Clifton, C., and Hicks, S. (2019). "Experimental behaviour of steel beam-column subassemblies with different slab configurations." *Journal of Constructional Steel Research*, 162(1), 105699. https://doi.org/10.1016/j.jcsr.2019.105699.

Chi, B., and Uang, C.-M. (2002). "Cyclic response and design recommendations of reduced beam section moment connections with deep columns." *Journal of Structural Engineering*, American Society of Civil Engineers, 128(4), 464–473. https://doi.org/10.1061/(ASCE)0733-9445(2002)128:4(464).

Chi, W. M., Deirlein, G. G., and Ingraffea, A. (1997). *Finite element fracture mechanics investigation of welded beam-column connections*. SAC Background Documents, Report No. SAC/BD-97/05, SAC Joint Venture, Sacramento, CA, USA.

Chi, W.-M., Deierlein, G. G., and Ingraffea, A. (2000). "Fracture toughness demands in welded beam-column moment connections." *Journal of Structural Engineering*, American Society of Civil Engineers, 126(1), 88–97. https://doi.org/10.1061/(ASCE)0733-9445(2000)126:1(88).

Christoph, A., Ibarra, L., and Krawinkler, H. (2004). "Evaluation of P-Delta effects in non-deteriorating MDOF structures from equivalent SDOF systems." *13th World Conference on Earthquake Engineering*, Vancouver, B.C., Canada.

Chung, K., Kishiki, S., Matsumoto, Y., and Yamada, S. (2006). "Experimental study on the hysteresis behavior of panel subjected to multi-axial cyclic loadings." *Journal of Structural and Construction Engineering*, 602, 203-210 (in Japanese).

Chung, K., Yamada, S., and Yang, I. (2010). "Simplified uni-axial hysteretic damage model for panel zone of structural steel under earthquake loads." *International Journal of Steel Structures*, 10(3), 267–281. https://doi.org/10.1007/BF03215836.

Ciutina, A. L., and Dubina, D. (2003). "Influence of column web stiffening on the seismic behaviour of beam-to- column joints." *Proceedings of the Conference on Behaviour of Steel Structures in Seismic Areas*, A. A. Balkema, Rotterdam, Netherlands, 269–275.

Ciutina, A. L., and Dubina, D. (2008). "Column web stiffening of steel beam-to-column joints subjected to seismic actions." *Journal of Structural Engineering*, American Society of Civil Engineers, 134(3), 505–510. https://doi.org/10.1061/(ASCE)0733-9445(2008)134:3(505).

Clark, P. W., Frank, K., Krawinkler, H., and Shaw, R. (1997). *Protocol for fabrication, inspection, testing and documentation of beam-column connection tests and other experimental specimens*. SAC Background Documents, Report No. SAC/BD-97/02, SAC Joint Venture, Sacramento, CA, USA.

Comerio, M. C. (2006). "Estimating Downtime in Loss Modeling." *Earthquake Spectra*, SAGE Publications Ltd STM, 22(2), 349–365. https://doi.org/10.1193/1.2191017.

CSA. (2019). *Design of steel structures*. CAN/CSA S16-19, Mississauga, Canada: CSA.

D'Aniello, M., Tartaglia, R., Costanzo, S., and Landolfo, R. (2017). "Seismic design of extended stiffened end-plate joints in the framework of Eurocodes." *Journal of Constructional Steel Research*, 128, 512–527. https://doi.org/10.1016/j.jcsr.2016.09.017.

Del Caprio, M., Mosqueda, G., and Lignos, D. (2014). *Hybrid simulation of the seismic response of a steel moment frame building structure through collapse*. Report No. MCEER-14-0003, University of Buffalo, State University of New York, USA.

Del Caprio, M., Mosqueda, G., and Lignos, D. G. (2016). "Seismic performance of a steel moment frame subassembly tested from the onset of damage through collapse." *Earthquake Engineering & Structural Dynamics*, 45(10), 1563–1580. https://doi.org/10.1002/eqe.2743.

deLorenzi, H. G. (1982). "On the energy release rate and the J-integral for 3-D crack configurations." *International Journal of Fracture*, 19(3), 183–193. https://doi.org/10.1007/BF00017129.

Eads, L., Miranda, E., Krawinkler, H., and Lignos, D. G. (2013). "An efficient method for estimating the collapse risk of structures in seismic regions." *Earthquake Engineering & Structural Dynamics*, 42(1), 25–41. https://doi.org/10.1002/eqe.2191.

Eads, L., Miranda, E., and Lignos, D. G. (2015). “Average spectral acceleration as an intensity measure for collapse risk assessment: Average Spectral Acceleration as an IM for Collapse Risk Assessment.” *Earthquake Engineering & Structural Dynamics*, 44(12), 2057–2073. https://doi.org/10.1002/eqe.2575.

El Jisr, H., Elkady, A., and Lignos, D. G. (2019). “Composite steel beam database for seismic design and performance assessment of composite-steel moment-resisting frame systems.” *Bulletin of Earthquake Engineering*, 17(6), 3015–3039. https://doi.org/10.1007/s10518-019-00564-w.

El Jisr, H., Kohrangi, M., and Lignos, D. G. (2022). “Proposed nonlinear macro-model for seismic risk assessment of composite-steel moment resisting frames (in press).” *Earthquake Engineering & Structural Dynamics*. https://doi.org/10.1002/eqe.3610.

Elkady, A., Güell, G., and Lignos, D. G. (2020). “Proposed methodology for building-specific earthquake loss assessment including column residual axial shortening.” *Earthquake Engineering & Structural Dynamics*, 49(4), 339–355. https://doi.org/10.1002/eqe.3242.

Elkady, A., and Lignos, D. G. (2014). “Modeling of the composite action in fully restrained beam-to-column connections: implications in the seismic design and collapse capacity of steel special moment frames.” *Earthquake Engineering & Structural Dynamics*, 43(13), 1935–1954. https://doi.org/10.1002/eqe.2430.

Elkady, A., and Lignos, D. G. (2015). “Effect of gravity framing on the overstrength and collapse capacity of steel frame buildings with perimeter special moment frames.” *Earthquake Engineering & Structural Dynamics*, 44(8), 1289–1307. https://doi.org/10.1002/eqe.2519.

Elkady, A., and Lignos, D. G. (2018a). “Full-scale testing of deep wide-flange steel columns under multiaxis cyclic loading: loading sequence, boundary effects, and lateral stability bracing force demands.” *Journal of Structural Engineering*, American Society of Civil Engineers, 144(2), 04017189. https://doi.org/10.1061/(ASCE)ST.1943-541X.0001937.

Elkady, A., and Lignos, D. G. (2018b). “Improved seismic design and nonlinear modeling recommendations for wide-flange steel columns.” *Journal of Structural Engineering*, American Society of Civil Engineers, 144(9), 04018162. https://doi.org/10.1061/(ASCE)ST.1943-541X.0002166.

El-Tawil, S. (2000). “Panel zone yielding in steel moment connections.” *Engineering Journal*, 37(3), 120–131.

El-Tawil, S., Mikesell, T., and Kunnath, S. K. (2000). “Effect of local details and yield ratio on behavior of FR steel connections.” *Journal of Structural Engineering*, American Society of Civil Engineers, 126(1), 79–87. https://doi.org/10.1061/(ASCE)0733-9445(2000)126:1(79).

El-Tawil, S., Mikesell, T., Vidarsson, E., and Kunnath, S. K. (1998). *Strength and ductility of FR welded-bolted connections*. SAC Joint Venture, Sacramento, CA, USA.

El-Tawil, S., Vidarsson, E., Mikesell, T., and Kunnath, S. K. (1999). “Inelastic behavior and design of steel panel zones.” *Journal of Structural Engineering*, American Society of Civil Engineers, 125(2), 183–193. https://doi.org/10.1061/(ASCE)0733-9445(1999)125:2(183).

Engelhardt, M. D., and Husain, A. S. (1993). “Cyclic-loading performance of welded flange-bolted web connections.” *Journal of Structural Engineering*, American Society of Civil Engineers, 119(12), 3537–3550. https://doi.org/10.1061/(ASCE)0733-9445(1993)119:12(3537).

Engelhardt, M. D., Venti, M. J., Fry, G. T., Jones, S. L., and Holliday, S. D. (2000). *Behavior and design of radius cut reduced beam section connections*. Report No. SAC/BD-00/17, SAC Joint Venture, Sacramento, CA, USA.

Erdogan, F., and Sih, G. C. (1963). “On the crack extension in plates under plane loading and transverse shear.” *Journal of Basic Engineering*, 85(4), 519–525. https://doi.org/10.1115/1.3656897.

Fardis, M. N. (2018). “Capacity design: Early history.” *Earthquake Engineering & Structural Dynamics*, 47(14), 2887–2896. https://doi.org/10.1002/eqe.3110.

FEMA. (1997). *Connection test summaries*. Report No. FEMA-289, Federal Emergency Management Agency, Washington, D.C., USA.

FEMA. (2000a). *State of the art report on connection performance*. Report No. FEMA-355D, Federal Emergency Management Agency, Washington, D.C., USA.

FEMA. (2000b). *State of the art report on past performance of steel moment-frame buildings in earthquakes*. Report No. FEMA-355E, Federal Emergency Management Agency, Washington, D.C., USA.

FEMA. (2009a). *Quantification of building seismic performance factors*. Report No. FEMA-P695, Federal Emergency Management Agency, Washington, D.C., USA.

FEMA. (2009b). *Effects of strength and stiffness degradation on seismic response*. Report No. FEMA-P440A, Federal Emergency Management Agency, Washington, D.C., USA.

FEMA. (2012). *Seismic performance assessment of buildings*. Report No. FEMA-P-58-1, Federal Emergency Management Agency, Washington, D.C., USA.

FEMA. (2018). *Seismic performance assessment of buildings*. Report No. FEMA -P-58-2, Federal Emergency Management Agency, Washington, D.C., USA.

Fielding, D. J., and Huang, J. S. (1971). "Shear in steel beam-to-column connections." *Welding Journal,* Research Supplement, 50(7), 313–326.

Flores, F. X., Charney, F. A., and Lopez-Garcia, D. (2014). "Influence of the gravity framing system on the collapse performance of special steel moment frames." *Journal of Constructional Steel Research,* 101, 351–362. https://doi.org/10.1016/j.jcsr.2014.05.020.

Foutch, D. A., and Yun, S.-Y. (2002). "Modeling of steel moment frames for seismic loads." *Journal of Constructional Steel Research*, 58(5–8), 529–564. https://doi.org/10.1016/S0143-974X(01)00078-5.

Fujisawa, K., Ichinohe, Y., Sugimoto, M., and Sonoda, M. (2013). *Statistical study on mechanical properties and chemical compositions of SN Steels*. In: Summary of technical papers of annual meeting, Architectural Institute of Japan, 699–700.

Furley, J., van de Lindt, J. W., Pei, S., Wichman, S., Hasani, H., Berman, J. W., Ryan, K., Daniel Dolan, J., Zimmerman, R. B., and McDonnell, E. (2021). "Time-to-functionality fragilities for performance assessment of buildings." *Journal of Structural Engineering*, American Society of Civil Engineers, 147(12), 04021217. https://doi.org/10.1061/(ASCE)ST.1943-541X.0003195.

Ghobarah, A., Korol, R. M., and Osman, A. (1992). "Cyclic behavior of extended end-plate joints." *Journal of Structural Engineering*, American Society of Civil Engineers, 118(5), 1333–1353. https://doi.org/10.1061/(ASCE)0733-9445(1992)118:5(1333).

Gomez, I. R., Kanvinde, A. M., Kwan, Y. K., and Grondin, G. Y. (2008). *Strength and ductility of welded joints subjected to out-of-plane bending*. American Institute of Steel Construction, Chicago, IL.

Gupta, A., and Krawinkler, H. (1999). *Seismic demands for performance evaluation of steel moment resisting frame structures*. Report No. 132, The John A. Blume Earthquake Engineering Research Center, Department of Civil Engineering, Stanford University, Stanford, CA, USA.

Gupta, A., and Krawinkler, H. (2000a). "Dynamic P-delta effects for flexible inelastic steel structures." *Journal of Structural Engineering*, American Society of Civil Engineers, 126(1), 145–154. https://doi.org/10.1061/(ASCE)0733-9445(2000)126:1(145).

Gupta, A., and Krawinkler, H. (2000b). "Estimation of seismic drift demands for frame structures." *Earthquake Engineering & Structural Dynamics*, 29(9), 1287–1305. https://doi.org/10.1002/1096-9845(200009)29:9<1287::AID-EQE971>3.0.CO;2-B.

Hajjar, J. F., Leon, R. T., Gustafson, M. A., and Shield, C. K. (1998). "Seismic response of composite moment-resisting connections. II: behavior." *Journal of Structural Engineering*, American Society of Civil Engineers, 124(8), 877–885. https://doi.org/10.1061/(ASCE)0733-9445(1998)124:8(877).

Han, S. W., Kwon, G. U., and Moon, K. H. (2007). "Cyclic behaviour of post-Northridge WUF-B connections." *Journal of Constructional Steel Research,* 63(3), 365–374. https://doi.org/10.1016/j.jcsr.2006.05.003.

Hartloper, A. R., de Castro e Sousa, A., and Lignos, D. G. (2021). "Constitutive modeling of structural steels: nonlinear isotropic/kinematic hardening material model and its calibration." *Journal of Structural Engineering,* American Society of Civil Engineers, 147(4), 04021031. https://doi.org/10.1061/(ASCE)ST.1943-541X.0002964.

Haselton, C. B., Baker, J. W., Liel, A. B., and Deierlein, G. G. (2011). "Accounting for ground-motion spectral shape characteristics in structural collapse assessment through an adjustment for epsilon." *Journal of Structural Engineering*, American Society of Civil Engineers, 137(3), 332–344. https://doi.org/10.1061/(ASCE)ST.1943-541X.0000103.

Hjelmstad, K. D., and Haikal, G. (2006). "Analysis of steel moment frames with deformable panel zones." *Steel Structures,* 6(2), 129–140.

Hobbs, M. (2014). *Effects of slab-column interaction in steel moment resisting frames with steel-concrete composite floor slabs*. Master Thesis, Department of Civil and Natural Resources Engineering, University of Canterbury Christchurch, New Zealand.

Hwang, S.-H., and Lignos, D. G. (2017). “Earthquake-induced loss assessment of steel frame buildings with special moment frames designed in highly seismic regions.” *Earthquake Engineering & Structural Dynamics*, 46(13), 2141–2162. https://doi.org/10.1002/eqe.2898.

Ibarra, L. F., and Krawinkler, H. (2005). *Global collapse of frame structures under seismic excitations*. Report No. 152, The John A. Blume Earthquake Engineering Research Center, Department of Civil Engineering, Stanford University, Stanford, CA, USA.

Ibarra, L. F., Medina, R. A., and Krawinkler, H. (2005). “Hysteretic models that incorporate strength and stiffness deterioration.” *Earthquake Engineering & Structural Dynamics*, 34(12), 1489–1511. https://doi.org/10.1002/eqe.495.

Ibrahim, O. A., Lignos, D. G., and Rogers, C. A. (2019). “Recommendations for improved welding procedures for thick steel plates through thermo-mechanical analysis.” *International Journal of Steel Structures*, 19(1), 193–212. https://doi.org/10.1007/s13296-018-0110-2.

Irwin, G. R. (1961). “Plastic zone near a crack and fracture toughness.” *Sagamore Research Conference Proceedings, Vol. 4*, Syracuse University Research Institute, Syracuse, NY, 63–78.

Jia, L.-J., and Kuwamura, H. (2014). “Ductile fracture simulation of structural steels under monotonic tension.” *Journal of Structural Engineering*, American Society of Civil Engineers, 140(5), 04013115. https://doi.org/10.1061/(ASCE)ST.1943-541X.0000944.

Jin, J., and El-Tawil, S. (2005). “Evaluation of FEMA-350 seismic provisions for steel panel zones.” *Journal of Structural Engineering*, American Society of Civil Engineers, 131(2), 250–258. https://doi.org/10.1061/(ASCE)0733-9445(2005)131:2(250).

Johnson, M. Q. (1997). *Evaluation of the effect of welding procedures on the mechanical properties of FCAW-S and SMAW weld metal used in construction of seismic moment frames*. SAC Background Documents, Report No. SAC/ BD-96/01 thru Report No. SAC/BD-00/30, SAC Joint Venture, Sacramento, CA, USA.

Jones, S. L., Fry Gary T., and Engelhardt Michael D. (2002). “Experimental evaluation of cyclically loaded reduced beam section moment connections.” *Journal of Structural Engineering*, American Society of Civil Engineers, 128(4), 441–451. https://doi.org/10.1061/(ASCE)0733-9445(2002)128:4(441).

Kanno, R. (2016). “Advances in steel materials for innovative and elegant steel structures in Japan–A review.” *Structural Engineering International*, 26(3), 242–253. https://doi.org/10.2749/101686616X14555428759361.

Kanvinde, A. M. (2017). “Predicting fracture in civil engineering steel structures: state of the art.” *Journal of Structural Engineering*, American Society of Civil Engineers, 143(3), 03116001. https://doi.org/10.1061/(ASCE)ST.1943-541X.0001704.

Kanvinde, A. M., Fell, B. V., Gomez, I. R., and Roberts, M. (2008). “Predicting fracture in structural fillet welds using traditional and micromechanical fracture models.” *Engineering Structures*, 30(11), 3325–3335. https://doi.org/10.1016/j.engstruct.2008.05.014.

Kato, B., Chen, W. F., and Nakao, M. (1988). “Effects of joint-panel shear deformation on frames.” *Journal of Constructional Steel Research*, 10, 269–320. https://doi.org/10.1016/0143-974X(88)90033-8.

Kaufmann, E. J., and Fisher, J. W. (1996). *Fracture analysis of failed moment frame weld joints produced in full-scale laboratory tests and buildings damaged in the Northridge earthquake*. SAC Joint Venture, Sacramento, CA, USA.

Kim, D.-W., Blaney, C., and Uang, C.-M. (2015). “Panel zone deformation capacity as affected by weld fracture at column kinking location.” *Engineering Journal*, 53(1), 27–46.

Kim, K. D., and Engelhardt, M. D. (2002). “Monotonic and cyclic loading models for panel zones in steel moment frames.” *Journal of Constructional Steel Research*, North American Special Issue, 58(5–8), 605–635. https://doi.org/10.1016/S0143-974X(01)00079-7.

Kim, S.-Y., and Lee, C.-H. (2017). “Seismic retrofit of welded steel moment connections with highly composite floor slabs.” *Journal of Constructional Steel Research*, 139, 62–68. https://doi.org/10.1016/j.jcsr.2017.09.010.

Kolednik, O., Predan, J., Shan, G. X., Simha, N. K., and Fischer, F. D. (2005). “On the fracture behavior of inhomogeneous materials—A case study for elastically inhomogeneous bimaterials.” *International*

Journal of Solids and Structures, Micromechanics of Materials, 42(2), 605–620. https://doi.org/10.1016/j.ijsolstr.2004.06.064.

Kolmogorov, A. (1933). "Sulla determinazione empirica di una legge di distributione." *Giornale dell' Instituto Italiano delgi Attuari*, 4, 83–91.

Kosarieh, A. H., and Danesh, F. (2016). "Effects of panel zone yielding on seismic behavior of welded-flange-plate connections." *Bulletin of Earthquake Engineering*, 14(10), 2805–2825. https://doi.org/10.1007/s10518-016-9915-6.

Krawinkler, H. (1978). "Shear in beam-column joints in seismic design of steel frames." *Engineering Journal*, 15(3), 82–91.

Krawinkler, H. (1995). "Earthquake design and performance of steel structures." *Pacific Conference on Earthquake Engineering, PCEE 95*, Melbourne, Australia.

Krawinkler, H. (1996). "Cyclic loading histories for seismic experimentation on structural components." *Earthquake Spectra*, SAGE Publications Ltd STM, 12(1), 1–12. https://doi.org/10.1193/1.1585865.

Krawinkler, H. (2009). "Loading histories for cyclic tests in support of performance assessment of structural components." *Proc., 3rd Int. Conf. on Advances in Experimental Structural Engineering*, Pacific Earthquake Engineering Research Center, San Francisco.

Krawinkler, H., Akshay, G., Medina, R., and Luco, M. (2000). *Development of loading histories for testing of steel beam-to-column assemblies*. Rep. prepared for SAC Steel Project, Department of Civil and Environmental Engineering, Stanford University, Stanford, CA, USA.

Krawinkler, H., Bertero, V. V., and Popov, E. P. (1971). *Inelastic behavior of steel beam-to-column subassemblages*. Report No. 71/07, University of California, Berkeley, CA, USA.

Krawinkler, H., and Deierlein, G. G. (2013). "Challenges towards achieving earthquake resilience through performance-based earthquake engineering." *Chapter 1, Performance-Based Seismic Engineering: Vision for an Earthquake Resilient Society*, Geotechnical, Geological and Earthquake Engineering, M. Fischinger, ed., M. Fischinger, ed., Springer, New York. https://doi.org/10.1007/978-94-017-8875-5_1.

Krawinkler, H., and Mohasseb, S. (1987). "Effects of panel zone deformations on seismic response." *Journal of Constructional Steel Research*, 8, 233–250. https://doi.org/10.1016/0143-974X(87)90060-5.

Krawinkler, H., and Popov, E. P. (1982). "Seismic behavior of moment connections and joints." *Journal of Structural Engineering*, American Society of Civil Engineers, 108(2), 372–391.

Krawinkler, H., and Seneviratna, G. D. P. K. (1998). "Pros and cons of a pushover analysis of seismic performance evaluation." *Engineering Structures*, Innovations in Stability Concepts and Methods for Seismic Design in Structural Steel, 20(4), 452–464. https://doi.org/10.1016/S0141-0296(97)00092-8.

Krishnan, S., and Hall, J. F. (2006). "Modeling steel frame buildings in three dimensions. I: panel zone and plastic hinge beam elements." *Journal of Engineering Mechanics*, American Society of Civil Engineers, 132(4), 345–358. https://doi.org/10.1061/(ASCE)0733-9399(2006)132:4(345).

Landolfo, R., D'Aniello, M., Costanzo, S., Tartaglia, R., Demonceau, J.-F., Jaspart, J.-P., Stratan, A., Jakab, D., Dubina, D., Elghazouli, A., and Bompa, D. (2018). *EQUALJOINTS PLUS - Volume with information borchures for 4 seimsically qualified joints*. European Convention for Constructional Steelwork.

Lee, C. H., Jeon, S. W., Kim, J. H., and Uang, C. M. (2005a). "Effects of panel zone strength and beam web connection method on seismic performance of reduced beam section steel moment connections." *Journal of Structural Engineering*, American Society of Civil Engineers, 131(12), 1854–1865. https://doi.org/10.1061/(ASCE)0733-9445(2005)131:12(1854).

Lee, D., Cotton, S. C., Dexter, R. J., Hajjar, J. F., Ye, Y., and Ojard, S. D. (2002). *Column stiffener detailing and panel zone behavior of steel moment frame connections*. Report No. ST-01-3.2, Department of Civil Engineering, Institute of Technology University of Minnesota, Minneapolis, Minnesota, USA.

Lee, D., Cotton, S. C., Hajjar, J., Dexter, R. J., and Ye, Y. (2005b). "Cyclic behavior of steel moment-resisting connections reinforced by alternative column stiffener details I. connection performance and continuity plate detailing." *Engineering Journal*, 42(4), 189–214.

Lee, D., Cotton, S. C., Hajjar, J. F., Dexter, R. J., and Ye, Y. (2005c). "Cyclic behavior of steel moment-resisting connections reinforced by alternative column stiffener details II. panel zone behavior and doubler plate detailing." *Engineering Journal*, 42(4), 215–238.

Léger, P., Paultre, P., and Nuggihalli, R. (1991). “Elastic analysis of frames considering panel zones deformations.” *Computers & Structures*, 39(6), 689–697. https://doi.org/10.1016/0045-7949(91)90212-5.

Lemaitre, J., and Chaboche, J. L. (1990). *Mechanics of solid materials*. Cambridge, UK: Cambridge University Press.

Leon, R. T., Hajjar, J. F., and Gustafson, M. A. (1998). “Seismic response of composite moment-resisting connections. I: performance.” *Journal of Structural Engineering*, American Society of Civil Engineers, 124(8), 868–876. https://doi.org/10.1061/(ASCE)0733-9445(1998)124:8(868).

Li, X.-S., and Goto, Y. (1998). “A three-dimensional nonlinear seismic analysis of frames considering panel zone deformations.” *Journal of Structural Mechanics and Earthquake Engineering, JSCE*, 1998(605), 1–13. https://doi.org/10.2208/jscej.1998.605_1.

Li, Y., Song, R., and Van De Lindt, J. W. (2014). “Collapse fragility of steel structures subjected to earthquake mainshock-aftershock sequences.” *Journal of Structural Engineering*, American Society of Civil Engineers, 140(12), 04014095. https://doi.org/10.1061/(ASCE)ST.1943-541X.0001019.

Liew, J. Y. R., and Chen, W. F. (1995). “Analysis and design of steel frames considering panel joint deformations.” *Journal of Structural Engineering*, American Society of Civil Engineers, 121(10), 1531–1540. https://doi.org/10.1061/(ASCE)0733-9445(1995)121:10(1531).

Lignos, D. G., Hartloper, A. R., Elkady, A., Deierlein, G. G., and Hamburger, R. (2019). “Proposed updates to the ASCE 41 nonlinear modeling parameters for wide-flange steel columns in support of performance-based seismic engineering.” *Journal of Structural Engineering*, American Society of Civil Engineers, 145(9), 04019083. https://doi.org/10.1061/(ASCE)ST.1943-541X.0002353.

Lignos, D. G., Hikino, T., Matsuoka, Y., and Nakashima, M. (2013). “Collapse assessment of steel moment frames based on E-Defense full-scale shake table collapse tests.” *Journal of Structural Engineering*, American Society of Civil Engineers, 139(1), 120–132. https://doi.org/10.1061/(ASCE)ST.1943-541X.0000608.

Lignos, D. G., and Krawinkler, H. (2011). “Deterioration modeling of steel components in support of collapse prediction of steel moment frames under earthquake loading.” *Journal of Structural Engineering*, American Society of Civil Engineers, 137(11), 1291–1302. https://doi.org/10.1061/(ASCE)ST.1943-541X.0000376.

Lignos, D. G., and Krawinkler, H. (2012). *Sidesway collapse of deteriorating structural systems under seismic excitations*. Report No. 177, The John A. Blume Earthquake Engineering Research Center, Department of Civil Engineering, Stanford University, Stanford, CA, USA.

Lignos, D. G., and Krawinkler, H. (2013). “Development and utilization of structural component databases for performance-based earthquake engineering.” *Journal of Structural Engineering*, American Society of Civil Engineers, 139(8), 1382–1394. https://doi.org/10.1061/(ASCE)ST.1943-541X.0000646.

Lignos, D. G., Krawinkler, H., and Whittaker, A. S. (2011). “Prediction and validation of sidesway collapse of two scale models of a 4-story steel moment frame.” *Earthquake Engineering & Structural Dynamics*, 40(7), 807–825. https://doi.org/10.1002/eqe.1061.

Lin, K. C., Tsai, K. C., Kong, S. L., and Hsieh, S. H. (2000). “Effects of panel zone deformations on cyclic performance of welded moment connections.” *In Proc., 12th World Conference on Earthquake Engineering (WCEE)*, New Zealand National Society for Earthquake Engineering, Auckland, New Zealand.

Lu, L. W., Ricles, J. M., Mao, C., and Fisher, J. W. (2000). “Critical issues in achieving ductile behaviour of welded moment connections.” *Journal of Constructional Steel Research*, 55(1–3), 325–341. https://doi.org/10.1016/S0143-974X(99)00092-9.

Luco, N., and Cornell, C. A. (2000). “Effects of connection fractures on SMRF seismic drift demands.” *Journal of Structural Engineering*, American Society of Civil Engineers, 126(1), 127–136. https://doi.org/10.1061/(ASCE)0733-9445(2000)126:1(127).

Lui, E. M., and Chen, W.-F. (1986). “Frame analysis with panel zone deformation.” *International Journal of Solids and Structures*, 22(12), 1599–1627. https://doi.org/10.1016/0020-7683(86)90065-X.

Mahin, S. A. (1998). “Lessons from damage to steel buildings during the Northridge earthquake.” *Engineering Structures*, 20(4–6), 261–270. https://doi.org/10.1016/S0141-0296(97)00032-1.

Mahin, S., Malley, J., and Hamburger, R. (2002). “Overview of the FEMA/SAC program for reduction of earthquake hazards in steel moment frame structures.” *Journal of Constructional Steel Research*, North American Special Issue, 58(5), 511–528. https://doi.org/10.1016/S0143-974X(01)00088-8.

Maison, B. F., and Speicher, M. S. (2016). “Loading protocols for ASCE 41 backbone curves.” *Earthquake Spectra*, SAGE Publications Ltd STM, 32(4), 2513–2532. https://doi.org/10.1193/010816EQS007EP.

Malley, J. O. (1998). “SAC steel project: summary of phase 1 testing investigation results.” *Engineering Structures*, 20(4–6), 300–309. https://doi.org/10.1016/S0141-0296(97)00033-3.

Malley, J. O., and Frank, K. (2000). “Materials and fracture investigations in the FEMA/SAC Phase 2 steel project.” *12th World Conference on Earthquake Engineering*, Auckland, New Zealand, Paper No. 2544.

Mao, C., Ricles, J., Lu, L. W., and Fisher, J. (2001). “Effect of local details on ductility of welded moment connections.” *Journal of Structural Engineering*, American Society of Civil Engineers, 127(9), 1036–1044. https://doi.org/10.1061/(ASCE)0733-9445(2001)127:9(1036).

McKenna, F. (1997). “Object oriented finite element programming frameworks for analysis, algorithms and parallel computing.” Ph.D. Thesis, University of California, Berkeley, CA, USA.

Miki, C., Homma, K., and Tominaga, T. (2002). “High strength and high performance steels and their use in bridge structures.” *Journal of Constructional Steel Research*, 58(1), 3–20. https://doi.org/10.1016/S0143-974X(01)00028-1.

Miller, D. K. (1998). “Lessons learned from the Northridge earthquake.” *Engineering Structures*, 20(4), 249–260. https://doi.org/10.1016/S0141-0296(97)00031-X.

Miller, D. K. (2017). *AISC steel design guide 21 welded connections - a primer for engineers, 2nd edition*. Chicago (IL): American Institute of Steel Construction.

von Mises, R. (1913). “Mechanik der festen körper im plastisch-deformablen zustand.” *Nachrichten von der Gesellschaft der Wissenschaften zu Göttingen, Mathematisch-Physikalische Klasse*, 1, 582–592.

Molina Hutt, C., Hulsey, A. M., Kakoty, P., Deierlein, G. G., Eksir Monfared, A., Wen-Yi, Y., and Hooper, J. D. (2021). “Toward functional recovery performance in the seismic design of modern tall buildings.” *Earthquake Spectra*, SAGE Publications Ltd STM, 87552930211033620. https://doi.org/10.1177/87552930211033620.

Mulas, M. G. (2004). “A structural model for panel zones in non linear seismic analysis of steel moment-resisting frames.” *Engineering Structures*, 26(3), 363–380. https://doi.org/10.1016/j.engstruct.2003.10.009.

Myers, A. T., Deierlein, G. G., and Kanvinde, A. M. (2009). “Testing and probabilistic simulation of ductile fracture initiation in structural steel components and weldments.” Report No. 170, The John A. Blume Earthquake Engineering Research Center, Department of Civil Engineering, Stanford University, Stanford, CA, USA.

Nakashima, M., Matsumiya, T., Suita, K., and Zhou, F. (2007). “Full-scale test of composite frame under large cyclic loading.” *Journal of Structural Engineering*, American Society of Civil Engineers, 133(2), 297–304. https://doi.org/10.1061/(ASCE)0733-9445(2007)133:2(297).

Nikolaidou, V., Rogers, C. A., and Lignos, D. G. (2013). “Finite element modelling of welding procedures in high strength W-shapes.” *3rd Specialty Conference on Material Engineering & Applied Mechanics*, Montréal, Québec, 11.

NIST. (2010). *Evaluation of the FEMA P-695 methodology for quantification of building seismic performance factors*. National Institute of Standards and Technology, Gaithersburg, MD, USA.

NIST. (2015). *Assessment of first generation performance-based seismic design methods for new steel buildings, Volume 1: Special Moment Frames*. Technical Note (NIST TN) 1863-1, National Institute of Standards and Technology, Gaithersburg, MD, USA.

NSF. (2004). “Network for earthquake engineers simulation-special report.” Accessed February 13, 2020. https://www.nsf.gov/news/special_reports/nees/NetworkforEarthquakeEngineeringSimulation_SR.pdf.

Ozkula, G., Harris, J., and Uang, C.-M. (2017). “Observations from cyclic tests on deep, wide-flange beam-columns.” *Engineering Journal*, 54(1), 45–60.

Paret, T. F. (2000a). “The W1 Issue. I: Extent of weld fracturing during Northridge earthquake.” *Journal of Structural Engineering*, American Society of Civil Engineers, 126(1), 10–18. https://doi.org/10.1061/(ASCE)0733-9445(2000)126:1(10).

Paret, T. F. (2000b). “The W1 Issue. II: UT reliability for inspection of T-joints with backing.” *Journal of Structural Engineering*, American Society of Civil Engineers, 126(1), 19–23. https://doi.org/10.1061/(ASCE)0733-9445(2000)126:1(19).

Parks, D. M. (1977). “The virtual crack extension method for nonlinear material behavior.” *Computer Methods in Applied Mechanics and Engineering*, 12(3), 353–364. https://doi.org/10.1016/0045-7825(77)90023-8.

PEER/ATC. (2010). *Modeling and acceptance criteria for seismic design and analysis of tall buildings*. PEER/ATC 72–1, Prepared for Pacific Earthquake Engineering Research Center (PEER) by Applied Technology Council (ATC): Redwood City, CA, USA.

Popov, E. P., Amin, N. R., Louie, J. J. C., and Stephen, R. M. (1985). “Cyclic behavior of large beam-column assemblies.” *Earthquake Spectra*, 1(2), 203–238. https://doi.org/10.1193/1.1585263.

Popov, E. P., Blondet, M., Stepanov, L., and Stojadinović, B. (1996). *Full-scale beam-column connection tests-Experimental investigations of beam-column subassemblages*. Report No. SAC-96/01, Part 2, Applied Technology Council (ATC), 555 Twin Dolphin Dr. Redwood City, CA, USA.

Popov, E. P., and Pinkney, R. B. (1969). “Cyclic yield reversal in steel building connections.” *Journal of Structural Division*, American Society of Civil Engineers, 95(3), 327–353.

Popov, E. P., Yang, T.-S., and Chang, S.-P. (1998). “Design of steel MRF connections before and after 1994 Northridge earthquake.” *Engineering Structures*, 20(12), 1030–1038. https://doi.org/10.1016/S0141-0296(97)00200-9.

Porter, K. A. (2021). “Should we build better? The case for resilient earthquake design in the United States.” *Earthquake Spectra*, SAGE Publications Ltd STM, 37(1), 523–544. https://doi.org/10.1177/8755293020944186.

Qi, L., Leon, R. T., Eatherton, M. R., and Paquette, J. L. (2020). “Parametric investigation on the design of RBS moment connections with jumbo beams and columns.” *Journal of Constructional Steel Research*, 177(1), 106436. https://doi.org/10.1016/j.jcsr.2020.106436.

Qi, L., Paquette, J., Eatherton, M., Leon, R., Bogdan, T., Popa, N., and Nunez, E. (2018). “Analysis of fracture behavior of large steel beam-column connections.” *In Proc., 12th International Conference on Advances in Steel-Concrete Composite Structures (ASCCS)*, Universitat Politècnica València. https://doi.org/10.4995/ASCCS2018.2018.7122.

Rahiminia, F., and Namba, H. (2013). “Joint panel in steel moment connections, part 1: experimental tests results.” *Journal of Constructional Steel Research*, 89, 272–283. https://doi.org/10.1016/j.jcsr.2013.07.002.

Ramirez, C. M., and Miranda, E. (2012). “Significance of residual drifts in building earthquake loss estimation.” *Earthquake Engineering & Structural Dynamics*, 41(11), 1477–1493. https://doi.org/10.1002/eqe.2217.

Reynolds, M., and Uang, C.-M. (2022). “Economical weld details and design for continuity and doubler plates in steel special moment frames.” *Journal of Structural Engineering*, American Society of Civil Engineers, 148(1), 04021246. https://doi.org/10.1061/(ASCE)ST.1943-541X.0003203.

Rice, R. H. (1968). “A path independent integral and the approximate analysis of strain concentration by notches and cracks.” *Journal of Applied Mechanics*, 35(2), 379–386.

Richard, R. M. (2003). “Discussion of ‘General issues influencing connection performance’ by Charles W. Roeder.” *Journal of Structural Engineering*, American Society of Civil Engineers, 129(6), 838–840. https://doi.org/10.1061/(ASCE)0733-9445(2003)129:6(838.2).

Ricles, J. M., Fisher, J. W., Lu, L.-W., and Kaufmann, E. J. (2002a). “Development of improved welded moment connections for earthquake-resistant design.” *Journal of Constructional Steel Research*, 58(5–8), 565–604. https://doi.org/10.1016/S0143-974X(01)00095-5.

Ricles, J. M., Mao, C., Lu, L. W., and Fisher, J. W. (2003). “Ductile details for welded unreinforced moment connections subject to inelastic cyclic loading.” *Engineering Structures*, 25(5), 667–680. https://doi.org/10.1016/S0141-0296(02)00176-1.

Ricles, J. M., Mao, C., Lu, L.-W., and Fisher, J. W. (2000). *Development and evaluation of improved details for ductile welded unreinforced flange connections*. SAC Background Documents, Report No. SAC/BD-00/24, SAC Joint Venture, Sacramento, CA, USA.

Ricles, J. M., Mao, C., Lu, L.-W., and Fisher, J. W. (2002b). "Inelastic cyclic testing of welded unreinforced moment connections." *Journal of Structural Engineering*, American Society of Civil Engineers, 128(4), 429–440. https://doi.org/10.1061/(ASCE)0733-9445(2002)128:4(429).

Ricles, J. M., Zhang, X., Fisher, J. W., and Lu, L.-W. (2004a). "Seismic performance of deep column-to-beam welded reduced beam section moment connections." *Connections in Steel Structures V*, Amsterdam.

Ricles, J. M., Zhang, X., Lu, L.-W., and Fisher, J. W. (2004b). *Development of seismic guidelines for deep-column steel moment connections*. ATLSS Report No. 04-13, Lehigh University, Bethlehem, PA, USA.

Sato, A., Newell, J., and Uang, C.-M. (2007). *Cyclic testing of bolted flange plate steel moment connections for special moment frames*. Report No. SSRP-07/10, University of California, San Diego, CA, USA.

Schneider, S. P., and Amidi, A. (1998). "Seismic behavior of steel frames with deformable panel zones." *Journal of Structural Engineering*, American Society of Civil Engineers, 124(1), 35–42. https://doi.org/10.1061/(ASCE)0733-9445(1998)124:1(35).

Schneider, S. P., and Teeraparbwong, I. (2000). *Bolted flange plate connections*. SAC Background Documents, Report No. SAC/BD-00/05, SAC Joint Venture, Sacramento, CA, USA.

Shapiro, S. S., and Francia, R. S. (1972). "An approximate analysis of variance test for normality." *Journal of the American Statistical Association*, 67(337), 215–216. https://doi.org/10.1080/01621459.1972.10481232.

Shapiro, S. S., and Wilk, M. B. (1965). "An analysis of variance test for normality (complete samples)." *Biometrika*, 52(3–4), 591–611. https://doi.org/10.1093/biomet/52.3-4.591.

Shaw, S. M., Stillmaker, K., and Kanvinde, A. M. (2015). "Seismic response of partial-joint-penetration welded column splices in moment-resisting frames." *Engineering Journal*, 52(2), 87–108.

Shin, S. (2017). "Experimental and analytical investigation of panel zone behavior in steel moment frames." PhD Thesis, Department of Civil, Architectural and Environmental Engineering, University of Texas at Austin, TX, USA.

Shin, S., and Engelhardt, M. D. (2013a). "Cyclic performance of deep column moment frames with weak panel zones." *Advances in Structural Engineering and Mechanics (ASEM13)*, Jeju, Korea.

Shin, S., and Engelhardt, M. D. (2013b). "Experimental study on panel zone behavior in steel moment resisting frames." *In Proc., 7th International Symposium on Steel Structures*, Jeju, Korea: Korean Society of Steel Construction.

Shirsat, P. S., and Engelhardt, M. D. (2012). "Preliminary analysis of doubler plate attachment details for steel moment frames." *15th WCEE*, Lisboa, Portugal: Sociedade Portuguesa de Engenharia Sismica.

Shokrabadi, M., Burton, H. V., and Stewart, J. P. (2018). "Impact of sequential ground motion pairing on mainshock-aftershock structural response and collapse performance assessment." *Journal of Structural Engineering*, American Society of Civil Engineers, 144(10), 04018177. https://doi.org/10.1061/(ASCE)ST.1943-541X.0002170.

Simha, N. K., Fischer, F. D., Kolednik, O., and Chen, C. R. (2003). "Inhomogeneity effects on the crack driving force in elastic and elastic–plastic materials." *Journal of the Mechanics and Physics of Solids*, 51(1), 209–240. https://doi.org/10.1016/S0022-5096(02)00025-X.

SIMULIA. (2019). *ABAQUS user's manual. Version 6.19*. Providence, RI: SIMULIA.

Skiadopoulos, A., Elkady, A., and Lignos, D. G. (2021). "Proposed panel zone model for seismic design of steel moment-resisting frames." *Journal of Structural Engineering*, American Society of Civil Engineers, 147(4), 04021006. https://doi.org/10.1061/(ASCE)ST.1943-541X.0002935.

Skiadopoulos, A., and Lignos, D. G. (2021). "Development of inelastic panel zone database." *Journal of Structural Engineering*, American Society of Civil Engineers, 147(4), 04721001. https://doi.org/10.1061/(ASCE)ST.1943-541X.0002957.

Skiadopoulos, A., and Lignos, D. G. (2022a). "Proposed backing bar detail in welded beam-to-column connections for seismic applications (accepted)." *Journal of Structural Engineering*, American Society of Civil Engineers. https://doi.org/10.1061/(ASCE)ST.1943-541X.0003374.

Skiadopoulos, A., and Lignos, D. G. (2022b). "Seismic demands of steel special moment frames with inelastic beam-to-column web panel zones (accepted)." *Earthquake Engineering & Structural Dynamics*. https://doi.org/10.1002/eqe.3629.

Slutter, R. G. (1981). *Tests of panel zone behavior in beam-column connections*. Report No. 200.81.403.1, Lehigh University, Bethlehem, PA, USA.

Smelser, R. E., and Curtin, M. E. (1977). "On the J-integral for Bi-material bodies." *International Journal of Fracture*, Vol. 13, 382–384.

Smirnov, H. (1939). "Sur les ecarts de la courbe de distribution empirique." *Recueil Mathematique*, 48(1), 3–26.

Soliman, A. A., Ibrahim, O. A., and Ibrahim, A. M. (2018). "Effect of panel zone strength ratio on reduced beam section steel moment frame connections." *Alexandria Engineering Journal*, 57(4), 3523–3533. https://doi.org/10.1016/j.aej.2018.07.017.

Song, J., and Ellingwood, B. R. (1999a). "Seismic reliability of special moment steel frames with welded connections: I." *Journal of Structural Engineering*, American Society of Civil Engineers, 125(4), 357–371. https://doi.org/10.1061/(ASCE)0733-9445(1999)125:4(357).

Song, J., and Ellingwood, B. R. (1999b). "Seismic reliability of special moment steel frames with welded connections: II." *Journal of Structural Engineering*, American Society of Civil Engineers, 125(4), 372–384. https://doi.org/10.1061/(ASCE)0733-9445(1999)125:4(372).

Song, R., Li, Y., and van de Lindt, J. W. (2014). "Loss estimation of a code-conforming steel building to mainshock-aftershock sequences." *Tenth U.S. National Conference on Earthquake Engineering*, Anchorage, Alaska: Frontiers of Earthquake Engineering.

Sousa, A., and Lignos, D. G. (2018). *On the inverse problem of classic nonlinear plasticity models*. Technical Report No. 231968, Ecole Polytechnique Federale de Lausanne, Lausanne.

Stillmaker, K., Kanvinde, A., and Galasso, C. (2016). "Fracture mechanics-based design of column splices with partial joint penetration welds." *Journal of Structural Engineering*, American Society of Civil Engineers, 142(2), 04015115. https://doi.org/10.1061/(ASCE)ST.1943-541X.0001380.

Stojadinović, B., Goel, S. C., Lee, K.-H., Margarian, A. G., and Choi, J.-H. (2000). "Parametric tests on unreinforced steel moment connections." *Journal of Structural Engineering*, American Society of Civil Engineers, 126(1), 40–49. https://doi.org/10.1061/(ASCE)0733-9445(2000)126:1(40).

Suita, K., Yamada, S., Tada, M., Kasai, K., Matsuoka, Y., and Shimada, Y. (2008). "Collapse experiment on 4-story steel moment frame: Part 2 detail of collapse behavior." *Proceedings of the 14th world conference on earthquake engineering*, Beijing, China, Vol. 1217: International Association for Earthquake Engineering.

Suzuki, Y., and Lignos, D. G. (2020). "Development of collapse-consistent loading protocols for experimental testing of steel columns." *Earthquake Engineering & Structural Dynamics*, 49(2), 114–131. https://doi.org/10.1002/eqe.3225.

Suzuki, Y., and Lignos, D. G. (2021). "Experimental evaluation of steel columns under seismic hazard-consistent collapse loading protocols." *Journal of Structural Engineering*, American Society of Civil Engineers, 147(4), 04021020. https://doi.org/10.1061/(ASCE)ST.1943-541X.0002963.

Terzic, V., Villanueva, P. K., Saldana, D., and Yoo, D. Y. (2021). "Framework for modelling post-earthquake functional recovery of buildings." *Engineering Structures*, 246, 113074. https://doi.org/10.1016/j.engstruct.2021.113074.

Tremblay, R., Tchebotarev, N., and Filiatrault, A. (1997). "Seismic performance of RBS connections for steel moment resisting frames: Influence of loading rate and floor slab." *Proceedings STESSA '97*, Kyoto, Japan: Salerno, Italy: Edizioni.

Tremblay, R., Timler, P., Bruneau, M., and Filiatrault, A. (1995). "Performance of steel structures during the 1994 Northridge earthquake." *Canadian Journal of Civil Engineering*, 22, 338–360.

Tsai, K. C., and Chen, W. Z. (2000). "Seismic responses of steel reduced beam section to weak panel zone moment joints." *In Proc., 3rd International Conference on Behavior of Steel Structures in Seismic Areas (STESSA)*, Montreal, Canada, 279–286.

Tsai, K. C., and Popov, E. P. (1988). *Steel beam-column joints in seismic moment resisting frames*. Report No. 88-19, University of California, Berkeley, CA, USA.

Tsai, K., and Popov, E. P. (1990). "Seismic panel zone design effect on elastic story drift in steel frames." *Journal of Structural Engineering*, American Society of Civil Engineers, 116(12), 3285–3301. https://doi.org/10.1061/(ASCE)0733-9445(1990)116:12(3285).

Uang, C.-M., and Bruneau, M. (2018). “State-of-the-art review on seismic design of steel structures.” *Journal of Structural Engineering,* American Society of Civil Engineers, 144(4), 03118002. https://doi.org/10.1061/(ASCE)ST.1943-541X.0001973.

Uang, C.-M., Yu, Q.-S. “Kent,” Noel, S., and Gross, J. (2000). “Cyclic testing of steel moment connections rehabilitated with RBS or welded haunch.” *Journal of Structural Engineering*, American Society of Civil Engineers, 126(1), 57–68. https://doi.org/10.1061/(ASCE)0733-9445(2000)126:1(57).

USGS. (2014). “Hazard curve application.” *United States Geological Survey, U.S. Department of the Interior*, United States Geological Survey, U.S. Department of the Interior: http://geohazards.usgs.gov/hazardtool/application.php.

Vamvatsikos, D., and Cornell, C. A. (2002). “Incremental dynamic analysis.” *Earthquake Engineering & Structural Dynamics*, 31(3), 491–514. https://doi.org/10.1002/eqe.141.

Wang, SJ. (1988). “Seismic response of steel building frames with inelastic joint deformation.” PhD Thesis, Department of Civil Engineering, Lehigh University, Bethlehem, PA, USA.

Wang, Y., Zhou, H., Shi, Y., and Chen, H. (2010). “Fracture behavior analyses of welded beam-to-column connections based on elastic and inelastic fracture mechanics.” *International Journal of Steel Structures*, 10(3), 253–265. https://doi.org/10.1007/BF03215835.

Wells, A. A. (1961). “Unstable crack propagation in metals: cleavage and fast fracture.” *Proceedings of the crack propagation symposium*, Vol. 1, Paper 84, Cranfield, UK: Cranfield [England] : College of Aeronautics.

Whittaker, A., Gilani, A., and Bertero, V. (1998). “Evaluation of pre-Northridge steel moment-resisting frame joints.” *The Structural Design of Tall Buildings*, 7(4), 263–283. https://doi.org/10.1002/(SICI)1099-1794(199812)7:4<263::AID-TAL118>3.0.CO;2-B.

Yang, T.-S., and Popov, E. P. (1995). *Behavior of pre-Northridge moment resisting steel connections*. Report No. UCB/EERC-95/08, Earthquake Engineering Research Center, University of California, Berkeley, CA, USA.

Yang, Y., Wang, Y., Yang, F., and An, Q. (2019). “Influence of weld details on fracture behavior of connections using high-strength steel.” *Journal of Constructional Steel Research*, 153, 578–587. https://doi.org/10.1016/j.jcsr.2018.11.004.

Young, B. W. (1971). “Residual stresses in hot-rolled members.” *Proc., Int. Colloquium on Column Strength, Int. Association for Bridge and Structural Engineering*, Zurich, Switzerland: International Association for Bridge and Structural Engineering, 25–38.

Youssef, N. F. G., Bonowitz, D., and Gross, J. L. (1995). *A survey of steel moment-resisting frame buildings affected by the 1994 Northridge earthquake*. National Institute of Standards and Technology, Gaithersburg, MD. https://doi.org/10.6028/NIST.IR.5625.

Yu, Q. S., Gilton, C., and Uang, C.-M. (2000). *Cyclic response of RBS moment connections: loading sequence and lateral bracing effects*. SAC Background Documents, Report No. SAC/BD-00/22, SAC Joint Venture, Sacramento, CA, USA.

Zareian, F., Krawinkler, H., Ibarra, L., and Lignos, D. (2009). “Basic concepts and performance measures in prediction of collapse of buildings under earthquake ground motions.” *The Structural Design of Tall and Special Buildings*, 19(1–2), 167–181. https://doi.org/10.1002/tal.546.

Zareian, F., and Medina, R. A. (2010). “A practical method for proper modeling of structural damping in inelastic plane structural systems.” *Computers & Structures,* 88(1), 45–53. https://doi.org/10.1016/j.compstruc.2009.08.001.

Zhang, X., and Ricles, J. M. (2006). “Experimental evaluation of reduced beam section connections to deep columns.” *Journal of Structural Engineering*, American Society of Civil Engineers, 132(3), 346–357. https://doi.org/10.1061/(ASCE)0733-9445(2006)132:3(346).

Skiadopoulos Andronikos | Curriculum Vitae

PERSONAL INFORMATION

Date of birth	29.11.1993
Nationality	Greek
Phone	+41 78 751 02 25
E-mail	andronikos.skiadopoulos@epfl.ch
Address	Avenue de la Gare 65, CH-1022, Chavannes, Switzerland

EDUCATION

01.2018-04.2022 **PhD, Civil Engineering**
École Polytechnique Fédérale de Lausanne (EPFL), Switzerland

- Thesis: Welded Moment Connections with Highly Dissipative Panel Zones for Enhanced Seismic Performance of Steel Moment Frames
- Supervisor: Prof. Dimitrios G. Lignos
- PhD defense date: 04.04.2022

09.2011-10.2016 **Diploma, M.Eng Civil Engineering (5-year joint degree)**
National Technical University of Athens (NTUA), Greece

- Thesis: Comparison of Alternative Methods for the Analysis and Design of Steel Frames (Grade: 10/10)
- Supervisor: Prof. Charis J. Gantes
- Specialization: Structural Engineering
- GPA: **9.41/10** (3rd of the year)

TEACHING

Teaching Assistant

02.2019/2020-07.2019/2020 **CIVIL-435, Advanced Steel Design**
École Polytechnique Fédérale de Lausanne (EPFL), Switzerland

- Graduate course; advanced topics in seismic design of steel structures

Supervision of Junior Researchers

09.2021-01.2022 **Master Thesis Advisor**
École Polytechnique Fédérale de Lausanne (EPFL), Switzerland

- Student: Schipani Carmine
- Thesis: Development of a Python-Based Simulation Tools Library for Composite Steel Concrete Structures

02.2021-07.2021 **Master Thesis Advisor**
École Polytechnique Fédérale de Lausanne (EPFL), Switzerland

- Student: Beqiraj Meriton
- Thesis: Finite Element Investigation of Stability Bracing Force Demands of Steel Moment Resisting Frame Columns under Cyclic Loading

09.2020-01.2021 **Master Thesis Advisor**
École Polytechnique Fédérale de Lausanne (EPFL), Switzerland

- Student: Falconi Gabriele
- Thesis: Influence of Residual Stresses on the Buckling Capacity of Axially Loaded Steel Columns

02.2019-07.2022 **Master Semester Projects**
École Polytechnique Fédérale de Lausanne (EPFL), Switzerland

- Fundamental Understanding of Structural Stability Using Educational Tools (1)
- Design of a Typical Earthquake Resilient Two-Story Steel Building (7)

(the parenthesis number indicates the number of projects supervised per subject)

Outreach Activities

11.2019/2021 **High-School Student Thematic Day**
École Polytechnique Fédérale de Lausanne (EPFL), Switzerland

- Annual high-school student thematic day to engage students in Civil Engineering
- Hands-on activities involving the design of a building resilient in gravity and seismic loading

PROFESSIONAL AND VOLUNTEERING EXPERIENCE

11.2016-08.2017 **Engineering Arm of Hellenic Army, Greece**

- Supervision of construction sites of refugee camps

06.2015-09.2015 **Engineering Intern**
HOCHTIEF Polska S.A., Warsaw

- Supervision of the following contruction cites: *Residential Houses JK51* and *The Business Garden Warszawa Office Complex*

11.2012-01.2018 **Founding Member and Website Administrator of the CEE portal of NTUA**
www.mqn.gr, Greece

- Organized events to promote the CEE portal and ensure funding
- Counting nearly 150.000 posts, 5.000 topics, 10.000 files and 10.000 users

HONORS AND AWARDS

Raymond C. Reese Research Prize, 2022
Awarded by the *American Society of Civil Engineers (ASCE)*
For the paper "Proposed Panel Zone Model for Seismic Design of Steel Moment-Resisting Frames"

17WCEE Early Career and Student Award, 2021
17th World Conference on Earthquake Engineering, Sendai, Japan, 2020-21
For the paper "Improved Panel Zone Model for Seismic Design of Steel Moment Resisting Frames"

Leventis Foundation Scholarship, 2017
Awarded by *A.G. Leventis Foundation*, Athens, Greece

Limmat Foundation Prize for Academic Excellence (3rd among all graduating students), 2016
Awarded by *Limmat Foundation*, Zürich, Switzerland

Scholarship for Extraordinary Achievement (Highest GPA), 2014-15
Awarded by *Sarafis Foundation*, N.T.U. Athens

Scholarship for Highest Nationwide University Entrance Grade in High School, 2011
Awarded by *Eurobank EFG*, "The big moment for education"

National Mathematics Olympiad Archimedes, 2011
Merits Awarded by the *Hellenic Mathematical Society* (H.M.S.)

Scholarship for Highest Grade in Dodecanese Islands among all High Schools, 2010
Awarded by *Lions*, Rhodes, Greece

JOURNAL PUBLICATIONS

J.1. **Skiadopoulos, A.**, and Lignos, D. G. (2022). “Seismic demands of steel moment resisting frames with inelastic beam-to-column web panel zones (accepted).” *Earthquake Engineering & Structural Dynamics*, Wiley. DOI: https://doi.org/10.1002/eqe.3629.

J.2. **Skiadopoulos, A.**, and Lignos, D. G. (2022). “Proposed backing bar detail in welded beam-to-column connections for seismic applications (accepted).” *Journal of Structural Engineering*, American Society of Civil Engineers. DOI: https://doi.org/10.1061/(ASCE)ST.1943-541X.0003374.

J.3. **Skiadopoulos, A.**, Elkady, A., and Lignos, D. G. (2021). “Proposed panel zone model for seismic design of steel moment-resisting frames.” *Journal of Structural Engineering*, American Society of Civil Engineers, 147(4), 04021006. DOI: https://doi.org/10.1061/(ASCE)ST.1943-541X.0002935.

J.4. **Skiadopoulos, A.**, and Lignos, D. G. (2021). “Development of inelastic panel zone database.” *Journal of Structural Engineering*, American Society of Civil Engineers, 147(4), 04721001. DOI: https://doi.org/10.1061/(ASCE)ST.1943-541X.0002957.

CONFERENCE PUBLICATIONS

C.1. **Skiadopoulos, A.**, and Lignos, D. G. (2022). “Seismic stability of steel moment resisting frames with inelastic panel zones.” 12th NCEE, Salt Lake City, UT, USA: Earthquake Engineering Re-search Institute.

C.2. **Skiadopoulos, A.**, Elkady, A., and Lignos, D. G. (2021). “Improved Panel Zone Model for Seismic Design of Steel Moment Resisting Frames.” 17th WCEE, Sendai, Japan: Japan Association for Earthquake Engineering.

SCIENTIFIC REVIEWS

(Publons: https ://publons.com/researcher/4834847/andronikos-skiadopoulos/)

- Eartquake Spectra

SKILLS

Languages

- Greek (Native)
- English (Fluent, Michigan proficiency certificate, TOEFL Score: 102/120)
- German (Conventional, Goethe-Zertifikat B1)
- French (Elementary proficiency, A1-A2)

Computer Skills

- MATLAB, Python, Fortran
- AutoCAD, OpenSees, Abaqus, SAP2000, ADINA, SOFiSTiK AG, Autodesk Fusion 360, Seismostruct, Plaxis